

2

# ANNUAL REPORT

University Research Initiative

Contract No.: N00014-92-J-1808

March 1992 - April 1993

AD-A266 398

DTIC  
ELECTE  
JUN 21 1993  
S A D

## The Processing and Mechanical Properties of High Temperature/High Performance Composites

by

A.G. Evans & F. Leckie  
University of California,  
Santa Barbara

University of Pennsylvania  
Harvard University  
Washington State University  
Carnegie Mellon University  
University of Virginia

This document has been approved  
for public release and sale; its  
distribution is unlimited.

93-13752

|||||

Book 5 of 5:

PROCESSING AND MISCELLANEOUS PROPERTIES

93 6 17 087

# SUMMARY OF TABLE OF CONTENTS

EXECUTIVE SUMMARY

BOOK 1: CONSTITUENT PROPERTIES OF COMPOSITES

BOOK 2: CONSTITUENT PROPERTIES AND MACROSCOPIC  
PERFORMANCE: CMCs

BOOK 3: CONSTITUENT PROPERTIES AND MACROSCOPIC  
PERFORMANCE: MMCs

BOOK 4: CONSTITUTIVE LAWS AND DESIGN

BOOK 5: PROCESSING AND MISCELLANEOUS PROPERTIES

DTIC QUALITY INSPECTED B

Accession For	
NTIS CR&I	<input checked="" type="checkbox"/>
DTIC TAB	<input type="checkbox"/>
Unannounced	<input type="checkbox"/>
Justification	
By per A216146	
Date	
Date	
A-1	

BOOK 5

PROCESSING AND MISCELLANEOUS PROPERTIES

- |     |   |  |
|-----|---|--|
| 69. | Computer Aided Manufacturing Through Selective Material Deposition  | F.B. Prinz<br>L.E. Weiss<br>M. Turk                        |
| 70. | Environmentally Compatible Double Coating Concepts for Sapphire Fiber-Reinforced $\gamma$ -TiAl             | T.J. Mackin<br>J. Yang<br>C.G. Levi<br>A.G. Evans          |
| 71. | Modeling the Fracture of Fibers During Metal Matrix Composite Consolidation                                 | D.M. Elzey<br>H.N.G. Wadley                                |
| 72. | The Effect of Processing on the Interface Structure/Property Relationship in a Ti-24Al-11Nb (at%) Composite | Cantonwine thesis<br>(part of Wadley contribution)         |
| 73. | The Evolution of Metastable $B_2$ Borides in a Ti-Al-B Alloy  | M. De Graef<br>J.P.A. Löfvander<br>McCullough<br>C.G. Levi |
| 74. | Measurement of Residual Stresses in Sapphire Fiber Composites Using Optical Fluorescence                    | Q. Ma<br>D.R. Clarke                                       |
| 75. | Compressive Failure of Fiber Composites   | B. Budiansky<br>N.A. Fleck                                 |
| 76. | Compressive Failure of Fiber Composites: The Roles of Multi-Axial Loading and Creep                         | W.S. Slaughter<br>N.A. Fleck<br>B. Budiansky               |
| 77. | Prediction of Kink Width in Fiber Composites  | N.A. Fleck<br>L. Deng<br>B. Budiansky                      |
| 78. | Mechanical Properties of Partially Dense Alumina Produced from Powder Compacts                              | D.C.C. Lam<br>F.F. Lange<br>A.G. Evans                     |

- |     |   |   |
|-----|---|---|
| 79. | Cracking Due to Localized Hot Shock                                     | V. Tvergaard<br>Z.C. Xia<br>J.W. Hutchinson |
| 80. | The Physics and Mechanics of Brittle<br>Matrix Composites               | A.G. Evans<br>F.W. Zok                      |
| 81. | <i>In Situ</i> Growth of SiC in MoSi <sub>2</sub> by Melt<br>Processing | D.J. Tilly<br>J.P.A. Löfvander<br>C.G. Levi |



## EXECUTIVE SUMMARY

### 1. GENERAL STRATEGY

The overall program embraces property profiles, manufacturing, design and sensor development (Fig. 1) consistent with a concurrent engineering philosophy. For this purpose, the program has created networks with the other composites activities. *Manufacturing* research on MMCs is strongly coupled with the 3M Model Factory and with the DARPA consolidation team. Major links with Corning and SEP are being established for CMC manufacturing. *Design Team* activities are coordinated by exchange visits, in February/March, to Pratt and Whitney, General Electric, McDonnell Douglas and Corning. Other visits and exchanges are being discussed. These visits serve both as a critique of the research plan and as a means of disseminating the knowledge acquired in 1992.

The program strategy concerned with design attempts to provide a balance of effort between *properties* and *design* by having studies of mechanisms and property profiles, which intersect with a focused activity devoted to design problems (Fig. 2). The latter includes two foci, one on MMCs and one on CMCs. Each focus reflects differences in the property emphases required for design. The intersections with the mechanism studies ensure that commonalities in behavior continue to be identified, and also facilitate the efficient transfer of models between MMCs and CMCs.

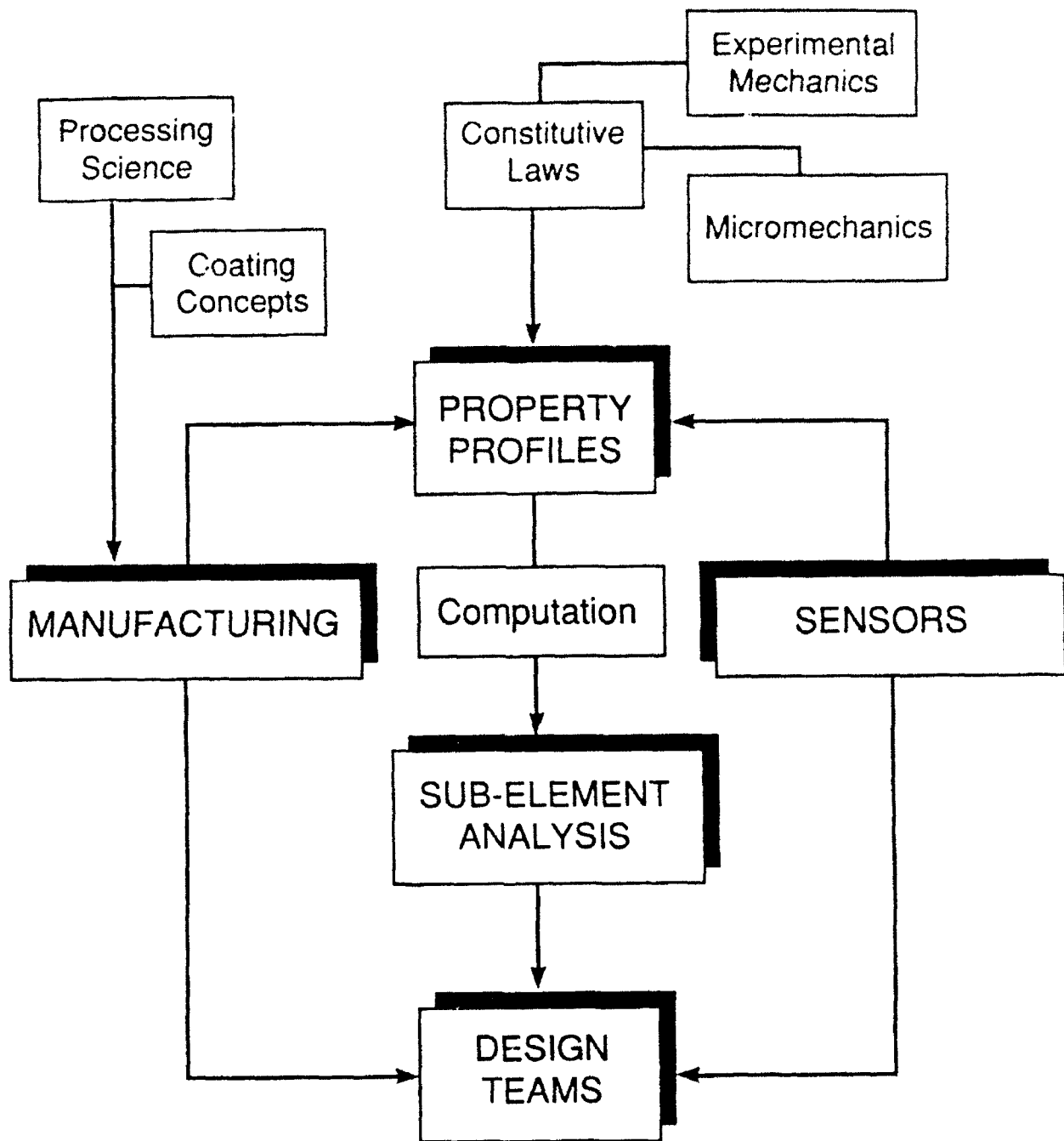


Fig. 1 The Concurrent Engineering Approach

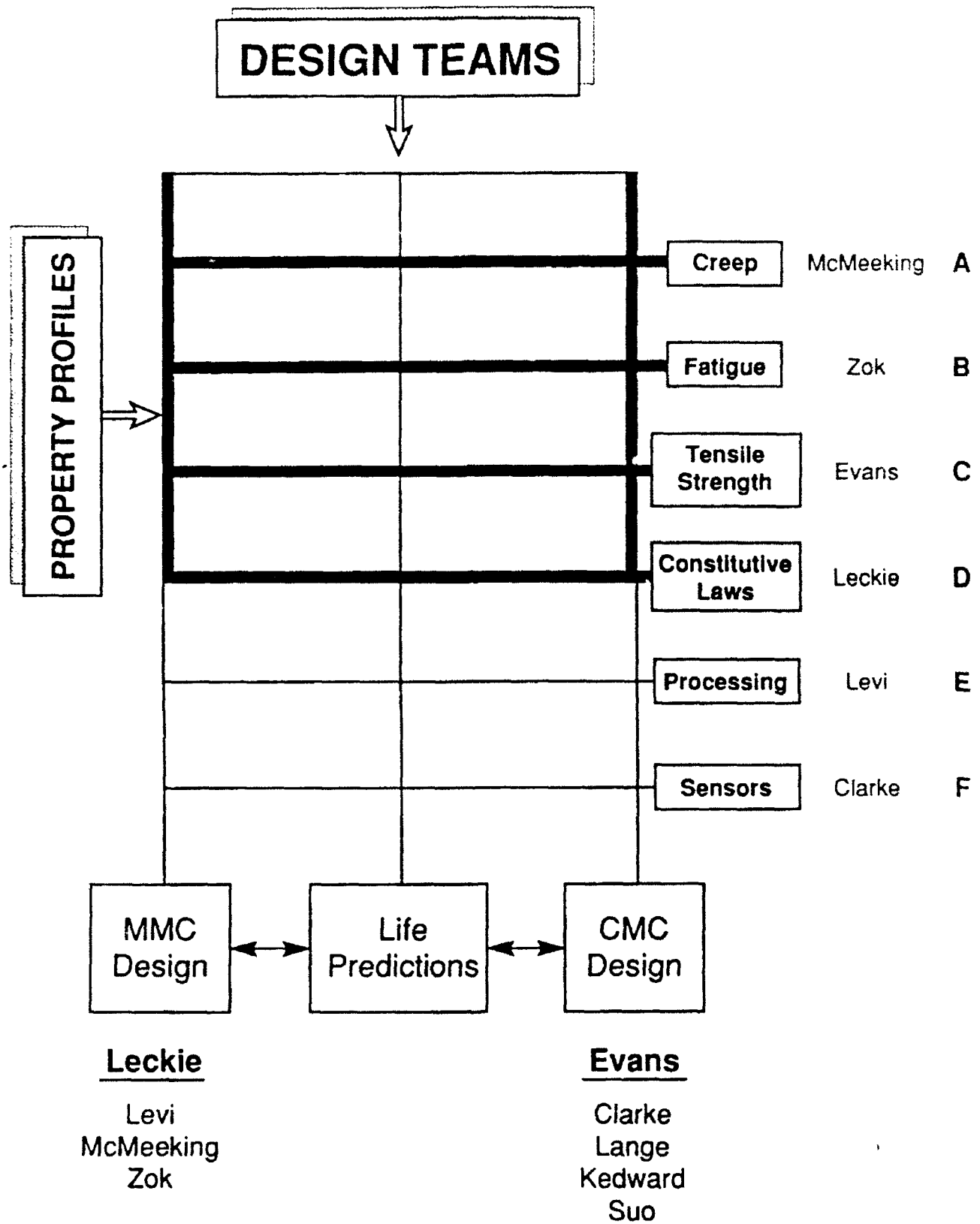


Fig. 2  
Matrix Structure of Program

## **2. PROPERTY PROFILES**

Each research activity concerned with properties begins with experiments that identify the principal property-controlling phenomena. Models are then developed that relate the physical response to constituent properties. These models, when validated, provide the constitutive laws required for calculating stress redistribution, failure and damage progression. They also provide a solid physics and mechanics understanding, which can be used to judge the effectiveness of the simplified procedures needed for design purposes.

### **2.1 Fatigue**

Studies of the propagation of dominant mode I fatigue cracks from notches in MMCs, including the role of fiber bridging and fiber failure, have been comprehensively addressed (Zok, McMeeking). Software programs that include these effects have been developed. These are being transferred to Pratt and Whitney and KAMAN Sciences. The effects of thermal cycling on crack growth in MMCs have also been modelled (McMeeking). The results highlight the opposing effects of cycling on matrix crack growth and fiber failure (the fatigue threshold), when thermal cycles are superposed onto load cycles. Notably, matrix crack growth is enhanced by out-of-phase thermomechanical cycling, but fiber failure is suppressed (and vice versa for in-phase cycling). Experimental studies that examine these predictions are planned (Zok).

Studies have also been conducted on systems that exhibit *multiple* matrix cracking (Zok). The tensile stress-strain behavior of composites containing such cracks is analogous to the behavior of unidirectional CMCs

under monotonic tensile loading. As a result, models developed to describe the tensile response of the CMCs have found utility in describing the MMCs. However, two important differences in the two classes of composite have been identified and are presently being addressed. The first deals with the nature of the crack patterns. In the CMCs, the cracks are more or less uniformly spaced and generally span across the entire composite section. In contrast, the MMCs exhibit a broader distribution of crack sizes, many of which are short compared with the specimen dimensions. Methodologies for measurement and interpretation of crack densities in MMCs are being developed. The second problem deals with degradation in the interfacial sliding properties with cyclic sliding in the MMCs. Such degradation is presently being studied using fiber push-out tests in fatigued specimens.

Thermal fatigue studies on MMCs subject to transverse loading have been performed and have established the conditions that allow shakedown (Leckie). The shakedown range is found to be strongly influenced by the extent of matrix creep, which defines a temperature limitation on the use of the material. The eventual outcome of this activity would be the specification of parameters that ensure shakedown and avoid ratcheting.

The next challenge for MMCs concern the quantification of transitions in fatigue behavior, especially those found at higher temperatures. These include multiple matrix cracking and shear band formation. Experimental studies are in progress which will be used to establish a mechanism map. The map, when developed, would explicitly identify the transitions (Zok). The analogous behavior found in CMCs will facilitate this development. Other high temperature phenomena to be explored include changes in the interfacial sliding behavior due to both relaxations in the thermal residual stresses and the growth of reaction products near the fiber-matrix interface.

Fatigue damage studies on 2-D CMCs will focus on interface and fiber degradation phenomena, especially at elevated temperatures (Evans, Zok). Cyclic loading into the stress range at which matrix cracks exist is known to modify the interface sliding stress and may weaken the fibers. These degradation effects can be distinguished, because they change the hysteresis loop and reduce the UTS, respectively. Experiments that probe these material responses are planned. In addition, models that include the influence of cyclic fiber failure and pull-out on fatigue damage will be developed (Suo).

## **2.2 Matrix Cracking**

Models of the plastic strain and modulus changes caused by various modes of matrix cracking have been developed. These solutions have provided a rationale for experimental studies on the tensile and shear behavior of CMCs and on the fatigue of MMCs (Hutchinson, Zok, Evans, Suo, Budiansky, McMeeking). The information has been used in two distinct ways. (i) Test methodologies have been devised that relate stress/displacement measurements to constituent properties (Table I). (ii) Stress/strain curves and matrix crack evolution have been simulated for specific combinations of constituent properties.

The development of the procedures and their implementation are still in progress. Independent solutions have been established for matrix cracks in  $0^\circ$  plies and  $90^\circ$  plies upon tensile loading. The former has been experimentally validated on 1-D materials (SiC/SiC and SiC/CAS). Measurements of plastic strain, hysteresis loops and crack densities have been checked against the models for consistency.

TABLE I

Relevant Constituent Properties and Measurement Methods

CONSTITUENT PROPERTY	MEASUREMENT
Sliding Stress, $\tau$	<ul style="list-style-type: none"> <li>• Pull-Out Length, <math>\bar{h}</math></li> <li>• Saturation Crack Spacing, <math>\bar{l}_s</math></li> <li>• Hysteresis Loop, <math>\delta \epsilon_{1/2}</math></li> <li>• Unloading Modulus, <math>\bar{E}_L</math></li> </ul>
Characteristic Strength, $S_c$ , m	<ul style="list-style-type: none"> <li>• Fracture Mirrors</li> <li>• Ultimate Strength, <math>S</math></li> </ul>
Misfit Strain, $\Omega$ (q)	<ul style="list-style-type: none"> <li>• Bilayer Distortion</li> <li>• Permanent Strain, <math>\epsilon_p</math></li> <li>• Residual Crack Opening</li> </ul>
Matrix Fracture Energy, $\Gamma_m$	<ul style="list-style-type: none"> <li>• Monolithic Material</li> <li>• Saturation Crack Spacing, <math>\bar{l}_s</math></li> <li>• Matrix Cracking Stress, <math>\bar{\sigma}_{mc}</math></li> </ul>
Debond Energy, $\Gamma_l$	<ul style="list-style-type: none"> <li>• Permanent Strain, <math>\epsilon_p</math></li> <li>• Residual Crack Opening</li> </ul>

The next challenge is to couple the models together in order to simulate the evolution of matrix cracks in 2-D materials, subject to tensile loading (Hutchinson, Budiansky). Related effects on the ultimate tensile strength caused by stress concentrations in the fibers in the presence of matrix cracks, would also be evaluated. Experimental measurements of stress/strain behavior in 2-D CMCs, with concurrent observations of matrix crack evolution, would be used to guide and validate such models (Evans, Kedward).

### **2.3 Constitutive Equations**

Constitutive equations provide the link between material behavior at the meso-scale and the performance of engineering components. The equations can be established from the results of uniaxial and transverse tensile tests together with in-plane shear loading. For a complete formulation, which describes accurately the growth of failure mechanisms and the conditions of failure at the meso-scale, it is also necessary to perform calculations which are valid at the micro-scale.

These procedures have been completed for metal-matrix composites (Jansson, Leckie), and the resulting constitutive equations are operational in the ABAQUS finite element code. The behavior of simple panels penetrated by circular holes have been studied and the results await comparison with experiments which are planned for the coming year. The constitutive equations are formulated in terms of state variables which include the hardening tensors and damage state variables which describe debonding at the interface and void growth in the matrix. The format is sufficiently general to allow the inclusion of failure mechanisms such as environmental attack as the appropriate understanding is available. For



example, the effect of matrix and fiber creep mechanisms (Aravas) have also been introduced into ABAQUS, and it is proposed to extend the creep conditions to include the effects of variable loading and temperature.

A similar approach has been taken towards the modulus of CMCs. In this case, efforts have been made to include the influence of matrix cracking, in-plane shearing and fiber breakage. The latter consideration is based on the global load sharing model (Hayhurst). The equations are also available in ABAQUS. At present, matrix cracking is introduced by assuming a matrix stress accompanied by an increase of strain. However, based on the more recent understanding of the growth of matrix cracks (above) it is intended to introduce these mechanisms into the constitutive equations for CMCs.

## **2.4 Creep**

The emphases of the creep investigations have been on the anisotropic characteristics of unidirectional layers in which the fibers are elastic, but the matrix creeps. Experiments and models of the longitudinal creep properties of such materials have been initiated (McMeeking, Leckie, Evans, Zok, Aravas). The critical issues in this orientation concern the incidence of fiber failure and the subsequent sliding response of the interface. A modelling effort has established an approach that allows the stochastic evolution of fiber failure to occur as stress is transferred onto the fibers by matrix creep (McMeeking). This approach leads to creep rates with a large power law exponent. Various attempts are underway to incorporate the interface sliding initiated by fiber breaks and to introduce sliding into the creep rate formulation. Experiments being performed on unidirectional Ti matrix materials are examining the incidence of fiber failures on the creep

deformation (Evans, Leckie, Zok). These results will guide the modelling effort concerned with interface sliding effects. Insight will also be gained about fiber failure stochastics during creep, especially differences from room temperature behavior.

The transverse creep properties are expected to have direct analogies with composite deformation for a power law hardening matrix (Section 2.3). In particular, the same effects of debonding and matrix damages arise and can be incorporated in an equivalent manner (Leckie, Aravas). Testing is being performed on Ti MMCs and on SiC/CAS to validate the models.

Experiments on Ti-matrix  $0^\circ/90^\circ$  cross-ply composites are planned. Creep models appropriate to cross-ply materials will be developed by combining those corresponding to the unidirectional materials in the longitudinal and transverse orientations, using a rule-of-mixtures approach. Such an approach is expected to be adequate for loadings in which the principal stresses coincide with the fiber axes. Alternate approaches will be sought to describe the material response in other orientations.

Some CMCs contain fibers that creep more extensively than the matrix. This creep deformation has been found to elevate the stress in the matrix and cause time dependent evolution of matrix cracks. This coupled process results in continuous creep deformation with relatively low creep ductility. Experiments on such materials are continuing (Evans, Leckie) and a modelling effort will be initiated (Suo). The models would include load transfer into the matrix by creeping fibers, with sliding interfaces, leading to enhanced matrix cracking.

## **2.5 Tensile Strength**

The ultimate strength (UTS) of both CMCs and MMCs (as well as fatigue and creep thresholds) is dominated by fiber failure. With the global load sharing (GLS) concept of fiber failure now well established, the recent emphasis has been on defining the constituent properties needed to ensure GLS. The approach has been to perform local load sharing calculations and then compare experimental UTS data with the GLS predictions (Curtin, Evans, Leckie). The situation is unresolved. However, initial calculations on CMCs (Curtin) and MMCs (Evans) have provided some insight. Two key remaining issues concern the magnitude of the stress concentration in intact fibers caused by matrix cracks and the role of fiber pull-out in alleviating those stresses. Calculations of these effects are planned (Budiansky, Suo).

Degradation of the fiber strength upon either high temperature (creep) testing, atmospheric exposure, or fatigue are other topics of interest. Rupture testing performed under these conditions will be assessed in terms of degradation in fiber properties.

## **3. DESIGN TEAMS**

### **3.1 The Approach**

The overall philosophy of the design effort is to eventually combine *material models*, with a *materials selector*, and a *data base*, within a unified software package (Prinz). One example of a composites data base is that developed for MMCs by KAMAN Sciences, which forms the basis for a potential collaboration. The materials selector has already been developed

for monolithic materials (Ashby) and is available for purchase. This selector requires expansion to incorporate phenomena that have special significance for high temperature composites, including creep and thermal fatigue. These new features will be developed and included in the advanced selector software (Ashby).

The modelling approach is illustrated in Table II. Failure mechanisms and their effect on material behavior have been introduced into constitutive equations. The stress, strain and damage fields which develop in components during the cycles of loading and temperature can then be computed. Experiments shall be performed on simple components such as holes in plates, and comparison made with the computational predictions. Since constitutive equations are modeled using the results of coupon tests, it is likely that additional failure modes shall come to light during component testing. These mechanisms shall be studied and the appropriate mechanics developed so that their influence is correctly factored into the constitutive equations. In this way, increased confidence in the reliability of the constitutive equations can be established in a systematic way.

In practice, it is most probable that the constitutive equations are too complex for application at the creative level of the design process. It is then that simple but reliable procedures are of greater use. Some success has been achieved in this regard for MMCs subjected to cyclic mechanical and thermal loading (Jansson, Ponter, Leckie), as well as for strength calculations of CMC panels penetrated by holes (Suo) and the fatigue of MMCs (Zok, McMeeking). In all cases simplifications are introduced after a complete and reliable analysis has been completed which provides a standard against which the effects of simplification can be assessed.

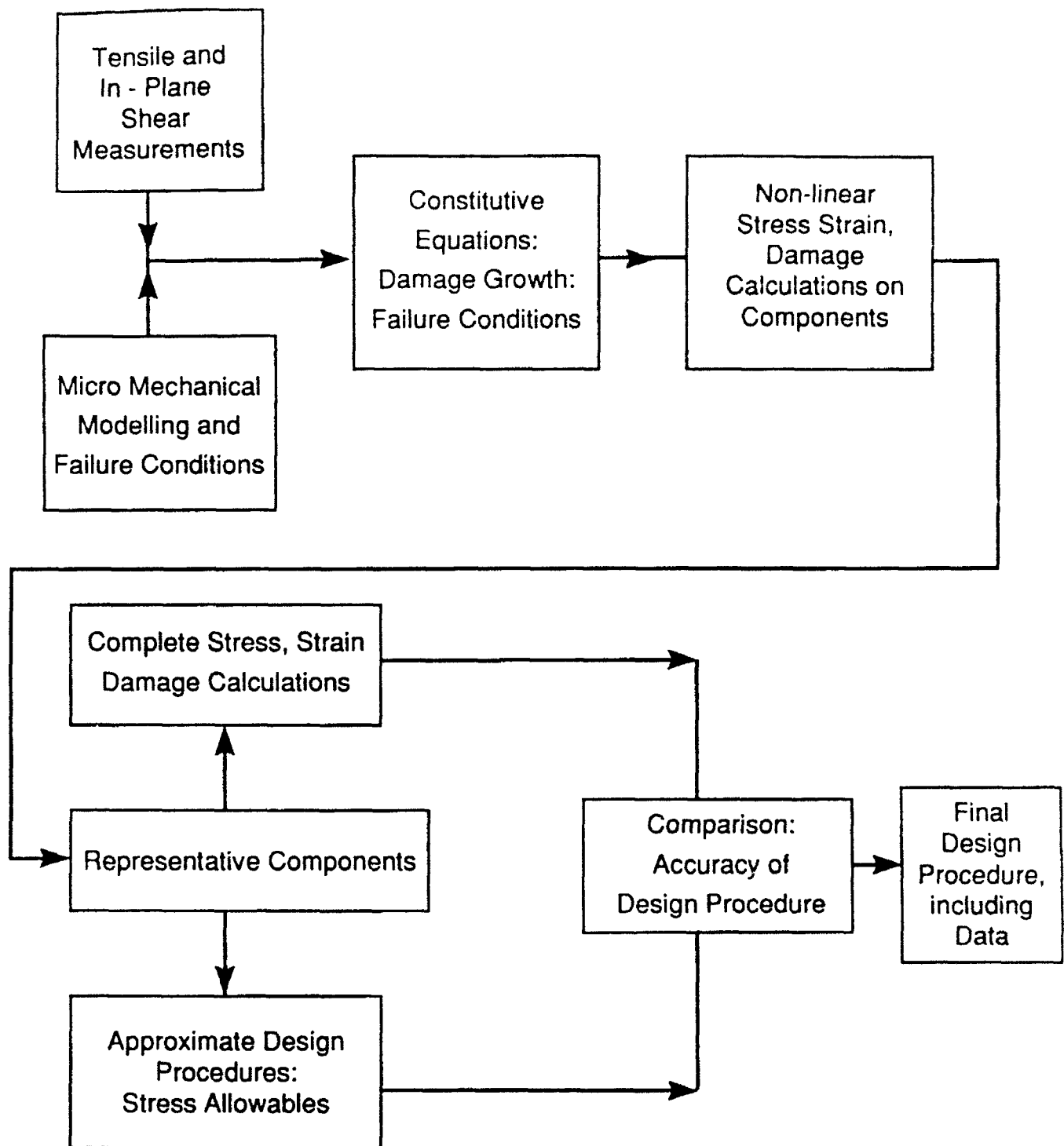


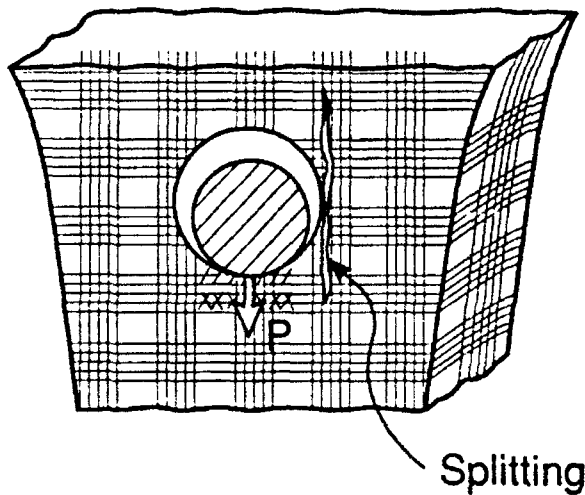
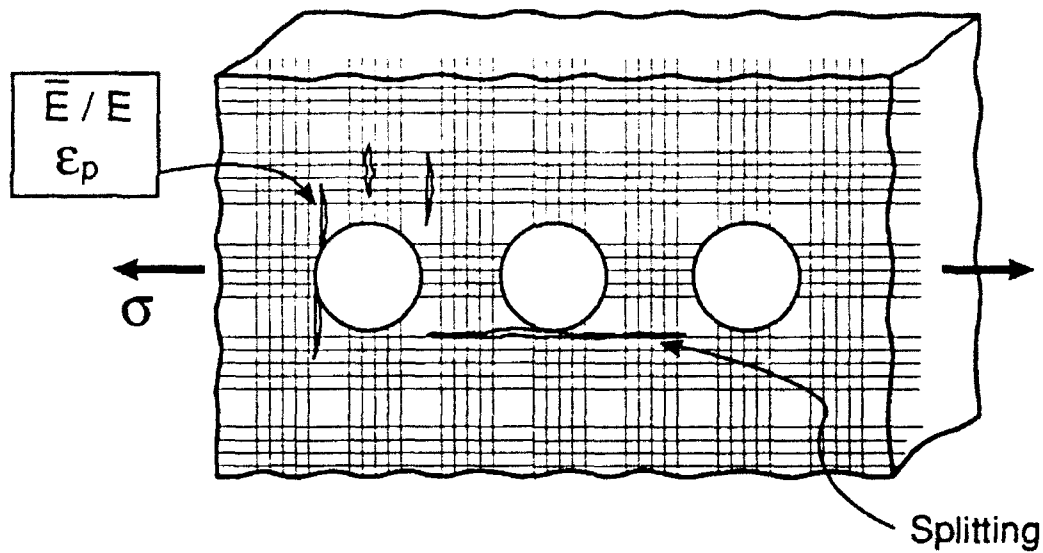
Table II  
The Modelling Approach

### 3.2 Ceramic Matrix Composite Design

The design effort on CMCs will have its major focus on pin-loaded holes used for attachments (Fig. 3). A smaller activity, expected to expand in 1994, will address delamination cracking. The hole design includes several related topics. Each topic is concerned with aspects of constitutive law development (Table III), highlighted during the study group. Combined experimental and modelling efforts on the *tensile properties* of CMCs have established that the plastic strains are dominated by matrix cracks in the 0° plies. The matrix cracking models developed in the program demonstrate that these strains are governed by four independent constituent properties [(Table I)  $\tau$ ,  $\Gamma_i$ ,  $\Omega$  and  $\Gamma_m$ ] which combine and interrelate through five non-dimensional parameters (Table IV). This modelling background suggests a concept for using model-based knowledge to develop constitutive laws. The following steps are involved (Table III). (i) A *model-based methodology* for inferring the constituent properties of unidirectional CMCs from macroscopic stress/strain behavior has been devised and is being experimentally tested on a range of materials (Evans). (ii) Upon validation, the models would allow stress/strain curves to be simulated (Hutchinson). This capability would facilitate a sensitivity study to be performed, in order to determine the minimum number of independent parameters that adequately represent the constitutive law. A strictly empirical law would require 3 parameters (yield strength, hardening rate and unloading modulus). Consequently, the objective might be to seek 3 combinations of the 4 constituent properties. (iii) Experiments would be performed and models developed that establish the matrix cracking sequence in 2-D materials (Hutchinson, Evans, Kedward). These would be conducted on

# DESIGN PROBLEM IN CMC's

## Design of Holes in Nozzles / Combustors



### Issues

Tensile Rupture  
Crushing  
Splitting

### Design Variables

Hole Size  
Hole Spacing  
Fiber Architecture  
Material Choice  
New Concepts

Fig. 3

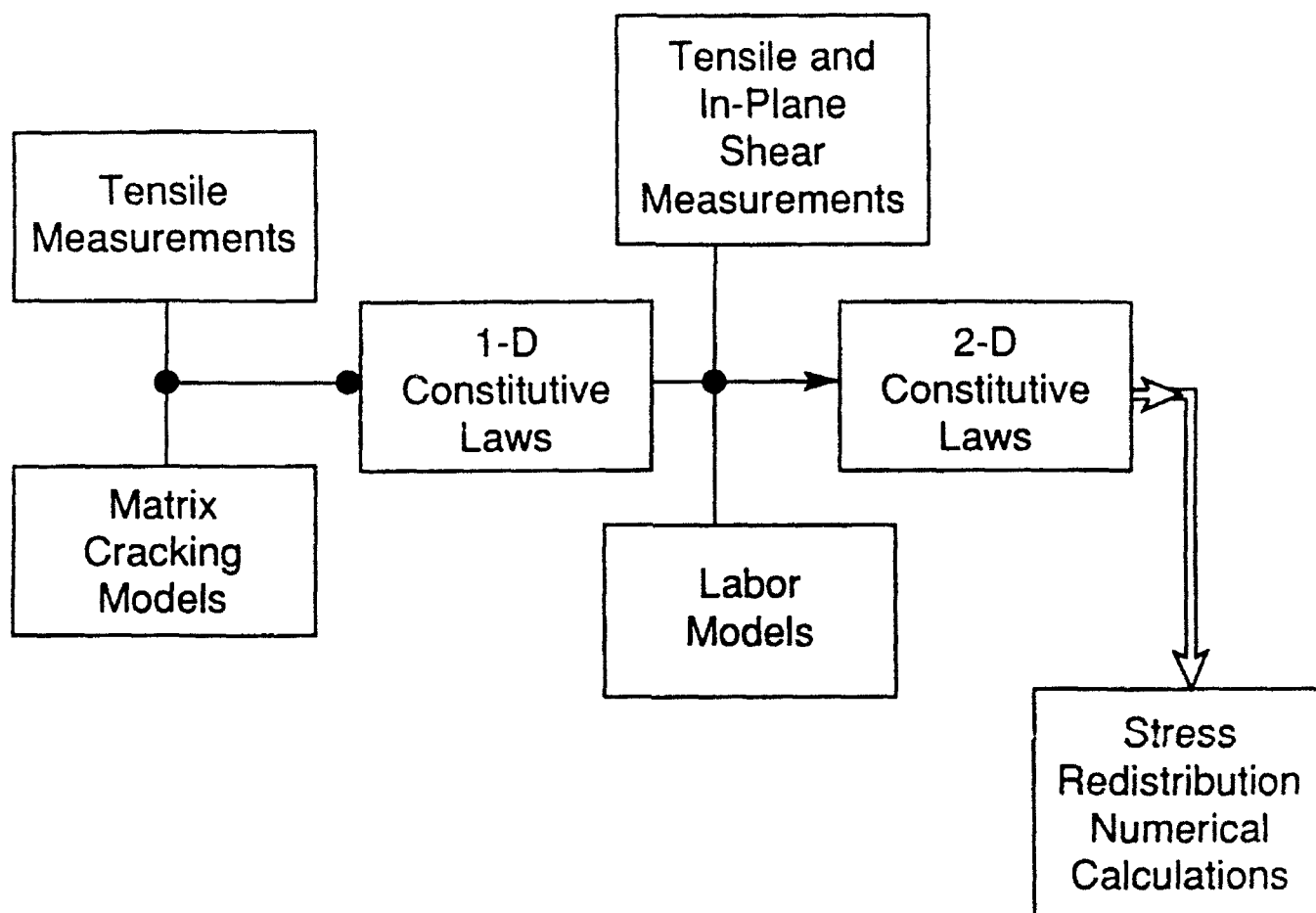


Table III

## Design Strategy for CMCs



TABLE IV

Summary of Non-Dimensional Coefficients

$$\mathcal{A}_b = [f/(1-f)]^2 (E_f E_L / E_m^2) (a_o \tau / RS_u), \text{ Flaw Index for Bridging}$$

$$\mathcal{A}_p = (a_o / \bar{h}) (S_p / E_L), \text{ Flaw Index for Pull-Out}$$

$$\mathcal{D} = \Gamma_m (1-f)^2 E_f E_m / f \tau^2 E_L R, \text{ Crack Spacing Index}$$

$$\mathcal{H} = b_2 (1-a_1 f)^2 R \bar{\sigma}_p^2 / 4 \bar{d} \tau E_m f^2, \text{ Hysteresis Index}$$

$$I = \bar{\sigma}_p / E_m \Omega, \text{ Misfit Index}$$

$$\mathcal{M} = 6 \tau \Gamma_m f^2 E_f / (1-f) E_m^2 R E_L, \text{ Matrix Cracking Index}$$

$$Q = E_p f \Omega / E_L (1-\nu), \text{ Residual Stress Index}$$

$$\Delta_l = (1/c_1 \Omega) \sqrt{\Gamma_i / E_m R}, \text{ Debond Index}$$

CMCs with a range of different constituent properties and fiber architectures. The plastic strains would be related to constituent properties by adapting the 1-D models.

The in-plane shear behavior will be characterized by performing experiments and developing models of matrix cracking that govern the plastic *shear strain* in 2-D CMC (Evans, Hutchinson, Bao). The information will be used to establish the constitutive laws for in-plane shear, as well as interlaminar shear. For continuity of interpolation between tension and shear, the shear models will include the same constituent properties as those used to represent the tensile behavior.

The model-based constitutive laws, based on matrix damage, will be built into a CDM (continuum damage mechanics) formulation, compatible with finite element codes (Hayhurst). Computations will be performed to explore *stress redistribution* around holes and other strain concentration sites. The calculations will establish visualizations of stress evolution that can be compared with experimental measurements performed using the SPATE method, as well as by Moiré interferometry (Mackin, Evans). These experiments will be on specimens with notches and holes, loaded in tension. The comparisons between the measured and calculated stress patterns will represent the ultimate validation of the constitutive law. The composite codes, when validated, will be made available to industry.

Some preliminary experimental work will be performed on pin-loaded holes. Damage patterns will be monitored and stress redistribution effects assessed using SPATE (Kedward, Evans, Mackin). These experiments will be conducted on SiC/CAS and SiC/C. The results will provide the focus for future CDM computations, based on the constitutive law for the material.

Smaller scale activities will involve basic aspects of stress redistribution around holes caused by fatigue and creep *damage*, using the experience gained from the matrix cracking studies. Some experimental measurements of these effects will be performed using SPATE (Zok, Evans).

Some delamination crack growth measurements and calculations are also envisaged (Ashby, Kedward, Hutchinson). Cantilever beam and C-specimens will be used for this purpose (Fig. 4). During such tests, crack growth, multiple cracking and stiffness changes will be addressed. Models of bridging by inclined fibers will be developed (Ashby) and used for interpretation.

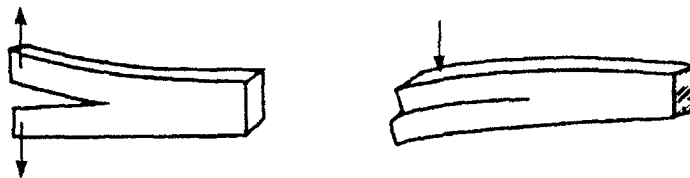
### **3.3 Metal Matrix Composite Design**

The 3D constitutive equations for MMCs are now available for use in the ABAQUS finite element code, and the immediate task is to use these equations to predict the behavior of representative components (Leckie). One such system is a ring-type structure which is being studied together with Pratt and Whitney. Clearly no experimental verification is possible with a component of this scale, but the experience of Pratt and Whitney shall provide invaluable input on the effectiveness of the calculations. A component sufficiently simple to be tested is the panel penetrated by holes. The holes shall be both unloaded and loaded (Jansson), and it is expected to include the effects of cyclic mechanical and thermal loading.

It is proposed to develop simplified procedures which are based on shakedown procedures (Jansson, Leckie). Demonstrations have already been made of the effectiveness of the Gohfeld method (which uses only simple calculations) in representing the behavior of MMCs subjected to cyclic thermal loading.

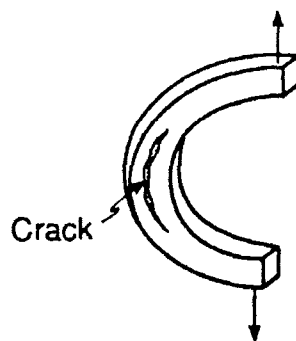
# TRANSVERSE CRACKING OF CMC

CONVENTIONAL  
COUPON  
TESTS



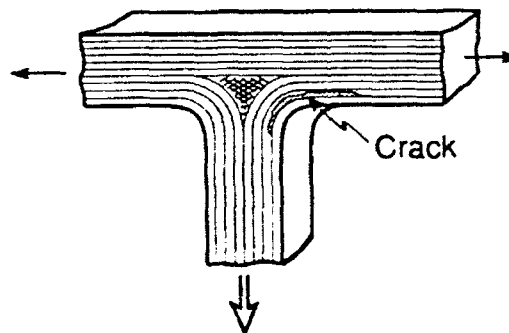
• Fiber Bridging Problem ( $G \gg \Gamma_T$ )

IMPROVED  
TESTS

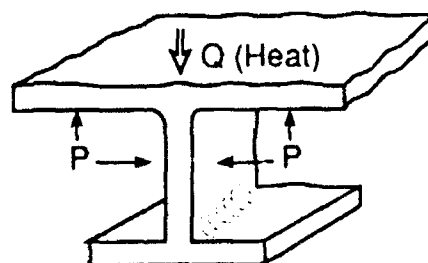


$da/dN$  vs.  $G$

SUB - ELEMENT  
TEST



DESIGN  
PROBLEM



- Thermal Conductivity
- Fiber Architecture
- Matrix Toughness

Fig. 4

During the complex histories of stress and temperature, it is known that the matrix-fiber interface properties change. Fatigue loading (Zok) is known to decrease the interface sliding stress. Transverse creep appears to cause matrix-fiber debonding (Jansson), which might result in loss of the ability to transfer stress between matrix and fiber. It is intended to study this effect of transverse creep on the integrity of the longitudinal strength of the material by performing tests on panels which shall allow rotation of the stress fields. A good understanding now exists of the fatigue properties of MMCs (Zok). It is intended to extend the ideas developed from earlier theoretical studies (McMeeking, Evans) to include cyclic thermal effects and experimental programs on holes in plates.

#### **4. MANUFACTURING**

The activities in processing and manufacturing have had the following foci:

- Matrix development to address specific requirements identified by the design problems, particularly first matrix cracking in CMCs (Lange) and creep strengthening in MMC/IMCs (Levi, Lucas).
- Hybrid architectures which offer possible solutions to environmental degradation and thermal shock problems (Evans, Lange, Leckie, Levi, Yang, Zok).
- Software development that predicts and controls fiber damage and interface properties during densification (Wadley).
- Processing techniques to generate model MMC sub-elements (Leckie, Levi, Yang).

#### 4.1 Metal Matrix Composites

Work on MMC matrix development has focused on dispersion strengthening approaches to increase the *transverse* tensile and creep strength of 1-D and 2-D fiber architectures. The initial work has emphasized a model system, Cu/Al<sub>2</sub>O<sub>3</sub>, wherein dispersoids are produced by internal oxidation of a dilute Cu-Al alloy deposited by PVD onto sapphire fibers. These are subsequently consolidated by HIP'ing. Specimens with fiber volume fractions of  $0.3 \leq f \leq 0.5$  and 2-3%  $\gamma$ -Al<sub>2</sub>O<sub>3</sub> dispersoids (~ 20 nm in size) have been produced in this manner and will be tested to assess their transverse creep behavior. The new emphasis will be on higher temperature matrices based on TiB dispersoids in Ti-(Cr/Mo)-B alloys (Levi). Initial solidification studies have demonstrated the potential of these materials as *in-situ* composites. Efforts are underway to develop sputtering capabilities to implement this concept.

Fiber damage during densification of composite prepregs generated by plasma-spray (GE) and PVD (3M) have also been emphasized (Wadley). Interdiffusion studies coupled with push-out tests have been used to study the evolution of reaction layers in Ti/SiC composites and their effect on the relevant interfacial properties as a function of process parameters. Additional efforts under other programs have focused on developing predictive models for fiber breakage during densification. The interdiffusion and breakage models are being incorporated into software that predicts pressure-temperature paths, which simultaneously minimize fiber damage and control the interface properties.

The feasibility of producing MMC sub-elements consisting of fiber reinforced rings (1-D) and tubes (2-D) has been demonstrated by using

liquid metal infiltration of Al alloy matrices (Levi). These are presently undergoing testing in combined tension/torsion modes. Future efforts will be directed toward extending the technique to other shapes (e.g., plates with reinforced holes), as well as devising methods to modify the (currently strong) interfaces. The identification of methods that provide the appropriate interfacial debonding/sliding characteristics should enable the use of these composites as *model systems* for higher temperature MMCs, such as Ti.

#### **4.2 Intermetallic Matrix Composites**

The focus of the IMC processing activities has been on the synthesis of  $\text{MoSi}_2/\beta\text{-SiC}_p$  composites by solidification processing. These materials are of interest as potential matrices for fiber composites. Significant progress was made in the elucidation of the relevant Mo-Si-C phase equilibria, the growth mechanisms of SiC from the melt and their impact on reinforcement morphology, as well as the orientation relationships between matrix and reinforcements, and the interfacial structure. An amorphous C layer,  $\leq 5$  nm thick, was found at the  $\text{MoSi}_2/\text{SiC}$  interface in the as cast condition, and persisted after 12 h heat treatments at  $1500^\circ\text{C}$ . This interfacial layer has been reproduced in  $\alpha\text{-SiC}_p/(\text{MoSi}_2 + \text{C})$  composites produced by powder metallurgy techniques and was found to exhibit promising debonding and pull-out behavior during fracture (Levi). Future efforts are aimed at implementing this *in-situ coating* concept in  $\alpha\text{-SiC}$  fiber composites.

#### **4.3 Ceramic Matrix Composites**

The processing issues for creating CMCs with high *matrix strength* continue to be explored (Lange, Evans). The basic concept is to create a strong ceramic matrix framework within a fiber preform, by means of slurry

infiltration followed by heat treatment. This strong framework would then be infiltrated by a polymer precursor and pyrolyzed to further densify the matrix. It has been demonstrated that strong matrices of  $\text{Si}_3\text{N}_4$  can be produced using this approach (Lange). Further work will address relationships between matrix strength and microstructure (Lange, Evans).

#### **4.4 Hybrids**

These activities cover materials consisting of thin monolithic ceramic layers alternating with layers containing high strength fibers bonded by a glass or metallic binder. The primary motivation behind this concept is the potential for manufacturing shapes that have a high resistance to environmental degradation and also have good thermal shock resistance. The concept has been demonstrated using alumina plates and graphite reinforced polymer prepregs (Lange). The availability of glass-ceramic bonded  $\text{SiC}_f$  prepregs and tape-cast  $\text{SiC}$  plates has facilitated the extension of this technique to high temperature systems (Lange). Future assessment will address new crack control concepts. These concepts would prevent damage from propagating into the fiber reinforced layers, especially upon thermal loading (Zok, Lange). If successful, this concept would allow the development of hybrid CMCs which impart resistance to environmental degradation, as well as high thermal strain tolerance.

Preliminary work has been performed on laminates consisting of alumina plates and sapphire-fiber reinforced Cu monotapes (Levi). The latter are produced by deposition of Cu on individual fibers which are subsequently aligned and bonded by hot pressing between two Cu foils. After suitable surface preparation, the alumina/monotape assemblies are



bonded by hot pressing. Future work is aimed at implementing the concept with Ni based alloys.

## **5. SENSORS**

The principal challenge being addressed is the non-destructive and non-evasive measurement of stresses in composites (Clarke, Wadley). The motivation is to make detailed measurements of stresses in components for incorporation into evolving design models, as well as validation of the stress distributions computed by finite element methods. A major emphasis has been placed on measuring the residual stresses in sapphire fibers in various matrices, using the recently developed technique of optical fluorescence spectroscopy. These measurements have provided data on the distribution of residual thermal stresses in the fiber reinforcement, as a function of depth below the surface. This approach will be extended, in conjunction with finite element modelling (Hutchinson), to measure the stresses during the process of fiber pull-out from a variety of metal and ceramic matrices. Initial experiments indicate that such in-situ measurements are feasible.

The technique will also be applied to the measurement of the stresses in sapphire fibers located in the vicinity of pin-loaded holes in order to understand the manner in which the stresses redistribute during loading. It is anticipated that this measurement will provide information about the detailed fiber loadings and also about the stresses that cause debonding of the fibers from the matrix. Moreover, in support of the activities on thermal ratcheting, the redistribution of stresses with thermal cycling will be established. This will be accomplished by using the fluorescence technique as well as Moiré interferometry, based on lithographically defined features.

## Computer Aided Manufacturing Through Selective Material Deposition

F. B. Prinz L.E. Weiss and M. Turk  
Engineering Design Research Center  
Carnegie Mellon University

### Introduction

The purpose of the research efforts at Carnegie Mellon is to create an environment in which a design, given geometry and material structure, can be automatically translated into a physical article. The methodology we have adopted is based on selective material deposition through thermal spraying, welding, and micro casting. The system is called MD\* which stands for recursive Material Deposition. There are also plans to integrate deposition methods like CVD into the manufacturing cell. The particular focus of the current research is the creation of a planning system enabling the user to conveniently generate the geometry and assign the desired material structures to the geometry. Once complete we envision a system accessible by all members of the URI community in which a design can be completed remotely followed by a manufacturing request through the network. The part will then be processed in the MD\* cell in Pittsburgh. Obviously, the initial version of this system will have limitations regarding complexity (geometry and micro structure) and size of the article which can be manufactured. The current system can be regarded as an experimental verifier of micro structure synthesis and analysis based research and tools developed by other URI researchers.

### Brief Description of the MD\* System

The MD\* System incorporates a plasma and two arc spraying stations, a welding and a microcasting process for layered material buildup. Material removal is accomplished through Computer Numerically Controlled Machining. Intermediate processing capabilities include shot peening grit blasting and cleaning. The parts are built on top of a pallet which is transferred from station-to-station using a robotic transfer/palletizing system. Examples of parts which were initially produced by the system are shown in Fig. 1.

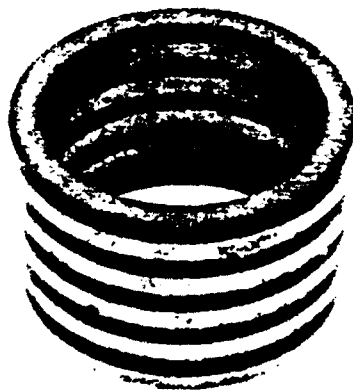


Figure 1:

The possibility exists to make ceramic parts with metal bearings embedded.(Fig. 2)

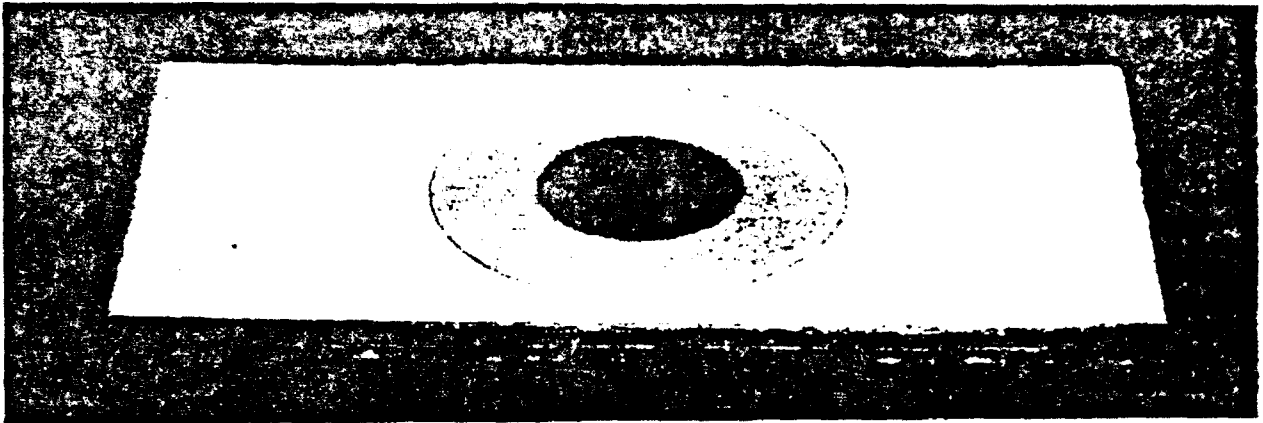


Figure 2:

Furthermore electronic structures with sensors and electronic processing capabilities can be manufactured as well. (Fig.3 )

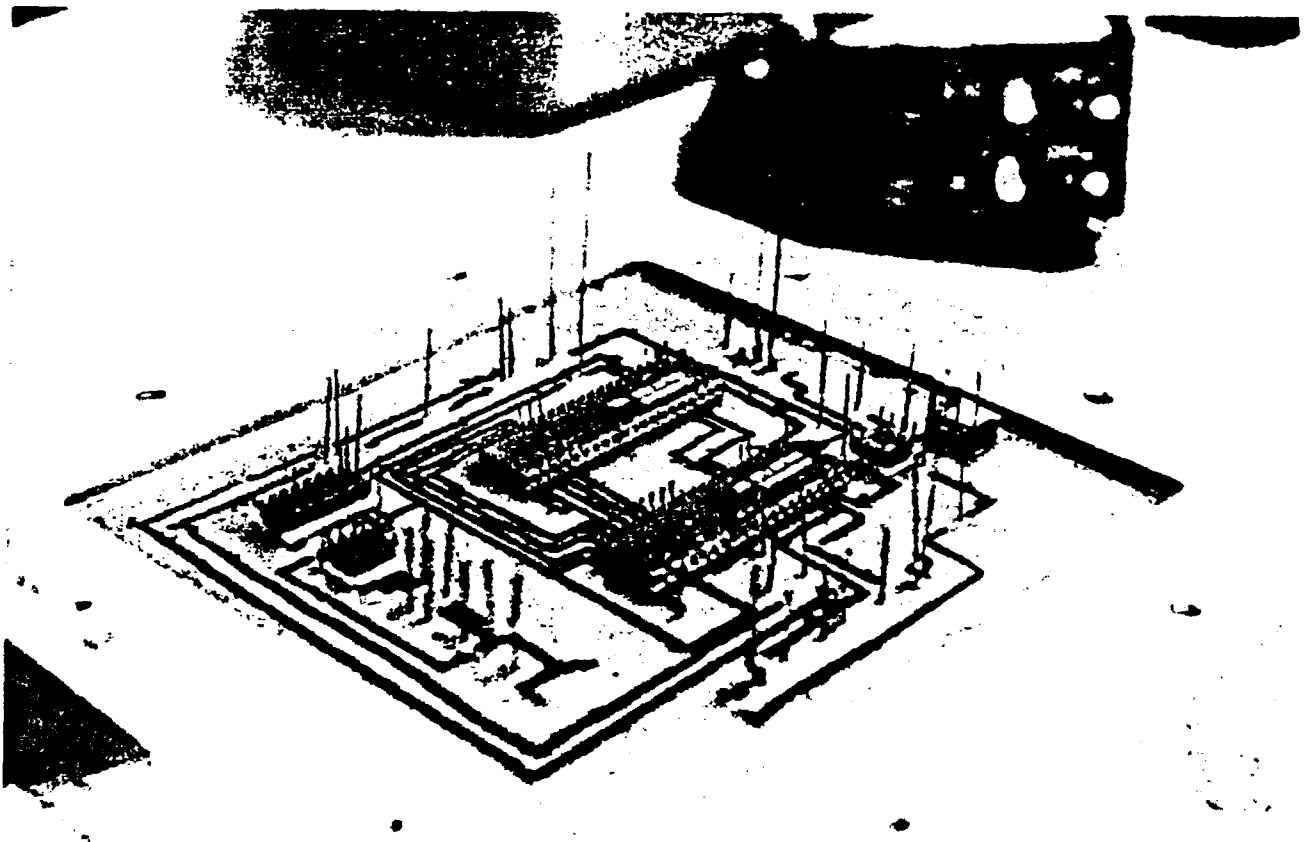


Figure 3:

## The Planning System

The MD\* planning system is a computer-aided system that will help in automating the planning stages of the MD\* family of manufacturing processes. The MD\* process builds up a part by successfully manufacturing cross-sectional layers. The planning module for MD\* process consists of seven major components shown in figure 4. The following is the summary of the functions performed by these modules during the planning process.

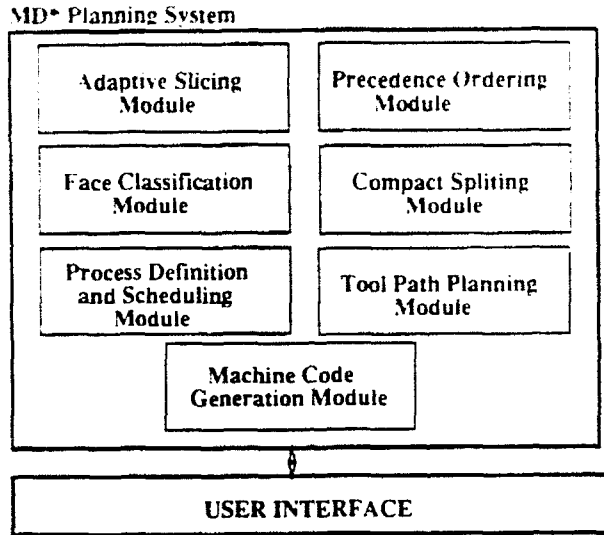


Figure 4: Planner Architecture

- *Adaptive Slicing Module.* This module analyses the CAD model of the part and splits the model into a set of layers. The location and thickness of these layers are a function of the process-imposed limits and the results of the manufacturability analysis of the part's geometry.
- *Process Definition and Scheduling Module.* This module defines a sequence of operations used to build a layer using MD\*. The definition of these operations includes values of all parameters associated with the tool used to perform them.
- *Face Classification Module.* This module determines the orientation of all faces in a CAD model of a layer and, if the selected process includes a machining operation, identifies if the face will be machined in the support material of the layer itself.
- *Precedence Ordering Module.* This module uses the CAD model of a layer and builds a graph describing the manufacturing precedence between all compacts present in the layer. A compact is defined as a distinct portion of a layer composed of single material. This module also identifies loops in the resulting precedence graph. The presence of a loop indicates a conflict in the scheduling of operations required to build a layer.
- *Compact Splitting Module.* This module tries to resolve problems in scheduling of operations on a layer by splitting one of compacts identified as contributing to the scheduling conflict. This module attempts to split the compact into several sub-compacts that do not pose any precedence problems.

- *Tool Planning Module.* This module uses the process definition to plan the motion of the various tools in the MD\* manufacturing cell.

- *Machine Code Generation Module.* This module generates command files used to drive the individual stations in the MD\* manufacturing cell. The flow of information between these models during a planning session is shown in figure 5. The remainder of this report describes the operations of these modules in greater details

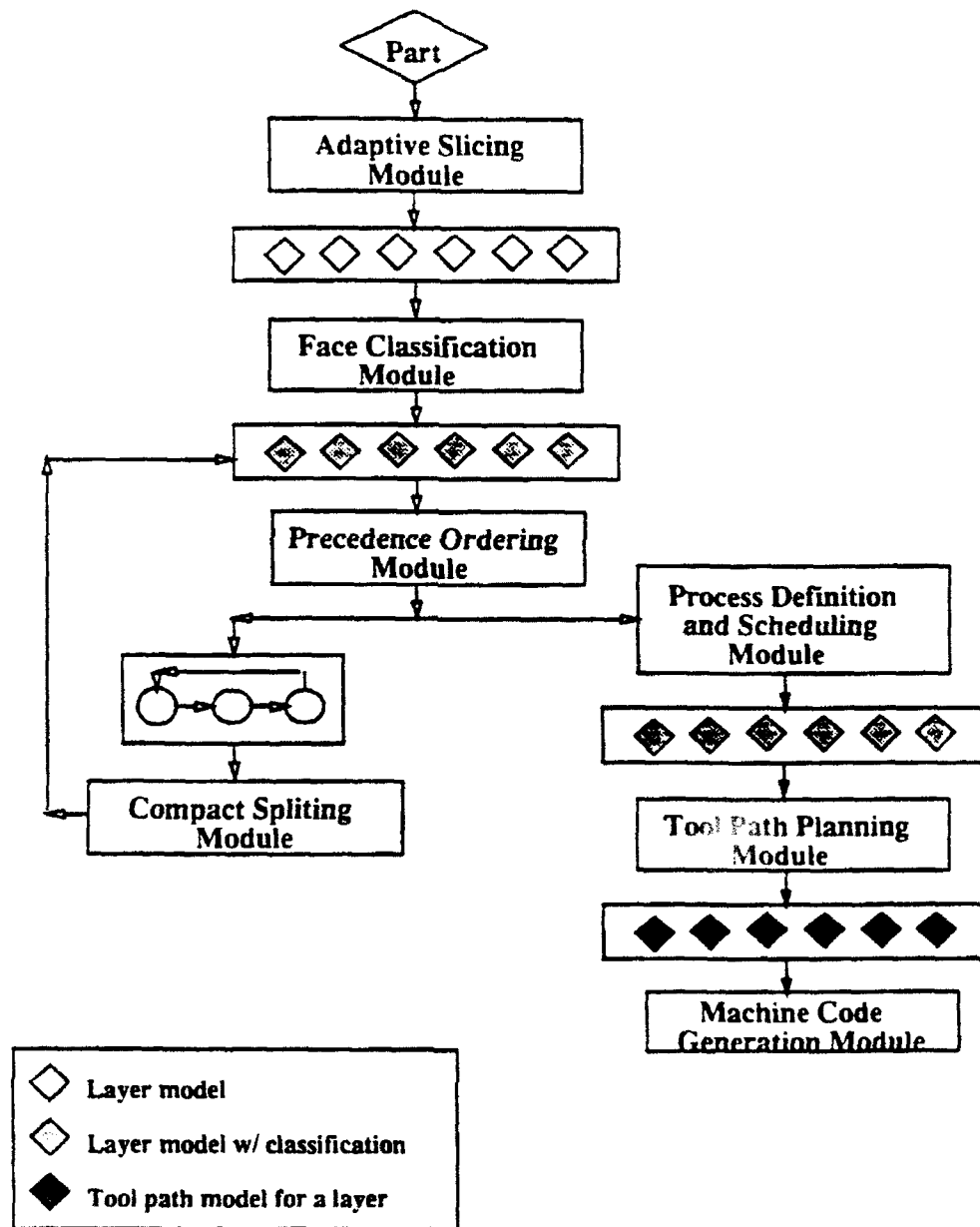


Figure 5: Data flow in MD\* Planning

### Adaptive Slicing Module.

The adaptive slicing module takes the CAD model of the part as its input and produces a set of CAD models representing the decomposition of the part into layers. The first step in this procedure is to classify the walls of the model based on the value of the Z component of their normal. Each wall is classified as either Up, Down, Undercut, Comp. Undercut, or Straight. The classification algorithm is shown in figure 6

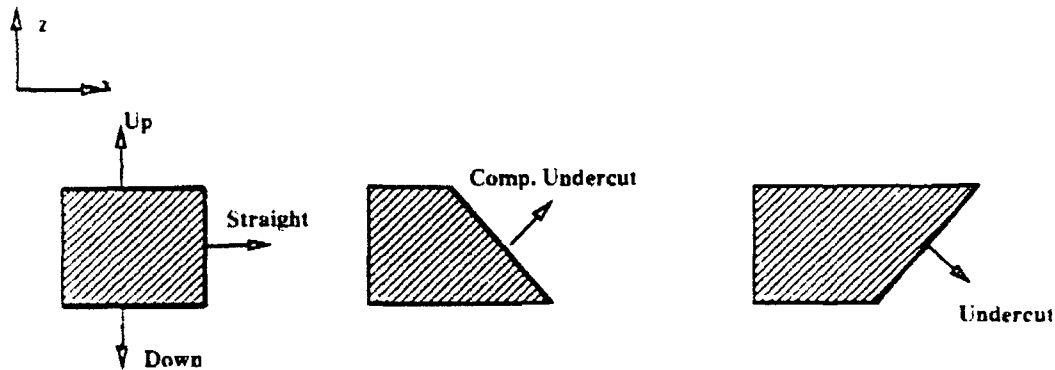


Figure 6: Wall classification Algorithm

Once all of the walls in the part model have been classified, the model is examined to determine the heights at which the model should be subdivided into layers. A boundary between any two walls of differing classification will cause the model to be partitioned. The four conditions used to trigger a partition of a model are shown in figure 7.

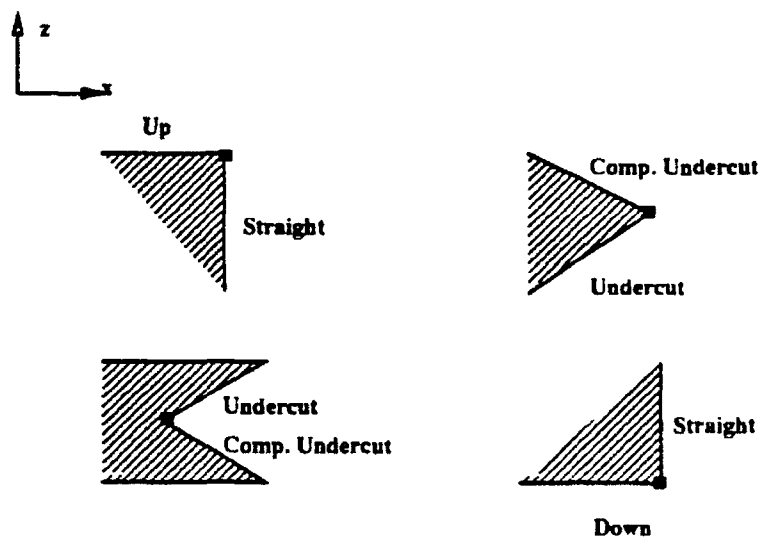


Figure 7: Adaptive Slicing Conditions

### Face Classification Module.

The face classification module takes a CAD model of a layer and classifies all of the faces in the model. The classification scheme determines whether a face is machined on the part or in the support material surrounding the part. The classification scheme can be summarized as follows:

- The faces classified as Straight or Undercut are machined on the support material.
- The faces classified as Comp. Undercut are machined on the part;
- The faces classified as Up will have to be planed in the object; and
- The remaining faces do not have to be machined.

### Precedence Ordering Module.

The MD\* manufacturing process is multi-material in its nature. Even if the part is completely homogeneous in its composition, each manufactured layer is encased in a support material that is different from the object. The precedence ordering module takes the CAD model of a layer and the surrounding support material and computes a graph representing relationships between various compacts in the model. A compact is defined as a solid entity in the CAD model. Each compact is marked with an attribute identifying the material used in manufacturing it. The procedure for determining the precedences between compacts relies on the classifications assigned to the walls of each compact. The approach used to determine precedence relationships is shown in figure 8. The resulting graph is examined for presence of precedence loops. A precedence loop indicated that there exists a conflict in the scheduling of manufacturing operations for two or more compacts. If no loops are found in the graph, the planning process can proceed, otherwise the precedence loops must be resolved by manipulating the geometry of the layer. This manipulation is the responsibility of the compact splitting module.

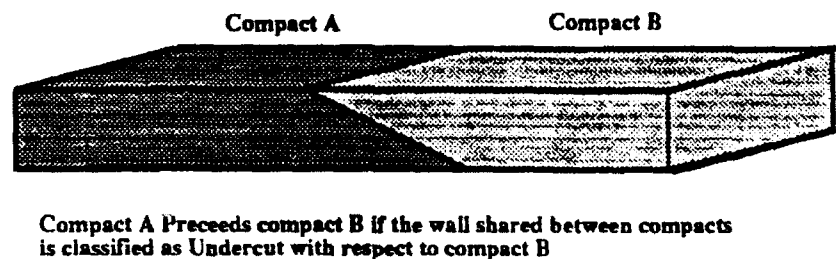


Figure 8: Compact Precedence Rule

### Compact Splitting Module.

The compact splitting module takes a CAD model of the a layer and the precedence graph produced by the precedence ordering module, and resolves the scheduling conflicts by subdividing compacts in a layer. The approach used by this module to resolve conflicts requires identifying a compact involved in a precedence loop and subdividing it as to break the loop. Each compact (C) identified in a precedence loop has a predecessor compact (P) and a successor compact (S). In order to clear up the scheduling conflict,

the compact has to be subdivided into two compacts sC1 and sC2 that meet the following three conditions:

1. Compact sC1 is not adjacent to compact P;
2. Compact sC2 is not adjacent to compact S; and
3. the boundary between sC1 and sC2 does not force any type of precedence between them.

Once a compact is selected for decomposition, the compact splitting module computes a parting surface that splits the compact into sub-compacts that meet these three conditions. The current approach involves identifying the common boundary between the compact C and its successor S. The nature of this boundary will determine how many sub-compacts will be produced by the decomposition. A continuous boundary will require two sub-compacts, each break in the boundary will require an additional sub-compact. The process of determining the parting surface uses the Medial Axis Transform (MAT) of the top of the compact. The segment of the MAT that connects the end-points of the common boundary serves to define the parting surface of the compact.

#### **Process Definition and Scheduling Module.**

The process definition and scheduling module determines the sequence of operation used to manufacture a layer. This process takes three pieces of information: the type of the MD\* process, a CAD model of the layer and the precedence graph for the compacts in the layer. The schedule is created by determining a sequence of compacts from the precedence graph and using that sequence to combine the operations used to manufacture each compact into a comprehensive schedule for the layer. The schedules for each layer are combined into a master command file that guides the manufacturing of the part.

#### **Tool Path Planning Module.**

The tool path planning module takes a CAD model of a compact and a set of parameters associated with an operation performed on it, and produces a CAD model of the path that the tool must follow in performing the operation.

#### **Machine Code Generation Module.**

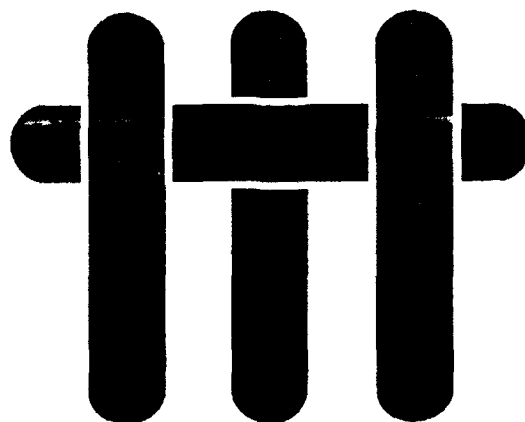
The machine code generation module takes a CAD model of the tool path and a set of parameter values for a operation and produces a station-specific command file.

#### **Plans for 1993/1994**

During 1993 a graduate student from Carnegie Mellon EDRC will spend time at the URI Santa Barbara. The purpose of that stay is to acquire knowledge about design methods for composite structures which will be later integrated into the MD\* system. In return the student will install the MD\* CAD and planning system for use of URI students in Santa Barbara.



# M A T E R I A L S



## Environmentally Compatible Double Coating Concepts for Sapphire Fiber-Reinforced $\gamma$ -TiAl

T.J. Mackin, J.Y. Yang, C.G. Levi and A.G. Evans

High Performance Composites Center  
Materials Department  
College of Engineering  
University of California  
Santa Barbara, CA 93106-5050

Accepted for publication in *Materials Science and Engineering* August, 1992

## ABSTRACT

Environmentally compatible interfaces based on double coating concepts have been developed for sapphire fibers in  $\gamma$ -TiAl matrix composites. The fiber coating design involves two layers with distinct functions: one in contact with the fiber which provides the debonding and sliding characteristics required for toughening, and a second one next to the matrix which protects the fiber and debond layer from diffusional interactions and mechanical degradation during processing. Three double coating systems were tested wherein the debond layer consisted of pyrolytic carbon, colloidal carbon or a mixture of carbon and alumina. The diffusion barrier was in all cases a dense alumina layer  $\leq 5 \mu\text{m}$  thick. With the exception of the pyrolytic carbon, all other coatings were applied by slurry processing techniques. After composite consolidation, the coatings were evaluated using fiber push-out tests, whereupon each double coating was found to successfully enable debonding and sliding of the sapphire fibers. The environmental compatibility of the coatings was tested by oxidizing the carbon in the debond layer at elevated temperatures. This produced measurable changes in the interfacial properties, but push-out tests confirmed that the coating design still allowed fiber debonding and sliding within the ranges desired for improving toughness.

## 1. INTRODUCTION

The mechanical properties of fiber-reinforced materials are known to be strongly influenced by the fiber/matrix interface.<sup>1-9</sup> Optimum longitudinal properties, for both brittle and ductile matrix materials, require that the interfaces debond and slide with a relatively low shear resistance,  $\tau$ , relative to fiber strength,  $S$ . Small values of  $\tau/S$  are needed to achieve a "rule-of-mixtures" composite tensile strength, by ensuring a global load sharing condition: generally,  $\tau/S$  must be smaller than  $\sim 0.05$ .<sup>10-13</sup> A high composite fracture resistance also requires small values of  $\tau/S$  as needed to achieve large fiber pull-out lengths and hence, a substantial contribution of frictional dissipation to the work of rupture.<sup>10,14,15</sup>

Single crystal sapphire fibers offer significant potential for both high temperature strengthening and toughening of intermetallic matrix composites, notably  $\gamma$ -TiAl. Unfortunately, directly bonded interfaces between  $\text{Al}_2\text{O}_3$  and  $\gamma$ -TiAl are "strong" and do not debond easily during fracture.<sup>16</sup> He and Hutchinson<sup>17</sup> have proposed that an interface should have a fracture energy,  $\Gamma_i$ , lower than  $1/4$  of the fiber fracture energy,  $\Gamma_f$ , if it is to fail ahead of an incident crack. (A detailed description of the debonding criterion is given in reference [17]). Reported  $\Gamma_f$  values for sapphire fibers<sup>18</sup> range from 7 to 23 J/m<sup>2</sup>, requiring in principle that  $\Gamma_i \leq 2$  J/m<sup>2</sup>. This suggests the use of fiber coatings to introduce "weak" interfaces with suitably small values of  $\Gamma_i$  and  $\tau$ .<sup>1-6,20</sup> The intent of this study was to devise and test fiber coatings that fulfill the requisite debonding/sliding characteristics for sapphire fibers in  $\gamma$ -TiAl matrix composites. The potential applications also require the coating to be thermochemically compatible with the composite constituents, sufficiently strong to maintain its integrity during processing, and capable of maintaining the toughening mechanisms operational after exposure to oxidative environments at temperatures in excess of 1000°C.

Prior studies have shown that many coating candidate materials which are environmentally stable would also bond strongly to sapphire.<sup>1</sup> Conversely, materials that have been found to debond easily from  $\text{Al}_2\text{O}_3$ , notably C and refractory metals like Mo and W,<sup>1</sup> are prone to diffusional interactions with the  $\gamma\text{-TiAl}$  matrix and are not oxidatively stable at high temperatures. The latter, however, could still be utilized if the coatings are designed in the double layer configurations proposed in Figure 1. The present work focuses on C-based coatings but similar approaches may be implemented with W and Mo.<sup>1</sup>

In one approach (Concept 1 in Figure 1), a thin layer of C is in direct contact with the fiber and covered with a thicker, dense  $\text{Al}_2\text{O}_3$  layer which separates it from the matrix and prevents interdiffusion during processing. The C coating would be fugitive<sup>21</sup> under oxidative environments, but can be designed to leave a gap between the fiber and the dense  $\text{Al}_2\text{O}_3$  layer which obviates the need for debonding (Concept 2). A sliding resistance could still be incorporated if the C layer is chosen to have a thickness smaller than the peak-to-peak amplitude of the fiber roughness. The "debond" (gap) surfaces would mimic the underlying fiber topography, as shown in Figure 1, and the fiber displacements would result in asperity interactions that give rise to a finite  $\tau$ . (In the particular case of the sapphire fibers, the surface has a sinusoidal roughness pattern which produces a modulated sliding response.<sup>22</sup>) Obviously, Concept 2 requires that the  $\text{Al}_2\text{O}_3$  layer does not sinter to the fiber in order to maintain the ease of sliding.

A desirable level of  $\Gamma_i$  could be achieved by using fugitive coatings as illustrated in Concept 3, Figure 1. In this case, the debond layer consists of a C +  $\text{Al}_2\text{O}_3$  mixture wherein the carbon may be subsequently eliminated by oxidation to yield a highly porous oxide. This provides discrete bridging between the fiber and the outer coating. Debonding occurs by fracture through the porous oxide<sup>20</sup> and the sliding resistance arises from the interaction of asperities on the debond surfaces. It is expected that  $\Gamma_i$  would depend on coating porosity, which may be varied through processing.<sup>20</sup>

## 2. MATERIALS AND PROCESSING

Sapphire fibers with c-axis orientation and  $\sim 130\ \mu\text{m}$  diameter were produced at Saphikon, Inc., by the Edge-defined Film-fed Growth (EFG) process. These were cut into 6 cm segments, washed in an ultrasonically stirred acetone bath to remove the sizing and subsequently heat treated at  $550^\circ\text{C}$  for 2 hrs to eliminate any combustible residue on the surface.

Three debond coatings were applied: carbon black (pyrolytic), colloidal carbon and a  $\text{C} + \text{Al}_2\text{O}_3$  mixture as a precursor to the porous oxide coating. Carbon black was simply deposited by passing fibers through an acetone flame, generating a sub-micron coating thickness. Both the colloidal carbon and the  $\text{C} + \text{Al}_2\text{O}_3$  slurries were applied by dipping, resulting in coatings with final thicknesses ranging from 1 to  $3\ \mu\text{m}$ . In the first case, fibers were dipped once into a commercially available colloidal carbon suspension (from Ted Pella, Inc.). The latter was diluted with isopropyl alcohol until its viscosity was suitable to create a uniform coating approximately  $1\ \mu\text{m}$  thick after drying. The  $\text{C} + \text{Al}_2\text{O}_3$  slurries were prepared by mixing graphite powder  $\leq 1\ \mu\text{m}$  in size (from Aldrich Chemical Co.) into an alumina sol (DISPAL 23N4-20, from Vista Chemical Co.), which had been diluted to the desired  $\text{Al}_2\text{O}_3$  content and mixed with sufficient nitric acid to adjust the pH to  $\sim 4$ . The ratios of alumina sol to graphite powder were varied from 6% to 10% to change the coating porosity after oxidation. (The exact porosity content of each coating was not determined, but the changes were inferred from fiber push-out tests which show an increase in interfacial fracture energy as the  $\text{Al}_2\text{O}_3$  content is increased. One should also note that the carbon must remain in the coating until composite densification is completed. Otherwise, the porous alumina layer would densify during the subsequent HIP'ing. This paper confines its attention to the 10% alumina porous coatings, deferring the issue of coating porosity to a future publication.) All dipped fibers were air dried prior to applying the second coating.

The outer coating was also applied by dipping the previously coated fibers into a slurry consisting of  $0.18\text{ }\mu\text{m}$   $\alpha\text{-Al}_2\text{O}_3$  particles (AKP-50 from Sumitomo Chemical Co.) and the commercial alumina sol cited above. Dispersion of the powders was promoted by adjusting the pH of the sol between 2-3.4 and by using ultrasonic agitation. The viscosity was later adjusted by adding de-ionized water and nitric acid to maintain the pH in the range specified. After the second coating, the fibers were air dried, heated in vacuum to  $500\text{-}600^\circ\text{C}$  and held for one hour to eliminate the volatile constituents, and finally heated to  $1350^\circ\text{C}$  in Ar and held for two hours to densify the outer  $\text{Al}_2\text{O}_3$  layer. The outer coating was typically  $5\text{-}10\text{ }\mu\text{m}$  thick and  $\sim 97\%$  dense. Further densification by increasing the sintering temperature was not attempted out of concern for the possible degradation of the fiber by reaction with the carbon. Studies reported elsewhere<sup>23</sup> have shown that the coating performs effectively as a diffusion barrier in spite of the small amount of residual porosity.

Coated fibers were carefully incorporated into a slurry of  $\gamma\text{-TiAl}$  powder (rapidly solidified Ti-48Al-2.3Nb-0.5Ta with an average particle size of  $\sim 120\text{ }\mu\text{m}$ , prepared by Pratt and Whitney Laboratories) in deionized water to produce green compacts with fiber volume fractions of  $\sim 20\text{-}30\%$ . The green compacts were canned, degassed in vacuum at  $300^\circ\text{C}$ , sealed and hot isostatically pressed in argon at  $276\text{ MPa}$  and  $1066^\circ\text{C}$  for 4 h. Typical cross sections of the resulting composites are shown in Figure 2. More extensive microstructural analysis is reported elsewhere.<sup>23</sup>

To simulate the potential effects of service environments on the coatings, slices of the various composites were exposed to heat treatments in air at either  $800^\circ\text{C}$  for one hour or  $1000^\circ\text{C}$  for 24 hours, and the interface characteristics re-evaluated.

### 3. TESTING PROCEDURES AND ANALYSIS

Push-out tests were conducted to determine the interfacial characteristics associated with each of the three double coatings using an apparatus and procedures described in detail elsewhere.<sup>24</sup> Thin wafers of the composite 400  $\mu\text{m}$  thick were cut perpendicular to the fiber axis and their surfaces were subsequently polished to a 1  $\mu\text{m}$  diamond finish. Each wafer was then mounted on a support base so that a fiber was positioned directly above a 220  $\mu\text{m}$ -diameter hole in its center. The fiber was pushed from the top into the hole using a 100  $\mu\text{m}$  diameter SiC cylindrical indenter. The fiber displacements were monitored by a transducer placed at the bottom of the specimen.

Push-out curves typically show a linear elastic loading region, followed by stable debond propagation down the fiber/matrix interface.<sup>24</sup> The debond crack becomes unstable at  $\sim 1.5$  fiber radii from the bottom side of the specimen resulting in a load drop,  $\Delta P$ . (The debond instability was determined from finite element calculations carried out by Liang and Hutchinson<sup>25</sup>.) Thereafter, the fibers slide relative to the matrix. The debond load drop,  $\Delta P$ , is related to the debond energy,  $\Gamma_i$ , by<sup>25</sup>

$$\Delta P = \left[ 2 \sqrt{\frac{\Gamma_i E_f}{B_2 R}} e^{3\mu B_1} + \frac{(\tau_0 + \mu n_R)}{\mu B_1} (e^{-3\mu B_1} - 1) + p_R \right] e^{2\mu B_1 h/R} \quad (1)$$

where

$$B_1 = \frac{\nu_f E}{(1 - \nu_f) E + (1 + \nu) E_f}$$

and

$$B_2 = 1 - 2\nu_f B_1$$

$E$  is the Young's modulus,  $\nu$  is Poisson's ratio, subscript  $f$  refers to the fiber,  $h$  is the section thickness,  $\mu$  is a coefficient of friction,  $R$  is the fiber radius,  $p_R$  is the residual axial compressive stress in the fiber,  $n_R$  is the residual radial compressive stress at the interface, and  $\tau_0$  is the shear strength at zero normal stress (mechanistically related to an asperity pressure that arises during fiber sliding).<sup>22,24,26-29</sup>

The nominal sliding strength,  $\tau$ , at push-out displacement,  $d$ , is obtained from the instantaneous load,  $P$ , using

$$\tau = \frac{P}{2\pi R(h-d)} \quad (2)$$

In general, the sliding stress is not constant, because of asperity effects and wear processes.<sup>22,26-28</sup> Consequently, the sliding stress just after the debond load drop is used for comparing coatings. It is also useful to compare the coefficients of friction for each of the sliding interfaces. For this purpose, since the fiber/matrix asperities are in near perfect registry at the onset of sliding ( $\tau_0 = 0$ ),  $\mu$  is given by

$$\mu = \frac{R}{2B_1 h} \ln \left( \frac{P/\pi R^2}{n_R - B_1 p_R} \right) \quad (3)$$

The stresses  $p_R$  and  $n_R$  are evaluated from the thermal expansion mismatch, using the formulae summarized in reference [30]. For this study, it is assumed that the axial mismatch pressure,  $p_R$ , is relieved by debonding. The relevant material properties used in Equations (1) through (3) are included in Table I.



#### 4. RESULTS AND DISCUSSION

Typical push-out curves for the as-HIPed specimens accompanied by SEM micrographs in Figure 3 reveal correspondences between surface texture and sliding stress. The *carbon black* interface (Figure 3a) exhibits a very small debond load drop and a relatively high sliding stress. Recall that this is the *thinnest* of the three debond coatings and will be most affected by the underlying fiber surface roughness. This feature is demonstrated in Figure 4, where the sinusoidal modulations in the load displacement trace are clearly visible. Prior work has shown that the wavelengths noted during sapphire fiber push-out are identical to those of the fiber surface roughness.<sup>22</sup> The fiber surface roughness was measured both by microscopy and profilometry, wherein profiles taken along the fiber axis showed a sinusoidal surface modulation with a predominant 10  $\mu\text{m}$  wavelength and a peak to peak amplitude of 0.3  $\mu\text{m}$ . Notably, the load modulations shown in Fig 4 also display a 10 micron wavelength. Push-outs for the *colloidal carbon* coating (Figure 3b) indicate a small debond load drop—though larger than that of the carbon black coating—and a low sliding stress. The low  $\tau$  arises because the relatively thick and brittle C coating provides a fracture propagation path that does not necessarily mimic the underlying fiber geometry. The C+10%  $\text{Al}_2\text{O}_3$  inner coating (Figure 3c) has the largest debond load drop, because the associated alumina network provides a bonded framework between the fiber and outer alumina coating (Fiber/matrix bonding is inferred from the relatively large debond load drops and is corroborated by the rough appearance of the debonded interface). However, once sliding commences, the sliding stress has an intermediate magnitude.

Push-out curves obtained after high-temperature oxidation exposure, plotted as bands in Figure 5 to show the range of variability, provide further insight into the coating performance. Experimental results indicate that these treatments eliminate the

carbon from the inner (debond) layers and, after prolonged exposure at 1000°C, reveal changes in the interfacial properties consistent with the development of discrete bonding between the fiber and the outer Al<sub>2</sub>O<sub>3</sub> coating.<sup>31</sup> The C+10% Al<sub>2</sub>O<sub>3</sub> coating transforms to a porous alumina layer during heat treatment, showing a significant drop in sliding stress after 1 hour at 800°C. Continued heat treatment results in an increase in sliding stress, Figure 5a. In the *carbon black* system, oxidation slightly relieves the mismatch pressure, such that the 1 hour heat treatment at 800°C reduces the sliding stress—Figure 5b. However, further exposure at 1000°C for 24 hours increased variability in the sliding behavior, attributed to some sintering of the outer Al<sub>2</sub>O<sub>3</sub> coating to the fiber. The *colloidal carbon* system exhibited characteristics similar to both the carbon black and porous alumina systems, Figure 5c, consistent with a reduction in the clamping pressure after an 800°C heat treatment in air. Treatments in air at 1000°C resulted in an increased variability in the sliding stress. The major difference between the coatings is in the fracture energy of the interface and the magnitude of the initial sliding stress.

Values of the debond and sliding parameters for each of the as-HIPed systems,  $\Gamma_i$ ,  $\tau$  and  $\mu$ , obtained from Equations (1–3) are summarized in Table II. Since the interfacial fracture energies,  $\Gamma_i$ , are less than the aforementioned  $\sim 2 \text{ J/m}^2$ , each of these coatings satisfies the debond criterion proposed by He and Hutchinson [17]. A bar chart comparison of  $\tau$  before and after heat treatment, Figure 6, facilitates comparisons and validates the features outlined above. For this purpose,  $\tau$  was computed at the peak load in order to emphasize effects of interfacial sintering during heat treatment. A statistical comparison of the results (using SYSTAT, a commercially available statistical analysis software package) demonstrates that heat treatment at 800°C for 1 hour significantly affects the sliding stress for both *carbon* coatings, but has no statistically significant effect on the C+10% Al<sub>2</sub>O<sub>3</sub> coating. However, continued heat treatment, at 1000°C for 24 hours, introduces substantial variability, resulting in similar sliding

behavior for all systems. Preliminary fracture tests conducted on beam specimens, both before and after heat treatment, revealed substantial fiber pull-out, e.g. Figure 7.

## 5. CONCLUDING REMARKS

Double coating concepts for sapphire fibers in  $\gamma$ -TiAl were implemented and evaluated using fiber push-out tests. These double coating systems employ an inner, debond coating of either carbon or carbon+alumina that provides a path for interfacial crack propagation and also protects the fiber during consolidation. These inner coatings are, in turn, protected from the matrix by a second, diffusion barrier consisting of dense alumina. Each coating system was found to permit debonding and sliding, in accordance with accepted criteria for strengthening and toughening. Thus, the double coating concept had been demonstrated to be viable for intermetallic-matrix composite systems.

Results from oxidation studies show distinct interfacial differences associated with removal of the inner carbon coatings. One effect, which is beneficial, concerns reduction of the mismatch strain, causing a decrease in sliding stress. Furthermore, when using fugitive coatings, fiber roughness plays a key role by allowing asperity interlock after the coating has oxidized. The second effect may be deleterious since, in the absence of the inner coating, the outer  $\text{Al}_2\text{O}_3$  layer may sinter to the sapphire fiber. This not only changes the debond characteristics of the interface, but may also change the *in-situ* fiber strength, both of which affect composite toughness. These deleterious effects can be controlled, however, by using a highly porous  $\text{Al}_2\text{O}_3$  network within the inner coating. Alternately, the outer coating may be replaced by another oxide which is less prone to sintering with sapphire.

## ACKNOWLEDGMENTS

This work was sponsored by the Defense Advanced Research Projects Agency under contract MDA972-90-K-0001, monitored by Dr. W. Coblenz, and the University Research Initiative grant N-00014-92-J-1808 monitored by Dr. S.G. Fishman. The authors would like to thank Dr. D.G. Backman of General Electric for making available the sapphire fibers, and Dr. M.L. Emiliani of Pratt and Whitney Laboratories for providing the TiAl powders. Technical assistance of Dr. Y.G. Deng and Mr. M. Zanner in the preparation of materials is gratefully acknowledged.

Table I  
Material properties

Property	$\gamma$ -TiAl	Sapphire Fiber
Young's Modulus, E (GPa)	173	434
Poisson's ratio, $\nu$	0.33	0.27
thermal expansion coefficient, $\alpha$ ( $\mu\text{m}/\text{m K}$ )	13	9

Table II  
Comparison of Interfacial Properties For Each Coating

Sample	$\Gamma_i$ (J/m <sup>2</sup> )	$\tau$ (MPa)	$\mu$
carbon black/alumina	0.01	100	0.23
colloidal carbon/alumina	0.01	40	0.09
porous alumina/alumina	0.05	75	0.09

## REFERENCES

1. A. G. Evans, F. W. Zok and J. Davis, "The Role of Interfaces in Fiber-Reinforced Brittle Matrix Composites," *Composites Science and Technology*, **42**, pp. 3-24, 1991.
2. R. J. Kerans, R. S. Hay, N. J. Pagano and T. A. Parasarathay, "The Role of the Fiber-Matrix Interface in Ceramic Composites," *Cer Bull*, Vol 68, No. 2, 1989.
3. A. G. Evans and D. B. Marshall, "The Mechanical Behavior of Ceramic Matrix Composites," *Acta Metall.*, 37[10] 2567-83 (1989).
4. R. Y. Kim and N. Pagano, "Crack Initiation in Unidirectional Brittle Matrix Composites," *J. Am. Ceram. Soc.*, 74[5] 1082-90 (1991).
5. A. Pryce and P. Smith, "Modelling the Stress/Strain Behaviour of Unidirectional Ceramic Matrix Composite Laminates," submitted to *J. Mater. Sci.*, (1991)
6. R. W. Rice, J. R. Spann, D. Lewis and W. Coblenz, "The Effect of Ceramic Fiber Coatings on the Room Temperature Mechanical Behavior of Ceramic Fiber Composites," *Ceramic Eng. Sci. Proc.*, 5 p 614 (1984).
7. H. C. Cao, E. Bischoff, O. Sbaizero, M. Ruhle, A. G. Evans, D. B. Marshall and J. J. Brennan, "Effect of Interfaces on the Properties of Fiber-Reinforced Ceramics," *J. Am. Ceram. Soc.*, 73[6] 1691-99 (1990).
8. K. M. Prewo and J. J. Brennan, "High Strength Silicon Carbide Fiber-Reinforced Glass Matrix Composites," *J. Mater. Sci.*, 15[2] 463-68 (1980).
9. D. Beyerle, S. M. Spearing, F. W. Zok and A. G. Evans, "Damage and Failure in Unidirectional Ceramic Matrix Composites," *J. Am. Ceram. Soc.*, in press.
10. W. Curtin, "Theory of Mechanical Properties of Ceramic-Matrix Composites," *J. Am. Cer. Soc.*, 74(11), 2837 (1991).
11. S. Ochai and K. Osamura, *Met Trans* 21A (1991) 971.

12. M. Y. He, A. G. Evans and W. A. Curtin, "The Ultimate Tensile Strength of Metal and Ceramic-Matrix composites," to be published
13. S. Jansson, H. E. Deve and A. G. Evans, "The Anisotropic Mechanical Properties of a Ti Matrix Composite Reinforced with SiC Fibers," *Met Trans A*, Vol. 22A, pp. 2973-2984, 1991.
14. M. D. Thouless and A. G. Evans, *Acta Metall.* 36 517 (1988).
15. M. Sutcu, *Acta Metall.*, 37 651 (1989).
16. J. Porter, private communication.
17. M-Y He and J. W. Hutchinson, *Int. J. Solids and Structures*, Vol. 25, No. 9, pp 1053-1067 (1989).
18. M. Isawa and R. C. Badt, Structures and Properties of MgO and Al<sub>2</sub>O<sub>3</sub> Ceramics, 767-779, ACS, Columbus, OH.
19. A. G. Evans, A. Bartlett, J. Davis, B. Flinn, M. Turner and I. Reimanis, *Scripta Met et Mat*, 25 (1991) 1003.
20. J. B. Davis, J.P.A. Lofvander, A. G. Evans, E. Bischoff and M. L. Emiliani, "Fiber Coating Concepts for Brittle Matrix Composites," submitted to *J. Am Cer Soc.*
21. T. Mah, K. Keller, T. A. Parthasarathy and J. Guth, "Fugitive Interface Coatings in Oxide-Oxide Composites: A Viability Study," *Ceram. Eng. Sci. Proc.*, 12[9-10] pp. 1802-1815 (1991).
22. T. J. Mackin, J. Y. Yang and P. D. Warren, "The Influence of Fiber Roughness on the Sliding Behavior of Sapphire Fibers in Glass and TiAl Matrices," *J. Amer. Cer. Soc.*, Vol. 75, 12, 1992.
23. C. H. Weber, J. Y. Yang, J. P. A. L, J. Y. Yang, J. P. A. Lofvander, C. G. Levi and A. G. Evans, "The Creep and Fracture Resistance of  $\gamma$ -TiAl Reinforced with Al<sub>2</sub>O<sub>3</sub> Fibers," to be published.

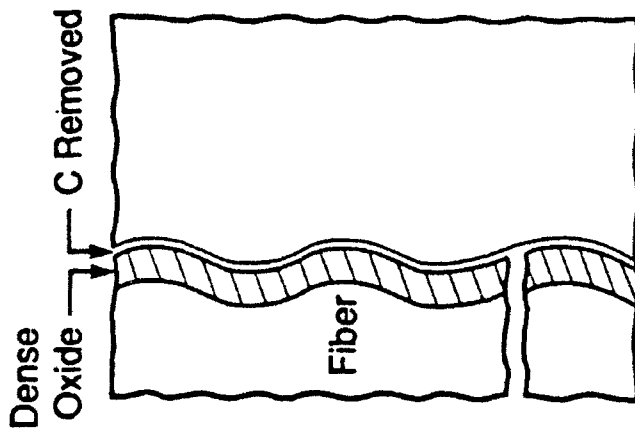
24. P. D. Warren, T. J. Mackin and A. G. Evans, "Design, Analysis and Application of an Improved Push-Through Test for the Measurement of Interface Properties in Composites," *Acta Metall et Mater.*, 40[6] pp 1243-49, 1992.
25. C. Liang and J. W. Hutchinson, "Mechanics of the Fiber Pushout Test," to be published.
26. T. J. Mackin, P. D. Warren and A. G. Evans, "Effects of Fiber Roughness on Interface Sliding in Composites," *Acta Metall et Mater.*, 40[6] pp 1251-57, 1992.
27. P. D. Jero and R. J. Kerans, "The Contribution of Interfacial Roughness to Sliding Friction of Ceramic Fibers in a Glass Matrix," *Scripta Met.* 25 (1991) 2457.
28. P. D. Jero, R. J. Kerans and T. A. Parthasarathy, "Effect of Interfacial Roughness on The Frictional Stress Measured Using Push-out Tests," *J. Am. Cer. Soc.*, 74(11), 2793, 1991.
29. W. C. Carter, E. P. Butler and E. R. Fuller, Jr., "Micro-Mechanical Aspects of Asperity-Controlled Friction in Fiber Toughened Ceramic Composites," *Scripta Met et Mat.*, Vol 25, pp. 579-584, 1991.
30. B. Budiansky, J. W. Hutchinson and A. G. Evans, *J Mech Phys Solids*, 2 (1986) 167.
31. D. J. Green, C. Nader and R. Brezny, "The Elastic Behavior of Partially-Sintered Alumina," *Sintering of Advanced Ceramics*, *Ceramic Transactions*, Vol. 7, edited by C. A. Handwerker, J. E. Blendell and W. Kaysser, ACERS, pp 345-356, 1990.



## FIGURE CAPTIONS

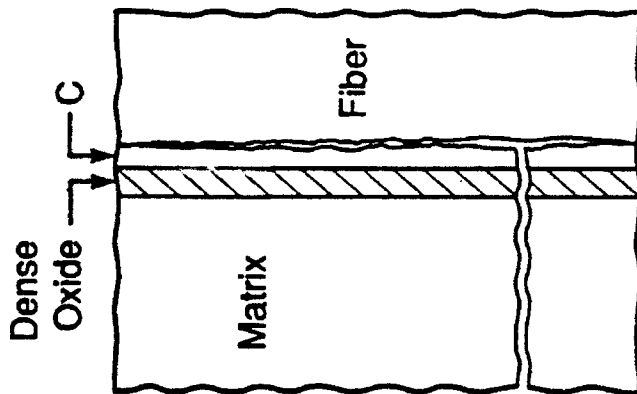
- Figure 1. Schematic representation of three double coating concepts for sapphire fibers in  $\gamma$ -TiAl matrix composites.
- Figure 2. Representative cross sections of double coated sapphire fibers: a) General view of a composite with 20-30 vol% of double coated fibers, b) Carbon black/dense alumina, c) colloidal carbon/dense alumina, and d) C+10%  $\text{Al}_2\text{O}_3$  precursor to porous alumina followed by dense alumina.
- Figure 3. A comparison of representative push-out curves and associated micrographs of pushed fibers with: a) carbon black debond coating, b) colloidal graphite debond coating and c) carbon+alumina debond coating. In all cases the fibers are covered with a layer of dense alumina that remains bonded to the matrix.
- Figure 4. Fiber roughness appears as a sinusoidal modulation in the push-out curve. Note the  $\sim 10\text{ }\mu\text{m}$  wavelength characteristic of the sapphire fiber surface topography.
- Figure 5. Range of results for push-out tests, comparing the behavior of as-HIP'ed and heat treated specimens. (a) carbon black, (b) colloidal carbon, and (c) carbon+alumina debond coating. In all cases the carbon is eliminated during the oxidative heat treatment.
- Figure 6. Comparison of the peak sliding stress for each coating and each heat treatment condition as calculated from the tests illustrated in Figure 5. Means and standard deviations are derived from a minimum of 5 push-outs for each coating and heat treatment.
- Figure 7. Evidence of fiber pull-out after fracture testing (courtesy of Weber et al., [23]).

### Concept 1



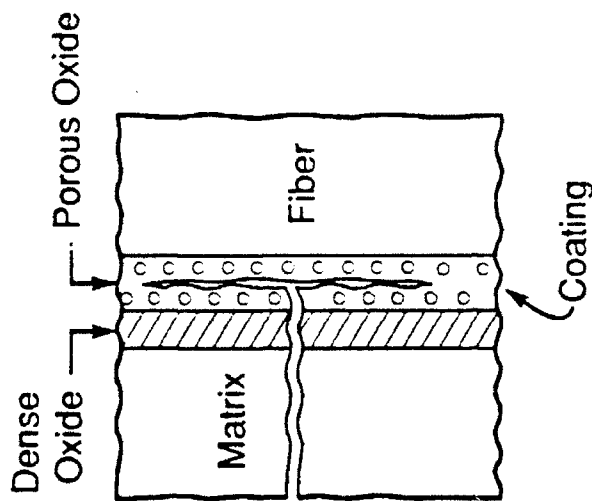
Carbon Coating and  
Dense  $\text{Al}_2\text{O}_3$   
(Mo,  $\omega$  also suitable  
for Inner Coating)

### Concept 2



Carbon Eliminated by  
Oxidation leaving gap  
between Fiber and  
Outer  $\text{Al}_2\text{O}_3$  Coating

### Concept 3



Porous Oxide  
and Dense  $\text{Al}_2\text{O}_3$

Figure 1

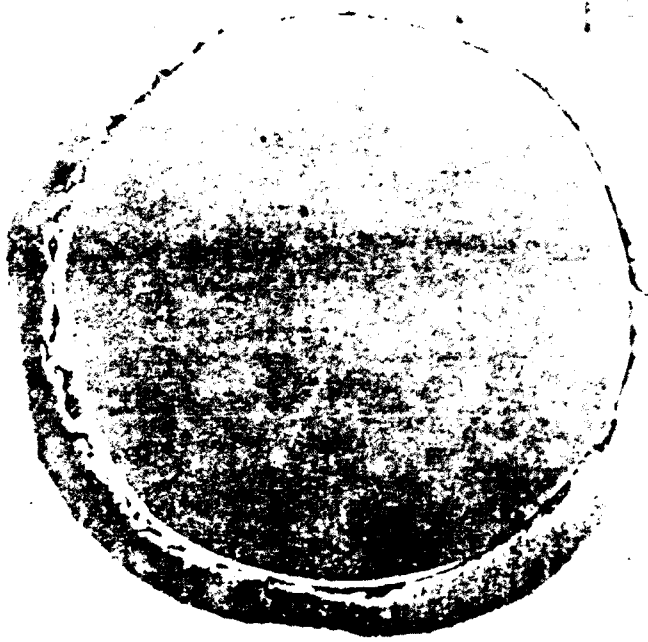
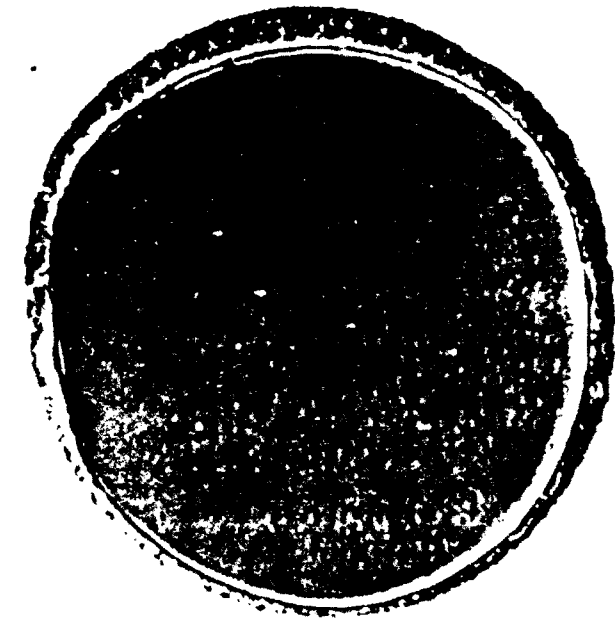
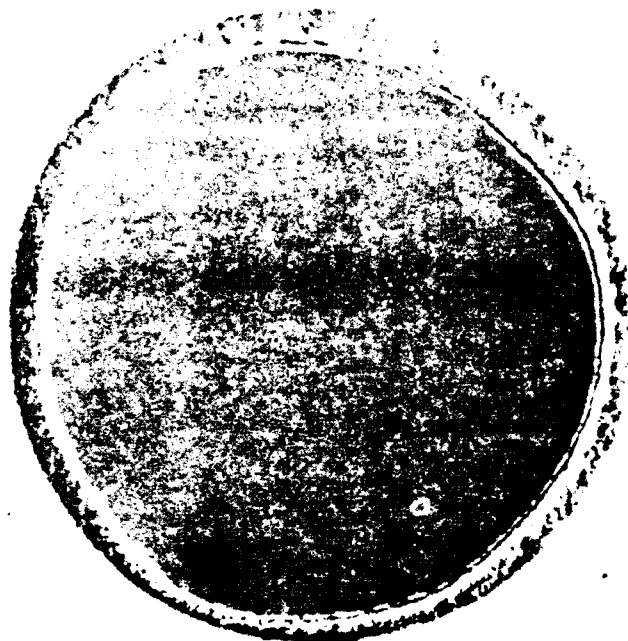
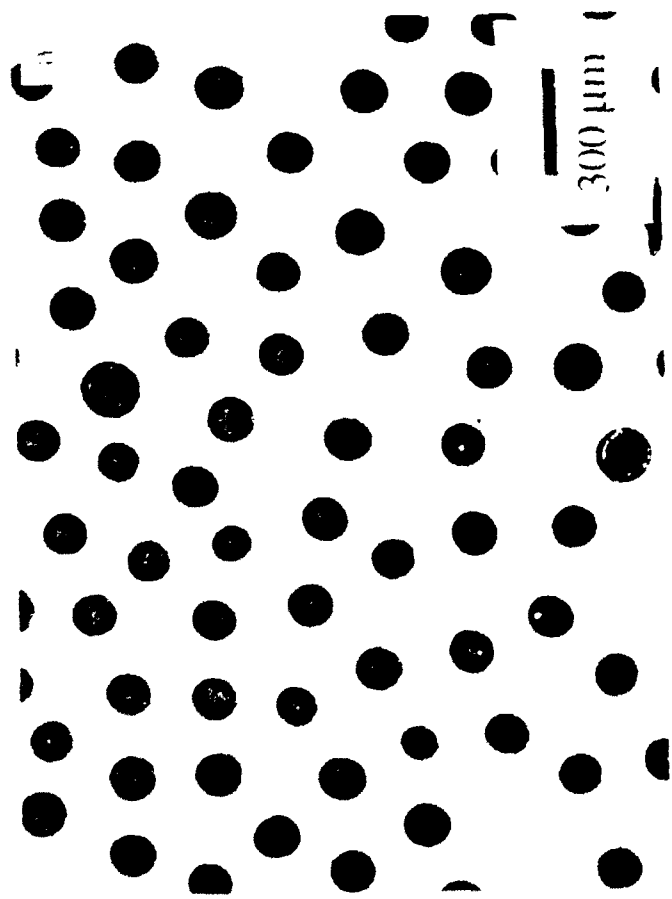


Figure 2

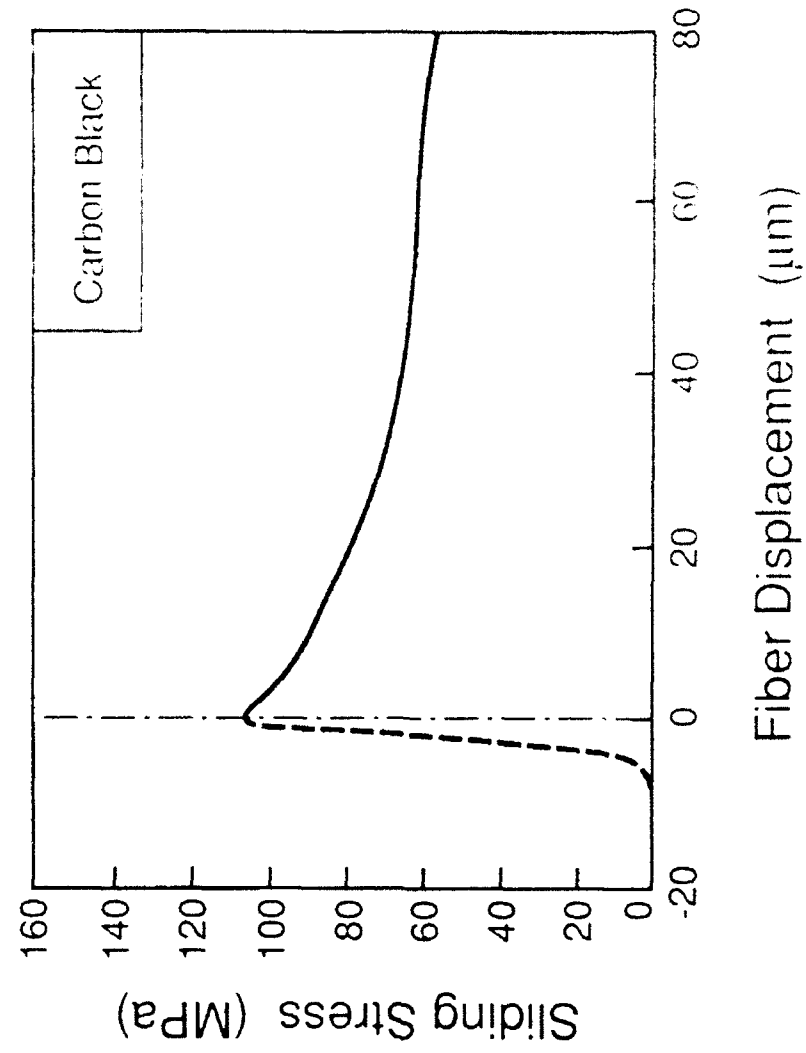


Figure 3 a

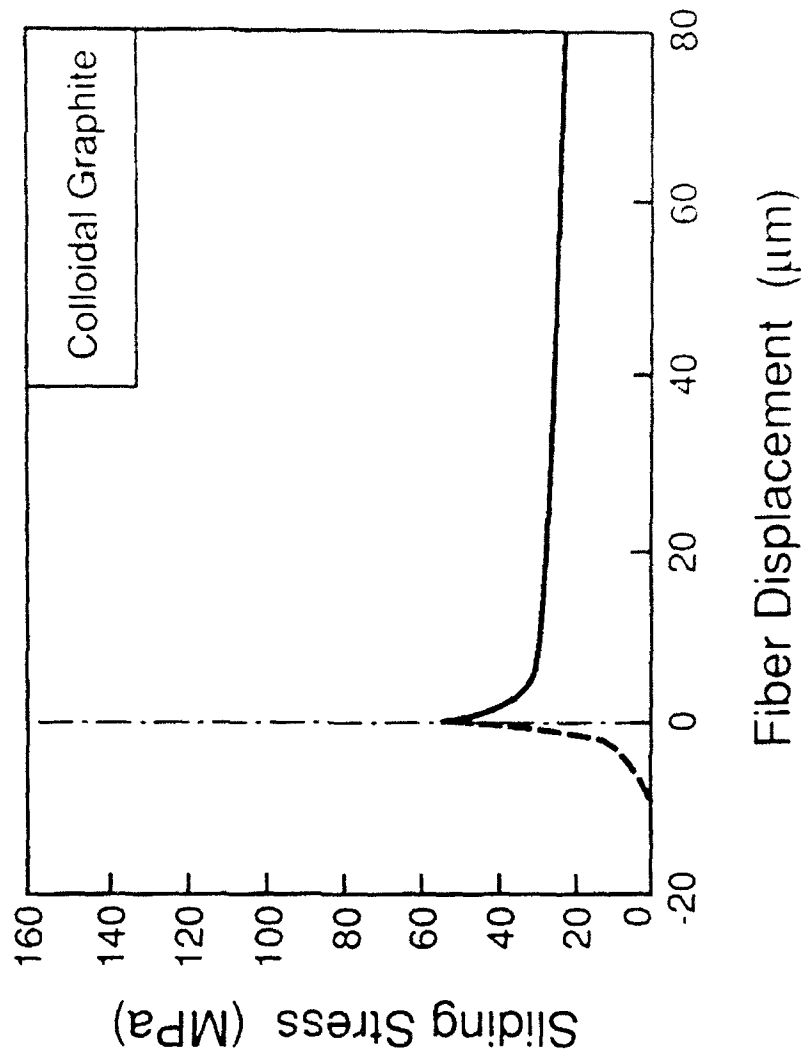


Figure 3b

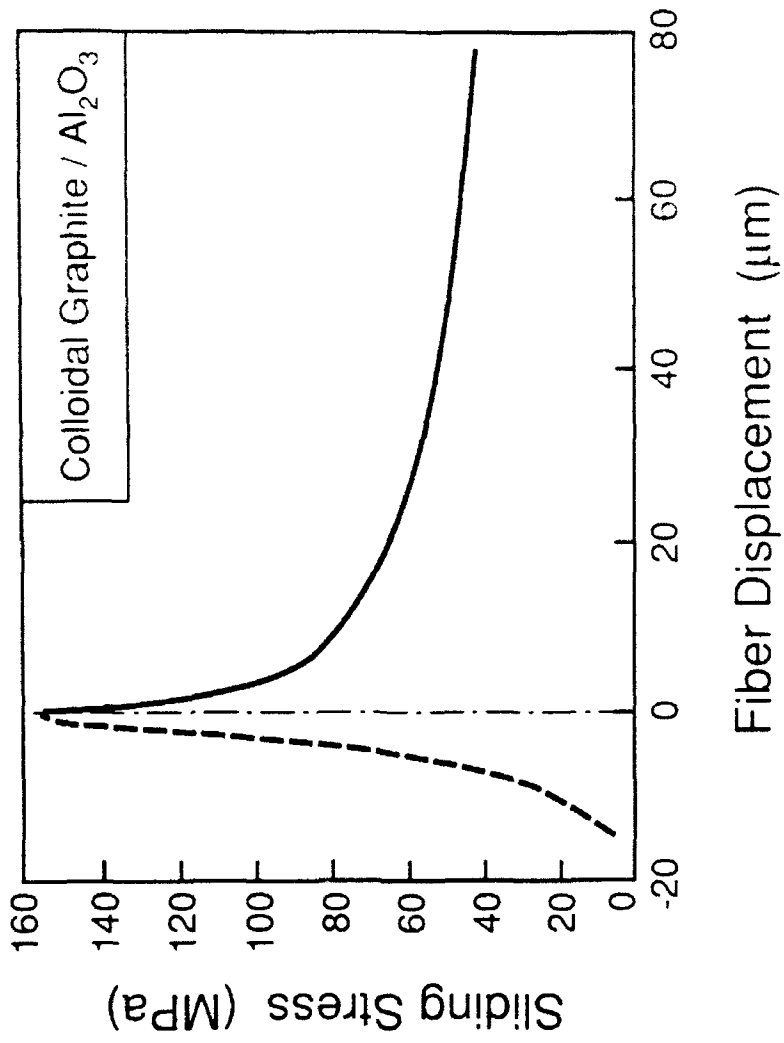


Figure 3c

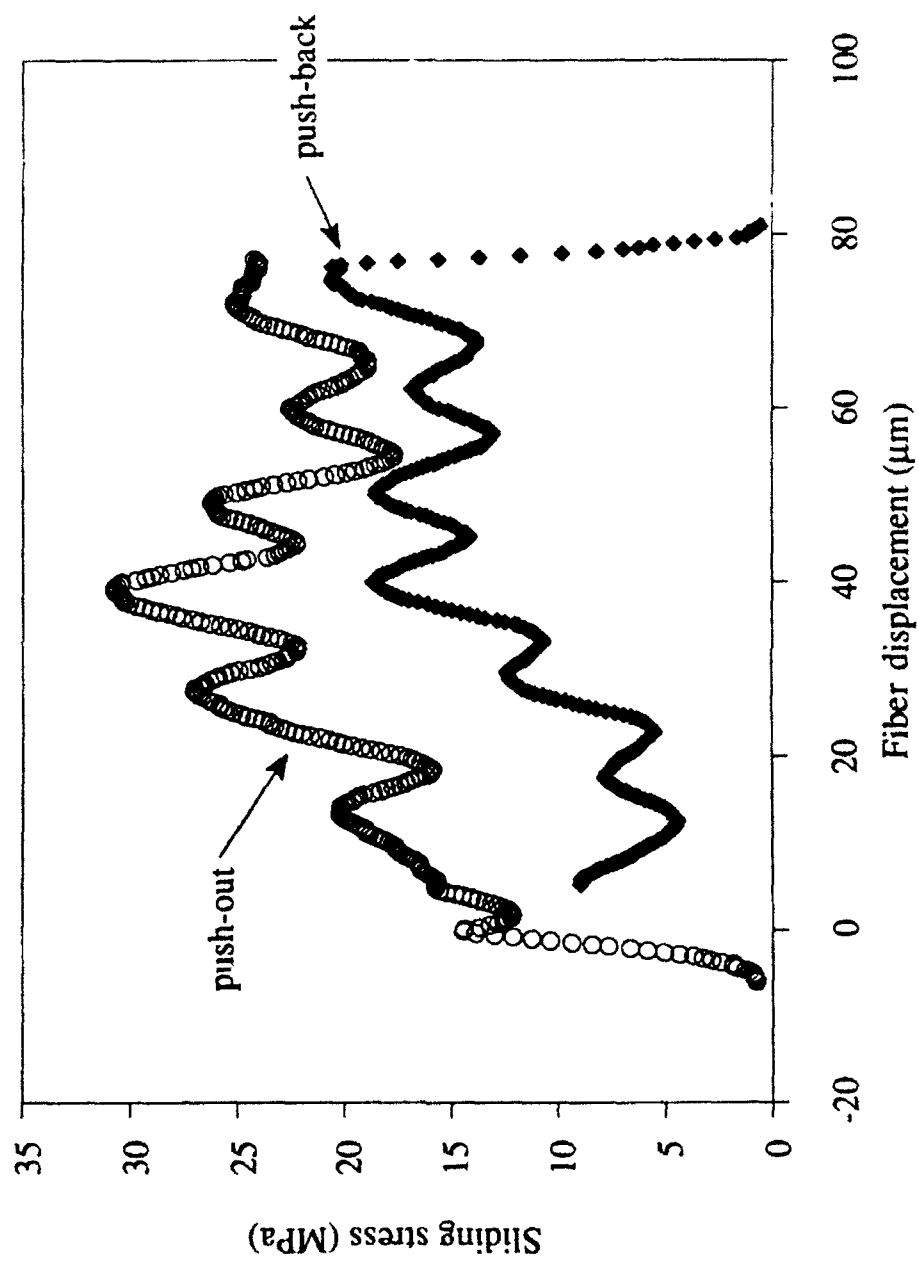


Figure 4

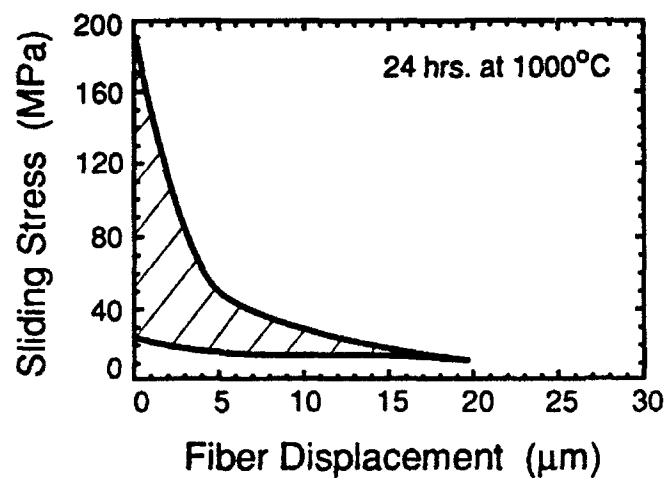
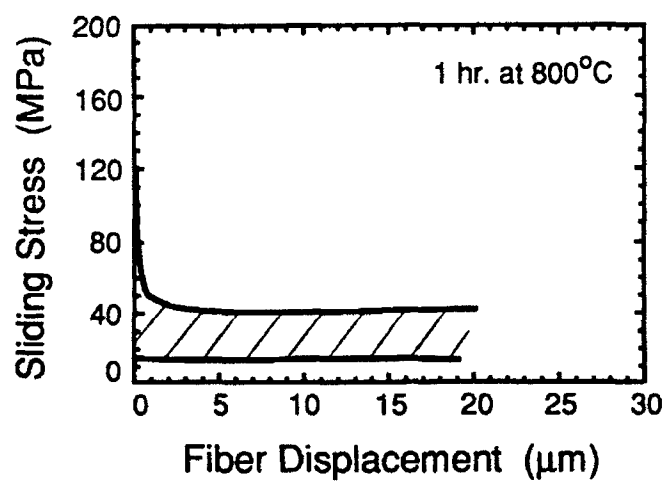
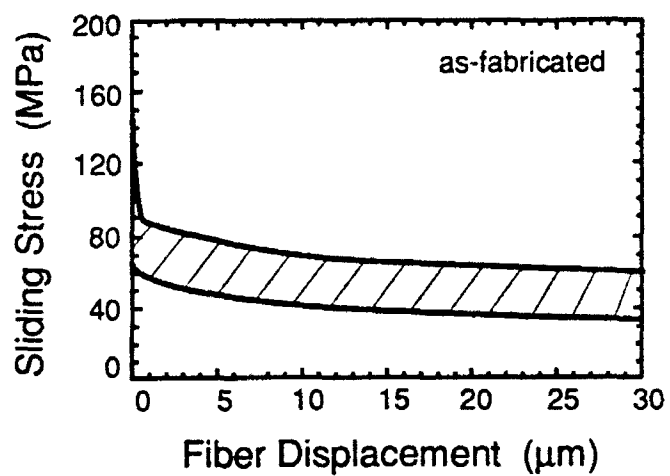


Figure 5a



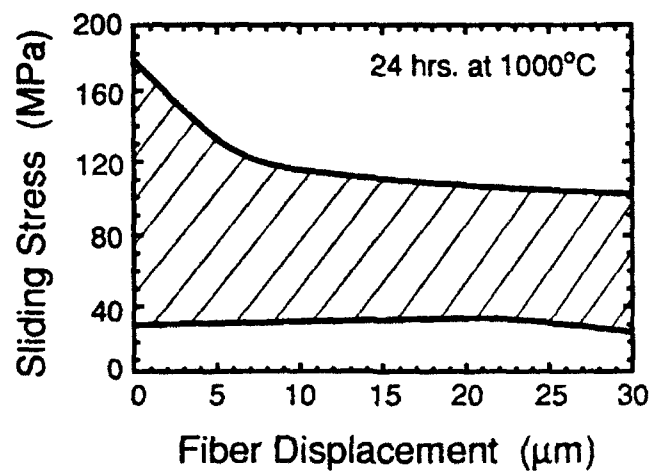
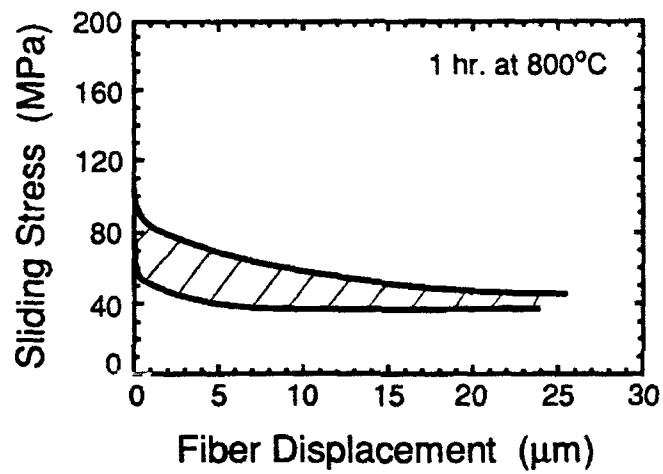
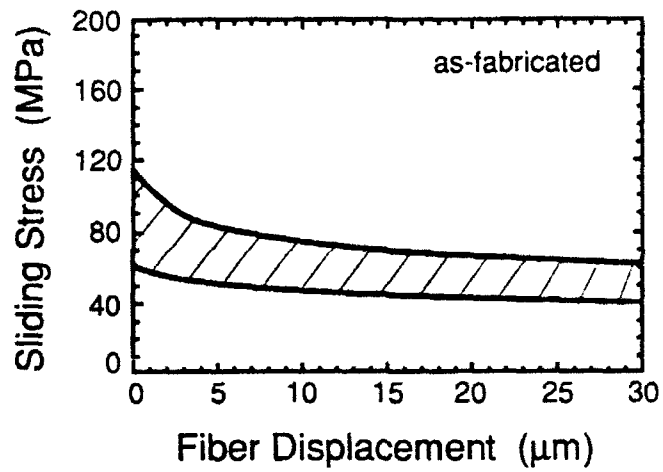


Figure 5b

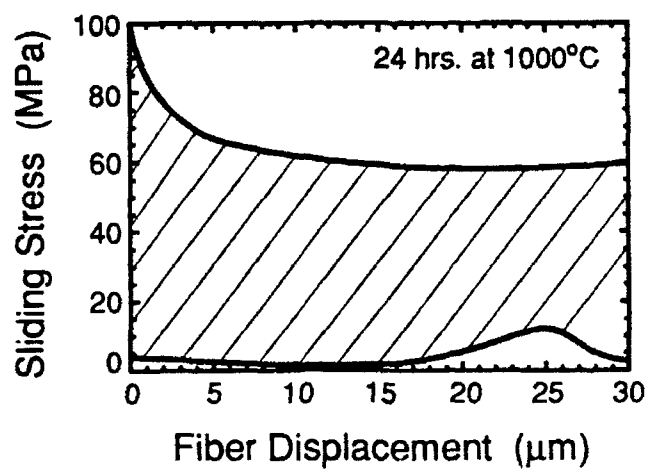
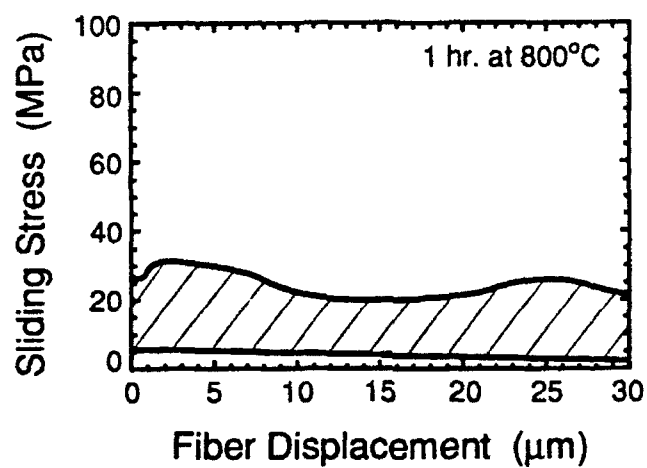
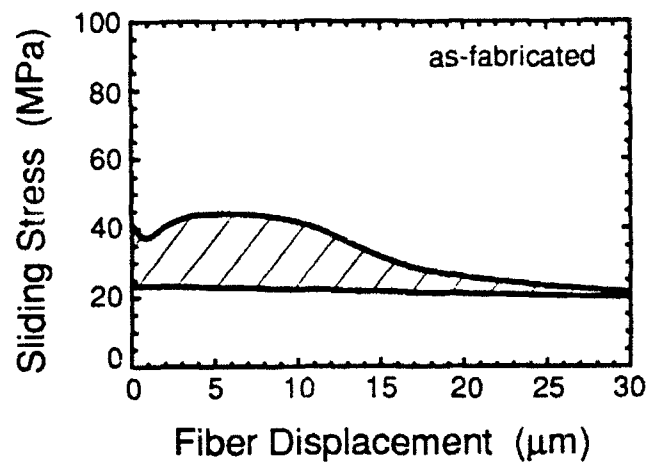


Figure 5c

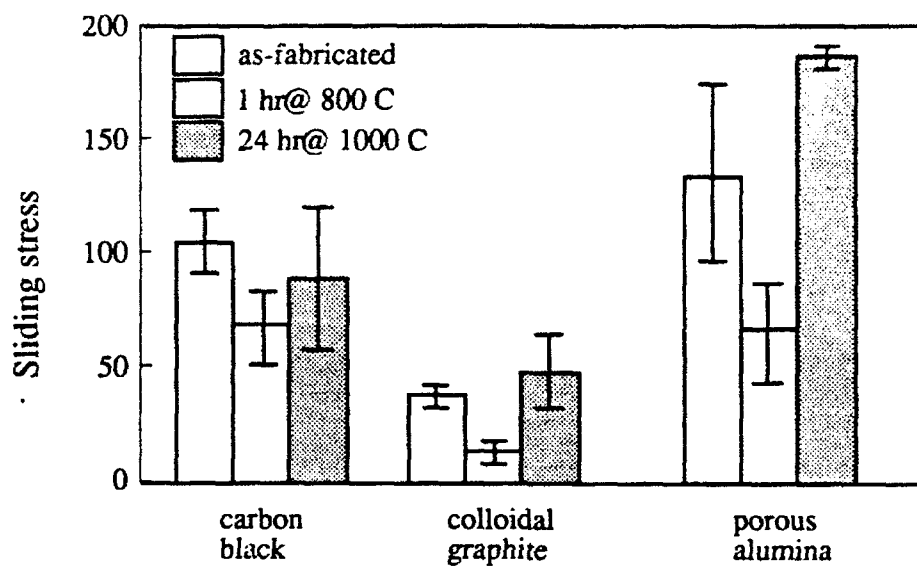


Figure 6



Figure 7

# MODELING THE FRACTURE OF FIBERS DURING METAL MATRIX COMPOSITE CONSOLIDATION

Dana M. Elzey and Haydn N. G. Wadley  
Department of Materials Science and Engineering  
University of Virginia  
Charlottesville, VA 22903

## ABSTRACT

Metal and intermetallic matrix composites reinforced with continuous fibers are increasingly being produced by the consolidation of plasma sprayed monotapes. Recently, there have been reports of significant fiber fracture during the consolidation, particularly when researchers have sought to use creep resistant matrix materials. A major cause of this fracture has been shown to be bending at monotape surface asperities (J.F. Groves, D.M. Elzey and H.N.G. Wadley, *Acta Metall. et Mater.*). The work reported here extends previous models of the densification process to predict the evolution of fiber fracture during hot isostatic or vacuum hot pressing. The model uses a statistical representation of the monotape roughness and computes bending forces when asperities are deforming (and the layup densifying) by plasticity, power law creep, or a combination of both. The model is used to identify where, during consolidation, damage occurs and how it is controlled by the surface roughness. Model predictions are compared with previously obtained experimental data for a Ti-24Al-11Nb/SCS6 composite.

## 1. INTRODUCTION

There is a growing interest in metal and intermetallic matrix composites reinforced with continuous fibers because of their superior specific modulus, strength and creep resistance[1,2]. For example, one emerging system based upon a Ti<sub>3</sub>Al+Nb matrix reinforced with 40 vol% of Textron's SCS-6 fibers has double the ambient specific strength of wrought superalloys and of some single crystal superalloys at 1100 C[3]. They are viewed as candidate materials for future aircraft engines and the airframes of high speed aircraft.

These composite systems are difficult to process by either traditional deformation processing methods because of the low ductility and high creep resistance of many of the matrix alloys or solidification pathways because of the reactivity between fiber and Ti-base matrices. Many novel methods are being investigated to bypass these limitations including foil-fiber-foil[4], powder cloth[5], vapor deposition[6] and various thermal spray processes such as induction coupled plasma deposition (ICPD)[7]. There is growing interest in the ICPD method because of the minimal contact time between the liquid alloy and the fiber. It results in sheets (usually called monotapes) containing a single layer of unidirectional fibers surrounded by matrix. These can be layed up and either hot isostatically or vacuum hot pressed (HIP/VHP) to densify and form a near net shape component. If this is done at low enough temperature there is only a small amount of further

fiber-matrix reaction.

Recent studies have identified the conditions required to achieve densification and the mechanisms by which this is accomplished[8]. It has led to the development of predictive models that are able to calculate the temporal evolution of density during an arbitrary temperature and pressure cycle. However experimental studies of monotape consolidation have identified the widespread occurrence of fiber fracture, a potentially serious drawback to this processing approach[9]. These studies showed that the extent of fiber fracture was sensitive to the conditions used to consolidate the monotapes. In particular they indicated that high consolidation temperatures and low densification rates greatly reduced the fiber damage, at least in the  $\text{Ti}_3\text{Al}+\text{Nb}/\text{SCS}-6$  system. Unfortunately, exposure of the monotapes to extended periods at high temperature during consolidation results in the dissolution of the fiber's protective coating, deleterious increases in the fiber-matrix sliding resistance[10] and eventually a loss in the fiber strength[11]. Therefore one needs to trade off fiber fracture, interfacial reaction severity and relative density in determining the best consolidation conditions.

This could be accomplished empirically but requires many tests and time consuming characterization with test materials that are expensive, sometimes irreproducible and often difficult to obtain. In addition, such an approach would have to be repeated each time the matrix alloy or the fiber or its coating were changed. This can add such great complexity and cost to the materials development process that it may undermine the incentive to continue a search for superior materials. Instead of this, we have resorted to a modeling approach that seeks to predict the fiber fracture rate for any (arbitrary) consolidation cycle. The development of this micromechanics model is presented here, together with the trends it predicts. It enables one to identify the properties of potential fiber and matrix systems that retard fiber fracture during consolidation. Together with the earlier model for densification, it has been explored for use in model-based, on-line simultaneous control of densification and fiber fracture[12].

## 2. PROBLEM DEFINITION

This study concentrates upon fiber damage during the consolidation of composite monotapes. The monotapes studied here were produced by winding silicon carbide fibers (Textron's SCS-6 fiber) on a drum, heating to  $\approx 850^\circ\text{C}$  and rotating/translating this under a stream of plasma melted  $\text{Ti}-14\text{wt}\%\text{Al}-21\text{wt}\%\text{Nb}$  ( $\text{Ti}-24\text{at}\%-11\text{at}\%\text{Nb}$ ) droplets forming a sample such as that shown in Fig. 1a[7]. The metal matrix composite monotapes produced this way are characterized by one, quite rough surface (the one built up by successive droplets), one, much smoother surface (the one

in contact with the mandrel) and internal porosity. A full characterization of this geometry can be found in [8,9] and a description of the deposit's microstructure (and evolution during the consolidation thermal cycle) in [13,14].

Near net shape components are subsequently produced by cutting and stacking the monotapes in a suitably shaped cannister or die (Fig. 1b) and subjecting them to a consolidation cycle (in a HIP or VHP) to eliminate porosity and cause diffusion bonding[8]. For sheet-like samples almost all the consolidation strain is accommodated by a reduction of thickness (widths and lengths show no appreciable strains) and so regardless of the process used, consolidation can be thought of as occurring under constrained uniaxial compression.

A number of potential mechanisms of fiber fracture can be envisioned (Fig. 2). Tensile stresses in the fiber could be generated because of the almost twofold higher thermal expansion coefficient of the matrix compared to the fiber[15]. A second possibility is that the crystallographic transformation of the metastable ICPD alloy on heating causes matrix dilatation and fiber stressing[13,14]. Both of these have been discounted because experiments in which the foils were thermally cycled (without an applied pressure) showed no fiber damage[9]. Additionally, fractures due to thermal mismatch can be quickly discounted because deposition of the alloy during monotape formation occurred at a temperature of 800–900° C[7]. Thus, at the start of consolidation the fibers would be in residual compression after cooling from the ICPD process, and go into tension only upon heating above the consolidation temperature (usually  $\leq 1050^{\circ}\text{C}$ ). A 100–200° C temperature increase could result in tensile fiber stress of 150–300 MPa, too little compared to measured fiber strengths of 3–4 GPa. A final possibility is that of nonuniform inelastic flow of the matrix as a result of a spatially nonuniform distribution of porosity; this leads to a nonuniform distribution of forces along the fiber, resulting in fiber distortion, i.e., axial, torsional or bend deformations. The experimental work of Groves et al[9] pointed to this as the source of the damage with the specific mechanism being fiber bending.

The effects due to nonuniform inelastic flow (i.e., fiber bending) can be thought to occur over two length scales. If on a macroscopic length scale (here, lengths greater than the fiber spacing), a region of the layup has a reduced fraction of matrix, fibers are induced to bend into this region as densifying matrix flow occurs. If this were sufficiently severe, the fibers might fail.

Microscopically (length scale on the order of a single fiber diameter or less), individual surface asperities on the rough foil surface may also result in fiber bending and fracture as shown by Fig. 3 reproduced from [9]. It is this latter mechanism which experimental observations indicate to be the most significant and the one for which we develop a model.

To be of greatest value, we require the model to predict the cumulative fiber damage during a consolidation cycle of arbitrary pressure and temperature profile. It must be statistical so that it fully captures the features of a randomly rough surface. The model should also be capable of generalization so that the effects of changing fiber properties or the matrix composition could be predicted. Lastly, since one would like to use the model for model-based process optimization and control, it should not require overly extensive computational requirements and in particular the use of human intervention during iterative application (i.e., it should not be a finite element model).

### 3. MODEL DEVELOPMENT

When two monotapes are pressed together fibers may bend (and possibly fracture) because they are loaded at only the contact points between the two foils (i.e., the points at which the asperities of one foil contact the other). As densification proceeds, and the foils are pressed more closely together, the number of contacting asperities increases and the average spacing decreases. Each fiber span suffers bending depending upon the span length and asperity height which are both statistical quantities determined by the surface roughness. Given an initial distribution of asperity spacings and heights, we seek to calculate the distribution of fiber deflections at any given density. The probability that a given fiber deflection causes fracture can be determined by calculating the maximum tensile stress (due to the bend deflection) and comparing this with the fiber strength distribution.

The density and densification rate, which could be obtained experimentally or predicted (given the applied pressure and temperature cycles) using the model described in [8], is presumed not to be affected by the bending and fracture of fibers. Conversely, we assume that the deflection of a given fiber segment is determined by the densification of the surrounding region. This amounts to saying that the number of fiber segments undergoing bending in a macroscopic volume of composite and the associated work required to do this, are insignificant relative to the work which must be expended to effect densification by inelastic matrix flow. Thus the current density and densification rate are used as input to the fiber fracture model; this results in a displacement controlled analysis of fiber bending/fracture rather than one based on equilibrium of applied and internal stresses.

The model's development is presented in two steps. First, we analyze (to obtain the fiber deflection) an isolated volume element consisting of a representative fiber segment and three contacting asperities causing bending. The fiber deflects due to the asperities' resistance to



deformation. The unit cell analysis results in a nonlinear differential equation relating the current density and densification rate (inputs to the model obtained using the results of [8]) to the fiber deflection (the model's output). The second step combines the unit cell response with a statistical model of a rough surface to calculate the distribution of fiber deflections (and therefore the probability of fiber fracture) in the macroscopic body.

### 3.1 Single Fiber Segment Analysis

Fig. 4 illustrates a typical fiber segment forced into three-point bending by asperity contacts. The fiber segment and associated asperities form a unit cell with a length,  $\ell$ , defined by the distance between contacting asperities, and a height,  $2 \cdot z(t)$  where  $z(t)$  is the current nominal thickness of a compressed foil. The thickness changes with time due to densification of the layup. If  $D$  and  $z$  are the current density and thickness, and  $D_0$  and  $z_0$  the initial values, then by conservation of mass,  $z = z_0 \cdot D_0 / D$  which can be calculated using the previously developed model for densification[8].

The initial dimensions of the unit cell to be analyzed are given by  $\ell$ , the distance between adjacent contacts, and by  $2h$ , where  $h$  is the undeformed asperity height. Both  $\ell$  and  $h$  vary statistically for a rough surface and are thus treated as random variables, but to begin we consider just one combination of these. The fiber segment is taken to be cylindrical and to remain elastic under all conditions. The asperities are treated as deforming plastically and by power-law creep. All asperities are assumed to have the same radius, corresponding to the mean value (as determined from profilometer data).

A lumped parameter representation of the composite bend unit cell can be used to analyze the cell's uniaxial response (Fig. 5). The uniaxial viscoplastic behavior of the asperities is modeled using a linear plastic element with stiffness coefficient,  $k_p$ , in series with a nonlinear, viscous dashpot. The response of the fiber in bending is represented by a linear elastic spring of stiffness,  $k_s$ . Input is the cell height,  $z$ , as a function of time and the output is the deformed asperity height,  $y$ , which is related to  $z$  and the fiber deflection,  $v$  by

$$(1) \quad v = 2(z - y)$$

Elementary analysis of a cylindrical, elastic beam in simply-supported, three-point bending gives the force-deflection relation for the fiber as:

$$(2) \quad F = k_s v$$

where, for central loading,  $k_s$  is given by:

$$k_s = \frac{3\pi}{4} \cdot E_f \cdot \frac{d_f^4}{l^3}$$

in which  $E_f$  is the Young's modulus and  $d_f$  is the diameter of the fiber.

The bending force,  $F$ , arises from the asperities' resistance to deformation. Consider first the plastic response of an asperity. The yield condition can be written:

$$(3) \quad \sigma \geq \beta \cdot \sigma_y$$

where  $\sigma$  is the average stress at the contact,  $\sigma_y$  is the uniaxial yield strength of the matrix obtained from a tensile test and  $\beta$  is a concentration factor ( $\beta > 1$ ). This factor accounts for the additional effort needed to overcome the elastic constraint of material surrounding the plastic zone, which forms within the interior of spherical bodies in contact [16,17]. Recent work [16] has shown  $\beta$  to be dependent upon the degree of deformation, reaching a maximum value of about 3 and then decreasing for a perfectly plastic material. For the case of Ti-24Al-11Nb, which undergoes work hardening during blunting,  $\beta$  can be approximated by  $\beta = 3$  over the range of densities concerned ( $D_0 \leq D \leq 0.9$ ). Rewriting (3) in terms of the applied force and the contact area,  $a_c$  gives:

$$(4) \quad F = 3\sigma_y a_c$$

Approximating  $a_c \cong 2\pi r(h-y)$  [17], where  $r$  and  $h$  are the undeformed asperity radius and height, respectively, and  $y$  is the deformed height gives

$$(5) \quad F = 6\pi r\sigma_y(y-h)$$

Since the change in asperity height due to plastic deformation is  $\Delta y_p = (y-h)$ ,  $F = 6\pi r\sigma_y \cdot \Delta y_p$ , or, defining a plastic stiffness coefficient,  $k_p$  as

$$(6) \quad k_p = 6\pi r\sigma_y,$$

the uniaxial plastic response of a single asperity is  $F = k_p \cdot \Delta y_p$ .

Equating (2) and (5), (since the force acting through each element in Fig. 5 must be equal), and using (1) gives  $\Delta y_p = 2k_s/k_p \cdot (z-y)$ , which differentiated, leads to the rate of plastic displacement

$$(7) \quad \dot{y}_p = \xi(\dot{z} - \dot{y})$$

where  $\xi (= 2k_s/k_p)$  is the ratio of fiber bend stiffness to the plastic stiffness of the asperity.

Next, consider the force when the asperity deforms by power law creep. We assume the uniaxial stress-strain rate relation for power law creep to be given as:

$$(8) \quad \dot{\epsilon} = B\sigma^n$$

where  $n$  is the creep exponent (often a function of stress and temperature) and where  $B$  is a temperature dependent constant conventionally expressed as  $B = B_0 \exp(-Q_c/RT)$ .  $Q_c$  is the activation energy for power law creep. Rewriting (8) in terms of the asperity height,  $y$  and the force applied to the asperity contact gives

$$(9) \quad \frac{\dot{y}_c}{y} = B \left[ \frac{F}{a_c} \right]^n$$

Solving (9) for the force ( $F$ ) and equating with the force required to bend the fiber (eq. 2) gives.

$$(10) \quad \dot{y}_c = -By \left[ \frac{2k_s(z-y)}{2\pi r(y-h)} \right]^n$$

The total displacement rate for an asperity is the sum of the rates due to creep and plasticity:  $\dot{y} = \dot{y}_p + \dot{y}_c$ . Inserting expressions (7) and (10) results in a single nonlinear ordinary differential equation in the asperity height:

$$(11) \quad \dot{y} = -\frac{By}{1+\xi} \cdot \left[ \frac{2k_s(z-y)}{2\pi r(y-h)} \right]^n + \frac{\xi}{1+\xi} \dot{z}$$

Solving (11) for the asperity height,  $y(t)$ , the fiber deflection is then obtained from (1). Results of the unit cell analysis are presented in §4.1.

### 3.2 Macroscopic Model

The spray-deposited monotape surface consists of asperities of varying size, height and spacing. As densification proceeds and the monotapes are pressed together, the number of contacting asperities increases. This is determined by the probability density function (PDF) describing the distribution of asperity heights,  $\varphi_h(h)$ . The cumulative fraction of contacting asperities is obtained by integrating the asperity height PDF (see Fig. 6):

$$(12) \quad \Phi_h = \int_z^{z_0} \varphi_h(h) dh$$

where  $z_0$  is the initial (undeformed) foil thickness and  $z$  is the current compacted foil thickness. If the lineal density of asperities (including those not yet in contact) is given by  $\rho$  [1/m], then the cumulative number of contacts per meter of fiber is

$$(13) \quad n_c(z) = \rho \Phi_h$$

Eqn (13) determines the density of contacts and thus of fiber segments assumed to be subjected to bending. Since the number of bend segments (per unit length of fiber) is increasing as the monotapes are pressed together, the mean segment length,  $\bar{\ell}$ , must be decreasing. In fact, the mean length is given by the reciprocal of (13):

$$(14) \quad \bar{\ell} = 1/n_c(z)$$

Thus although the distribution of asperity heights can be used to determine the mean asperity spacing, the probability density for the distribution of spacings cannot be inferred. We shall assume the asperity spacing PDF to be given by  $\varphi_\ell(\ell, z)$  and to be independent of  $\varphi_h$ . The probability that two asperities of undeformed height,  $h$ , are separated by a distance,  $\ell$ , is then  $\varphi_h(h) \cdot \varphi_\ell(\ell, z)$ .

Considering a segment of fiber (again of length,  $\ell$ ), in contact with two asperities (of undeformed height,  $h$ ), we wish to know the probability that it will fracture at any given deflection. The unit cell model for the response of a single fiber segment described above can be used to determine the deflection, given  $\ell$ ,  $h$ , and  $z$ . The maximum tensile stress,  $\sigma_b$ , in the fiber is related to the fiber deflection:

$$(15) \quad \sigma_b = 6E_f \cdot \frac{d_f}{\bar{\ell}^2} \cdot v$$

The stress required to cause fracture during bending is proportional to the more normally measured tensile fracture stress,  $\sigma_f$ , by a factor that depends on the fiber volume loaded in tension[18]:

$$(16) \quad \sigma_b = \sigma_f \left[ \frac{V_{\text{tension}}}{V_{\text{bending}}} \cdot \frac{1}{k} \right]^{\frac{1}{m}}$$

where  $V_{\text{tension}}$  and  $V_{\text{bending}}$  are the volumes of fiber stressed during tension and bending, respectively. The factor  $k$  depends only on the Weibull modulus,  $m$  when the fracture strength follows weakest link statistics. It is found to be  $1.45 \cdot 10^{-2}$  for the SiC fibers considered here ( $m = 13$ [9]). Taking  $V_{\text{tension}}$  to be the gage length of tensile fiber samples and  $V_{\text{bending}}$  to be the mean asperity spacing (considering asperities of all heights),  $V_{\text{tension}}/V_{\text{bending}} \approx 100$ , which gives

$$(17) \quad \sigma_b \approx 1.9 \cdot \sigma_f$$

The expression in (17) is fairly insensitive to values of  $V_{\text{bending}}$  such that for the entire range of beam lengths encountered in practice (i.e., asperity spacings), the ratio of  $\sigma_b/\sigma_f$  remains  $1.9 \pm 0.1$ . The tensile fiber stress is then, from (15) and (17),

$$(18) \quad \sigma_f \approx 6E_f \cdot \frac{d_f}{\ell^2} \cdot |z-y|$$

where eqn. (1) has been used for the deflection. The deformed asperity height,  $y$ , in (18) is obtained by solution of (11) for a given  $\ell$ ,  $h$  and foil thickness as a function of time,  $z(t)$ .

Therefore the fiber stress at time  $t$  depends on  $\ell$ ,  $h$  and the densification history,  $z(t')$ :

$\sigma_f = \sigma_f(\ell, h, z(t'), t)$ . With the fiber stress given by (18), the probability of fracture is  $\varphi_f(\sigma_f)$ .

Now, the probability that a fiber of length,  $\ell$  spanning neighboring asperities of undeformed height,  $h$  will fracture at time  $t$ , (when each monotape has been compressed to a nominal thickness,  $z(t)$ ), is  $\varphi_h(h) \cdot \varphi_l(\ell, t) \cdot \varphi_f(\ell, h, z(t'), t)$ . Integrating this joint probability over all cell heights and lengths and over time from 0 to  $\tau$  gives:

$$(19) \quad n_d(\tau) = \rho \int_{z(\tau)}^{z_0} \int_{\ell_{\min}}^{\ell_{\max}} \int_0^{\tau} \{ \varphi_h(h) \cdot \varphi_l(\ell, t) \cdot \varphi_f(\sigma_f) \cdot \frac{\partial \sigma_f}{\partial t} \} dt d\ell dh$$

where  $\partial \sigma_f / \partial t$  (found by differentiating eqn. 18) has been introduced to allow integration of  $\varphi_f$  with respect to time. The integral represents a cumulative probability and must therefore be less than

or equal to 1. This limits the number of fractures to less than or equal to the number of fiber segments ( $n_d \leq \rho$ ), an obvious physical requirement.

Application of the model as given by (19) requires determination of the lineal density,  $\rho$  and the PDF's,  $\varphi_h$ ,  $\varphi_l$  and  $\varphi_r$ . The asperity density and  $\varphi_l$  and  $\varphi_h$  characterize the rough surface and are easily determined experimentally by stylus profilometry. The surface, which is assumed to be isotropic, (confirmed in the case of plasma-sprayed foils considered here), is scanned by a fine stylus which traces a surface profile and provides digitized output for statistical analysis. Typically the distributions of both asperity heights and spacings are found to be roughly normal (see Fig. 7) and are thus described by

$$(20a) \quad \varphi_h(h) = \frac{1}{\sqrt{2\pi} \cdot \sigma_h} \exp \left[ -\frac{1}{2} \left[ \frac{h - \bar{h}}{\sigma_h} \right]^2 \right]$$

$$(20b) \quad \varphi_l(l) = \frac{1}{\sqrt{2\pi} \cdot \sigma_l} \exp \left[ -\frac{1}{2} \left[ \frac{l - \bar{l}}{\sigma_l} \right]^2 \right]$$

where  $\bar{h}$  and  $\bar{l}$  are the mean asperity height and spacing, respectively and  $\sigma_h$  and  $\sigma_l$  are the corresponding standard deviations.

The distribution of asperity spacings (20b) changes with time in that  $\bar{l}$  and  $\sigma_l$  both depend on the current monotape thickness,  $z(t)$ . The mean spacing is given by (14) while the standard deviation,  $\sigma_l$ , is determined by assuming that the ratio of  $\sigma_l/\bar{l}$  remains constant. Denoting the mean spacing and standard deviation determined for the total asperity population, i.e., irrespective of heights, by  $\bar{l}_0$  and  $\sigma_{l0}$ , the standard deviation is then given as a function of  $z$  as:

$$(21) \quad \sigma_l(z) = \frac{\bar{l}(z)}{\bar{l}_0} \cdot \sigma_{l0}$$

Eqn. (21) states that the standard deviation of asperity spacings decreases with further compaction, approaching  $\sigma_{l0}$  as the relative density approaches 1.

Table I lists the experimentally determined values of all statistical parameters needed to characterize the surface.

Table I.

Surface Statistical Data  
(plasma sprayed Ti-24Al-11Nb/SCS-6)

$\bar{h} = 91.06 \mu\text{m}$	mean asperity height
$\sigma_h = 39.82 \mu\text{m}$	std. dev. of asperity heights
$\bar{z}_0 = 258.18 \mu\text{m}$	mean asperity spacing
$\sigma_{z_0} = 108.19 \mu\text{m}$	std. dev. of asperity spacings
$\rho = 3.87 \cdot 10^{-3} \mu\text{m}^{-1}$	lineal density of asperities

With the statistical quantities needed to characterize the surface in hand, we turn now to the PDF for fiber strengths,  $\varphi_f$ . Single fiber pull tests (described in detail elsewhere[19]) on as-received SCS-6 (SiC) fibers as well as on fibers removed from the spray-deposited monotapes by acid etching revealed a distribution of strengths well described by a Weibull PDF:

$$(22) \quad \varphi_f(\sigma_f) = \frac{m}{\sigma_0} \cdot \sigma_f^{m-1} \exp\left[-\left(\frac{\sigma_f}{\sigma_0}\right)^m\right]$$

where  $\sigma_f$  is the fiber stress as given by (18),  $\sigma_0$  is the reference stress (stress below which 37% of fibers survive) and  $m$  the Weibull modulus. The experimentally determined values for  $\sigma_0$  and  $m$  are[9]:

$$\begin{aligned} \sigma_0 &= 4.45 \pm 0.19 \text{ [GPa]} \\ m &= 13.0 \pm 2.1 \end{aligned}$$

### 3.3 Implementation

Implementation of (19) to simulate the evolution of fiber fracture with densification was carried out as follows: for a given (small) time step, an increment of densification is determined using a previously developed model[8] which takes as input, an increment in applied stress and temperature. The resulting density is used to calculate a corresponding monotape thickness,  $z$ : ( $z = z_0 D_0/D$  for uniaxial compaction), which is then input to the fiber fracture model. For any given cell size ( $\ell$  and  $h$ ), the unit cell model (11) is solved over the time range, 0 to  $\tau$ . The unit cell solution gives the asperity height within the cell as a function of time, which is used to calculate the deflection and so the fiber stress and then  $\varphi_f$ . As long as the stress in the fiber is increasing the probability of fracture increases, as indicated by (22). If however, the fiber begins to relax, as can happen when the creep rate of the asperities exceeds the rate of consolidation, the probability of fracture is set equal to zero. This corresponds with the physical reasoning that if

the fiber has not failed at a stress  $\sigma_f$ , it will not fail at some stress less than  $\sigma_f$ . The probability of fracture is explicitly set equal to zero for asperities which have not yet made contact with an adjacent foil, (i.e., those for which  $h < z(t)$ ).

By considering the creep response of the asperities in addition to plastic deformation, time-dependence is entered into the problem formulation and consequently, the cumulative number of fractures depends not only on the total change in compacted laminate thickness, but on the densification path as well. A process controller has been described which couples the models with a realtime optimization algorithm to achieve interactive control of densification and fracture during monotape consolidation[12].

As mentioned previously, the monotape thickness is related to the relative density by  $z = z_0 D_0 / D$ , which can be used to show that full density is reached before all asperities are brought into contact with an adjacent foil. For constrained uniaxial compression, the limiting value of  $z$ , which we denote by  $z^*$ , is obtained as  $z^* = z_0 D_0$ . Inserting values measured experimentally for plasma-sprayed Ti-24Al-11Nb/SCS-6 foils,  $z_0 = 91.06 + 3(39.82) = 210 \mu\text{m}$  and  $D_0 = 0.35$ , gives  $z^* = 74 \mu\text{m}$ . If every asperity contact is associated with one fracture, the maximum number of fractures is  $n^* = \rho \int_{z^*}^{z_0} \phi_h(h) dh = 3.87 \cdot 10^{-3} \cdot \int_{74}^{210} \frac{1}{(\sqrt{2\pi} \cdot 39.82)} \cdot \exp \left[ -\frac{1}{2} \left( \frac{h - 91.06}{39.82} \right)^2 \right] dh = 2.57 \cdot 10^{-3}$  or 2.57 fractures/mm. Therefore the contact density ( $\rho$ ) actually used in (19) is about 2/3 of the value in given in Table I.

#### 4. Results

The fiber fracture model (19) can be used to predict the evolution of fiber fracture during any arbitrary process cycle. The only data required are yield and creep strengths of the matrix, elastic stiffness and fracture strength of the fiber and statistical parameters needed to characterize the monotape surface. Figure 8 shows the evolution of fiber fractures for a laminate of Ti-24Al-11Nb/SCS-6 monotapes, all subjected to the same applied stress cycle, but different consolidation temperatures. Plotted is the predicted fractures normalized by the number of potential fractures ( $n^*$ ) versus relative density. The effect of increasing the processing temperature in reducing fractures is apparent: at 950 C, only about 2-3% of potential fractures are expected. It is also evident from Fig. 8 that most of the damage to fibers is expected to occur before 80-85% density is reached. It is during this early stage of consolidation that surface asperity deformation plays a dominant role both in densifying and in causing fiber bending and fracture. It has been shown experimentally that fewer fractures result if the composite is allowed



to densify very slowly at first by applying a low consolidation pressure at high temperature[9] – after the density has reached 80–85%, the pressure can be increased with little additional fiber damage.

As an example of input to the model, Figure 9 shows the consolidation cycle used to generate the curve in Fig. 8 at 850° C; the temperature is first allowed to reach its soak value before ramping the pressure to 100 MPa. The resulting densification curve (predicted using the densification model in [8]) is shown at right.

Experimental study of the fiber damage evolution during VHP and HIP of MMC laminates[9] has shown that lower densification rates result in fewer fractures. This is predicted by the model: Figure 10 shows the normalized number of fractures occurring upto a density of 0.8 as a function of the average densification rate. The values shown represent a variety of different combinations of pressure and temperature; the scatter merely indicates that damage is not purely a function of the average densification rate. Nonetheless a clear trend is visible: lower densification rates cause fewer accumulated fractures.

Figure 11 illustrates the relative behavior of two composites, TiAl ( $\gamma$ ) and Ti–24Al–11Nb ( $\alpha_2+\beta$ ) matrices reinforced with SiC fibers, under identical processing conditions. The higher creep resistance of the  $\gamma$ –matrix composite leads to a significantly greater number of fractures.

Experimental results[9] are compared with model predictions in Figure 12. Here, the number of fractures is shown as a function of process temperature (i.e., the soak temperature at which the sample was held throughout most of the process cycle). The contours represent different applied (average soak) pressures. The experimentally determined density of fractures was obtained by removing the matrix material (acid etch) and then counting fiber segments. The observed agreement is reasonably good, especially at higher temperatures. Below about 850° C, the model overestimates the actual number of fractures.

## 5. DISCUSSION

Damage or fracture of fibers is a significant technical problem when subjecting continuously reinforced metal/intermetallic matrix composites to deformation processing; the inherently brittle (ceramic) fibers are suspended in a porous (compressible) matrix of inelastically flowing metal/alloy. The observation that fibers may be subjected to bending forces as matrix material flows inelastically to fill voids, thus leading to densification, underlies a more general premise:

that the susceptibility to consolidation induced fiber fracture scales with the initial degree of inhomogeneity in the spatial distribution of matrix material. In the case of MMC monotapes produced by plasma spray deposition, this inhomogeneity is present in the form of a substantial surface roughness arising as the plume of molten metal droplets impact, spread and freeze on the growing substrate. As a consequence of this surface irregularity, which leads to a substantial volume of trapped void when the monotapes are stacked prior to consolidation, the transmission of applied loads from one foil to the next is initially, very nonuniform. The model we have described is based on experimental observations (ref [9]), which appear to indicate that fractures are primarily the result of fiber bending caused by forces transmitted at the statistically distributed asperity contacts.

While little work has been undertaken to date to study the mechanisms of fiber damage and fracture during deformation processing of MMC's, the current investigation indicates that mechanical forces imposed on the fibers by the densifying metal matrix may be the most crucial concern at densities below say, 0.85. Once the matrix is fully dense, attention may shift to mechanisms which have routinely been identified as sources of failure during component service, such as the matrix/fiber CTE mismatch. The reason for this may be that the matrix transmits shear stresses much less effectively when highly porous (with areas in which the fibers may have only a thin coating of matrix), whereas loads normal to the fiber axis are unaffected at the point of application. A central result is that the initial distribution of matrix material must be made to be as homogeneous (spatially) as possible – large volume fractions of void will be much more benign if the void is present in the form of evenly distributed pores which are small relative to the fiber diameter. The utility of the fiber bend fracture model in this respect, is that the benefit of refining the monotape manufacturing process (e.g. to reduce surface roughness), can be quantitatively weighed against the costs.

In view of the complexity of the deformation and loading geometry, a truly accurate representation of the evolution of fiber fracture during consolidation cannot realistically be expected. Rather, the model is intended merely to capture the influence of process variables (e.g. pressure, temperature, time), easily obtained matrix mechanical properties and certain characteristics of spray deposited monotapes. In attempting to keep the model formulation as simple as possible, (since the model must be able to operate in real time), a number of idealizations have been introduced: (i) the fiber segments are treated as bare, although they are actually bonded with the surrounding porous matrix, (ii) the fiber segments are assumed to be simply supported as though isolated – the fact that the fibers are continuous and bonded to the deforming metal matrix makes the actual end constraints much more complicated, (iii) perfect three-point bending is treated – in reality, the intermediate loading may occur anywhere between

the end supports, and (iv) the deforming asperity contacts are treated as point loads rather than distributed. As a result of these simplifying assumptions, all of which are associated with the unit cell analysis, the model developed is conservative, i.e., it tends to overestimate the number of fractures. Further comparison with experimental results is needed before actual inadequacies can be identified and the model refined.

## SUMMARY

A micromechanics model for predicting the rate of fiber fracture during consolidation processing of spray deposited metal matrix composite monotapes has been presented. Fibers are assumed to fracture by a mechanism in which segments of the continuous fibers are subjected to bending caused by nonuniform contact stresses associated with surface roughness. The model incorporates statistical parameters characterizing the distribution of matrix material and the fracture strength of the fibers. Simulations of fiber fractures during consolidation indicate that most fractures occur prior to reaching 80–85% density. It is therefore most crucial to monitor and control this type of fiber damage in the early stages of densification. The model can be used to compare the susceptibility of various metal matrix composite systems to fiber fracture during consolidation processing and to optimize process conditions such that fiber damage (in balance with other requirements) can be minimized.

## Acknowledgements

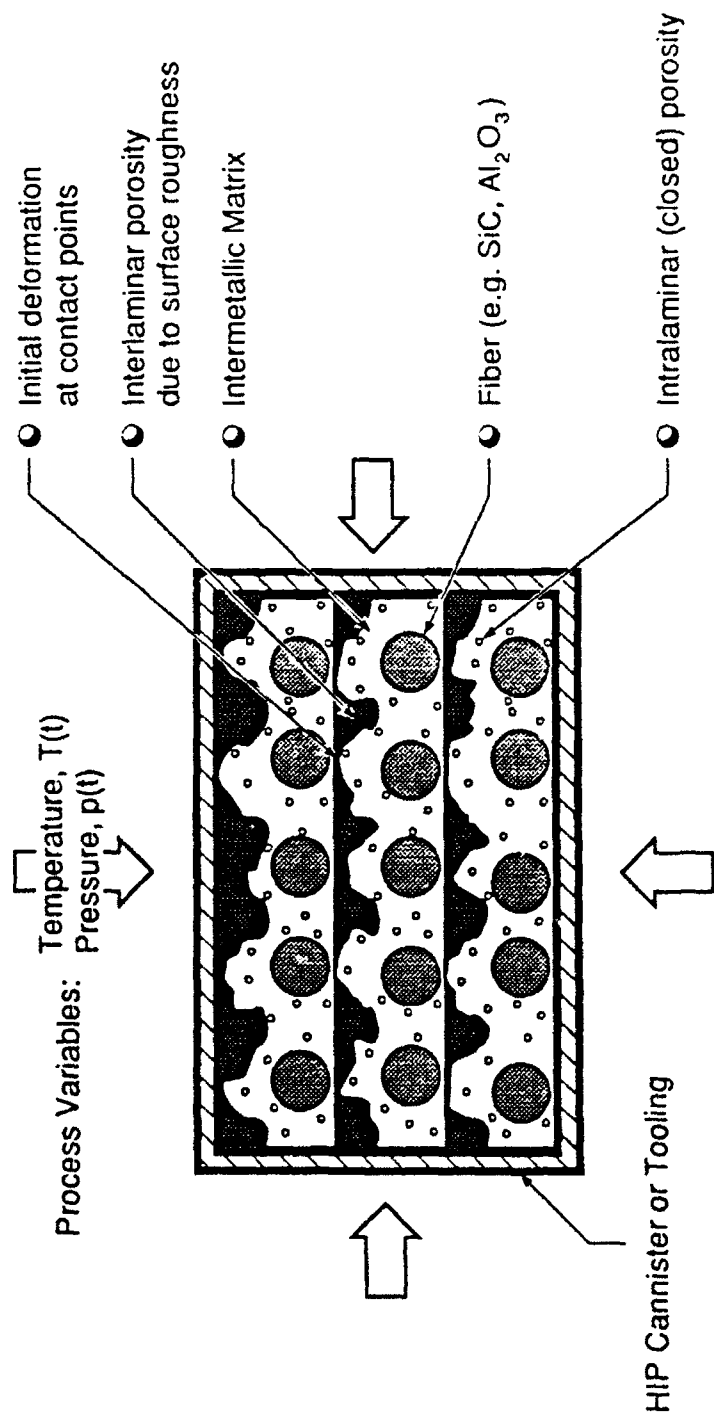
The authors gratefully acknowledge the partial support of DOD/DARPA/NASA (contract No. 4179–89R) and the UCSB–URI (No. 5158–91).

## REFERENCES

1. R.A.MacKay, P.K.Brindley and F.H.Froes, JOM, 43(5), 23 (1991).
2. J.Doychak, JOM, 44(6), 46 (1992).
3. J.R.Stephens and M.V.Nathal, "Status and Prognosis for Alternative Engine Materials" in: Superalloys 1988, ed., D.N.Duhl, TMS (Warrendale, PA), p.183 (1988).
4. P.D.Nicolaou, H.R.Piehler and S.Saigal, "Finite Element Analysis of the Consolidation Behavior of Composite Materials Using the Foil/Fiber/Foil Technique" in: Concurrent Engineering Approaches to Materials Processing, eds., A.J.Paul, S.N.Dwivedi and F.R.Dax, TMS (Warrendale, PA), 1992 (In Press).
5. P.K.Brindley, "SiC Reinforced Aluminide Composites" in: High Temperature Ordered Intermetallic Alloys II, eds., N.S.Stoloff, C.C.Koch, C.T.Liu and O.Izumi, MRS (Pittsburgh, PA), 81, p.419 (1987).
6. D.A.Hardwick and R.C.Cordi, "Intermetallic Matrix Composites by Physical Vapor Deposition" in: Intermetallic Matrix Composites, eds., D.L.Anton, P.L.Martin, D.B.Miracle and R.McMeeking, MRS (Pittsburgh, PA) 194, p.65 (1990).
7. E.S.Russell, "Thermomechanical Effects in Plasma-Spray Manufacture of MMC Monotapes" in: Thermal Structures and Materials for High Speed Flight, ed., E.A.Thornton, Progress in Astronautics and Aeronautics 140, AIAA (Washington D.C.), p. 437 (1992).
8. D.M.Elzey and H.N.G.Wadley, Acta Metall. et Mater., 1993 (In Press).
9. J.F.Groves, D.M.Elzey and H.N.G.Wadley, Acta Metall. et Mater., 1993 (Submitted).
10. J.-M.Yang and S.M.Jeng, JOM, 44(6), 52 (1992).
11. J.-M.Yang, S.M.Jeng and C.J.Yang, Mat. Sci. & Eng., A138, 155 (1991).
12. D.G.Meyer, R.Vancheeswaran and H.N.G.Wadley, "Application of Micromechanical Models for On-Line Control of MMC Consolidation" in: Model-Based Design of Materials and Processes, eds., E.S.Russell, D.M.Elzey and D.G.Backman, TMS (Warrendale, PA), (1993).
13. L.M.Hsiung, W.Cai and H.N.G.Wadley, Mat. Sci. & Eng., A125, 295 (1992).
14. L.M.Hsiung, W.Cai and H.N.G.Wadley, Acta Metall. et Mater., 40(11), 3035 (1992).
15. T.A.Kuntz, H.N.G.Wadley and D.G.Black, Met. Trans. A, 1993 (In Press).
16. R.Gampala, D.M.Elzey and H.N.G.Wadley, Acta Metall. et Mater., 1993 (Submitted).
17. K.L.Johnson, Contact Mechanics, Cambridge Univ. Press, Cambridge, p.412 (1985).
18. P.A.Siemers, R.L.Mehan and H.Moran, JOM, 23, 1329 (1988).
19. J.F.Groves, M.S.Thesis, University of Virginia, p.32 (1992).

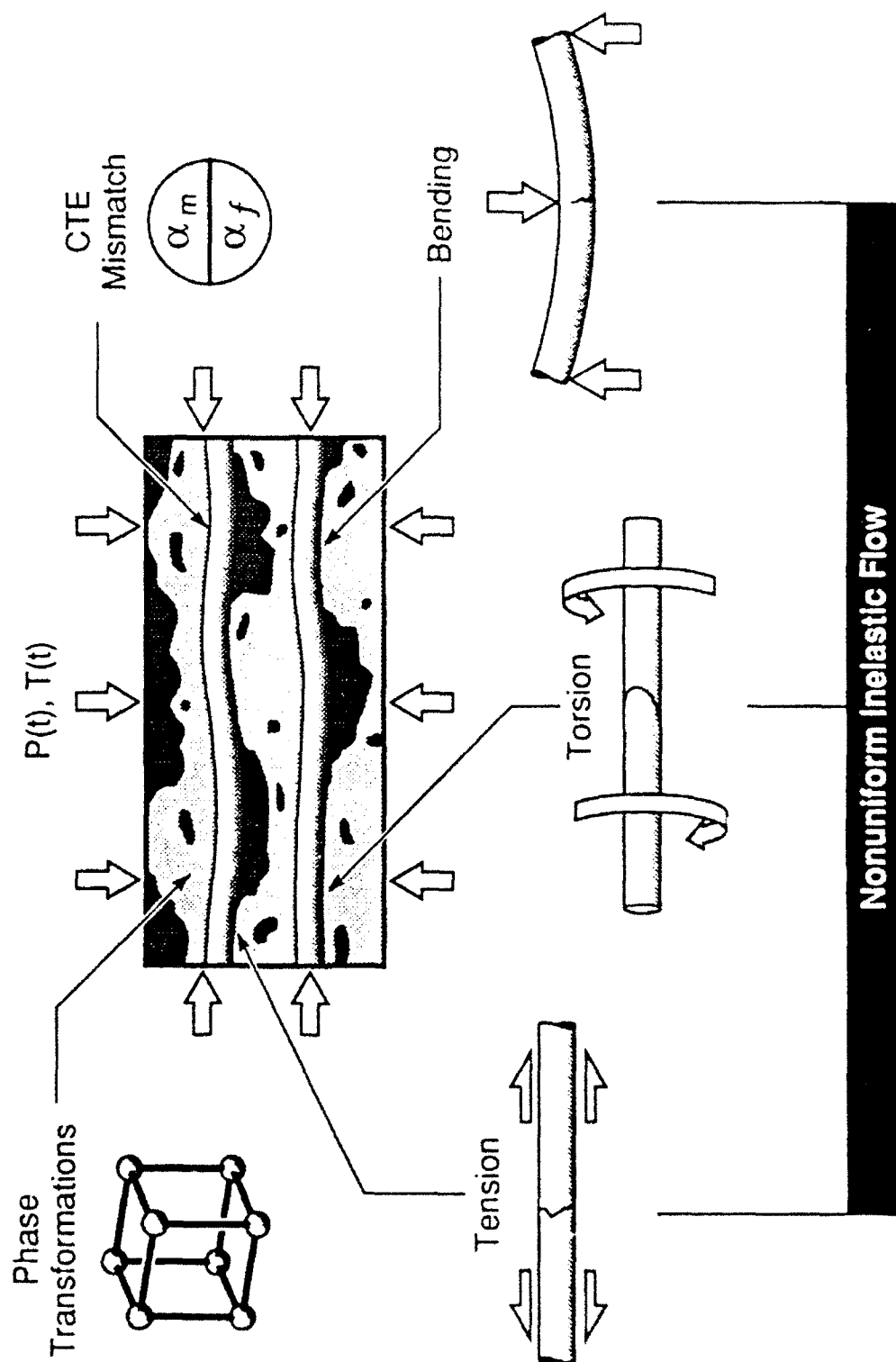


1a. Cross-section of a SiC fiber-reinforced metal matrix composite monotape produced by plasma deposition showing surface roughness and internal porosity.

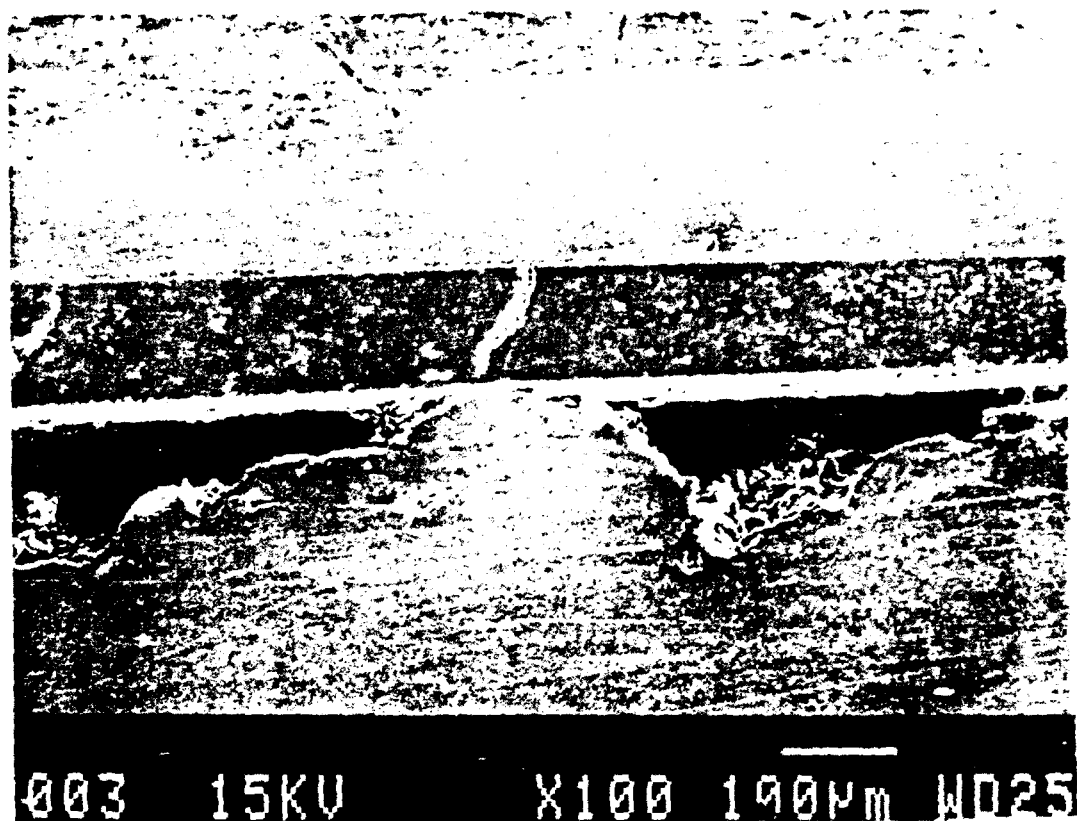


1b. Schematic representation of the consolidation of plasma sprayed MMC monotapes. The initial distribution of porosity is very nonuniform due to the surface roughness.

## POTENTIAL MECHANISMS FOR FIBER FRACTURE DURING CONSOLIDATION PROCESSING

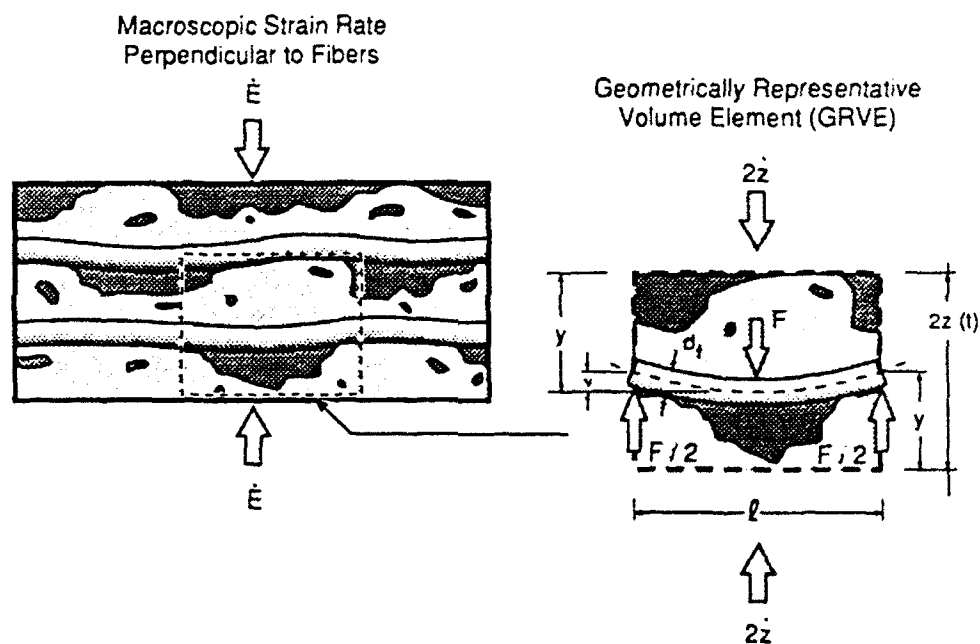


2. Potential mechanisms for fiber fracture during consolidation processing include internal stresses due to CTE mismatch or to volume changes associated with phase transformations and nonuniform mechanical forces associated with rough surface contact deformation

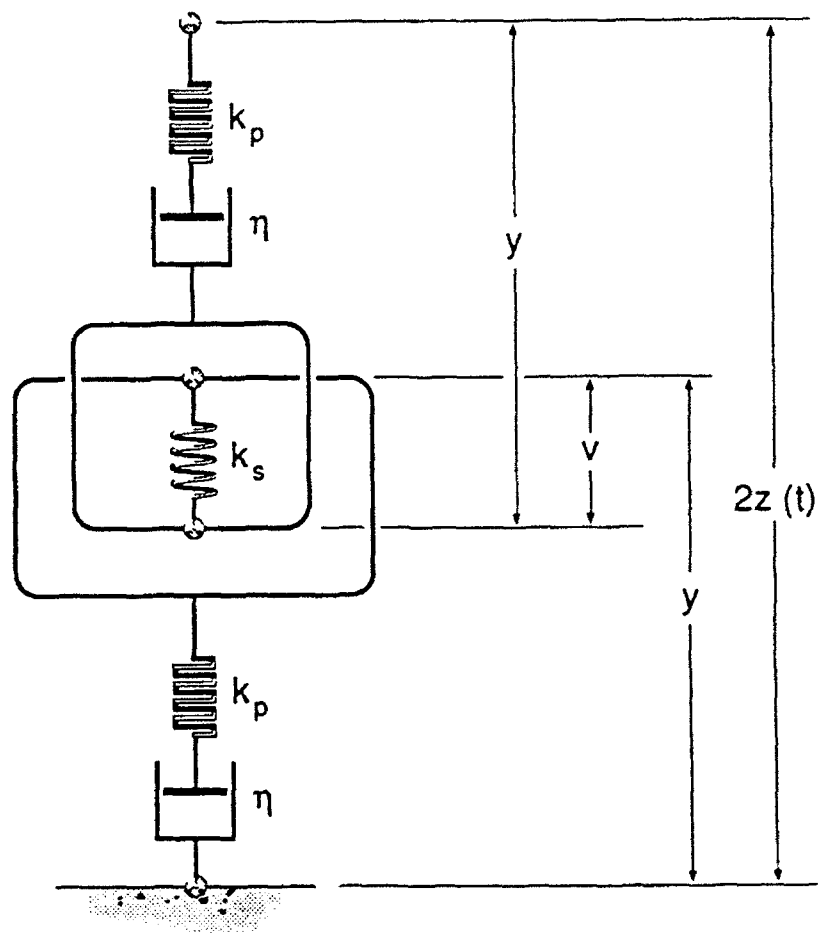


3. Experimental study has shown the principal cause of fiber fracture during consolidation to be fiber bending due to nonuniform surface contact loading. (reproduced from [9])

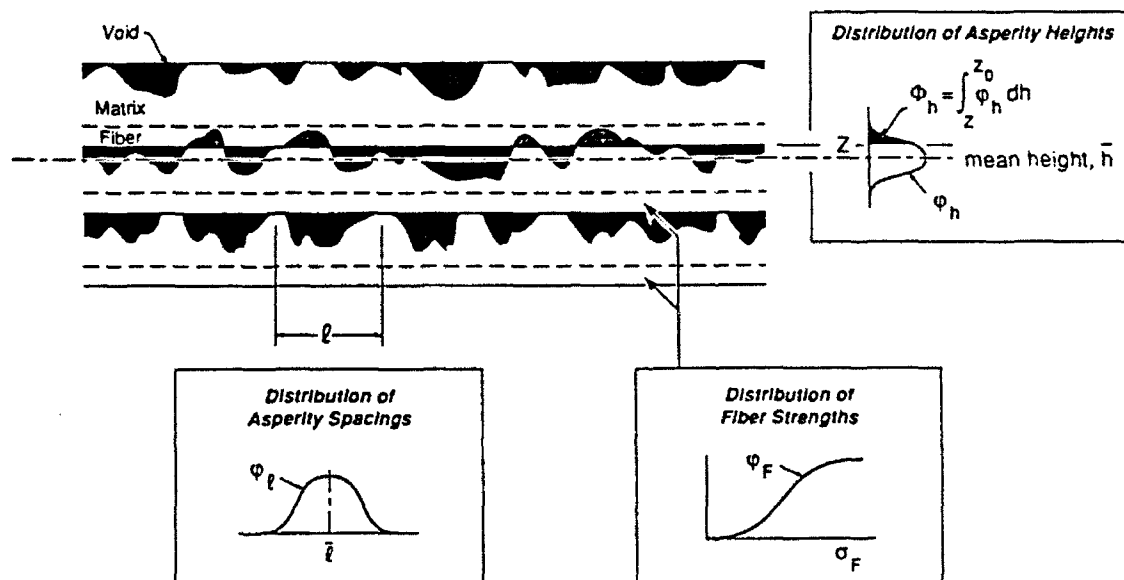




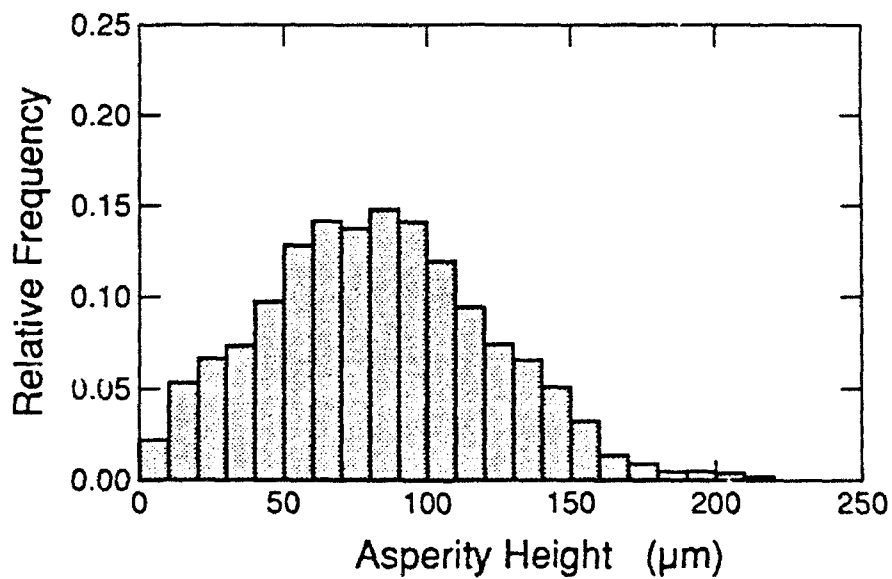
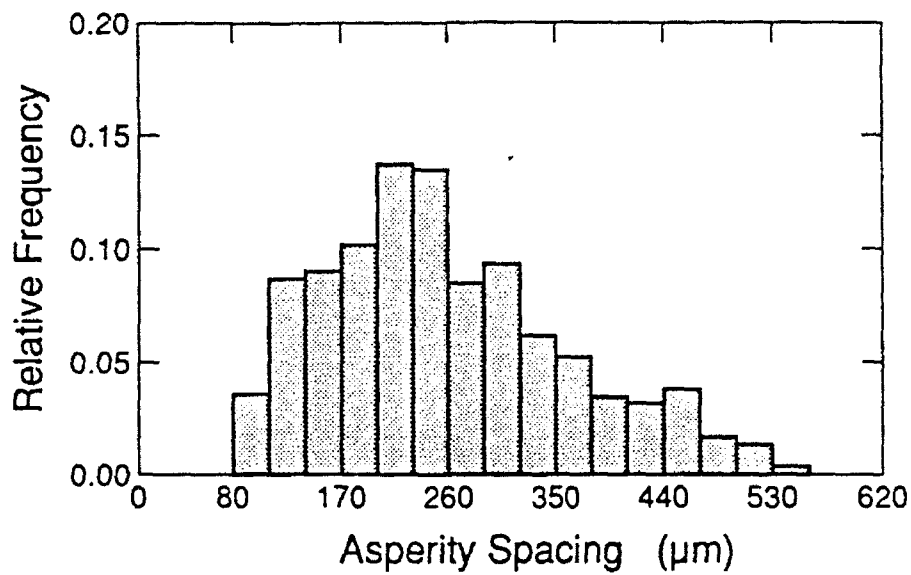
4. The evolution of fiber damage during consolidation is predicted based on the analysis of a representative volume element: the element contains a fiber segment subjected to bending by the action of contacting asperities (matrix).



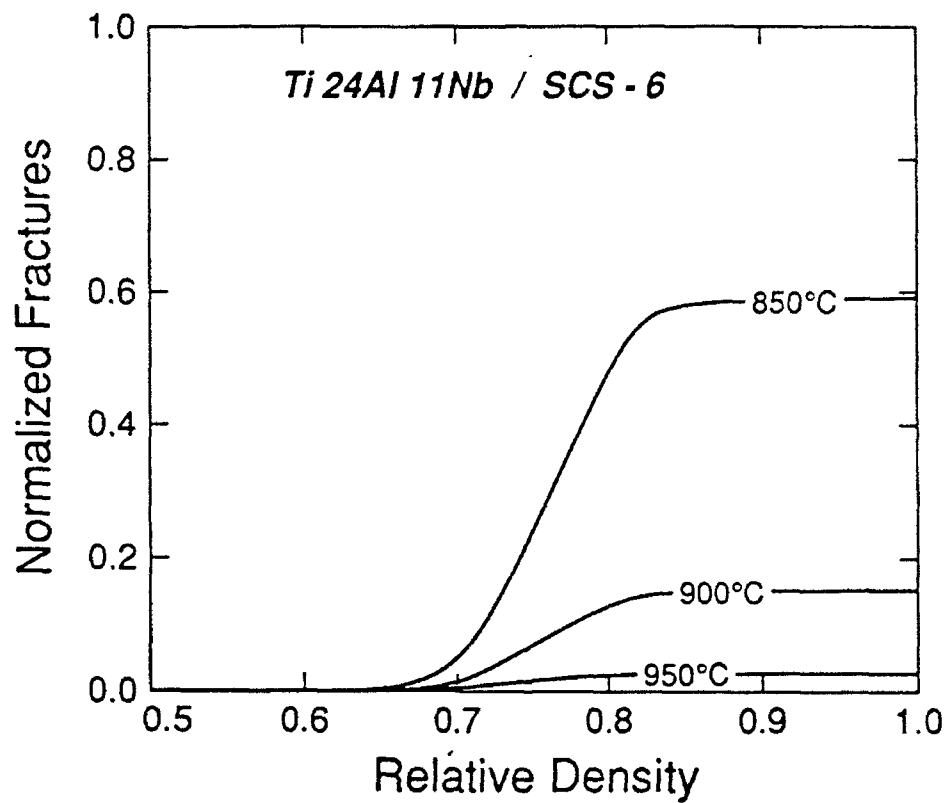
5. Lumped parameter representation of the fiber bend unit cell shown in Fig. 4; the asperities are treated using a Maxwell-type viscoplastic model while the fiber is considered to be elastic with spring constant,  $k_s$ .



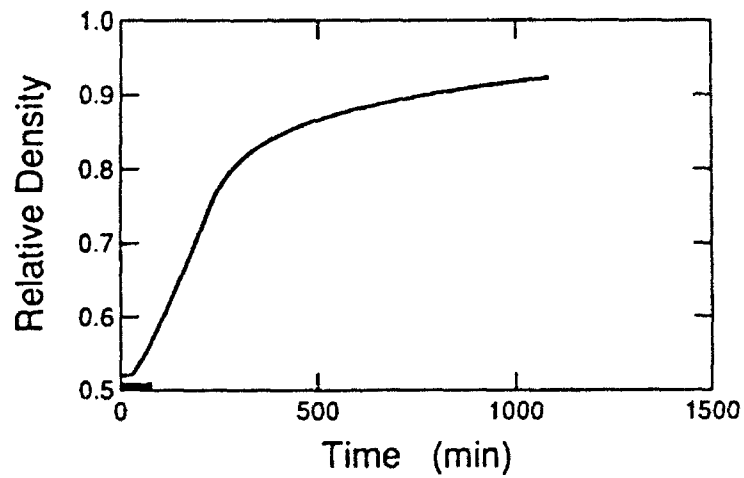
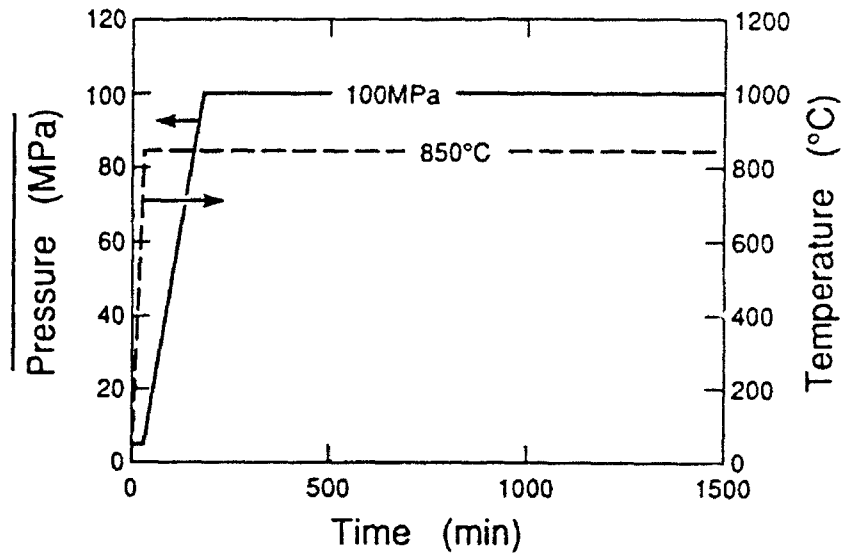
6. Macroscopically, the material is treated as an assemblage of fiber bend unit cells of statistically varying size (given by the distribution of asperity heights and spacings) and fiber strengths.



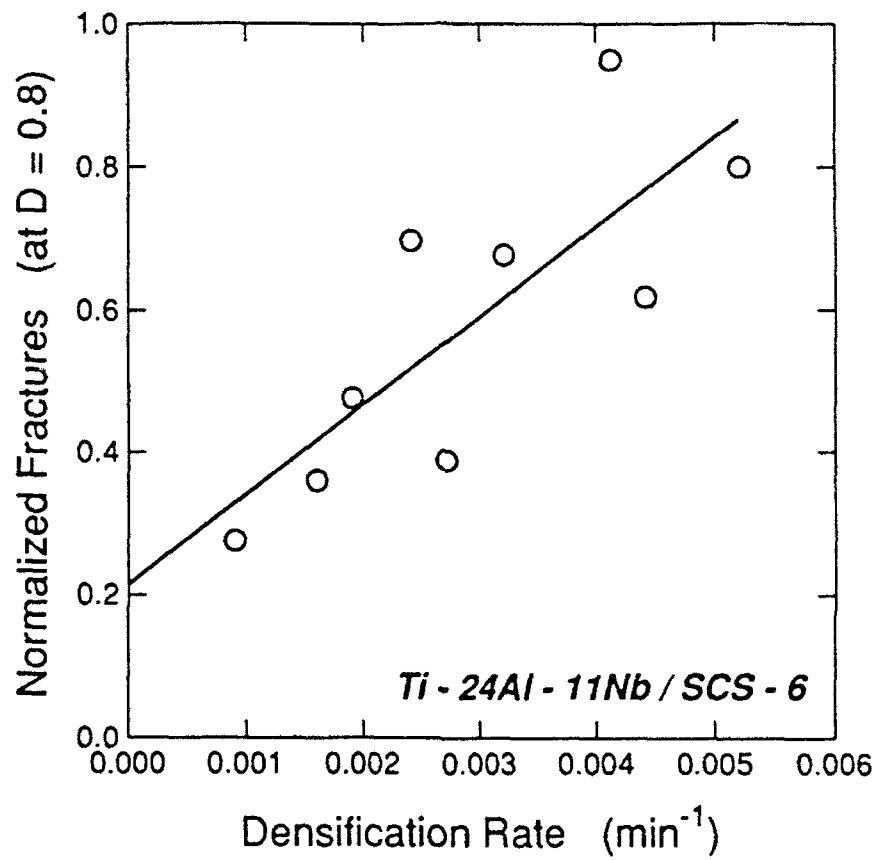
7. Representative frequency histograms for the distribution of asperity spacings and heights as obtained by stylus profilometry.



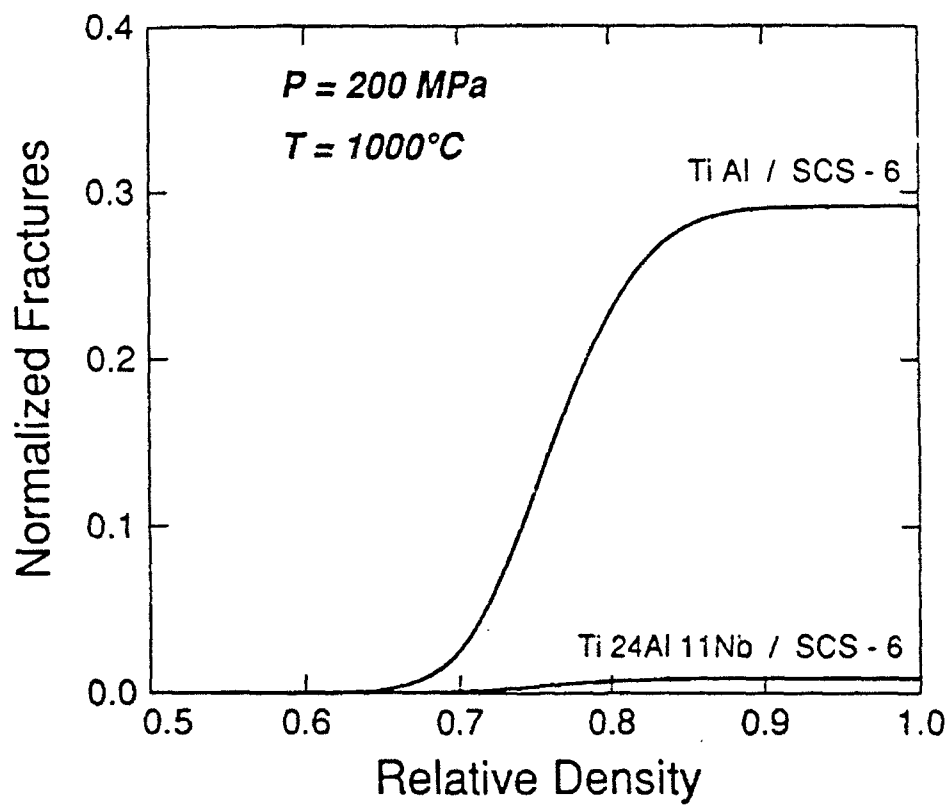
8. Predicted temperature dependence of fiber fracture: successful consolidation requires temperatures at which the plastic and creep strength of the matrix material are low relative to the bend stiffness of the fiber.



9. Input to the fracture model is the density as a function of time, which can be predicted for a given pressure and temperature cycle using the densification model in [8].

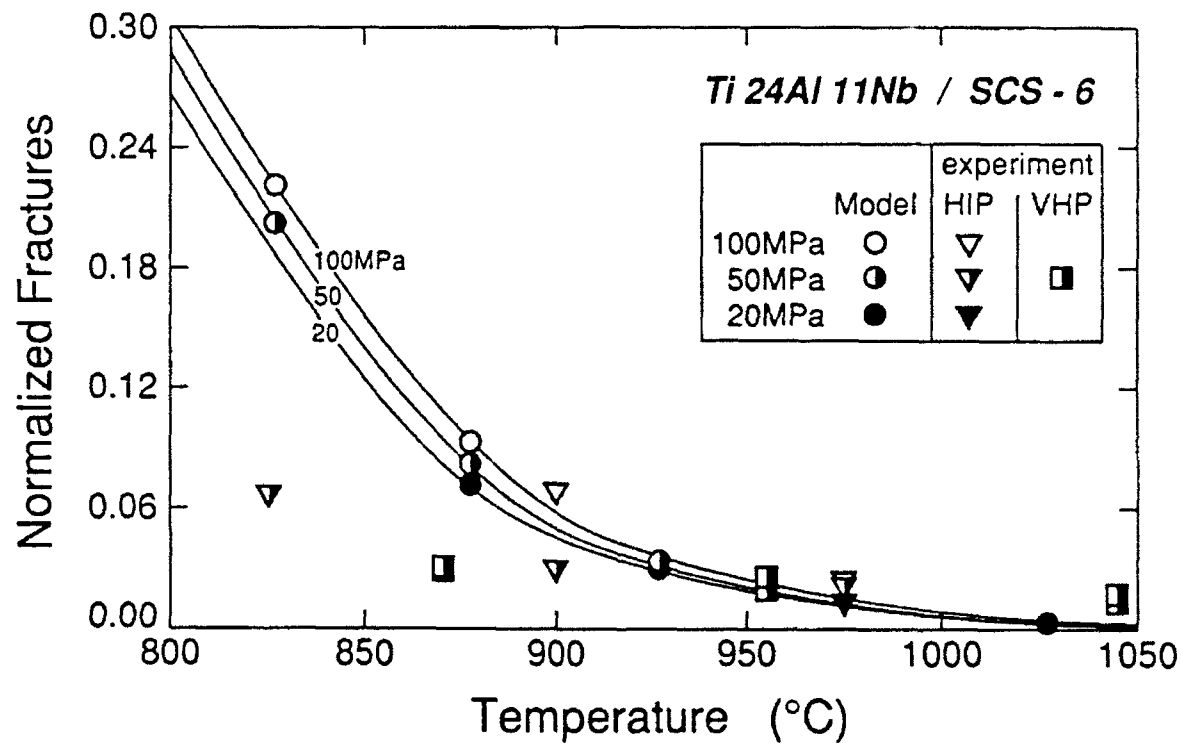


10. Predicted dependence of fiber damage on the average densification rate: lower rates lead to smaller fiber bend deflections since more time is available for stress relaxation within the matrix.



11. The model can be used to compare the relative processability of fiber/matrix combinations. Matrices with high creep resistance, such as  $\gamma$ -TiAl, tend to heavily load fibers, leading to increased damage.





12. Predicted and experimentally determined dependence of damage on processing temperature and applied stress: reasonably good agreement is obtained at temperatures above 850° C.

# **The Effect of Processing on the Interface Structure/Property Relationship in a Ti 24Al 11Nb (at%) Composite**

A Thesis  
Presented to the  
Faculty of the School of Engineering and Applied Science  
University of Virginia

In Partial Fulfillment  
of the Requirement for the Degree  
Masters of Science (Material Science)

Paul E. Cantonwine

May 1993

## Abstract

Composite toughness is well known to be a function of the fiber/matrix interface properties. The effect of processing on the interface properties however is not well understood. This investigation is concerned with studying interface properties of a SCS-6/Ti 24Al 11Nb (at%) composite. The composite was consolidated with a foil/fiber/foil technique at 1040 °C for 30 to 240 min. A uniaxial constrained pressure of 100 MPa was applied in a vacuum hot-press (VHP). The reaction zone thickness increased with processing time and a model was proposed to predict the measured reaction zone thickness. Radial cracking was observed in the matrix around the fiber. Radial damage increased with processing time indicating a possible decrease in residual stress. A push-out test measured the debond strength ( $\tau_d$ ) and sliding resistance ( $\tau_s$ ) of the fiber/matrix interface. Both  $\tau_d$  and  $\tau_s$  are constant until the reaction zone thickness reaches a value of 1.4 to 1.5  $\mu\text{m}$ . An increase in  $\tau_d$  and  $\tau_s$  was observed for reaction zone thicknesses greater than 1.5  $\mu\text{m}$ . The increase is attributed to a change in the debond crack during the pushout test. These results can then be incorporated into existing densification [13] and fiber fracture [111] models to determine optimal processing conditions.

# 1 Introduction

In a continuous unidirectional reinforced (CUR) composite, fibers are added to a matrix material to improve its stiffness, strength, creep resistance and (in some cases) toughness. Properties such as stiffness and strength in the fiber direction are often modeled as a weighted average of the fiber and matrix properties using the rule of mixtures [1,2]. However other properties such as toughness [2,3] (and strength [4,5]) depend on fiber debond and pullout from the matrix (especially in brittle matrix composites) and do not obey a model as simple as the rule of mixtures. The work of fiber pullout usually enhances the fracture toughness over a rule of mixtures prediction [2,3] and is a function of the properties of the fiber/matrix interface. Thus, the performance of composites depends both on the properties of their constituents (fiber and matrix) and the interface between them.

The extreme reactivity between today's typical metal matrix materials (e.g. Ti alloys and intermetallics) and fiber reinforcements (such as SiC or  $\text{Al}_2\text{O}_3$ ) has led to the development of several solid state methods for composite synthesis. One technique alternates layers of matrix alloy foil and aligned fibers to produce a foil/fiber/foil preform. A derivative of this foil/fiber/foil technique was developed at NASA Lewis Research Center in Cleveland, OH. They produced porous foils (or powder cloths) by tape casting alloy powders combined with an organic binder [112,113]. The third process involves consolidation of a composite preform composed of spray deposited foils (monotapes) which contain embedded fibers [9,10]. More recently a technique has been developed which deposits matrix material on cold single fibers by a vapor deposition process [11,12]. The matrix coated fibers are randomly or closed packed into a composite preform and consolidated without additional alloy foil or powder. All of these preforms are consolidated using either vacuum hot-press (VHP) or hot-isostatic press (HIP) techniques [7,8]

The consolidation process is difficult to optimize. First an appropriate temperature

and pressure cycle must be determined to ensure complete consolidation. Until recently such a processing cycle was determined by trial and error and had to be repeated for each new fiber/matrix combination. Today with densification models such as that of Elzey and Wadley [13], a good estimate of a processing cycle to accomplish densification can be determined at a work station before conducting any experimentation.

A second issue in CUR composite processing is fiber fracture [6,14]. Pank et al [6] found a significant decrease in composite tensile strength and connected this with the fracture of fibers during processing. More recently, Groves [14] and Elzey and Wadley [11] have systematically evaluated the conditions that lead to fiber fracture during the processing of monotape preforms, and a detailed predictive model has been developed. This model can be used with the densification models already developed to define process cycles that both densify the preform and eliminate fiber fracture.

Fiber/matrix reactions have also been reported to accompany consolidation [15-29] and cause a loss of composite performance [30,31]. These reactions and their kinetics have been quite thoroughly studied after consolidation [15-29], and their properties have been investigated in some detail [32-39]. However, little has been done to determine the effect of processing on these interfaces or to establish the effect of interfacial structure (which must be a function of processing conditions) on properties. Thus, there is not a clear understanding of the interface structure/property/process relationships for interfaces in metal/intermetallic matrix composites. Since interface properties affect the bulk composite properties (i.e. toughness), it is essential that they be understood and modelled so that optimal consolidation processing pathways can be found. The work reported here seeks to contribute to this.

The objective of the study has been to begin to develop a basic understanding of the structure/property relationships of the fiber/matrix interface as a function of processing condition for a representative  $\text{Ti}_3\text{Al}$  aluminide matrix (Ti 24at%Al 11at%Nb) reinforced with three reinforcements of topical interest; SiC (SCS-6 and Sigma SM1040) and  $\text{Al}_2\text{O}_3$

(Saphikon) fibers. Foil/fiber/foil preforms consolidated in a vacuum hot-press produced composite test coupons. The effect of systematic variations of the process conditions on the interface reaction kinetics has been observed and analyzed. A model is developed to predict the evolution of the reaction thickness during processing. In addition, accompanying changes to the microstructure of the fiber/matrix interface and surrounding matrix have been observed. They appear to have a significant effect on the radial cracking behavior and this may affect the interfacial properties by relaxation of residual stresses. A pushout test method was used to estimate the debond and sliding properties of these interfaces. These were then correlated with the debond surfaces to identify the microstructural features that control them. The results have been used (in conjunction with recently developed models of densification and fiber damage) to design optimal consolidation cycles for this difficult to process material class of composites.

## 2 Background

The work of this thesis addresses the processing of a two specific composite systems - Ti 24Al 11Nb reinforced with either SiC (both Textron's SCS-6 and Sigma SM1040 fiber) or a single crystal  $\text{Al}_2\text{O}_3$ . It is helpful to the non-expert to review some important background: namely composite processing, characteristics of the constituents (fiber and matrix), and the current understanding of the microstructure and properties of the fiber/matrix interface.

### 2.1 Processing

Processing of metal and intermetallic matrix composites with reactive matrices and fibers proceeds by a sequence of (sometimes complicated) steps. The first is the formation of a composite preform. The preform can be a stack of foil/fiber/foils (fig. 1a), monotapes of aligned fibers embedded in plasma sprayed foil (fig. 1b), matrix coated fibers randomly (or closed) packed (fig. 1c) or a fiber mat in between powder cloth foils (fig. 1d)

Processing with foil/fiber/foil preforms has been widely used in the fabrication of CUR composites. However, the lack of ductility for some matrices (e.g. aluminides) makes the production of foil difficult. If the foil cannot be rolled to the proper thickness, it is often chemically milled [41], but this is an expensive solution. Another technique of making foils from difficult to roll materials is called the powder cloth method [112]. A powder cloth is a mixture of alloy powder and organic binder which is tape casted into a foil [113]. The aligned fibers of the preform must also be held in position by an organic binder (often an acrylic polymer) or by a cross-weave of metallic ribbon such as Nb or Mo (but preferably the matrix alloy composition if this can be fashioned into a ribbon). Prior to consolidation any organic binder must be fully off-gassed to minimize interstitial contamination of the matrix [41,42]. A high interstitial content (particularly oxygen in Ti

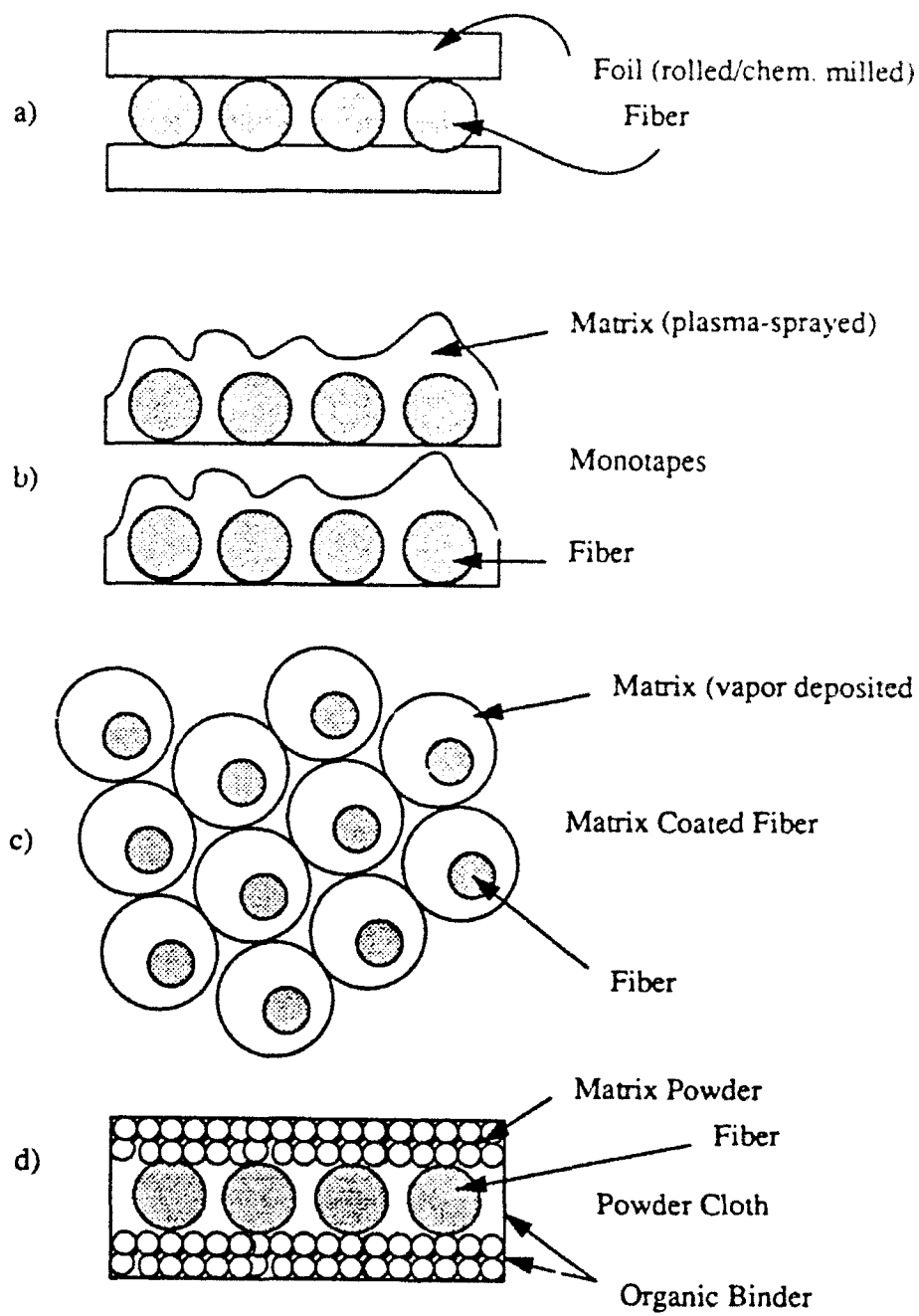


**Figure 1 Composite Preforms**



alloys) decreases the ductility of Ti 24Al 11Nb significantly [42,43]. Doble et al. [41] have also suggested that interstitial contamination (from the vacuum environment or by surface diffusion of elements from the fiber) may result in foil surfaces resistant to bonding and prone to later delamination. The cross-weave ribbon also may decrease composite properties such as high temperature time dependent creep/fatigue properties for reasons that are not fully understood [41].

The search for solutions to these problems led to the development of monotape and matrix coated fiber preforms. For these the matrix material is either vapor deposited (sputtered, or e-beam evaporated) to form a matrix coated fiber or melted and sprayed onto fibers wound around a mandrel to form a monotape [9-12]. The monotapes produced by molten droplet deposition typically have one smooth side corresponding to the side in contact with the mandrel during deposition and a much rougher side corresponding to the last deposited matrix (see figure 9 in ch. 3). To fabricate a composite from monotapes, one stacks the tapes with the fibers oriented unidirectionally or in any other configuration (i.e.  $0^\circ/\pm 90^\circ/0^\circ$ ). The obvious advantage of this technique is that no binder or cross-weaving ribbon is needed. However, spalling of fiber coatings sometimes occurs during the spraying process and fiber fracture during consolidation can be extensive unless a high (usually higher than is required to densify) consolidation temperature is used [14]. Though binder contamination is not a problem, interstitial contamination of the matrix may occur during plasma spraying and should be controlled [44]. Matrix coated single fiber preforms have many of the same advantages and disadvantages of monotapes. But there is an added flexibility of fabricating hoop or radially reinforced ring structures [11] and the difficulty of consolidation is significantly lessened for close-packed preforms [114].

Preform consolidation can be conducted in either a vacuum hot-press (VHP) or hot-isostatic press (HIP); the preform is placed in a vacuum environment and an appropriate temperature and pressure profile is chosen to achieve full density. A typical temperature and pressure profile to accomplish this is shown in figure 2. The specific

conditions of pressure, temperature and time are determined by the composite system and preform. Generally, foil/fiber/foil preforms are the most difficult to densify because

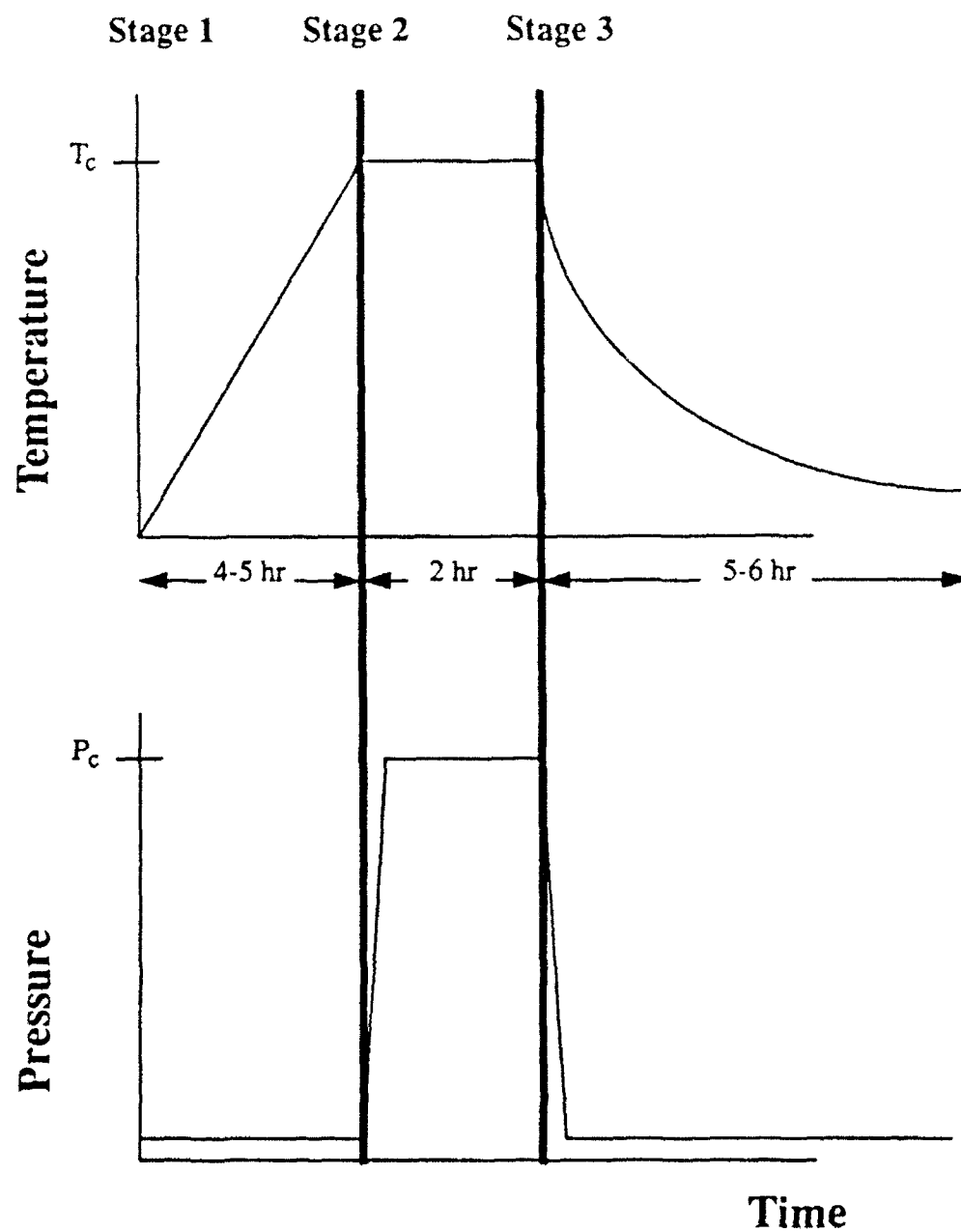


Figure 2 Temperature and pressure profiles for consolidation of metal matrix composites (for Ti 24Al 11Nb,  $T_c \approx 1000^\circ\text{C}$  and  $P_c \approx 100\text{ MPa}$ )

matrix material must flow a significant distance to fully densify. The matrix coated fiber preform with hexagonal closed-packed fiber arrays are the easiest [114]. Conditions are chosen so that both densification and fiber fracture reach desired goals.

In general, the process cycle can be divided into three stages. Stage 1 constitutes the ramp to consolidation temperature. Stage 2 begins as the pressure is applied (usually after the consolidation temperature is achieved to avoid fiber fracture) and includes the time at the "soak" temperature ( $T_c$ ) and pressure ( $P_c$ ). Stage 3 corresponds to the decrease in temperature and pressure from the Stage 2 levels. The process parameters that define these stages in combination with material properties determine the densification rate, matrix microstructure, fiber/matrix reactions, fiber integrity (damage) and ultimate coefficient of thermal expansion (CTE) mismatch residual stress. For a given composite system, the properties of the consolidated composite depend both on the chosen preform type and the processing parameters. Understanding the effect of both on composite properties is critical to the development of "best practices" for producing high performance composites.

Consolidation process development has thus far largely been a trial and error process. Doble and Kumnick's review of the consolidation of (SCS-6 (SiC fiber) reinforced Ti 24Al 11Nb) composites from foil/fiber/foil preforms reported the process as a collection of empirical rules [41]. They ranked the fabrication variables in order of their importance to composite performance:

- 1) Clean vacuum environment
- 2) Minimize residual stress
- 3) Minimize temperature and pressure

The purpose of keeping the vacuum system clean was to avoid interstitial absorption by the foil. Residual stress between the fiber and matrix should be minimized because the

resulting tensile hoop stress in the matrix induces radial cracks to form around the fiber [41,82-86]. Although Doble and Kumnick list the temperature and pressure as important fabrication variables, they viewed the most important affect of temperature to be on the fiber/matrix reaction which were neglected as sufficiently small. However, intuitively one would expect the extent of interfacial reactions (a function of processing) to affect debond/sliding properties and it is well known that decreasing the sliding resistance between the fiber and matrix affects both fatigue and toughness [2,3,45,46]. Hanusiak et al. [43] discussed the fiber/matrix interface solely from the viewpoint of the role of a fiber coating in protecting fiber strength during processing; the effects of processing on the structure and properties of the interface were neglected. It is probably the case that an interface coating must be "engineered" to provide the desired interfacial mechanical properties in the as processed state (Optimal sliding properties in intermetallic composites are thought to be around 100 MPa [116]). This lack of insight results in selection of sub-optimal processing conditions and a failure to realize the full potential of these types of composite systems.

Trial and error may find consolidation parameters that produce a fully dense material, but when additional factors such as fiber fracture, fiber/matrix reactions and residual stress are considered, a new set of parameters for densification experiments are required. A large test matrix is require to examine each factor which would be time consuming and very costly. Thus, the large number of quality concerns that must be controlled during composite processing (density, residual stress, matrix microstructure/ductility, fiber strength/integrity, and fiber/matrix reactions) make it almost impossible to use trial and error to optimize all concerns.

Predictive model development seems to be the only realistic approach to the optimization of composite design and processing. Recently several pertinent models have been published. Elzey and Wadley developed a densification model for the plasma spray monotape preforms [13]. Whilst at Rockwell Science Center, Bampton et al. [47] developed a densification model for foil/fiber/foil preforms. Residual stresses due to the

CTE mismatch have long been the subject of predictive models [48-51]. Fiber integrity or damage has been modelled for monotape preforms by Elzey and Wadley [111] and Elzey, Groves and Wadley [52]. The simultaneous use of these models at a workstation allows an "intelligent" temperature and pressure profile to be chosen for any system with known mechanical properties. However, models are lacking for the prediction of fiber/matrix reactions (and their affect on the interface properties) for the fibers and coatings of interest today.

## 2.2 Material

### 2.2.1 Fiber

Today's most common fiber for use in Ti alloy (or intermetallic) matrices is a SiC fiber. The SiC fiber (or monofilament) was first developed in the 1960's. Today there are two sources of this basic SiC monofilament: British Petroleum (BP) and Textron Specialty Materials (Textron - formally Avco Corp.). Both monofilaments are produced by chemical vapor deposition (CVD) of SiC on either a heated tungsten wire or carbon fiber substrate [53]. BP produces Sigma monofilaments that are almost identical to the SiC fibers developed in the 60's and 70's. It has a 12  $\mu\text{m}$  tungsten core and a diameter of about 100  $\mu\text{m}$  [54]. These monofilaments have either no coating (SM1040) or a dual coating of carbon and titanium diboride (SM1240). Textron produces SiC monofilaments using a 33  $\mu\text{m}$  carbon core with a total diameter of about 140  $\mu\text{m}$  [55]. They have developed a series of fibers; designated SCS-2, SCS-6, and SCS-8. The most significant difference between these SCS type fibers are their surface coatings. The SCS-2 fiber has a single 1  $\mu\text{m}$  thick C-rich (SCS) coating. The SCS-6 fiber has a dual C-rich coating that is 3-5  $\mu\text{m}$  thick. The coating on the SCS-8 fiber is C-rich near the fiber and increases to stoichiometric SiC at the surface and is 1  $\mu\text{m}$  thick [55]. Both the SCS-2 and SCS-8 fibers were originally intended as reinforcements for aluminum matrices whereas the thicker coated SCS-6 has become the preferred choice for the more reactive titanium matrices

[56].

Single crystal  $\text{Al}_2\text{O}_3$  monofilaments with c-axis orientations are now also available from Saphikon Inc. and is one of growing interest for reinforcement of aluminides (and ceramic matrix composites). The diameters are produced in diameters that from 25 to 150  $\mu\text{m}$ . The fibers are grown by an edge-defined, film-fed growth process (patented in 1971 by Labelle [57]). It entails drawing molten  $\text{Al}_2\text{O}_3$  out of a molybdenum capillary tube using an  $\alpha\text{-Al}_2\text{O}_3$  seed. At present Saphikon is available as an uncoated fiber (there is a polymeric sizing for handling purposes [58]), but work is in progress at several institutions to design an appropriate coating to expand its use in reactive Ti alloys matrices where its CTE is a better match with the matrix than SiC.

Some typical properties of the Sigma, SCS-6 and Saphikon fibers are given in Table 1.

**Table 1: Fiber Properties**

Fiber	Ultimate Strength (GPa)	Elastic Modulus (GPa)	Density ( $\text{g/cm}^3$ )	CTE ( $10^6/^{\circ}\text{C}$ ) R.T.	Ref.
Sigma (SM1040)	3.75	400	3.86	3.4 [103]	54
Textron (SCS-6)	3.5 - 4.4	410	3.15	3.4 [103]	55
Saphikon	2.5	460	3.97	5.0 <sup>a</sup>	59

a. C-axis

### 2.2.2 Fiber Coatings

Wawner [53] has reviewed some of the underlying reasons for SiC fiber coating development. Originally a thin carbon coating was used on SiC fibers to improve handlability (i.e. to reduce the generation of surface flaws). The coating was also thought to minimize the stress concentration ability of the SiC grain structure known as the Joffe

Effect. However, it was found that this type of coating caused wettability problems with both metal and epoxy matrices and in the case of metals, failed to protect the fibers from reactions with the matrix. The  $\text{TiB}_2/\text{C}$  and SCS coatings of the Sigma and SCS fibers are the result of attempts to solve these problems. Other coatings suggested by Kieschke et al. [60] include diffusion barrier oxide coatings ( $\text{Y}_2\text{O}_3$ ,  $\text{HfO}_2$ ,  $\text{ZrO}_2$ ) and duplex coatings consisting of various refractory metallic layers overlaid with a rare earth oxide.

The polymeric sizing (methylcellulose) on the Saphikon fiber is a water soluble coating developed only for protection during handling. It must be removed before consolidation in any matrix. The  $\text{Al}_2\text{O}_3$  does react in titanium matrices [61-63] and therefore, should have an additional coating to protect it during consolidation.  $\text{HfO}_2$  and  $\text{Y}_2\text{O}_3$  coatings have been studied as well as duplex coatings of  $\text{Y}_2\text{O}_3$  and Mo [12]. Mackin et al. [39] has also studied duplex coatings with an outer coating of a dense  $\text{Al}_2\text{O}_3$  and an inner coating of either carbon or a carbon/ $\text{Al}_2\text{O}_3$  mixture.

One purpose for protecting fibers from reactions is to avoid strength degradation [30,31,77]. Theoretically if perfect bonding is assumed, fiber strength degrades after the reaction zone has reached a critical thickness [30,31]. However, Smith et al. [64] suggested that when fiber/matrix debonding occurs, fiber strength degrades when the reaction reaches the load bearing portion of the fiber. Indeed, the strength of SCS-6 fibers do not apparently degrade in titanium matrices until the SCS layers are entirely consumed [65-67] suggesting fiber/matrix debonding occurs [64]. If the interface reacts during service conditions, minimizing the extent of reactions during processing will extend the useful high temperature life of the composite. Understanding the reaction kinetics during processing is necessary if this is to be accomplished.

### 2.2.3 Matrix

The alloy chosen for this study, Ti 24Al 11Nb, is an  $\alpha_2 + \beta$  alloy. The  $\alpha_2$  phase of the Ti - Al system is an ordered phase with a  $\text{DO}_{19}$  crystal structure. The  $\beta$  precipitates

have a bcc structure [72,73]. The  $\beta$ -phase improves ductility and its volume fraction can be increased by the addition of niobium, a beta stabilizer [72,74]. The  $\alpha_2 + \beta$  alloy has a distinct improvement in room temperature ductility over a stoichiometric  $\text{Ti}_3\text{Al}$ ,  $\alpha_2$  alloy [72,74]. The service temperature in air is limited to less than 650 °C due to oxidation problems. If the alloy is in a protected environment where creep is the concern, the alloy could be used up to 815 °C [74]

The microstructure of this alloy is sensitive to thermal history and may differ widely depending on the processing conditions used. Koss et al. [72] indicate that the microstructure may have a basketweave, aligned Widmanstatten or an equiaxed  $\alpha_2 +$  transformed  $\beta$  structure. The final microstructure depends on the solution heat treatment and whether the material is aged. A pseudo binary diagram of  $\text{Ti}_3\text{Al}$  and Nb is shown in figure 3. Processing in the  $\beta$  - phase region followed by a slow cool or rapid cool with a

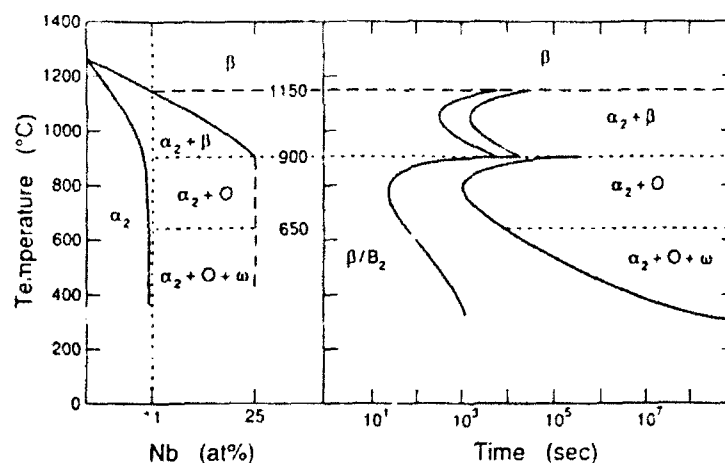


**Figure 3** Pseudo binary diagram of  $\text{Ti}_3\text{Al}$  and Nb

subsequent high temperature age produces an aligned Widmanstatten or basketweave structure respectively. Equiaxed  $\alpha_2$  grains with precipitated  $\beta$  on the grain boundaries are produced when processing in the  $\alpha_2 + \beta$  region with no subsequent aging [72]. Since the



temperature of processing for a Ti 24Al 11Nb matrix composite is in the  $\alpha_2 + \beta$  region ( $\approx 1000^\circ\text{C}$ ), an equiaxed  $\alpha_2$  structure with  $\beta$  on the grain boundaries is typically observed [75,76,].

The mechanical properties are dependent on the microstructure [117,118]. For example the yield strength as a function of temperature is shown in figure 4 for an equiaxed  $\alpha_2 + \beta$  microstructure (rolled sheet [76]) and a Widmanstätten or basketweave microstructure ( $\beta$  solutioned [107]). Other properties are given in table 2.

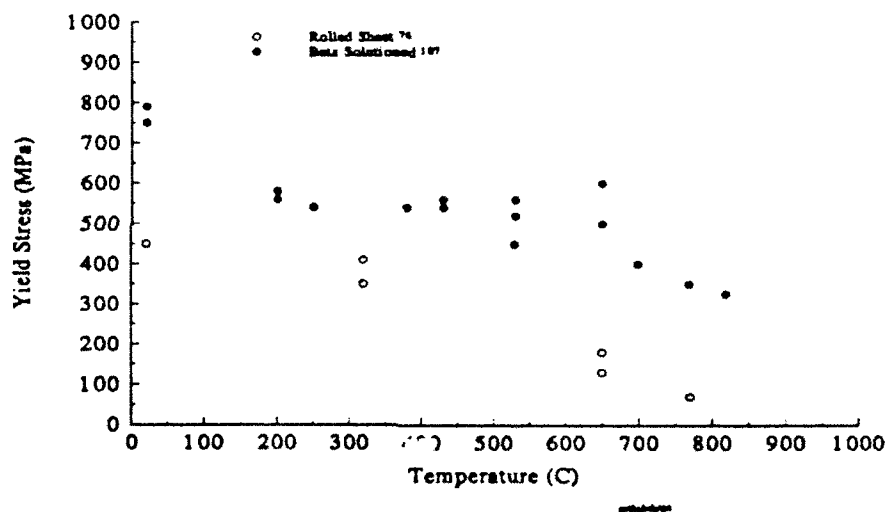


Figure 4 Temperature dependence of yield strength for Ti 24Al 11Nb

Table 2: Material Properties for Ti 24Al 11Nb

Young's Modulus (GPa)	Density (g/cm <sup>3</sup> )	CTE (R.T.) 10 <sup>6</sup> /°C	Ductility R.T.
100 [13]	4.6 [13]	9.0 [51]	2 - 5% [40]

## 2.3 Fiber/Matrix Interface

Understanding why certain reaction products are formed at the fiber/matrix

interface, analyzing the reaction kinetics, and measuring the subsequent interface properties is necessary for process optimization. The majority of work reported to date characterizes the reaction products and models isothermal kinetics for service conditions which are lower in temperature than processing [15-29]. Only recently - with the development of pushout and pullout tests - have the interface properties been directly studied [32-39,68]. Their relationship with structure has not yet been established.

### 2.3.1 Characterization of Interface Reaction

SiC (Sigma, SCS-6) fibers react in titanium alloys [77-81]. The reaction product of the Sigma (SM1040 an uncoated fiber) and commercially pure titanium results mainly in TiC and  $Ti_5Si_3$  [78,79]. Small amounts of  $Ti_3SiC_2$  were also reportedly found adjacent to the fiber [78]. It is suspected that similar carbides and silicides with variations due to Al and Nb would be present in a Ti 24Al 11Nb/Sigma reaction zone. The reaction between SCS-6, a coated fiber, and Ti 24Al 11Nb has been extensively studied and shown to result in a two phase reaction zone [77,80,81]. The inner zone consisted of a mixture of  $(Ti,Nb)C_{(1-x)} + (Ti,Nb,Al)_5Si_3$  while the outer zone was determined to be  $(Ti,Nb)_3AlC + (Ti,Nb,Al)_5Si_3$  [80]. As yet there is not a fundamental understanding of how the reaction product evolves. Bowden et al. [28] viewed the formation of a multi-layered reaction zone as a sequence of individual events, but they state that it is more likely that the different layers are formed simultaneously. The kinetics of the individual reaction layers is unknown because researchers have only measured the total thickness of the reaction zone which includes all the reaction layers. The difficulty is that TEM is often required to observe the individual reaction layers. This leaves the reaction zone thickness as the only parameter for the evolution of the interface structure.

In  $\alpha_2 + \beta$  alloys such as Ti 24Al 11Nb, a  $\beta$  depleted zone is also observed around the fibers [77,80,81]. In addition, radial cracking in the  $\beta$  depleted zone is observed [41,75,82-86]. There is evidence the radial cracks initiate in the reaction zone and propagate into the  $\beta$  depleted zone [83]. Generally, the cracks are arrested at the edge of

the  $\beta$  depleted zone, but after processing under extreme conditions (100 hrs at 980 °C) they may propagate into the  $\alpha_2 + \beta$  region [83]. The radial cracking problem is found in a number of titanium alloy matrix composites [84,85,88], but is more prevalent in the  $\alpha_2 + \beta$  alloys where an embrittled  $\beta$  depleted zone forms [41,82,86]. Since the interface properties are a function of residual stress acting on the fiber [33-39], relieving stress by cracking may affect these properties.

Single crystal  $\text{Al}_2\text{O}_3$  reacts readily with titanium [61-63]. Tressler et al [62] concluded the reaction zone consisted of a titanium oxide layer adjacent to the fiber and a  $\text{Ti}_3\text{Al}$  phase adjacent to the titanium matrix. More recently Misra [61] found only  $\text{Ti}_3\text{Al}$  as a reaction product in  $\text{Al}_2\text{O}_3/\text{Ti}$  diffusion couples. While for  $\text{Al}_2\text{O}_3/\text{Ti}_3\text{Al}$  diffusion couples, he found only  $\text{TiAl}$  to be the reaction product. For a  $\text{Al}_2\text{O}_3/\text{Ti 24Al 11Nb}$  composite, Hisung [87] has observed a dual phase reaction zone. Hisung reported an amorphous titanium oxide phase with embedded  $\text{TiO}$  crystals adjacent to the fiber. The second phase corresponded to  $\text{TiAl}$ . A  $\beta$  depleted zone and radial cracking are also observed to accompany processing.

### 2.3.2 Interface Reaction Kinetics

The growth of the reaction and  $\beta$  depleted zones are believed to be diffusion controlled processes [20,33,94]. The diffusion of titanium through the reaction zone appears to be the rate controlling process (in SCS-6 and Sigma composites) during the growth of the reaction zone in isothermal heat treatments (800 - 1000 °C) [77,89]. In the  $\text{Al}_2\text{O}_3/\text{Ti}$  and  $\text{Al}_2\text{O}_3/\text{Ti 24Al 11Nb}$  composite systems, a diffusion mechanism is also thought to control the growth of the reaction zone [61,62], but the rate controlling step and diffusing element are unknown. Two possible mechanisms for the growth of the  $\beta$  depleted zone in a SCS-6/Ti 24Al 11Nb composite have been proposed [82]. In one carbon (an  $\alpha_2$  stabilizer) from the C-rich SCS layer could diffuse into the  $\beta$  phase causing the  $\beta$  precipitates to transform into  $\alpha_2$ . Alternatively Ti and Nb may be consumed (to

form carbides and silicides) proportionally faster than the Al (an  $\alpha_2$  stabilizer). The enhanced aluminum concentration would then be available to stabilize the  $\alpha_2$  against  $\beta$  transformations. Similar mechanisms could explain the  $\beta$  depleted zones in the  $\text{Al}_2\text{O}_3/\text{Ti}$  24Al 11Nb system where now oxygen assumes the previous role of carbon.

By assuming diffusion of a matrix element through the reaction zone to be the rate controlling step, Gundel [77] has derived a growth rate equation

$$\frac{d\delta}{dt} = \frac{k^2}{2\delta} \quad [1]$$

where  $\delta$  is the reaction zone thickness;  $t$  is the time and  $k$  is a rate constant. Assuming  $k$  is constant with time, eqn. 1 can be integrated to give:

$$\delta = kt^{1/2} \quad [2]$$

The rate constant obeys an Arrhenius relationship of the form

$$k = k_0 \exp\left(-\frac{Q}{RT}\right) \quad [3]$$

where  $R$  and  $T$  are the gas constant and absolute temperature respectively;  $k_0$  is a preexponential constant;  $Q$  is an apparent activation energy defined as one half the activation energy for diffusion of the matrix element (probably Ti) in the reaction zone [90]. Since  $k$  is assumed constant with time, both  $Q$  and  $T$  must be constant with time. In other words eqn. 2 is valid for isothermal temperatures and an unchanging mechanism of growth (matrix element diffusing through the reaction zone). The kinetic constants for the reactions between SCS-6 and  $\text{Al}_2\text{O}_3$  fibers and titanium alloy matrices are well documented [16,18,77], and summarized in table 3.

Processing kinetics may be more complicated than the above model. There are

concerns about the mechanisms of growth. It is uncertain if diffusion of a matrix element through the reaction zone will control the reaction during initial growth. In addition, a significant portion of processing time is spent in a temperature ramp or cooling (non-isothermal conditions).

**Table 3: Reaction Kinetic Properties**

Fiber	Matrix	Q (KJ/mole)	$k_0$ (m/s <sup>1/2</sup> )	Temp. Range * (°C)	Reference
SCS-6	Ti 24Al 11Nb	134	$2.9 \times 10^{-3}$	800 - 1000	[77]
"	"	142			[16]
"	"	132	$2.0 \times 10^{-3}$	800 - 1000	[18]
Al <sub>2</sub> O <sub>3</sub>	Ti	108	$2.1 \times 10^{-3}$	650 - 925	[17]
"	Ti 24Al 11Nb	110	$4.5 \times 10^{-4}$	800 - 1000	[18]

\* Temp. Range defines the range of temperatures used in experimentally determining Q and  $k_0$ . These constants are often taken as valid at lower temperatures.

### 2.3.3 Interface Property Measurement

The recent immergence of pushout/pullout tests for single fibers in composites has allowed the study of interface mechanical properties [33-39,68,75,92,96]. It is convenient

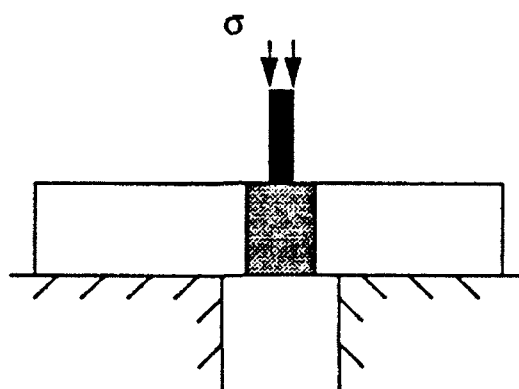


**Figure 5 Pushout test schematic**

to divide interface properties into two categories: debonding and sliding. Debond properties measure the ability of a matrix crack to deflect and propagate along a fiber/matrix interface (figure 6). They can be characterized by a mode 2 fracture energy,  $\Gamma_i$  and a debond sliding resistance,  $\tau_s$ . Physically  $\Gamma_i$  measures the energy required to create two new surfaces at an interface (i.e. chemical debonding) and the ability of the region to dissipate energy (e.g. through crack tip plasticity or reaction product cracking). After a crack has propagated over an interface, debond sliding may subsequently occur between the newly formed surfaces (it may also accompany the stable crack growth during the debonding event of a pushout test).  $\tau_s$  measures the resistance to these typically small sliding displacements that occur in practice (believed to be  $< 5 \mu\text{m}$ ) [33,93]. The sliding resistance is often considered a function of the radial residual clamping pressure [33,34,36,38,39,92,96]. At large fiber displacement ( $\geq 5 \mu\text{m}$ ), sliding resistance can be affected by fiber roughness [34,38,91,92] in addition to residual clamping stresses. In a pushout test, large displacement sliding resistance can be measured. Thus a pullout/pushout sliding resistance,  $\tau_p$ , (initially equal to but distinguished from  $\tau_s$ ) is introduced to describe the large displacement behavior and should be used when discussing the effects of fiber pullout on composite properties. In the limiting case when large displacement concerns can be neglected,  $\tau_p$  equals  $\tau_s$ .

In both ceramic and titanium matrix composites, research has focused on the effect of fiber roughness on sliding properties [34,36,38,39,91,92] and the effect of fiber coatings on both debond and sliding properties [39,68,91,94]. Although, the effect of reactions on interface properties has been investigated in thin plate samples [95], a clear understanding of its effect on interface properties in composites is still lacking.

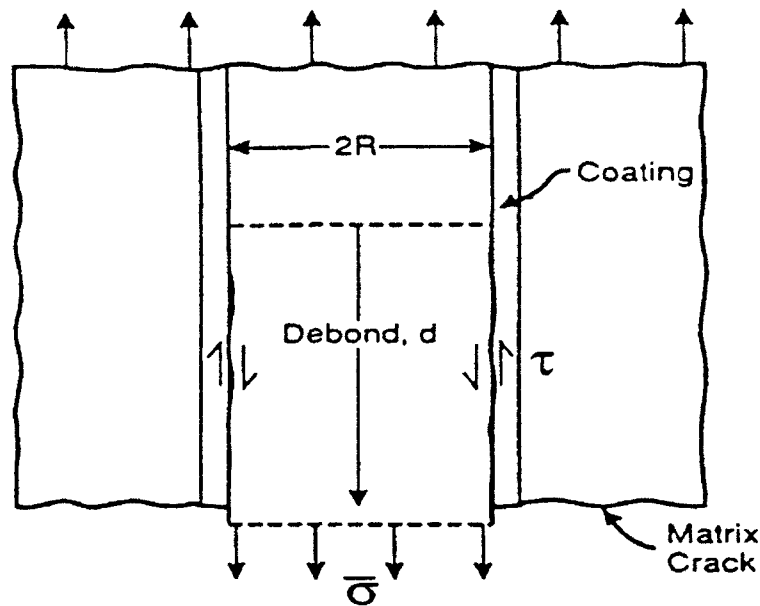


Figure 6 Fiber/Matrix debonding in a brittle matrix composite [from ref. 91]

Pullout more accurately simulates composite tensile failure, but a single fiber pullout specimen is difficult (and time consuming) to prepare. By comparison, specimens for pushout tests are relatively easy to prepare and multiple tests can be performed on a single multi-fiber specimen. The concern with the pushout test is the interpretation of the measurements. Difficulties arise because of the complexity of the stress state in the compressed fiber, relief of residual stresses [33] and bending effects [35].

Micromechanical models [33,35,92,96] have recently been developed to aid the analysis and design of pushout tests and to enable one to calculate  $\Gamma_i$  and  $\tau_s$  from pushout data (figure 7). Koss, Kallas and Hellmann [35,105] investigated the possibility of debond initiation at the specimen back-face (opposite the applied stress) because of induced bending stresses. They found to in order to avoid significant bending affects (which can cause mode 1 interface failure at the sample back-face) from corrupting the measurements, the ratio of the specimen thickness to the diameter of the support base hole (figures 5 and 11) must be greater then two. More recently this group also concluded that

even when the bending stresses are avoided by electroplating Ni on the back-face leaving a hole equal in size to the fiber, crack initiation still occurs at the back-face [106].

However, in general when bending stresses can be ignored, debond crack initiation is assumed to occur on the top-face and propagate down to the back-face [33,34,36,38,39,92,96]. The most extensive analysis to date using this assumption is by Liang and Hutchinson (LH) [33].

They determined the applied stress,  $\sigma_{ai}$  (defined as positive), required to initiate the debond crack is given by

$$\sigma_{ai} = \sigma_z + 2 \sqrt{\frac{\Gamma_i E_f}{B_2 R_f}} \quad [4]$$

where

$$B_2 = \frac{(1 + \nu_f)(1 - 2\nu_f)E + (1 + \nu)E_f}{(1 - \nu_f)E + (1 + \nu)E_f} \quad [5]$$

$\sigma_{ai}$  is the stress in the embedded fiber being pushed out.  $E_f$  and  $\nu_f$  are the Young's modulus and Poisson ratio of the fiber while  $E$  and  $\nu$  are for the surrounding region (matrix).  $\sigma_z$  is the axial residual compressive stress in the fiber (defined as positive). It opposes the applied stress and must be overcome to initiate debonding [92,93];  $\Gamma_i$  is the mode 2 debond toughness (or fracture energy) of the interface and  $R_f$  is the fiber radius.  $\sigma_{ai}$  is represented in the applied/displacement curve as the first point of deflection from linearity (figure 7). The non-linear portion represents stable crack extension along the interface.



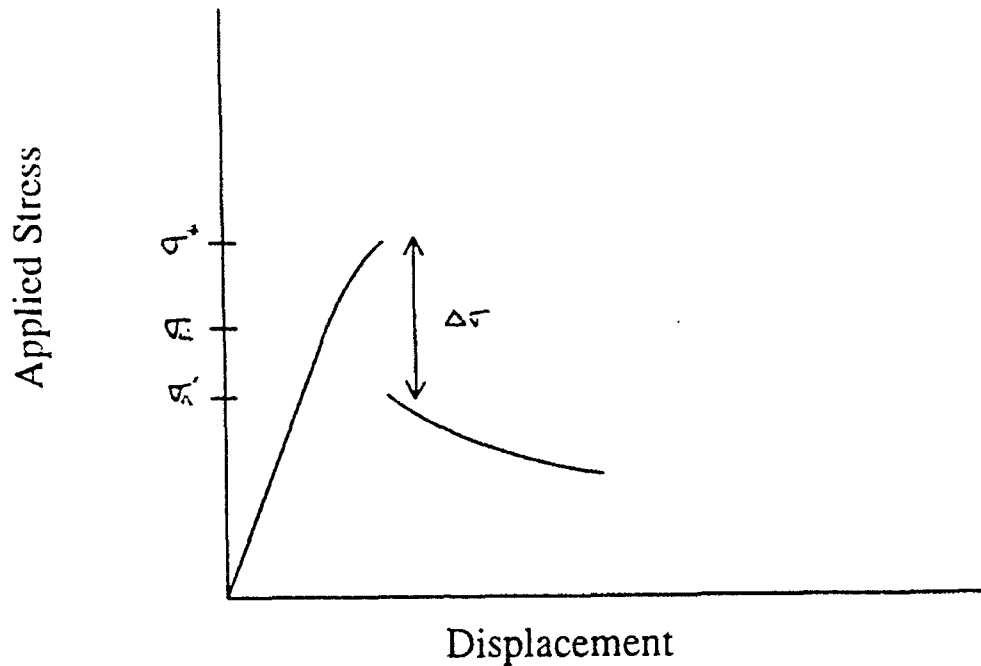


Figure 7 Applied Stress/Displacement Curve for Push-out

In this test as the debond crack propagates, the debonded portion of the fiber may slide relative to the matrix with a “debond” sliding resistance characterized by  $\tau_s$  [33].  $\tau_s$  is measure from the applied stress after the load drop ( $\Delta\sigma$ ):  $\tau_s = 2\sigma_d'/R_f$ . At this point the fiber has only been displaced a few microns [33], therefore the effects of large fiber displacement ( $\geq 5 \mu\text{m}$ ) are neglected. LH models the  $\tau_s$  as a combination of a constant term ( $\tau_0$ ) and a coulombic friction term:

$$\tau_s = \tau_0 + \mu\sigma_r \quad [6]$$

where  $\mu$  and  $\sigma_r$  are the coulomb friction coefficient and the radial (compressive) stress across the interface (compressive stress is defined here as positive).  $\sigma_r$  is controlled mostly by the CTE mismatch between the fiber and matrix and only weakly by the difference in Poissons ratio [97]. LH have speculated that  $\tau_0$  is controlled by fiber roughness. However fiber roughness is not thought to be significant until after large fiber displace-

ment ( $\geq 5 \mu\text{m}$ ) [93]. Thus it is reasonable to assume  $\tau_0 = 0$  during debonding and  $\tau_s$  is defined only as coulombic

$$\tau_s = \mu \sigma_r \quad [7]$$

Now a frictional contribution due to sliding of the debonded portion of the fiber can be added to eqn. 3 to describe the non-linear portion of the curve from  $\sigma_{ai}$  to  $\sigma^*$  in figure 7. The applied stress ( $\sigma_a$ ) becomes

$$\sigma_a = \sigma_z + 2 \sqrt{\left( \frac{\Gamma_i E_f}{B_2 R_f} \right)} (e^\zeta) + \frac{\sigma_r}{B_1} (e^\zeta - 1); \zeta = 2\mu B_1 \frac{l}{R_f} \quad [8]$$

where

$$B_1 = \frac{v_f E}{(1 - v_f) E + (1 + v) E_f} \quad [9]$$

$\Gamma_i$ ,  $E_f$ ,  $v_f$ ,  $E$ ,  $v$ ,  $\sigma_z$ ,  $\sigma_r R_f$ ,  $B_2$  and  $\mu$  are defined above.  $e^\zeta$  is a function of the debond crack length,  $l$ . LH determined that complete debonding (the point which defines the debond strength  $\tau_d$ ;  $\tau_d = 2\sigma^*/R_f$ ) occurs at the onset of unstable crack growth when  $l = t - 1.5R_f$  where  $t$  is the specimen thickness.

After debonding, the compressive axial stress ( $\sigma_z$ ) of the pushed out fiber section is relieved and the radial compressive stress across the interface becomes  $\sigma_r - B_1 \sigma_z$ . The applied stress to cause further sliding ( $\sigma_a'$ ) then becomes

$$\sigma_a' = \frac{(\sigma_r - B_1 \sigma_z)}{B_1} (e^{\zeta_d} - 1); \zeta_d = \frac{2B_1 \mu d}{R_f} \quad [10]$$

where  $d$  is the fiber length remaining in contact with the matrix and equals  $t$  just after debonding.<sup>1</sup>  $\Delta\sigma$  is calculated by subtracting eqn. 10 from eqn. 8 where  $l = t - 1.5R_f$ .

$$\Delta\sigma = \left[ 2\sqrt{\frac{\Gamma_i E_f}{B_2 R_f}} e^{-3\mu B_1} + \frac{\sigma_r}{B_1} (e^{-3\mu B_1} - 1) + \sigma_z \right] e^{\zeta_d} \quad [11]$$

With equations 7,10 and 11, the measured results for  $\sigma^*$  (or  $\tau_d$ ),  $\sigma_a'$  (or  $\tau_s$ ) and  $\Delta\sigma$  and either predicted or measured values for the residual stresses, both  $\Gamma_i$  and  $\mu$  may be calculated.

In brittle matrix composites a debond criteria has been developed [98] to determine the fiber and interface properties required to cause crack deflection at the interface. This debond criteria is a function of the ratio  $\Gamma_i/\Gamma_f$  (where  $\Gamma_f$  is the mode I fracture energy of the fiber). A matrix crack approaching perpendicular to an interface will be deflected up (or down) rather than penetrating through the interface if  $\Gamma_i/\Gamma_f$  is less than the ratio of the energy release rate of deflection to the energy release rate of penetration. This critical value depends on the elastic mismatch constant,  $\alpha = \frac{\bar{E}_f - \bar{E}_m}{\bar{E}_f + \bar{E}_m}$  ( $\bar{E} = \frac{E}{1 - \nu^2}$ ), and is shown on the following page.

---

1. LH assumed no significant changes occurred in the sliding properties at large displacements (i.e.  $\tau_p = \tau_s$ )

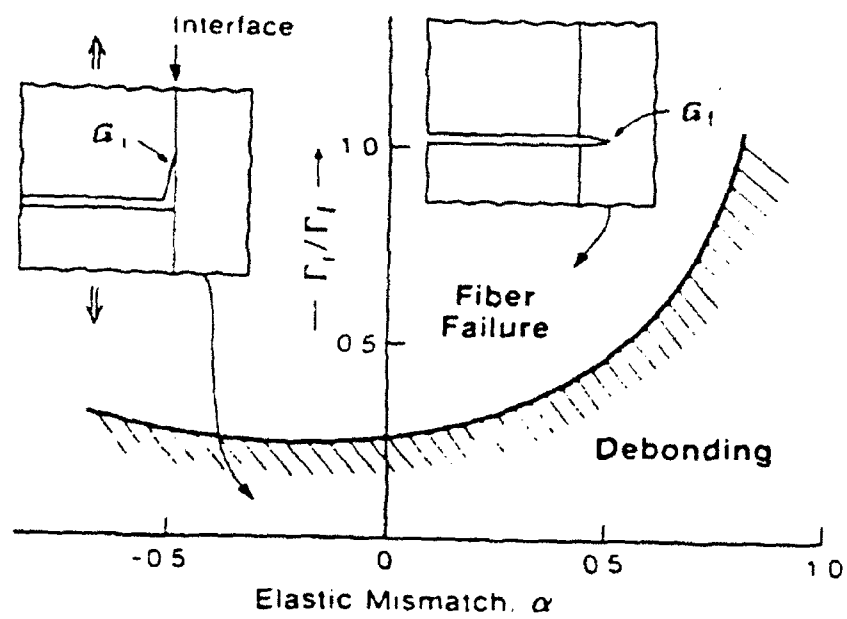


Figure 8 Debond diagram for brittle matrix composites [from ref. 91]

### 3 Experimental Procedure

The objective of this research was to begin to understand the structure/property/processing relationships for the fiber/matrix interface of SiC (and to lesser extent  $\text{Al}_2\text{O}_3$ ) fiber reinforced composites. Processing temperature and pressure profiles were chosen to vary the reaction zone thickness and the residual stresses, and both coated and uncoated fibers were consolidated in a Ti 24Al 11Nb matrix to determine their effect on interface properties. An investigation was also conducted to observe Stage 1 consolidation of a foil/fiber/foil preform.

#### 3.1 Material

Plasma sprayed Ti 24Al 11Nb (at%) foil (figure 9) was supplied by GE in Lynn, Ma. The plasma spray process [9,10,14] deposits molten matrix material onto a spinning drum. The resulting foil is about 250  $\mu\text{m}$  thick and has one rough side and one smooth side. To avoid the detrimental effects of surface roughness upon fiber damage [14], the roughness was removed. The foil was cut into discs (3.2 cm in diameter) by electrodischarge machining or grinding. The smooth side of the discs were then attached to the bottom of a cylinder (diameter  $\approx$  3.8 cm, height  $\approx$  7.5 cm) using double sided tape. The rough side was then ground to a 180 grit finish. In addition, a flat edge was created as a reference when aligning the fibers.

A number of different fiber were chosen for study. Two SiC fibers - SCS-6 (Textron) and Sigma (BP - SM1040) - were studied as well as the uncoated single crystal  $\text{Al}_2\text{O}_3$  fiber (Saphikon Inc.). A few coated Saphikon fibers (outer coating of  $\text{Y}_2\text{O}_3$  and a refractory metal on the fiber surface) were supplied by 3M. Room temperature properties for the matrix and fibers are given in table 4.

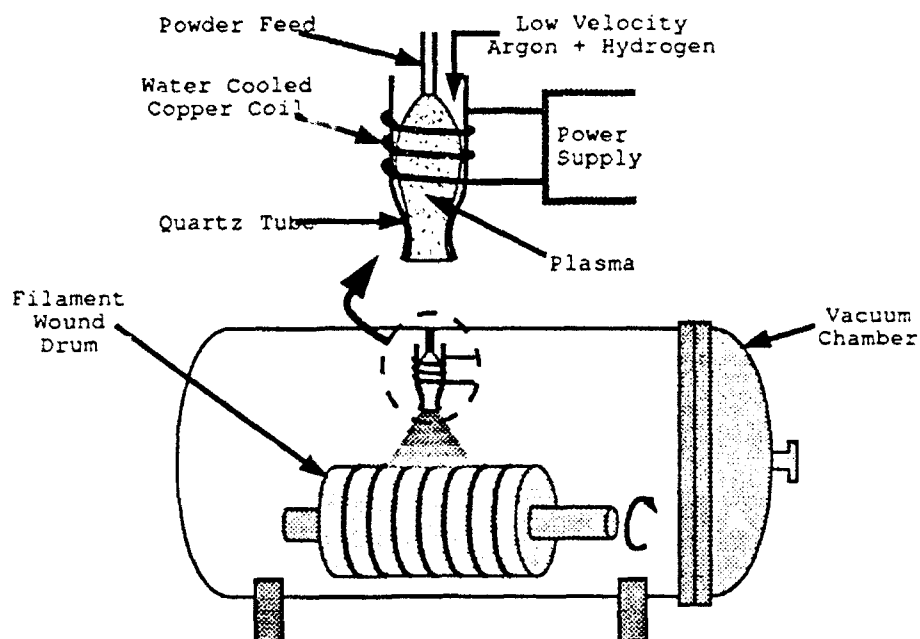


Figure 9 Plasma Spray Process for producing neat foil or monotapes (from ref. 54)

Table 4: Material Properties (Room Temperature)

	Young's Modulus (GPa)	Yield Strength (MPa)	Ultimate Tensile Strength (MPa)	Coefficient of Thermal Expansion ( $10^{-6} \text{ }^{\circ}\text{C}^{-1}$ )
Ti 24 11	110-145 [74]	500 [74]	600 [102]	8.2 [103]
SCS-6	400 [55]		3300 - 4400 [55]	3.4 [103]
Sigma	410 [54]		3750 [54]	3.4 [103]
Saphikon	414 [104]		2100 - 3400 [58]	5.0 <sup>a</sup> [58]

a. C-Axis

### 3.2 Processing

To produce foil/fiber/foil preforms, the fibers were first placed in file grooves to ensure a parallel array and subsequently taped to a surface covered with wax paper. A foil disc was then placed under the array of fibers aligning them perpendicular to the flat edge. The fiber array was bonded to the foil discs using an organic binder that would burn off in the VHP process.

The foil/fiber/foil preforms were consolidated under uniaxial constrained condition in an Astro HP20 vacuum hot press (VHP). The preforms were placed between graphite ram rods and constrained with a graphite collar. A furnace was brought down over the sample and about a 60 millitorr vacuum was created with a mechanical pump. A three stage temperature ramp was used in Stage 1 (figure 2 and 10). The ramp rate to the hold temperature of 150 °C and 450 °C was 8 °C/min. The temperature was held at these temperatures to remove absorbed H<sub>2</sub>O and organics from surfaces and the binder holding the fibers to the foil discs. The final ramp rate was decreased to 4 °C/min to keep the vacuum under 100 millitorr. Only the consolidation temperature and the time of Stage 2 were varied. Eight different consolidation temperatures and times were chosen (table 5)

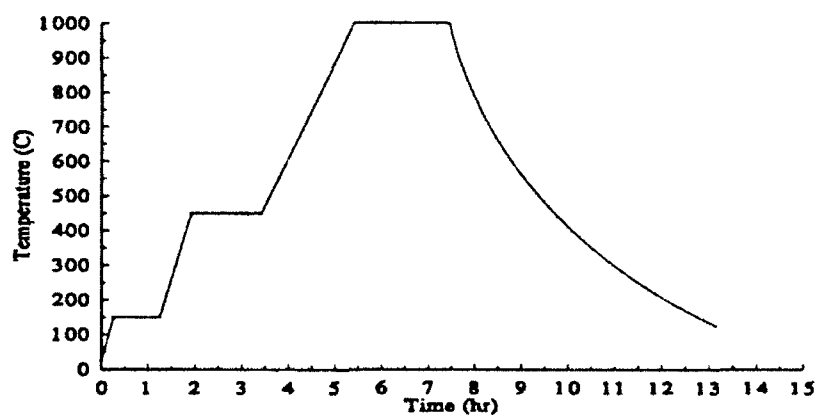


Figure 10 Typical temperature cycle during VHP

**Table 5: Processing Conditions**

Process	Temperature (°C)	Pressure (MPa)	Time (minutes)
Time Dependence			
1	1040	100	30
2	1040	100	60
3	1040	100	90
4	1040	100	120
5	1040	100	240
Temperature Dependence			
6	980	100	120
7	1000	100	120
8	1020	100	120
4	1040	100	120

To investigate the effects of Stage 1 on the structure of the interface, three experiments were done. First a consolidated sample was fabricated at 1040 °C / 100 MPa / 30 min. with an extended ramp in Stage 1. The foil/fiber/foil preform was held above 850 °C for 3 hrs. longer than in the previously described Stage 1 ramp. In a second experiment, the foil/fiber/foil preform was held at 875 °C for 2 hrs. before ramping up to 1040 °C at 4 °C/min and then furnace cooled without applying pressure. The effect of the Stage 1 ramp used in the consolidation experiments was also investigated.

### 3.3 Characterization

A JOEL 840 scanning electron microscope (SEM) was used to characterize the consolidated composites before and after pushout testing (described in 3.4.2). The consolidated samples were sectioned perpendicular to the fiber direction, polished to a 1



$\mu\text{m}$  finish, and Kroll etched (10% HF, 5%  $\text{HNO}_3$ , 85%  $\text{H}_2\text{O}$  - 10 to 20 sec. at R.T.) to reveal the fiber/matrix interface and matrix microstructure. The grain size was measured with the line intercept method described in ASTM E112-85. The volume and size of  $\beta$  phase particles was determined with an image analysis. The characterization of the interface consisted of measuring the reaction and beta depleted zone thicknesses from both SEM micrographs and the SEM screen - after calibrating the screen with a calibration grid. The extent of the radial cracking was quantified by measuring the average number and length of the cracks. The debond path in the pushout tests was determined from SEM micrographs of pushed out fibers.

### 3.4 Interface Properties

#### 3.4.1 Specimen Preparation

Specimens from each of the consolidated samples were prepared for pushout testing conducted at both the University of California at Santa Barbara (UCSB) with Dr. Tom Mackin and at the University of Virginia (UVA). The specimens tested at the two sites were prepared somewhat differently because of different metallography equipment existing at each facility. In both cases a 400 - 500  $\mu\text{m}$  thick specimen was cut perpendicular to the fiber direction with a diamond saw. At UVA the composite was embedded in a cold mounting resin before sectioning. This simplified the manual polishing of the (0.5 x 2.0 x 15 mm) specimen. Both surfaces of the sectioned sample were ground to the appropriate thickness - 400  $\mu\text{m}$  (UCSB), 480  $\mu\text{m}$  (UVA) - with a 600 grit finish..

The specimens tested at UCSB were then polished to a 1  $\mu\text{m}$  finish using a Malvern Multipol automatic lapping machine. The automatic lapping machine allowed specimens from all eight VHP samples to be prepared at the same time. The specimens were attached with crystal bond to a disc and lined up parallel to an outer support ring. After both sides had been polished, the thickness was optically measured with a scaled eye

piece. It was always  $250\text{ }\mu\text{m} \pm 15\text{ }\mu\text{m}$ . The diameter of the support base hole was about  $220\text{ }\mu\text{m}$ ; thus, the ratio of the specimen thickness to the support base hole was less than two.

The specimens tested at UVA were polished to a  $1\text{ }\mu\text{m}$  finish using manual metallography techniques. A  $6\text{ }\mu\text{m}$  polish using SiC paper or diamond paste on a nylon or lapping wheel was followed by a light  $1\text{ }\mu\text{m}$  polish ( $\text{Al}_2\text{O}_3$  slurry on a cloth wheel). The thickness was optically measured with a scaled eye piece to be about  $450\text{ }\mu\text{m} \pm 10\text{ }\mu\text{m}$ . Therefore the ratio of specimen thickness to the support base hole is slightly greater than two.

### 3.4.2 Pushout Tests

The pushout tests were performed on either a 1400 series Instron (UCSB) or an Applied Test System (ATS) 900 (UVa) tensile/compression testing machine. A  $300\text{ }\mu\text{m}$  (height) Sigma fiber,  $100\text{ }\mu\text{m}$  in diameter, was used as the push-rod or indenter (see fig. 8). The specimen was held on the support base with double sided scotch tape. Using a microscope to magnify the specimen and a needle to control the push-rod, it was first aligned over the fiber to be tested. Vacuum grease was applied to the specimen surface to ensure the push-rod did not move while transporting the support base to the test machine. The fiber and push-rod were then positioned over the hole in the support base (diameter  $\approx 220\text{ }\mu\text{m}$ ). Vacuum grease was again used to hold the specimen over the hole. Centering the fiber over the support base hole was done by first centering the hole with a scaled eye piece. The fiber was then positioned over the hole without moving the support base.

The fixture in the testing machine consisted of a sectioned ceramic ball set in the machined hemisphere of a steel bar and a platen for the support base. A ceramic surface was required to avoid the indenter deforming the fixture surface rather than pushing to fiber out. Before the specimen and the support base were put into the fixture, the ceramic ball was set in the steel bar by loading the fixture to seventy pounds. Vacuum grease was used to hold the ball in the hemisphere.

In the tests performed at UCSB, the loads were directly measured from a 200 lb load cell using a volt meter (1V/lb). The deflection at the bottom of the fiber was measured with a lever arm deflection gage (figure 11). The signal from the strain gage was amplified, digitized and stored in an ASCII file with the load and time measurements.

At UVa the loads were measured from a 5000 lb load cell on the 10 percent setting essentially giving a 500 lb load cell. A deflection gage was not available, therefore, only the load verses time was measured. A chart recorder was used for this purpose.

The pushout test started by first optically centering the specimen and the support base under the ceramic ball. The bar/ball fixture was brought down slowly (CHS = 0.1 mm/sec. UCSB; = 0.3 mm/sec UVA). When the ceramic surface was close to the push-rod, the speed was changed to about 0.015 mm/sec at UCSB and 0.025 mm/sec at UVa. When a load was measure the data collection began, giving typical results as shown in fig. 9. The peak load is used to define the debond strength -  $\tau_d = (\text{peak load})/2\pi R_{ft}$  - and the load after  $\Delta\sigma$ ,  $\sigma_a'$ , defines the debond sliding resistance -  $\tau_s = \sigma_a'/2\pi R_{ft}$ .

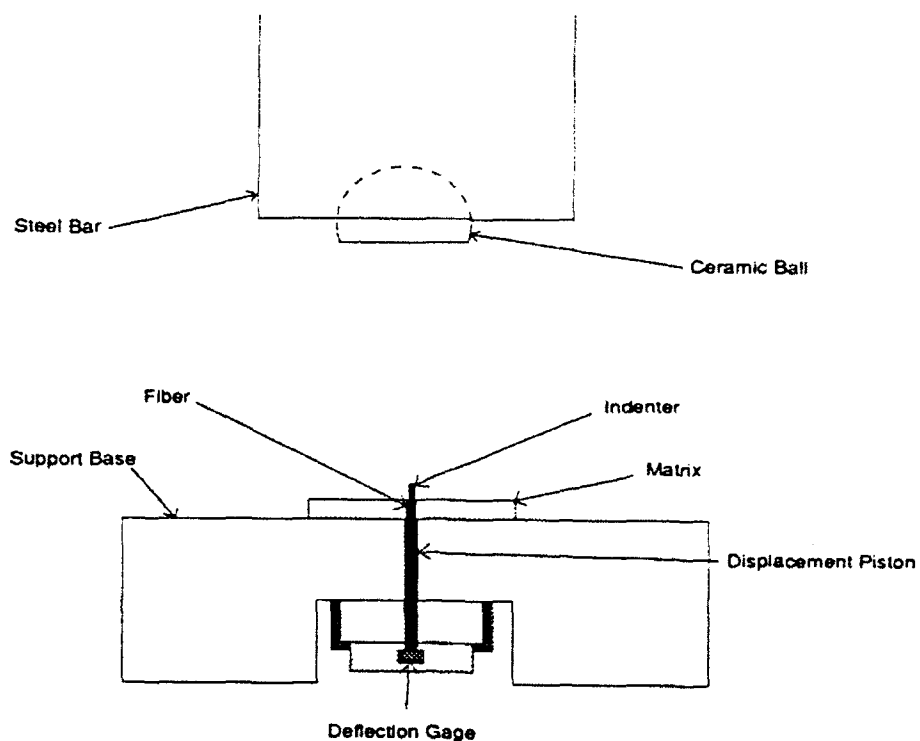


Figure 11 pushout test set-up

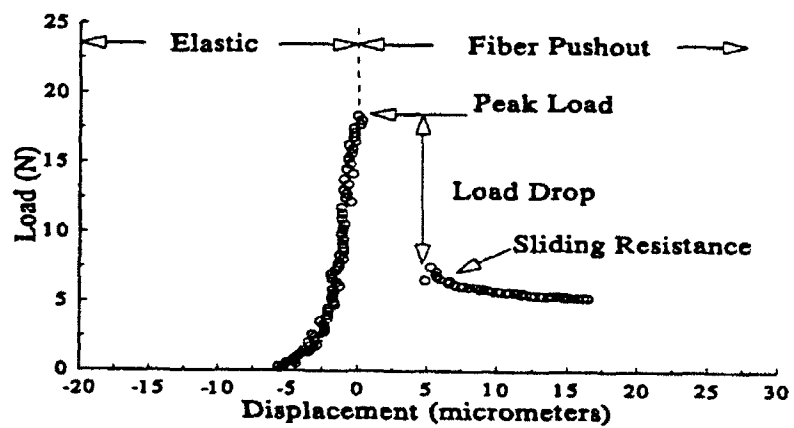


Figure 12 Typical pushout test data (UCSB Method)

## 4 Results

### 4.1 Characterization

#### 4.1.1 Matrix

The matrix microstructure (far from the fibers) depended upon the consolidation process conditions. Typically it consisted of equiaxed  $\alpha_2$  grains with  $\beta$  phase particles precipitated at the  $\alpha_2$  grain boundaries (figures 13-16). The  $\alpha_2$  grain size increased with increase in processing temperature and time (table 6). The volume fraction of  $\beta$  also increased with processing temperature, but did not change with processing time. As the processing temperature was increased from 980 °C to 1040 °C, the  $\beta$  fraction increased from about 4 to 10 %. In addition, the  $\beta$  distribution changed from heterogeneous to homogeneous with increasing temperature (figures 13 and 16). The origin of the non-uniformity of the  $\beta$  precipitates at 980 °C may reflect niobium segregation in the as-sprayed foils.

**Table 6: Quantitative Metallography**

Process Conditions	Grain Size ( $\mu\text{m}$ )	Volume Percent $\beta$	Size ( $\mu\text{m}^2$ ) $\beta$	Distribution of $\beta$
1040 °C / 30 min.	4.5	10	0.4	uniform
1040 °C / 120 min.	6.4	10	0.6	uniform
1040 °C / 240 min.	8.4	11	0.7	uniform
980 °C / 120 min.	5.5	4	0.4	non-uniform

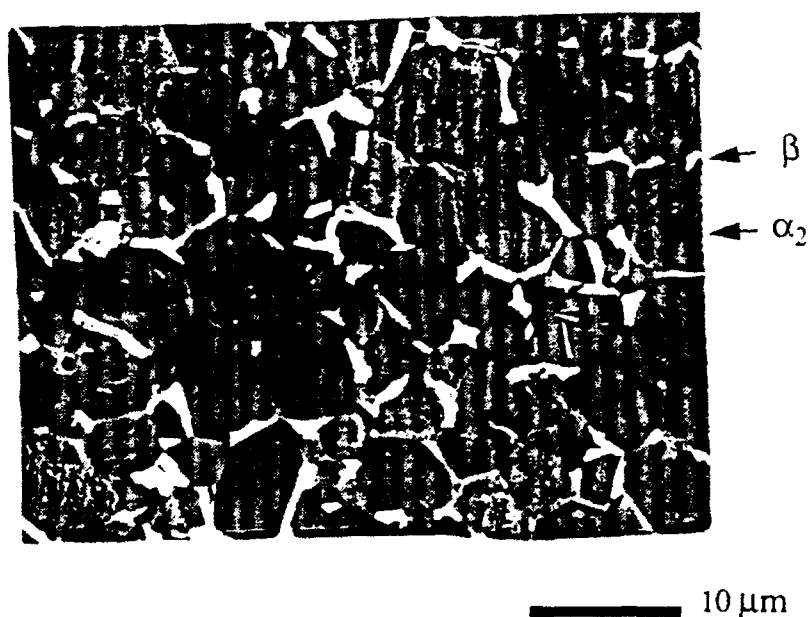


Figure 13 Matrix Microstructure (VHP 1040 °C / 100 MPa / 30 min)

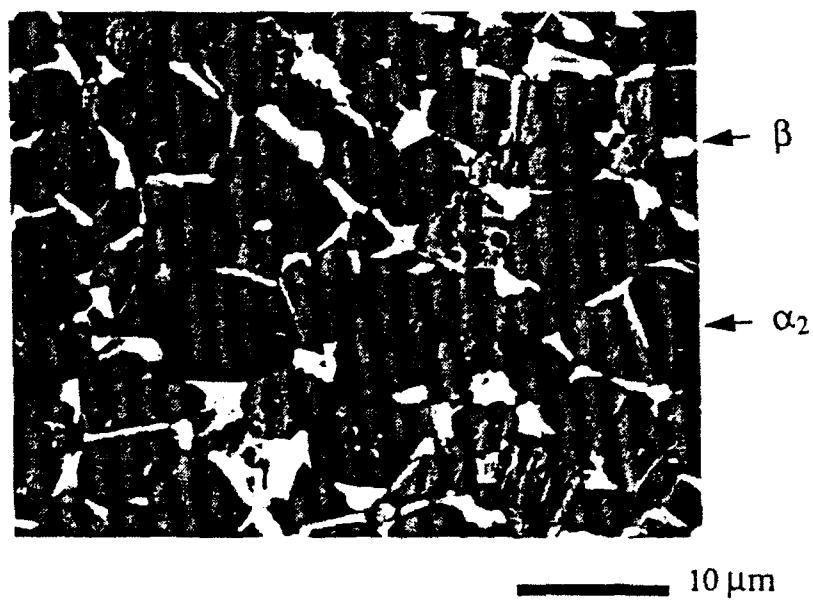


Figure 14 Matrix Microstructure (VHP 1040 °C / 100 MPa / 120 min)

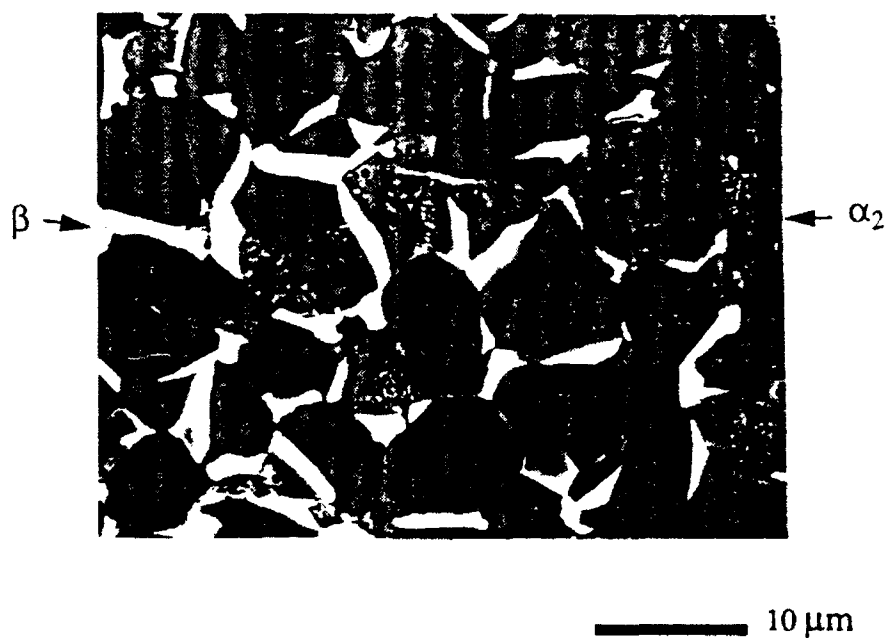
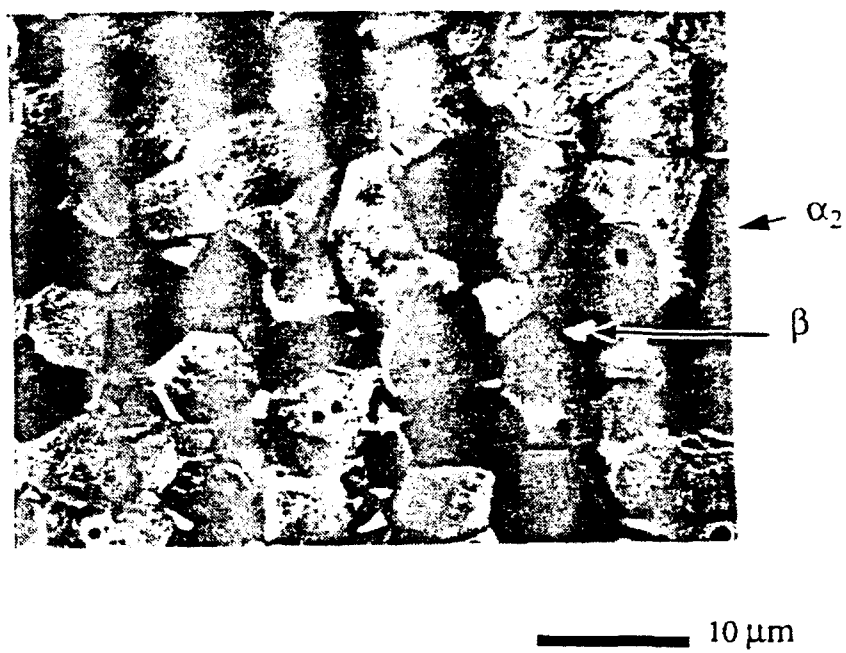
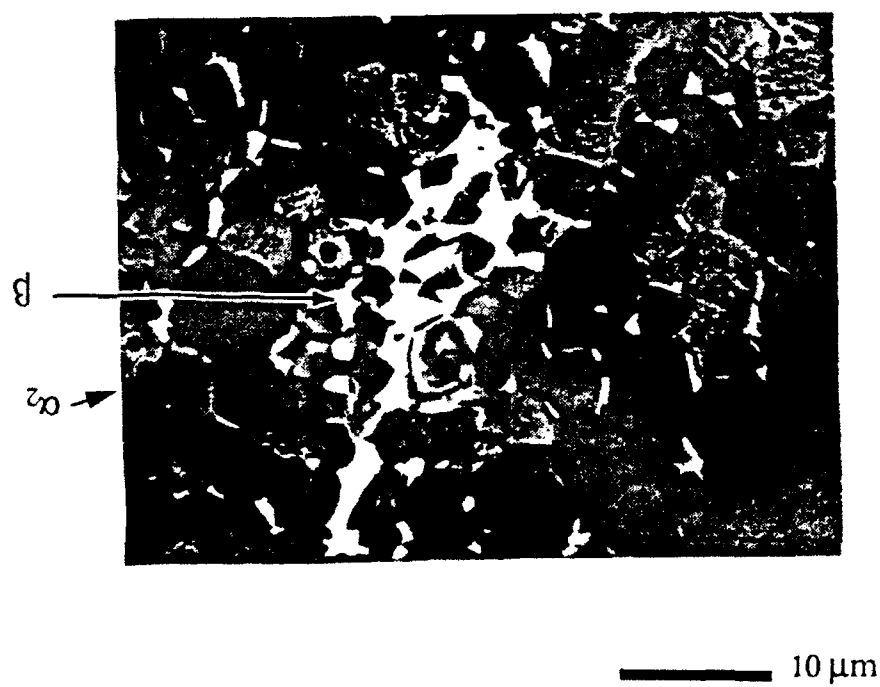


Figure 15 Matrix Microstructure (VHP 1040 °C / 100 MPa / 240 min)



a)



b)

Figure 16 Matrix Microstructure (VHP 980 °C / 100 MPa / 120 min)



### 4.1.2 $\beta$ - Depleted Zone

Near the fiber/matrix interface, a  $\beta$  - depleted zone was observed for all the consolidation conditions (Figures 17-19). The  $\beta$  depleted zone thickness depended both on the type of fiber present and the processing conditions (figures 20 and 21). It increased with processing time for all three fiber types (SCS-6, Sigma - SM1040 and Saphikon -  $\text{Al}_2\text{O}_3$ ). However, the SCS-6 fibers always had the smallest zone while the uncoated  $\text{Al}_2\text{O}_3$  had the largest. There was only a weak dependence of  $\beta$  - depleted zone thickness upon processing temperature for the SCS-6 fiber. A more significant dependence upon temperature was observed for the other two fibers (figure 21).

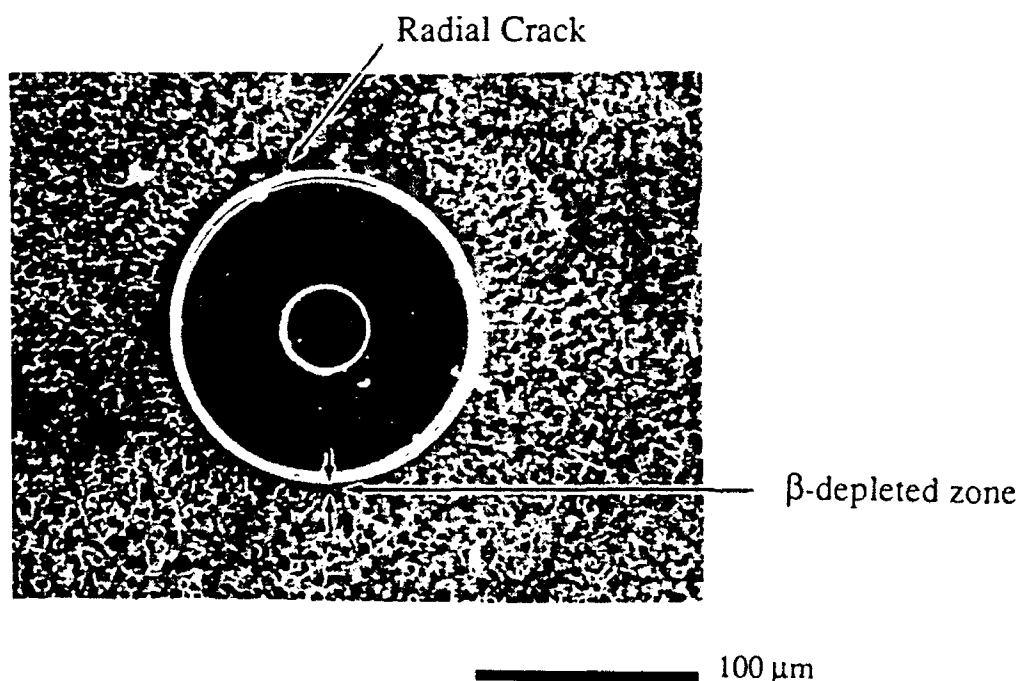


Figure 17 SCS-6 / Ti 24Al 11Nb (VHP 1040  $^{\circ}\text{C}$  / 100 MPa / 30 min)

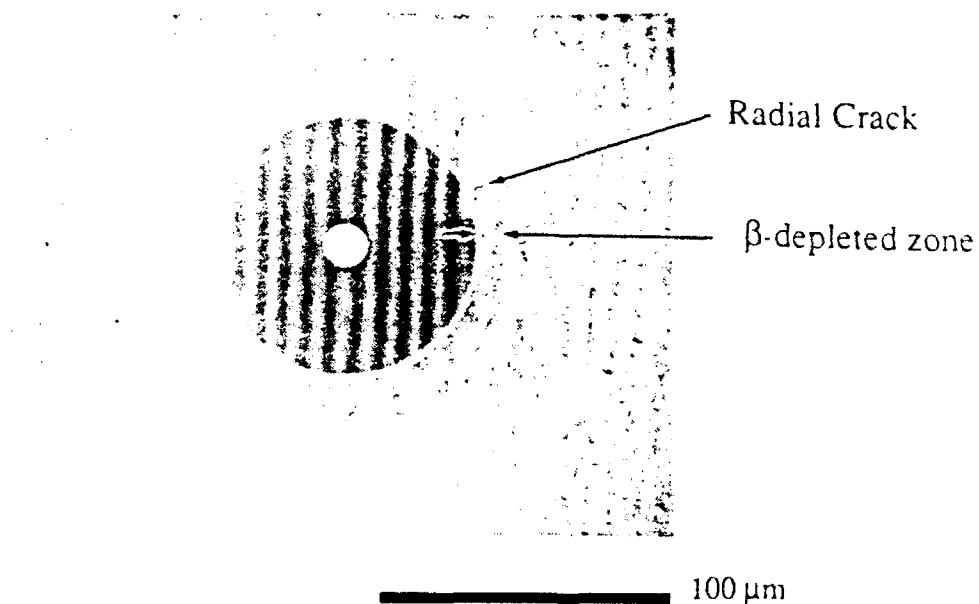


Figure 18 Sigma / Ti 24Al 11Nb (VHP 1040 °C / 100 MPa / 30 min)

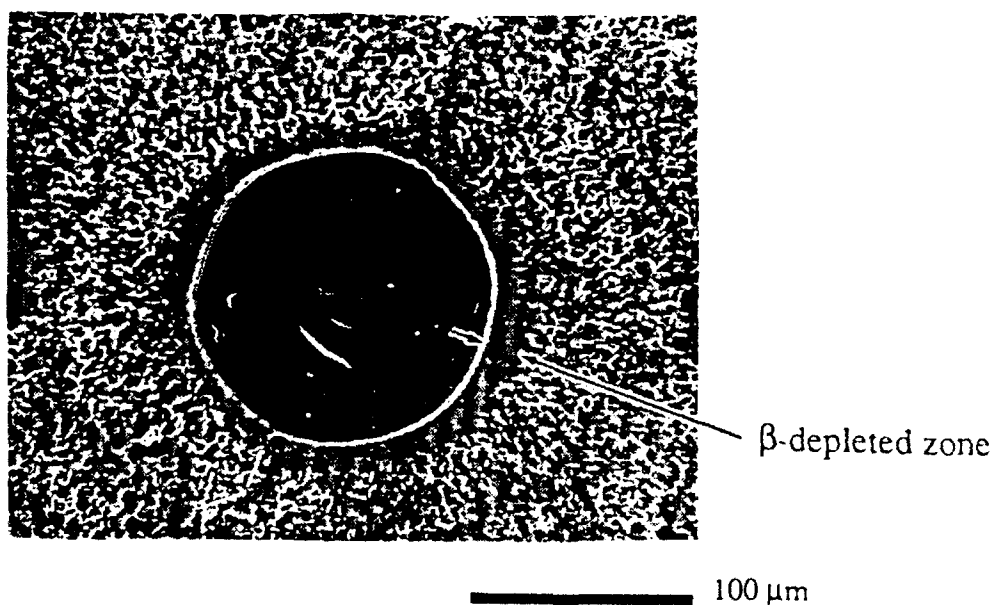


Figure 19 Saphikon / Ti 24Al 11Nb (VHP 1040 °C / 100 MPa / 30 min)

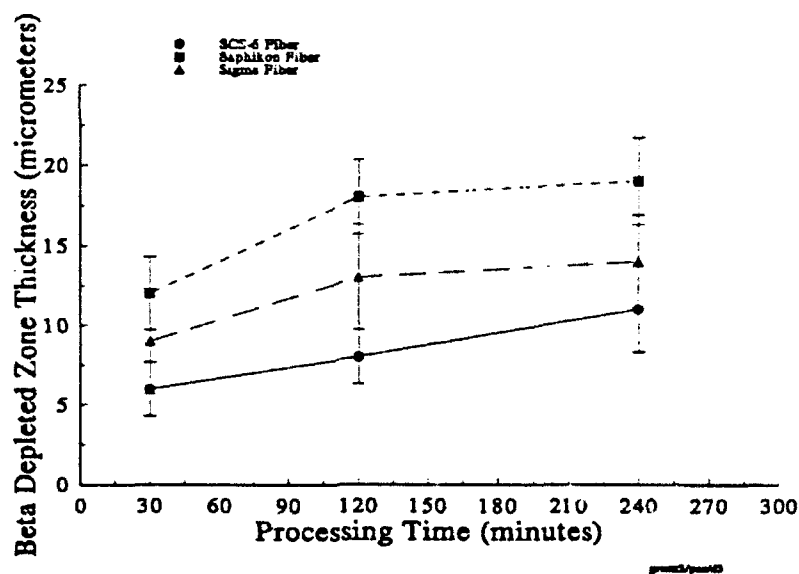


Figure 20  $\beta$  Depleted Zone Thickness vs. Processing Time

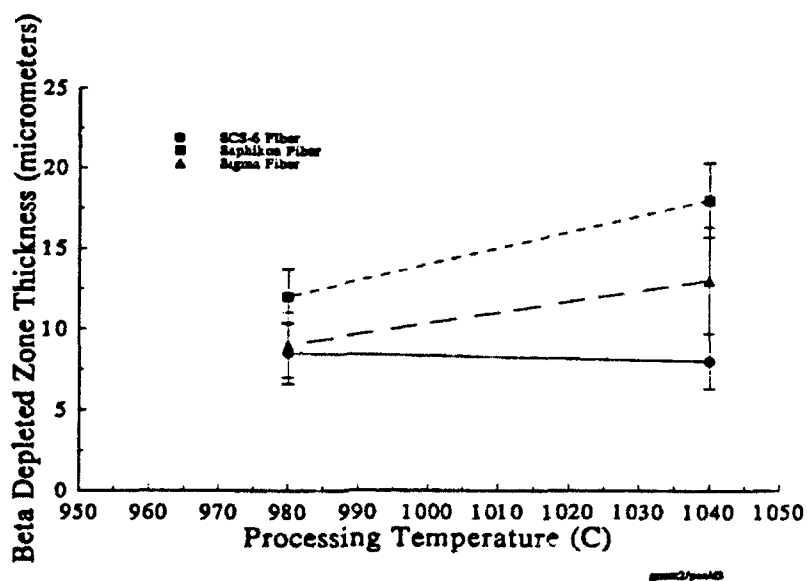


Figure 21  $\beta$  Depleted Zone Thickness vs. Processing Temperature

### 4.1.3 Radial Cracks

Radial matrix cracks were consistently present around both the SCS-6 and Sigma fibers (figures 17 and 18), but significantly more cracking was observed around the Sigma fibers. These cracks were generally arrested at or before the  $\beta$  depleted zone boundary, (figures 17 and 18) often by the more ductile  $\beta$  precipitates. Radial cracks were only occasionally observed around the Saphikon fibers; presumably a consequence of the smaller CTE mismatch compared with the SiC case (tables 1,4 and 9)

To quantify these cracks, a convenient damage parameter was defined as the average number of cracks per fiber multiplied by the average length of cracks. Figure 22 shows the effect of processing time on the damage around the both SiC fiber types. As the processing time increased the damage parameter increased. The difference in the damage parameters for the SCS-6 and Sigma fibers confirms the observation that more cracking occurs around a Sigma fiber. The damage parameter for both fibers shows a weaker trend with temperature in figure 23 than was shown in figure 22. For the SCS-6 composites, the damage parameter was essentially independent of consolidation temperature while the Sigma composite showed a small increase.

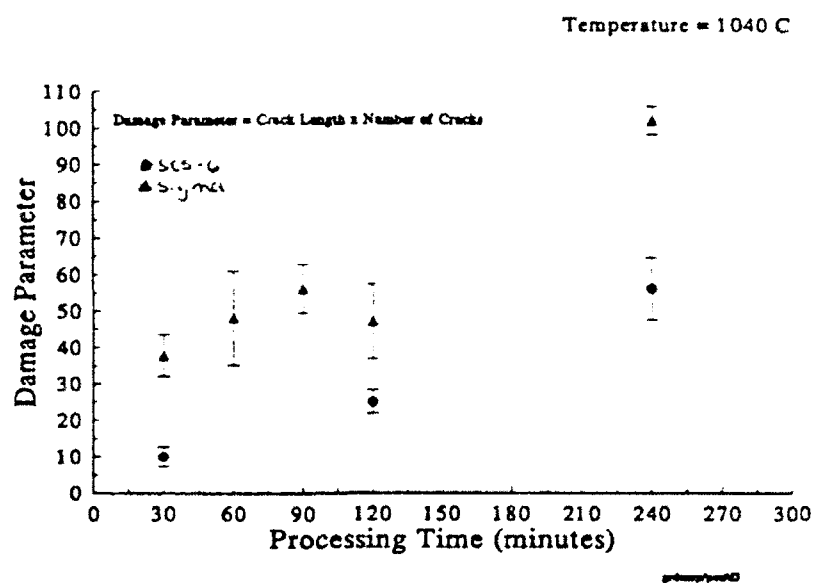


Figure 22 Damage Parameter vs. Processing Time

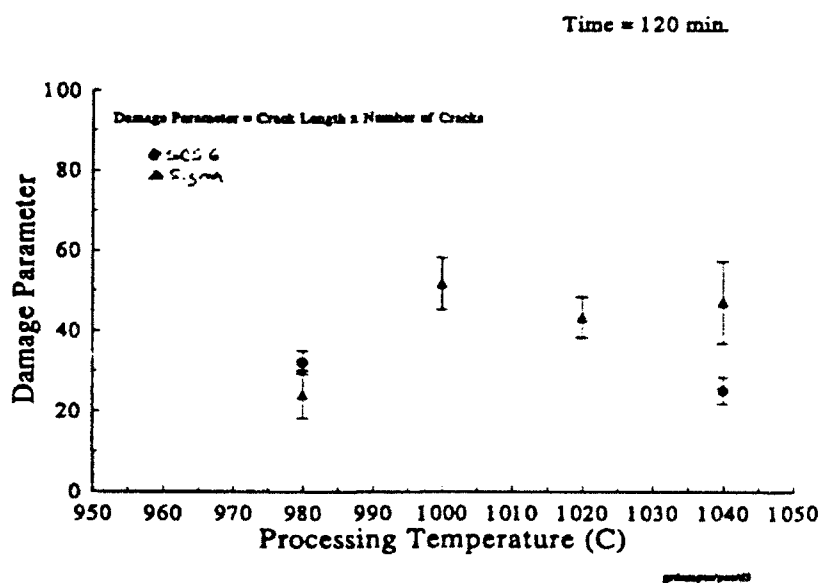


Figure 23 Damage Parameter vs. Processing Temperature

#### 4.1.4 Interface Reaction Zone

SRM Observations at high magnifications have revealed that the fiber and matrix always reacted to form interfacial reaction products (figures 24-26). The reaction zone of SCS-6 samples had two reaction layers (figure 24). Baumann et al. [82] reported the inner layer consisted of a mixture of  $(\text{Ti, Nb})\text{C}_{(1-x)}$  and  $(\text{Ti, Nb, Al})_5\text{Si}_3$  while the outer layer was likely a mixture of two phases:  $(\text{Ti, Nb})_3\text{AlC}$  and  $(\text{Ti, Nb, Al})_5\text{Si}_3$ .

The total reaction zone thickness ( $\delta$ ) was measured as a function of process conditions. In figures 27 and 28,  $\delta$  can be seen to increase with both processing time and temperature for all three fiber types. The SCS-6 fibers exhibited the smallest reaction zones while the Sigma fiber had the largest. The kinetics of growth appeared parabolic with processing time (figure 27) and the growth rate appeared to increase with temperature (figure 28).

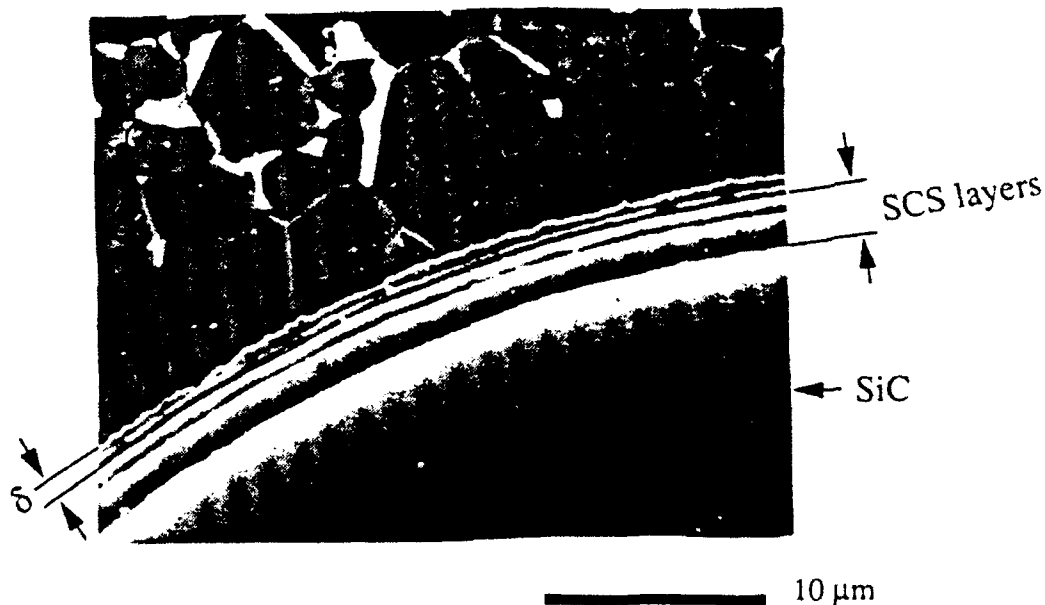


Figure 24 SCS-6 / Ti 24Al 11Nb Interface (VHP 1040 °C / 100 MPa / 30 min.)

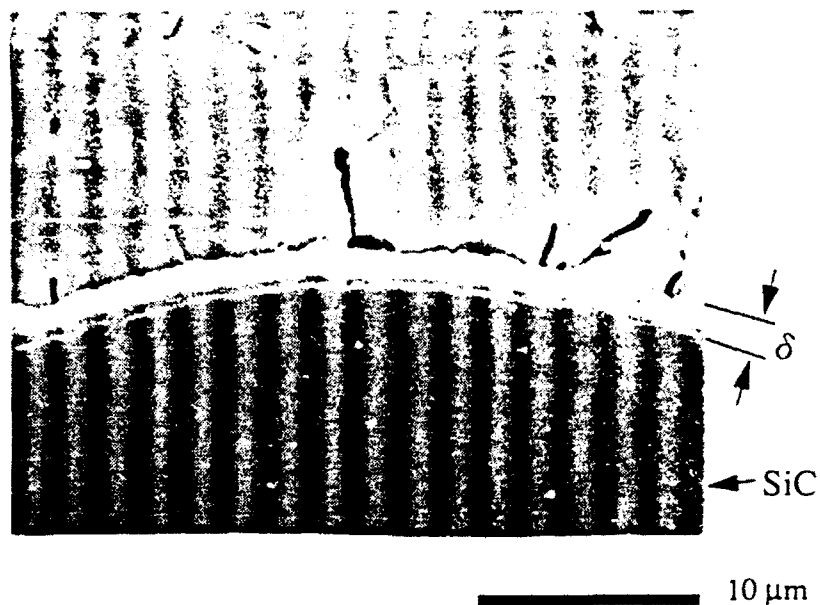


Figure 25 Sigma / Ti 24Al 11Nb Interface (VHP 1040 °C / 100 MPa / 30 min.)

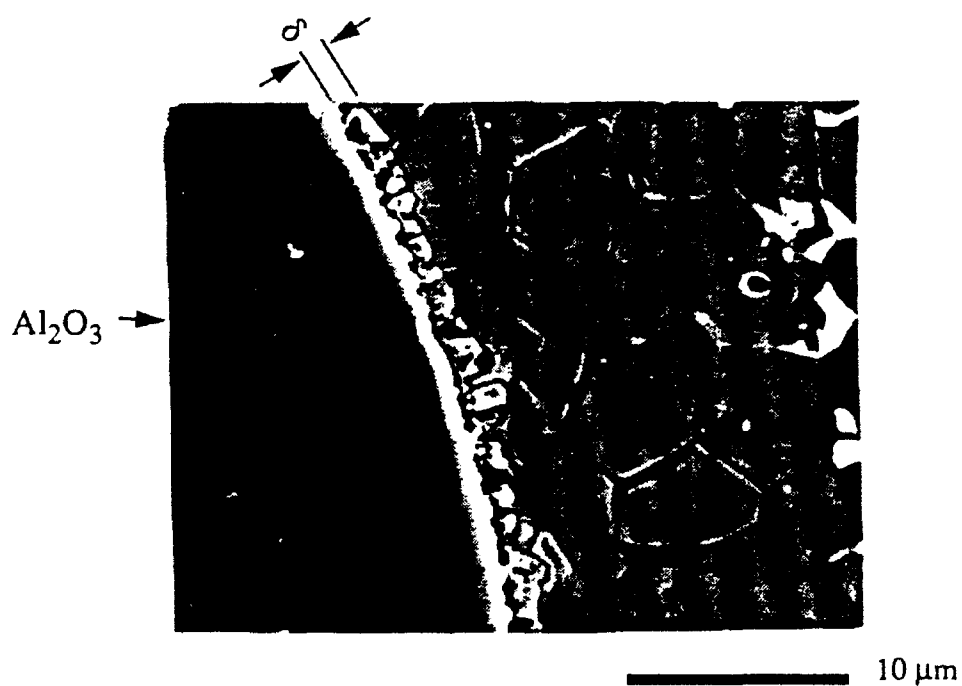


Figure 26 Saphikon / Ti 24Al 11Nb Interface (VHP 1040 °C / 100 MPa / 30 min.)

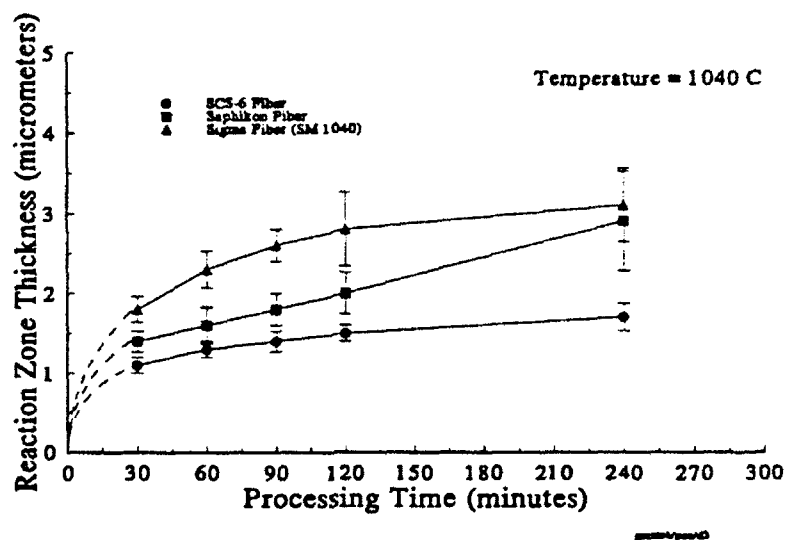


Figure 27 Reaction Zone Thickness ( $\delta$ ) vs. Processing Time

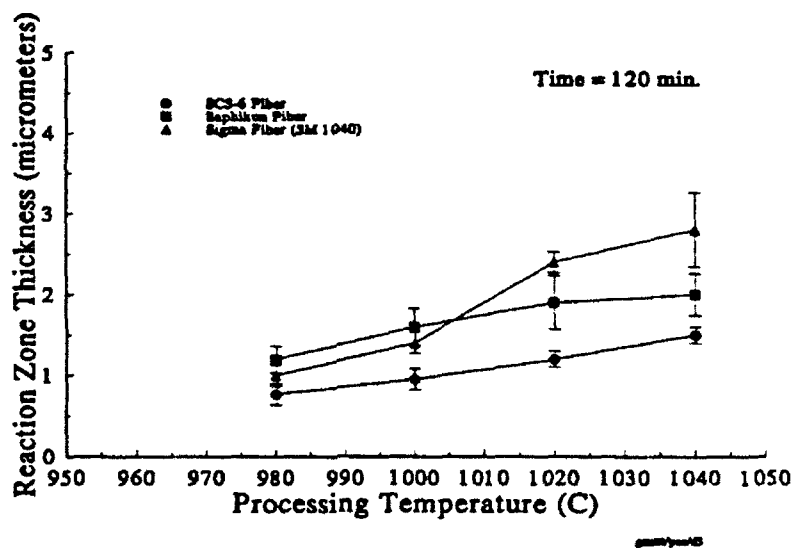


Figure 28 Reaction Zone Thickness ( $\delta$ ) vs. Processing Temperature



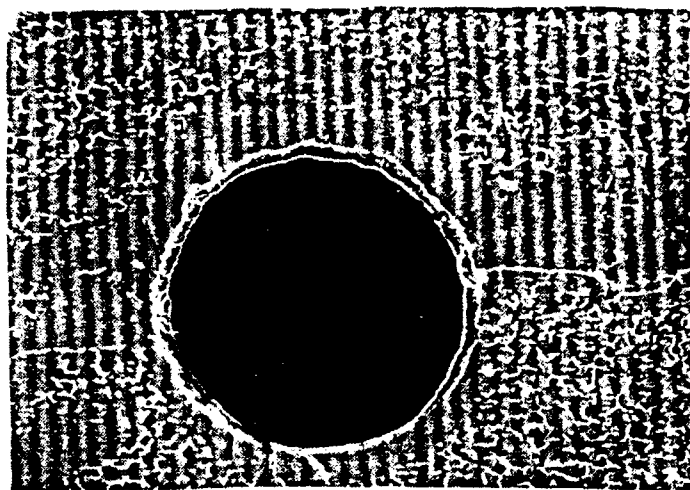
#### 4.1.5 Stage 1 Effects

Stage 1 effects on the reaction of a Saphikon fiber sample were first investigated by extending the time of Stage 1 (an extra 3 hrs. between 850 - 875 °C) followed by conventional processing at 1040 °C. The morphology of the resultant interface (figures 29 and 30) was significantly different to that of the conventional processed sample (figures 19 and 26). Using Energy Dispersive X-Ray analysis (EDS), quantitative analysis of the regions marked in figure 30 were conducted (Appendix A). Region 1 corresponded to the matrix alloy composition. Region 2 had a high Nb content; its average composition was 41% Ti, 24% Al, 35% Nb (at%). Region 3 was titanium rich with almost no Nb; its average composition was 91% Ti, 8% Al, 1% Nb (at%). Region 4 contained a larger concentration of Al than region 3; its overall composition was 71% Ti, 28.5% Al, 0.5% Nb, and probably corresponds to the  $Ti_3Al$  phase. This has previously been reported to be the reaction product between Ti and  $Al_2O_3$  [17,61,62].

The high Ti concentration in region 3 further suggests a Ti rich layer may have formed on the fiber surface during Stage 1 prior to the application of pressure. This hypothesis was tested by heat treating foil/fiber/foil samples in Stage 1 (holding at 875 °C for 2 hrs.) and furnace cooling from the consolidation temperature without applying any pressure. In these experiments the fibers could be physically removed from the foils and their surfaces characterized in the SEM. In figure 31 the surface of the Saphikon fibers are shown. EDS analysis of Saphikon fiber surfaces indicated the presence of a Ti layer that coated the fiber.

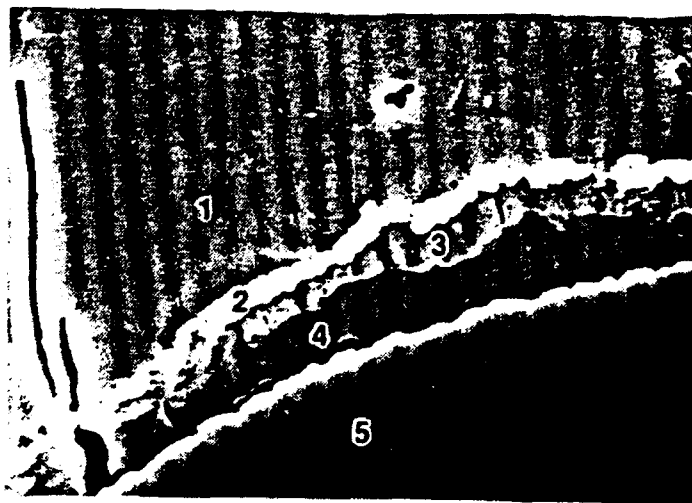
A similarly results was obtained for a SCS-6 fiber. EDS analysis of the lighter regions in figure 32 indicated the presence of Ti; with little or no Al or Nb present. The darker regions of figure 32 (regions where the coating had broken off) contained no Ti (see Appendix A for EDS data).

The morphologies of Ti-rich coatings on both the SCS-6 and Saphikon fibers are different and probably a function of the fiber surface composition and morphology.



100  $\mu\text{m}$

Figure 29 Saphikon/Ti 24Al 11Nb (VHP 1050 °C / 100 MPa / 30 min. - held above 850 °C for about 3 hrs. before pressing)



10  $\mu\text{m}$

Figure 30 Saphikon/Ti 24Al 11Nb (VHP 1050 °C / 100 MPa / 30 min. - held above 850 °C for about 3 hrs. before pressing)

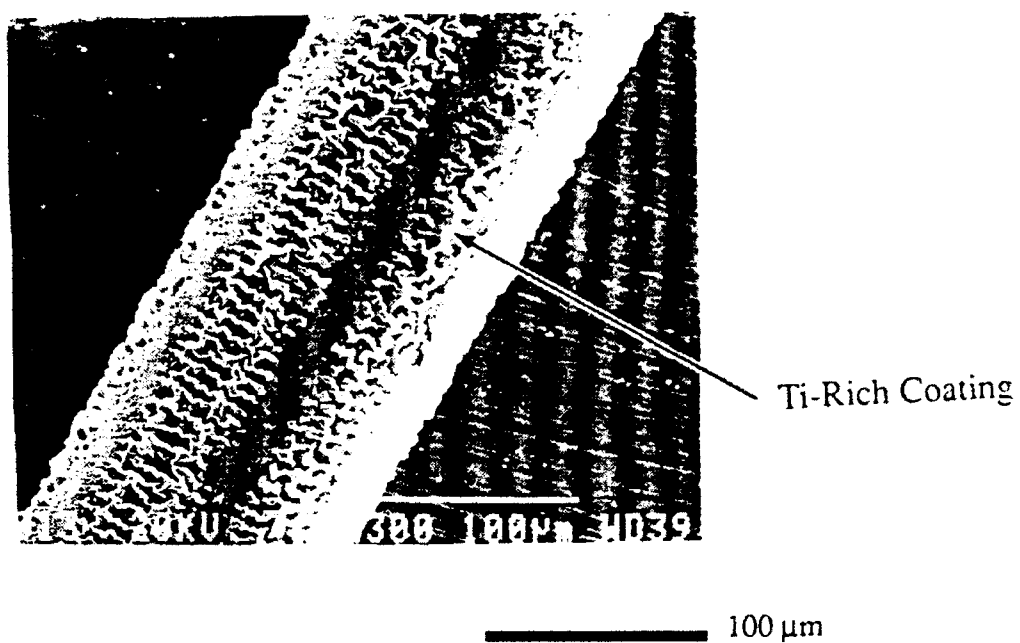


Figure 31 Saphikon Exposed fiber (VHP ramp to 875 °C / hold 2 hrs.; ramp to 1050 °C / furnace cool)

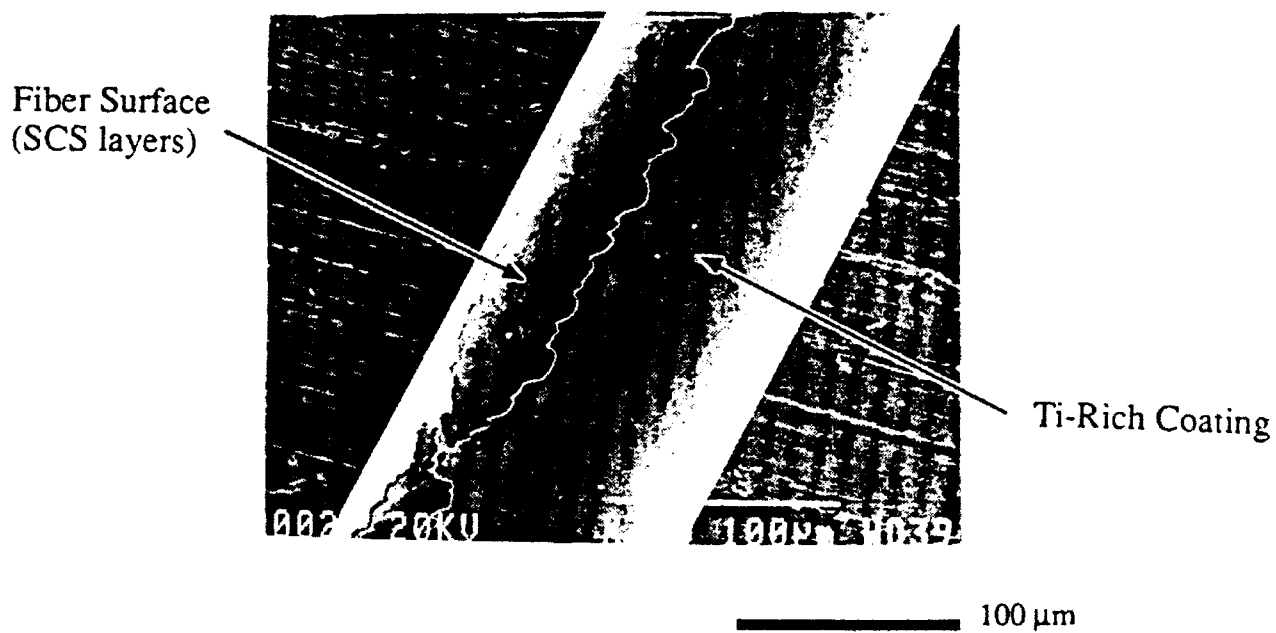
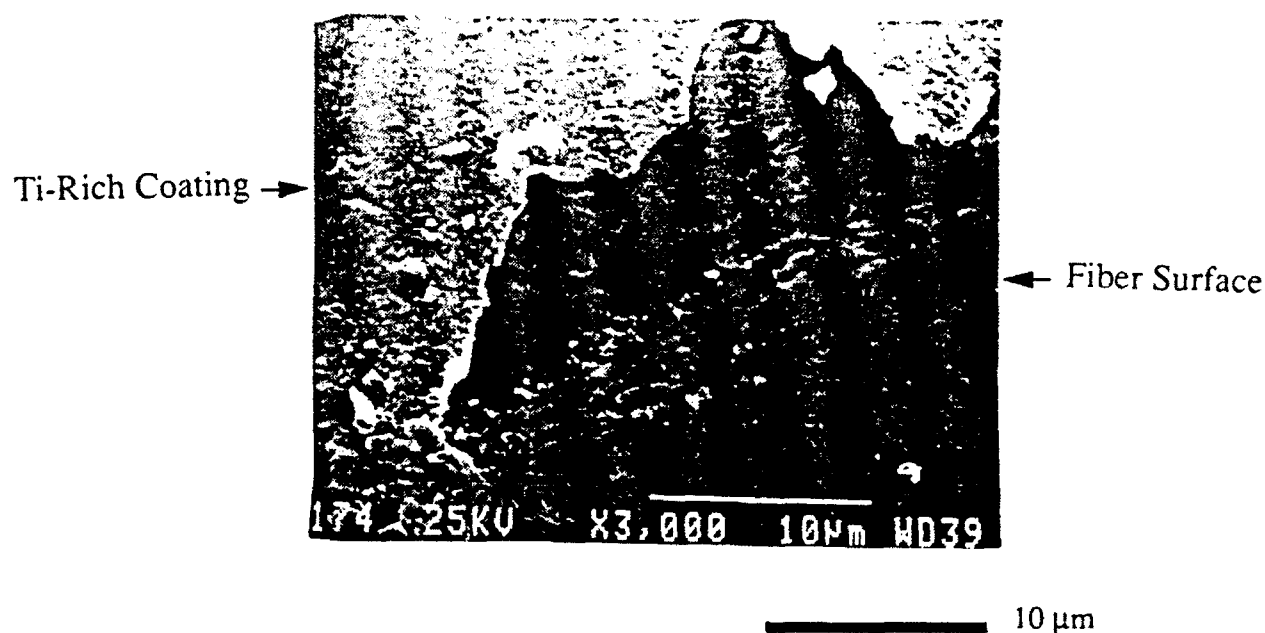


Figure 32 SCS-6 Exposed fiber (VHP ramp to 875 °C / hold 2 hrs.; ramp to 1050 °C / furnace cool)

In a final VHP experiment, a foil/Saphikon fiber/foil preform was ramped to 150 °C and 450 °C at 8 °C/min and held for 60 and 90 minutes respectively before ramping to 1040 °C at 4 °C/min and furnace cooled. A Ti-rich coating on the surface of the Saphikon fiber was again observed (figure 33). The coating was thinner than before and had flaked off in areas revealing the fiber surface below. The once smooth fiber surface was now filled with surface defects. These surface defects formed on uncoated fibers caused significant loss of fiber strength [119]. The results indicate that uncoated fiber strength is degraded even during Stage 1 of consolidation.



**Figure 33 Saphikon Exposed Fiber (VHP ramp to 1050 °C / furnace cool)**

## 4.2 Interfacial Mechanical Properties

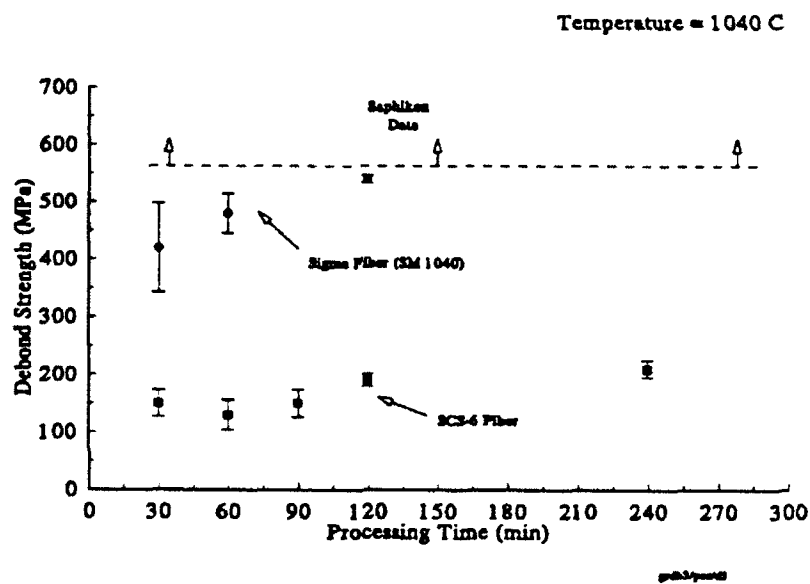
The debond strength,  $\tau_d$ , for composites with the three fiber types is shown as a function of processing time (temperature = 1040 °C) in figure 34. Each data point is the average of 3 to 5 tests. The error bars represent standard deviations of the measurements. These results are for specimens with a 250  $\mu\text{m}$  thickness. Thicker specimens (450  $\mu\text{m}$ ) had slightly higher values of  $\tau_d$  (table 7), but exhibited the same trends with processing.

Dramatic differences in  $\tau_d$  between the three fiber types were observed. The coated SCS-6 fiber had only a third (or less) of the debond strength of the uncoated Sigma SM1040 fiber. A significant increase in the debond strength with processing time was observed for both fibers - though for the SCS-6 fibers  $\tau_d$  did not significantly increase until the processing time exceeds 90 min. The Saphikon fiber (in all processed conditions) was so strongly bonded to the matrix that it could not be debonded before failure of the push-rods. This failure load corresponded to a interface shear stress of around 560 MPa and represents a lower bound for  $\tau_d$ . As an aside, a coated Saphikon fiber provided by 3M (outer coating of  $\text{Y}_2\text{O}_3$  and an inner refractory metal coating) did allow debonding and sliding.  $\tau_d$  varied from 125 (process 4 - table 5) to 175 MPa (process 6 - table 5) suggesting that this duplex coating for Saphikon fibers may be a technically feasible approach to producing desirable values of debond strength.

The debond sliding characteristics ( $\tau_s$ ) of the two SiC fiber types are shown in figure 35. A drastic difference is observed between the two fibers. For the SCS-6 case,  $\tau_s$  mirrored the trends observed for  $\tau_d$ . There was no significant difference in  $\tau_s$  for samples processed for 30,60 or 90 minutes at 1040 °C. After 90 minutes  $\tau_s$  increased. For a Sigma (SM1040) reinforced composite,  $\tau_s$  appeared to initially decrease and then rapidly increase with processing time.

Table 7: Pushout Test Results (SCS-6)

Process	Debond Strength $\tau_d$ 250 $\mu\text{m}$ (MPa)	Debond Sliding Resistance $\tau_s$ 250 $\mu\text{m}$ (MPa)	Debond Strength $\tau_d$ 450 $\mu\text{m}$ (MPa)	Debond Sliding Resistance $\tau_s$ 450 $\mu\text{m}$ (MPa)
VHP 1040 °C/30 min	150	73	150	95
VHP 1040 °C/240 min	210	155	240	206

Figure 34 The effect of processing time on Debond Strength ( $\tau_d$ ) ( $t=250 \mu\text{m}$ )

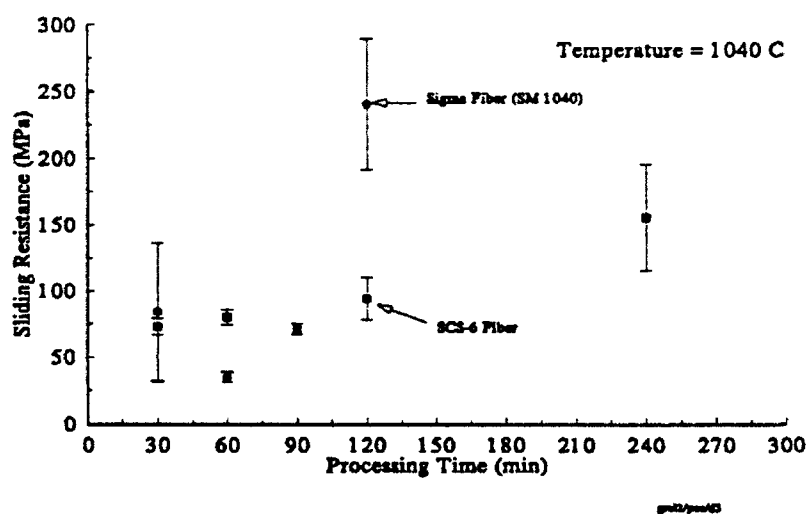


**Figure 35** The effects of processing time on Debond Sliding Resistance ( $\tau_s$ ) ( $t=250 \mu\text{m}$ )

For the SCS-6 fiber composite,  $\tau_d$  and  $\tau_s$  are plotted verses the reaction zone

thickness ( $\delta$ ) in figure 36. The results of the samples processed at 980 °C ( $\delta=0.77\mu\text{m}$ ), 1000 °C ( $\delta=0.95\mu\text{m}$ ) and 1020 °C ( $\delta=1.2\mu\text{m}$ ) are also included. Both  $\tau_d$  and  $\tau_s$  remain roughly constant until  $\delta$  reaches 1.4 or 1.5  $\mu\text{m}$  at which point they begin to increase significantly.

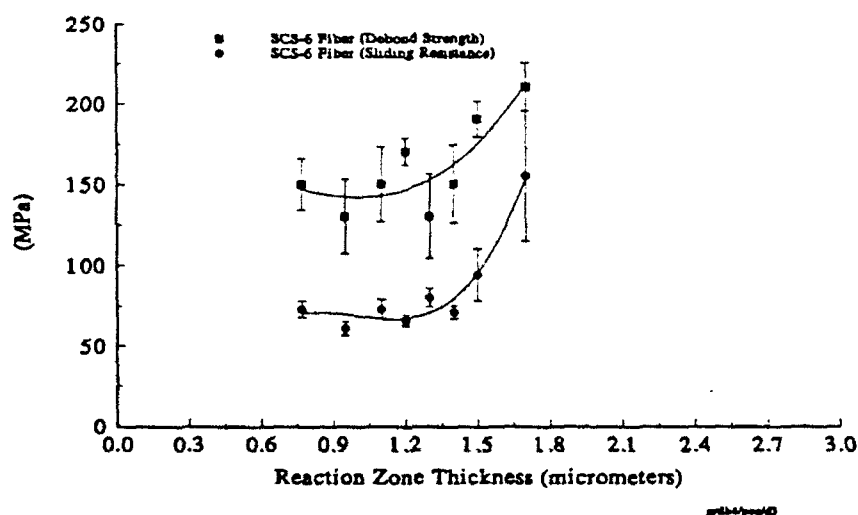
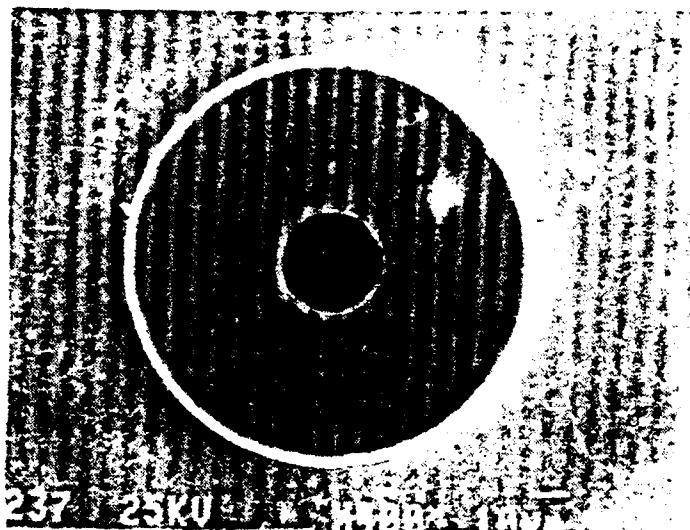


**Figure 36** Debond Strength ( $\tau_d$ ) and Debond Sliding Resistance ( $\tau_s$ ) vs. Reaction Zone Thickness ( $\delta$ ) ( $t=250\mu\text{m}$ )

An SEM examination of the pushout specimens after testing was performed. The differences in the debond strength for the Sigma fibers compared to the SCS-6 fiber (figure 34) was clearly related to a difference in the debond path. In the pushed out SCS-6 samples, a mode 2 interface crack had propagated along the interface between the outer SCS layer and the reaction product (figure 37). In contrast, both the Sigma fiber and matrix appeared to have failed in shear along a complex set of radial and circumferential planes (figure 38). In part this appeared aided by the radial cracks in both the fiber and matrix. No significant differences were observed (by SEM examination) between the Sigma (SM1040) interfaces with high and low  $\tau_s$  values shown in figure 35 (figures 39

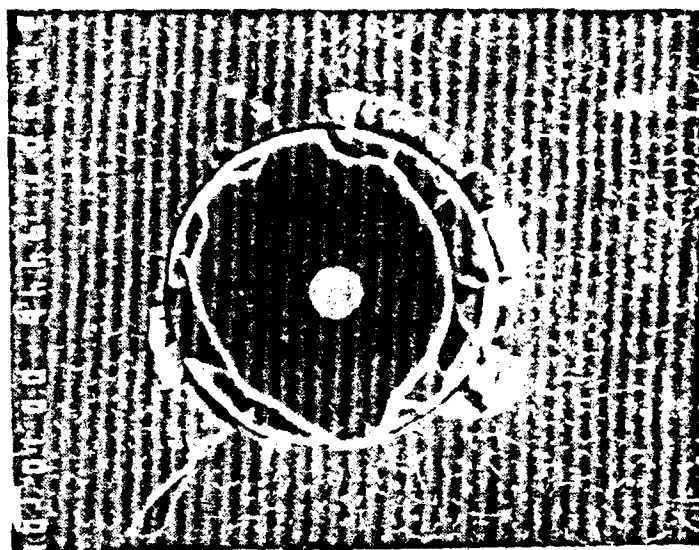


and 40), so the origin of the differences in  $\tau_s$  are at present unknown.



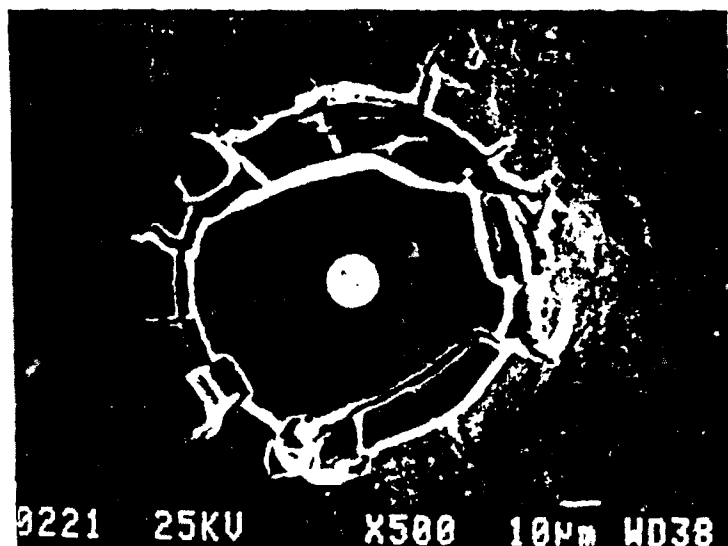
100  $\mu\text{m}$

Figure 37 Fiber Surface Pushout Test (SCS-6 / VHP 1040 °C - 30 min. - 100 MPa  $t \approx 450 \mu\text{m}$ )



100  $\mu\text{m}$

Figure 38 Fiber Surface Pushout Test (Sigma / VHP 1040 °C - 30 min. - 100 MPa  $t=450\mu\text{m}$ )



100  $\mu\text{m}$

Figure 39 Fiber Surface Pushout Test (Sigma / VHP 1040 °C - 30 min. - 100 MPa  $t=250\mu\text{m}$ )

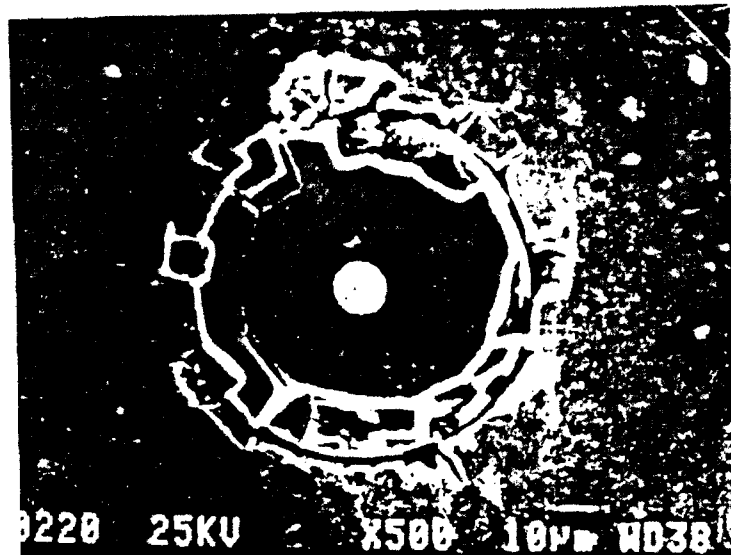
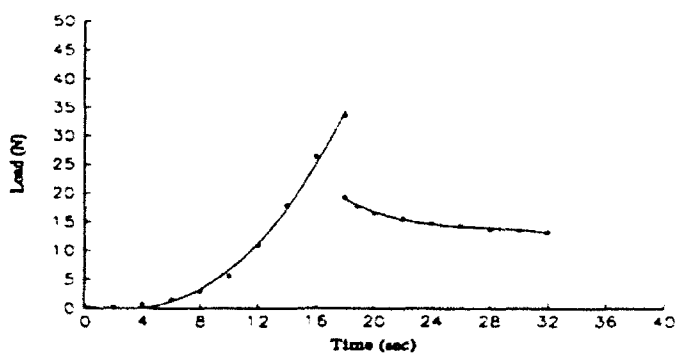
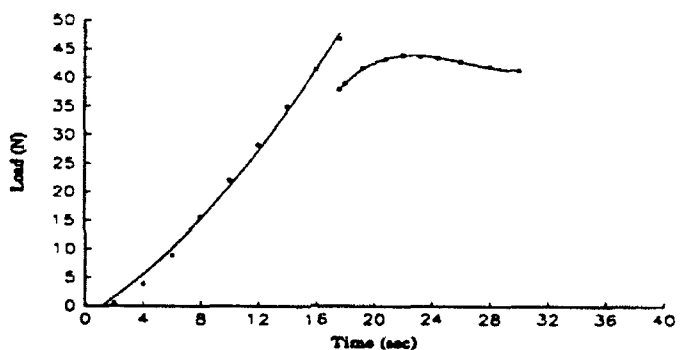


Figure 40 Fiber Surface Pushout Test (Sigma / VHP 1040 °C - 90 min. - 100 MPa  $t \approx 250 \mu\text{m}$ )

Lastly, a significant difference was observed in the sliding properties for large pushout displacements ( $\geq 5 \mu\text{m}$ ) i.e. in  $\tau_p$ . Typical pushout data are shown in figure 41 for  $450 \mu\text{m}$  thick specimens (whose properties are reported in table 7). When  $\delta$  equals  $1.1 \mu\text{m}$ , the pushout sliding resistance ( $\tau_p$ ) decreased after debonding, but the opposite behavior was observed when  $\delta$  equals  $1.7 \mu\text{m}$ .



a)



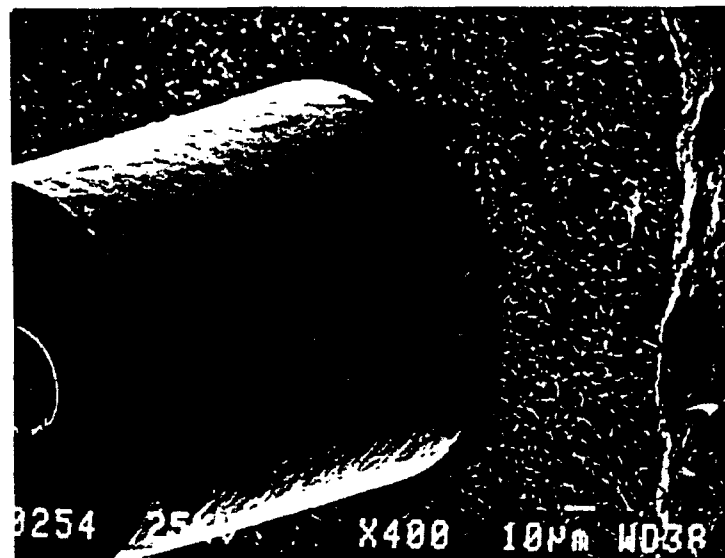
b)

**Figure 41** Typical load vs. time plots for SCS-6 fibers a)  $\delta = 1.1 \mu\text{m}$  b)  $\delta = 1.7 \mu\text{m}$

Figures 42 and 43 show both the fiber and matrix surfaces of a pushed out SCS-6 fiber with the thinner reaction zone thickness ( $\delta = 1.1 \mu\text{m}$ ). In this case, both the SCS C-rich layers were found to have adhered to the fiber while the reaction product was bonded to the matrix. Thus, the interface failed at the SCS/reaction product interface.

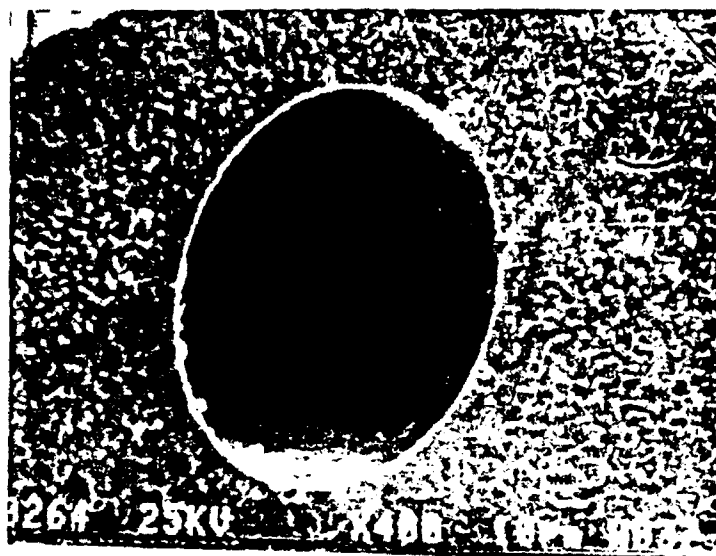
Different fiber and matrix surfaces were observed for the thicker reaction product ( $\delta = 1.7 \mu\text{m}$ ), Figure 44. Some areas of the fiber surface resembled that of the  $\delta = 1.1 \mu\text{m}$

specimen, however, large rough regions were also present. Examination of the matrix surface (figure 45) indicated that large areas of the SCS layers had adhered to the matrix. Thus, the interface fracture (debond) path appeared to have alternated between an unknown path in the SCS layers (either at the SiC/SCS interface, between (a) - the SCS layers or some combination of both - and (b) - the SCS/reaction product interface. More extended heat treatments may show a transition to only the former.



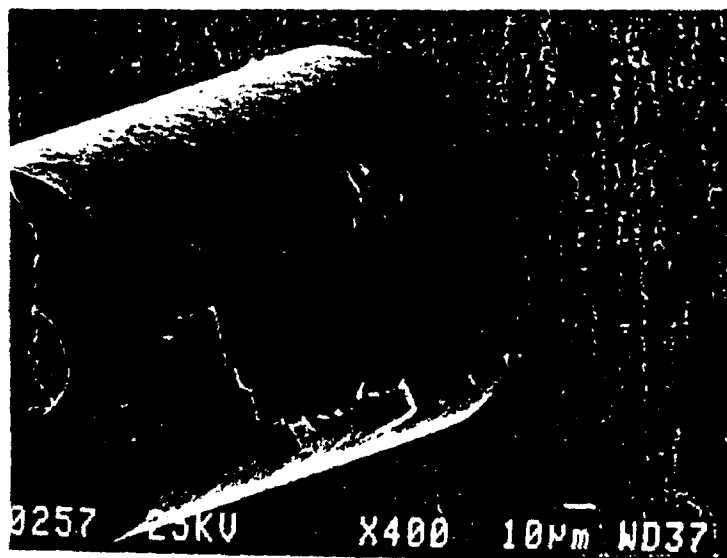
100 µm

**Figure 42** Fiber Surface of Pushout Test (SCS-6 /  $\delta=1.1\mu\text{m}$  / VHP 1040 °C - 30 min. - 100 MPa  $t\approx 450\mu\text{m}$ ). Note the SCS layers are bonded to the fiber and the reaction product to the matrix



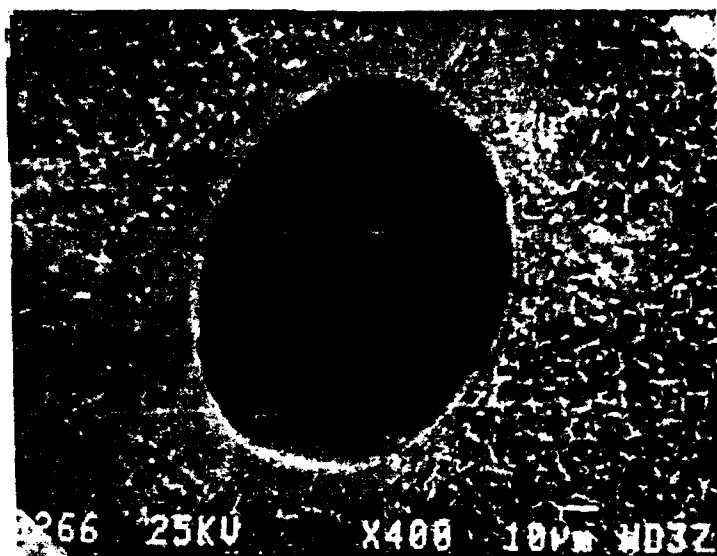
100 µm

Figure 43 Matrix Surface of Pushout Test (SCS-6 /  $\delta=1.1\mu\text{m}$  / VHP 1040 °C - 30 min. - 100 MPa  $t=450\mu\text{m}$ )



100 µm

Figure 44 Fiber Surface of Pushout Test (SCS-6 /  $\delta=1.7\mu\text{m}$  / VHP 1040 °C - 240 min. - 100 MPa  $t=450\mu\text{m}$ )



100 µm

Figure 45 Matrix Surface of Pushout Test (SCS-6 /  $\delta=1.7\mu\text{m}$  / VHP 1040 °C - 240 min. - 100 MPa  $t\approx 450\mu\text{m}$ ). Note much of the SCS layers had adhered to the matrix

## 5 Discussion

It is clear from the results that a strong relationship exists between interfacial reactions (characterized by  $\delta$ ) and the interface mechanical properties. Since the interface reaction zone thickness ( $\delta$ ) depends upon the process conditions, it is important to characterize and model  $\delta$  as a function of processing. A quantitative trade-off can then perhaps be made between densification, fiber fracture and interface properties (as determined by the optimal  $\delta$  value).

### 5.1 Reaction Kinetic Model during Consolidation

Each stage of processing may contribute to the interfacial reaction zone growth. To understand the effect of each stage, Stage 2 and 3 are first separately analyzed. The effect of Stage 1 in consolidating a foil/fiber/foil preform can be inferred when the effects of Stage 2 and 3 are understood and compared to the measured values after consolidation. In monotape and matrix coated fiber preforms (where the fiber is continuously in contact with the matrix), Stage 1 is treated by extending the model over the entire process cycle.

#### 5.1.1 Stage 2 and 3

We begin by assuming that diffusion of a matrix element through the reaction product controls the growth kinetics of the reaction product during processing. It is further assumed, that the reaction product only grows during Stage 2 of the consolidation process and the fiber is considered to be everywhere in contact with the matrix from the moment pressure is first applied. This corresponds to the situation analyzed by Gundel [77] and leads to a parabolic growth law of the form given in eqn. 2. The appropriate kinetic data are taken from the literature for SCS-6 and Saphikon fibers in Ti 24Al 11Nb and given in table 3 (no data is available for Sigma SM1040 fibers in Ti 24Al 11Nb).



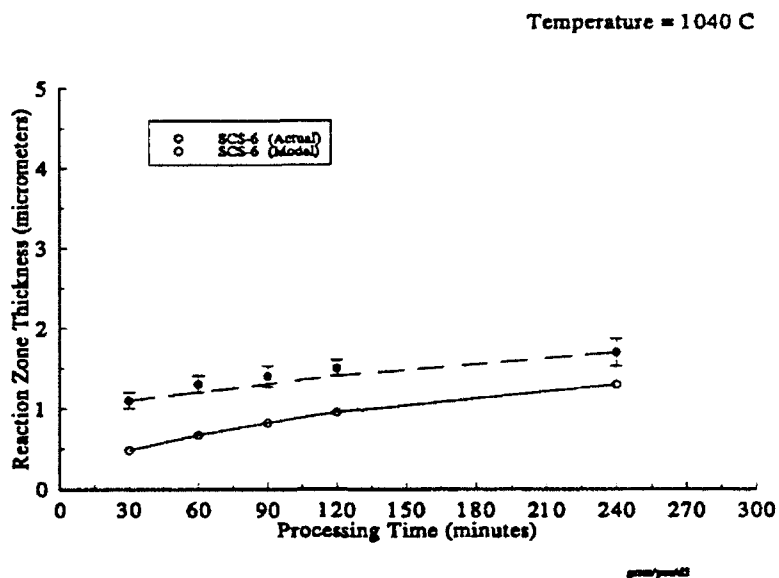


Figure 46 Comparison of Measured and Modeled Reaction Zone Thickness vs. Processing Time for the SCS-6 (SiC) Fiber

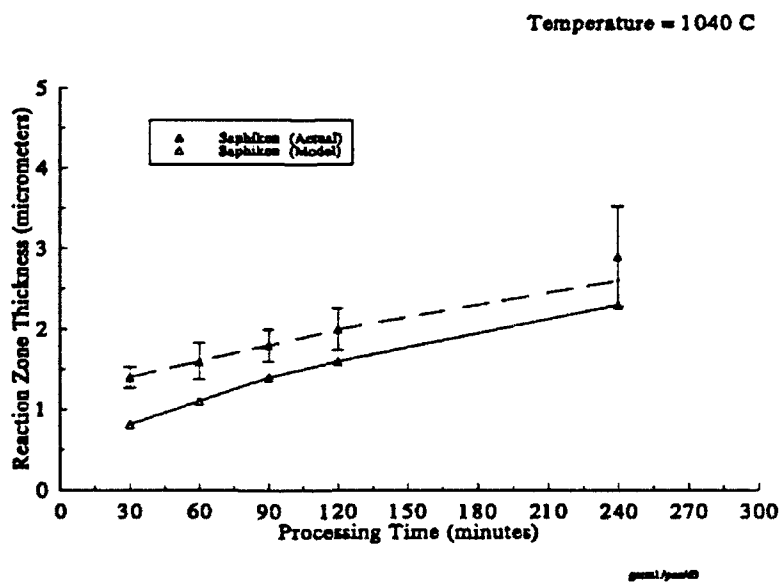


Figure 47 Comparison of Measured and Modeled Reaction Zone Thickness vs. Processing Time for the Saphikon ( $\text{Al}_2\text{O}_3$ ) fiber.

Figures 46 and 47 show a comparison between the predictions of this model and the measured values. The predictions are significantly lower than the measured values. Thus, either the growth law itself is invalid or the kinetic data is incorrect or reactions occurring in consolidation Stages 1 and 3 (where temperature varies with time) are important.

The contribution to the reaction in Stage 3 is presumably controlled by the same diffusional mechanism as in Stage 2. This it is possible to use the parabolic law (eqn. 2), to compute the incremental increase in  $\delta$  during cooling. The time-dependent temperature in Stage 3 is modelled as a sequence of steps as shown in figure 48. In figure 45  $T_c$  is the consolidation temperature,  $t_c$  is the time in Stage 2 and  $\Delta t$  equals the amount of time required to decrease the temperature  $1^\circ\text{C}$ ; for a rate of decrease in temperature ( $R_c$ ) equal to  $-12^\circ\text{C/min}$ ,  $\Delta t$  equals 5 sec. At each step, eqn. 2 is valid because temperature is constant.  $\delta$  is determined by summing eqn. 2 over each step.

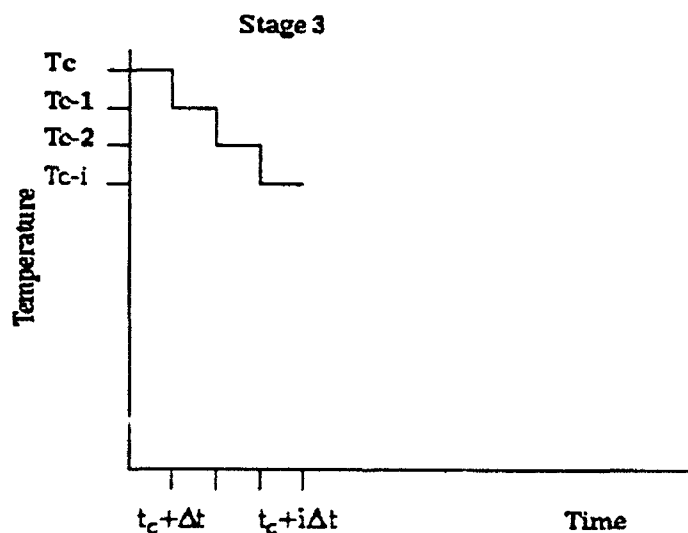


Figure 48 Step function of temperature vs. time

But before doing the summation, a new form of eqn. 2 must be derived to take into consideration the previous reaction growth that occurred in Stage 2 (recall the rate of

growth decreases as  $\delta$  increases). Eqn. 1 is integrated from  $\delta = 0$  to  $\Delta\delta_i$  (where  $\Delta\delta_i$  is the amount of reaction growth at each increment) and from  $t = t_c + \Delta t(i-1)$  to  $t_c + \Delta t(i)$  (where  $t_c$  is the time of Stage 2 and  $i$  is the current increment). Thus  $\Delta\delta_i$  becomes:

$$\Delta\delta_i = k(t) \left[ (t_c + \Delta t \times i)^{\frac{1}{2}} - (t_c + \Delta t \times (i-1))^{\frac{1}{2}} \right] \quad [12]$$

where  $T = T_c - i$  in eqn. 3.

$\Delta\delta_i$  may now be summed over  $i$  to give the total growth in Stage 3.

$$\delta_{Stage3} = \sum_{i=1}^x \Delta\delta_i \quad [13]$$

$x$  is defined as the  $v/\Delta t$  when  $k(t) \approx 0$ ; for consolidating a SCS-6/Ti 24Al 11Nb composite at 1040 °C,  $x \approx 500$ .

Table 8 shows the calculated contribution to  $\delta$  from Stage 3. The calculations indicate the amount of reaction occurring in Stage 3 compared to Stage 2 is insignificant and can possibly be ignored. The implication is the discrepancies in figures 46 and 47 are due to either reactions in Stage 1 or an error in the assumptions of the mechanism controlling the reactions (i.e. bad kinetic data). During Stage 1 of processing foil/fiber/foil preforms, it has indeed been shown that almost pure titanium can deposit on the fibers (by a transport mechanism that is somewhat unclear). Thus the beginning of the reaction may well occur early in Stage 1. It is well established that pure titanium reacts faster with fibers than a Ti 24Al 11Nb matrix [15,22,77].

**Table 8: Model and Measured Results for SCS-6/Ti 24Al 11Nb**

Consolidation Parameters	Model Stage 2 $\delta$ ( $\mu\text{m}$ )	Model Stage 3 $\delta$ ( $\mu\text{m}$ )	Model Total $\delta$ ( $\mu\text{m}$ )	Measured $\delta$ ( $\mu\text{m}$ )
1040 °C / 30 min	0.5	0.05	0.55	1.1
1040 °C / 60 min	0.7	0.04	0.74	1.3
1040 °C / 90 min	0.8	0.03	0.83	1.4
1040 °C / 120 min	0.95	0.03	0.98	1.5
1040 °C / 240 min	1.3	0.02	1.32	1.7

### 5.1.2 Stages 1,2 and 3

The fibers in a monotape or matrix coated fiber preform are surrounded by matrix throughout the stages of consolidation, and reactions may readily occur throughout. Although, these preforms were not used in this investigation, they are important to consider when modelling reaction zone growth. A continuous function has been defined to represent the temperature history for processing monotapes of SCS-6 and Ti 24Al 11Nb (VHP 1040 °C/100 MPa/30 min. sample - see Appendix C).

$$T(t) = 335 - 0.081t + 2.14 \times 10^{-5}t^2 - 7.8 \times 10^{-10}t^3 \quad [14]$$

where  $t$  is time in seconds and  $T(t)$  is in units of Kelvin. This continuous function,  $T(t)$ , can be substituted into the Arrhenius equation for  $k$

$$k(t) = k_o \exp\left(-\frac{Q}{RT(t)}\right) \quad [15]$$

$k(t)$  was then substituted into the growth rate equation (eqn. 1) derived by Gundel [77] and

Integrated to give.

$$\delta = \sqrt{\int_0^t k(t)^2 dt} \quad [16]$$

The results for  $\delta$  (delta) and the temperature profile are shown in figures 49 and 50. The temperature reaches 1040 °C at about 15000 sec. The model predicts a significant amount of reaction ( $\approx 0.3 \mu\text{m}$ ) occurs during the Stage 1. At the end of Stage 2 ( $t \approx 17000$  sec),  $\delta$  is about  $0.58 \mu\text{m}$ . The reaction zone grows approximately  $0.08 \mu\text{m}$  during the furnace cool which correlates well to the results of the previous model for the growth in Stage 3. The slightly higher value ( $0.08$  compared to  $0.05$ ) is probably due to the fact that the continuous function is at higher temperature for a longer period during Stage 3. The total reaction zone thickness is about  $0.66 \mu\text{m}$  which is on the order typically observed for this system [6,42,77]. These results are encouraging evidence of the model's predictive capability.

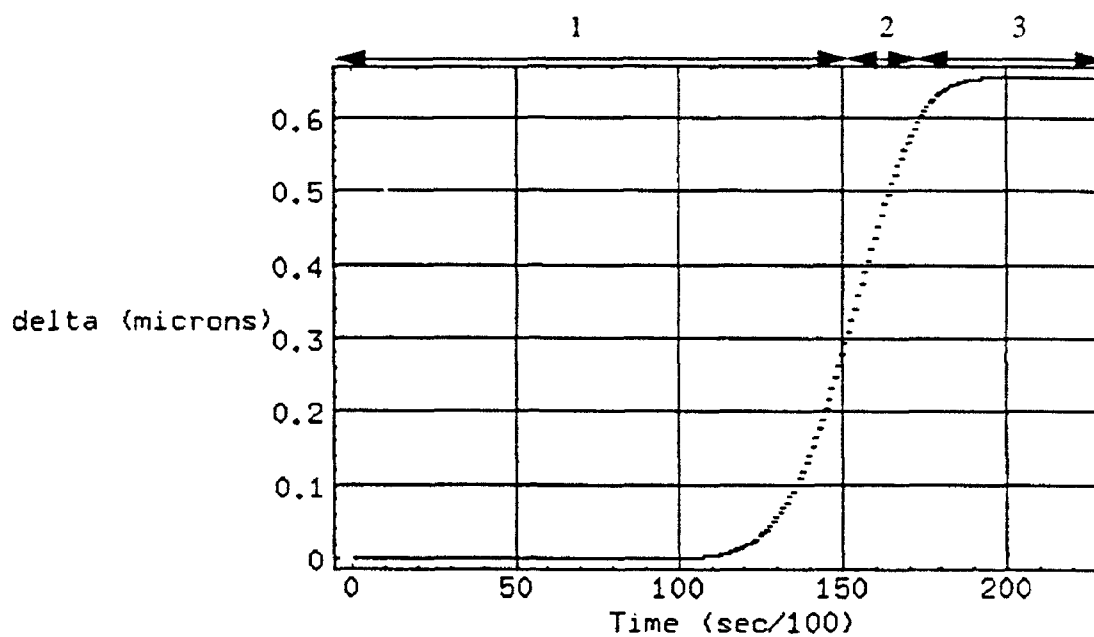


Figure 49 Growth of  $\delta$  for temperature profile in fig. 66

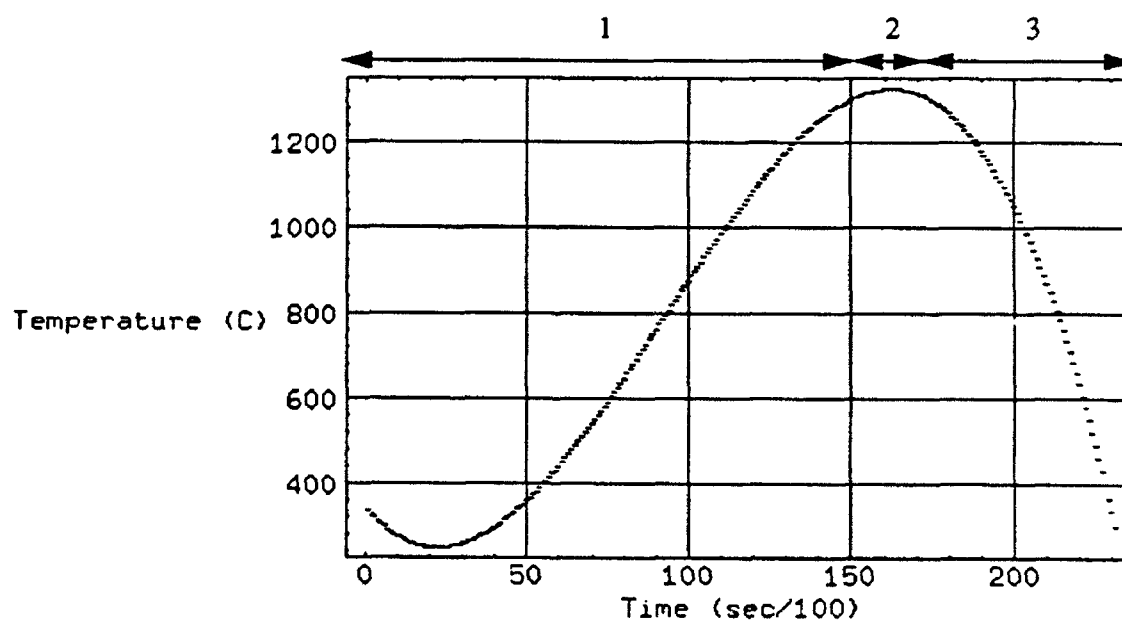


Figure 50 Temperature profile representing (VHP 1040 °C/100 MPa/ 30 min.)

## 5.2 Stage 1 Effects

The effects of Stage 1 during the consolidation processing have in the past been ignored with the exception of work on a  $\text{Al}_2\text{O}_3/\text{Cr}_2\text{O}_3$  system [71]. Evidence given in section 4.1.5 indicates there is a significant interaction in a foil/fiber/foil preform. The interaction results in a titanium rich coating on both the SiC and  $\text{Al}_2\text{O}_3$  fibers prior to the start of consolidation. Reactions occurring between this coating and the fibers may account for the discrepancy in the reaction kinetic model (ignoring Stage 1 effects) and the measured values (figures 46 and 47).

The transport process that takes titanium from the foil to the fiber is unclear, but there are two possible mechanisms. Titanium may be transported by surface diffusion onto the fibers at various fiber/matrix contact points. As an example, calculations for surface diffusion on fcc metals indicated an average diffusion distance ( $x \approx (2Dt)^{0.5}$  [99]) for the temperatures and times experienced in Stage 1 to be on the order of 100 to 1000  $\mu\text{m}$ . However, there is no known surface diffusion data for titanium on single crystal  $\text{Al}_2\text{O}_3$  which prohibits a true estimation of the diffusion distance. A second transport mechanism may be via the vapor phase since there exists a vacuum environment within the preform. The vapor pressure of pure titanium at 1000 °C is about  $10^{-8}$  torr (the vapor pressure of Ti over a Ti 24Al 11Nb alloy is unknown). Using Langmuir's evaporation rate equation [69] results in an evaporation rate of  $1.13 \times 10^{-10}$  g/cm<sup>2</sup>/sec. For a single fiber between two foils (8cm x 0.8cm) at 1000 °C for 30 min., a 0.02  $\mu\text{m}$  coating is predicted to form. Either one or both of these mechanisms could contribute to the development of the Ti-rich coatings.

When foil/fiber/foil preforms were encapsulated in quartz tubing - a cleaner system (15 millitorr) than the VHP vacuum (60 to 100 millitorr) - a thicker Ti-rich coating is observed for the same heat treatment (see Appendix B). This suggests that the vapor path may be more significant than surface diffusion. There are still many questions that need to be addressed to fully determine how this phenomenon occurs and to fully

understand its affect on the reaction kinetics.

### 5.3 Interface Properties

To compare the effects of processing history on interfacial debond properties, the coefficient of friction,  $\mu$  for debond sliding (small fiber displacements) and the mode 2 debond toughness,  $\Gamma_i$ , are calculated from the pushout data ( $\tau_d$  and  $\tau_s$ ) presented in section 4.2. The sliding properties (i.e. large fiber displacements) are also discussed.

#### 5.3.1 Debond Properties

From eqn. 6,  $\mu$  is defined as

$$\mu = \frac{\tau_s}{\sigma_r} \quad [17]$$

where  $\tau_s$  is measured just after the load drop (or  $\Delta\sigma$ ) and  $\sigma_r$  is radial residual compressive stress.  $\mu$  may also be calculated from eqn. 9

$$\mu = \frac{P_f}{2B_1d} \ln \left( \frac{\sigma_a' B_1}{\sigma_r - B_1 \sigma_z} + 1 \right) \quad [18]$$

Here,  $\sigma_z$  is the axial residual compressive stress and  $\sigma_a'$  is the applied stress on the fiber after the load drop ( $\sigma_a' = 2\tau_s/R_f$ ).  $\mu$  is calculated from both equation to see if there are any discrepancies.

$\Gamma_i$  may be calculated by rearranging eqn 10 to give;

$$\Gamma_i = \frac{B_2 R_f}{E_f} \left[ \left[ \frac{\Delta\sigma}{e^{\zeta d}} - \sigma_z - \frac{\sigma_r}{B_1} (e^{-3\mu B_1} - 1) \right] \frac{e^{3\mu B_1}}{2} \right]^2 \quad [19]$$

After measuring  $\tau_s$  (or  $\sigma_a'$ ) and  $\Delta\sigma$ , the only unknowns in equation 11,12 and 13 are the axial residual stress,  $\sigma_z$  and the radial residual stress,  $\sigma_r$ .

Ideally the residual stresses should be directly measured, but techniques for this are only just emerging in metal and ceramic composites [88,115]. Instead the residual



stresses must be calculated. The models used to calculate the residual stresses often assume the fiber to be a homogeneous, linear elastic, isotropic (or transversely isotropic) cylinder and the matrix to be linearly elastic and isotropic [48-50]. These calculations do not allow for matrix plasticity (or creep at high temperatures) which may relax stresses. However, recently Pindera et al. [51] developed a model to analyze CTE mismatch stresses in fibers like SCS-6 when they are embedded in matrices that have an elastic-plastic constitutive response. The model requires CTE data as a function of temperature which is shown for both SCS-6 and Ti 24Al 11Nb in table 9.

To obtain a sense of the sensitivity of the predicted residual stresses to the differences in published CTE data, two sets of parameters (SCS-6[108]/Ti 24Al 11Nb[51] and SCS-6[108]/Ti 24Al 11Nb[51]) have been substituted into Pindera's model - the data for the yield strength as a function of temperature was taken from ref. [51] and essentially corresponded to the rolled sheet results shown in figure 4. The model gives the residual stresses after cooling from  $T_c = 1040^\circ\text{C}$  (figure 51).

The axial compressive stress ( $\sigma_z$ ) in the fiber ranged from 2.39 - 1.59 GPa and radial compressive stress at the interface ( $\sigma_r$ ) varied from 420 to 340 MPa.

**Table 9: Tangent CTE data for SCS-6 and Ti 24Al 11Nb**

Temperature ( $^\circ\text{C}$ )	SCS-6 [108] <sup>1</sup> $10^6/^\circ\text{C}$	SCS-6 [51] $10^6/^\circ\text{C}$	Ti 24Al 11Nb [109] <sup>1</sup> $10^6/^\circ\text{C}$	Ti 24Al 11Nb [51] $10^6/^\circ\text{C}$
21	4.35	3.53	9.9	9.0
200	4.42	3.62	10.1	9.4
425	4.62	3.9	11.2	10.3
600	4.82	4.2	12.8	10.5
650	4.89	4.28	13.3	10.6
815	5.22	4.5	15.4	11.1
1040	6.4	4.8	19.2	11.7

1. Reported data transformed from Secant CTE to Tangent CTE (see Appendix D)

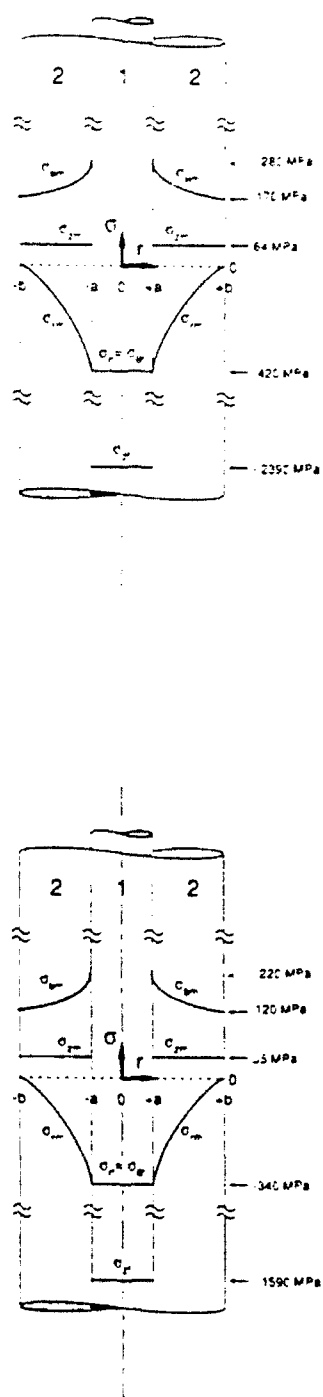


Figure 51 Elastic-plastic model predicted residual stress ( $a/b = 1/3$ )

With the results shown in figure 51, Eqns. 11 and 12 can now be used to determine  $\mu$ . Table 10 lists values of the friction coefficient deduced from both eqns. 11 and 12.

**Table 10: Debond Sliding in a SCS-6/Ti 24Al 11Nb composite**

$\delta$ ( $\mu\text{m}$ )	$\sigma_r$ (MPa)	$\tau_s$ (MPa)	$\sigma'_{\beta}$ (GPa)	Eqn. 11 $\mu$	Eqn. 12 $\mu$
1.1	340	95	1.2	0.28	0.31
1.1	420	95	1.2	0.23	0.27
1.7	340	206	2.65	0.60	0.63
1.7	420	206	2.65	0.49	0.56

The fairly good agreement between eqn. 11 and 12 indicates the accuracy of the LH model when the coulombic friction law (eqn. 6) is applicable, and  $\mu$  is relatively insensitive to the increase in  $\sigma_r$ . However, as expected there is a significant difference in all cases between the samples  $\delta = 1.1 \mu\text{m}$  and  $\delta = 1.7 \mu\text{m}$ .

Table 11 lists deduced values of  $\Gamma_i$  using eqn. 19 and the values:  $E_f = 400 \text{ GPa}$ ,  $\nu_f = 0.25$ ,  $E = 100 \text{ GPa}$ ,  $\nu = 0.26$ ,  $R_f = 70 \mu\text{m}$ .  $\Gamma_i$  is more sensitive to changes in the residual stresses. For both the  $1.1 \mu\text{m}$  and  $1.7 \mu\text{m}$  samples,  $\Gamma_i$  for the larger stresses is about four times larger than for the smaller stresses. There is little sensitivity as  $\mu$  changes for given residual stresses, but  $\Gamma_i$  generally decreases as  $\mu$  increases. This seems reasonable since the frictional contribution to  $\Delta\sigma$  would increase as  $\mu$  increased leaving less of a contribution due to the interface toughness. One interesting result is that there is not much variation in  $\Gamma_i$  between the  $1.1 \mu\text{m}$  and  $1.7 \mu\text{m}$  samples. This seems to indicate that although the debond interface changes as the reaction zone thickness increases, the toughness of either interface is equivalent to roughly the same.

Table 11: Interface Toughness in a SCS-6/Ti 24Al 11Nb composite

$\delta$ ( $\mu\text{m}$ )	$\sigma_r$ (MPa)	$\sigma_z$ (GPa)	$\mu$	$\Delta\sigma$ (MPa)	$\Gamma_i$ (J/m <sup>2</sup> ) $T_c=1040^\circ\text{C}$
1.1	420	2.39	0.23	710	99
1.1	420	2.39	0.27	710	96
1.1	340	1.59	0.28	710	23
1.1	340	1.59	0.31	710	21
1.7	420	2.39	0.49	440	103
1.7	420	2.39	0.56	440	95
1.7	340	1.59	0.60	440	24
1.7	340	1.59	0.63	440	22

The actual purpose of calculating  $\Gamma_i$  is to determine if fiber/matrix debonding will occur which is necessary for fiber pullout and to subsequently increase composite toughness. The elastic mismatch,  $\alpha$ , for a SCS-6/Ti 24Al 11Nb composite is about 0.5. This corresponds to a debond criteria of  $\Gamma_i/\Gamma_f \leq 0.5$  (figure 8). If  $\Gamma_f$  is estimated as 50 J/m<sup>2</sup> from bulk SiC properties given in Ashby and Jones [2],  $\Gamma_i$  is required to be less than 25 J/m<sup>2</sup>. The lower residual stress predictions give a  $\Gamma_i$  slightly less than 25 J/m<sup>2</sup> while the larger predictions give a much greater  $\Gamma_i$ . Since, the actual residual stresses are unknown, no conclusions on debonding can be made because of the discrepancies in  $\Gamma_i$ .

However, the predictions for  $\sigma_r$  and  $\sigma_z$  do not take into account creep or the radial cracking which would both tend to decrease the residual stresses and thus decrease the calculated interface toughness. Presently, Pindera and Williams are attempting to include creep into the elastic-plastic model [110], but presently the extent to which creep will affect the residual stresses is unknown. The effect of radial cracking on the residual stresses has also not been included in models but may be significant.

There is also an effect of slicing upon the residual stresses acting on the fibers

which must be considered in the thin specimens used for pushout tests. This has been addressed by LH who showed that the residual stresses within a region of about one fiber radius from the sectioned surface are relieved. If the residual stresses acting on the fiber are to be representative of a bulk composite, a sample at least  $3R_f$  thick is necessary (but  $t = 6R_f$  or  $12R_f$  is preferable) [33]. In addition, as already pointed out to avoid bending stresses in thin specimens, Kallas et al. [35] determined  $t \geq 2d_b$  where  $t$  is the specimen thickness and  $d_b$  is the diameter of the support base hole ( $\approx 220 \mu\text{m}$ ). The results in figures 34-36 are from specimens with a thickness of  $250 \mu\text{m}$  ( $\approx 2R_f$ ,  $\approx d_b$ ). To minimize problems of stress relief and bending when  $\mu$  and  $\Gamma_i$  were calculated, the pushout test results of  $450 \mu\text{m}$  ( $\approx 3.5R_f$ ,  $\approx 2d_b$ ) thick specimens (prepared for the shortest and longest processing times at  $1040^\circ\text{C}$  - see table 5) were used. There was an increase in  $\tau_d$  and  $\tau_s$  with thickness indicating there may have been some bending affects in the thinner specimens. However, the results of the thicker specimens mirrored the trends observed in the thinner specimens and the optical observation of the debond interface during testing of the thinner specimens agreed with the results shown in figures 42 -45.

### 5.3.2 Large Displacement Sliding Properties

The debond properties determine if fiber pullout can occur while the sliding properties describe fiber pullout when it does occur. Fiber pullout enhances composite toughness due to the additional work required to pull fibers out of the fracture surface [2,3]. It is possible to estimate the contribution of sliding to toughness as follows [2]. The work ( $W$ ) done to pullout a single fiber is defined as

$$W = \int_0^l \pi d_f \tau_p x dx \quad [20]$$

where  $d_f$  is the fiber diameter,  $\tau_p$  is the sliding resistance during pullout, fiber displacements greater than  $5 \mu\text{m}$  ( $\tau_p = \tau_s$  at  $x=0$ ), and  $l$  is the average pullout length. In a unidirec-

tional composite in which fiber fragmentation has occurred prior to crack extension, the average pullout length is  $l_f/2$  [2, 5].  $l_f$  is the critical (stress transfer) length [1]

$$l_f = \frac{\sigma_f d_f}{2\tau_s} \quad [21]$$

where  $\sigma_f$  is the average tensile strength of the fiber and  $\tau_s$  is the debond sliding resistance discussed earlier. It is more appropriate to use  $\tau_s$  in eqn. 15 than  $\tau_p$ , since  $l_f$  is determined before large fiber displacement occurs.

The pullout contribution to composite toughness,  $G_{po}$ , is determined by multiplying  $W$  by the number of fibers per unit crack area ( $4V_f/\pi d^2$ ).

$$G_{po} = \frac{4V_f}{d_f} \int_0^l \tau_p(x) x dx \quad [22]$$

If  $\tau_p$  is assumed constant with respect to  $x$  (i.e. if we disregard the effect of fiber roughness and asperity wear during sliding) and equate it to  $\tau_s$  (the value at the start of sliding)

$$G_{po} = \frac{V_f d_f \sigma_f^2}{8\tau_s} \quad [23]$$

Thus as  $\tau_s$  increases with  $\delta$  as shown in figure 36, the composite toughness will decrease. For a volume fraction of 10%,  $d_f$  equal to 140  $\mu\text{m}$  and  $\sigma_f$  equal to 3.9 GPa,  $G_{po}$  would be about 280  $\text{KJ}/\text{m}^2$  ( $\tau_s = 95$  MPa,  $\delta = 1.1$   $\mu\text{m}$ ) and 130  $\text{KJ}/\text{m}^2$  ( $\tau_s = 206$  MPa,  $\delta = 1.7$   $\mu\text{m}$ ).

When roughness is an important factor, the load often increases in the first 5 or 10  $\mu\text{m}$  just after debonding and is thought to be the result of decorrelation of asperities [34,38]. Figure 41 shows that the sliding resistance of the  $\delta = 1.7$   $\mu\text{m}$  sample exhibits a decorrelation pressure after debonding. The SEM analysis (figures 44-45) of this sample confirms there is a distinct roughness not observed in the  $\delta = 1.1$   $\mu\text{m}$  sample (figures 42-

43). There is also no evidence of a decorrelation pressure in figure 41 for the  $\delta = 1.1 \mu\text{m}$  pushout tests.

From this evidence when debonding occurs in samples where  $\delta \leq 1.4 \mu\text{m}$ ,  $\tau_s$  may reasonably estimate  $\tau_p$ . However, this may not be the case when reaction zone thickness becomes larger than  $1.4 \mu\text{m}$ . Besides the roughness effect, wear associated with sliding may require redefining the friction law followed by  $\tau_p$ .

## 5.4 Composite Processing Optimization

Future composite processing will entail modelling properties (i.e. density, matrix microstructure, fiber damage and fiber/matrix reactions,  $\delta$ ) as a function of processing parameters (i.e. temperature, pressure and time), sensing those parameters and properties and using feedback to effectively control the process. The first step is the development of models to predict properties for given processing parameters. Elzey and Wadley [13] have developed a densification model for consolidation of monotape preforms. This model is best represented by densification maps similar to the densification maps developed for powders [101]: the relative density vs. normalized stress at constant temperature and relative density vs. homologous temperature at a given stress are plotted in figures 52 and 53. The time contours, defined as time in Stage 2, show how densification progresses. For example, the first contour in figure 52 represents the instantaneous response of applying a 10 MPa pressure. If  $T/T_m$  is given as 0.7, the relative density would be about 0.85 in 15 minutes. These maps allow one to choose an appropriate temperature ( $T_c$ ) and time ( $t_c$ ) to fabricate a fully dense composite.

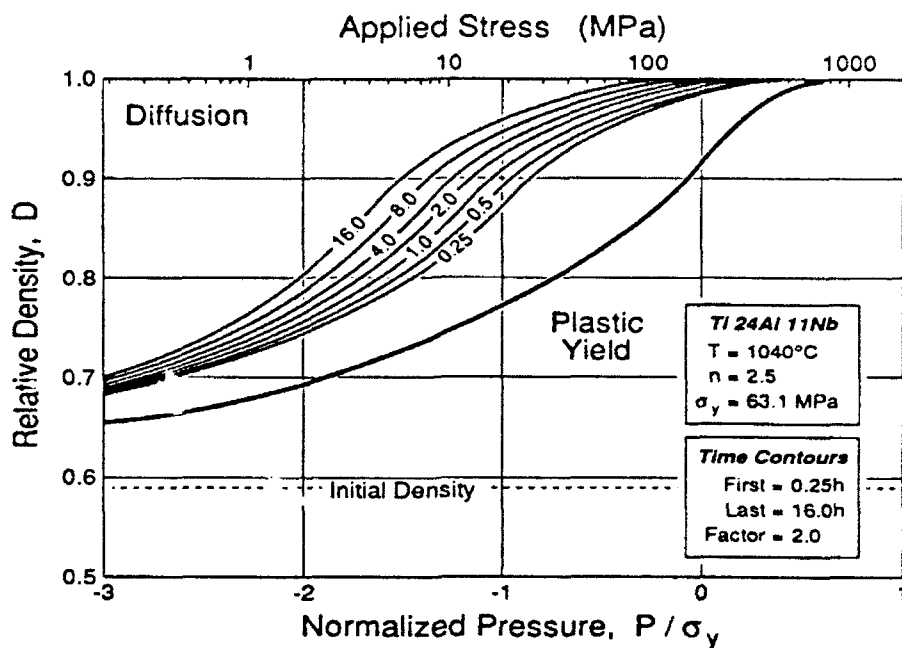


Figure 52 Predicted densification of SCS/6/Ti 24Al 11Nb monotapes verses normalized applied stress

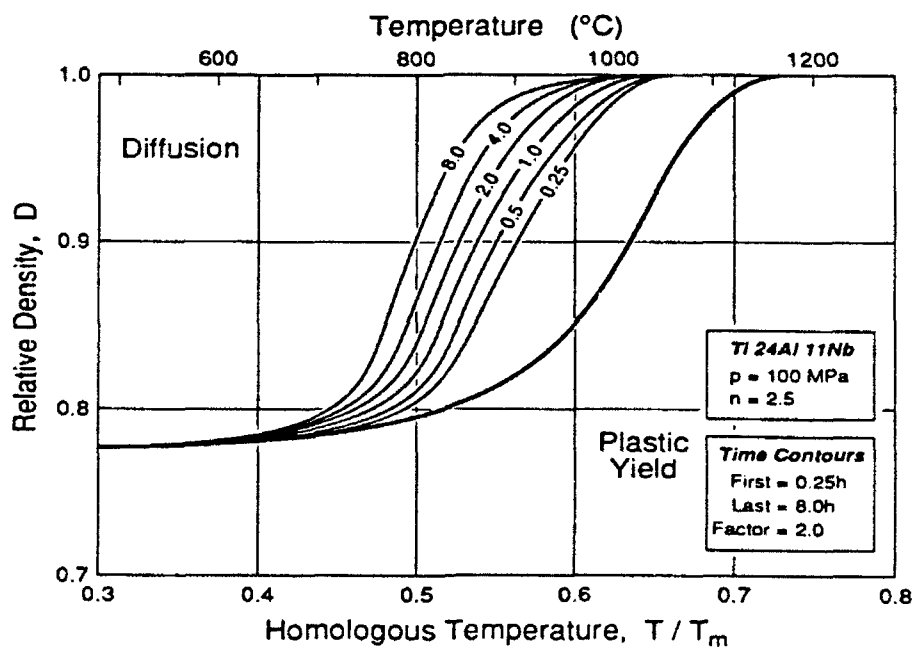
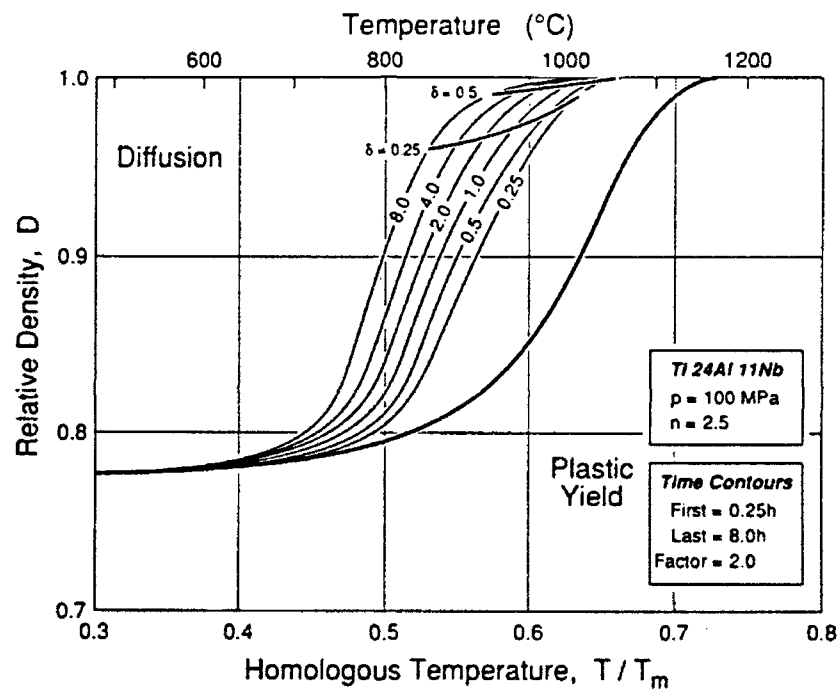


Figure 53 Predicted densification of SCS/6/Ti 24Al 11Nb monotapes verses homologous temperature



The models for the reaction zone thickness,  $\delta$ , discussed in section 5.1 can be integrated into these densification maps. Since the time contours are defined as time in Stage 2,  $\delta$  is modelled with eqn. 2 as in section 5.1.1 and the  $\delta$  contours are added to the densification map (see figure 54). The knowledge that the interface properties increase when  $\delta \geq 1.4$  to  $1.5 \mu\text{m}$  can now be taken into consideration. From figure 54 processing above about  $1050^\circ\text{C}$  for short periods of time will both minimize reaction and give full density. Although it is not shown on this plot the amount of fiber fracture is lessened by also processing at high temperature for short periods of time [52, 111]



**Figure 54** Predicted densification of SCS/6/Ti 24Al 11Nb monotapes verses homologous temperature with  $\delta$  contours

## 6 References

- 1) T.H. Courtney, Mechanical Behavior of Materials, Magraw-Hill, 1990
- 2) M. Ashby, D. Jones, "Engineering Materials 2", 1986
- 3) A. Kelly, "The Nature of Composites", Materials, Scientific American Book, W.H.Freeman and Company, pp. 97-110, 1967
- 4) Rosen, "Tensile Failure of Fibrous Composites," AIAA Journal, Vol. 2 No 11, Nov. 1964
- 5) W.A. Curtin, "Theory of Mechanical Properties of Ceramic-Matrix Composites", J. Am. Ceram. Soc., 74[11]2837-45, 1991
- 6) D.R. Pank, A.M. Ritter, R.A. Amato, J.J. Jackson, "Structure-Property Relationships in  $Ti_3Al$ /SCS-6 Composites," Titanium Aluminide Composite Workshop, pp. 383 - 398, Orlando, FL, May 1990
- 7) C. Thaw, "Fabrication of Sigma Silicon Carbide Monofilament Reinforced Metal Matrix Composites," Titanium Aluminide Composite Workshop, pp. 242 - 245, Orlando, FL, May 1990
- 8) J.P. Sorensen, "Titanium Metal Matrix Composite Subcomponent Fabrication," Titanium Aluminide Composite Workshop, pp. 246 - 362, Orlando, FL, May 1990
- 9) P.A. Siemers, J.J. Jackson, " $Ti_3Al$  / SCS-6 MMC Fabrication by Induction Plasma Deposition", Titanium Aluminide Composite Workshop, pp. 233 - 250, Orlando, FL, May 1990
- 10) H.Gigerenzer, P.K. Wright, "Plasma Sprayed SCS-6 / Titanium Aluminide Composite Test Panels," Titanium Aluminide Composite Workshop, pp. 251 - 264, Orlando, FL, May 1990
- 11) S. Singerman, R. Boucher, B. Doehnert, R. Tucker, G. Doble, "Techniques for Matrix Coating Monofilaments," Titanium Aluminide Composite Workshop, pp. 289 - 299, Orlando, FL, May 1990
- 12) H.M. Meyer III, R.R. Kieschke and J. Storer, "Material Development in the 3M

- Continuous-Fiber Metal Matrix Composites Model Factory," Titanium Matrix Composites Workshop Proceedings, Nov. 91, pp. 174-199
- 13) D.M. Elzey and H.N.G. Wadley, "Modeling the Densification of Metal Matrix Composite Monotapes," *Acta Metall. Mater.*, in press
  - 14) J.F. Groves, "Fiber Damage During the Consolidation of Metal Matrix Composites", Masters Thesis, University of Virginia, 1992
  - 15) D.B. Gundel and F.E. Wawner, "Interfacial Reaction Kinetics of Coated SiC fibers With Various Titanium Alloys", *Scripta Met.*, vol. 25, pp. 437-441, 1991
  - 16) J.M. Yang and S.M. Jeng, "Interfacial Reaction Kinetics of SiC Fiber-Reinforced  $Ti_3Al$  Matrix Composites", *Scripta Met.*, Vol 23, pp. 1559-1564, 1989
  - 17) R.E Tressler and T.L. Moore, "Mechanical Property and Interface Reaction Studies of Titanium-Alumina Composites", *Met. Eng. Quart.*, pp. 16-22, Feb. 1971
  - 18) P.E. Cantonwine, unpublished research
  - 19) A.K. Misra, *Interfaces in Metal-Ceramic Composites*, pp 85-102, TMS, 1989
  - 20) G.H. Reynolds, J.H. Norman, and W.Bell, *Titanium Aluminide Composite Workshop*, pp. 202-216, Orlando, FL, May 1990
  - 21) A.K. Misra, "Reaction of Ti and Ti-Al Alloys with Alumina", *Met Trans*, Vol 22A, pp. 715-721, March 1991
  - 22) R.E. Tressler, T.L. Moore, and R.L. Crane, "Reactivity and interface characteristics of titanium-alumina composites", *J. Mat. Sci*, pp. 151-161, 1973
  - 23) J.H. Selverian, F.S. Ohuchi, M. Bortz, and M.R. Notis, "Interface reactions between titanium thin films and (1-1 2) sapphire substrates, *J. Mat. Sci.*, pp. 6300-6308, 1991
  - 24) D.B. Gundel, "Investigation of the Interaction Between Silicon Carbide Fibers and Titanium Alloys", Masters Thesis University of Virginia, 1991
  - 25) P. Martineau, R. Pailler, M. Lahaye, R. Naslain, "SiC Filament/Titanium Composites Regarded as Model Composites II," *J. Mat. Sci.*, 19, pp 2749-2770, 1984
  - 26) J.L. Ratliff, G.W. Powell, "Research on Diffusion in Multiphase System: Reaction in

- the Ti-SiC and Ti-6Al-4V-SiC Systems," AFML-TR-65-2, Part V, 1984
- 27) S.F. Baumann, P.K. Brindley, S.D. Smith, "Reaction Zone Microstructure in a  $\text{Ti}_3\text{Al}$  + Nb/SiC Composite." Met. Trans., 21A, pp. 1559-1568, 1990
  - 28) D.M. Bowden, J.E. O'Neal, J.E. Deffeyes, D.S. Schwartz, D.J. Peterman, "Effects of Matrix Chemistry on Interface Development in  $\alpha_2 + \beta$  Titanium Aluminide Alloys Containing SCS-6 SiC Reinforcement," Titanium Aluminide Composite Workshop, pp. 149 - 164, Orlando, FL, May 1990
  - 29) S.M. Jeng, W. Kai, C.J. Shih, J.M. Yang, "Interface Reaction Studies of  $\text{B}_4\text{C}/\text{B}$  and SiC/B Fiber-Reinforced  $\text{Ti}_3\text{Al}$  Matrix Composites," Mat. Sci Eng., A114,(1-2), PP. 189-196, 1989
  - 30) A.G Metcalfe, 'Fiber-Reinforced Titanium Alloys," in Composite Materials, V.4, Metallic Matrix Composites, K.G. Kreider, ed., Academic Press, New York, pp. 269-318 (1974)
  - 31) S. Ochiai, K. Osamura, "A Computer Simulation of Strength of Metal Matrix Composites with a Reaction Layer at the Interface", Met Trans, V 18A, pp. 673-679, April 1987
  - 32) J.-M. Yang, S.M. Jeng and C.J. Yang, "Fracture mechanisms of fiber-reinforced titanium alloy matrix composites Part 1: Interfacial behavior", Mat. Sci. and Eng., A138, pp. 155-167, 1991
  - 33) C. Liang, J.W. Hutchinson, "Mechanics of the Fiber Pushout Test", To be published
  - 34) P.D. Warren, T.J. Mackin, A.G. Evans, "Design, Analysis and Application of an Improved Push-Through Test for the Measurement of Interface Properties in Composites", Acta Metall. Mater., Vol 40, No. 6, PP 1243-1249, 1992
  - 35) M.N. Kallas, D.A. Koss, H.T. Hahn, J.R. Hellmann, "Interfacial Stress State Present in a "Thin Slice" Fibre Push-Out Test", J. Mat. Sci., 27, pp. 3821-3826, 1992
  - 36) D.B. Marshall, M.C. Shaw and W.L. Morris, "Measurement of Interfacial Debonding and Sliding Resistance in Fiber Reinforced Intermetallics," Acta Metall Mater., Vol.

- 40, No. 3, pp. 443-454, 1992
- 37) M.C. Watson, T.W. Clyne, "The use of Single Fibre Pushout Testing to Explore Interfacial Mechanics in SiC Monofilament-Reinforced Ti-II. Application of the Test to Composite Material, *Acta Metall. Mater.*, Vol. 40, No. 1, pp. 141-148, 1992
  - 38) T.J. Mackin, P.D. Warren, A.G. Evans, "Effects of Fiber Roughness on Interface Sliding in Composites", To be published
  - 39) T.J. Mackin, J. Y. Yang, C.G. Levi, A.G. Evans, "Environmentally Compatible Double Coating Concepts for Sapphire Fiber-Reinforced Gamma-TiAl", To be published
  - 40) H.A. Lipsitt, "Titanium Aluminides - An Overview", *Mat. Res. Soc. Symp.*, Vol 39, 1985, MRS
  - 41) G.S. Doble and A.J. Kumnick, "Fabrication of Silicon Carbide Reinforced Aluminide Composites for Engine and Airframe Application," *Titanium Matrix Composites Workshop Proceedings*, Nov. 91, pp. 200-214
  - 42) P.K. Brindley, S.L. Draper, M.V. Nathal and J.I. Eldridge, "Factors Which Influence Strength of a SiC/Ti 24Al 11Nb (at%) Composite," *Fundamental Relationships Between Microstructure and Mechanical Properties of Metal-Matrix Composites*, edited by P.K. Liaw and M.N. Gungor, TMS 1990
  - 43) W. Hansiak, C. Rowe, M. Abraham, "Fabrication of Titanium Aluminide Metal Matrix Composites", *Titanium Aluminide Composite Workshop*, pp. 251-264, Orlando, FL, May 1990
  - 44) J.W. Pickens and G.K. Watson, "Fabrication of Titanium Aluminide Composites via Powder Cloth and Wire Arc Spray Techniques," *Titanium Aluminide Composite Workshop*, pp. 576-585, Orlando, FL, May 1990 (Wright-Pat AFB)
  - 45) P. Kantzos, J.J. Eldridge, D. Koss and L.I. Ghosn, "The Effect of Fatigue on the Interfacial Friction Properties of SCS-6/Ti-15-3 Composite," *HiTemp Review 1991 - Advance High Temperature Engine Materials Technology Program*
  - 46) T.P. Gabb, J. Gayda and R.A. MacKay, "Isothermal and Nonisothermal Fatigue

- Behavior of a Metal Matrix Composite," J. Comp. Mat., Vol 24, June 1990
- 47) C.C. Bampton, J.A. Graves, K.J. Newell and R.H. Lorenze, "Process Modeling for Titanium Matrix Composites," Titanium Matrix Composites Workshop Proceedings, Nov. 91, pp. 145-157
  - 48) K.Chawla, Composite Materials: Science and Engineering, Ch. 10, 1987 (Springer-Verlag)
  - 49) R.A. Naik, "Simplified Micromechanical Equations for Thermal Residual Stress Analysis of Coated Fiber Composites," J. Comp. Tech. & Res., Vol 14, No 3, Fall 1992 pp. 182-186
  - 50) J.W. Hutchinson and H.J. Jensen, "Models of Fiber Debonding and Pullout in Brittle Composites with Friction," Mechanics of Material, 9, 1990, pp. 139-163
  - 51) M.J. Pindera, A.D. Freed and S.M. Arnold, "Effects of Fiber and Interfacial Layer Architectures on the Thermoplastic Response of Metal Matrix Composites," NASA Technical Memorandum 105802
  - 52) J. Groves, D. Elzey and H.N.G. Wadley, research to be published
  - 53) F.E. Wawner, "Boron and Silicon Carbide / Carbon Fibers", Fibre Reinforcements for Composite Materials, edited by A.R.Bunsell, pp. 371-424, 1988
  - 54) British Petroleum
  - 55) Textron Specialty Material
  - 56) H. DeBolt, R. Suplinskas, J. Cornie, T. Henze and A. Henze U.S. Patent 4340636, July, 20 1982
  - 57) H.E. Labelle, Jr. "Method for growing crystalline materials", U.S. Patent 3,591,348 (1971)
  - 58) Saphikon Inc.
  - 59) G.F. Hurley, H.F. Labelle, Jr., C.R. Mitchell, and F.H. Cocks, "Elevated Temperature Strengthening of Melt-Grown Sapphire by Alloying" Appl. Polymer. Sym. #29, New and Specialty Fibers, John Wiley and Sons, pp. 131-149, 1976

- 60) R.R. Kieschke, R.E. Somekh, and T.W. Clyne, "Sputter Deposited Barrier Coatings on SiC Monofilaments for Use in Reactive Metallic Matrices - I. Optimization of Barrier Structure," *Acta metall. mater.*, vol 39, No 4 pp. 427-435
- 61) A.K. Misra, "Reaction of Ti and Ti-Al Alloys with Alumina", *Met Trans*, Vol 22A, pp. 715-721, March 1991
- 62) R.E. Tressler, T.L. Moore, and R.L. Crane, "Reactivity and interface characteristics of titanium-alumina composites", *J. Mat. Sci.*, pp. 151-161, 1973
- 63) J.H. Selverian, F.S. Ohuchi, M. Bortz, and M.R. Notis, "Interface reactions between titanium thin films and (1-1 2) sapphire substrates, *J. Mat. Sci.*, pp. 6300-6308, 1991
- 64) P.R. Smith, F.H. Froes, Cammett J.T., "Correlation of Fracture Characteristics and Mechanical Properties for Titanium Matrix Composites," in *Mechanical Behavior of Metal Matrix Composites*, J.E. Hack, M.F. Amateau, eds., TMS-AIME, Warrendale, PA (1983)
- 65) J.P. Sorensen, *Proceedings of 14th Annual Conf. on Composite Materials and Structures*, Cocoa Beach, FL, Jan. 17-19 (1990)
- 66) F.E. Wawner, Whatley, W.J., "The Effect of Elevated Temperature Exposure on the Properties of SiC/Ti6Al4V Composites," *Space Age Metals Technology V2*, Eds F.H. Froes, R.A. Cull, SAMPE, pp. 470-479 (1988)
- 67) R. Pailler, P. Martineau, M. Lahaya, Y. Le Patitcorps, R. Naslain, "Influence of Diffusion Formed Brittle Layers at Filament-Matrix Interfaces on the Mechanical Properties of SiC/Ti Composite Material," in *Reactivity of Solids Part B*, P. Barret, L.C. Dufour, eds., pp. 1113-1117, Elsevier, New York (1985)
- 68) R.R. Kieschke and T.W. Clyne, "Control over Interfacial Bond Strength in Ti/SiC Fibrous Composites," *Fundamental Relationships Between Microstructure and Mechanical Properties of Metal-Matrix Composites*, edited by P.K. Liaw and M.N. Gungor, TMS 1990
- 69) J. Langmuir, "The Vapor Pressure of Metallic Tungsten," *Phys. Rev.* 2(1913) 5,

pp.329-342

- 70) H. Hertz, Ann. Physik, 47, 697(1882)
- 71) C.A. Handwerker, J.W. Cahn and J.R. Manning, "Thermodynamic and kinetics of Reactions at Interfaces in Composites," Mat. Sci. and Engr., A126(1990 173-189
- 72) D.A. Koss, D. Banerjee, D.A. Lukasak, and A. K. Gorgia, "A Review of the Deformation and Fracture of  $Ti_3Al$  - Based Alloys", High Temperature Aluminides and Intermetallics, TMS 1990
- 73) L.M. Hsiung, W. Cai, H.N.G. Wadley, "Microstructure and Phase evolution in rapidly-solidified Ti-24Al-11Nb", Mat. Sci. Eng., A152, pp. 295-303, 1992
- 74) J.M. Larson, K.A. Williams, S.J. Balsone, and M.A. Stucke, "Titanium Aluminides for Aerospace Applications," High Temperature Aluminides and Intermetallics, TMS 1990
- 75) Brindley et al. Nasa Lewis Research Center, personal communication
- 76) M.L. Gambone, "Fatigue and Fracture of Titanium Aluminides", WRDC-TR-89-4145, February 1990
- 77) D.B. Gundel, "Investigation of the Interaction Between Silicon Carbide Fibers and Titanium Alloys", Masters Thesis University of Virginia, 1991
- 78) P. Martineau, R. Pailler, M. Lahaye, R. Naslain, "SiC Filament/Titanium Composites Regarded as Model Composites II," J. Mat. Sci., 19, pp 2749-2770, 1984
- 79) J.L. Ratliff, G.W. Powell, "Research on Diffusion in Multiphase System: Reaction in the Ti-SiC and Ti-6Al-4V-SiC Systems," AFML-TR-65-2, Part V, 1984
- 80) S.F. Baumann, P.K. Brindley, S.D. Smith, "Reaction Zone Microstructure in a  $Ti_3Al$  + Nb/SiC Composite." Met. Trans., 21A, pp. 1559-1568, 1990
- 81) D.M. Bowden, J.E. O'Neal, J.E. Deffeyes, D.S. Schwartz, D.J. Peterman, "Effects of Matrix Chemistry on Interface Development in  $\alpha_2 + \beta$  Titanium Aluminide Alloys Containing SCS-6 SiC Reinforcement," Titanium Aluminide Composite Workshop, pp. 149 - 164, Orlando, FL, May 1990



- 82) S.F. Baumann, P.K. Brindlley, and S.D. Smith, "Reaction Zone Microstructure in a  $\text{Ti}_3\text{Al} + \text{Nb} / \text{SiC}$  Composite", *Met. Trans. A*, 21A June 1990, 1559-1569
- 83) P.R. Smith, C.G. Rhodes and W.C. Revelos, "Interfacial Evaluation in a Ti-25Al-17Nb/SCS-6 Composite," *Interfaces in Metal-Ceramic Composites*, eds. R.Y. Lin, R.J. Arsenault, G.P. Martins and S.G. Fishman, TMS (1989)
- 84) G. Das, "Interfacial Reactions in SiC Fiber-Reinforced Titanium Alloy and Titanium Aluminide Composites," *Metal and Ceramic Matrix Composites: Processing, Modeling and Mechanical Behavior*, eds. R.B. Bhagat, A.H. Clauer, P. Kumar and A.M. Ritter, TMS (1990)
- 85) A.M. Ritter, E.L. Hall and N. Lewis, "Reaction Zone Growth in Ti-Base/SiC Composites," *Mat. Res. Soc. Symp. Proc. Vol 194*, MRS (1990)
- 86) Y. W. Kim and J.J. Kleek, "Heat Treatments and Thermal Fatigue of SCS-6/Alpha-2 Titanium Aluminide Composites," *Mat. Res. Soc. Symp. Proc. Vol 194*, MRS (1990)
- 87) L. Hisung, Unpublished research
- 88) H Hough, Masters Thesis, University of Virginia, 1993
- 89) I.W Hall, J.L. Iirn, Y. Lepetitcorps and K. Bilba, "Microstructural Analysis of Isothermally Exposed Ti/SiC Metal Matrix Composites," *J. Mat. Sci* 27(1992) 3835-3842
- 90) Melcalf [30]
- 91) A.G. Evans, F.W. Zok and J. Davis, "The Role of Interfaces in Fiber-Reinforced Brittle Matrix Composites," *Composite Science and Technology*, 42, 1991, pp 3-24
- 92) R.J. Kerans and T.A Parthasarthy, "Theoretical Analysis of the Fiber Pullout and Pushout Tests," *J. Am. Ceram. Soc.*, 74(7), pp. 1585-96 (1991)
- 93) T.J. Mackin, personal communication
- 94) J.B. Davis, J.P.A. Löfvander, A.G. Evans, E. Bischoff and M.L. Emiliani, "Fiber Coating Concepts for Brittle Matrix Composites," to be published
- 95) A. Barlett and A.G. Evans, "The Effect of Reaction Products on the Fracture

- Resistance of a Metal/Ceramic Interface," to be published
- 96) D.B. Marshall, "Analysis of Fiber Debonding and Sliding Experiments in Brittle Matrix Composites," *Acta Metall. Mater.*, Vol 40, No 3, pp. 427-441, 1992
  - 97) A.G. Evans, T.J. Mackin, "The Mechanical Performance of Ceramic Matrix Composites", To be published
  - 98) MY. He, J.W. Hutchinson, "Crack Deflection at an Interface Between Dissimilar Elastic Materials," In *J. Solid Structures*, Vol. 25, No. 9, pp. 1053-1067, 1989
  - 99) J. Wert, personal communication (MS 606)
  - 100) D. Gundel unpublished research
  - 101) E. Artz, M.F. Ashby and K.E. Easteling, "Practical Application of Hot-Isostatic Pressing Diagrams: Four Case Studies, *Met. Trans. A*, Vol. 14, 1983, pp. 211-22
  - 102) P.K. Brindley, S.L. Draper, M.V. Nathal, J.I. eldridge, "Factors Which Influence Tensile Strength of a SiC/ Ti -24Al-11Nb (at%) Composite", *Fundamental Relationships Between Microstructure and Mechanical Properties of Metal Matrix Composites*, P.K. Liaw and M.N. Gungor, eds., TMS 1990
  - 103) J.L. Kroupa, "Elastic-Plastic Finite Element Analysis of MMC Subjected to Thermomechanical Fatigue", *Titanium Aluminide Composite Workshop*, pp. 576-585, Orlando, FL, May 1990
  - 104) G. Das, "Microstructural Characterization of Ceramic Reinforcements for Composites", *Titanium Aluminide Composite Workshop*, pp. 20 - 58, Orlando, FL, May 1990
  - 105) D.A. Koss, M.N. Kallas and J.R. Hellmann, "Mechanics of Interfacial Failure During Thin-Slice Fiber Pushout Tests," *Intermetallic Matrix Composites II*, ed. D.B. Miracle, D.L. Anton and J.A. Graves (Pittsburgh, PA MRS, 1992)
  - 106) D.A. Koss, J.R. Hellmann and M.N. Kallas, "Fiber Pushout and Interfacial Shear in Metal Matrix Composites," *JOM*, March 1993
  - 107) M.J. Blackburn and M.P. Smith, "Research to Conduct an Exploratory Experimental

and Analytical Investigation of Alloys", Report AFWAL-TR-81-4046, Wright-Patterson Air Force Base, OH, 1981

- 108) R.P. Nimmer, P.A. Siemers, M.R. Eggleston, E.R. Russel, "Fiber Array Geometry Effects upon Composite Transverse Tensile Behavior," Titanium Matrix Composites Workshop Proceedings, WPAFB, Ohio, Nov. 91
- 109) J.L. Kroupa, J.A. Sherwood, N.E. Ashbough, H.M. Quimby and M.J. Boyle, "Comparison of Responses of a MMC using Classical and unified Constitutive Matrix Behaviors," Titanium Matrix Composites Workshop Proceedings, Nov. 91
- 110) M.J. Pindera, personal communication
- 111) D.Elzey and H.N.G. Wadley, "Modeling the Fracture of Fibers During Metal Matrix Composite Consolidation," to be submitted to Acta Met.
- 112) J.W. Pickens and G.K. Watson, "Fabrication of Titanium Aluminide Composites via Powder Cloth and Wire Arc-Spray Techniques," Titanium Aluminide Composite Workshop, Orlando, FL, May 1990
- 113) J.T. Niemann and J.F. Edd, "Fabrication of Titanium-Aluminide Composites by Tape Casting," Titanium Aluminide Composite Workshop, Orlando, FL, May 1990
- 114) H.N.G. Wadley, Private Communication
- 115) Todd Kunze, Masters Thesis, University of Virginia, 1991
- 116) Anthony Evans, personal communication
- 117) Yong Mei, Lui, "Densification by Power Law Creep," Masters Thesis, University of Virginia, Jan. 93
- 118) Yong, Mei, H.N.G. Wadley, M. Duva, research to be published
- 119) P. Cantonwine, "Titanium attack in the temperature ramp of processing a titanium aluminide composite using a foil/fiber/foil technique," to be published

## Appendix A

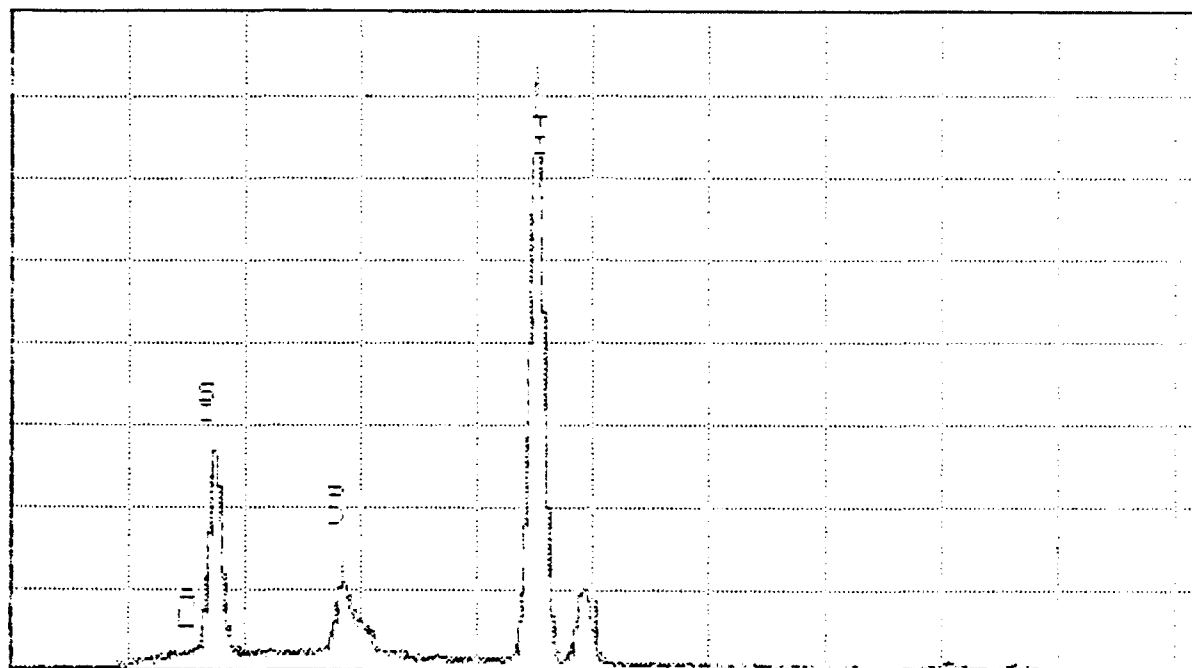
### 1.1 EDS Data

Series II University of Virginia

SRT 00-JRN-93 15:15

Cursor: 0.000keV = 0

ROI (44) 0.000: 0.000



0.000

VFS = 1024 10.240

30

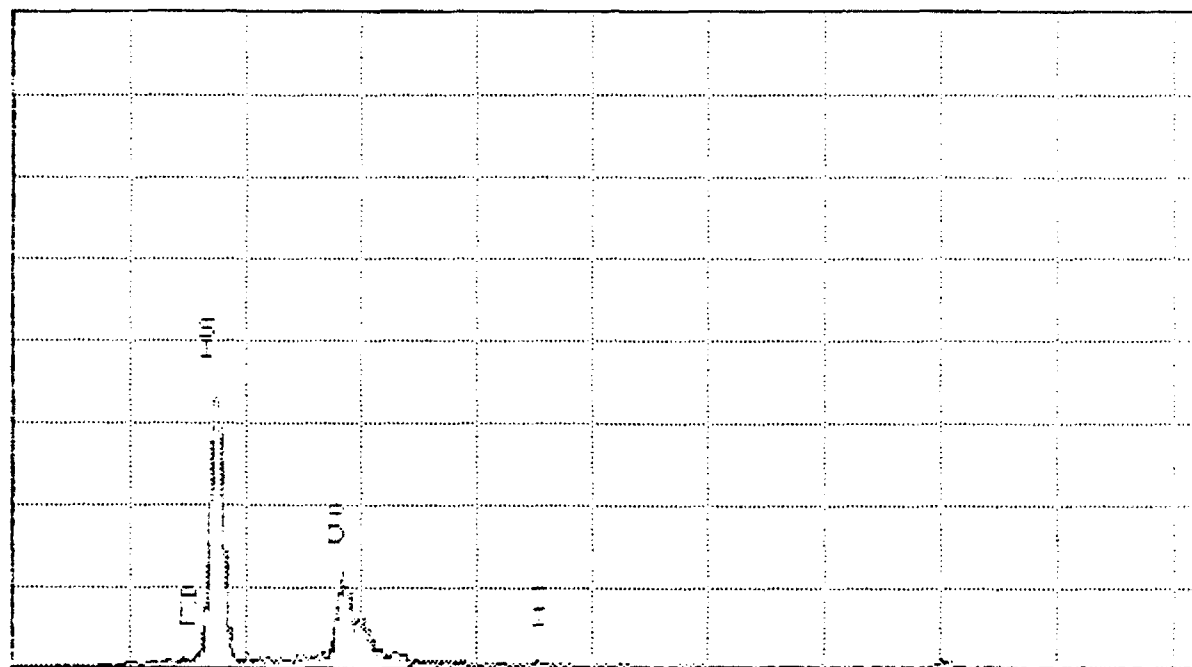
SCS-6/ TI COATING

Series II University of Virginia

ERT 20-JFK-53 15:20

Durchf: 0.000keV = 0

ROI (44) 0.000: 2.000



0.000

VFS = 1024 10.240

30

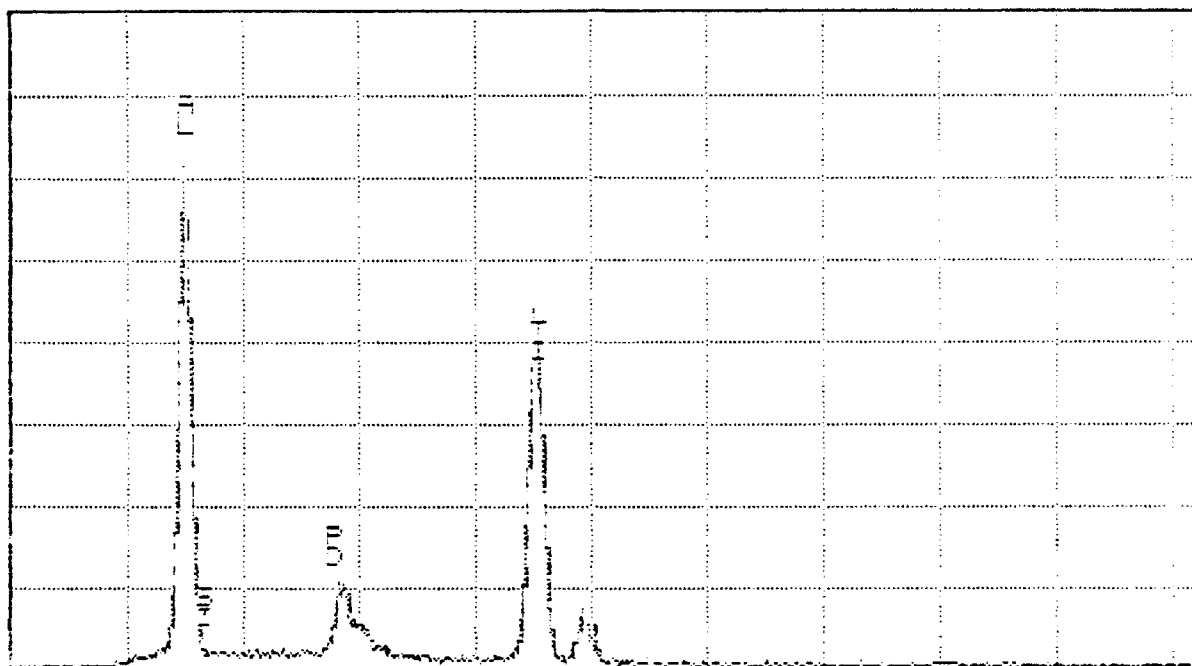
SCS-6/ SCS COATING

Series II University of Virginia

SAT 80-JAN-88 16:18

Cursor: 0.000keV = 0

ROI (44) 0.000: 0.000



0.000

VFS = 1024 10.240

20

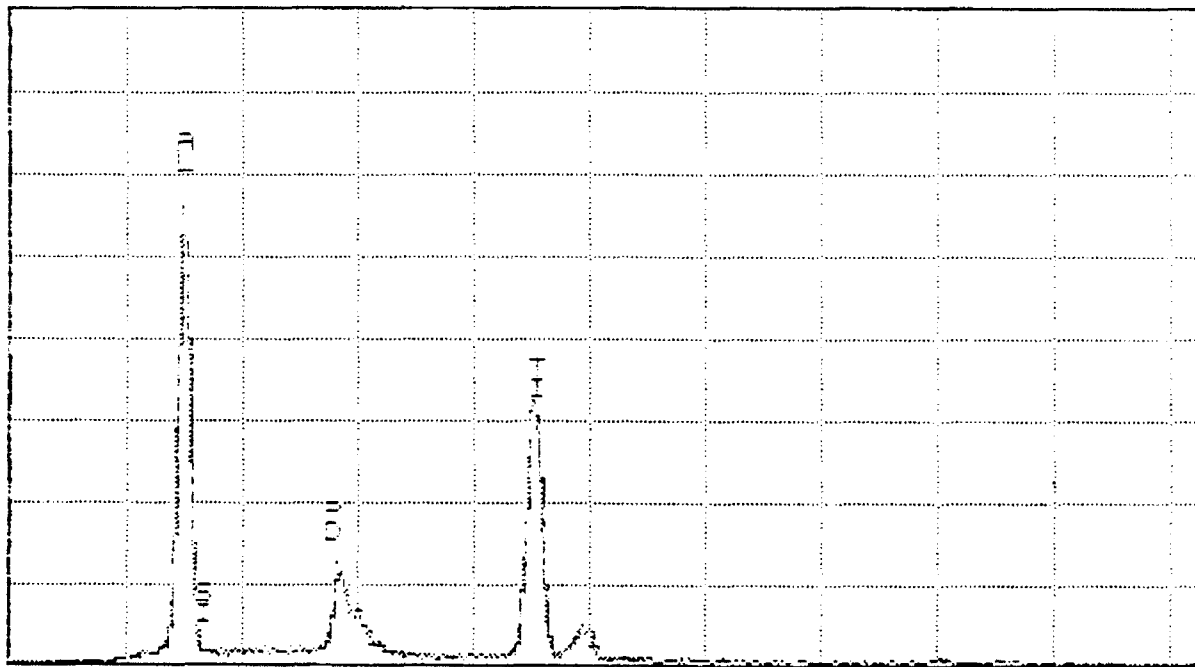
ALUMINA/ SMOOTH STREEK OF TC COATING

Series II University of Virginia

SAT 00-JAN-80 16:24

Cursor: 0.000keV = 0

ROI (44) 0.000: 0.000



0.000

VFS = 1024 10.240

20

ALUMINA/ ROUGH STREEK OF TI COATING



## Appendix C

In the actual processing of the VHP 1040 °C/100 MPa/30 min. sample, the temperature was held at 150 °C and 450 °C for 60 and 90 min. respectively. It is believed the reaction kinetics at these temperatures are slow enough to ignore and the results of the model indicate this is a valid assumption. The temperature profile can be defined by three different linear equations

$$T_{Stage1} = 0.067t + 20; t = 0 \rightarrow 15200 \quad [1]$$

$$T_{Stage2} = 1040; t = 15200 \rightarrow 17000 \quad [2]$$

$$T_{Stage3} = -0.17t + 3930; t = 17000 \rightarrow 23000 \quad [3]$$

T is in °C and t is in seconds.

A third order polynomial is chosen to model the defined temperature profile

$$T(t) = K_1 + K_2t + K_3t^2 + K_4t^3 \quad [4]$$

To find the unknown constants, four points from the temperature profile defined four equations with four unknowns.

**Table 3: Temperature/Time Points**

Temperature (°C)	Time (sec)
40	300
1040	15200
1040	17000
20	23000

Setting  $t = t/300$  to reduce the magnitude and using matrix notation the problem becomes.

$$\begin{bmatrix} 1 & 1 & 1 & 1 \\ 1 & 50.7 & 50.7^2 & 50.7^3 \\ 1 & 56.7 & 56.7^2 & 56.7^3 \\ 1 & 76.7 & 76.7^2 & 76.7^3 \end{bmatrix} \begin{bmatrix} K_1 \\ K_2 \\ K_3 \\ K_4 \end{bmatrix} = \begin{bmatrix} 40 \\ 1040 \\ 1040 \\ 20 \end{bmatrix} \quad [5]$$

This equation was solved in mathematica using the following commands.

```
In[27]:= m = {{1, 1, 1, 1}, {1, 50.7, 50.7^2, 50.7^3},
               {1, 56.7, 56.7^2, 56.7^3}, {1, 76.7, 76.7^2, 76.7^3}}
Out[27]= {{1, 1, 1, 1}, {1, 50.7, 2570.49, 130324.},
           {1, 56.7, 3214.89, 182284.}, {1, 76.7, 5882.89, 451218.}}
>
In[28]:= LinearSolve[m, {40, 1040, 1040, 20}]
Out[28]= {62.3359, -24.2451, 1.93035, -0.0211401}
```

Plugging  $t/300$  back in for  $t$  gives

$$T(t) = 62.3 - 0.081t + 2.14 \times 10^{-5}t^2 + 7.8 \times 10^{-10}t^3 \quad [6]$$

A comparison of the temperature profiles defined by equations 1-3 and eqn. 6 is shown on the following page.

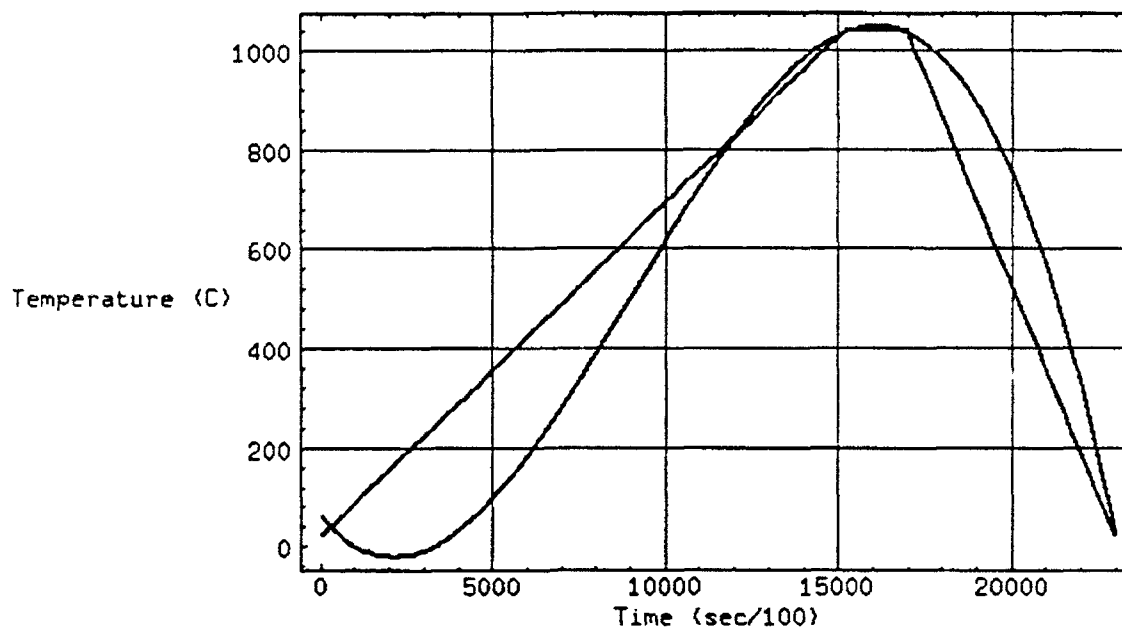


**Figure 25 Comparison of defined and modelled temperature profile**

The integration and plotting of eqn. 24 in mathematica required defining a table and numerically integrating over  $t$  from 0 to  $i$  where  $i$  went from 0 to 23000 in steps of 100. The mathematica commands where

```
In[7]:= ko = .0025;
In[8]:= q = 135000;
In[9]:= r = 8.314;
In[10]:= temp = 335 - 0.081 t + 2.14 10^-5 t^2 - 7.8 10^-10 t^3;
In[11]:= Table[10^6 Sqrt[NIntegrate[ko^2 Exp[-2q/(r temp)],
    {t, 0, i}]], {i, 0, 23000, 100}];
In[12]:= ListPlot[%11];
```

## Appendix A

### 1.1 Secant CTE vs. Tangent CTE

Secant CTE,  $\alpha_s$ , is defined as

$$\alpha_s = \frac{\Delta \epsilon}{\Delta T} \quad [1]$$

where  $\Delta T = (T - T_{ref})$ .  $T$  is the Temperature of concern and  $T_{ref}$  is the reference temperature which  $\alpha_s$  was measure.  $\Delta \epsilon = (\epsilon - \epsilon_{ref})$ ; for convenience  $\epsilon_{ref}$  is defined as zero. Thus  $\alpha_s$  will have the form

$$\alpha_s = \frac{\epsilon}{\Delta T} \quad [2]$$

The tangent CTE,  $\alpha_t$ , is defined as

$$\alpha_t = \frac{d\epsilon}{dT} \quad [3]$$

Graphically  $\alpha_s$  and  $\alpha_t$  are shown in figure 1.

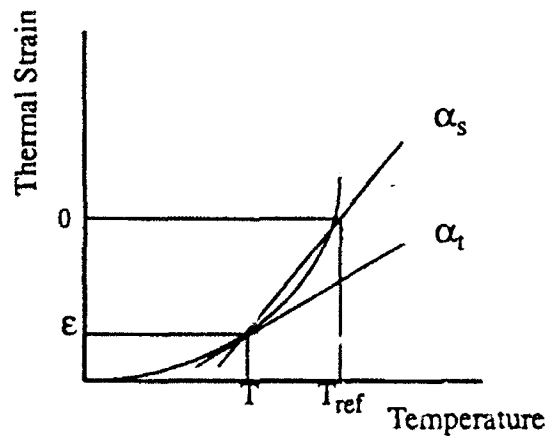


Table 1. Structure type, space group, lattice parameters, Wyckoff positions and fractional atomic coordinates for the TiB (B27) and B (TiB<sub>2</sub>) and TiB<sub>2</sub> structures [4]. The lattice parameters for the B structure were determined from the lattice parameters of TiB. From the values of  $V_B = V_{TiB}/2$  and  $a_B = a_{TiB}/2$  it is calculated that the volume of the trigonal prism is nearly independent of the crystal structure.

Structure	Space group	Unit cell (nm)	Atom	Fractional coordinate
TiB B27	R $\bar{3}m$ (no. 62)	$a = 0.611$ $b = 0.305$ $c = 0.486$	Ti (4c)	0.177, 0.25, 0.125
			B (4c)	0.026, 0.25, 0.675
TiB B	Cmm (no. 63)	$a = 0.323$ $b = 0.856$ $c = 0.305$	Ti (4c)	0.000, 0.146, 0.250
			B (4c)	0.000, 0.444, 0.250
TiB <sub>2</sub> D7 <sub>h</sub>	Inmm (no. 71)	$a = 0.326$ $b = 1.375$ $c = 0.302$	Ti (2c)	0.500, 0.500, 0.000
			Ti (4g)	0.000, 0.18, 0.000
			B (4g)	0.000, 0.375, 0.000
			B (4h)	0.000, 0.443, 0.500
TiB <sub>2</sub> C32	P6 $\bar{3}$ mm (no. 191)	$a = 0.303$ $c = 0.323$	Ti (12c)	0.000, 0.000, 0.000
			B (32d)	0.333, 0.000, 0.500

## 1. INTRODUCTION

Alloys based on the intermetallic compounds  $\gamma$ -TiAl (L1<sub>0</sub>) and  $\alpha_2$ -Ti<sub>3</sub>Al (DO<sub>19</sub>) are of current interest for structural applications at high temperature. Boron additions to these alloys are known to form highly stable refractory borides which enhance high temperature strength and creep resistance of the material, and also refine the microstructural scale during casting and subsequent thermomechanical processing [1-3]. A better understanding of the relative stability and evolution of boride phases in the Ti-Al-B system is thus clearly desirable as a foundation for microstructural design.

The Ti-B equilibrium diagram in Fig. 1 shows three intermediate boride phases: TiB (B27), Ti<sub>3</sub>B<sub>4</sub> (D7<sub>h</sub>) and TiB<sub>2</sub> (C32). (The crystallographic data for the different borides are listed in Table 1 [4].) The existence of Ti<sub>3</sub>B<sub>4</sub> has been the subject of substantial debate [5-7], especially in solidification microstructures, presumably because it can only form directly from the melt over a very narrow range of temperatures and liquid compositions as noted in Fig. 1. A simple Scheil [8] analysis of the solidification of a melt with a Ti:B ratio of 3:4 reveals that the majority of the boron would be present in TiB<sub>2</sub> and TiB, assuming that there is no significant kinetic hindrance to the nucleation and growth of any of the borides. Ti<sub>3</sub>B<sub>4</sub> has been detected by transmission electron microscopy (TEM) of samples produced by *in situ* reaction of B and Ti [9], and by X-ray diffraction on ingot samples annealed at 1963 K [10].

The ternary Ti-Al-B diagram is reported to be divided by a quasibinary between TiB<sub>2</sub> and Al, with the congruent maximum in Fig. 1 projecting into the ternary liquidus along the line of constant Ti:B = 2 [11]. The Ti-TiB eutectic extends into the ternary as a line of two-fold saturation  $L \rightarrow M + B$ , with the metallic phase M switching from  $\beta$ -(Ti) to  $\alpha$ -(Ti) near the equiatomic Ti:Al composition, as depicted in Fig. 2. The boride phase B also changes with

increasing Al content, from TiB to possibly\* TiB<sub>2</sub> and finally Ti<sub>3</sub>B<sub>4</sub> as the corresponding liquid surfaces join the monovariant line. The lines separating the primary boride fields on the liquidus surface in Fig. 2 are the extensions of the peritectics  $L + TiB_2 \rightarrow Ti_3B_4$  and  $L + Ti_3B_4 \rightarrow TiB$  in the binary Ti-B system, and thus represent only changes in slope [12]. An interesting consequence of the opposite trends in liquidus temperature with increasing B or

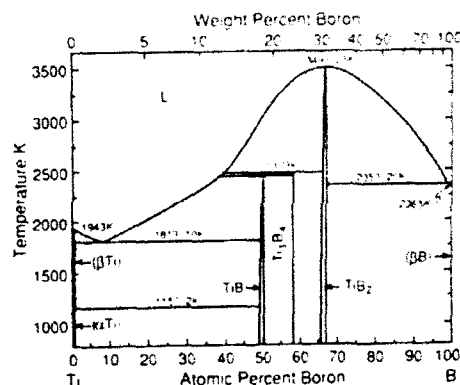


Fig. 1. Binary Ti-B phase diagram

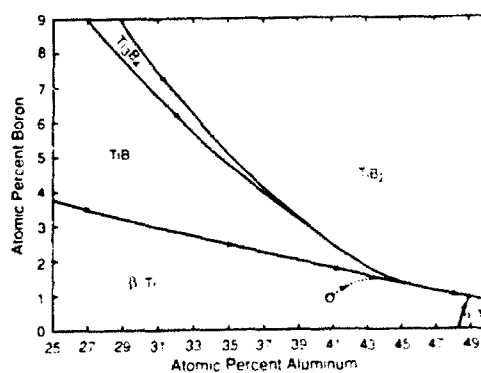


Fig. 2. Ternary liquidus projection [12] for the Ti-Al-B system in the vicinity where the liquidus of primary boride crystallization intersect with the primary metallic phase liquid emerging from the Ti-Al edge binary. The alloy used in this work is indicated by (O).

\*It has not been established whether the Ti<sub>3</sub>B<sub>4</sub> liquidus actually terminates at the monovariant line or is encroached by the TiB and TiB<sub>2</sub> liquidus before reaching it.

Al along the binaries is that the sequence of evolution of the borides with decreasing temperature along the monovariant line is the reverse of that noted along the Ti-B binary liquidus, i.e.  $\text{TiB} \rightarrow \text{TiB}_2 \rightarrow \text{TiB}$ .

Recent investigations on the solidification of Ti-Al-B alloys near the  $\alpha_2$  range of the Ti-Al binary in Fig. 2 revealed the presence of second phases with the B crystal structure typical of the refractory metal monoborides. This phase has not been reported in the Ti-Al-B diagram but has been consistently observed in primary boride rods grown from Ti-Al-R-B melts, where  $R = \text{Ta}, \text{Nb}$  [13, 14]. The B phase in these quaternary alloys was commonly found as coherent lamellar precipitates within the  $\text{B27}$  structure typical of TiB, with both structures containing Ti and the refractory metal in similar proportions. The present article addresses the characterization of the seemingly metastable B boride in the ternary alloys and presents a possible scenario to explain their evolution.

## 2. EXPERIMENTAL TECHNIQUES

The alloy of interest to the present study was prepared by non-consumable tungsten electrode arc-melting on a water-cooled copper hearth in an atmosphere of purified argon ( $<0.1$  ppb  $\text{O}_2$ ). Following the

procedure outlined by Haman *et al.* [15], titanium and Al evaporation B powder ( $<60$  mesh,  $99.7\%$  pure) was first melted with pure Ti ( $<200$  ppm O), to form a eutectic master alloy, to which additional Ti and Al ( $99.999\%$  pure) were subsequently added to reach the desired composition. The arc-melted button weighed approx. 35 g and was repeatedly flipped and remelted to ensure chemical homogeneity. The final analysis of the sample was Ti-40.9Al-0.97B, which places it on the  $\beta$  liquidus in Fig. 2. Samples for heat treatment were wrapped in Ta-foil and encapsulated in a quartz tube which was repeatedly evacuated to  $10^{-5}$  Pa while being heated to approx. 600 K and backfilled with high purity Ar. The sealed ampoule was annealed at 1423 K for 100 h.

Specimens for transmission electron microscopy were prepared by cutting 400  $\mu\text{m}$  thin slices from the arc-melted material using a low speed diamond saw. These were ground to a thickness of roughly 200  $\mu\text{m}$  and then discs 3 mm in diameter were ultrasonically drilled out. The discs were polished and dimpled with diamond paste. Finally, ion-milling at 5 kV at an incidence angle of  $13^\circ$  yielded thin sections containing electron transparent boride particles. The specimens were examined in both a JEOL 2000FX TEM, equipped with a LINK energy dispersive X-ray detector and a side-entry JEOL 4000FX

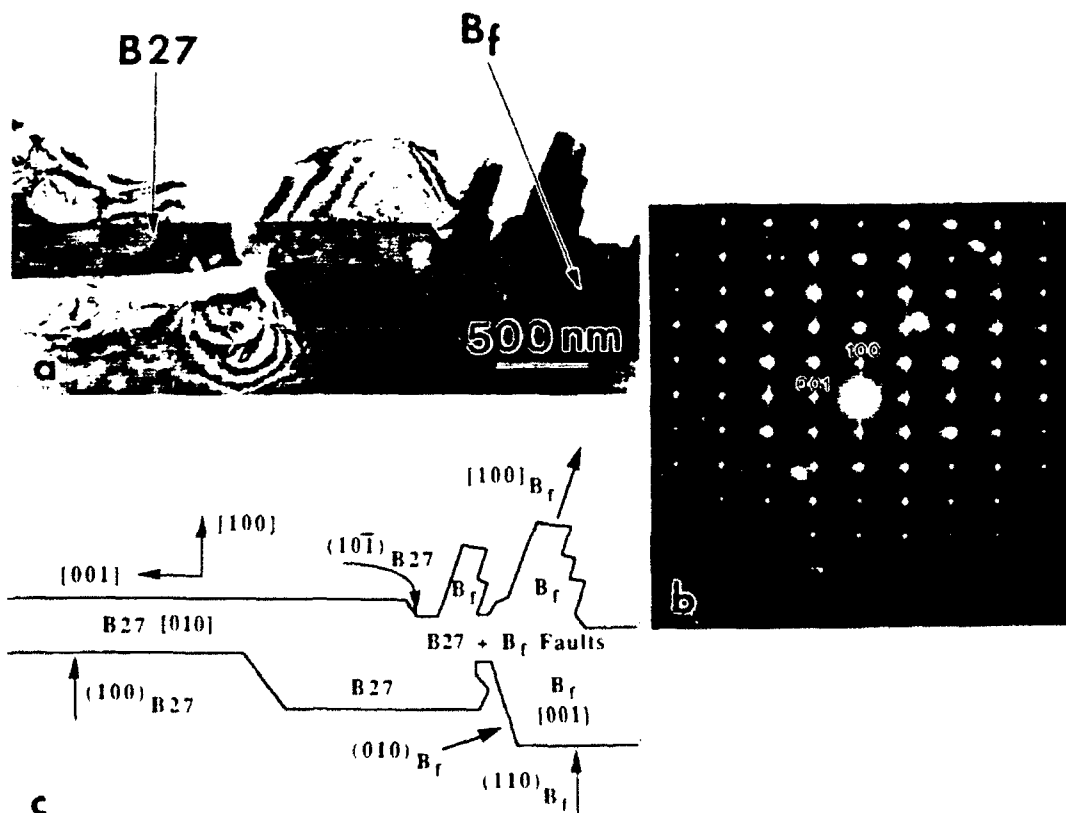


Fig. 3. Boride particle in a matrix of  $\alpha_2$ . (a) Whole particle with B27 and B<sub>f</sub> regions indicated by arrows. (b)  $[010]_{B_f}$  zone axis pattern. (c) schematic diagram of the particle in (a).

microscope equipped with a Gatan image intensifier for high-resolution transmission electron microscopy (HRTEM). The microscopes were operated at 200 and 400 kV, respectively. High-resolution image simulations (multi-slice algorithm), orientation relationships and diffraction patterns were all computed with EMS [16] and DIFFRACT 317 software. Computed images were convolved with filtered and averaged digitized micrographs.

### 3. MICROSTRUCTURAL OBSERVATIONS IN CONVENTIONAL TEM

Figure 3(a) shows a  $\gamma$ -boride particle in the as-cast sample oriented such that the edge facets are parallel with the incident electron beam. The elongated section ( $\approx 200$  nm wide) on the left side of the micrograph was identified by electron diffraction as the stable B27 form of TiB. The corresponding zone axis pattern was labeled as  $[010]_{B27}$ , which is the fastest growth direction in this crystal [15] and suggests that the particle grew as a plate with its longer dimension normal to the plane of the image. The long facets normal to the plate thickness are  $(100)_{B27}$  planes, whereas the planes bounding the width are of the  $(101)_{B27}$  type, as indicated in the schematic of

Fig. 3(c). In the diffraction pattern, there are extra spots arising from the  $\gamma$ -phase, which are visible as streaks in the  $[010]_{B27}$  selected area electron diffraction pattern lying parallel to the  $(100)_{B27}$  face of the B27 particles.

The portion of the boride particle on the right of the B27 plate in Fig. 3(a) is depicted again in Fig. 4(a) at higher magnification. It also contains plate-like faults, but now along three different sets of planes in three directions. The center of the faulted  $\gamma$ -phase is the center of the B27 plate with faults marked in the  $(100)_{B27}$  plane, as indicated by the schematic in Fig. 3(c). In addition, there are two near-orthogonal cracks with their faults oriented at  $\approx 75^\circ$  from the  $(100)_{B27}$  planes. An electron diffraction pattern from the image in Fig. 4(a) revealed three zones (see Fig. 4b). One zone corresponds to the  $[010]_{B27}$  axis described above, whilst the other two were identified as twin-related  $[001]$  zone axes of the B structure. The orientation relationship between the B27 and B crystals was established as

$$\begin{aligned} [010]_{B27} &= [001]_B \\ (100)_{B27} &= (110)_B \end{aligned}$$

The bounding planes of the B crystal are  $(010)_B$  and  $(100)_B$  as illustrated in Fig. 3(c). Figure 4(a) shows

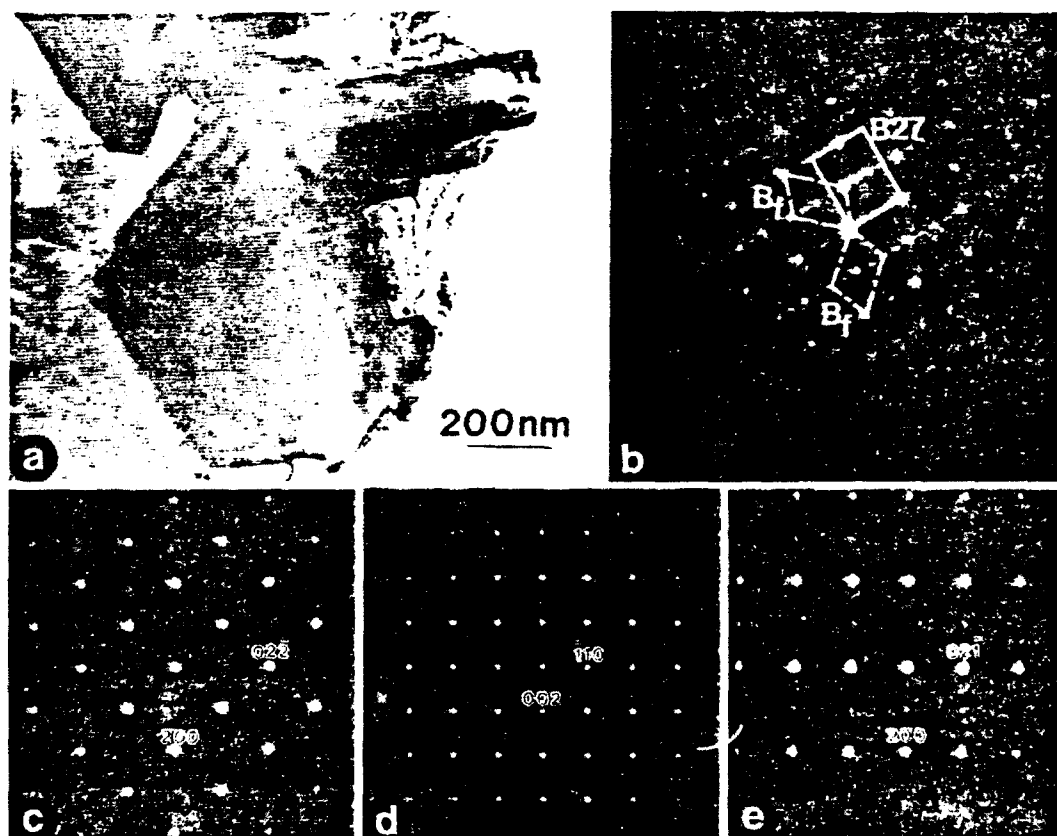


Fig. 4 (a) Enlarged section of Fig. 3(a) with faults on three different sets of planes. (b) zone axis pattern corresponding to (a). (c)  $[011]$ , (d)  $[110]$  and (e)  $[012]$  zone axis patterns of the untwinned B region marked by an arrow in Fig. 3(a).

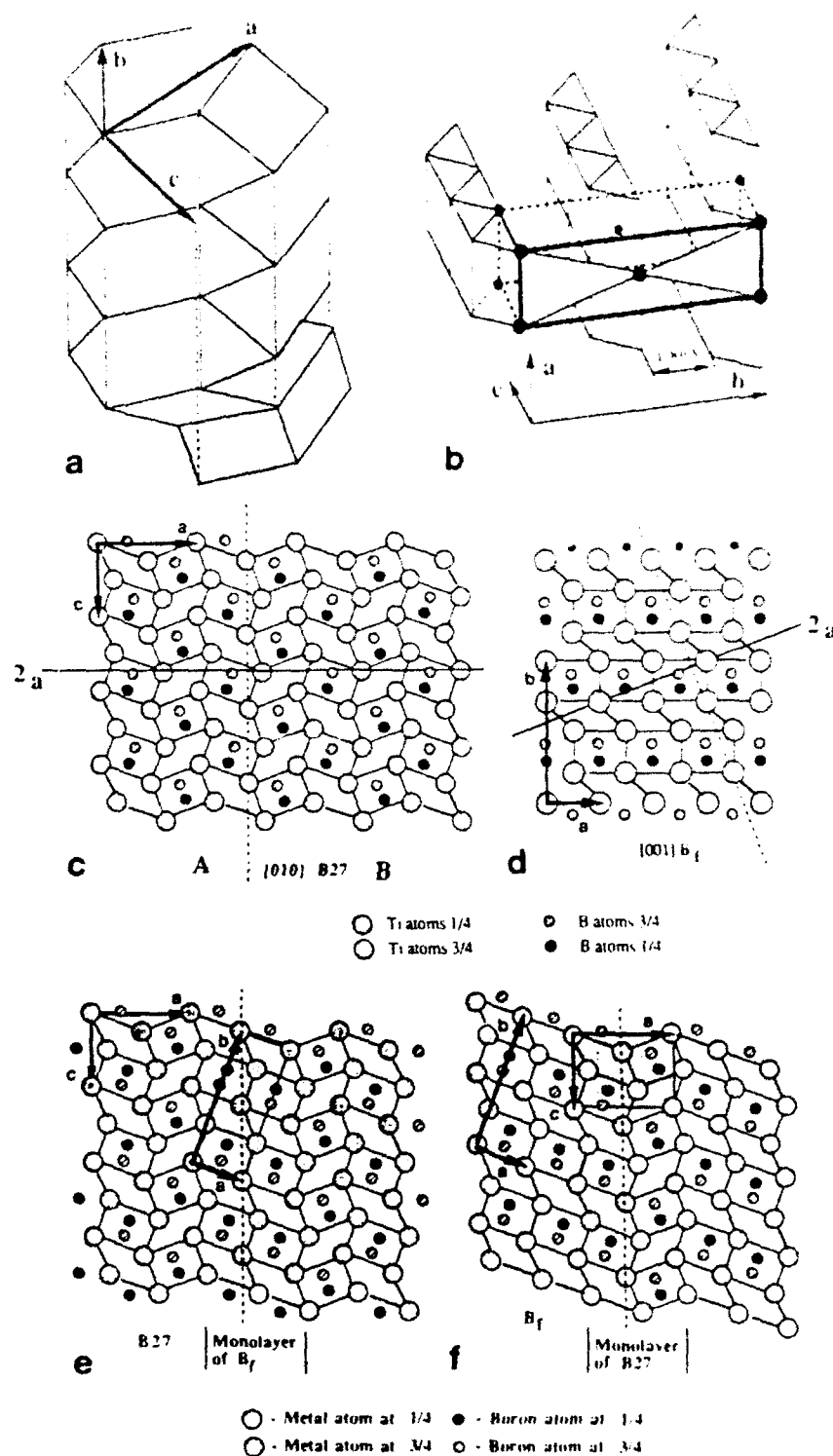


Fig. 5. (a) Construction of the B27 structure from edge-connected columns with the orthorhombic unit cell vectors indicated. (b) Perspective drawing of the Bf structure; unit cell vectors and C-centering are shown. (c) and (d)  $[010]_{B27}$  and  $[001]_{Bf}$  structure projections showing rectangular and parallelogram shaped building blocks. (e) Monolayer of Bf in B27 obtained by 180° rotational twinning around the axis denoted 2 in (c) and (f) similar projection for a bilayer of B27 in a Bf crystal.



a large area 500–600 nm wide (marked by an arrow) which appears to be unfaulked. Electron diffraction from this region gave intensity maxima indicating only one single crystal structure which was conclusively identified as the B monoboride (CrB type). The  $[011]_B$ ,  $[110]_B$  and  $[012]_B$  zone axis patterns are shown in Figs. 4(c–e). They contain no streaking or any evidence of the B27 structure. Inspection of other boride particles in the as-cast material revealed an abundance of the B structure, which is not reported to be an equilibrium phase in the Ti-B or the Ti-Al-B system. Microchemical analysis by EDS was unable to detect any elements other than Ti within the B particles. Moreover, examination of the borides after 100 h at 1423 K revealed that the majority of the particles were of the B27 type with only traces of B remaining, suggesting that the B structure is metastable.

Planar faults were observed in other B particles which could not be readily identified by means of electron diffraction. The application of HREM was essential for the elucidation of these nanoscale features and the origin of the B phase. However, it is first necessary to establish the crystallographic foundation of the different borides and their potential structural relationships.

#### 4. CRYSTALLOGRAPHIC CONSIDERATIONS

All the boride phases of interest are based on different arrays of the same basic building block: the trigonal prism consisting of six metal atoms surrounding each boron atom [18]. The prisms may be stacked sharing two of the three rectangular faces to form columns as shown in Fig. 5(a). The boron atoms are strongly bonded forming a zig-zagging chain along the main axis of the column. In the B27 structure, the columns are connected only along their edges, as shown in Fig. 5(a), and the B chains are parallel to the  $[010]_{B27}$  axis. The B chains and surrounding rows of metal atoms are evident in the  $[010]_{B27}$  projection in Fig. 5(c). Conversely, in the B structure the columns are stacked in parallel sheets sharing the triangular faces of the trigonal prisms. These sheets are displaced by a vector  $\frac{1}{2}(a+b)_B$  relatively to one another as shown in Fig. 5(b). The array of B chains and surrounding metal atoms as well as the relative displacement of the sheets is clearly evident in the  $[010]_B$  projection shown in Fig. 5(d). The similarity between the B27 and B structure projections are striking. In fact, it has been shown that a 180° rotational twinning on the  $(001)_{B27}$  along the two-fold screw axes [labeled as  $2_1$  in Fig. 5(c)] results in a monolayer of B, in an otherwise undistorted B27, as shown in Fig. 5(e). Similarly, 180° rotational twinning on the  $(110)_B$  gives rise to a monolayer of B27 in a B matrix—see Fig. 5(f). The full orientation relationship in both cases is described by

$$[010]_B \parallel [001]_{B27}$$

$$[100]_B \parallel [110]_{B27}$$

which is consistent with the experimental observations described above. The close crystallographic relationship between the B27 and B phases has been further documented by high resolution microscopy of (Ti,Ta)B rods in a Ti-Ta-Al-B alloy [19] revealing a nanoscale intergrowth of both structures with perfectly coherent interfaces as predicted by Figs. 5(e) and (f). Whereas no obvious orientation relationship can be deduced between B27 and the other equilibrium borides in the Ti-B system, namely D7<sub>1</sub> and C32, the latter structures can be shown to be more closely related to the B form of TiB, as discussed below.

The  $[100]_B$  structure projection is shown in Fig. 6(a). If one  $(010)_B$  metal atom plane is removed (marked A) and the incomplete layer of trigonal prisms is translated by a vector parallel to  $[\frac{1}{2}a, \frac{1}{2}b]$  with respect to the original unit cell origin, and joined to the metal atoms of the next layer (labeled B), then a monolayer of the D7<sub>1</sub> structure is created as illustrated in Fig. 6(b). The orientation relationship derived from this non-conservative operation is

$$[100]_B \parallel [100]_{D7_1}$$

$$(010)_B \parallel (010)_{D7_1}$$

The removal of one Ti plane accounts for the difference in composition between TiB and TiB<sub>2</sub>. If the operation is repeated in one out of every four Ti planes the B crystal can be transformed into D7<sub>2</sub>, as illustrated in Fig. 6(c).

Given the close relationship between D7<sub>1</sub> and C32, one could also define a monolayer of the C32 structure within the D7<sub>1</sub> layer in Fig. 6(b). Thus, the removal of every second Ti plane in the B structure perpendicular to  $[010]_B$ , following the sequence described in Figs. 6(a) and 6(c) would generate the C32 structure in Fig. 6(d), which consists of a "close packed" stacking of prism sheets. Accordingly, the orientation relationship between B and C32 is given by:

$$[100]_B \parallel [0001]_{C32}$$

$$(010)_B \parallel (10\bar{1}0)_{C32}$$

As before, the introduction of two non-conservative faults in the B<sub>1</sub> unit cell accounts for the difference in stoichiometry between TiB and TiB<sub>2</sub>.

It will be useful for the analysis of the HREM images to establish the differences between the B<sub>1</sub>, D7<sub>1</sub> and C32 structures in terms of the relative positions of the metal atom rows. In each of the projections in Fig. 6 one can readily define a rectangular array of metal atom rows with a characteristic (length/height) aspect ratio. For example, Fig. 6(d) shows the symmetric rectangular array of metal atoms in the C32 structure with an aspect ratio of 1.73 (hexagonal

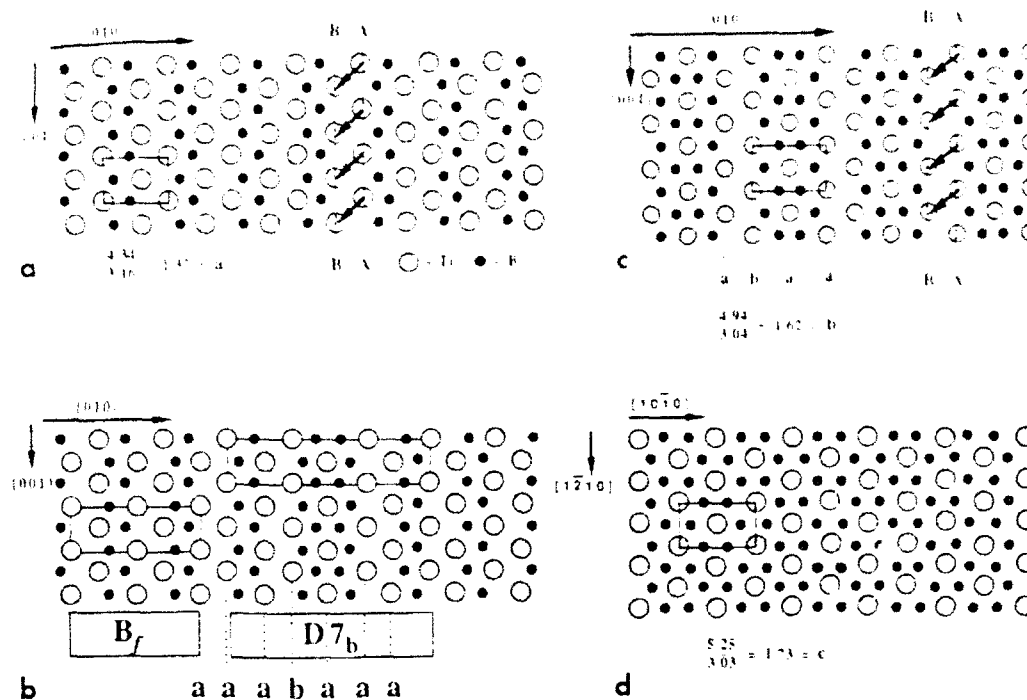


Fig. 6. (a)  $[100]_B$  projection of the B structure.  $[010]$  and  $[001]$  directions are marked. The arrows indicate a non-conservative planar fault on  $(010)_B$  with translation vector  $[-\frac{1}{2}a]$ . (b) A single D7 monolayer in a B matrix. The B unit cell is shaded dark grey, whereas the D7 unit cell is light grey. (c) Monolayers of C32 in the D7 structure created by non-conservative faults on the original  $(010)_B$  planes. The  $[010]$  and  $[001]$  directions in D7 are marked. (d)  $[0001]$  projection of the ideal C32 structure with  $[1010]$  and  $[1210]$  directions marked. The characteristic ratios  $a$ ,  $b$  and  $c$  of the metal atom rectangle dimensions are indicated for each structure.

lattice of projected metal atoms). In contrast, the array in the B structure is asymmetric (off-centered middle atom) and has an aspect ratio of 1.37, as shown in Fig. 6(a). Finally, two different configurations occur in the D7 structure: one symmetric based on the hexagonal array within each close packed sheet, with an aspect ratio of 1.62, and one asymmetric with an aspect ratio of 1.37 similar to that identified in the B crystal. These ratios are particularly useful in the analysis of intergrowth of the three phases, for which the diffraction pattern would only give statistically averaged information.

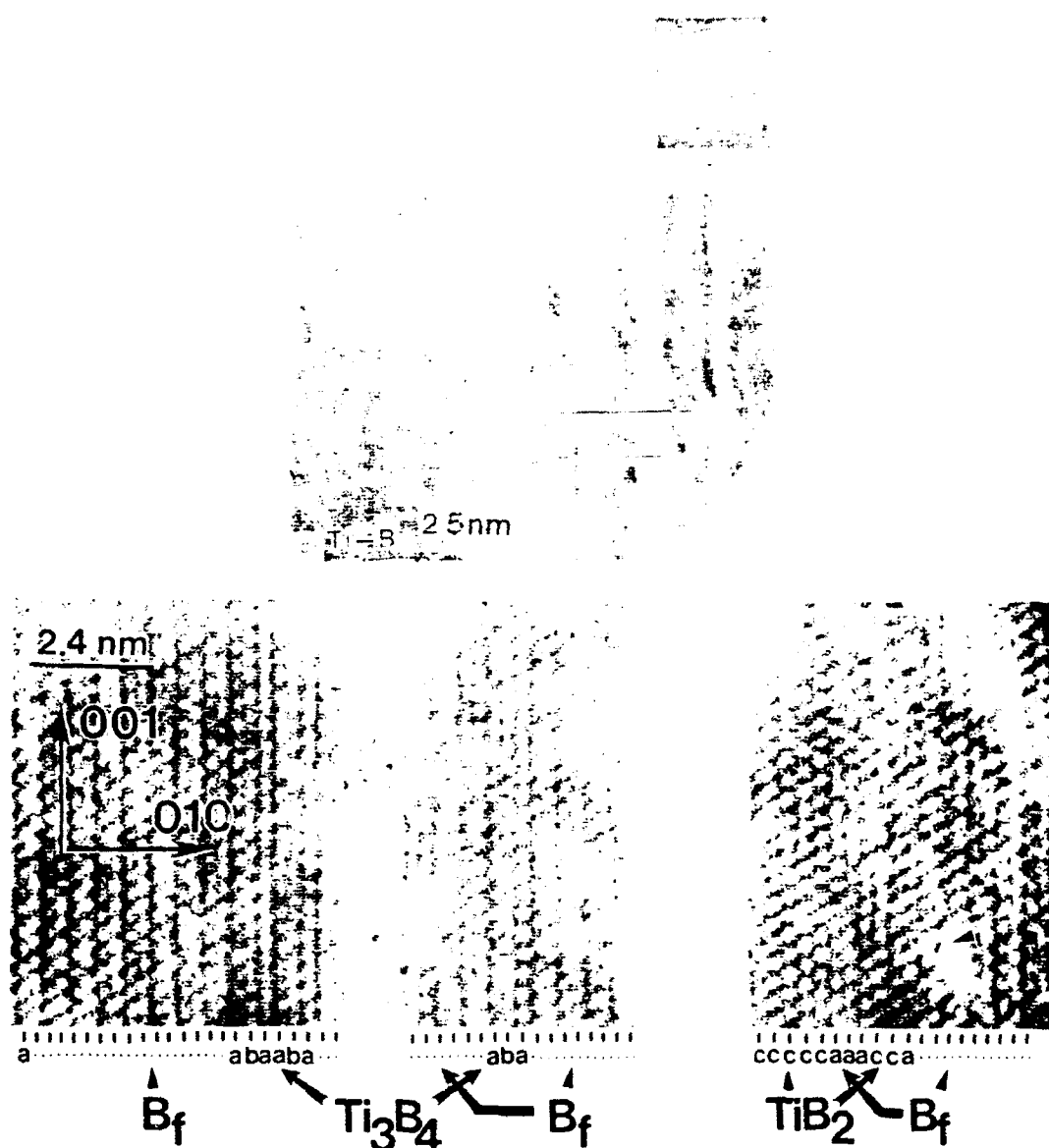
If we denote every Ti-plane parallel to  $(010)_B$  by a letter corresponding to the aspect ratio of the rectangle of metal atoms to the immediate right of the plane (see Fig. 6), then all three structures can be expressed as a string of letters. With  $a = 1.37$ ,  $b = 1.62$  and  $c = 1.73$ , the perfect B structure is described by the stacking sequence  $\dots aaaaa \dots$ , D7 by  $\dots abaabaaba \dots$  and C32 by  $\dots ccccc \dots$ . A monolayer of one phase in a matrix formed by another phase is then easily represented by the appropriate sequence, e.g. one monolayer of D7 in B is described by  $aaabaaba$ , as shown in Fig. 6(b). This shorthand notation will be used in the following section to identify a complex stacking sequence in a boride particle.

## 5. HIGH RESOLUTION ANALYSIS OF THE B<sub>2</sub> STRUCTURE

From the crystallographic relationships described in Section 4, it can be seen that the B phase could form intergrowths with B27, D7, or C32 with a virtually arbitrary stacking sequence. The coexistence of B27 and B, in the complex (Ti,Ta)B monoborides has been extensively documented in a separate publication [19] and will not be further discussed. It should be noted, however, that the interfaces between neighboring B27 and B crystals such as those in Figs 3 and 4 are also coherent in this case, strongly suggesting the nucleation of one phase on the other.

Based on the description of Fig. 6, the  $[100]_B$  zone axis is obviously the most suited for observations of the intergrowths with D7, and C32. A high resolution micrograph from a boride particle and its corresponding diffraction pattern are shown in Fig. 7. Note the streaks along the  $[010]_B$  direction in inset of Fig. 7(a) indicating a random array of planar faults parallel to the  $(010)_B$  plane. Random mixing of B27, D7, and C32 regions in a B matrix is consistent with the experimentally observed diffraction pattern.

Multislice image simulations were performed for the B form of TiB<sub>2</sub>, the D7 structure of Ti<sub>2</sub>B<sub>3</sub> and the C32 structure of TiB<sub>2</sub> along the respective  $[100]_B$ .



(b)

Fig. 7. (a) High resolution electron micrograph of the tip of a boride rod in the  $[100]_B$  zone axis orientation (diffraction pattern in inset). (b) Enlarged section of the micrograph of (a), showing the sequence of rectangle ratios indicated at the bottom. The three boride phases are clearly distinguished.

$[100]_B$ , and  $[0001]_C$  directions. Identical microscope conditions were used in each computation. Careful comparison of the images of these three structures indicates they share common contrast features for identical thickness and defocus values. For a given thickness and defocus, all Ti-columns are represented by black (or white) dots in all four structures. For both B<sub>1</sub> and C32, the aspect ratio of the metal atom rectangles (1.37 and 1.73, respectively) is determined by the symmetry of the lattice and consequently does not depend on crystal thickness and microscope defocus. However, for  $Ti_3B_4$ , the rectangle aspect ratio

does depend on both thickness and defocus: the ratio can vary almost continuously from 1.37 to 1.62. Therefore, it is possible to identify each structure from a single high resolution micrograph by measuring the aspect ratios of rectangles of white or black dots.

This procedure was used to interpret the micrograph of Fig. 7(a): the region delineated by the rectangular inset is shown enlarged in (b). This image was digitized as a  $1280 \times 512$  pixel image and Fourier filtered to remove random intensity fluctuations. Then the pixel values (intensities) of rows parallel to

the  $[001]_B$  direction were projected onto one line (i.e. integrated intensity along the  $[001]_B$  direction). The positions of the intensity maxima in the resulting profile were carefully measured and from these the aspect ratios of the metal atom rectangles were deduced. The results are shown underneath the electron micrograph of Fig. 7(b) using the structural codes introduced in Section 4.

Thin slabs of  $D7'$  and C32 structures are clearly identified within the B monoboride in Fig. 7(b). The structures are not perfect along the  $[100]_B$  direction as there are several locations where the Ti-planes seem to jump or jog sideways, i.e. the stacking sequence changes from e.g. *aaaaaaa* to *aaabaaa*. Such a change is indicated by an arrow in Fig. 7(b). The abruptness of the change precludes any thickness effects. The occurrence of "defects" in the nanoscale intergrowth is likely to arise during the crystallization process, as discussed below. The size and frequency of such defects suggest there is a small energy difference between the adjacent intergrowth regions. These non-conservative faults are somewhat analogous to the crystallographic shear faults (CSF) observed in the oxygen-deficient  $TiO_{2-x}$  phases [20].

## 6. DISCUSSION

The conventional and high resolution TEM evidence have unequivocally established the existence of a binary titanium monoboride with the B<sub>1</sub> structure. This phase was often found to contain planar faults identified as thin layers of  $Ti_3B_4$  ( $D7_c$ ) and  $TiB_2$  (C32). This section will attempt to rationalize the origin of the B<sub>1</sub> structure within the context of the overall microstructure evolution in this alloy.

Since the B<sub>1</sub> monoboride has not been reported in the Ti-B or the Ti-Al-B system and it is found to transform to the normal B27 form of TiB upon prolonged heat treatment, one may reasonably conclude that the B<sub>1</sub> structure is metastable. Two hypotheses may thus be advanced to explain its occurrence in Ti-Al-B alloys. Firstly, TiB could have a stable high temperature B<sub>1</sub> allotrope which forms from the melt and is retained at the cooling rates typical of arc-button solidification. In this scenario, the

$B_1 \leftrightarrow B27$  allotropic transformation temperature should be between the peritectic temperatures (2453 K) and 1473 K, wherein most of the boride is converted to B27. This hypothesis is unlikely since the B27 form of TiB is also present in the solidification structure and has been established to form from the melt in other alloys [12, 21]. Furthermore, Lush [5] reported finding the B27 structure in TiB samples quenched from temperatures as high as 2285 K.

The second hypothesis considers the formation of B<sub>1</sub> from the melt as a metastable structure which supersedes the B27 form. This is rather unusual as the metastable phase evolves *after* the more stable B27 form and probably nucleates epitaxially on it, as suggested by the coherent interface. The understanding of this phase evolution sequence requires a combination of thermodynamic and kinetic factors which are discussed below.

The relative stability of the B27-TiB,  $TiB_2$  and  $Ti_3B_4$  is well established for the Ti-B system and in principle can be quantified for the ternary Ti-Al-B system from the free energy functions used to model the different binaries. However, the available experimental information is not sufficient to accurately determine the boundaries of the different liquid surfaces and hence the relative thermodynamic ranking of the phases in the regions where several liquids meet. Furthermore, there is no accurate method to assess the differences in free energy between B<sub>1</sub> and the stable phases based on the information currently available. A cursory analysis of the transition metal borides in Table 2 reveals that the B<sub>1</sub> structure is more common than B27, especially amongst the elements that form both C32 and D7<sub>c</sub> phases. Moreover, the monoborides often exhibit melting points close to those of the corresponding  $M_3B_4$  ( $D7_c$ ) compounds, suggesting that within each system the MB and  $M_3B_4$  phases may be relatively close in energy. This is particularly true in the case of Ti, where there is a difference of only ~20 K in the melting temperature of the two borides as noted in Fig. 1.

Additional evidence that the B27 and B<sub>1</sub> phases for TiB have relatively similar energies may be obtained from lattice energy calculations. The lattice parameters of the different boride structures in Table 1 suggest that the volume of the trigonal prism (i.e. the

Table 2. Crystal structures of some transition metal borides

Boride	Element							
	Sc	Ti	V	Cr	Mn	Fe	Co	Ni
MB	—	B27	B <sub>1</sub>	B	B27	B27	B27	B
$M_3B_4$	—	D7 <sub>c</sub>	D7 <sub>c</sub>	D7 <sub>c</sub>	D7 <sub>c</sub>	—	—	—
MB	—	C32	C32	C32	C32	—	—	—
<hr/>								
MB	Y	Zr	Nb	Mo	Ta	Ru	Rh	Pd
$M_3B_4$	—	—	B	$B_3B_4$	—	B <sub>1</sub>	—	—
MB	—	—	D7 <sub>c</sub>	—	—	—	—	—
MB	C32	C32	C32	C32	—	—	—	—
<hr/>								
MB	La	Hf	Ta	W	Re	Os	Ir	Pt
$M_3B_4$	—	B27	B <sub>1</sub>	$B_3B_4$	—	B <sub>1</sub>	B <sub>1</sub>	B
MB	—	—	D7 <sub>c</sub>	—	—	—	—	—
MB	—	C32	C32	—	—	—	—	—

Table 3. 12-Mie type potential parameters from [22]

	$\epsilon$	$l$
Ti-Ti	1.4	0.26
Ti-B <sub>1</sub>	1.4	0.26
Ti-B <sub>2</sub>	1.4	0.26
B-B	1.4	0.26
Ti-B <sub>3</sub>	1.4	0.26

coordination polyhedron of each boron atom is fairly independent of the structure composition. This suggests that the energy differences between the four structures may actually be quite small and could be attributed mainly to next-nearest neighbor interactions. To assess these differences in energy it is necessary to have models describing the relevant interatomic potentials. The only available potentials are for TiB<sub>2</sub> developed by Abdel-Hamid *et al.* [22] as part of a simple model to predict the morphology of TiB<sub>2</sub> crystals grown from the melt. Based on the observed bond lengths and the sublimation or fusion energies of the pure substances Ti, B and TiB<sub>2</sub>, they derived a set of three 6-12 Mie type interaction potentials of the form

$$E_{ij}(l) = \epsilon \left[ \left( \frac{l}{l_0} \right)^{12} - 2 \left( \frac{l}{l_0} \right)^6 \right] \quad (1)$$

where  $E$  is the bond energy between atoms  $i$  and  $j$ ,  $l$  is the actual bond length,  $\epsilon$  and  $l_0$  are adjustable parameters, which are given in Table 3 for the Ti-Ti, B-B and TiB bonds [22]. Only nearest neighbor interactions were taken into account for the fitting procedure.

A first estimate of the relative stability of the borides can be obtained from the potential parameters listed in Table 3. Careful analysis of the values suggested by Abdel-Hamid *et al.* shows that none of the four structures considered is mechanically stable when higher order neighbor interactions are taken into account, i.e. the lattice energy vs hydrodynamic deformation is not minimal for the experimental lattice parameters. Thus, a least squares fitting procedure was used to modify the potential well parameters such that TiB<sub>2</sub> and both structural variants of TiB would show a minimum in the energy vs hydrostatic deformation curve for strains smaller than 0.1%. (The TiB<sub>2</sub> structure could not be rendered stable with coefficients in the same range as those used for the other borides.) The modified parameters are also shown in Table 3.

Figure 8 shows the energy vs deformation curves for the listed potential parameters and for four crystal structures; the calculations include all neighbor shells within a truncation radius of 2.5 nm. The energies at the minima are given by: -39.12 kJ/mole for the B27

form of TiB<sub>2</sub> (-39.14 kJ/mole for the B form of TiB<sub>2</sub>) and -45.62 kJ/mole for TiB<sub>2</sub>. It should be noted that these calculations are for a perfect state of stress and ignore entropy contributions. The least squares procedure a reasonably first assessment of crystal stability. It is evident from the calculations that the lattice stabilities of the B<sub>1</sub> and B27 structures are quite similar and considerably less than that of B<sub>2</sub>. B<sub>1</sub> is only slightly more competitive with that of B27. Moreover, work reported elsewhere [3, 14, 19] indicates that relatively modest additions of Ti or Nb to Ti-Al-B alloys in this composition range render the B phase stable, although in those cases the monoboride contains both Ti and Ta or Nb. The cumulative evidence suggests that the B<sub>1</sub> structure of TiB may indeed be only slightly metastable relative to the B27 form.

Having established that the B27 and B<sub>1</sub> structures may have similar energies it remains to be explained why the seemingly more stable B27 form is superseded by the metastable B phase.\* Consider the solidification path of the present alloy on the ternary liquidus projection in Fig. 2. Solidification starts with the formation of primary  $\beta$ -Ti dendrites (which subsequently transform to  $\alpha$  upon cooling), with B partitioning more strongly than Al toward the liquid, thus driving the composition of the latter toward the two-fold saturation line  $L \rightarrow \beta + \text{TiB}$ . When this line is reached, crystals of TiB with the B27 structure form and grow concurrently with  $\beta$ -Ti, driving the composition of the liquid toward higher Al and somewhat lower B contents as indicated by the arrows in Fig. 2.

With continued solidification down the line of two-fold saturation, Fig. 2, there comes a point when TiB no longer is the boride which has the largest driving force for solidification, and in the absence of kinetic constraints should be replaced by TiB<sub>2</sub> (or perhaps Ti<sub>3</sub>B<sub>4</sub> since there is some uncertainty on the liquidus projection as noted before). In any event, thermodynamic considerations would favor the formation of a boride with a higher boron content from

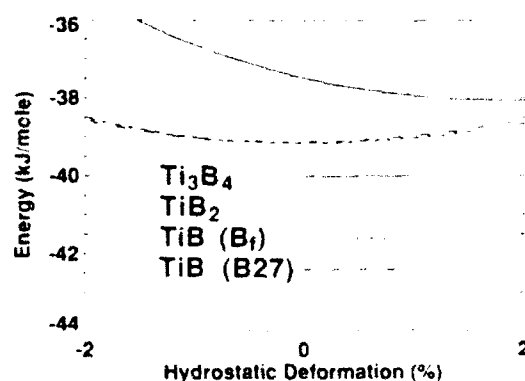


Fig. 8. Energy vs hydrostatic deformation curves for the four boride phases, using the modified potential parameters of Table 3. The minima for the three lower curves are within 0.1% of zero deformation.

\*The B27 structure is believed to form first based on TEM observations such as those on Fig. 3, where the B27 phase is surrounded by B<sub>1</sub> crystals which grew epitaxially on it.

a melt which is quite dilute in B. The new boride phase could nucleate homogeneously from the melt, but a preferred mechanism would be heterogeneous nucleation on one of the existing solid phases. Previous work has shown that there is rarely a clear orientation relationship between Ti and the secondary boride phases formed during solidification, suggesting that the metal phase may not be a very favorable site for boride nucleation. In contrast, the crystallographic analysis of the present borides indicates that the B phase is an excellent opportunity for nucleating on the B27 in the manner depicted on Fig. 9(a). Note in this figure the close match between the  $(100)_{B_2}$  and  $(110)_{B_1}$  planes which facilitates the observed epitaxial growth of the B crystal. Stoichiometric considerations indicate that growth normal to the  $(100)_{B_1}$  planes is probably faster than growth normal to the  $(010)_{B_1}$  planes [13–15, 19, 21], giving rise to the elongated morphology of the B<sub>1</sub> crystals with habit planes at 70° from the  $(100)_{B_2}$  facets evident in Fig. 3.

Consider now the potential nucleation of TiB<sub>2</sub> or TiB<sub>1</sub> on the preexisting B27 phase. The mismatch between TiB<sub>2</sub> and the predominant  $(100)_{B_2}$  facets of the TiB crystal is quite evident, as shown by the schematic on Fig. 9(b). Analysis of other possible interfaces suggests that there is no better fit between B27 and

D7<sup>+</sup> than that illustrated in the figure. A similar conclusion may be reached from studying the mismatch interfaces between C32 and B27, indicating that the nucleation of B<sub>1</sub> or B27 would be a more favorable process than that for either of the stable phases. Growth of the B monoboride may also be kinetically easier than that of the stable phases which require more B to form, given the dilute concentration of B in the melt.

In summary, it is proposed that the B monoboride in the Ti-Al-B system forms in response to a change in the chemistry of the melt during solidification which in the absence of kinetic constraints should produce TiB<sub>2</sub> or TiB<sub>1</sub>. The B<sub>1</sub> phase is metastable relative to the D7<sup>+</sup> or C32 structures, but it must necessarily become more stable than the B27 phase as the melt becomes enriched in Al, or it would not be able to supersede the latter. The occurrence of thin layers of D7<sup>+</sup> and C32 phases within the B<sub>1</sub> phase, perhaps in response to local fluctuations in B concentration, may be taken as a sign that the system is indeed trying to form TiB<sub>2</sub> or TiB<sub>1</sub>. However, growth of the latter phases is likely to require more significant B redistribution within the melt, which may be constrained at the solidification rates characteristic of arc buttons.

## 7. CONCLUSIONS

Conventional and high resolution transmission electron microscopy have shown that two monoborides with essentially the same chemical composition but different crystal structures are present within the solidification microstructure of a Ti-40.9Al-0.97B alloy. These monoborides were identified as having the B27 and B crystal structures, the latter nucleating and growing epitaxially on the former. Both structures are typically faulted, the B27 crystals containing thin layers of B<sub>1</sub>, and the B<sub>1</sub> crystals exhibiting nanoscale intergrowths of the D7<sup>+</sup> and C32 structures. Clear orientation relationships were established in all cases and rationalized on the basis of the common crystallographic features of the boride phases, all of which are based on the same fundamental building block. By and large, the interfaces were typically coherent as expected from the similar interatomic distances in the different boride structures.

A simple lattice stability calculation coupled with a cursory analysis of the prevalent monoboride structures in transition metal systems led to the conclusion that the B and B27 forms of TiB are probably very close in energy. Since the metastable B<sub>1</sub> phase nucleates and grows epitaxially on preexisting B27 particles, its evolution is believed to obey to local changes in the melt chemistry due to normal segregation effects during solidification. The B<sub>1</sub> phase forms instead of the more stable D7<sup>+</sup> (TiB<sub>2</sub>) and C32 (TiB) phases owing to its closer orientation relationship with the existing B27 phase, which favors

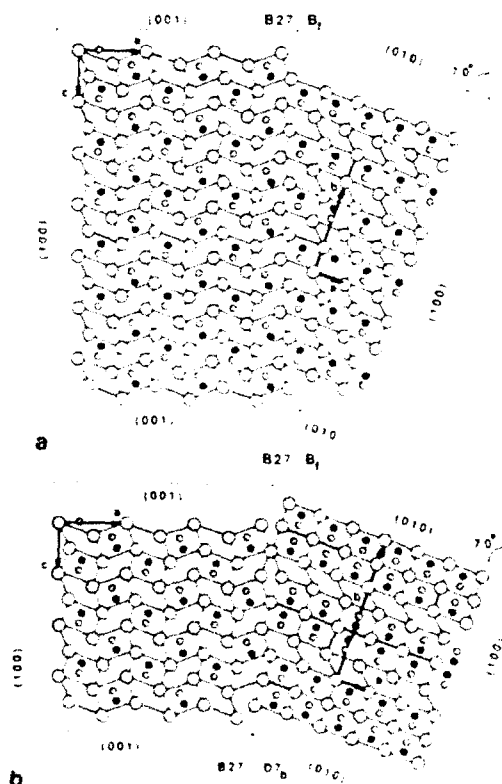


Fig. 9. (a) B27 D7<sup>+</sup> interface in  $(010)_{B27}$  projection; there is no mismatch across the interface. (b) B27 D7<sup>+</sup> interface in same projection; notice the mismatch at the interface.

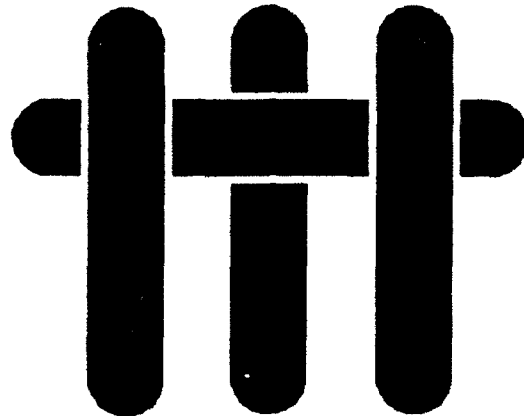
nucleation on the  $\{100\}_{\alpha}$  planes, as well as its lower requirements for B which facilitates growth from a melt dilute in this element.

**Acknowledgments**—The authors are grateful to Dr M. E. Hyman for preparing the alloys and to Mr A. Peres for his contributions to the photographic analysis of the electron micrographs. This work was sponsored by the Defense Advanced Research Projects Agency under the University Research Initiative (grant No. 004-80-K01753) supervised by Dr W. Coblenz and monitored by Dr S. G. Fishman at the Office of Naval Research. M. De Graet is a Research Associate with the Belgian National Fund for Research. Additional support for C. McCullough and C. G. Levi under grant DMR89-15209 from the National Science Foundation, monitored by Dr Bruce A. MacDonald, is gratefully acknowledged.

## REFERENCES

1. L. S. Kampe, J. A. Clarke and L. Christodoulou, *Mater. Res. Soc. Symp. Proc.*, **194**, 225 (1990).
2. D. I. Carsen Jr, S. Kampe and L. Christodoulou, *ibid.*, 285.
3. L. Robertson and P. L. Martin, *ibid.*, 233.
4. Pearson, in *Handbook of Crystallographic Data for Intermetallic Phases* (edited by P. Villars and L. D. Calvert), pp. 1369, 1372. American Society for Metals (1985).
5. R. G. Fenish, *Trans. metall. Soc. AIME*, **236**, 804 (1966).
6. E. Rudy and St. Windisch, Air Force Tech. Rep. AFML-TR-65-2, P. I, Vol. 7 (1966).
7. K. E. Spear, in *Application of Phase Diagrams in Metallurgy and Ceramics* (edited by G. C. Carter), pp. 144-162. NBS, Gaithersburg, Md. (1977).
8. E. Scheel, *Z. Metall.*, **34**, 70 (1942).
9. V. A. Neronov, M. A. Korzhakov, V. A. Aksenov and S. N. Gusevskii, *Dokl. Akad. Nauk SSSR*, **82**, 127 (1981).
10. K. E. Spear, P. McDowell, and E. McManis, *J. Appl. Cryst.*, **69**, C4 (1986).
11. I. Maxwell and A. Hewitell, *Metal. Trans. A*, 1457 (1972).
12. M. Hyman, Ph.D. thesis, Univ. of California (1989).
13. J. J. Valencía, J. P. A. Loivander, C. McCullough, C. G. Levi and R. Mehrabian, *Mater. Sci. Engn.*, **144**, 25 (1991).
14. J. J. Valencía, C. McCullough, J. Rosier, C. G. Levi and R. Mehrabian, in *Solidification of Composite Materials* (edited by P. Rohatyn), pp. 133-150. TMS (1990).
15. M. E. Hyman, C. McCullough, J. J. Valencía, C. G. Levi and R. Mehrabian, *Metal. Trans.*, **20A**, 1847 (1989).
16. P. A. Stadelman, *Ultramicrosc.*, **21**, 131 (1987).
17. Reg. Trademark of Virtual Laboratories, 37 Highland Court, Ukiah, CA 95482, U.S.A.
18. T. Lundström, in *Boron and Boronates, Borates* (edited by V. F. Matkovich), pp. 351-376. Springer, Berlin (1977).
19. M. De Graet, J. P. A. Loivander and C. G. Levi, *Acta metall. mater.*, **39**, 2381 (1991).
20. J. Van Landuyt and S. Amelnekkx, *Mater. Res. B*, **5**, 267 (1970).
21. M. E. Hyman, C. McCullough, C. G. Levi and R. Mehrabian, *Metal. Trans.*, **22A**, 1647 (1991).
22. A. A. Abdel-Hamid, S. Hamar-Thibault and R. Hamar, *J. Cryst. Growth*, **71**, 744 (1985).

MATERIALS UCSB



**MEASUREMENT OF RESIDUAL STRESSES  
IN SAPPHIRE FIBER COMPOSITES  
USING OPTICAL FLUORESCENCE**

Qing Ma and David R. Clarke

Materials Department  
University of California  
Santa Barbara, California 93106

**Abstract**

The residual stresses in c-axis sapphire fibers in a  $\gamma$ -TiAl matrix and in a polycrystalline  $\text{Al}_2\text{O}_3$  matrix as a function of distance below a surface are determined. They are obtained from the shift in frequency of the characteristic R2 fluorescence line of chromium in sapphire obtained by focussing an optical probe at different depths in a sapphire fiber intersecting the surface of the composite. The method is described together with its calibration. Both the axial and radial components of the residual stress in the fiber are observed to vary over a depth of approximately the fiber diameter and are then almost independent of depth.



## 1 Introduction

When a composite material is cooled down from its fabrication temperature, thermal mismatch residual stresses develop, which can have a profound influence on the mechanical properties of the composite. For example, in many ceramic fiber reinforced metal matrix or glass matrix composites the thermal expansion coefficient of the matrix  $\alpha_m$  is considerably larger than that of the fiber  $\alpha_f$  and so large compressive stresses can develop in the fiber. The axial compressive stress creates a large stress difference between debonded and bonded regions of the interface when the material is under applied tension, facilitating interfacial crack growth [1,2], a pre-requisite for fiber pull-out. On the other hand, the large radial compressive stress produces large friction forces in the debonded region, which retards fiber sliding and consequently shortens fiber pull-out length [2,3]. It is therefore possible to optimize the mechanical properties of such composites by tailoring the residual stresses through appropriate processing conditions and the use of interfacial coatings [4].

Unfortunately, accurate information about the residual stresses in embedded fibers is usually unavailable since their measurement is particularly difficult. As a result, estimations based on the thermal and elastic properties of the individual material components are usually used in various analyses. This approach requires accurate knowledge of the effective temperature change  $\Delta T$ , which is usually an unmeasurable quantity, and is difficult to estimate without detailed knowledge of the stress relaxation mechanisms, especially near the interface. Furthermore, such estimates can not take into account the variations from fiber to fiber due to irregularities in coatings and interfacial roughness: details which are important in understanding individual fiber pull-out/push-out tests. Direct measurement of the residual stresses in fibers is, in principle, possible by a variety of diffraction techniques. For

instance, X-ray diffraction using ultra-fine beams can provide strain information of individual fibers. However, it suffers from having a relatively small penetration depth ( $\sim 50 \mu\text{m}$ ) [5,6] and can therefore only measure stresses near the surface, which could be significantly different from those deeper inside the composite. Neutron scattering, whilst capable of probing fiber stresses throughout the composite [7,8], has insufficient spatial resolution to study individual fibers or to ascertain stress distributions along the fibers.

An alternative method of measuring stresses in fibers is by using piezo-spectroscopic effects. The basis of such methods is that the characteristic luminescence lines (Raman or fluorescence) of the material shift with stress. By utilizing an optical microscope to define a probe, it is relatively easy to select regions of interest with spatial resolution of only a few microns [9] either on the surface of a composite, or if the matrix is transparent, within the composite. For example, in the case of polydiacetylene fibers embedded in an optically transparent epoxy [10], Raman spectra were collected from different positions along a fiber to obtain the stress distribution along it. Since optical spectrum can be collected and analyzed with relative ease compared to most diffraction methods, such measurements can be performed routinely.

In this paper, we present a new method of measuring residual stresses in embedded transparent fibers, one that utilizes optical fluorescence, and illustrate its application to determining the residual stresses in sapphire fibers in  $\gamma\text{-TiAl}$  and  $\text{Al}_2\text{O}_3$  matrices. The theoretical basis of the fluorescence method was described in detail in an earlier work [11]. Briefly, the frequency shift of a characteristic fluorescence line is stress dependent and is given by:

$$\Delta\nu = \Pi_{ij} \sigma_{ij}^* \quad (1)$$

where  $\Pi_{ij}$  are the piezo-spectroscopic coefficients relating frequency shift to stress, and  $\sigma_{ij}^*$  is the stress tensor represented in the crystallographic frame of reference.

The method is to use an optical microscope to focus a light beam on the end of an exposed sapphire fiber (figure 1), measure the frequency shift of a characteristic luminescence line and then repeat the measurement at successively deeper points of focus into the fiber. Using the lenses of the microscope to form an optical probe enables the luminescence to be collected, for any particular point of focus, from a relatively small depth of field. This facilitates high spatial resolution [12,13] along the fiber but at the same time means that the observed frequency shifts have to be deconvoluted using a previously established calibration of the microscope convolution function (the depth of field function). This is described in the following section. Also described is a test of the accuracy of the stress profiling method in which the stress through the thickness of a ruby beam under four-point loading is measured and compared with the known elastic solution.

To illustrate the application of the technique we have measured the residual stresses in Saphikon sapphire fibers. They have sufficient levels of chromium impurity to produce sufficiently intense fluorescence lines  $R_1$  and  $R_2$  of ruby when excited by an argon ion laser. Because the fibers are single crystal with their  $c$ -axis along the fiber axis, the residual stresses inside the fibers are expected to have cylindrical symmetry. As a result, there are only two independent stress components, the radial component  $\sigma_r$  and the axial component  $\sigma_a$ . This simplifies equation 1 to be:

$$\Delta\nu = 2\Pi_a \sigma_r + \Pi_c \sigma_a \quad (2)$$

where  $\Pi_a$  and  $\Pi_c$  are the piezo-spectroscopy coefficients for the  $a$  and  $c$  directions. They have been measured to have values of 2.70 and 2.15  $\text{cm}^{-1}\text{GPa}^{-1}$ , respectively [14]. A positive

shift implies tension and a negative one implies compression. In section 3, measurements of line shifts along fibers in both  $\gamma$ -TiAl and  $\text{Al}_2\text{O}_3$  matrices as a function of depth are made. Since the frequency shifts are dependent on both the axial and radial stress components, their separation requires the solution of the appropriate elastic equations. This is described, using the results of a finite element computation in section 4. From this, the stresses as a function of depth are determined.

## 2 The Through-Focus Depth Profiling Method <sup>1</sup>

### 2.1 Depth of Field Function

The depth resolution of the optical microprobe used for the fluorescence measurements is determined by the numerical aperture of the objective lens and the size of the collection aperture used [12,13]. As illustrated in figure 2, when the excitation laser is focused at a distance  $z$  below the top surface of a transparent material with uniform concentration of fluorescing species, only the signal generated in a small volume above and below the focal plane is collected. The total signal collected is then the integral of the fluorescence from different depths:

$$I(z) = \int_{-z}^{t-z} g(u) du \quad (3)$$

where  $g(u)$  is the depth of field function of the lens used to describe the relative collection efficiency as a function of  $u$ , the distance from the focal plane.

By moving the focal plane from a position above the top surface to a position below the surface of a thick sapphire disk ( $t \rightarrow \infty$ ) containing adequate chromium concentration,

---

<sup>1</sup> The general procedures for optical fluorescence measurement and analysis were described in detail in [11] and therefore not included in this work.

and recording the fluorescence line intensity as a function of depth  $z$ , the depth resolution function  $g$  is obtained from equation 3, namely:

$$g(z) = \frac{dI(z)}{dz} . \quad (4)$$

The depth resolution function for our optical microprobe using a 50/0.55 objective lens and a 200  $\mu\text{m}$  collection aperture was measured using the above method and is shown in figure 3. As can be seen, the collection efficiency is maximum at the focal plane, and decrease rapidly with distance on either side of the focal plane.

## 2.2 Measurement of the Frequency Shift Depth Profile

We now suppose that there exists a stress field that only varies with depth  $z$ . From equation 2, the shift of a fluorescence line associated with the increment in signal from a narrow slice of material at depth  $z + u$  is

$$\Delta\nu(z + u) = 2\Pi_a \sigma_r(z + u) + \Pi_c \sigma_z(z + u) \quad (5)$$

The measured shift with focal point positioned at depth  $z$  is then a weighted average of the signals from all depths:

$$\overline{\Delta\nu(z)} = \frac{\int_{-z}^{t-z} \Delta\nu(z + u) g(u) du}{\int_{-z}^{t-z} g(u) du} \quad (6)$$

Provided the depth of field function  $g(z)$  is known, the real depth profile  $\Delta\nu(z)$  can be deconvoluted from equation 6.

To establish that the foregoing methodology is correct, the stress field through the thickness of a dilute ruby beam in 4-point loading was measured and compared with the elastic solution for the stress. A number of fluorescence spectra were taken as the laser beam was

focused at different depths from the top, tension surface to the bottom, compression surface of the beam. The measured shifts are plotted in figure 4 as the solid dots. The deconvoluted data is shown by the solid line. The deconvolution was obtained by assuming that the real shift  $\Delta\nu(z)$  is a linear function of depth  $a + bz$  since it is known that the stress distribution varies linearly with the depth  $z$  for a rectangular beam under 4-point loading. This function is then convoluted with the depth of field function  $g(z)$ . By fitting the resulting convoluted function to the measured shifts, the coefficients  $a$  and  $b$  are obtained. The initially assumed function, with the coefficients obtained by fitting, is then regarded as the deconvoluted shift  $\Delta\nu(z)$  directly related to the stress distributions by equation 2. The straight solid line in figure 4 therefore represents the real shifts. As expected, and required, the zero shift position coincides with the neutral plane of the beam. The stress distribution calculated by using equation 2 is also in good agreement with that obtained from beam theory and loading conditions. As a further check, the convoluted shift, obtained by convoluting the derived values of the real shift with the instrument function  $g(z)$  is shown by the dashed curve. It has excellent fit with the measured data except for the slight deviation near the compression surface which, we believe, is due to the fact that the focus deteriorates after light has passed all the way through the ruby beam. These observations thus confirm that the through-focus method can indeed accurately measure the depth profile of the stresses.

### 3 Measured Frequency Shifts From Embedded Sapphire Fibers

The depth profiling method has been applied to two different sapphire fiber composites: the first, a  $\gamma$ -TiAl matrix composite with carbon black/alumina double fiber coatings on the sapphire fibers and, the second, a polycrystalline  $\text{Al}_2\text{O}_3$  matrix with a thin molybdenum

coating on the fibers. In each case, the fiber diameter is about 120  $\mu\text{m}$ . Thin slices of composite with parallel surfaces perpendicular to the sapphire fibers were cut to about 450  $\mu\text{m}$  and 600  $\mu\text{m}$  thick for the  $\gamma$ -TiAl matrix and the  $\text{Al}_2\text{O}_3$  matrix composites respectively. The top surface of the specimens were then polished to obtain an optical finish at the fiber ends.

The measured and the deconvoluted frequency shift as a function of depth into a sapphire fiber in  $\gamma$ -TiAl matrix, as well as the convoluted function are plotted in figure 5. Since  $\gamma$ -TiAl has considerably larger thermal expansion coefficient than sapphire (table 1), the residual stress developed by thermal mismatch in the fiber should be compressive in both radial and axial directions. This is consistent with the large negative shifts observed when the probe is focused deep in the interior of the specimen. Near the surface, the axial stress approaches zero as required by force balance. The deconvoluted shift becomes positive near the surface indicating that the radial stress becomes tensile near the surface. In the case of the sapphire fibers in polycrystalline  $\text{Al}_2\text{O}_3$ , the residual stress is mainly caused by the anisotropy of the thermal expansion coefficient of sapphire. As show in figure 6, the relatively large negative shifts near the surface indicate that the radial stress near the surface is compressive, since the axial stress must approach zero due to force balance requirement, and thus does not contribute to the shift. The magnitude of the negative shift becomes progressively smaller with increasing of depth implying that the negative shift associated with the radial compressive stress is partially compensated by the positive shift resulting from the build up of the axial tensile stress. These observations are consistent with the fact that the thermal expansion coefficient of polycrystalline  $\text{Al}_2\text{O}_3$  is larger than that of the sapphire in the  $a$ -direction, but smaller than that in the  $c$ -direction. A notable feature of the depth profile of the shift, in both systems, is the near exponential dependence. This

is indicative of the fibers being fully bonded to the matrices and the fiber/matrix systems being elastic.

#### 4 Analysis

The residual stresses in the sapphire fibers are related to the observed frequency shifts presented in the previous section by equation 2. In order to obtain actual values of the two stress components, an additional relationship between the two components is evidently required. Two difficulties are associated with establishing such a relationship. First, the residual stresses originate from thermal expansion mismatch but the temperature on cooling at which stress relaxation no longer is effective, and stresses begin to build up, is not known. Secondly, existing equations relating the residual stresses in a fiber embedded in an infinite matrix [2] to the thermal mismatch strain  $\Delta\alpha\Delta T$  are unfortunately not valid for the thin specimens used in this work. Furthermore, rigorous analytical solutions for the residual stress field are not available and the approximate models used in analyzing stresses in fibers, e.g. those in analyzing fiber pull-out/push-out tests [15-17] breakdown near the fiber end. We have therefore had to resort to finite element calculations of the residual stress field for the sapphire/ $\gamma$ -TiAl and sapphire/ $\text{Al}_2\text{O}_3$  systems and use an iterative, self consistent procedure to calculate the residual stresses and the temperature at which the stresses become frozen in. This is described in the following paragraphs. First, however, it should be noted that the stresses can be *estimated* directly from equation 2. For the  $\gamma$ -TiAl matrix system, the residual stresses in the fiber are expected to be compressive. If it is assumed that the magnitude of the radial component is similar to the axial component in the interior of the



composite, then using the shift from deep in the fiber we have from equation 2

$$\sigma_r^{int} \sim \sigma_z^{int} \sim \frac{\Delta\nu^{int}}{2\Pi_a + \Pi_c} \sim 500 \text{ MPa}$$

For the  $\text{Al}_2\text{O}_3$  matrix system, due to the anisotropy of the thermal expansion coefficient of sapphire, the fiber should be under axial tension and radial compression. If we assume that the radial compression stress is about the same in the interior and near the surface, we again can estimate that

$$\sigma_r^{int} \sim \sigma_r^{sur} \sim \frac{\Delta\nu^{sur}}{2\Pi_a} \sim -100 \text{ MPa}$$

and

$$\sigma_z^{int} \sim \frac{\Delta\nu^{int} - 2\Pi_a\sigma_r^{int}}{\Pi_c} \sim 200 \text{ MPa}$$

Quantitative stress distributions can be obtained by comparing in detail the measured shifts with those calculated from the elastic field in the fiber/matrix system. Since the fiber coatings are relatively thin in both composites, we expect their effects on the elastic field to be negligible compared to those of the fiber and matrix. Therefore, in the calculations, the elastic system is simplified as consisting solely of an isotropic matrix of modulus  $E_m$  and Poisson's ratio  $\nu_m$  and a fiber of modulus  $E_f$  and Poisson's ratio  $\nu_f$  (Table 1). The specimen was represented by a thin disk of the same thickness as the corresponding specimen with one cylindrical fiber sitting at the symmetry axis. The diameter of the disk was chosen to be about ten times that of the fiber in order to be consistent with the low fiber volume fraction of both composite systems. The thermal expansion coefficients of the sapphire fiber in both the radial direction  $\alpha_a$  and axial direction  $\alpha_c$  are also listed in Table 1. The mean thermal expansion coefficient for  $\gamma\text{-TiAl}$  is known to be  $11 \sim 13 \times 10^{-6}/^\circ\text{C}$  depending on

the stress frozen-in temperature. However, that of the polycrystalline  $\text{Al}_2\text{O}_3$  is expected to vary from sample to sample depending on the residual matrix porosity. As a result of the complicated stress relaxation processes that occur during cooling, particularly near the interface, the effective thermal expansion coefficient  $\alpha_m$  for both matrices and the effective temperature change  $\Delta T$  were adjusted in the computation to obtain the best agreement with the experimental frequency shift data. The following procedure was adopted. First, reasonable estimates for the matrix thermal expansion coefficient and temperature change  $\alpha_m^{est}$  and  $\Delta T^{est}$  were used in the finite element calculation. The resulting stresses  $\sigma_r^{est}(z)$  and  $\sigma_z^{est}(z)$  were then used in equation 2 to calculate the shift as a function of  $z$ ,  $\Delta\nu_{cal}^{est}(z)$ . This function and the measured shifts are then normalized by their values in the interior of the material:

$$\Delta\nu^{norm} = \frac{\Delta\nu}{\Delta\nu^{int}} \quad (7)$$

By comparing the calculated and measured normalized shifts for a series of values of  $\alpha_m^{est}$ , the value that gives the best agreement is considered as the true  $\alpha_m$ . Then, by requiring that the calculated shift be equal to the measured shift in the interior, the effective temperature difference is proportionally scaled:

$$\Delta T = \Delta T^{est} \frac{\Delta\nu_{meas}^{int}}{\Delta\nu_{cal}^{int}} \quad (8)$$

Finally, the stress distributions are obtained:

$$\begin{aligned} \sigma_r &= \sigma_r^{est} \frac{\Delta T}{\Delta T^{est}} \\ \sigma_z &= \sigma_z^{est} \frac{\Delta T}{\Delta T^{est}} \end{aligned} \quad (9)$$

Since the thermal expansion coefficient of  $\gamma$ -TiAl is considerably larger than  $\alpha_s$  and  $\alpha_c$  of sapphire, the difference between  $\alpha_s$  and  $\alpha_c$  was unimportant. As a result, it was observed that the fitting of the normalized shift was not sensitive to the actual value of  $\alpha_m$ . Figure 7 illustrates the fitting between the measured and the calculated normal shifts for  $\alpha_m = 12$ . The effective temperature drop  $\Delta T$  calculated from equation 8 is  $\sim 750^\circ\text{C}$ , which agrees with  $\alpha_m$ - $T$  curve for  $\gamma$ -TiAl [18]. This temperature change is about  $300^\circ\text{C}$  smaller than the difference between the processing temperature and the room temperature indicating significant stress relaxation occurring during cooling. The stress distributions along the fiber calculated from equation 9 are plotted in figure 8. The axial stress approaches zero as expected and the radial component is positive at the surface as was indicated by the frequency shift measurement. The differences between the calculated and the measured normalized shifts as shown in figure 7 are due to the simplifications used in the model, e.g., neglecting the effects of coatings and assuming perfect interfacial bonding. However, the finite element calculations shows that the stress distributions in the interior of the specimen are not sensitive to small changes in the value of the elastic modulus and the thermal expansion coefficient of the matrix. This is because the values of the stresses are bounded by the measured shifts through equations 2 and scaled by equations 8 and 9. These observations suggest that the stress distributions deduced from the fluorescence data and illustrated in figure 8 are relatively accurate especially in the interior of the specimen. The possibility of some interfacial debonding will be discussed in more detail in the next section.

As expected, the normalized shift calculated for the  $\text{Al}_2\text{O}_3$  matrix system depends much more sensitively on the value of  $\alpha_m$  used in the computation. As show in figure 9,  $\alpha_m = 8.73$  gives the best fit between the calculated and the measured normalized shifts. The effective temperature difference obtained using equation 8 is about  $1300^\circ\text{C}$ , which is about  $200^\circ\text{C}$

lower than the processing temperature again as indication of stress relaxation occurring during cooling. The stress distributions in the sapphire fiber are plotted in figure 10. The observation that the calculated stress distributions in the interior are not sensitive to changes of  $E_m$  also applies in this system. The values of stress in the interior differ less than 5% for the three  $\alpha_m$ 's shown in figure 9. Since the shape of the shift profile depends sensitively to the change of  $\alpha_m$ , the fitting in figure 9 also provides means of estimating the local thermal expansion coefficient of the  $\text{Al}_2\text{O}_3$  matrix, which could be different from the average value of the whole sample because the density of the matrix is slightly lower near the fibers. The resulting value of  $\alpha_m$  can then be used in other analyses, such as for push-out tests.

## 5 Discussion

The analysis in the last section is based on the assumption that the fiber/matrix systems are elastic without any debonding occurring at the interface. This requires that the interfacial shear strength be larger than the maximum interface shear stress. To examine this assumption, the interfacial shear stress is also calculated in the finite element computation. The results corresponding to the best fit conditions determined in the last section are plotted for the sapphire/ $\gamma$ -TiAl and the sapphire/ $\text{Al}_2\text{O}_3$  systems in figure 11. In both systems, the magnitude of the shear stress has a maximum at the surface and decreases to zero with increasing depth. This is expected from the stress distributions in figures 8 and 10 and the force balance requirement:

$$\tau = \frac{R_f}{2} \frac{d\sigma_z}{dz} \quad (10)$$

Whilst the calculated interfacial shear stress for the sapphire/ $\text{Al}_2\text{O}_3$  system is smaller than the interfacial shear strength for the molybdenum/sapphire interface ( $\sim 100 - 300$

MPa) [19] and therefore insufficient to produce any debonding, the shear stress calculated for the sapphire/ $\gamma$ -TiAl system is considerably larger than any reasonable value for the carbon/sapphire interface ( $\sim 100 - 150$  MPa) [4,18]. It is likely that the thin carbon coating on this fiber is not continuous so that the sapphire fiber has direct contact with the polycrystalline  $\text{Al}_2\text{O}_3$  outer coating to form a strongly bonded interface. This has been often observed in the same composite specimen during push-out tests [18]. As mentioned in the last section, the fitting between the calculated and measured frequency shifts near the surface is not perfect. As shown in figure 7, the calculated shift changes more rapidly than that measured within one fiber diameter from the surface. Therefore, the change of the axial stress and consequently the magnitude of the interfacial shear (equation 10) in the real system should be smaller than that calculated. This further suggest that the interface may be debonded for a distance about one fiber diameter from the surface. However, this debonding does not seem to change the stress field significantly, so that the fiber/matrix system still behaves in an elastic manner. This is consistent with the fact that the friction is sufficiently large in this system, due to asperities at the interface [4,20], that the stress distribution is similar to a system with perfect bonding [3]. Therefore, we believe that the residual stresses determined for the sapphire/ $\gamma$ -TiAl system, especially in the interior of the composite, are not significantly affected by possible debonding near the surface.

## 6 Conclusions

By utilizing the optical fluorescence from chromium impurities in sapphire fibers, we have determined the residual stress distributions in embedded fibers in both a  $\gamma$ -TiAl matrix and a polycrystalline  $\text{Al}_2\text{O}_3$  matrix composite. The axial and radial components of the residual

stress, produced by differential thermal contraction on cooling after fabrication, in the fibers are determined as a function of depth below the composite surface. For both composites, the two stress components vary over a distance of about the fiber diameter from the surface and then are almost independent of distance further into the composite.

### **ACKNOWLEDGMENT**

This work was supported by the Office of Naval Research under grant N00014-91-J-1875 (QM) and the DARPA URI program at UCSB under contract N00014-92-J-1808 (DRC). The authors are grateful to Dr. T.J. Machin and J. Davis, UCSB, for providing the composite samples used in this work.

## References

1. J.W. Hutchinson and H.M. Jensen, *Mech. Materials*, 9, 139 (1990).
2. R.J. Kerans and T.A. Parthasarathy, *J. Am. Ceram. Soc.*, 74, 1585 (1991).
3. K.T. Faber, S.H. Advani, J.K. Lee, and J.T. Jinn, *J. Am. Ceram. Soc.*, 69, C-208 (1986).
4. T.J. Machin, J.Y. Yang, C.G. Levi and A.G. Evens, submitted to *Mat. Sci. Eng.*
5. P. Predecki, A. Abuhasan, and C.S. Barrett, *Adv. X-ray Anal.*, 31, 231, (1988).
6. A. Abuhasan, C. Balasingh, and P. Predecki, *J. Am. Ceram. Soc.*, 73, 2474 (1990).
7. S. Majumdar, D. Kupperman, and J. Singh, *J. Am. Ceram. Soc.*, 71, 858 (1988).
8. A.J. Allen, M.A.M. Bourke, S. Dawes, M.T. Hutchings and P.J. Withers, *Acta Metall. Mater.*, 40, 2361 (1992).
9. S. E. Molis and D. R. Clarke, *J. Am. Ceram. Soc.*, 73, 3189 (1990).
10. I.M. Robinson, R.J. Young, C. Galotis and D.N. Batchelder, *J. Mater. Sci.*, 22, 3642 (1987).
11. Q. Ma and D. R. Clarke, *J. Am. Ceram. Soc.*, submitted.
12. M. Pluta, *Advanced Light Microscopy 1*, Elsevier, Amsterdam, 1988.
13. F. Adar and D.R. Clarke, "Raman Microprobe Spectroscopy of Ceramics", pp 307-310 in *Microbeam Analysis*. Edited by K.F.J. Heinrich, San Francisco Press, San Francisco, 1982.

14. R.G. Munro, G.J. Piermarini, S. Block and W.B. Holzapfel. *Journal of Applied Physics*, 57, 165 (1985).
15. A. Takaku and R.G.C. Arridge, *J. Phys. D6*, 2038 (1973).
16. D.K. Shetty, *J. Am. Ceram. Soc.*, 71, C-107 (1988).
17. Y.C. Gao, Y.W. Mai, and B. Cotterell, *J. Appl. Math. Phys.*, 39, 550 (1988).
18. T.J. Machin, private communication.
19. J. Davis and A.G. Evans. to be published.
20. T.J. Machin, P.D. Warren and A.G. Evans. *Acta Metall. Mater.*, 40, 1251 (1992).



TABLE I

PROPERTY	Sapphire	$\gamma$ -TiAl	Al <sub>2</sub> O <sub>3</sub>
$E$ (GPa)	434	173	250
$\nu$	0.27	0.33	0.27
$\alpha$ (10 <sup>-6</sup> /°C)	8.3 (a), 9.0 (c)	11 ~ 13	8.3 < $\alpha$ < 9.0

## Figure Captions

Figure 1. Schematic diagram of the optical arrangement used to collect fluorescence from a region in an embedded, transparent fiber below its surface. The stress induced shift in frequency of a characteristic luminescence line is used to determine the stress in the probed region.

Figure 2. Illustration of the effect of the finite depth of field of the optical system used. When the excitation laser is focused at a distance  $z$  below the top surface, only the signal generated in a small volume above and below the focal plane is effectively collected.

Figure 3. The depth of field function of the microprobe used. It describes the relative collection efficiency as a function of distance from the focal plane. Details are given in the text.

Figure 4. The fluorescence line shift in the region between the tension surface ( $z = 0$ ) and the compression surface ( $z = 513 \mu\text{m}$ ) of a ruby beam under 4-point bending. The solid line representing the true shift is obtained by deconvoluting the measured shift with the depth of field function.

Figure 5. The line shift depth profiles ( $z = 0$  at the surface) in a  $c$ -axis sapphire fiber embedded in the  $\gamma$ -TiAl matrix.

Figure 6. The line shift depth profiles ( $z = 0$  at the surface) in a  $c$ -axis sapphire fiber embedded in a polycrystalline  $\text{Al}_2\text{O}_3$  matrix.

Figure 7. A comparison of the calculated and the measured normalized shifts as a function of depth for the sapphire/ $\gamma$ -TiAl system.

Figure 8. The radial and axial stresses as a function of depth in the sapphire/ $\gamma$ -TiAl system determined from the fluorescence data.

Figure 9. A comparison of the calculated and the measured normalized shifts as a function of depth for the sapphire/ $\text{Al}_2\text{O}_3$  system.

Figure 10. The radial and axial stresses as a function of depth in the sapphire/ $\text{Al}_2\text{O}_3$  system determined from the fluorescence data.

Figure 11. The interfacial shear stresses in the sapphire/ $\gamma$ -TiAl and the sapphire/ $\text{Al}_2\text{O}_3$  systems calculated from the finite element computation and the fluorescence data.

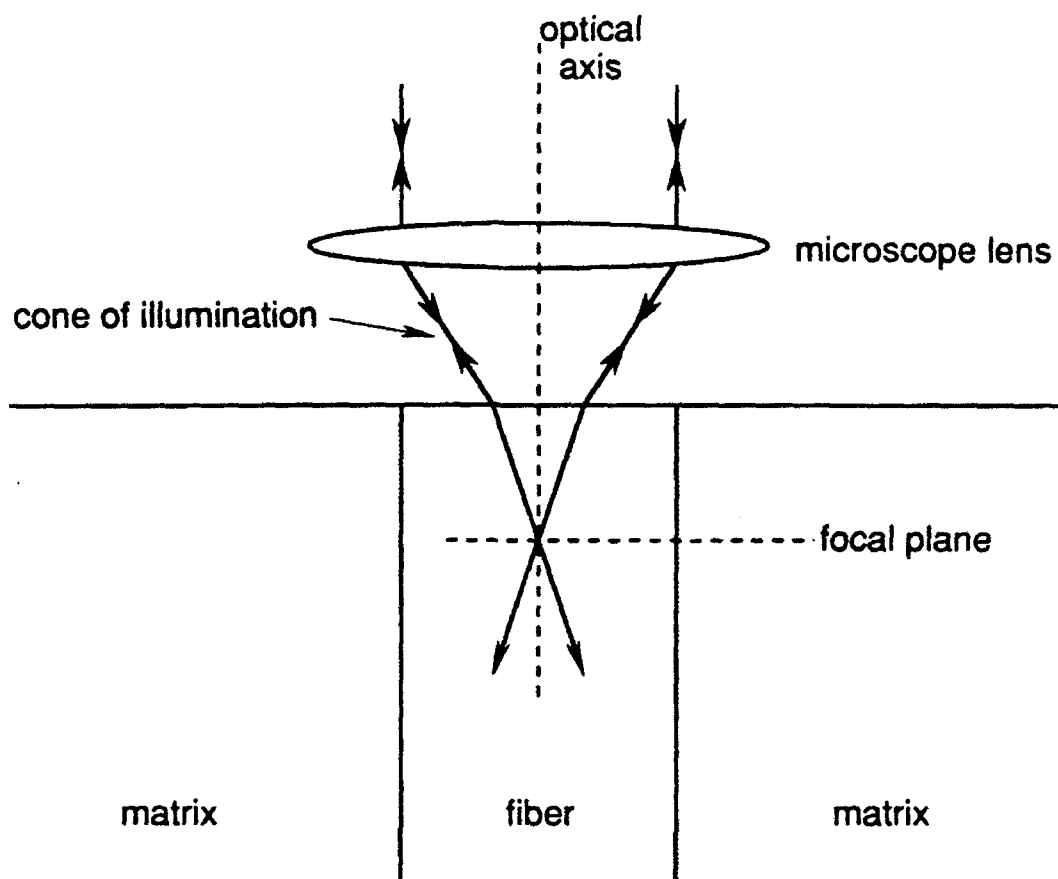


Fig.1

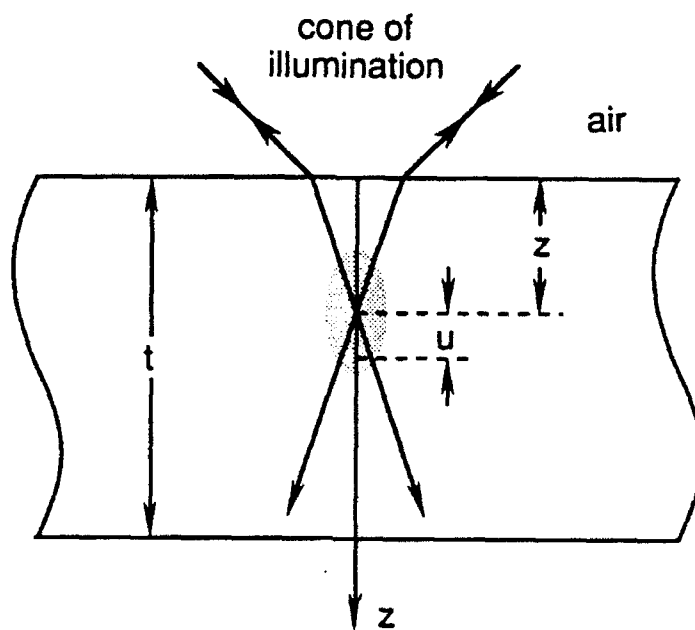


Fig. 2

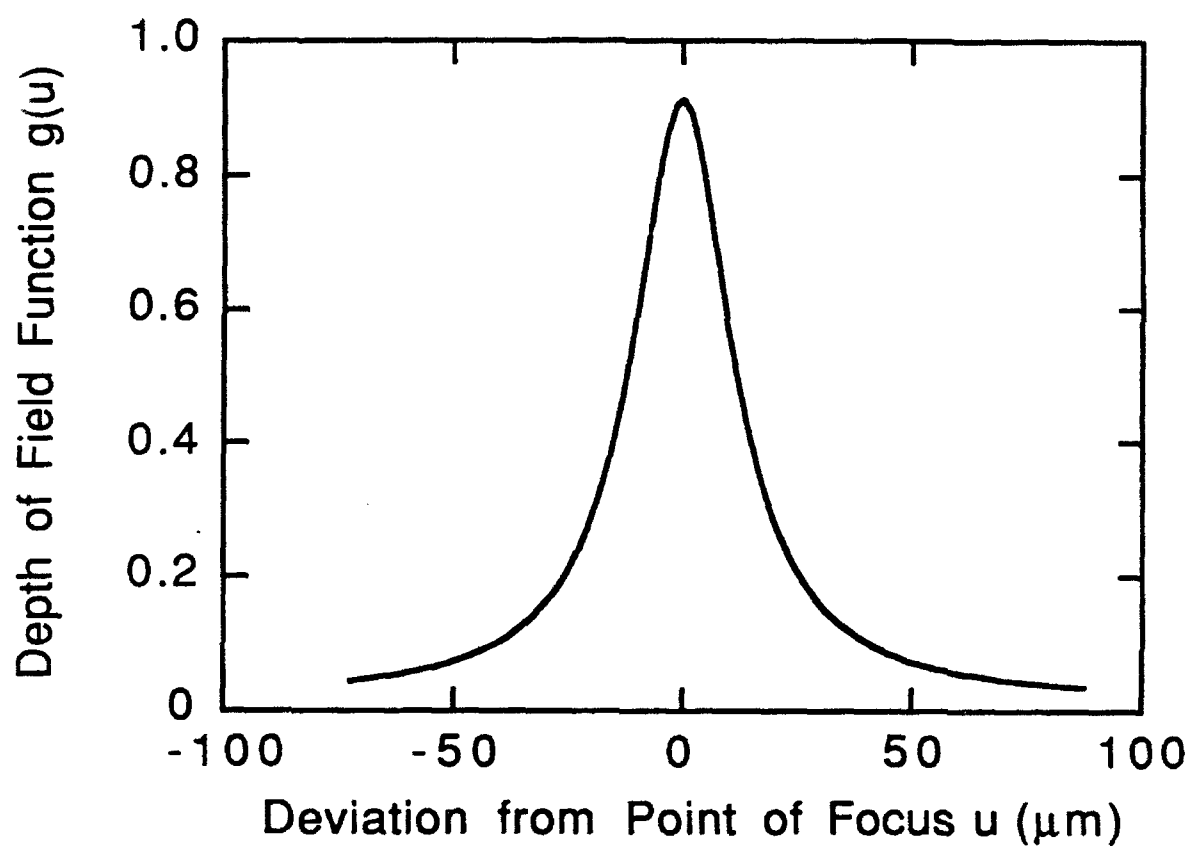


Fig. 3

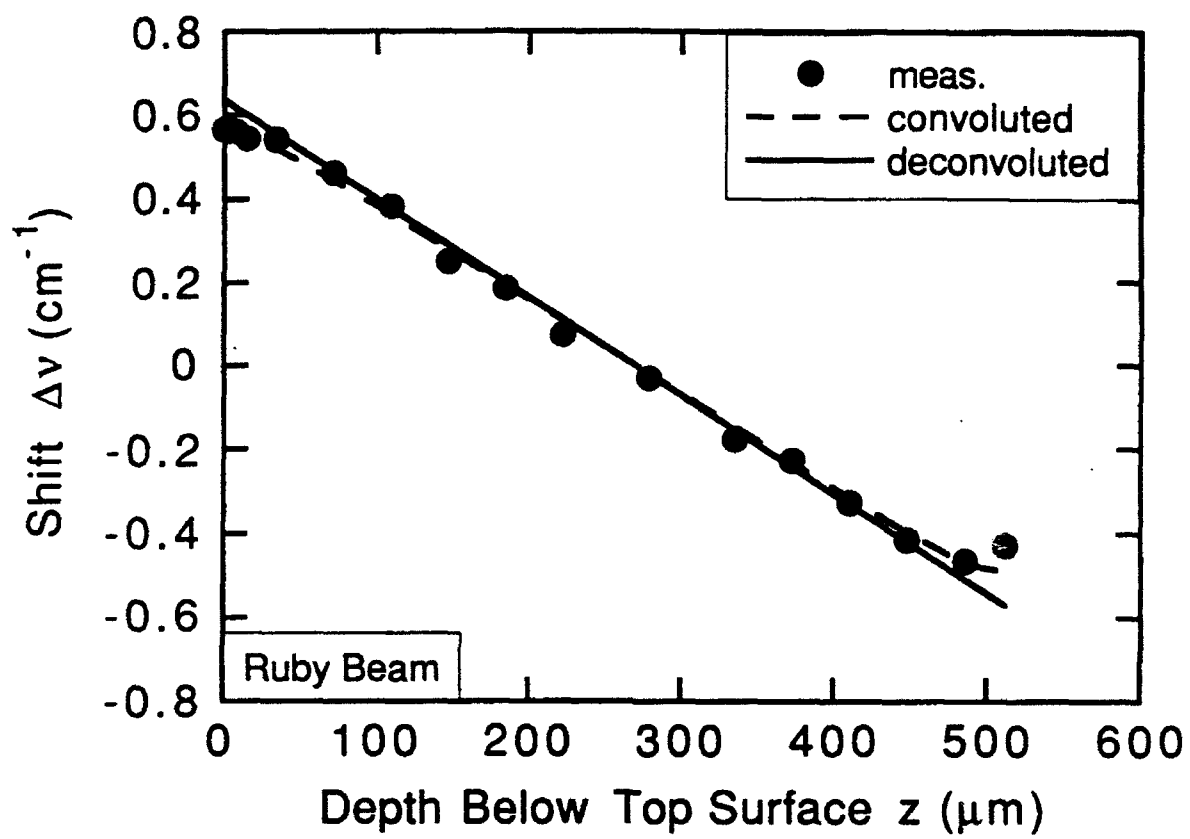


Fig. 4

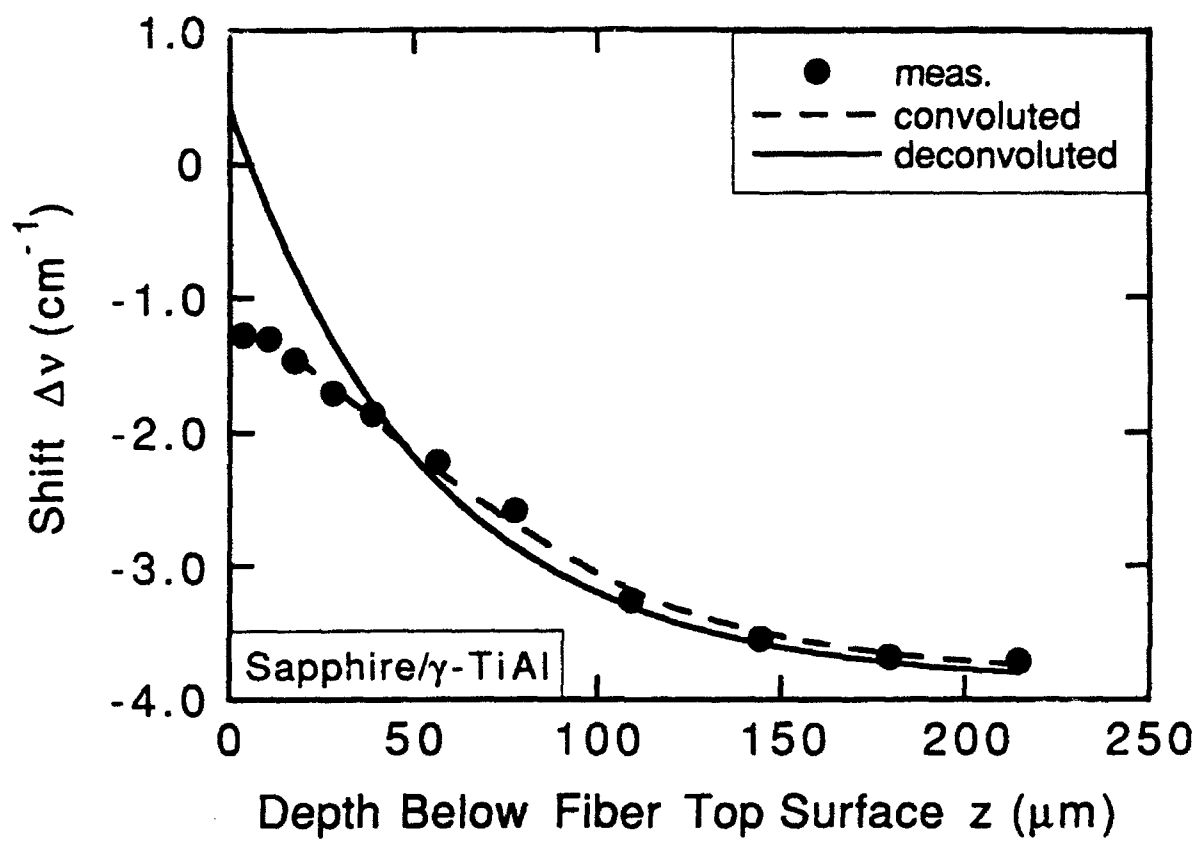


Fig. 5



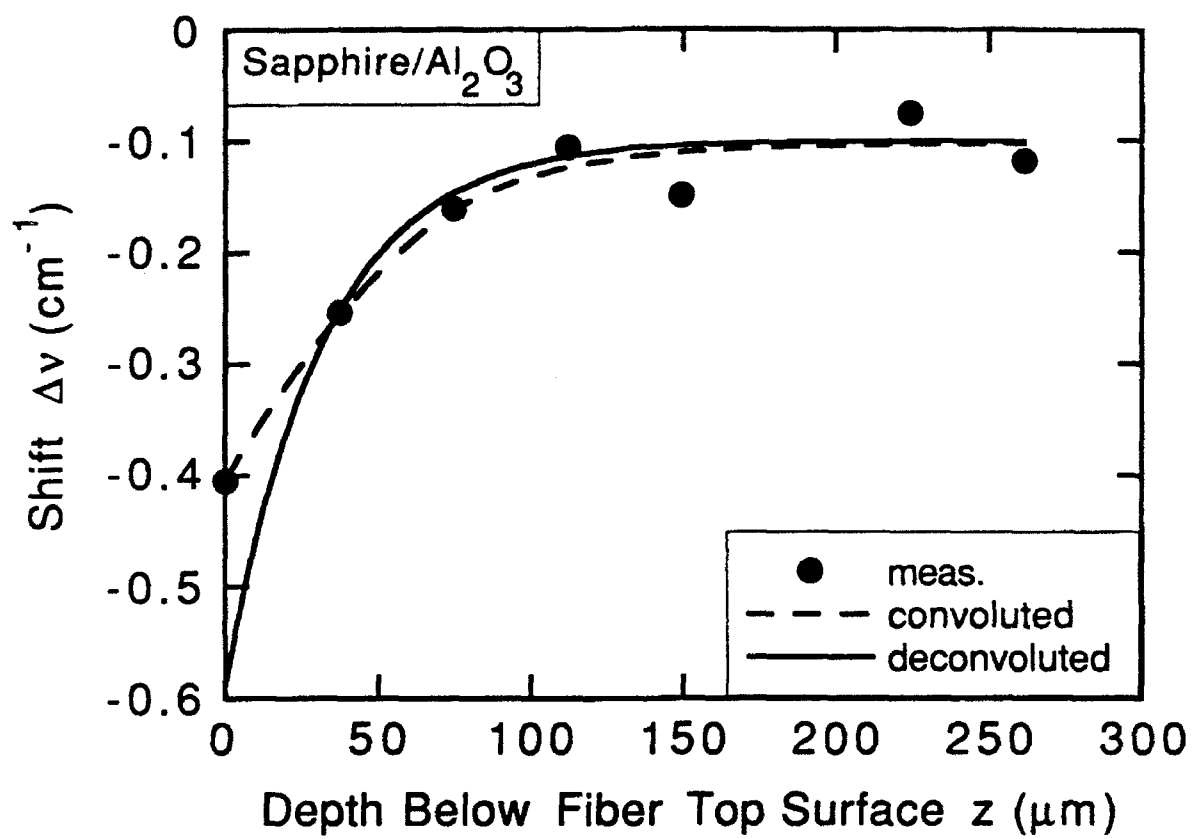


Fig. 6

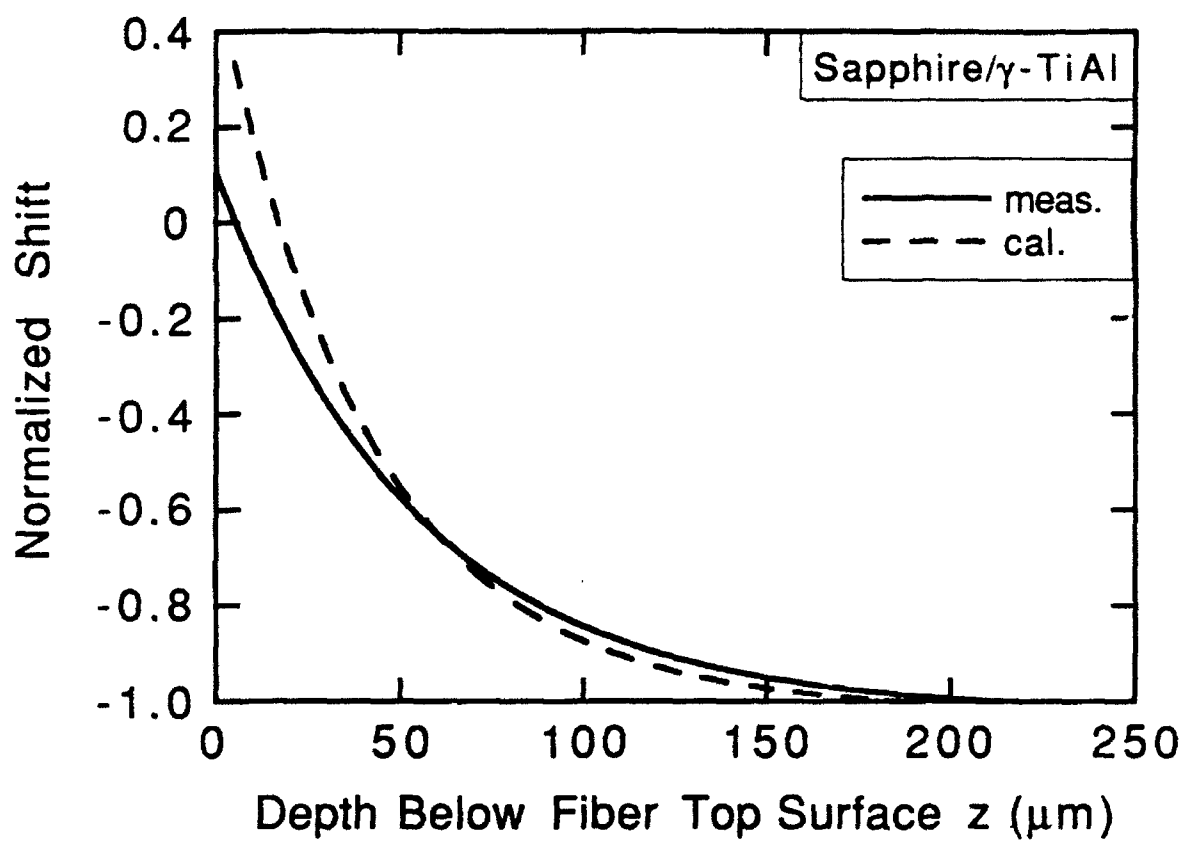


Fig. 7

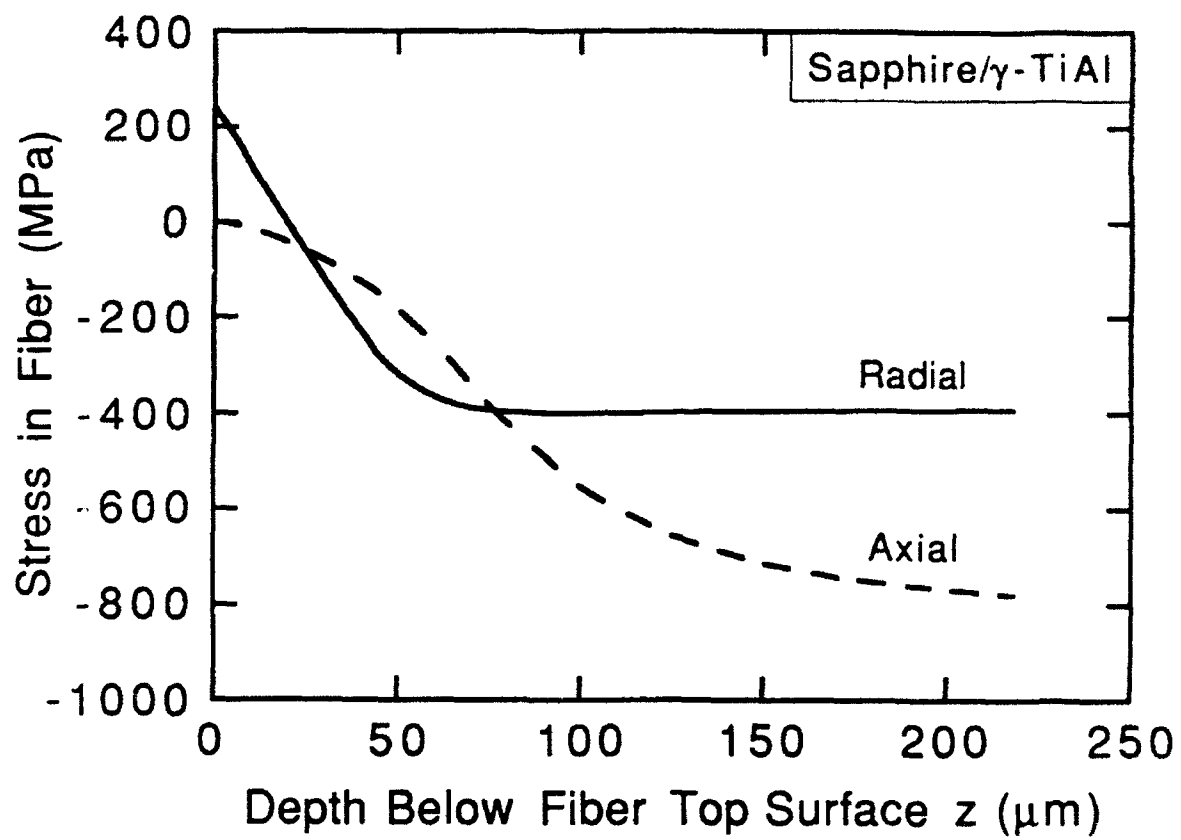


Fig. 8

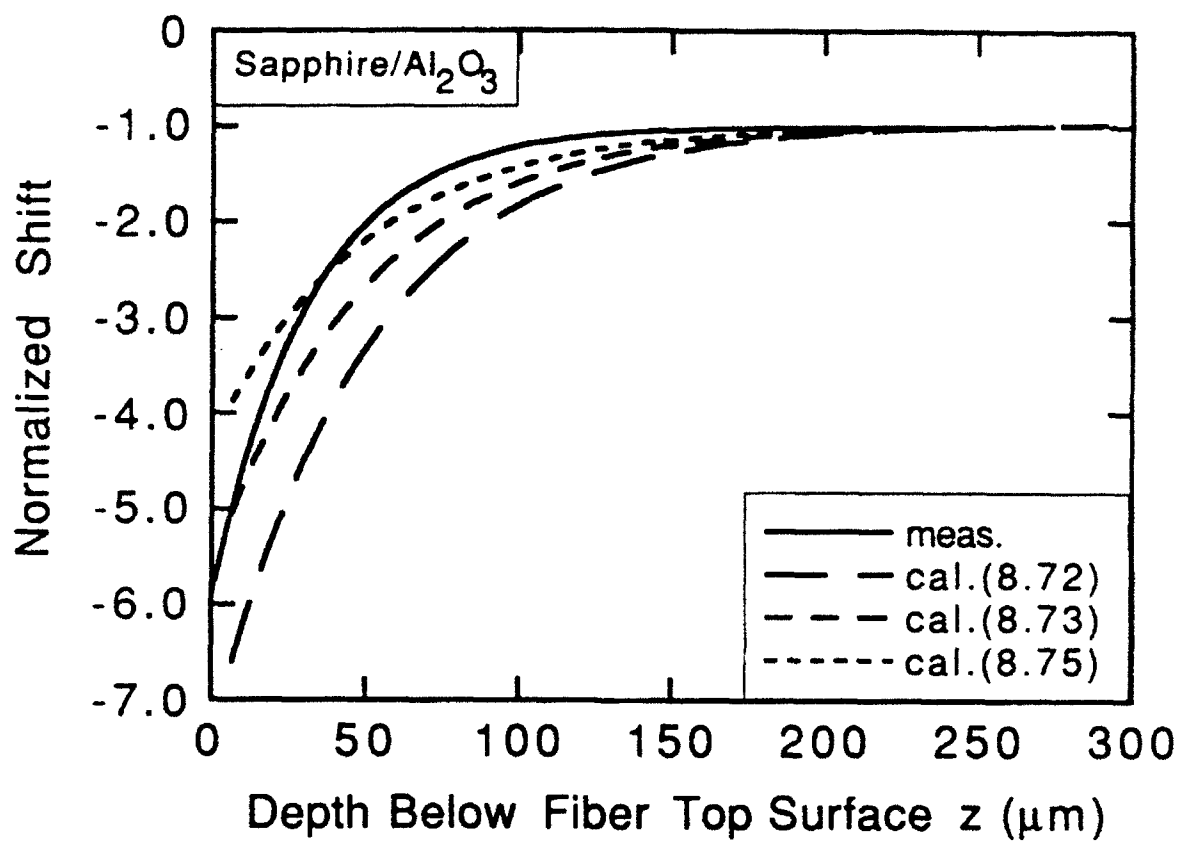


Fig. 7

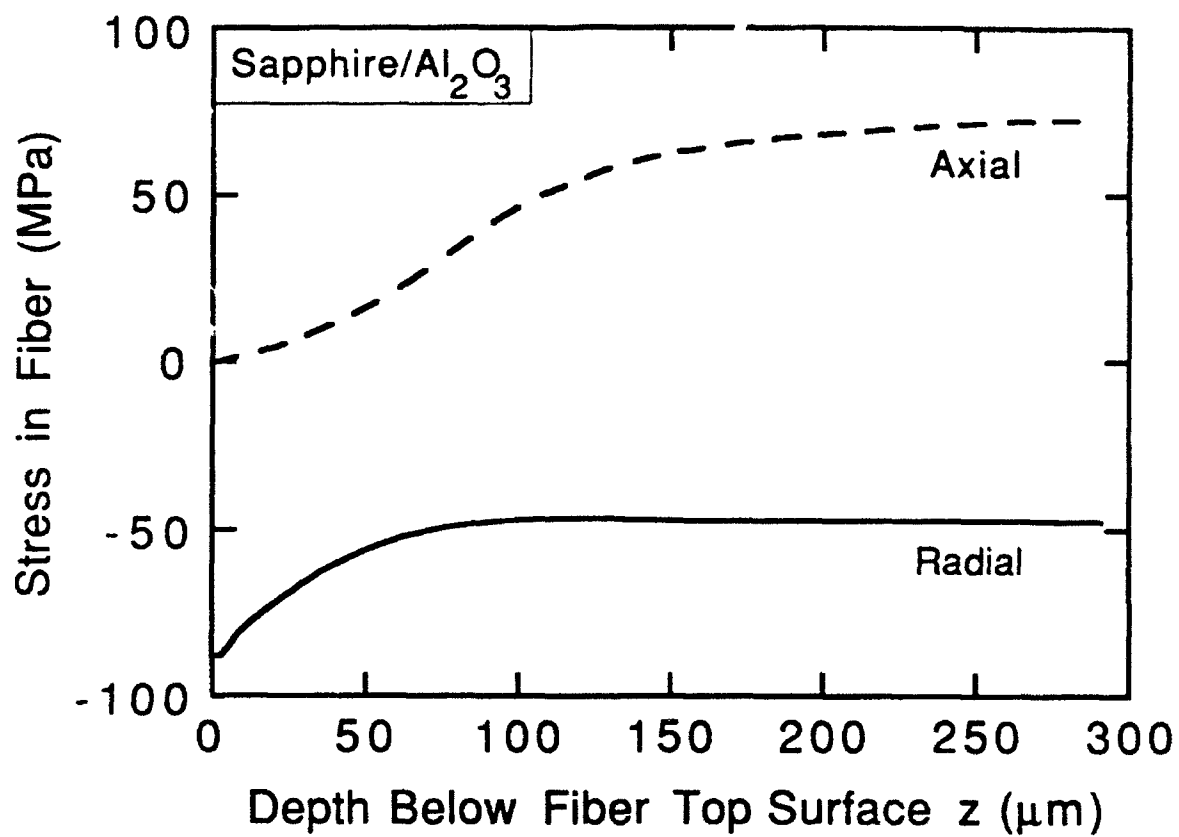


Fig. 10

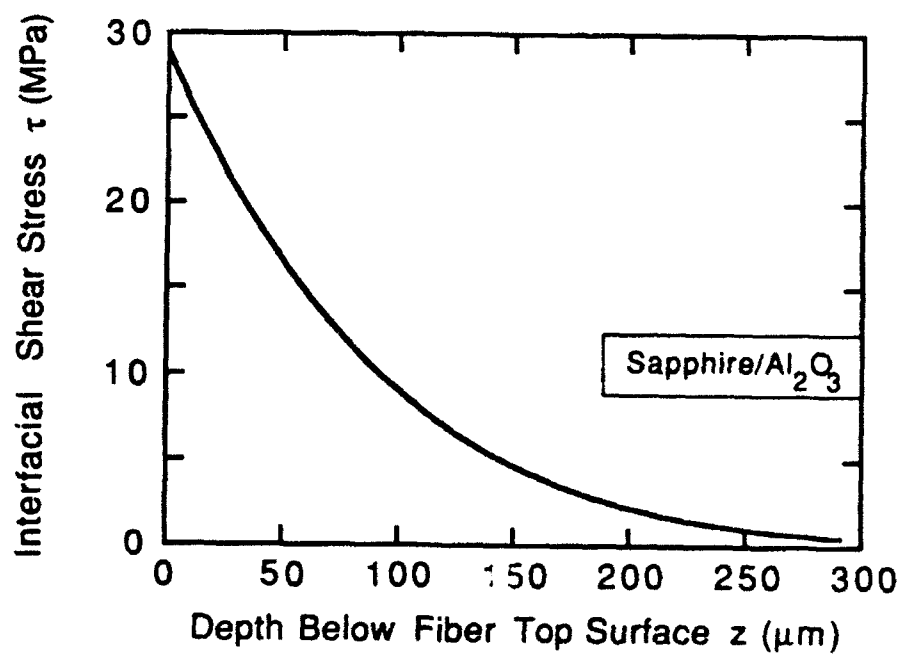
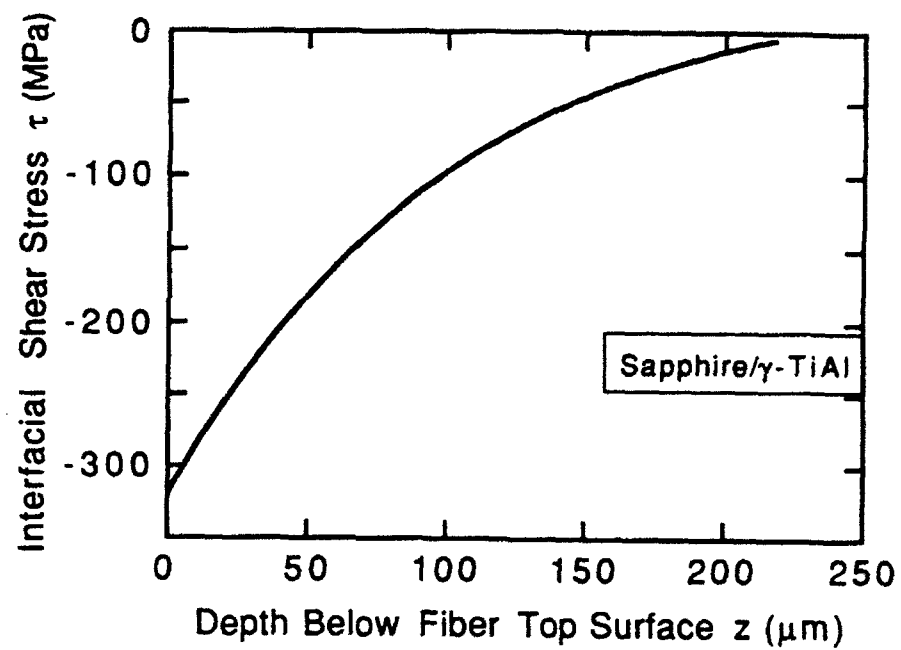


Fig. 11

## COMPRESSIVE FAILURE OF FIBRE COMPOSITES

B. BUDIANSKY

Division of Applied Sciences, Harvard University, Cambridge, MA 02138, U.S.A.

and

N. A. FLECK

Cambridge University Engineering Department, Trumpington Street, Cambridge,  
CB2 1PZ, U.K.

(Received 2 December 1991)

### ABSTRACT

A REVIEW of experimental data and elementary theoretical formulas for compressive failure of polymer matrix fibre composites indicates that the dominant failure mode is by plastic kinking. Initial local fibre misalignment plays a central role in the plastic kinking process. Theoretical analyses and numerical results for compressive kinking are presented, encompassing effects of strain-hardening, kink inclination, and applied shear stress. The assumption of rigid fibres is assessed critically, and the legitimacy of its use for polymer matrix composites is established.

### INTRODUCTION

COMPRESSION FAILURE is a design limiting feature of aligned, continuous fibre composite materials. For example, the compressive strengths of unidirectional carbon fibre-epoxy laminates are often less than 60% of their tensile strengths. The dominant compressive failure mode in aligned-fibre, polymeric matrix composites is localized compressive buckling, or kinking; other failure modes, such as fibre crushing, can also occur. Although fibre kinking limits the compressive strength of carbon-matrix composites, and has often been observed in wood, the importance of kinking in metal-matrix and ceramic-matrix composites generally is not yet clear.

The present paper, continuing the recent studies of FLECK and BUDIANSKY (1991), is concerned primarily with various aspects of the compressive kinking problem. A preliminary discussion invokes theoretical arguments and existing experimental information to support the belief that the kinking mechanism in polymer-matrix and carbon-matrix fibre composites is dominated by fibre misalignment together with plastic shear deformation in the matrix. This sets the stage for the extension of previous theoretical results for static kinking strength under combined compression and shear to include effects of composite strain-hardening.

As in most treatments of compressive kinking the fibres in these calculations are





right-hand side of (1) is just an approximation for  $G$ . ARGON (1972) took the alternative view that long-fibre composites undergo *plastic* microbuckling. He assumed, in effect, that kinking occurs in a  $\beta = 0$  band within which fibres have suffered an initial misalignment angle  $\bar{\phi}$  (see Fig. 1). In a rigid-perfectly plastic composite having yield stress  $\tau_y$  in longitudinal shear, additional rotation  $\phi$  cannot develop until the critical compressive stress

$$\sigma_c = \frac{\tau_y}{\bar{\phi}} \quad (2)$$

is applied, and subsequently the compressive stress decreases with increasing  $\phi$ .

The Argon formula (2) for the plastic kinking stress was extended by BUDIANSKY (1983) to an *elastic*-perfectly plastic composite, with yield strain  $\gamma_y = \tau_y/G$  in longitudinal shear, for which the kinking stress is

$$\sigma_c = \frac{\tau_y}{\gamma_y + \bar{\phi}} = \frac{G}{1 + \bar{\phi}\gamma_y} \quad (3)$$

This result (still for  $\beta = 0$ ) is uniformly valid for all  $\bar{\phi}$ , giving the Rosen bifurcation stress for  $\bar{\phi} = 0$ , and asymptotically equivalent to the Argon result (2) for  $\bar{\phi}$  large.

JELF and FLECK (1991) measured the microbuckling stresses of linear elastic composites made from glass fibres and a silicone rubber matrix. They observed microbuckles having half-wavelengths equal to the specimen length, and found that as the specimen length was increased the compressive strength decreased towards the Rosen limit (1). However, available experimental evidence for more conventional polymer matrix composites supports the hypothesis that microbuckling is a plastic rather than an elastic event. Test data from a variety of sources for the axial compressive strength  $\sigma_c$  of aligned-fibre polymer matrix composites are plotted against  $G$  in Fig. 2. [The

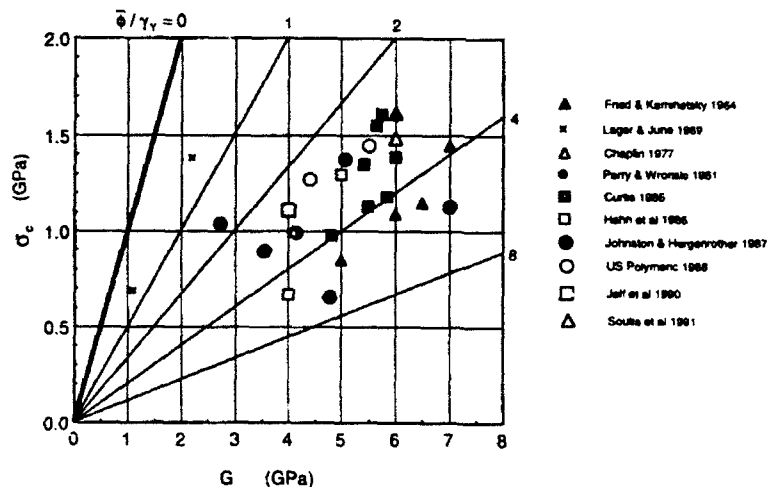


FIG. 2. Test data and elastic-ideally plastic predictions, compressive strength  $\sigma_c$  vs composite shear modulus  $G$ , for zero-inclination kink bands ( $\beta = 0$ ). Fibre misalignment =  $\bar{\phi}$ , shear yield strain =  $\gamma_y$ .

composite  $G$  values were estimated via the right-hand side of (1), and, in turn, each  $G_m$  was calculated from estimates, measurements or handbook values of the Young's modulus  $E_m$  and Poisson's ratio  $\nu_m$  of the matrix.] The elastic kinking stress is given by the heavy line (corresponding to  $\bar{\phi} = 0$ ) and the other slanted straight lines are plots of (3) for several values of  $\bar{\phi}$  ( $\gamma_0 > 0$ ). The simplifying assumptions (e.g.,  $\beta = 0$ , ideal plasticity) used in the derivation of (3) limit its direct applicability: indeed, more realistic analyses, taking into account strain-hardening as well as  $\beta > 0$  will be made in this paper. We note, nevertheless, that most of the data in Fig. 2 fall well below the elastic buckling line, and are consistent with (3) for a range of values of  $\bar{\phi}$  near 4. If we set  $\gamma_0$  equal to some nominal magnitude—say  $1^\circ$ —this gives values of  $\bar{\phi}$  scattered about a mean value in the vicinity of 2. As we shall see later, this rough estimate for typical values of  $\bar{\phi}$  may change somewhat in the light of more refined calculations, but it is in good agreement with measured values of the misalignment of fibre bundles when a laminate was sectioned and examined under a light microscope by YURGARTIS (1987). Yurgartis found that most of the fibres in a carbon fibre-PEEK unidirectional composite were oriented within  $\pm 3^\circ$  of the mean fibre direction, and the standard deviation of the distribution was  $1.9^\circ$ .

Indirect evidence to support (3) comes from compression tests on woven carbon fibre cloth by WILKINSON *et al.* (1986). They found that the compressive strength of T300 914 carbon-epoxy cloth ( $G \approx 6$  GPa) decreased from about 1 GPa to 200 MPa when they inserted brass wires into the cloth normal to the fibre direction in order to increase the waviness. From these strength measurements the inferred value of  $\bar{\phi}$  increases from 5 to 29 via (3). With  $\gamma_0 \approx 0.01$  ( $0.57^\circ$ ) this corresponds to an increase of  $\bar{\phi}$  from 3 to 17. These theoretical values agree well with our measurements of the maximum fibre bundle waviness from the micrographs published by WILKINSON *et al.* (1986), which show increases from approximately  $3^\circ$  to approximately  $20^\circ$ .

The compressive strength of composites shows a large degree of scatter, with nominally identical specimens often varying in strength by 25%. This is consistent with plastic microbuckling, for which the analytic prediction (3) shows high imperfection sensitivity, with strength strongly dependent upon the misalignment angle. In contrast, the elastic microbuckling collapse load is fairly insensitive to imperfections (BUDIANSKY, 1979), and would not show much scatter.

The simple formula (3) for the kinking stress of an elastic-ideally plastic composite under pure longitudinal compression, kinking in a band normal to the fibre direction, provides an indication of the relative importance of the physical parameters that govern the kinking strength. It follows from (3) that variations  $\delta\tau_0$ ,  $\delta G$  and  $\delta\bar{\phi}$  in the shear yield stress, elastic shear modulus, and initial misalignment are related to a change  $\delta\sigma_k$  in the kinking stress by

$$\frac{\delta\sigma_k}{\sigma_k} = \left(\frac{\sigma_k}{G}\right) \frac{\delta G}{G} + \left(1 - \frac{\sigma_k}{G}\right) \frac{\delta\tau_0}{\tau_0} - \left(1 - \frac{\sigma_k}{G}\right) \frac{\delta\bar{\phi}}{\bar{\phi}}. \quad (4)$$

Thus, to give a typical example, if  $\sigma_k/G = 1/4$ , a fractional increase of yield stress is three times as effective in raising the kinking stress as is a similar relative change in the shear modulus, and the same is true for a fractional decrease in the initial imperfection.

*Plastic kinking vs fibre crushing*

In an illuminating set of tests (PIGGOTT and HARRIS, 1980; PIGGOTT, 1981), the modulus of a polyester resin matrix was varied by partial curing, and it was found that the matrix yield strength varied proportionally. With reinforcing fibres of either glass or Kevlar, and  $v_f = 0.31$ , a nominal, uniform value of  $\gamma_f \approx 0.024$  (1.4) for the composites can be estimated from their data. Figure 3 shows the measured composite strengths on another plot of  $\sigma_c$  versus  $G$ . Again we infer a value  $\bar{\phi} \approx 2$  for both the glass and Kevlar fibres from the initial, nearly linear ranges of the data, presumed to reflect plastic kinking. However, above transitional values of the composite stiffness  $G$ , the failure-stress levels, shown by the arrows in Fig. 3, become more-or-less independent of  $G$  (or of  $\tau_f = G/v_f$ ). Piggott and Harris surmise that in this range failure was due to *fibre crushing*.

Fibre failure in compression crushing occurs when the uniaxial strain in the composite equals the intrinsic crushing strain  $\epsilon_{fc}$  of the fibres. A variety of mechanisms may be associated with fibre crushing. In the case of steel fibres local crushing is due to plastic yielding (MONCUNILL DE FERRAN and HARRIS, 1970; PIGGOTT and WILDE, 1980). Glass fibres tend to fail in compression by longitudinal splitting. In the case of carbon, Kevlar and wood fibres, local buckling or kinking occurs *within* each fibre (GRESZCZUK, 1972, 1975; PRANDY and HAHN, 1990; YOUNG and YOUNG, 1990; PIGGOTT and HARRIS, 1980; GIBSON and ASHBY, 1988); kink bands within the fibres of width less than the fiber radius are observed (PRANDY and HAHN, 1990). Pitch-based carbon fibres have a very well aligned longitudinal microstructure, and they fail in compression by a combination of internal buckling and longitudinal splitting. Typical values of crushing strain are  $\epsilon_{fc} = 0.5\%$  for Kevlar and pitch-based carbon fibres, and  $\epsilon_{fc} = 2.5\%$  for PAN-based carbon fibres.

The average axial stress in the composite at which fibre crushing occurs is given

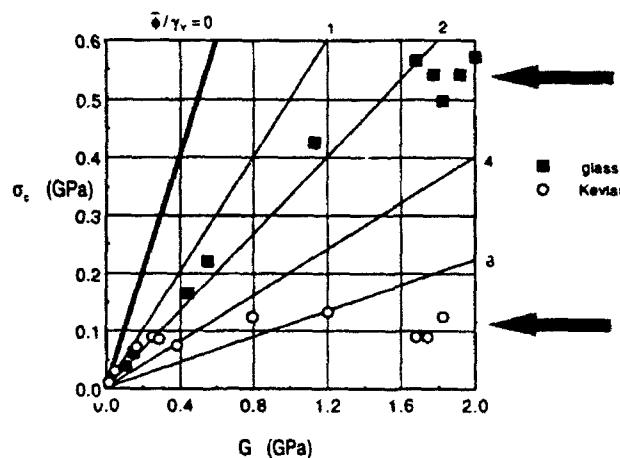


FIG. 3. Test data (PIGGOTT and HARRIS, 1980; PIGGOTT, 1981) for compressive strengths of glass and Kevlar fibre reinforced, partially cured resins. Arrows indicate presumed stress levels at transitions from kinking to fibre crushing.

approximately by the rule-of-mixtures formula  $\sigma_c = [v_f E_f + (1 - v_f) E_m]$ , where  $E$  is the Young's modulus of the fibres. In the Piggott-Harris tests,  $E_f/E_m \approx 1$ , and so the fibre crushing strengths  $\sigma_{cf} = E_f \epsilon_{cf}$  can be estimated as  $\sigma_{cf} \approx \sigma_{cm}$  from the upper-shelf values of  $\sigma_{cm}$ . This gives fibre crushing strengths of about 1.7 and 0.4 GPa for the glass and Kevlar, respectively; these values are plausible.

Early carbon fibre-epoxy matrix systems were manufactured from carbon fibres of low crushing strength and epoxies of high yield strength. These materials failed by fibre crushing at test temperatures below approximately 100°C (EWINS and POTTER, 1980). At higher temperatures the yield strength of the early epoxies drops sufficiently for the failure mechanism to switch to kinking. More modern carbon fibre-epoxy systems possess carbon fibres of higher crushing strength, and a tougher, lower yield strength matrix. The transition temperature from fibre crushing to kinking is shifted from 100°C to -40°C, and modern carbon fibre-epoxy laminates fail by kinking at both ambient and elevated temperatures (BARKER and BALASUNDARAM, 1987).

#### *Shear banding*

Finally, we remark that besides fibre crushing and localized kinking, another distinct failure mode has been observed in aligned-fibre polymer-matrix composites with very low fibre volume fractions, namely *shear-banding*, oriented at about 45° with respect to the loading axis (FRIED, 1963). This is a failure mode essentially identical to that which would occur in the unreinforced matrix material, to which the few fibres present offer little resistance, and is not expected to be significant at conventional fibre volume fractions.

#### *Carbon, ceramic and metal matrices*

Microbuckling in carbon-carbon composites has been observed by EVANS and ADLER (1978) and CHATTERJEE and McLAUGHLIN (1979). The latter found compressive strengths as low as 1/20 of the elastic kinking stress (1), and suggested plastic kinking as the operative failure mechanism. The plasticity of the carbon matrix is probably due primarily to microcracking. Similar nonlinear stress-strain behaviour due to matrix microcracking and consequent kinking mechanisms might also be expected in some ceramic-matrix composites. Although little experimental evidence is available, LANKFORD (1989) did observe kinking at high compressive strain rates in a pyroceramic matrix reinforced with silicon carbide fibres. His measured compressive strength of  $\sigma_c \approx 1500$  MPa, and our roughly estimated values of  $\tau_y \approx 115$  MPa and  $\gamma_y \approx 0.01$ , when substituted into the plastic kinking formula (3), give  $\bar{\phi} \approx 4$  for the fibre misalignment.

Compressive failure in metal-matrix fibre composites has received little study, and the importance of kinking as a failure mode in such composites has not been established.

### MATRIX STRAIN-HARDENING EFFECTS ON KINKING

We shall now analyse the kinking of an aligned-fibre composite, taking into account the influence of plastic strain-hardening in the matrix. Combined compression and

shear loading of the composite will be considered, as will arbitrary kink-band orientations. As in previous studies (e.g., FLECK and BUDIANSKY, 1991), fibre inextensibility will be assumed, and fibre bending resistance will be neglected. A critical assessment of the assumptions of fibre inextensibility will be made later in this paper. The significance of fibre bending will be addressed in a future publication.

We presume that in the presence of remotely applied compressive and shear stresses  $\sigma'$  and  $\tau'$ , there exists a kinked band (see Fig. 1) of infinite extent and finite width  $w$ , currently oriented at an angle  $\beta$ . With  $\sigma' = \tau' = 0$ , the band is imagined to have an initial orientation angle  $\beta_0$ , and is given an initial imperfection characterized by a uniform fibre rotation  $\bar{\phi}$ . We smear out the material to obtain an anisotropic continuum in a state of plane strain. Neglecting the fibre bending stiffness implies that the continuum is free of couple stresses, and that, in effect, the fibres are broken at the two boundaries of the kink band. The deformation state is considered to be homogeneous but different inside and outside of the band. By asserting the continuity of tractions and displacements on the boundary of the band, and making use of the equations of equilibrium, kinematics and assumed constitutive relations for the anisotropic solid, the additional rotation  $\phi$  inside the band, and its relation to the externally applied compressive and shear stresses  $\sigma'$  and  $\tau'$ , may be deduced.

### Kinking equilibrium

As shown in Fig. 1, we let  $(\mathbf{e}_1, \mathbf{e}_2)$  and  $(\mathbf{e}_1, \mathbf{e}_2)$  be unit vectors parallel and perpendicular to the fibres outside and inside the kink band, respectively. Equating the tractions on each side of the band boundary gives

$$\mathbf{n} \cdot \boldsymbol{\sigma}' = \mathbf{n} \cdot \boldsymbol{\sigma}, \quad (5)$$

where  $\mathbf{n} = \mathbf{e}_1 \cos \beta + \mathbf{e}_2 \sin \beta$  is the unit normal to the band, the remote stress tensor  $\boldsymbol{\sigma}'$  is

$$\boldsymbol{\sigma}' = -\sigma' \mathbf{e}_1 \mathbf{e}_1 + \tau' (\mathbf{e}_1 \mathbf{e}_2 + \mathbf{e}_2 \mathbf{e}_1) \quad (6)$$

and the stress tensor  $\boldsymbol{\sigma}$  inside the band is

$$\boldsymbol{\sigma} = \sigma_L \mathbf{e}_1 \mathbf{e}_1 + \sigma_T \mathbf{e}_2 \mathbf{e}_2 + \tau (\mathbf{e}_1 \mathbf{e}_2 + \mathbf{e}_2 \mathbf{e}_1). \quad (7)$$

Substitution of (6) and (7) into (5), and use of the connections

$$\mathbf{e}_1 = \mathbf{e}_1 \cos (\phi + \bar{\phi}) - \mathbf{e}_2 \sin (\phi + \bar{\phi}), \quad (8a)$$

$$\mathbf{e}_2 = \mathbf{e}_1 \sin (\phi + \bar{\phi}) + \mathbf{e}_2 \cos (\phi + \bar{\phi}), \quad (8b)$$

gives the two equilibrium statements

$$-\sigma' \cos \beta \cos (\bar{\phi} + \phi) + \tau' \sin (\beta + \bar{\phi} + \phi) = \tau \sin (\beta - \bar{\phi} - \phi) + \sigma_L \cos (\beta - \bar{\phi} - \phi), \quad (9)$$

$$\sigma' \cos \beta \sin (\bar{\phi} + \phi) + \tau' \cos (\beta + \bar{\phi} + \phi) = \tau \cos (\beta - \bar{\phi} - \phi) + \sigma_T \sin (\beta - \bar{\phi} - \phi). \quad (10)$$

The longitudinal stress  $\sigma_L$  along the fibre direction in the band is of limited interest (because the fibres are inextensible) and we need consider (9) no further. The stress

components and  $\sigma_T$  and  $\tau$  will appear in the constitutive relations of the composite material, and (10) will play a central role in the calculation of the kinking response.

We assume henceforth that the initial imperfection  $\bar{\phi}$  is small, and we anticipate that consideration of only small additional rotations  $\phi$  will suffice to determine kinking strengths. Accordingly, it is appropriate to linearize (10) with respect to  $\phi$  and  $\bar{\phi}$ . The linearized equation can be written in the form

$$(\phi + \bar{\phi})(\sigma' \cos \beta - 2\tau' \sin \beta) = [\tau - \tau'][\cos \beta + (\phi + \bar{\phi}) \sin \beta] + \sigma_T[\sin \beta - (\phi + \bar{\phi}) \cos \beta]. \quad (11)$$

We can simplify further, dropping the terms containing  $(\phi + \bar{\phi})$  in each of the square brackets on the right-hand side of (11) to get

$$\sigma' - 2\tau' \tan \beta = \frac{\tau - \tau' + \sigma_T \tan \beta}{\phi + \bar{\phi}} \quad (12)$$

as the connection between the applied stresses ( $\sigma'$ ,  $\tau'$ ), the rotation  $\phi$ , and the stresses  $\tau$  and  $\sigma_T$  that develop in the kinked band.

(We note, incidentally, that the time derivatives  $\dot{\sigma}_T$  and  $\dot{\tau}$  of the stresses defined, as shown in Fig. 1, with respect to the rotating fibre directions are objective stress rates which are *not* equal to the Jaumann stress rates. Nevertheless, they appear to be the natural choices to appear in constitutive relations that involve stress rates.)

#### Kinking kinematics

In both the kinked and unkinked regions, inextensibility implies zero strain in the fibre direction. Outside of the kink band we stipulate zero rotation, and zero direct strain transverse to the fibre direction. Accordingly, to within rigid body motion, the velocity  $\mathbf{v}$  in the unkinked region to the left of the kink (Fig. 1) is simply

$$\mathbf{v} = \dot{\gamma}^{\text{far}} \mathbf{e}_1, \quad (13)$$

where  $\dot{\gamma}^{\text{far}}$  is the remote shear strain rate parallel to the fibres. Inside the kink band the velocity of a point  $P$  is

$$\mathbf{v} = \dot{\gamma}^{\text{far}} \mathbf{e}_1 + x\dot{\phi}\mathbf{e}_2. \quad (14)$$

The strain rate tensor in the band is

$$\dot{\boldsymbol{\epsilon}} = \frac{1}{2}[\nabla \mathbf{v} + (\nabla \mathbf{v})^T], \quad (15)$$

where the superscript  $T$  denotes the transpose, and the gradient operator  $\nabla$  is

$$\nabla = \mathbf{e}_1 \frac{\partial}{\partial \xi_1} + \mathbf{e}_2 \frac{\partial}{\partial \xi_2}. \quad (16)$$

The position  $\mathbf{r}$  of point  $P$  is

$$\mathbf{r} = \xi_1 \mathbf{e}_1 + \xi_2 \mathbf{e}_2 = y(-\mathbf{e}_1 \tan \beta + \mathbf{e}_2) + x\mathbf{e}_1. \quad (17)$$

The unit-vector connections (8) then give

$$\begin{aligned} x &= \xi_1 + \xi_2 \tan(\beta - \phi - \bar{\phi}) \\ y &= \xi_2 \cos \beta \sec(\beta - \phi - \bar{\phi}) \end{aligned} \quad (18)$$

and the velocity (14), rewritten in terms of  $(\xi_1, \xi_2, \epsilon_1, \epsilon_2)$ , may be used in (15) to give the strain velocity tensor

$$\begin{aligned} \dot{\epsilon} &= \frac{1}{2}[\epsilon_1 \epsilon_2 + \epsilon_2 \epsilon_1][\dot{\phi} + \dot{\gamma}' \cos \beta \sec(\beta - \phi - \bar{\phi}) \cos(\phi + \bar{\phi}) \\ &\quad + \epsilon_2 \epsilon_2[\dot{\phi} \tan(\beta - \phi - \bar{\phi}) - \dot{\gamma}' \cos \beta \sec(\beta - \phi - \bar{\phi}) \sin(\phi + \bar{\phi})] \end{aligned} \quad (19)$$

in the kink band. However,  $\dot{\epsilon} \equiv \frac{1}{2}[\dot{\epsilon}_1 \epsilon_2 + \epsilon_2 \dot{\epsilon}_1] + \dot{\epsilon}_T \epsilon_2 \epsilon_2$ , where by definition  $\dot{\gamma}$  is the shear strain rate in the band and  $\dot{\epsilon}_T$  is the direct strain rate transverse to the fibres. Identification of this expression for  $\dot{\epsilon}$  with (19) gives

$$\dot{\gamma} = \dot{\phi} + \dot{\gamma}' \cos \beta \sec(\beta - \phi - \bar{\phi}) \cos(\phi + \bar{\phi}) \quad (20a)$$

and

$$\dot{\epsilon}_T = \dot{\phi} \tan(\beta - \phi - \bar{\phi}) - \dot{\gamma}' \cos \beta \sec(\beta - \phi - \bar{\phi}) \sin(\phi + \bar{\phi}). \quad (20b)$$

From (17),  $\dot{\mathbf{r}} = (-\gamma \beta \sec^2 \beta) \mathbf{e}_1 + x \dot{\epsilon}_1 \equiv \mathbf{v}$ , and with  $\dot{\epsilon}_1 = \dot{\phi} \epsilon_2$ , it follows from (14) that

$$\dot{\beta} = -\dot{\gamma}' \cos^2 \beta. \quad (21)$$

This integrates to

$$\tan \beta = \tan \beta^0 - \gamma'^x, \quad (22)$$

where  $\beta^0$  corresponds to the kink angle associated with vanishing remote shear strain.

For  $\gamma'^x \equiv 0$ ,  $\beta = \beta^0$  and (20a, b) may be integrated to give

$$\gamma = \phi \quad (23a)$$

and

$$e_T = \log \left[ \frac{\cos(\beta - \phi - \bar{\phi})}{\cos(\beta - \bar{\phi})} \right]. \quad (23b)$$

For small values of  $\gamma'^x$ ,  $\phi$  and  $\bar{\phi}$ , we can ignore the difference between  $\beta$  and  $\beta^0$ , linearize (20a, b), and integrate to get

$$\dot{\gamma} = \dot{\phi} + \gamma'^x, \quad (24a)$$

$$e_T = \phi \tan \beta. \quad (24b)$$

We remark here that a non-zero  $e_T$ , together with the assumptions of inextensibility and plane strain, implies that the kinked material undergoes volumetric straining. The early stages of plastic deformation in polymers (and also carbon matrices) may indeed be associated with volume changes attributable to the opening of microcracks and voids (PURSLOW, 1986). This is consistent with the observation that the von Mises effective stress for flow in polymers increases with an increase of pressure (WARD, 1983).

## Constitutive relations

The combined-stress yield condition

$$\left(\frac{\tau}{\tau_0}\right)^2 + \left(\frac{\sigma_T}{\sigma_{T0}}\right)^2 = 1 \quad (25)$$

has been used by BUDIANSKY (1983) and FLECK and BUDIANSKY (1991) for the ideally-plastic, inextensible composite. Here  $\tau_0$  and  $\sigma_{T0}$  are the plane-strain yield stresses in pure shear and pure transverse tension. This may be generalized to the strain-hardening case by defining

$$\tau_e = \sqrt{\tau^2 + \sigma_T^2} R^2 \quad (26)$$

as an effective stress that must increase during plastic straining, and using  $\tau_e(\tau, \sigma_T)$  as a plastic potential for the plastic strain rates  $\dot{\gamma}_e^p$  and  $\dot{e}_T^p$ . Note that  $\tau_e(\tau, \sigma_T)$  is a homogeneous function of degree one, that the current yield ellipse in  $(\tau, \sigma_T)$  space expands homogeneously with increasing  $\tau_e$ , and that the constant parameter  $R$ , defining the eccentricity of the yield ellipse, is the ratio  $\sigma_{T0}/\tau_0$  of the yield stresses in transverse tension and shear.

For monotonically increasing  $\tau_e$ , the flow-theory relations connecting plastic strain rates with the plastic potential may be postulated as

$$\begin{aligned} \dot{\gamma}_e^p &= F(\tau_e) \frac{\partial \tau_e}{\partial \tau} \dot{\tau}_e, \\ \dot{e}_T^p &= F(\tau_e) \frac{\partial \tau_e}{\partial \sigma_T} \dot{\tau}_e. \end{aligned} \quad (27)$$

Let  $\dot{\gamma}_e^p$  be a *work-equivalent* effective strain rate (HILL, 1979) defined by

$$\tau_e \dot{\gamma}_e^p + \sigma_T \dot{e}_T^p = \tau_e \dot{\gamma}_e^p. \quad (28)$$

It follows that

$$\dot{\gamma}_e^p = F(\tau_e) \dot{\tau}_e \quad (29)$$

and that (27) are equivalent to

$$\begin{aligned} d\gamma_e^p &= \frac{\partial \tau_e}{\partial \tau} d\tau_e, \\ de_T^p &= \frac{\partial \tau_e}{\partial \sigma_T} d\tau_e, \end{aligned} \quad (30)$$

where  $\gamma_e^p$  is an effective plastic strain that depends only on  $\tau_e$ . Further, the relationship between  $\dot{\gamma}_e^p$  and  $\tau_e$  must be the same as that between  $\dot{\gamma}^p$  and  $\tau$  in pure shear.

For proportional loading, during which  $\tau$  and  $\sigma_T$  maintains a constant ratio, the partial derivatives in (30) remain constant, and integration gives

$$\dot{\gamma}_e^p = \frac{\partial \tau_e}{\partial \tau} \dot{\gamma}^p.$$



$$e_T^p = \frac{\dot{\gamma} \tau_c}{\dot{\gamma} \sigma_T} \dot{\gamma}^p. \quad (31)$$

These relations have the form of a loading-path-independent *deformation theory* of plasticity, that we shall use in the rest of this paper, even if proportional loading conditions are not quite met. (Briefly, the justification for pursuing the easier calculations afforded by deformation theory is as follows: in the kinking problem, the kink stresses, at least up to maximum load, do stay approximately proportional, and deformation theory, reinterpreted as a *corner* theory of plasticity, is then physically acceptable (BUDIANSKY, 1959); and in plastic buckling problems, deformation theories are well-known to give better answers than flow theories.)

We can rewrite (31) as

$$\begin{aligned} \dot{\gamma}^p &= \left( \frac{\dot{\gamma}^p}{\tau_c} \right) \tau = \left( \frac{1}{G_s(\tau_c)} - \frac{1}{G} \right) \tau, \\ e_T^p &= \left( \frac{\dot{\gamma}^p}{\tau_c} \right) \frac{\sigma_T}{R^2} = \left( \frac{1}{G_s(\tau_c)} - \frac{1}{G} \right) \frac{\sigma_T}{R^2}, \end{aligned} \quad (32)$$

where the function  $G_s(\tau)$  is the pure-shear secant modulus. The total strains, elastic plus plastic, are then

$$\dot{\gamma} = \frac{\tau}{G} + \left( \frac{\dot{\gamma}^p}{\tau_c} \right) \tau = \frac{\tau}{G_s(\tau_c)} \quad (33)$$

and

$$e_T = \frac{\sigma_T}{E_T} + \left( \frac{\dot{\gamma}^p}{\tau_c} \right) \frac{\sigma_T}{R^2} = \frac{\sigma_T}{E_T} + \left( \frac{1}{G_s(\tau_c)} - \frac{1}{G} \right) \frac{\sigma_T}{R^2}, \quad (34)$$

where  $E_T$  is an effective transverse Young's modulus. (It is appreciated that imposition of the condition of plane strain on the *total* strains in the kink band would really couple the constitutive rules for the elastic and plastic components of strain, but the simple decoupled formulation should suffice for the purpose of the present exploratory studies.) We now make a final simplification of these constitutive relations, by arbitrarily setting

$$\frac{E_T}{G} = R^2 = \left( \frac{\sigma_T}{\tau_c} \right)^2 \quad (35)$$

and this lets us write

$$\begin{aligned} \dot{\gamma} &= \frac{\tau}{G_s(\tau_c)}, \\ e_T &= \frac{\sigma_T}{R^2 G_s(\tau_c)}. \end{aligned} \quad (36)$$

We note also that if we define

$$\gamma = \frac{\tau}{G(\tau)}, \quad (37)$$

we have

$$\gamma = \gamma_0 + R^2 c_f \quad (38)$$

and (36) can be rewritten as

$$\begin{aligned} \tau &= \begin{pmatrix} n \\ \tau_0 \end{pmatrix} \tau_0 \\ c_f &= \begin{pmatrix} n \\ \tau_0 \end{pmatrix} \frac{\sigma_0}{R}. \end{aligned} \quad (39)$$

To implement the constitutive relations explicitly, we shall adopt the three-parameter  $(G, \tau_0, n)$  Ramberg-Osgood representation

$$\tau = \frac{\tau_0}{G} \left[ 1 + \frac{3}{n} \left( \frac{\tau}{\tau_0} \right)^{n-1} \right] \quad (40)$$

for the shear stress-strain curve of the composite. Here, for strain-hardening,  $\tau_0$  is defined as a nominal composite yield stress for which the secant modulus  $G(\tau) = \tau/\gamma$  of the composite is reduced to 70% of its initial elastic value  $G$ . For  $n = \infty$ , (40) gives the elastic-ideally plastic stress-strain relation;  $\tau_0 = \infty$  provides elastic behaviour. If we define

$$\gamma_0 \equiv \frac{\tau_0}{G} \quad (41)$$

as the elastic strain of the composite at  $\tau = \tau_0$ , we can write the non-dimensional relations

$$\frac{\tau}{\tau_0} = \frac{\tau}{\tau_0} + \frac{3}{n} \left( \frac{\tau}{\tau_0} \right)^n \quad (42)$$

and

$$\frac{G}{G_0(\tau)} = 1 + \frac{3}{n} \left( \frac{\tau}{\tau_0} \right)^{n-1}. \quad (43)$$

Under combined stressing (40), (42) and (43) remain valid with  $\tau$  and  $\gamma$  replaced by  $\tau_c$  and  $\gamma_c$ .

#### *Kinking analysis and results for pure compression loading: experimental data*

We consider first the case of zero kink angle  $\beta$ , for which  $c_f = 0$  for small rotation  $\phi$ . For a given initial rotation  $\bar{\phi}$  (assumed positive here and henceforth) and a pure compressive loading stress  $\sigma'$ , the equilibrium equation (12) gives

$$\sigma' = \frac{\tau}{\phi + \bar{\phi}} \quad (44)$$

in the kink band. With  $\phi = \gamma$  from (23a), we get

$$\frac{\sigma}{G} = \frac{\tau \gamma}{\gamma \gamma + \bar{\phi} \gamma} \quad (45)$$

and with the use of the Ramberg-Osgood relation (42) this is found to be a maximum with respect to  $\tau \gamma$ , and hence  $\phi$ , at

$$\tau \gamma = \left[ \frac{7(\bar{\phi} \gamma)}{3(n-1)} \right]^{1/n} \quad (46)$$

and

$$\phi \gamma = \tau \gamma = \left[ \frac{7(\bar{\phi} \gamma)}{3(n-1)} \right]^{1/n} + \frac{\bar{\phi} \gamma}{n-1}. \quad (47)$$

The corresponding maximum value of (45) provides the kinking stress  $\sigma_c$  given by

$$\frac{\sigma_c}{G} = \frac{1}{1 + n \left( \frac{1}{3} \right)^{1/n} \left( \frac{\bar{\phi} \gamma}{n-1} \right)^{n-1/n}} \quad (48)$$

For  $n = \infty$ , this reduces to the elastic-perfectly plastic result of (4).

Equation (48) may be regarded as a knockdown factor that must be applied to the elastic (Rosen) kinking stress due to plasticity and initial imperfections. Figure 4 shows how  $\sigma_c/G$  varies with  $\bar{\phi} \gamma$  for  $n = 3, 5, 9$  and  $\infty$ . Note that strain-hardening does not change the elastic-perfectly plastic value of  $\sigma_c$  very much.

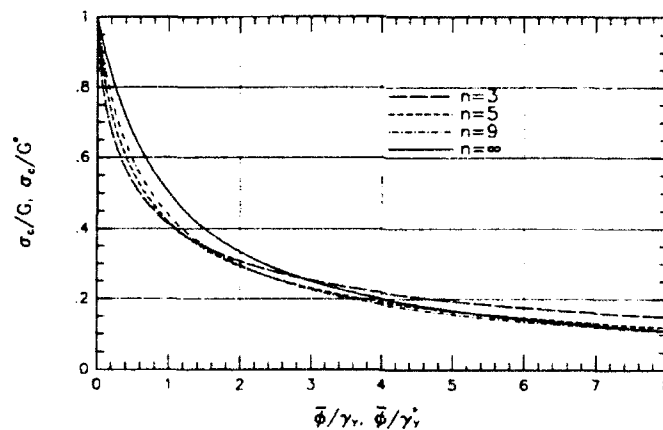


FIG. 4. Non-dimensional kinking stress ratio  $\sigma_c/G$  vs imperfection ratio  $\bar{\phi} \gamma$  ( $\beta = 0$ ), or  $\sigma_c/G^*$  vs  $\bar{\phi} \gamma^*$  ( $\beta > 0$ ), for various values of the Ramberg-Osgood hardening parameter  $n$  ( $G^* = \alpha^2 G$ ,  $\gamma^* = \gamma/\alpha$ ,  $\alpha^2 = 1 + R^2 \tan^2 \beta$ ,  $R = \sigma_{T1}/\tau_{11}$ ).

For a given imperfection size  $\bar{\phi} \gamma_1$  we can minimize (48) with respect to  $n$  in order to determine the largest possible effect of strain-hardening plasticity on the kinking stress. The resulting minimum value of  $\sigma_c/G$  is

$$\left(\frac{\sigma_c}{G}\right)_{\min} = (1 + \bar{\phi} \gamma_1)^{-1} \quad (49)$$

for the value

$$n = 1 + \frac{1}{2}(\bar{\phi} \gamma_1) \quad (50)$$

of the strain-hardening index.

For a given  $\bar{\phi} \gamma_1$ , the result (49) and the largest prediction of (48) for  $n$  in the range  $(3, \infty)$  prescribe plausible theoretical bounds for  $\sigma_c$ . These bounds are compared in Fig. 5 with the experimental data of Fig. 2, as well as with the portion of the Piggott-Harris data for kinking of Fig. 3. The lower boundary of each shaded band represents the minimum  $\sigma_c$  given by (49); the top boundary is given by  $n = \infty$  for  $\bar{\phi} \gamma_1 = 1$  and 2, and by  $n = 3$  for  $\bar{\phi} \gamma_1 = 4$  and 8. The conclusion we draw from this comparison is that the inferred predominant values of  $\bar{\phi} \gamma_1 \approx 4$  are hardly changed from the earlier estimate made on the basis of  $n = \infty$ . However all of this, of course, is still for an assumed kink angle  $\beta = 0$ .

We can now easily modify the analysis to cover  $\beta > 0$ . Equation (12) becomes (with  $\tau'$  still zero)

$$\sigma' = \frac{\tau + \sigma_T \tan \beta}{\phi + \bar{\phi}} \quad (51)$$

With  $\gamma_1' = 0$ , and  $\phi$  positive, (24), (38)–(39) imply

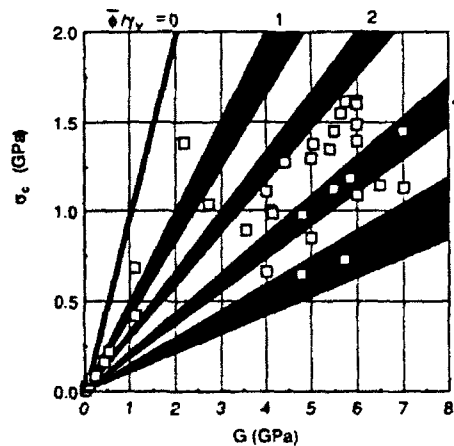


FIG. 5. Test data and elastic strain-hardening predictions for  $\beta = 0$ ; the shaded region for each  $\bar{\phi} \gamma_1$  shows the range of the theoretical results for  $n$  in  $(3, \infty)$ .

$$\tau + \sigma_f \tan \beta = \tau_c \sqrt{1 + R^2 \tan^2 \beta} \quad (52)$$

and

$$\gamma_c = \phi_c \sqrt{1 + R^2 \tan^2 \beta}. \quad (53)$$

If we introduce the definitions

$$x \equiv \sqrt{1 + R^2 \tan^2 \beta}, \quad (54)$$

$$\gamma^* \equiv \gamma_c x, \quad (55)$$

$$G^* \equiv x^2 G, \quad (56)$$

then (51) implies

$$\frac{\sigma_c}{G^*} = \frac{\tau_c}{\gamma_c} \frac{\tau_c}{\gamma_c + \bar{\phi} \gamma^*}. \quad (57)$$

Comparing this with (45), and remembering that (42) holds with  $\tau$  and  $\gamma$  replaced by  $\tau_c$  and  $\gamma_c$ , shows that the earlier result for the kinking stress given by (48) continues to apply with  $G$  and  $\gamma$ , replaced by  $G^*$  and  $\gamma^*$ . Hence,

$$\frac{\sigma_c}{G^*} = \frac{1}{1 + n(\frac{1}{2})^{1/n} \left( \frac{\bar{\phi} \gamma^*}{n-1} \right)^{(n-1)/n}}, \quad (58)$$

which provides the curves previously plotted in Fig. 4.

To see how the comparison with experimental data is modified for a typical kink angle, it is convenient to rewrite (58) in the form

$$\frac{\sigma_c}{G} = \frac{1 + R^2 \tan^2 \beta}{1 + n(\frac{1}{2})^{1/n} \left[ \frac{\bar{\phi} \gamma_c}{n-1} \sqrt{1 + R^2 \tan^2 \beta} \right]^{(n-1)/n}}. \quad (59)$$

For a given value of  $\bar{\phi} \gamma_c$ , this has the minimum value

$$\left( \frac{\sigma_c}{G} \right)_{\min} = [1 + R^2 \tan^2 \beta]^{1/2} + (\bar{\phi} \gamma_c) \sqrt{1 + R^2 \tan^2 \beta} \quad (60)$$

for

$$n = 1 + \frac{2}{3} (\bar{\phi} \gamma_c) \sqrt{1 + R^2 \tan^2 \beta}. \quad (61)$$

Once again, we show the experimental data for  $\sigma_c$  vs  $G$  in Fig. 6, but the theoretical bands for each  $\bar{\phi} \gamma_c$  are now based on (60)–(61) for  $n$  in (3,  $\infty$ ), with  $\beta = 20^\circ$  and  $R^2 = E_T/G = (\sigma_{T1}/\tau_1)^2 = 4$ . (The heavy solid line has been kept at the elastic prediction for  $\beta = 0$ .) The inferred characteristic average values of  $\bar{\phi} \gamma_c \approx 5$ , and hence  $\bar{\phi} \approx 3$ , are now somewhat larger than those estimated on the basis of  $\beta = 0$ .

The present analysis does not predict observed kink angles; for any given  $n$  and  $\bar{\phi} \gamma_c$ , the lowest value of  $\sigma_c$  predicted by (59) always corresponds to  $\beta = 0$ . A separate study (BUDIANSKY, 1983) suggests that the non-uniform waviness induced by com-

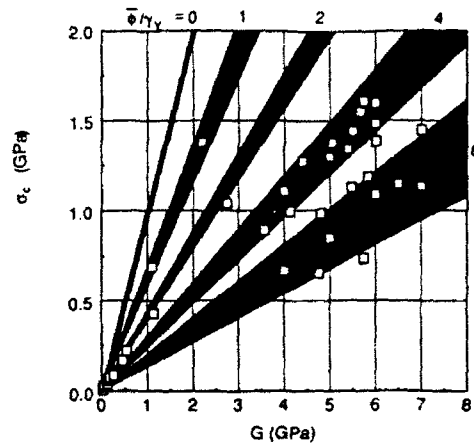


FIG. 6. Test data and strain-hardening predictions for  $\beta = 20$  and  $E_T G = (\sigma_T/\tau_Y)^2 = 4$ ; the shaded region for each  $\bar{\phi}/\gamma_Y$  shows the range of the theoretical results for  $n$  in (3,  $\infty$ ).

pressive load acting on localized fibre misalignments tends to organize itself into skewed patterns that lock the kinking into inclined bands.

The Ramberg-Osgood stress-strain equation has facilitated numerical studies of strain-hardening effects, but its use is not, of course, essential. [Some early plastic kinking calculations by CHATTERJEE and McLAUGHLIN (1979) for  $\beta = 0$  were, in fact, based on (44), and the use of a bilinear  $\tau$ - $\gamma$  relation.] We conclude this section by showing, for an arbitrary  $\tau_c$ - $\gamma_c$  relation, a simple graphical interpretation of the maximization of  $\sigma'$ , as given by (51), to get  $\sigma_c$ . [The same kind of construction has been described by BATDORF and KO (1987) and others for similar equations: the idea may be traced back to Considère in the last century, in connection with the ultimate tensile strength of ductile bars.] It is convenient to work with (57) for  $\sigma'/G^*$ , with  $\gamma_Y$  now defined arbitrarily, but  $\gamma_Y^*$  and  $G^*$  still given by (55)–(56). Figure 7 shows the normalized stress-strain curve of  $\tau_c/\tau_Y$  vs  $\gamma_c/\gamma_Y$ . The point  $A$  has the coordinates  $(-\bar{\phi}/\gamma_Y^*, 0)$ , and so, by (57), as the point  $P$  moves up along the stress-strain curve,

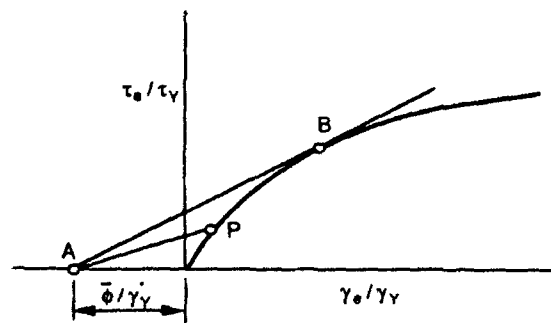


FIG. 7. Considère diagram:  $\sigma_c/G^*$  is equal to the slope of line  $AB$ .

the slope of the line  $AP$  is  $\sigma' / G^*$ . This slope is a maximum, and therefore equal to  $\sigma_c / G^*$ , when  $P$  reaches the point  $B$  where  $AB$  is tangent to the curve.

#### *Kinking analysis and results, combined compression and shear*

We shall assume that the remotely applied shear stress  $\tau'$  is fixed during the subsequent compressive loading (see Fig. 1), and consider first the case  $\beta = 0$ . Using  $\phi = \gamma - \gamma'$  (24a) in (12) gives

$$\sigma' = \frac{\tau - \tau'}{\gamma - \gamma' + \phi} \quad (62)$$

(This differs slightly from the equation given by BATDORF and KO (1987), who appear to have been the first to consider the effect of applied shear stress on kinking: they omit the term  $\gamma'$ .) Non-dimensionalizing, we get

$$\frac{\sigma'}{G} = \frac{\tau/\tau_y - \tau'/\tau_y}{(\gamma/\gamma_y - \gamma'/\gamma_y) + \bar{\phi}/\gamma_y} \quad (63)$$

Figure 8(a) shows how to modify the Considère diagram of Fig. 7 in order to represent (63). The slope of the tangent line  $AB$  still gives  $\sigma_c/G$ , but now the coordinates of the point  $A$  are at  $(-\bar{\phi}/\gamma_y + \gamma'/\gamma_y, \tau'/\tau_y)$ . The modified Considère diagram for the case of an elastic-ideally plastic material ( $n = \infty$ ) is shown in Fig. 8(b). Ideal plasticity requires that we keep  $\tau' < \tau_y$ . The slope of  $AB$  is  $(1 - \tau'/\tau_y)/(1 - \gamma'/\gamma_y + \bar{\phi}/\gamma_y)$ , and so

$$\frac{\sigma_c}{G} = \left[ 1 + \left( \frac{\bar{\phi}/\gamma_y}{1 - \tau'/\tau_y} \right) \right]^{-1} \quad (64)$$

for ideal plasticity. In this case, therefore, the effect of an applied shear stress is exactly equivalent to that of an increased initial fibre misalignment.

To compute  $\sigma_c$  in the case of strain-hardening, we write

$$t = \tau/\tau_y, \quad \eta = \gamma/\gamma_y, \quad t^x = t^x/\tau_y, \quad \text{and} \quad \eta^x = \gamma^x/\gamma_y \quad (65)$$

in (63) and set  $d(\sigma^x/G)/dt = 0$  to get

$$\begin{aligned} \sigma_c/G &= 1/\eta'(t), \\ \bar{\phi}/\gamma_y &= \frac{t - t^x}{\sigma_c/G} - \eta + \eta^x \end{aligned} \quad (66)$$

as combinations of  $\sigma_c/G$  and  $\bar{\phi}/\gamma_y$  generated parametrically by values of  $t > t^x$ . This holds for smooth stress-strain curves, for which  $\eta(t)$  is a continuously differentiable, monotonically increasing function of  $t$ , and  $\eta'(t) \equiv d\eta/dt$ .

For Ramberg-Osgood stress-strain relations, the formula for  $\eta(t)$  given by (42) was used in (66) to generate the curves for  $n = 3$  in Fig. 9(a), for  $\tau^x/\tau_y = 0, 0.5$  and  $0.8$ . The corresponding curves for  $n = \infty$ , based on (65), are shown in Fig. 9(b).

Turning next to the consideration of  $\beta \neq 0$ , we substitute the constitutive relations (39) and the strain-rotation formulas (24) in the equilibrium equation (12) to get

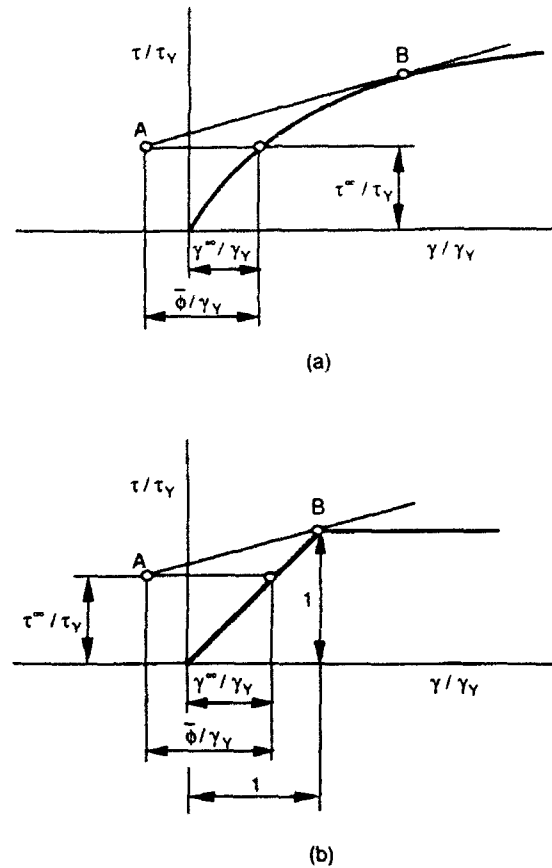


FIG. 8. Modified Considère diagrams for combined compression and shear, with  $\beta = 0$ . For both (a) strain-hardening and (b) ideal plasticity,  $\sigma_c/G$  is equal to the slope of line AB.

$$\sigma' - 2\tau' \tan \beta = \frac{[(1 + R^2 \tan^2 \beta)\phi + \gamma']\tau_c - \tau' \gamma_c}{(\phi + \bar{\phi})\gamma_c}, \quad (67a)$$

where

$$\gamma_c^2 = (1 + R^2 \tan^2 \beta)\phi^2 + 2\phi\gamma' + (\gamma')^2. \quad (67b)$$

With the adjusted definitions  $t = t_c/\tau_c$ ,  $\eta = \gamma_c/\gamma'$ , the notational substitutions  $\omega = \phi/\gamma'$ ,  $\bar{\omega} = \bar{\phi}/\gamma'$ , and the definition (54) for  $\alpha$ , we find

$$A \equiv \frac{\sigma' - 2\tau' \tan \beta}{G} = \frac{(t\eta)[\alpha^2\omega + \eta'] - t'}{\omega + \bar{\omega}}, \quad (68)$$

where



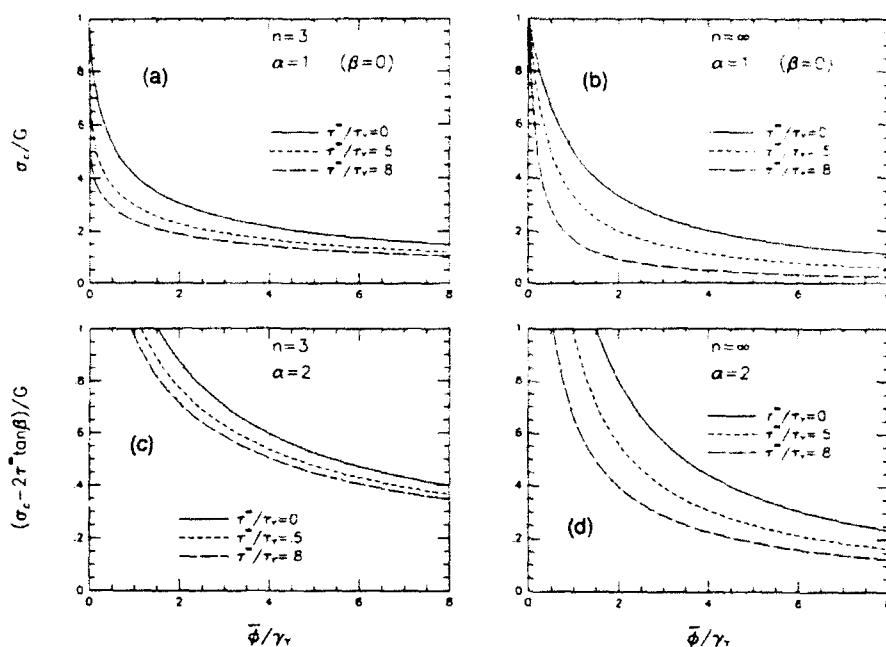


FIG. 9. Theoretical results for kinking under combined shear and compression:  $x^2 = 1 + R^2 \tan^2 \beta$ ,  $R = \sigma_r / \tau_r$ .

$$\eta = \sqrt{x^2 \omega^2 + 2\omega \eta^x + (\eta^x)^2}. \quad (69)$$

Setting  $dA/d\omega = 0$  leads to the parametric equations

$$A_c \equiv \frac{\sigma_c - 2\tau^* \tan \beta}{G} = x^2 \frac{dt}{d\eta} + \left[ \frac{t}{\eta} - \frac{dt}{d\eta} \right] \left[ \frac{\eta^x}{\eta} \right]^2 [x^2 - 1],$$

$$\bar{\omega} \equiv \frac{\bar{\phi}}{\gamma_r} = \frac{(\tau/\eta)[x^2 \omega + \eta^x] - t^x}{A_c} - \omega \quad (70)$$

for  $A_c$  vs  $\bar{\omega}$ . An efficient procedure to generate the solution for a given value of  $t^x$  (and hence  $\eta^x$ ) is to assume values of  $\omega$ , get  $\eta$  via (69), and find  $t$  and  $dt/d\eta$  from the shear stress-strain relation, inverting it numerically, if necessary. Unfortunately, there does not appear to be a neat Considère diagram that goes with these results for  $\beta > 0$ . Furthermore, although we were able to parameterize  $x$  out of the results for  $\tau^* = 0$  [see (58a, b)], this is not possible for  $\tau^* > 0$ . For this reason, it is no longer useful to show results for the kinking stress as a function of the modified imperfection parameter  $\bar{\phi}/\gamma_r^*$ . Thus, Fig. 9(c) shows the numerical results produced by (70) for  $A_c$  vs  $\bar{\omega} = \bar{\phi}/\gamma_r$ , for  $n = 3$  and  $x = 2$ .

For  $n = \infty$ , we must again assume  $\tau^* / \tau_r < 1$ , as we did for  $\beta = 0$ , and in the expression (68) for  $A$  we can set  $\eta^x = t^x$ . For  $\tau^* = 0$ , the maximum value of  $A$  is attained at the onset of plasticity, but not necessarily for  $\tau^* > 0$ . For any given value

of  $\tau'/\tau_y$ , there is a critical transition value  $\bar{\phi}_T$  such that, for  $\bar{\phi}/\gamma_y < \bar{\phi}_T$ ,  $A_c$  is given by the yield condition  $\eta = 1$  in (68). For higher values of  $\bar{\phi}/\gamma_y$ , (70) (with  $dt/d\eta = 0$ ) govern the relation between  $A_c$  and  $\bar{\phi}$ . In the examples shown in Fig. 9(d) for  $n = \infty$ , the transition values  $\bar{\phi}_T$  were found to be 1.411 and 0.174, for  $\tau'/\tau_y = 0.5$  and 0.8, respectively. For  $\bar{\phi} > \bar{\phi}_T$  the stress state  $(\tau, \sigma_f)$  moves around the yield locus (25) between the onset of yield and the attainment of the maximum applied stress  $\sigma_a$ , and so the loading is far from proportional. The applicability of a deformation theory therefore becomes questionable, but as in buckling problems generally, the results for  $\sigma_c$  are lower than those that would be given by a possibly more realistic flow theory, and are therefore conservative. However these reservations should not be taken too seriously, since the yield condition (25) is anyhow arbitrary, imperfection magnitudes are uncertain, and the present results for  $\beta \neq 0$  should be regarded as indicative of trends rather than precise predictions.

It should be noted that for  $\tau'/\tau_y \leq 1$ , the term containing  $\tau'$  in the numerator of the expression in (70) for  $A_c$  is usually negligible compared to  $\sigma_c$ , because  $\tau' \cdot G \approx \gamma_y(\tau'/\tau_y)$  is small compared to  $A_c$ . So  $A_c$  is a good approximation to  $\sigma_c/G$ . Note, however, that  $\sigma_c$  will be slightly smaller for  $\beta < 0$  than for  $\beta > 0$ .

Fairly straightforward solution techniques can be used on (68)–(70) to generate results for  $A_c$  vs  $\tau'/\tau_y$  for assigned values of  $\bar{\phi}/\gamma_y$ . This has been done to evaluate the *shear knockdown factor*  $T$ , defined as

$$T \equiv \frac{A_c}{(\sigma_c/G)_{\tau'=0}} = \frac{\sigma_c - 2\tau' \tan \beta}{\sigma_c|_{\tau'=0}}. \quad (71)$$

Here, for a Ramberg–Osgood material, the denominator is simply specified by (48). The results for  $T$  vs  $\tau'/\tau_y$  are shown in Fig. 10, for  $\bar{\phi}/\gamma_y = 2, 4$  and 8, for  $\alpha = 1, 2$ , and  $n = 3, 5$  and  $\infty$ . Again, since we can usually neglect the second term in the numerator of (71),  $T$  represents the *extra* knockdown factor that should be applied to the result (48) for  $\sigma_c$  to account for the presence of applied shear stress, while (48) itself is the knockdown factor applied to the Rosen result to account for fibre imperfection. Note that for  $\bar{\phi}/\gamma_y \geq 2$ ,  $T$  does not vary much with the size of the fibre misalignment.

#### EFFECTS OF FINITE FIBRE STIFFNESS

In this part of the paper we shall study and assess the simplifying assumption made in the kinking analysis that the fibres are infinitely stiff in their longitudinal directions. The main effect of finite axial fibre stiffness is to let the matrix carry a portion of the applied compressive stress, which can then interact with matrix shear and transverse stress to raise the level of plasticity, and lower the resistance to kinking. We shall demonstrate that, at least as far as organic-matrix composites are concerned, the rigid-fibre simplifying assumption does not have much effect on the validity of our kinking-stress calculations.

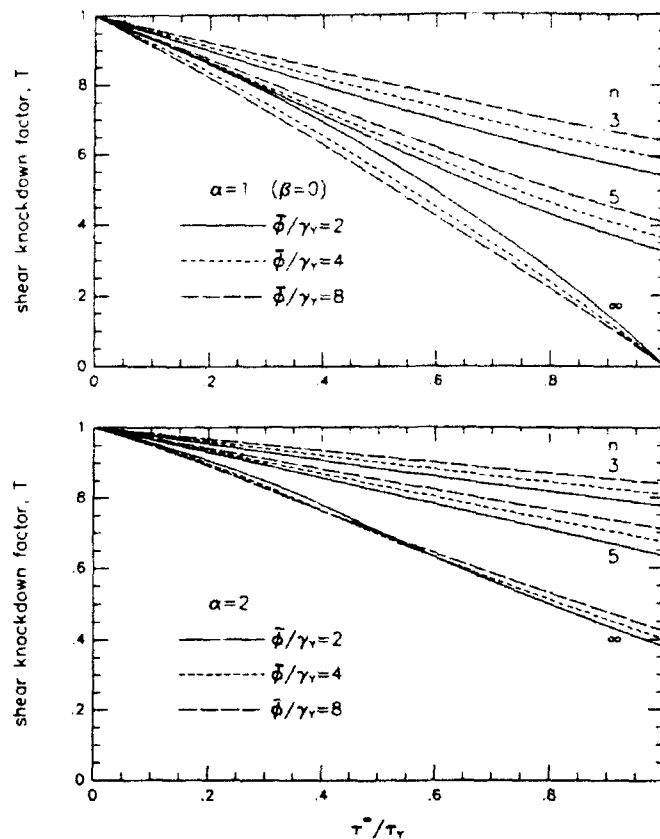


FIG. 10. Shear knockdown factor  $T$  vs  $\tau^*/\tau_c$ . For  $\beta = 0$ ,  $T$  is the ratio of the compressive kinking stress when shear is present to the pure-compression kinking stress, and is close to this ratio for  $\beta > 0$ .

#### Perfectly aligned fibres

In a recent paper, ROSEN (1989) considered the influence of axial matrix compression on the microbuckling stress of composites having straight, perfectly aligned fibres, and for a Ramberg-Osgood value of  $n = 3$ , calculated a kinking stress on the basis of an effective, plasticity-reduced shear modulus used in place of the elastic shear modulus in his classical formula (1). In effect, Rosen used a deformation theory of plasticity to calculate this reduced modulus, and so shall we, but with a more accurate analysis of the pre-buckling stress state, and with more generality. We simplify matters greatly by limiting this study to  $\beta = 0$ , which lets us consider just combinations of shear  $\tau_m$  and axial stress  $\sigma_m$  in the matrix.

Under the assumptions of initial isotropy and plastic incompressibility, *all* deformation theories of plasticity give the following result for the effective, initial shear modulus  $\bar{G}_m$  of the matrix material when it is subjected to a purely uniaxial stress (PETERS *et al.*, 1950):

$$\bar{G}_m = \left[ \frac{1}{G_m} + \frac{3}{E_{m_s}(\sigma_m)} - \frac{3}{E_m} \right]^{-1} \quad (72)$$

where, as indicated, the secant modulus  $E_{m_s}$  of the matrix is a function of  $\sigma_m$ . It follows that the plastic bifurcation-buckling stress [see (1)] is now

$$\sigma_c = \frac{\bar{G}_m}{1 - \nu_f} \quad (73)$$

and with  $G \equiv G_m (1 - \nu_f)$ ,

$$\frac{\sigma_c}{G} = \left[ 1 + \rho \left( \frac{E_m}{E_{m_s}(\sigma_m)} - 1 \right) \right]^{-1} \quad (74)$$

where

$$\rho = 3G_m/E_m = 3/2(1 + \nu_m). \quad (75)$$

Here  $E_{m_s}$  depends on the value of  $\sigma_m$  when the critical stress  $\sigma_c$  is applied. These stresses, and the corresponding fibre stress  $\sigma_f$ , are connected by the very accurate rule-of-mixtures relation

$$\sigma_c = (1 - \nu_f)\sigma_m + \nu_f\sigma_f \quad (76)$$

and the compatibility equation

$$\sigma_m/E_{m_s}(\sigma_m) = \sigma_f/E_f \quad (77)$$

where  $E_f$  is the modulus of the fibre, presumed to stay elastic. From these two relations we can derive another equation that relates  $\sigma_c$  and  $\sigma_m$ , to wit:

$$\frac{\sigma_c}{G} = \frac{\sigma_m(1 - \nu_f)}{G_m} \left[ 1 - \nu_f + \nu_f \frac{E_f}{E_{m_s}(\sigma_m)} \right] \quad (78)$$

In principle, then, for any uniaxial relation between  $E_{m_s}$  and  $\sigma_m$ , (74) and (78) can be solved simultaneously to get  $\sigma_c$ . It will be convenient, however, to show an explicit result for a Ramberg-Osgood family of matrix compression curves having the form

$$\frac{\epsilon_m^*}{\epsilon_{mY}} = \frac{\sigma_m}{\sigma_{mY}} + a \left( \frac{\sigma_m}{\sigma_{mY}} \right)^n \quad (79)$$

Here  $\sigma_{mY}$  is a nominal matrix yield stress,  $\epsilon_{mY} \equiv \sigma_{mY}/E_m$ , and  $a$  is a constant that, for the moment, we need not specify, except to note that  $E_m/E_{m_s} = (1 + a)$  at  $\sigma_m = \sigma_{mY}$ . It follows that

$$\left( \frac{E_m}{E_{m_s}} - 1 \right) = a \left( \frac{\sigma_m}{\sigma_{mY}} \right)^{n-1} \quad (80)$$

and  $\sigma_m$ ,  $\sigma_{mY}$  can be eliminated from (74) and (78) to give

$$\epsilon_m = \frac{\Lambda \left[ \frac{\rho d \Lambda}{1 - \Lambda} \right]^{1/(n-1)}}{2(1 - \nu_f)(1 + \nu_m) \left[ 1 - \nu_f + \frac{\nu_f E_f}{E_m} \left( 1 + \frac{1 - \Lambda}{\rho \Lambda} \right) \right]} \quad (81)$$

where  $\Lambda \equiv \sigma_f/G = \bar{G}_m/G_m$  is the *plasticity knockdown factor* for bifurcation buckling. This provides an explicit relation between the plasticity knockdown factor for the perfect-fibre composite and the nominal compressive yield strain of the matrix material.

We emphasize that this result is valid for *all* deformation theories of plasticity. We also mention, in passing, that all flow theories having smooth yield surfaces would predict *no* plasticity knockdown, because in such theories the initial shear modulus in the presence of an arbitrary axial stress remains equal to elastic value.

Before we show numerical examples, it will be useful to specialize to the familiar  $J_2$ -deformation theory in which the effective matrix stress for combined shear and compression is defined by

$$\sigma_{me} = \sqrt{\sigma_m^2 + 3\tau_m^2} \quad (82)$$

and the plastic strains are given by

$$\epsilon_m^p = \left[ \frac{E_m}{E_m(\sigma_{me})} - 1 \right] \frac{\sigma_m}{E_m} \quad (83a)$$

$$\gamma_m^p = 3 \left[ \frac{E_m}{E_m(\sigma_{me})} - 1 \right] \frac{\tau_m}{E_m} \quad (83b)$$

Here the bracketed quantities are given by (80) with  $\sigma_m$  replaced by  $\sigma_{me}$ . We can then touch base with our previous formulations in which the shear stress-strain curve of the *composite* was given by the Ramberg-Osgood form

$$\frac{\gamma}{\gamma_y} = \frac{\tau}{\tau_y} + b \left( \frac{\tau}{\tau_y} \right)^n \quad (84)$$

with  $b = 3/7$ . As was implicit in the original Rosen equation (1), we make the rough approximations

$$\gamma = (1 - \nu_f)\gamma_m, \quad \gamma_y = (1 - \nu_f)\gamma_{my}, \quad \tau = \tau_m, \quad \tau_y = \tau_{my}, \quad (85)$$

appropriate for composites in which the longitudinal shear stiffness of the fibres is much greater than that of the matrix, to find that

$$\frac{\gamma_m}{\gamma_{my}} = \frac{\tau_m}{\tau_{my}} + b \left( \frac{\tau_m}{\tau_{my}} \right)^n \quad (86)$$

is the shear stress-strain relation of the matrix. Then, since  $\sigma_m = \tau_m \sqrt{3}$  for pure shear, comparison of (86) with (83b) shows that

$$\left[ \frac{E_m}{E_m} - 1 \right] = \frac{b}{\rho} \left( \frac{\sigma_m}{\tau_y \sqrt{3}} \right)^n \quad (87)$$

and if we introduce the definitions

$$\sigma_m = \tau_y \sqrt{3} \quad \text{and} \quad \epsilon_m = \sigma_m / E_m \quad (88)$$

we find from (83a) that for pure compression we recover (79), with  $a = b/\rho$ . Also, we have

$$\epsilon_m = \frac{\gamma_y \sqrt{3}}{2(1+\nu_m)(1-\nu_f)} \quad (89)$$

and so (81) can be rewritten in the neat form

$$\gamma_y = \frac{\Lambda \left[ \frac{b\Lambda}{1-\Lambda} \right]^{1/(n-1)}}{\sqrt{3} \left[ \frac{E}{E_m} + \left( \frac{E}{E_m} - 1 + \nu_f \right) \left( \frac{1-\Lambda}{\rho\Lambda} \right) \right]} \quad (90)$$

where we have used the rule-of-mixtures formula for the composite modulus  $E = (1-\nu_f)E_m + \nu_f E_f$  in order to express the relation between  $\Lambda$  and  $\gamma_y$  in terms of  $E/E_m$  instead of  $E_f/E_m$ .

Figure 11 shows the results given by (90) for  $\Lambda \equiv \sigma_f/G$  vs  $\gamma_y$ , for  $n = 3$  and  $\infty$ , and for  $E/E_m = 10, 30$  and  $50$ . These values of  $E/E_m$  more than cover the practical range for organic-matrix composites, which usually have values in the interval 20–40. The curves were calculated for  $\nu_f = 0.6$ , but it should be noted that for large values of  $E/E_m$ ,  $\gamma_y$  is nearly independent of  $\nu_f$ . The other constants used were  $\rho = 9/8$ , corresponding to  $\nu = 1/3$  and  $b = 3/7$ .

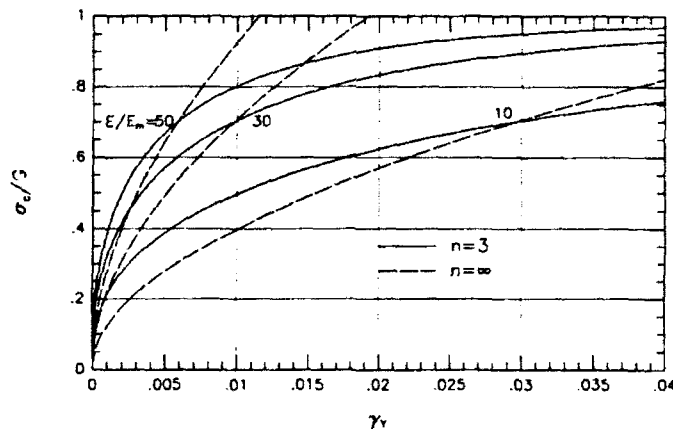


FIG. 11. Non-dimensional kinking stress ratio  $\sigma_f/G$  vs shear yield stress  $\gamma_y$  of the composite, perfectly aligned, extensional fibres. Ramberg-Osgood hardening index  $= n$ ; ratio of composite and matrix moduli  $= E/E_m$ .

It is interesting to note from (90) that for any given value of  $E/E_m$ , the curves of  $\sigma_c/G$  vs  $\gamma_1$  for all values of  $n$  intersect at the value  $\sigma_c/G = 0.7$ . Thus, for  $E/E_m = 30$ ,  $\sigma_c/G = 0.7$  at  $\gamma_1 = 0.0098$  at each  $n$ . Above this critical value of  $\gamma_1$ ,  $\sigma_c/G$  is an increasing function of  $n$ , and below it decreases with  $n$ .

The main conclusion we draw from the curves is that for realistic values of  $\gamma_1$  in the vicinity of 0.01, the reduction of  $\sigma_c/G$  from the Rosen value of unity is quite insufficient to account for most of the experimental data in Fig. 2. The typically observed experimental knockdown factors of around 1.4 are predicted by (90) only for unrealistically low values of  $\gamma_1$  and  $E/E_m$ . This further strengthens the case for the necessity of invoking initial misalignments to account for observed kinking stresses.

It remains reasonable to inquire about the plasticity effect of finite fibre stiffness on the kinking stress when initial imperfections are present. We study this question in the next section.

#### Initially misaligned fibres

If the fibres are presumed to have an initial rotation  $\bar{\phi}$  in a narrow,  $\beta = 0$  kink band, application of the remote stress  $\sigma'$  will induce a state of combined axial compression and shear ( $\sigma_m, \tau_m$ ) in the matrix, and the  $J_2$ -deformation theory relations may be written as

$$\epsilon_m = \frac{\sigma_m}{E_m(\sigma_m)} \quad (91)$$

$$\gamma_m = \left[ \frac{1}{G_m} + \frac{3}{E_m(\sigma_m)} - \frac{3}{E_m} \right] \tau_m \equiv \frac{\tau_m}{\bar{G}_m} \quad (92)$$

where  $E_m$  is now a function of the effective stress  $\sigma_{me}$  given by (82). (We are presuming a state of plane stress in the kink band, whereas it would be more appropriate to impose the condition that transverse strains in the narrow kink are constrained to equal those produced by  $\sigma'$  in the unknicked regions; but this minor simplification is unlikely to affect our conclusions very much.) Following the calculations of the previous section, we rewrite the connection (78) between  $\sigma'$  and  $\sigma_m$  as

$$\frac{\sigma'}{G} = \sqrt{3}\gamma_1 \left[ \frac{E}{E_m} + \left( \frac{E}{E_m} - 1 + \nu_f \right) \left( \frac{E_m}{E_m(\sigma_{me})} - 1 \right) \right] \frac{\sigma_m}{\sigma_m} \quad (93)$$

and the use of (92) and the approximations (85) in the equilibrium equation (45) gives

$$\frac{\sigma'}{G} = \frac{\tau \cdot \tau_1}{(\tau \cdot \tau_1)(G_m \bar{G}_m) + \bar{\phi} \cdot \gamma_1} \quad (94)$$

Rewriting (82) for  $\sigma_m$  in the form

$$\left( \frac{\sigma_m}{\sigma_m} \right)^2 = \left( \frac{\sigma_m}{\sigma_m} \right)^2 + \left( \frac{\tau}{\tau_1} \right)^2 \quad (95)$$

and using (93)–(94) to eliminate  $\sigma_m/\sigma_m$  and  $\tau/\tau_1$  gives

$$\begin{pmatrix} \sigma_{\infty} \\ \sigma_{n+1} \end{pmatrix} = \begin{pmatrix} \sigma_G \\ \bar{\sigma} \end{pmatrix} \begin{pmatrix} \bar{\phi} \\ \gamma \end{pmatrix} + \begin{pmatrix} \sigma_G \\ \bar{\sigma} \end{pmatrix} \quad (96)$$

$$\left[ 1 - \begin{pmatrix} \sigma_G \\ \bar{\sigma} \end{pmatrix} \begin{pmatrix} \bar{\phi} \\ \gamma \end{pmatrix} \right] = \lambda_{n+1} \left[ \frac{E}{E_{\infty}} - \left( \frac{E}{E_{\infty}} - 1 + \nu \right) \left( \frac{L}{L_{\infty}} - 1 \right) \right]$$

Note that the defining relation (92) for  $\bar{\sigma}$ , together with the Ramberg-Osgood formulas imply

$$\frac{G_{\infty}}{\bar{G}_{\infty}} - 1 = \rho \left( \frac{E_{\infty}}{E_{\infty}} - 1 \right) = h \left( \frac{\sigma_{\infty}}{\sigma_{n+1}} \right) \quad (97)$$

where  $\rho$  is defined by (75), and so (96) relates  $\sigma^*/G$  to  $\sigma_{\infty}/\sigma_{n+1}$ . For increasing values of  $\sigma_{\infty}/\sigma_{n+1}$ , we can solve (96) numerically for  $\sigma^*/G$ , and so find the non-dimensional kinking stress  $\sigma^*/G$  when  $\sigma^*/G$  reaches a maximum. Numerical results for  $\sigma^*/G$  vs  $\bar{\phi}/\gamma$  are shown in Fig. 12 for  $n=3$  and several values of  $\gamma$  that cover the practical

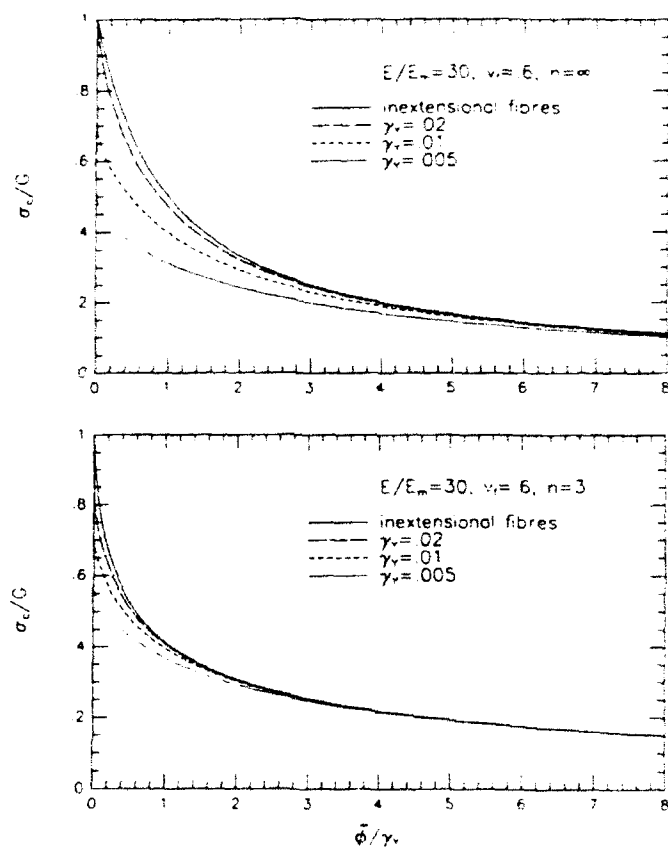


FIG. 12. Non-dimensional kinking stress ratio  $\sigma_c/G$  vs fibre imperfection ratio  $\bar{\phi}/\gamma$ , extensional fibres.



range: the inextensional-fibre result of Fig. 4 is shown for comparison. The parameters  $E/E_m = 30$  and  $\nu_r = 0.6$  were used, and it is striking that for these values, typical for polymer matrices, plasticity effects on  $\sigma_c$  of finite fibre stiffness become negligible for  $\bar{\phi}/\gamma_0 > 2$ .

The analogous set of curves for  $n = \infty$ , shown in the top part of Fig. 12 show that for high values of  $n$ , larger, but still quite small, effects of finite fibre stiffness might occur at moderate values of  $\bar{\phi}/\gamma_0$ . (The calculation of these results for  $n = \infty$  required a special set-up. Under increasing  $\sigma'/G$  the composite responds elastically until the yield condition  $\sigma_m/\sigma_{m0} = 1$  is satisfied. From (96) this implies that

$$\frac{\left(\frac{\sigma'}{G}\right)^2 \left(\frac{\bar{\phi}}{\gamma_0}\right)^2}{\left[1 - \left(\frac{\sigma'}{G}\right)^2\right]^2} + \frac{\left(\frac{\sigma'}{G}\right)^2}{3\gamma_0^2 \left[\frac{E}{E_m}\right]^2} = 1 \quad (98)$$

at yield. Thereafter, we can track the evolution of  $\sigma'/G$  by using

$$1 = \frac{\left(\frac{\sigma'}{G}\right)^2 \left(\frac{\bar{\phi}}{\gamma_0}\right)^2}{\left[1 - \left(\frac{\sigma'}{G}\right)^2 \left(\frac{G_m}{G_m^0}\right)\right]^2} + \frac{\left(\frac{\sigma'}{G}\right)^2}{3\gamma_0^2 \left[\frac{E}{E_m} + \frac{1}{\rho} \left(\frac{E}{E_m} - 1 + \nu_r\right) \left(\frac{G_m}{G_m^0} - 1\right)\right]^2} \quad (99)$$

to solve for  $\sigma'/G$  as  $G_m/G_m^0$  is increased from unity, as the independent variable. The maximum value of  $\sigma'/G$  can occur either at or beyond yield.

We conclude that when realistic imperfections are present, and the longitudinal stiffness of the composite is large ( $> 20$ ) compared to the elastic matrix stiffness, and the yield strain of the composite is not unusually low ( $< 0.005$ ), then the assumption of axially rigid fibres is well justified.

#### CONCLUDING DISCUSSION

The theoretical and experimental evidence presented in this paper shows that long fibre polymeric composites, such as carbon fibre in an epoxy matrix or glass fibre in a polyester matrix, tend to fail in compression by plastic kinking. These kinking strengths are sensitive to the initial misalignment of the fibres, and show considerable scatter. For misaligned fibres, kinking stresses in the vicinity of 25% of the elastic microbuckling stresses of composites having perfectly straight, aligned fibres are typical. The basic analyses and quantitative results presented in this paper, encompassing effects of strain-hardening, kink inclination, and applied shear stress, provide a broad basis for the understanding of the kinking phenomenon. The analysis given of the effects of finite fibre stiffness provide theoretical justification for the assumption of rigid fibres in the study of many aspects of the kinking problem. However, the present treatment of kinking is unable to predict the width of the kink band and its

inclination: in order to make these predictions, a study of the initiation and growth of kinking patterns, with explicit inclusion of fibre bending resistance, is required.

A paucity of experimental data remains on the compressive failure of long-fibre ceramic-matrix and metal-matrix composites. In such composites the fibre-matrix stiffness ratios are substantially lower than those for polymer matrices. It is therefore clear from the trends established concerning the effects of finite fibre stiffness that the rigid-fibre assumption in the theoretical study of kinking in ceramic and metal matrix composites might not be justified. The importance of kinking as a failure mode in such composites has not been established.

#### ACKNOWLEDGMENTS

This work was supported in part by the National Science Foundation under a Material Research Laboratory grant (DMR-89-20490), in part by a DARPA University Research Initiative grant (Subagreement P.O. No. VB38639-0 with the University of California, Santa Barbara, ONR Prime Contract 00014-86-K-0753), and by the Division of Applied Sciences, Harvard University. The authors are also grateful for funding from the Procurement Executive of the Ministry of Defence, under a joint SERC MOD contract, and for support from the ONR contract 00014-91-J-1916.

#### REFERENCES

- |  |      |  |
|--|------|--|
| ARGON, A. S.                               | 1972 | In <i>Treatise of Materials Science and Technology</i> , Vol. 1. Academic Press, New York.   |
| BARKER, A. J. and<br>BALASUNDARAM, V.      | 1987 | <i>Composites</i> <b>18</b> (3), 217.  |
| BATDORI, S. B. and KO, R. W. C.            | 1987 | Internal report, School of Engineering and Applied Science, University of California, Los Angeles, CA 90024.   |
| BUDIANSKY, B.                              | 1959 | <i>J. Appl. Mech.</i> <b>26</b> , 259.   |
| BUDIANSKY, B.                              | 1979 | In Preliminary Reports, Memoranda and Technical Notes of the Materials Research Council Summer Conference, La Jolla, CA, July 1979. Sponsored by DARPA.                    |
| BUDIANSKY, B.                              | 1983 | <i>Comp. Struct.</i> <b>16</b> (1), 3.   |
| CHAPLIN, C. R.                             | 1977 | <i>J. Mater. Sci.</i> <b>12</b> , 347.   |
| CHATTERJEE, S. N. and<br>McLAUGHLIN, P. V. | 1979 | <i>Proc. 3rd Engineering Mechanics Div. Specialty Conf.</i> , 17-19 Sept., 1979, University of Texas at Austin, pp. 649-652. ASCE, New York.                               |
| CURTIS, P. T.                              | 1986 | RAE Tech. Report 86021.  |
| EVANS, A. G. and ADLER, W. F.              | 1978 | <i>Acta Metall.</i> <b>26</b> , 725.   |
| EWINS, P. D. and POTTIER, R. T.            | 1980 | <i>Phil. Trans. R. Soc. Lond.</i> <b>A294</b> , 507.   |
| FLECK, N. A. and BUDIANSKY, B.             | 1991 | <i>Proc. IUTAM Symp. on Inelastic Deformation of Composite Materials</i> , Troy, New York, 29 May-1 June, 1990 (edited J. DVORAK), pp. 235-273. Springer-Verlag, New York. |
| FRIED, N.                                  | 1963 | <i>Proc. 18th Annual Meeting of the Reinforced Plastics Division, Society of Plastics Industry</i> , Section 9-A, pp. 1-10.  |

- FRIED, N. and KAMINSKY, J. 1964 *Proc. 19th Annual Meeting of the Reinforced Plastics Division, Society of Plastics Industry*, Section 9-A, pp. 1-10.
- GIBSON, L. J. and ASHBY, M. F. 1988 *Cellular Solids: Structure and Properties*. Pergamon Press, Oxford.
- GRISZCZUK, L. B. 1972 AFML-TR-72107, U.S. Air Force.
- GRISZCZUK, L. B. 1975 *AIAA J.* **13**(10), 1311.
- HAHN, H. T., SOHL, M. and MOON, S. 1986 NASA CR 3988.
- HILL, R. 1979 *Math. Proc. Camb. Phil. Soc.* **55**, 179.
- JILL, P. M. and FLECK, N. A. 1991 Submitted to *J. Comp. Mater.*
- JILL, P. M., SOUTIS, C. and FLECK, N. A. 1990 Presented at 3rd. International Symposium on Composites, Patras, Greece, Sept. 1990.
- JOHNSTON, N. J. and HERGENROTHER, P. M. 1987 32nd Int. SAMPE Symposium, 6-9 April 1987.
- LAGER, J. B. and JUNI, R. R. 1969 *J. Comp. Mater.* **3**(1), 48.
- LANKFORD, J. 1989 *Mat. Sci. Engng.* **A107**, 261.
- MONCUNILL DE FERRAN, E. and HARRIS, B. 1970 *J. Comp. Mater.* **4**, 62.
- PARRY, T. V. and WRONSKI, A. S. 1981 *J. Mat. Sci.* **16**, 439.
- PETERS, R. W., DOW, N. F. and BATDORI, S. B. 1950 *Proc. Soc. Exp. Stress Analysis* **7**, 27.
- PIGGOTT, M. R. 1981 *J. Mat. Sci.* **16**, 2837.
- PIGGOTT, M. R. and HARRIS, B. 1980 *J. Mat. Sci.* **15**, 2523.
- PIGGOTT, M. R. and WILDE, P. 1980 *J. Mat. Sci.* **15**, 2811.
- PRANDY, J. M. and HAHN, H. T. 1990 *Proc. 35th International SAMPE Symposium*, 2-5 April 1990, pp. 1657-1670.
- PURSLow, D. 1986 RAE Technical Report 86046.
- RHODES, M. D., MIKULAS, M. M. and MCGOWAN, P. E. 1984 *AIAA J.* **22**(9), 1283.
- ROSEN, B. W. 1965 *Fibre Composite Materials*, Am. Soc. Metals Seminar, Chapter 3, Am. Soc. Metals.
- ROSEN, B. W. 1989 *Proc. 1st U.S. USSR Symposium on Mechanics of Composite Materials*, Riga, Latvia, May 1989. To be published by ASME.
- SOUTIS, C., FLECK, N. A. and SMITH, P. A. 1991 *J. Compos. Mater.* **25**, 1476.
- STARNES, J. H. and WILLIAMS, J. G. 1982 *Mechanics of Composites Materials—Recent Advances* (Edited by Z. HASHIN and C. T. HERAKOVICH), pp. 283-306. Pergamon Press, Oxford.
- U.S. POLYMERIC 1990 Data sheets on properties of carbon fibre epoxy composites, 700E Dyer Rd., Santa Ana, CA, 92707, USA.
- WARD, I. M. 1983 *The Mechanical Properties of Solid Polymers*, 2nd edn. Wiley, New York.
- WILKINSON, E., PARRY, T. V. and WRONSKI, A. S. 1986 *Comp. Sci. Technol.* **26**, 17.
- YOUNG, R. J. and YOUNG, R. 1990 *Proc. 4th European Conference on Composite Materials*, 25-28 September, Stuttgart, pp. 685-690. Elsevier Applied Science, Amsterdam.
- YURGARTIS, S. W. 1987 *Comp. Sci. Technol.* **30**, 279.



MECH-199

COMPRESSIVE FAILURE OF FIBRE COMPOSITES: THE ROLES OF  
MULTI-AXIAL LOADING AND CREEP

W.S. Slaughter<sup>†</sup>, N.A. Fleck<sup>†</sup>, and B. Budiansky<sup>\*</sup>

<sup>†</sup>Cambridge University Engineering Department  
Cambridge CB2 1PZ  
England

<sup>\*</sup>Division of Applied Sciences  
Harvard University  
Cambridge, Massachusetts 02138  
U.S.A.

Division of Applied Sciences  
HARVARD UNIVERSITY  
Cambridge, Massachusetts 02138

October 1992

To appear in *J. Engineering Materials and Technology*

# COMPRESSIVE FAILURE OF FIBRE COMPOSITES: THE ROLES OF MULTI-AXIAL LOADING AND CREEP

W.S. Slaughter<sup>†</sup>, N.A. Fleck<sup>†</sup>, and B. Budiansky<sup>\*</sup>

<sup>†</sup> Cambridge University Engineering Department  
Cambridge CB2 1PZ  
England

<sup>\*</sup> Division of Applied Sciences  
Harvard University  
Cambridge, Massachusetts 02138  
U.S.A.

## ABSTRACT

The roles of multi-axial loading and creep in compressive failure of aligned fibre composites are considered. Analytical models are developed based on the model given by Budiansky and Fleck (1992). The critical microbuckling stress in multi-axial loading is calculated for a rigid-perfectly plastic solid and an elastic-plastic strain hardening solid. The rigid-perfectly plastic results predict a plane compressive failure surface in stress space. The rigid-perfectly plastic results are sufficiently accurate, when compared to the strain hardening results, so long as the remote shear stress and stress normal to the fibre direction are not too large relative to the remote stress in the fibre direction. The model given for creep microbuckling is suitable for power-law viscous composite behaviour. Deformation within a localised kink band is computed as a function of time. A creep life is predicted, based on a critical strain failure criterion.

## INTRODUCTION

An important failure mechanism for aligned fibre composites in compression is microbuckling. Microbuckling is an event in which the composite suffers localised buckling within a kink band (Hull, 1981). Aligned fibre composites include polymer matrix composites, which are widely used in applications in which the benefits from their high specific tensile moduli and tensile strengths outweigh competing cost considerations, and metal matrix and ceramic matrix composites, which remain largely in the developmental stage. The mechanical properties of metal matrix and ceramic matrix composites are not as well understood as those of polymer matrix composites. Wood, in many circumstances, also behaves as an aligned fibre composite (Dinwoodie, 1981).

A serious limitation for aligned fibre composites is that they often have compressive strengths less than 60% of their tensile strengths. The dominant failure mechanism for aligned

fibre-polymer matrix composites in compression is microbuckling (Argon, 1972; Budiansky and Fleck, 1992). Microbuckling is also an important failure mechanism in woods (Grossman and Wold, 1971; Dinwoodie, 1981). The role played by microbuckling in the compressive failure of metal matrix and ceramic matrix composites is less clear, though microbuckling has been observed in aluminium alloy matrix composites (Schulte and Minoshima, 1991) and in carbon-carbon composites (Evans and Adler, 1978). Theoretical studies by Argon (1972) and Budiansky and Fleck (1992) have shown that, in polymer matrix composites, microbuckling is associated with a non-linear plastic response of the matrix. The analysis of Budiansky and Fleck (1992) for plastic microbuckling considers the effects of initial imperfections, plastic strain hardening, and combined remote shear stress and axial compression. Here we extend the Budiansky and Fleck (1992) analysis to general multi-axial loading.

Many fibre composites are known to exhibit time *dependent* deformation behaviour, or creep. These include polymer matrix composites (Horoschenkoff, *et. al.*, 1988; Ha, *et. al.*, 1991) and woods (Dinwoodie, 1981). A theoretical analysis assuming linear viscoelastic composite behaviour has previously been presented (Slaughter and Fleck, 1992). At elevated temperatures, metal matrix and ceramic matrix composites also creep. An alternative theoretical analysis of creep microbuckling, suitable for power-law viscous composite behaviour, is given here.

The structure of this paper is as follows. First, plastic kinking is analysed for general remote loading. Results are presented for a rigid-perfectly plastic solid and for a strain hardening deformation theory solid. Creep microbuckling is then addressed for a power law creeping matrix.

## GENERAL MULTI-AXIAL LOADING

Microbuckling is characterised by the formation of a kink band in which the aligned fibre composite undergoes localised failure. This kink band is on the order of ten fibre diameters in width and is *not*, in general, normal to the fibre axes. The analysis to follow, for microbuckling under general remote loading, expands upon that given by Budiansky and Fleck (1992). A schematic of the kink band is shown in Fig. 1. The kink band is of width  $w$  and forms an angle  $\beta$  with the direction normal to the fibre axes, hereafter called the transverse direction. It is assumed that the fibres are inextensible and that uniform straining within the kink band is associated with a change in fibre orientation,  $\phi$ . It is further assumed that initial misalignment within the composite is represented by the angle  $\bar{\phi}$ .

Two cartesian coordinate systems,  $(\underline{e}_1, \underline{e}_2)$  and  $(\underline{\epsilon}_1, \underline{\epsilon}_2)$ , are defined such that  $\underline{e}_1$  and  $\underline{e}_2$  are parallel and normal to the fibre axes outside the kink band, and  $\underline{\epsilon}_1$  and  $\underline{\epsilon}_2$  are parallel and normal to the fibre axes inside the kink band. These two coordinate systems are related by

$$\left. \begin{aligned} \underline{e}_1 &= \underline{e}_1 \cos(\bar{\phi} + \phi) - \underline{e}_2 \sin(\bar{\phi} + \phi) \\ \underline{e}_2 &= \underline{e}_1 \sin(\bar{\phi} + \phi) + \underline{e}_2 \cos(\bar{\phi} + \phi) \end{aligned} \right\} \quad (1)$$

The stress components outside the kink band are defined by

$$\underline{\sigma}^- = -\sigma_L^- \underline{e}_1 \underline{e}_1 + \sigma_T^- \underline{e}_2 \underline{e}_2 + \tau^- (\underline{e}_1 \underline{e}_2 + \underline{e}_2 \underline{e}_1) \quad (2)$$

and those within the kink band are defined by

$$\underline{\sigma} = \sigma_L \underline{e}_1 \underline{e}_1 + \sigma_T \underline{e}_2 \underline{e}_2 + \tau (\underline{e}_1 \underline{e}_2 + \underline{e}_2 \underline{e}_1) \quad (3)$$

In the analysis by Budiansky and Fleck (1992) the remote transverse stress,  $\sigma_T^-$ , was assumed to be zero.

#### *Continuity of tractions*

Continuity of tractions across the kink band interface can be expressed as

$$\underline{n} \cdot \underline{\sigma}^- = \underline{n} \cdot \underline{\sigma} \quad (4)$$

where  $\underline{n} = \underline{e}_1 \cos \beta + \underline{e}_2 \sin \beta$  is the unit normal to the kink band interface. Equations (1) - (4) lead to the two scalar equations for continuity of tractions in the  $\underline{e}_1$  and  $\underline{e}_2$  directions, respectively,

$$\begin{aligned} -\sigma_L^- \cos \beta \cos(\bar{\phi} + \phi) + \sigma_T^- \sin \beta \sin(\bar{\phi} + \phi) + \tau^- \sin(\beta + \bar{\phi} + \phi) \\ = \sigma_L \cos(\beta - \bar{\phi} - \phi) + \tau \sin(\beta - \bar{\phi} - \phi) \end{aligned} \quad (5)$$

$$\begin{aligned} \sigma_L^- \cos \beta \sin(\bar{\phi} + \phi) + \sigma_T^- \sin \beta \cos(\bar{\phi} + \phi) + \tau^- \cos(\beta + \bar{\phi} + \phi) \\ = \sigma_T \sin(\beta - \bar{\phi} - \phi) + \tau \cos(\beta - \bar{\phi} - \phi) \end{aligned} \quad (6)$$

Because the fibres are assumed to be inextensible, the axial stress in the kink band,  $\sigma_L$ , is of no interest in the analysis to follow and equation (5) need not be considered further.

It is assumed that the initial misalignment,  $\bar{\phi}$ , is small. Furthermore, it is anticipated that consideration of small deformation angles,  $\phi$ , will be sufficient to examine the critical events associated with microbuckling. For small  $\bar{\phi} + \phi$ , linearisation of equation (6) provides the result

$$(\bar{\phi} + \phi)(\sigma_L^- \cos \beta - 2\tau^- \sin \beta) \\ = (\sigma_T - \sigma_T^-) \sin \beta - (\bar{\phi} + \phi) \sigma_T \cos \beta + (\tau - \tau^-) [\cos \beta + (\bar{\phi} + \phi) \sin \beta] . \quad (7)$$

Equation (7) can be further approximated, when  $(\pi/2) - \beta \gg 0$ , by dropping the term  $(\tau - \tau^-)(\bar{\phi} + \phi) \sin \beta$  from the right hand side, to give

$$\sigma_L^- - 2\tau^- \tan \beta \approx \frac{\tau - \tau^- + (\sigma_T - \sigma_T^-) \tan \beta}{\bar{\phi} + \phi} - \sigma_T . \quad (8)$$

This form of the approximation is chosen so that, when the composite behaves elastically, a proper account of the terms involving the remote stresses is maintained. This will be shown explicitly later.

#### Kinematic relations

Kinematic conditions for kink band deformation are now examined. Consider a material point  $P$  within the kink band. The position vector  $\underline{r}$  to point  $P$  is

$$\underline{r} = \xi_1 \underline{e}_1 + \xi_2 \underline{e}_2 = y(-\underline{e}_1 \tan \beta + \underline{e}_2) + x \underline{e}_1 \quad (9)$$

where the scalar lengths  $\xi_1$ ,  $\xi_2$ ,  $x$ , and  $y$  are defined as shown in Fig. 1 and related by

$$\left. \begin{aligned} x &= \xi_1 + \xi_2 \tan(\beta - \bar{\phi} - \phi) \\ y &= \xi_2 \cos \beta \sec(\beta - \bar{\phi} - \phi) \end{aligned} \right\} . \quad (10)$$

The velocity of point  $P$  is

$$\underline{v} = y \dot{\gamma}^- \underline{e}_1 + y \dot{e}_T^- \underline{e}_2 + x \dot{\phi} \underline{e}_2 \quad (11)$$

where  $\dot{\gamma}^-$  and  $\dot{e}_T^-$  are, respectively, the shear strain rate and transverse strain rate outside the kink band and  $\dot{f}(t) \equiv df(t)/dt$ . In the analysis by Budiansky and Fleck (1992), the remote transverse strain rate,  $\dot{e}_T^-$ , was zero.

The strain rate tensor within the kink band is related to the velocity field by



$$\dot{\underline{\epsilon}} = \frac{1}{2} \left[ \underline{\nabla} \underline{v} + (\underline{\nabla} \underline{v})^T \right] \quad (12)$$

where the superscript T denotes the transpose, and the gradient operator  $\underline{\nabla}$  is

$$\underline{\nabla} = \underline{\epsilon}_1 \frac{\partial}{\partial \xi_1} + \underline{\epsilon}_2 \frac{\partial}{\partial \xi_2} \quad (13)$$

With the strain rate components within the kink band defined by

$$\dot{\underline{\epsilon}} = \dot{e}_T \underline{\epsilon}_2 \underline{\epsilon}_2 + \frac{1}{2} \dot{\gamma} (\underline{\epsilon}_1 \underline{\epsilon}_2 + \underline{\epsilon}_2 \underline{\epsilon}_1) \quad (14)$$

equation (12), along with equations (1) and (9) - (11), gives the kinematic conditions

$$\left. \begin{aligned} \dot{e}_T &= \dot{\phi} \tan(\beta - \bar{\phi} - \phi) + [\dot{e}_T^* \cos(\bar{\phi} + \phi) - \dot{\gamma}^* \sin(\bar{\phi} + \phi)] \cos \beta \sec(\beta - \bar{\phi} - \phi) \\ \dot{\gamma} &= \dot{\phi} + [\dot{\gamma}^* \cos(\bar{\phi} + \phi) + \dot{e}_T^* \sin(\bar{\phi} + \phi)] \cos \beta \sec(\beta - \bar{\phi} - \phi) \end{aligned} \right\} \quad (15)$$

Differentiating equation (9), and noting that  $\dot{\underline{r}} = \underline{v}$ ,  $\dot{y} = y \dot{e}_T^*$ , and  $\dot{\underline{\epsilon}}_1 = \dot{\phi} \underline{\epsilon}_2$ , it follows from equation (11) that

$$\dot{\beta} = -(\dot{e}_T^* \sin \beta + \dot{\gamma}^* \cos \beta) \cos \beta \quad (16)$$

For  $\bar{\phi} + \phi$ ,  $e_T^*$ , and  $\gamma^*$  small, equations (15) and (16) reduce to the approximate kinematic equations

$$\left. \begin{aligned} e_T &\approx e_T^* + \phi \tan \beta \\ \gamma &\approx \gamma^* + \phi \\ \beta &\approx \beta_0 \end{aligned} \right\} \quad (17)$$

where  $\beta_0$  is the kink band angle associated with zero remote straining.

#### Constitutive relations

If the composite deforms elastically, then the kinematic conditions, equations (17), lead to

$$\left. \begin{aligned} \sigma_T &= \sigma_T'' + E_T \phi \tan \beta \\ \tau &= \tau'' + G \phi \end{aligned} \right\} \quad (18)$$

where  $E_T$  and  $G$ , respectively, are the transverse and shear elastic moduli for the composite. The *exact* equation for continuity of tractions, equation (6), combined with this result and then linearised gives the approximate elastic kink band response

$$\sigma_L'' + \sigma_T'' - 2\tau'' \tan \beta = [G + E_T \tan^2 \beta] \frac{\phi}{\phi + \phi_0} \quad (19)$$

An examination of equation (8), the *approximate* equation for continuity of tractions, shows that it also reduces to the correct result for elastic kink band response, equation (19).

The following constitutive equations for plastic deformation have previously been derived by Budiansky and Fleck (1992) and, unlike the equations for continuity of tractions and the kinematic conditions, are unchanged by the consideration of general multi-axial loading. Consequently, the derivation is only outlined here. Assume that the composite is characterised by the quadratic yield condition

$$\left( \frac{\tau_e}{\tau_y} \right)^2 = \left( \frac{\tau}{\tau_y} \right)^2 + \left( \frac{\sigma_T}{\sigma_{Ty}} \right)^2 \quad (20)$$

where  $\tau_y$  and  $\sigma_{Ty}$  are the plane strain yield stresses in pure shear and pure transverse tension in the case of perfect plasticity (when  $\tau_e = \tau_y$ , a constant). The effective stress,  $\tau_e$ , which can be rewritten as

$$\tau_e \equiv \sqrt{\tau^2 + (\sigma_T/R)^2} \quad (21)$$

is used as a plastic potential for the plastic strain rates,  $\dot{\gamma}^p$  and  $\dot{\epsilon}_T^p$ . The parameter  $R = \sigma_{Ty}/\tau_y$ , defines the eccentricity of the yield ellipse which expands homogeneously with increasing  $\tau_e$  due to strain hardening.

Discounting the possibility of elastic unloading, the associated flow theory relations for plastic strain rates, based on  $\tau_e$  as a plastic potential, can be written as

$$\left. \begin{aligned} \dot{\gamma}^p &= F(\tau_s) \frac{\partial \tau_s}{\partial \tau} \dot{\tau}_s \\ \dot{e}_T^p &= F(\tau_s) \frac{\partial \tau_s}{\partial \sigma_T} \dot{\sigma}_T \end{aligned} \right\} \quad (22)$$

where  $F(\tau_s)$  is a measure of the rate of strain hardening. A work-equivalent effective plastic strain rate,  $\dot{\gamma}_e^p$ , is defined by

$$\tau \dot{\gamma}^p + \sigma_T \dot{e}_T^p = \tau_s \dot{\gamma}_e^p \quad (23)$$

and it follows that

$$\dot{\gamma}_e^p = F(\tau_s) \dot{\tau}_s = \sqrt{(\dot{\gamma}^p)^2 + R^2 (\dot{e}_T^p)^2} \quad (24)$$

Thus, we interpret  $F(\tau_s)$  as the inverse of the tangent modulus in pure shear. Substituting equation (24) into equation (22) and assuming proportional loading leads to

$$\left. \begin{aligned} \gamma^p &= \left( \frac{\gamma_e^p}{\tau_s} \right) \tau \\ e_T^p &= \left( \frac{\gamma_e^p}{\tau_s} \right) \frac{\sigma_T}{R^2} \\ \gamma_e^p &= \sqrt{(\gamma^p)^2 + R^2 (e_T^p)^2} \end{aligned} \right\} \quad (25)$$

Note that the functional dependence of  $\gamma_e^p$  on  $\tau_s$  must be the same as that of  $\gamma^p$  on  $\tau$  for pure shear. Equations (25) have the form of a *deformation theory* of plasticity. Since microbuckling is a plastic buckling phenomenon, and deformation theories are known to give more accurate predictions to plastic buckling problems than flow theories, we adopt a deformation theory of plasticity and use equations (25) in the remainder of the paper, even though proportional loading may not always be maintained. The microbuckling stress is now derived for the rigid-perfectly plastic solid, and then for a Ramberg-Osgood strain hardening solid.

*Rigid-perfectly plastic solid*

Assume that the composite behaves in a rigid-perfectly plastic manner, with plastic yielding within the kink band only. The elastic components of strain vanish and the constitutive equations (25) can be combined with the approximate kinematic equations (17) to give, after eliminating  $\gamma_p$ ,

$$\sigma_T = \tau R^2 \tan \beta \quad (26)$$

Combining equation (26) with the yield condition, equation (20) (with  $\tau_s/\tau_y = 1$ ), yields

$$\tau = \tau_y / \alpha \quad (27)$$

where

$$\alpha \equiv \sqrt{1 + R^2 \tan^2 \beta} \quad (28)$$

Finally, the rigid-perfectly plastic load response of the kink band is obtained by substituting equations (26) and (27) into the approximate expression for continuity of tractions across the kink band interface, equation (8),

$$\sigma_L^- = \frac{\alpha \tau_y - \tau^- - \sigma_T^- \tan \beta}{\bar{\phi} + \phi} - \frac{1}{\alpha} \tau_y R^2 \tan \beta + 2 \tau^- \tan \beta \quad (29)$$

Since  $\bar{\phi} + \phi$  is small, the expression can be further approximated by dropping the last two terms, leaving

$$\sigma_L^- \approx \frac{\alpha \tau_y - \tau^- - \sigma_T^- \tan \beta}{\bar{\phi} + \phi} \quad (30)$$

Equation (30) reduces to the solution given by Fleck and Budiansky (1991) when there is zero transverse stress outside the kink band,  $\sigma_T^- = 0$ .

The critical microbuckling stress,  $(\sigma_L^-)_c$ , for an applied constant remote shear and transverse stresses,  $\tau^-$  and  $\sigma_T^-$ , is given by equation (30) when  $\phi = 0$ . Both the remote shear stress and the remote transverse stress reduce the critical microbuckling stress in a linear fashion. The microbuckling stress is inversely proportional to the initial imperfection  $\bar{\phi}$ . Note that when  $\beta = 0$  the remote transverse stress ceases to affect microbuckling when the composite is a rigid-perfectly plastic solid.

*Strain-hardening solid*

Consider the case where the composite behaves as an elastic-plastic strain-hardening solid. As previously noted, the functional dependence of  $\gamma_e^p$  on  $\tau_e$  is assumed to equal that of  $\gamma^p$  on  $\tau$  in pure shear, so that

$$\gamma_e^p = \left[ \frac{1}{G_s(\tau_e)} - \frac{1}{G} \right] \tau_e \quad (31)$$

where the function  $G_s(\tau_e)$  is the pure shear secant modulus. Combining the elastic and plastic strain components from equation (25), using equation (31), and, for simplicity, imposing the arbitrary condition

$$\frac{E_T}{G} = R^2 = \left( \frac{\sigma_{Ty}}{\tau_e} \right)^2, \quad (32)$$

leads to

$$\left. \begin{aligned} \gamma &= \frac{\tau}{G} + \gamma^p = \left( \frac{1}{G} + \frac{\gamma_e^p}{\tau_e} \right) \tau = \frac{\tau}{G_s(\tau_e)} \\ e_T &= \frac{\sigma_T}{E_T} + e_T^p = \left[ \frac{1}{E_T} + \frac{1}{R^2} \left( \frac{\gamma_e^p}{\tau_e} \right) \right] \sigma_T = \frac{\sigma_T}{R^2 G_s(\tau_e)} \end{aligned} \right\} \quad (33)$$

A total effective strain is defined by

$$\gamma_e \equiv \frac{\tau_e}{G_s(\tau_e)} \quad (34)$$

so that

$$\gamma_e = \sqrt{\gamma^2 + R^2 e_T^2} = \gamma_e^p + \frac{\tau_e}{G} \quad (35)$$

Thus,  $\gamma_e$  is the sum of an elastic part,  $\tau_e/G$ , and a plastic part,  $\gamma_e^p$ , defined in equation (25). Equations (33) can be rewritten simply as

$$\left. \begin{aligned} \gamma &= \left( \frac{\gamma_e}{\tau_e} \right) \tau \\ e_T &= \left( \frac{\gamma_e}{\tau_e} \right) \frac{\sigma_T}{R^2} \end{aligned} \right\} \quad (36)$$

The three parameter  $(G, \tau_y, n)$  Ramberg-Osgood representation is used to explicitly implement constitutive equations in this paper. With  $\tau_y$  defined as the stress at which the secant modulus is equal to 70% of the elastic modulus, i.e.  $G_s(\tau_y) = 0.7G$ , the Ramberg-Osgood representation for pure shear of the *composite* is

$$\frac{\gamma}{\gamma_y} = \frac{\tau}{\tau_y} + \frac{3}{7} \left( \frac{\tau}{\tau_y} \right)^n \quad (37)$$

where  $\gamma_y \equiv \tau_y/G$  is the elastic component of strain at  $\tau = \tau_y$ . Also, the secant modulus  $G_s(\tau)$  is given by

$$\frac{G}{G_s(\tau)} = 1 + \frac{3}{7} \left( \frac{\tau}{\tau_y} \right)^{n-1} \quad (38)$$

The Ramberg-Osgood representation reduces to the elastic representation when  $\tau_y \rightarrow \infty$  and gives the elastic-perfectly plastic response when  $n \rightarrow \infty$ . The relations are applied to equations (31) - (36) by replacing  $\tau$  and  $\gamma$  with  $\tau_y$  and  $\gamma_y$ .

Combining continuity of tractions, equation (8), with the kinematic constraints, equations (17), and the constitutive equations (36) leads to

$$\sigma_L^- - 2\tau^- \tan \beta = \frac{(\alpha^2 \phi + \gamma^- + R^2 e_T^- \tan \beta) \frac{\tau_e}{\gamma_e} - \tau^- - \sigma_T^- \tan \beta}{\bar{\phi} + \phi} - R^2 (e_T^- + \phi \tan \beta) \frac{\tau_e}{\gamma_e} \quad (39)$$

where

$$\gamma_e^2 = \alpha^2 \phi^2 + R^2 \left[ (e_T^-)^2 + 2e_T^- \phi \tan \beta \right] + 2\gamma^- \phi + (\gamma^-)^2 \quad (40)$$

and  $\alpha$  has been previously defined in equation (28). Define the following non-dimensional

parameters:  $t \equiv \tau_s/\tau_y$ ,  $\eta \equiv \gamma_s/\gamma_y$ ,  $t^- \equiv \tau^-/\tau_y$ ,  $\eta^- \equiv \gamma^-/\gamma_y$ ,  $s^- \equiv \sigma_T^-/\tau_y$ ,  $\epsilon^- \equiv e_T^-/\gamma_y$ ,  $\omega \equiv \phi/\gamma_y$ ,  $\bar{\omega} \equiv \bar{\phi}/\gamma_y$ . Equations (39) and (40) may now be rewritten in non-dimensional form,

$$A \equiv \frac{\sigma_L^- - 2\tau^- \tan \beta}{G} = \frac{(\alpha^2 \omega + \eta^- + R^2 \epsilon^- \tan \beta) \frac{t}{\eta} - t^- - s^- \tan \beta}{\bar{\omega} + \omega} - \gamma_y R^2 (\epsilon^- + \omega \tan \beta) \frac{t}{\eta} \quad (41)$$

$$\eta = \sqrt{\alpha^2 \omega^2 + R^2 [(\epsilon^-)^2 + 2\epsilon^- \omega \tan \beta] + 2\eta^- \omega + (\eta^-)^2} \quad (42)$$

The critical microbuckling load is achieved when  $dA/d\omega = 0$ . Setting  $dA/d\omega = 0$  leads to the parametric equations

$$A_c = \alpha^2 \frac{dt}{d\eta} + \left( \frac{t}{\eta} - \frac{dt}{d\eta} \right) \left( \frac{\eta^-}{\eta} \right)^2 \left[ \alpha^2 - 1 + R^2 \left( \frac{\epsilon^-}{\eta^-} \right)^2 - 2R^2 \frac{\epsilon^-}{\eta^-} \tan \beta \right] - \gamma_y R^2 (\bar{\omega} \tan \beta + \epsilon^- + 2\omega \tan \beta) \frac{t}{\eta} \quad (43)$$

$$+ \gamma_y \frac{R^2}{\eta^2} (\alpha^2 \omega + R^2 \epsilon^- \tan \beta + \eta^-) (\epsilon^- + \omega \tan \beta) (\bar{\omega} + \omega) \left( \frac{t}{\eta} - \frac{dt}{d\eta} \right) \\ \bar{\omega} = \frac{(\alpha^2 \omega + \eta^- + R^2 \epsilon^- \tan \beta) \frac{t}{\eta} - t^- - s^- \tan \beta - \gamma_y R^2 \omega (\epsilon^- + \omega \tan \beta) \frac{t}{\eta} - \omega A_c}{A_c + \gamma_y R^2 (\epsilon^- + \omega \tan \beta) \frac{t}{\eta}} \quad (44)$$

where  $A_c \equiv [(\sigma_L^-)_c - 2\tau^- \tan \beta]/G$ . To generate solutions for the microbuckling stress  $(\sigma_L^-)_c$  for given constant values of  $t^-$  and  $s^-$  (and, therefore,  $\eta^-$  and  $\epsilon^-$ ), first assume a value for the kink band deformation angle,  $\omega$ , at maximum load and calculate the corresponding effective strain,  $\eta$ , from equation (42). Use the constitutive relations, e.g. the Ramberg-Osgood equation (37), to calculate, numerically if necessary, the effective stress,  $t$ , and its first derivative,  $dt/d\eta$ . A good initial guess for  $A_c$  is given by equation (43) without the terms involving  $\gamma_y$ . Equations (43) and (44) can then be solved iteratively for  $A_c$  and  $\bar{\omega}$  and, thus,  $(\sigma_L^-)_c$ .

In the elastic-perfectly plastic limit of the Ramberg-Osgood relation, when  $n \rightarrow \infty$ , there exists a transition value of initial imperfection,  $\bar{\omega}_T$ , such that for  $\bar{\omega} < \bar{\omega}_T$  the maximum value of  $A$  is obtained at initial yield. In this case,  $t = \eta = 1$  and  $A_c$  is given by equation (41). Otherwise, if  $\bar{\omega} > \bar{\omega}_T$ , the previously described procedure is followed with  $t = 1$  and  $dt/d\eta = 0$ . For a more detailed discussion, see Budiansky and Fleck (1992).

The critical microbuckling stress is shown as a function of the remote transverse stress  $\sigma_T^*$  in Fig. 2 and 3. Results are given for different values of the remote shear stress, Ramberg-Osgood parameter,  $n$ , and kink band angle,  $\beta$ . There is a strong dependence of the microbuckling stress  $(\sigma_L^*)_c$  on the remote shear stress  $\tau^*$  and a weaker dependence on remote transverse stress  $\sigma_T^*$ . Note that when  $\beta = 0$  the dependence on remote transverse stress nearly vanishes. This agrees with the results from the rigid-perfectly plastic analysis. The ratio of the strain hardening results to the rigid-perfectly plastic results are plotted in Fig. 4 and 5. This comparison is intended to assess the accuracy of the simple, analytical rigid-perfectly plastic result, equation (30). There is considerable variability with Ramberg-Osgood parameter,  $n$ , but when the remote shear stress and remote transverse stress are not too large the rigid-perfectly plastic result, equation (30), gives acceptable results.

### CREEP MICROBUCKLING

In the following creep microbuckling analysis, it is presumed that under a state of constant remote stress, localised deformation within a kink band proceeds as a function of time. The conventions and assumptions of the previous section are retained to describe the state of stress, strain, and deformation of the composite (Fig. 1). For a given general multi-axial loading,  $\sigma^*$ , and initial imperfection,  $\bar{\phi}$ , fibres rotate in the kink band with increasing time. The function  $\phi(t)$  is sought.

Failure is associated with debonding of the fibre-matrix interface, matrix microcracking, or with other mechanisms which result in a sharp decrease in the load bearing ability of the kink band. The failure criterion proposed by Slaughter and Fleck (1992) will be used here. This criterion is based on the quadratic condition

$$\left(\frac{e_T}{e_{Tf}}\right)^2 + \left(\frac{\gamma}{\gamma_f}\right)^2 = 1 \quad (45)$$

where  $e_{Tf}$  is the transverse failure strain and  $\gamma_f$  is the shear failure strain. Assuming that  $e_{Tf} \ll \gamma_f$ , then the failure criterion simplifies to

$$e_T \approx e_{Tf} \quad (46)$$

For the purposes of this paper,  $e_{Tf} = 0.01$  or  $0.02$ .



Assume that the effective stress,  $\tau_e$ , defined in equation (21) can be used as a creep potential, so that

$$\left. \begin{aligned} \dot{\gamma} &= H(\tau_e) \frac{\partial \tau_e}{\partial \tau} \\ \dot{\epsilon}_T &= H(\tau_e) \frac{\partial \tau_e}{\partial \sigma_T} \end{aligned} \right\} \quad (47)$$

Let  $\dot{\gamma}_e$  be a work rate conjugate of  $\tau_e$  defined by

$$\tau \dot{\gamma} + \sigma_T \dot{\epsilon}_T = \tau_e \dot{\gamma}_e \quad (48)$$

from which it follows that

$$\dot{\gamma}_e = H(\tau_e) \quad (49)$$

Using equations (21) and (47) - (49) leads to

$$\left. \begin{aligned} \dot{\gamma} &= \frac{\tau}{\tau_e} \dot{\gamma}_e \\ \dot{\epsilon}_T &= \frac{\sigma_T}{R^2 \tau_e} \dot{\gamma}_e \end{aligned} \right\} \quad (50)$$

and

$$\dot{\gamma}_e = \sqrt{\dot{\gamma}^2 + R^2 \dot{\epsilon}_T^2} \quad (51)$$

The analysis is simplified if one considers only pure axial compression ( $\sigma_T = \tau = 0$ ). In this case the kink band angle,  $\beta$ , is constant and the kinematic conditions can be expressed approximately, for small  $\bar{\phi} + \phi$ , as

$$\left. \begin{aligned} \dot{\epsilon}_T &= \dot{\phi} \tan \beta \\ \dot{\gamma} &= \dot{\phi} \end{aligned} \right\} \quad (52)$$

which along with equation (51) leads to the expression for the effective strain rate,  $\dot{\gamma}_e$ , in terms of  $\dot{\phi}$ ,

$$\dot{\gamma}_s = \alpha \dot{\phi} \quad (53)$$

where  $\alpha$  has been previously defined in equation (28). In the expression for continuity of tractions, equation (8), the last term on the right hand side can be neglected, since  $\bar{\phi} + \phi$  is assumed small. This, along with equations (50), (52), and (53), leads to an expression for the effective stress,  $\tau_s$ , in terms of the axial compressive stress,  $\sigma_L^-$ ,

$$\tau_s = \frac{1}{\alpha} (\bar{\phi} + \phi) \sigma_L^- \quad (54)$$

It is assumed that the creep behaviour is described by the functional relation

$$\dot{\gamma}_s = g(\tau_s) \quad (55)$$

where  $g(\tau_s)$  is an unspecified function of  $\tau_s$ . Thus the deformation rate,  $\dot{\phi}$ , is related to the deformation,  $\phi$ , and axial load,  $\sigma_L^-$ , by

$$\dot{\phi} = \frac{1}{\alpha} g \left[ \frac{1}{\alpha} (\bar{\phi} + \phi) \sigma_L^- \right] \quad (56)$$

Let  $\phi_f$  be the kink band deformation angle at failure, i.e. when equation (46) is satisfied. Integration of equation (52) gives the relation between  $\phi_f$  and  $e_{\eta}$ ,

$$\phi_f = \frac{e_{\eta}}{\tan \beta} \quad (57)$$

The failure time  $t_f$ , or creep life, is deduced by integrating equation (56) from  $\phi = 0$  at  $t = 0$  to  $\phi = \phi_f$  at  $t = t_f$ , giving

$$t_f = \int_0^{\phi_f} \frac{\alpha}{g \left[ \frac{1}{\alpha} (\bar{\phi} + \phi) \sigma_L^- \right]} d\phi \quad (58)$$

One possible form of creep behaviour is that of a power-law viscous solid,

$$\tau_s = \tau_0 \dot{\gamma}_s^n \quad (59)$$

where  $\tau_0$  and  $m$  (with  $m < 1$ ) are material properties. In this case,  $g(\tau_*) = (\tau_*/\tau_0)^{1/m}$ , which when inserted into equation (58) yields

$$t_f = \alpha^{\frac{m+1}{m}} \left( \frac{m}{1-m} \right) \left( \frac{\tau_0}{\sigma_L^*} \right)^{\frac{1}{m}} \left[ \bar{\phi}^{\frac{m-1}{m}} - (\bar{\phi} + \phi_f)^{\frac{m-1}{m}} \right] \quad (60)$$

as the creep life.

The creep life  $t_f$  is shown as a function of  $\bar{\phi}$ ,  $\beta$ , and  $e_{\eta}$  in Fig. 6 for the power-law viscous solid. Note that  $t_f$  scales with  $\sigma_L^*$  as  $(\sigma_L^*)^{-1/m}$ ; also,  $t_f$  decreases rapidly with increasing  $\bar{\phi}$  and decreasing  $\beta$ . That  $t_f$  decreases with decreasing  $\beta$  is due solely to the  $\beta$  dependence of  $\alpha$ . The tendency of the  $\beta$  dependence of  $\phi_f$  to increase  $t_f$  with decreasing  $\beta$  is comparatively small. Most of the creep life is spent with  $\phi$  close to  $\bar{\phi}$ : the creep life is relatively insensitive to the magnitude of  $e_{\eta}$ . When  $\beta = 0$  the approximate equation for the kink band deformation angle at failure  $\phi_f$ , equation (57), is no longer appropriate. However, provided  $\bar{\phi}$  is small, the creep life  $t_f$  in this case is approximated by equation (60) without the term involving  $(\bar{\phi} + \phi_f)$  and is independent of  $e_{\eta}$ .

## CONCLUDING DISCUSSION

The microbuckling analysis presented in this paper follows the collapse response of an imperfect structure. It is not a bifurcation analysis. The effects of fibre bending stiffness are neglected, with the result that there is no length scale in the analysis. Previous studies have shown that this is a valid approximation (Budiansky, 1979). Fibres are implicitly assumed to be broken at the kink band interface, but without fibre bending stiffness this is not an issue.

The critical stress state for microbuckling of a rigid-perfectly plastic solid is given by equation (30), with  $\phi = 0$ . This failure criterion defines a plane in  $(\sigma_L^*, \sigma_T^*, \tau^*)$  space, and serves as a useful engineering guide-line for the significance of plastic kinking under multi-axial loading. It is noted that the axial microbuckling stress  $(\sigma_L^*)_c$  is sensitive to the degree of fibre waviness  $\bar{\phi}$ . As a rough guide, we deduce from equation (30) that plastic microbuckling is an important mechanism in the compressive failure of unidirectional aligned fibre composites when the in-plane shear strength of the composite  $\tau_y$  is significantly less than the axial compressive stress associated with fibre crushing,  $\sigma_f$ , times the fibre waviness  $\bar{\phi}$ , i.e.  $\tau_y < \bar{\phi} \sigma_f$ . Consider the case of ceramic matrix and metal matrix composites, reinforced with ceramic fibres such as silicon carbide or carbon. The axial strength of unidirectional material associated with fibre compressive fracture is

of the order of  $\sigma_f = 2000$  MPa. A fibre misalignment angle  $\bar{\phi}$  of  $3^\circ$  is assumed. Then, the criterion  $\tau_c < \bar{\phi} \sigma_f$  implies that microbuckling is expected, in ceramic matrix and metal matrix composites, when the composite has a shear strength of less than 100 MPa. This is the case for ceramic matrix composites which are severely microcracked during processing. The above argument is unaffected by the degree of fibre-matrix debonding. The effect of fibre debonding is to reduce the compressive shear strength to approximately  $v_m \tau_c$ , where  $v_m$  is the matrix volume fraction.

Little is known about the compressive creep behaviour of ceramic matrix and metal matrix composites. The analysis given in this paper suggests that creep microbuckling becomes of concern when the in-plane shear creep rate of the composite is appreciable at a shear stress of the order  $\bar{\phi} \sigma_f$ . For the purposes of the discussion assume a kink band angle  $\beta = 0$ . Then material in the kink band suffers simple shear at a rate  $\dot{\gamma} = \dot{\phi}$ . Assuming that the creep life is governed by the initial rotation rate of material in the kink band, then  $\dot{\phi} \approx \phi_f / t_f$  where  $\phi_f$  is the fibre rotation at failure and  $t_f$  is the creep life.

Thus creep microbuckling is expected when the in-plane creep response of the composite under shear is such that the creep rate  $\dot{\gamma}$  is of the order  $\phi_f / t_f$  at a shear stress of  $\bar{\phi} \sigma_f$ . Again taking some approximate values for a metal matrix or ceramic matrix composite,  $\phi_f = 5^\circ$ ,  $\bar{\phi} = 3^\circ$ ,  $\sigma_f = 2000$  MPa, then for a creep life  $t_f$  of 100 hours, the composite must creep at a rate  $\dot{\gamma}$  of as little as  $10^{-7} \text{ s}^{-1}$  under an in-plane shear stress of 100 MPa. It is thought that such creep rates are achievable even at only moderate temperatures. Therefore, creep microbuckling is of potential concern in the design of metal matrix and ceramic matrix composites.

#### ACKNOWLEDGEMENTS

The authors are grateful for financial support from the Office of Naval Research (Contract 0014-91-J-1916), Procurement Executive of the Ministry of Defence (Contract 2029/267), National Science Foundation (Contract MSS-9216135), Department of Engineering, Cambridge University and the Division of Applied Sciences, Harvard University.

REFERENCES

- Argon, A.S. (1972). Fracture of composites. *Treatise of Materials Science and Technology*, vol. 1, Academy Press, New York.
- Budiansky, B. (1979). Remarks on kink formation in axially compressed fiber bundles. *Preliminary Reports, Memoranda and Technical Notes of the Materials Research Council Summer Conference*, La Jolla, CA, July 1979. Sponsored by DARPA.
- Budiansky, B. and Fleck, N.A. (1992). Compressive failure of fibre composites. To appear in *J. Mech. Phys. Solids*.
- Dinwoodie, J.M. (1981). *Timber: Its Nature and Behaviour*. Van Nostrand Reinhold Company, Berkshire, England.
- Evans, A.G. and Adler, W. F. (1978). Kinking as a mode of structural degradation in carbon fiber composites. *Acta Metallurgica* 26, 725-738.
- Fleck, N.A. and Budiansky, B. (1991). Compressive failure of fibre composites due to microbuckling. *Proc. IUTAM Symp. on Inelastic Deformation of Composite Materials*, Troy, New York, May 29 - June 1, 1990, ed. J. Dvorak, 235-273, Springer-Verlag.
- Grossman, P.U.A. and Wold, M.B. (1971). Compressive fracture of wood parallel to the grain. *Wood Sci. Tech.* 5, 147-156.
- Ha, S.K., Wang, Q., and Chang, F. (1991). Modeling the viscoplastic behavior of fiber-reinforced thermoplastic matrix composites at elevated temperatures. *J. Comp. Mat.* 25, 335-373.
- Horoschenkoff, A., Brandt, J., Warnecke, J., and Brüller, O.S. (1988). Creep behaviour of carbon fibre reinforced polyetheretherketone and epoxy resin. *New Generation Materials and Processes*, Milan.
- Hull, D. (1981). *An Introduction to Composite Materials*. Cambridge University Press, Cambridge.
- Schulte, K. and Minoshima, K. (1991). Mechanisms of fracture and failure in metal matrix composites. *12th Risø Int. Symp. on Materials Science: Metal Matrix Composites Processing, Microstructure, and Properties*, ed. N. Hansen, et. al., 123-147.
- Slaughter, W.S. and Fleck, N.A. (1992). Viscoelastic microbuckling of fibre composites. Submitted for publication to *J. Appl. Mech.*



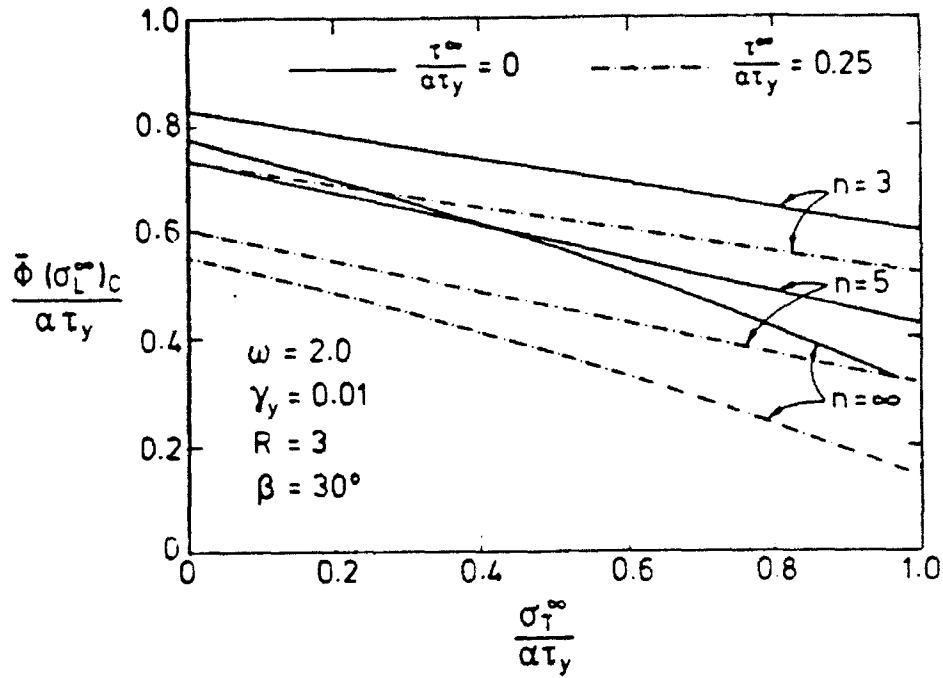


Fig. 2 - The critical microbuckling stress versus the remote transverse stress from the Ramberg-Osgood strain hardening analysis, for  $\beta = 30^\circ$ .

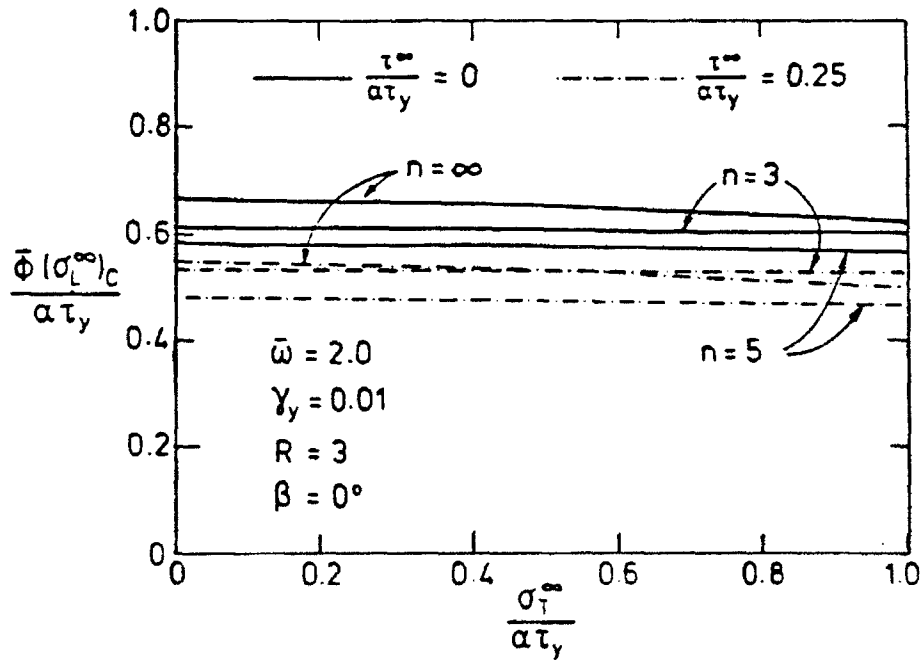


Fig. 3 - The critical microbuckling stress versus the remote transverse stress from the Ramberg-Osgood strain hardening analysis, for  $\beta = 0^\circ$ .

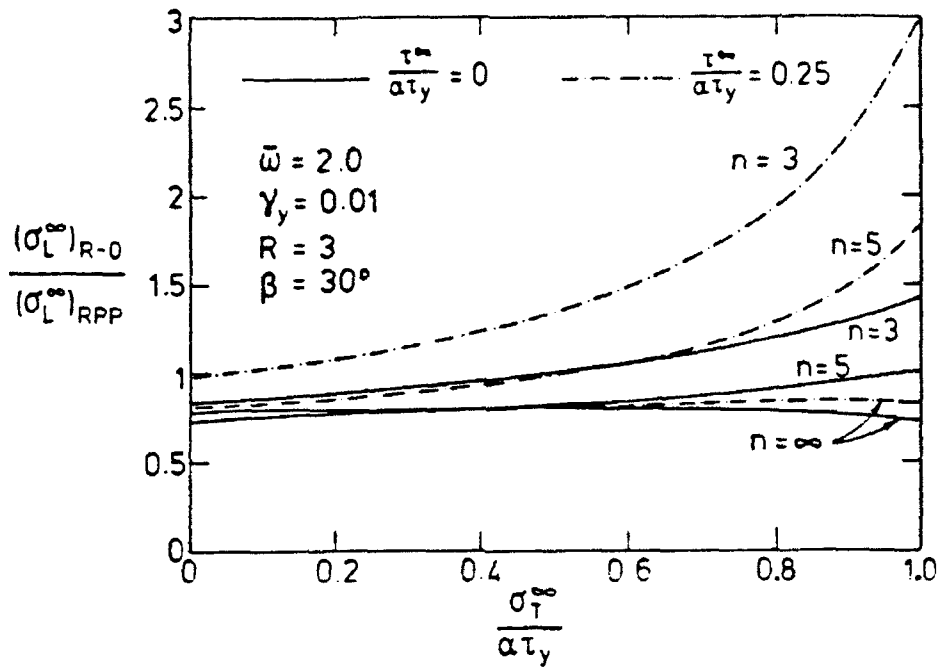


Fig. 4 - Ratio of the critical microbuckling results from the Ramberg-Osgood strain hardening analysis to the results from the rigid-perfectly plastic analysis as a function of the remote transverse stress, for  $\beta = 30^\circ$ .

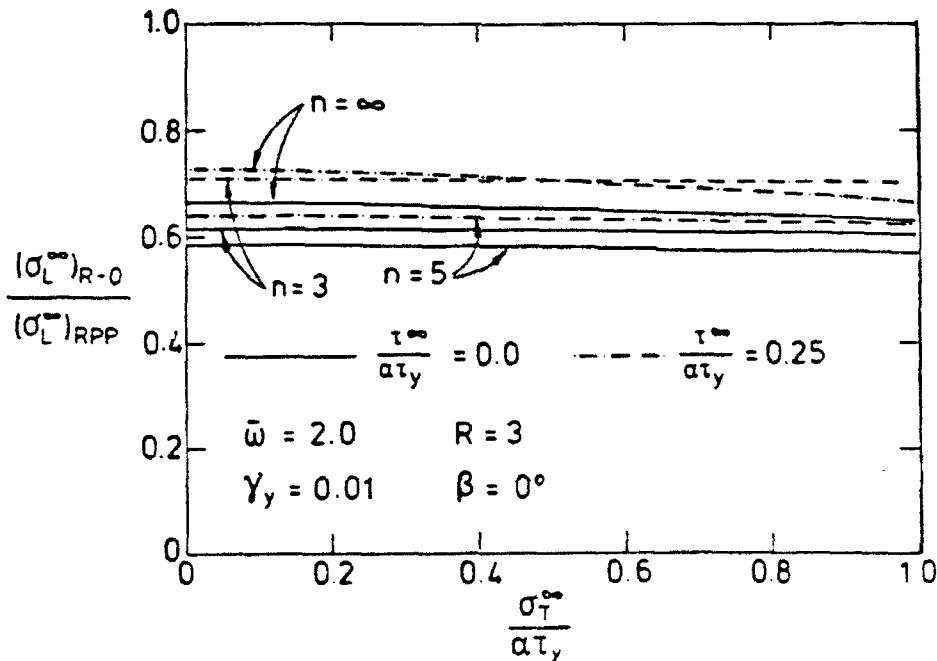


Fig. 5 - Ratio of the critical microbuckling results from the Ramberg-Osgood strain hardening analysis to the results from the rigid-perfectly plastic analysis as a function of the remote transverse stress, for  $\beta = 0^\circ$ .



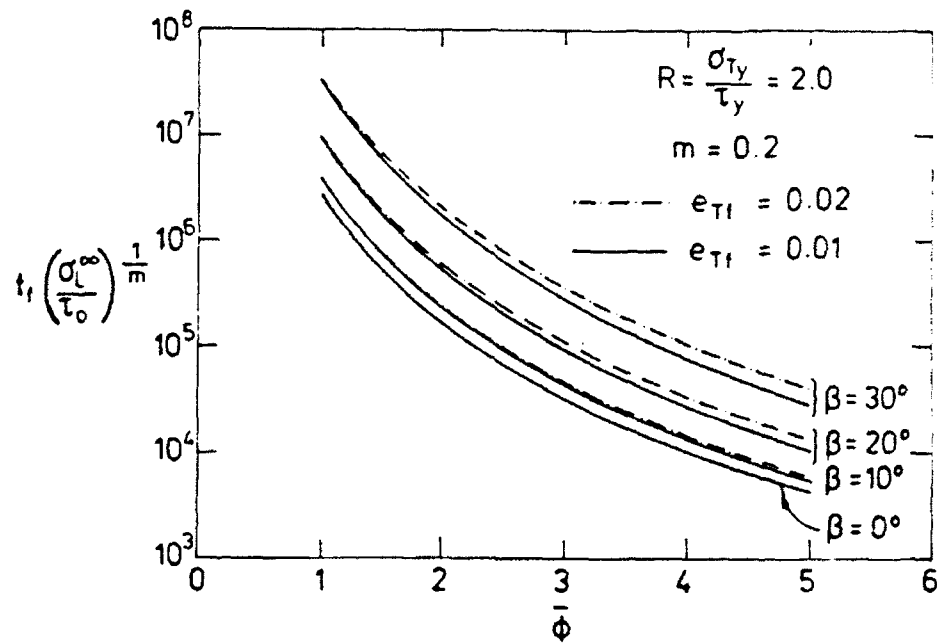


Fig. 6 - Creep life as a function of fibre waviness and kink band inclination, for a power-law viscous material.



MECH-203

## PREDICTION OF KINK WIDTH IN FIBER COMPOSITES

N. A. Fleck, L. Deng and B. Budiansky

Division of Applied Sciences  
HARVARD UNIVERSITY  
Cambridge, Massachusetts 02138

January 1993

## PREDICTION OF KINK WIDTH IN FIBER COMPOSITES

N. A. Fleck\*, L. Deng† and B. Budiansky†

Division of Applied Sciences

Harvard University

Cambridge, MA 02138

### ABSTRACT

Couple stress theory is used in the prediction of the size of the kink band width that occurs in the compressive failure of a fiber composite by microbuckling. The composite is assumed to be inextensible in the fiber direction, and to deform as a Ramberg-Osgood solid in shear and in transverse tension. Predictions are given for the kink width as a function of the fiber diameter, modulus and strength; the material non-linearity of the composite; and the amplitude and wavelength of fiber waviness. The kink width scales with fiber diameter but is fairly insensitive to variations in other material properties and in the amplitude and wavelength of initial fiber waviness. For typical polymer matrix composites, the predicted kink width is of the order of 10-15 fiber diameters, in agreement with observed values.

The couple stress theory is also used to assess the role of fiber bending resistance in the compressive strength of fiber composites that fail by microbuckling. It is found that although the compressive strength is sensitive to the amplitude of the initial waviness, it is not very sensitive to its wavelength.

### INTRODUCTION

Fiber microbuckling is recognized as the dominant compressive failure mechanism in aligned-fiber polymeric matrix composites. Microbuckling occurs in a localized band, which is inclined typically at an angle  $\beta = 10^\circ - 30^\circ$  to the transverse direction, as shown in Fig. 1. The width of the kink band at failure is of the order of 10-15 fiber diameters, as reviewed by Jelf and Fleck (1992).

---

\* Engineering Department, Trumpington Street, Cambridge University, Cambridge, CB2 1PZ, England.

† Division of Applied Sciences, Harvard University, Cambridge, MA 02138, U.S.A.

Several authors have attempted to predict the compressive strength due to microbuckling. The pioneering analysis of kinking by Rosen (1965) was based on the assumption of elastic microbuckling. The evidence is now compelling that non-linear deformation of the matrix, together with the presence of small initial fiber misalignments, are essential features of the kinking process. On the basis of a one-dimensional theory that assumes inextensible fibers and neglects fiber bending resistance, Budiansky and Fleck (1993) found that small fiber misalignments of the order of  $2^\circ$  can account for the observed compressive strengths. They further showed that the assumption of fiber inextensibility is justified for the large fiber to matrix stiffness ratios typical of polymer matrices reinforced with ceramic fibers. We shall refer to the Budiansky-Fleck theory as kinking theory in this paper.

Little attention has been paid to the prediction of kink width. Any analysis capable of predicting kink band width must include an internal material length scale, which may be taken to be the fiber diameter. The material length scale enters the constitutive response via the elastic bending resistance of the fibers. Hahn (1987) has predicted kink widths for a kink band inclination  $\beta=0$  by treating the fibrous composite as a layered solid, with the fibers undergoing bending and the matrix deforming predominantly in shear. Budiansky (1983) used a couple-stress analysis to calculate kink width in a composite comprising perfectly aligned fibers of zero tensile strength in a rigid, ideally plastic matrix. For  $\beta=0$ , he derived the formula

$$\frac{w}{d} = \frac{\pi}{4} \left( \frac{E}{2\tau_y} \right)^{1/3} \quad (1)$$

for the ratio of the kink width  $w$  to fiber diameter  $d$ , in terms of the shear yield stress  $\tau_y$  and the axial modulus  $E$  of the composite.

In the present paper, a couple stress theory is used to take fiber bending resistance into account; we shall refer to this theory as bending theory. The bending theory is used to calculate the dependence of kink width and failure stress upon fiber diameter, modulus and strength, matrix non-linearity and the amplitude and wavelength of fiber waviness. A comparison is also made between the collapse response predicted by the bending theory and by the previous kinking theory of Budiansky and Fleck (1993).

The basic problem analyzed is shown in Fig. 1. A unidirectional fiber composite is subjected to a compressive stress in the fiber direction. The fibers are assumed to have an initial, isolated half-sinusoid of waviness due to manufacturing deficiencies. The waviness is taken to be perfectly correlated in a direction inclined at an angle  $\psi$  to the transverse direction. Upon loading, additional deformation occurs mainly within a finite band, not necessarily coincident with the band of initial imperfection. With continued rotation of the fibers, the load attains a maximum and then drops continuously until the fibers break in bending. Fiber breakage sets the width of the resulting kink band.

## KINK BAND ANALYSIS

We smear out the fibers and matrix, and consider the composite to behave as a homogeneous anisotropic solid. A couple stress formulation is used to take fiber bending resistance into account. We start with descriptions of kinematics and equilibrium, and then set up constitutive laws and a criterion for fiber fracture.

### *Kinematics*

In the initial stress free configuration, the fibers are assumed to possess a small initial angular misalignment  $\bar{\phi}$  which is perfectly correlated along a direction inclined at an angle  $\beta$  to the transverse direction. Thus  $\bar{\phi}$  depends upon the single variable  $x + y \tan \beta$ , where the Cartesian coordinates  $(x, y)$  are parallel and transverse to the ideal fiber direction, respectively, as shown in Fig. 2. For  $y=0$ , we will assume that  $\bar{\phi}$  is an even function of  $x$ .

When the unidirectional composite is loaded by a compressive stress  $\sigma$ , the fibers suffer an additional rotation  $\phi$ ; by symmetry  $\phi$  is also a function of the combined coordinate  $(x + y \tan \beta)$ . Upon invoking fiber inextensibility and the assumption that  $\phi$  is small, we find that the displacement field  $(u, v)$  associated with  $\phi$  satisfies

$$u = 0, \quad \frac{\partial v}{\partial x} = \phi \quad (2)$$

Now define a shear strain  $\gamma_S$  along the fiber direction, and a transverse strain  $\epsilon_T$  which is transverse to the fiber direction. The usual strain-displacement relations for small strains and rotations give the shear strain  $\gamma_S$  and transverse strain  $\epsilon_T$  in terms of  $\phi$  as

$$\gamma_S = \frac{\partial v}{\partial x} = \phi \quad (3)$$

$$\epsilon_T = \frac{\partial v}{\partial y} = \frac{\partial v}{\partial x} \tan \beta = \phi \tan \beta \quad (4)$$

### *Equilibrium*

We consider equilibrium of a representative material element in the deformed configuration (see Fig. 3). The element is subjected to a longitudinal compressive stress  $\sigma_L$  aligned with the fiber direction, a sliding shear stress  $\tau_S$ , a transverse shear stress  $\tau_T$  and a transverse tensile stress  $\sigma_T$ . The fibers embedded in the material offer bending resistance; thus the representative material element carries a bending moment per unit area, or couple stress,  $m$ .

Equilibrium of forces in the fiber direction gives to first order

$$\frac{\partial \sigma_L}{\partial x} = 0 \quad (5)$$

and so  $\sigma_L$  is related to the remote compressive stress  $\sigma$  by

$$\sigma_L = -\sigma \quad (6)$$

Force equilibrium in the transverse direction gives

$$\frac{\partial \sigma_T}{\partial y} + \frac{\partial \tau_T}{\partial x} - \sigma_L \left( \frac{\partial \phi}{\partial x} + \frac{\partial \bar{\phi}}{\partial x} \right) = 0 \quad (7)$$

and moment equilibrium gives

$$\frac{\partial m}{\partial x} = \tau_S - \tau_T \quad (8)$$

We note that the presence of couple stresses makes the stress tensor unsymmetric, with  $\tau_S \neq \tau_T$ .

Elimination of  $\sigma_L$  and  $\tau_T$  from the equilibrium equation (7) gives via (6) and (8)

$$\frac{\partial^2 m}{\partial x^2} + \sigma \left( \frac{\partial \phi}{\partial x} + \frac{\partial \bar{\phi}}{\partial x} \right) = \frac{\partial \tau_S}{\partial x} + \frac{\partial \sigma_T}{\partial y} \quad (9)$$

Since all dependent variables are functions only of the combined co-ordinate  $(x + y \tan \beta)$ , (9) can be rewritten as

$$\frac{\partial^2 m}{\partial x^2} + \sigma \left( \frac{\partial \phi}{\partial x} + \frac{\partial \bar{\phi}}{\partial x} \right) = \frac{\partial \tau_S}{\partial x} + \frac{\partial \sigma_T}{\partial x} \tan \beta \quad (10)$$

and from now on we can set  $y=0$ , and regard  $m$  as an odd function, and  $\phi$ ,  $\tau_S$ , and  $\sigma_T$  as even functions, of the single independent variable  $x$ . Finally, Eq. (10), now an ordinary differential equation, may be integrated with respect to  $x$  to provide the governing differential equation of equilibrium

$$\frac{dm}{dx} + \sigma (\phi + \bar{\phi}) = \tau_S + \sigma_T \tan \beta \quad (11)$$

In order to proceed, we need a constitutive law in order to relate the generalized stress components ( $m$ ,  $\tau_S$ ,  $\sigma_T$ ) to the fiber rotation  $\phi$ .

#### Constitutive law

We assume that the fibers behave as linear elastic beams undergoing inextensible bending, and we neglect matrix contributions to couple stresses. Simple beam theory for circular fibers of diameter  $d$ , Young's modulus  $E_f$  and volume fraction  $c_f$  gives the relation between the couple stress  $m$  on the composite and the associated curvature  $d\phi/dx$  as

$$m = \frac{c_f E_f d^2}{16} \frac{d\phi}{dx} \quad (12)$$

The shear and transverse responses of the composite are taken to be those of a non-linear deformation-theory solid, as suggested by Budiansky and Fleck (1993). They proposed an effective shear stress  $\tau_e$  defined by

$$\tau_e^2 = \tau_s^2 + \frac{\sigma_T^2}{R^2} \quad (13)$$

where the constant  $R$  is interpreted as the ratio of yield stresses in transverse tension and in shear. The constitutive relations for the combined stress state were given as\*

$$\gamma_s = \frac{\gamma_e}{\tau_e} \tau_s \quad (14a)$$

$$\epsilon_T = \frac{\gamma_e}{\tau_e} \frac{\sigma_T}{R^2} \quad (14b)$$

where the effective shear strain  $\gamma_e$ , defined via the virtual work relation  $\tau_e \gamma_e \equiv \tau_s \gamma_s + \sigma_T \epsilon_T$ , is

$$\gamma_e^2 = \gamma_s^2 + R^2 \epsilon_T^2 \quad (15)$$

The three parameter  $(\gamma_Y, \tau_Y, n)$  Ramberg-Osgood representation for the in-plane shear stress-strain curve of the composite is taken as the connection

$$\frac{\gamma_e}{\gamma_Y} = \frac{\tau_e}{\tau_Y} + \frac{3}{7} \left( \frac{\tau_e}{\tau_Y} \right)^n \quad (16)$$

between the effective stress and effective strain. Here  $\tau_Y$  is defined as the composite shear yield stress and  $\gamma_Y$  is the shear yield strain. We note from (16) that  $\tau_Y$  is the shear stress and  $\frac{10}{7} \gamma_Y$  is the shear strain at the point on the stress-strain curve where the secant modulus is 70% of its initial elastic value  $G \equiv \tau_Y / \gamma_Y$ . The strain hardening parameter  $n$  ranges from 1 to  $\infty$ . For  $n > 1$ , equation (16) gives  $\left( \frac{d\tau_e}{d\gamma_e} \right)_{\gamma_e=0} = \frac{\tau_Y}{\gamma_Y} = G$ . In the limit of  $n=1$ , equation (16) gives the misleading law  $\gamma_e = \frac{10}{7} \left( \frac{\tau_e}{G} \right)$ , and so for  $n=1$  we replace (16) by the law  $\gamma_e = \tau_e / G$ ; we refer to this as the elastic case.

#### *Fiber fracture criterion*

It is found experimentally (see for example Soutis and Fleck 1990) that the width of the kink band is set by fiber fracture in tension due to local fiber bending. The strain in the fibers is the sum of the bending strain and the compressive strain associated with the axial stress  $\sigma$ . We equate the maximum tensile strain in each fiber to the tensile fracture strain of the fiber  $\epsilon_F$  to get the fracture criterion

$$\epsilon_F = \left( \frac{d}{2} \right) \left| \frac{d\phi}{dx} \right|_{\max} - \frac{\sigma}{E} \quad (17)$$

---

\* An additional simplifying assumption made in the development of the constitutive relations was that  $R$  is also equal to  $\sqrt{E_T / G}$ , where  $E_T$  is the transverse elastic modulus and  $G$  is the elastic shear modulus of the composite.

where  $\left| \frac{d\phi}{dx} \right|_{\max}$  is the maximum absolute value of curvature along each fiber and  $E$  is the longitudinal Young's modulus of the composite. This fracture condition will be satisfied at two locations  $x = \pm x_F$ , and the width of the kink band is defined as the distance  $2|x_F|$  along the fibers between the points of fiber fracture.

It is noted that the assumption of inextensible fibers was made in the kinematics and equilibrium relations, but axial straining of the fibers is implicit here in the fiber fracture condition. Budiansky and Fleck (1993) have included fiber extensibility in the kinematic and equilibrium relations of a particular version of their kinking analysis, and found that for typical polymer-matrix composites fiber extensibility has little effect upon the collapse response.

### *Solution method*

In this section, we combine the equations of kinematics, equilibrium and constitutive response in order to obtain a single non-linear differential equation. The equations are non-dimensionalised and the solution method is outlined. Details of the analytic and numerical procedures are given in the Appendix.

It is clear from equations (3) and (4) that straining is proportional at each material point, and so the constitutive relations (14-16) imply that loading is also proportional, with

$$\sigma_T = \tau_s R^2 \tan \beta \quad (18)$$

Thus deformation and flow theories of plasticity give identical predictions.

The equilibrium equation (11) may be reduced to a differential equation in  $\phi$  by eliminating  $m$ ,  $\tau_s$  and  $\sigma_T$  via (12), (13) and (18); then

$$\frac{E d^2}{16} \frac{d^2 \phi}{dx^2} + \sigma(\phi + \bar{\phi}) = \tau_s \sqrt{1 + R^2 \tan^2 \beta} \quad (19)$$

where the composite modulus  $E$  has been used as an approximation for  $c_t E_t$ . The effective stress  $\tau_s$  is related to the effective strain  $\gamma_s$  by the non-linear Ramberg-Osgood relation (16), and in turn,  $\gamma_s$  may be written in terms of  $\phi$  on the basis of (3), (4) and (15) as

$$\gamma_s = \phi \sqrt{1 + R^2 \tan^2 \beta} \quad (20)$$

We treat (19) as the governing non-linear differential equation to be solved, together with (20) and the Ramberg-Osgood relation (16), for the rotation  $\phi(x)$ .

The imperfection in fiber alignment  $\bar{\phi}(x)$  is assumed to take the form

$$\left. \begin{aligned} \bar{\phi}(x) &= \bar{\phi}_0 \cos\left(\frac{\pi x}{\bar{w}}\right) & |x| < \frac{\bar{w}}{2} \\ \bar{\phi}(x) &= 0 & |x| > \frac{\bar{w}}{2} \end{aligned} \right\} \quad (21)$$

where the magnitude of the fiber waviness  $\bar{\phi}_0$  and the wavelength  $\bar{w}$  characterize the imperfection.



To proceed, we non-dimensionalise the problem by introducing the non-dimensional quantities

$$\Lambda \equiv \frac{\sigma}{G^*}, \quad \omega \equiv \frac{\phi}{\gamma_Y^*}, \quad \bar{\omega} = \frac{\bar{\phi}_0}{\gamma_Y^*}, \quad g \equiv \frac{\tau_e}{\tau_Y}, \quad \xi \equiv \frac{4x}{d} \sqrt{\frac{G^*}{E}}, \quad \xi_1 \equiv \frac{2\bar{w}}{d} \sqrt{\frac{G^*}{E}} \quad (22)$$

where

$$G^* \equiv \alpha^2 G, \quad \gamma_Y^* \equiv \gamma_Y / \alpha, \quad \text{and} \quad \alpha \equiv \sqrt{1 + R^2 \tan^2 \beta} \quad (23)$$

Then

$$\bar{\omega} = \begin{cases} \frac{\bar{\phi}_0}{\gamma_Y^*} \cos\left(\frac{\pi \xi}{2\xi_1}\right) & \xi < \xi_1 \\ 0 & \xi > \xi_1 \end{cases} \quad (24)$$

and the governing differential equation (19) gives

$$\frac{d^2 \omega}{d\xi^2} + \Lambda(\omega + \bar{\omega}) = g \quad (25)$$

where  $g$  is defined implicitly in terms of  $\omega$  by the non-dimensional form

$$\omega = g + \frac{3}{7} g^3 \quad (26)$$

of the constitutive relation (16). Eq. (25) applies, of course, only for plastic "loading", for which  $\omega$  is increasing. For the elastic case, equation (26) is replaced by the relation  $\omega = g$ . In the elastic-ideally plastic limit of  $n=\infty$ , the Ramberg-Osgood solid possesses a shear yield stress  $\tau_Y$  and a shear modulus  $G \equiv \tau_Y / \gamma_Y$ , and then equation (25) is replaced by

$$\frac{d^2 \omega}{d\xi^2} + (\Lambda - 1)\omega = -\Lambda \bar{\omega} \quad (27a)$$

in the elastic region ( $\omega = g < 1$ ) and

$$\frac{d^2 \omega}{d\xi^2} + \Lambda \omega = 1 - \Lambda \bar{\omega} \quad (27b)$$

in the plastic region ( $g = 1; \omega > 1, \omega$  increasing).

Recall that the width  $w$  of the kink band is defined as the length of broken fibers. Fiber breakage occurs at the locations  $\xi = \pm \xi_F$  where (17) is first satisfied; in non-dimensional form, this condition is

$$\epsilon_F = 2 \sqrt{\frac{\tau_Y^*}{E}} \sqrt{\gamma_Y^*} \left| \frac{d\omega}{d\xi} \right|_{\max} - \frac{\Lambda}{\gamma_Y^*} \left( \frac{\tau_Y^*}{E} \right) \quad (28)$$

where

$$\tau_Y^* \equiv \alpha \tau_Y \quad (29)$$

The kink band width  $w$  is related to  $\xi_F$  via (22) by

$$\frac{w}{d} = \frac{\xi_F}{2} \sqrt{\frac{E}{G^*}} \quad (30)$$

We note in passing that the inclination  $\beta$  of the kink band has been absorbed into the material properties  $\tau_Y^*$ ,  $\gamma_Y^*$  and  $G^*$ .

## RESULTS AND DISCUSSION

We begin by describing the collapse response  $\sigma$  versus  $\phi_0 \equiv \phi(0)$  for the composite over a range of values of imperfection magnitude  $\bar{\phi}_0$  and imperfection wavelength  $\bar{w}$ . Before proceeding to kink-width prediction, we will digress to discuss the dependence of the maximum compressive stress  $\sigma_c$  on the imperfection parameters  $\bar{\phi}_0$  and  $\bar{w}$  and the material non-linearity index  $n$ , and the accuracy of the bending theory vis-a-vis kinking theory will be assessed. Finally, calculated results for the width of kink band will be presented. Rather remarkably, we will find that the predicted width of kink band is in the range 10-15 fiber diameters for a wide range of material properties and imperfection magnitudes and wavelengths.

### *Collapse Response*

The collapse response was calculated by solving the non-linear second order differential equations (25) or (27), as described in Appendix. In all cases, it was found that plastic unloading never occurred.

Consider first the elastic-ideally plastic solid. A typical collapse response is given in Fig. 4 for the perfectly aligned composite ( $\bar{\phi}_0 = 0$ ) and in Fig. 5 for a misaligned composite ( $\bar{\phi}_0/\gamma_Y^* = 4, \bar{w}/d = 20$ ). The values  $\gamma_Y^* = .01$ ,  $\epsilon_F = .01$ , and  $\tau_Y^*/E = .0004$  in these figures are typical for polymer-matrix composites. The insert of each figure displays the deformed shape of a representative fiber at four stages of loading; an enhanced line thickness is used to depict the extent of the plastic zone at each stage.

For the perfectly aligned composite (see Fig. 4), and any assumed value of  $\beta$ , the fibers start to rotate at the bifurcation stress  $G^*$ , in agreement with the Rosen (1965) result for  $\beta=0$ . The bifurcation mode consists of uniform rotation, with the composite deforming elastically and the fibers suffering no bending. Between points 1 and 2 of Fig. 4, elastic deformation continues as the fibers rotate uniformly, until the matrix yields at  $\phi_0 = \gamma_Y^*$ . Active plastic loading then occurs immediately in the finite interval

$$|x| \leq \frac{\pi d}{8} \sqrt{\frac{E}{G^*}} \quad (31)$$

and elsewhere the composite unloads elastically. With further increase of the maximum rotation  $\phi_0$ , the collapse response shown in Fig. 4 obeys the relation

$$\frac{\phi_0}{\gamma_Y^*} = \frac{1 + \sqrt{1 - \sigma/G^*}}{\sigma/G^*} \quad (32)$$

as the load drops smoothly, and the plastic zone extends in width. Fiber bending now occurs everywhere, but is concentrated within the plastic zone. When the maximum surface strain in the fibers equals the tensile fracture strain of the fibers, the fibers break in accordance with the fracture criterion (28). Point 4 on the main plot of Fig. 4 shows the remote stress  $\sigma$  and fiber rotation  $\phi_0$  at the point of fiber fracture; the solid circles on the curve labeled 4 in the figure insert depict the sites of fiber fracture. The length of fiber between the two fracture locations is taken as the definition of the width of the resulting kink band, to be discussed in the next section. After fiber fracture, the fibers are unable to carry a bending moment at the locations of fiber fracture, and the load on the composite drops discontinuously to a lower value (not shown). Thereafter the fibers in the kink band suffer no further bending and the collapse response is given by the kinking theory. This regime is of little practical relevance and is not explored further.

Now consider the typical collapse response of the misaligned composite, as shown in Fig. 5. Since the composite possesses an initial waviness, deformation begins at zero load. The initial response of the composite is elastic and involves elastic bending of the fibers. At  $\phi_0 = \gamma_Y^*$  the matrix yields at the single location  $x=0$ ; we term the corresponding load the yield load. The plastic zone spreads quickly and a maximum in the load (point 2) is attained at a load only slightly above the yield load. In fact, for the elastic-ideally plastic body, the maximum load occurs at the yield load for imperfections of sufficiently large wavelength. Post maximum load, the load drops smoothly with increasing fiber rotation  $\phi_0$ , and the plastic zone continues to spread. Finally, at point 4 the fiber fracture criterion (28) is met, and a kink band is formed. The solid circles on curve 4 of the insert of Fig. 5 show the locations of fiber fracture. The response of the misaligned composite in Fig. 5 asymptotes towards the response of the perfect composite in Fig. 4 at sufficiently large  $\phi_0$ . Since fiber fracture occurs at large  $\phi_0$ , the width of the kink band determined by fiber fracture can be expected to be little influenced by the existence of initial fiber waviness.

This last point is amplified in Fig. 6, wherein the curves for  $n=\infty$  of Figs. (4) and (5) are reproduced, together with response curves for  $n=3$ . In addition, the fiber fracture points on each curve are shown for  $\epsilon_F=0, .01$ , and  $.02$ . These results show that for each  $n$  the values of rotation  $\phi_0$  and load  $\sigma$  at fiber fracture are insensitive to the initial misalignment. Thus, even for small values of  $\epsilon_F$ , for which  $\phi_0$  at fracture is not large, we expect kink widths to be insensitive to the size of the imperfection  $\bar{\phi}_0$ .

*Comparisons of collapse response via bending and kinking theories*

The collapse response predicted by kinking theory is compared with that given by bending theory in Fig. 7, for the elastic solid, elastic-ideally plastic solid and the intermediate case of a Ramberg-Osgood solid with  $n=3$ . Results are shown for a typical imperfection magnitude of  $\bar{\phi}_0/\gamma_Y^* = 4$ , and for the bending theory with imperfection widths of  $\frac{\bar{w}}{d}\sqrt{\frac{G^*}{E}} = 5$  and  $\infty$ . (For typical values of  $G^*/E$ , the finite width corresponds to  $\bar{w}/d \approx 25$ .) In the case of the elastic solid, the normalized load  $\sigma/G^*$  increases monotonically with normalized fiber rotation  $\phi_0/\gamma_Y^*$  and tends to unity at large fiber rotations. For  $\frac{\bar{w}}{d}\sqrt{\frac{G^*}{E}} = \infty$  (and  $\frac{\bar{w}}{d}\sqrt{\frac{G^*}{E}} = 0$ ) uniform fiber rotation occurs with no fiber bending, and the response predicted by the bending theory is identical to that predicted by the kinking theory. Otherwise fiber bending occurs and the bending theory gives a stiffer response than kinking theory.

Now examine the case  $n=3$ . The bending theory suggests a small influence of wavelength of initial waviness upon the collapse response. Plastic deformation of the matrix with elastic bending of the fibers begins at zero load, and the composite is everywhere in a plastic state at finite loads. A mild maximum in the load is attained, which is a consequence of the competition between geometric softening associated with fiber rotation and strain hardening. The kinking theory prediction lies very slightly below the bending theory prediction for  $\frac{\bar{w}}{d}\sqrt{\frac{G^*}{E}} = \infty$ . Note that this limiting value of normalized width of initial waviness should be interpreted as the limit  $\bar{w} \rightarrow \infty$  rather than the limit  $d \rightarrow 0$ . In the limit  $d \rightarrow 0$  the bending theory formally reduces to the kinking theory.

For the elastic-ideally plastic solid, both theories give an initial elastic response. The bending theory with  $\frac{\bar{w}}{d}\sqrt{\frac{G^*}{E}} = 5$  gives a maximum load which is slightly greater than the yield load. In contrast, the bending theory with  $\frac{\bar{w}}{d}\sqrt{\frac{G^*}{E}} = \infty$  and the kinking theory predict that maximum load occurs at the onset of yield; thereafter the load drops in a smooth manner until fiber fracture intervenes. In the plastic range the kinking response is given by

$$\frac{\sigma}{G^*} = \left( \frac{\phi_0}{\gamma_Y^*} + \frac{\bar{\phi}_0}{\gamma_Y^*} \right)^{-1} \quad (33)$$

while in the limit of large  $\phi_0/\gamma_Y^*$  and  $\frac{\bar{w}}{d}\sqrt{\frac{G^*}{E}} = \infty$  an asymptotic formula may be derived for the collapse response by bending theory as

$$\frac{\sigma}{G^*} = \left( \frac{\phi_0}{2\gamma_Y^*} + \frac{\bar{\phi}_0}{\gamma_Y^*} \right)^{-1} \quad (34)$$

The above two formulas show that at large values of  $\phi_0/\gamma_Y^*$  the load carrying capacity is nearly doubled by the presence of fiber bending resistance.

Regardless of the degree of material non-linearity the strongest response is consistently shown in Fig. 7 by the bending theory for a short wavelength of initial misalignment, and the weakest response is given by the kinking theory. However, the effect of fiber bending resistance upon the response up to the critical load is small. Furthermore, the maximum stress  $\sigma_c/G^*$  is little influenced by the value of  $n \geq 3$  for the non-linear solid.

The normalized critical stress  $\sigma_c/G^*$  is a function of the non-dimensional groups  $\bar{\phi}_0/\gamma_Y^*$  and  $n$  in the kinking analysis, and of the groups  $\bar{\phi}_0/\gamma_Y^*$ ,  $\frac{\bar{w}}{d} \sqrt{\frac{G^*}{E}}$  and  $n$  in the bending analysis. The dominant independent group for both theories is the imperfection magnitude  $\bar{\phi}_0/\gamma_Y^*$ . Budiansky and Fleck (1993) have given an analytic formula for the effect of imperfection magnitude upon the critical compressive strength  $\sigma_c^k/G^*$  by the kinking theory. They find

$$\frac{\sigma_c^k}{G^*} = \frac{1}{1 + n \left( \frac{3}{7} \right)^{\frac{1}{n}} \left( \frac{\bar{\phi}_0/\gamma_Y^*}{n-1} \right)^{\frac{n-1}{n}}} \quad (35)$$

The ratio of the critical load  $\sigma_c^b$  predicted by bending theory to the value  $\sigma_c^k$  by kinking theory is given in Fig. 8 as a function of  $\bar{\phi}_0/\gamma_Y^*$ , for  $n=3$  and  $\infty$  and two finite imperfection wavelengths.

For the limiting case of  $\frac{\bar{w}}{d} \sqrt{\frac{G^*}{E}} = \infty$  (omitted from Fig. 8 for the sake of clarity), the ratio  $\sigma_c^b/\sigma_c^k$  equals unity to within 0.1% for  $\bar{\phi}_0/\gamma_Y^* = 2$  and 4, and for all  $n$  in the range  $1 \leq n \leq \infty$ . The effect of the imperfection-wavelength parameter  $\frac{\bar{w}}{d} \sqrt{\frac{G^*}{E}}$  on the value of  $\sigma_c/G^*$  given by bending theory is shown explicitly in Fig. 9, for the two imperfection sizes  $\bar{\phi}_0/\gamma_Y^* = 2$  and 4. The results in Figs. 8 and 9 imply that, in general, the strength predictions of the bending and kinking theories differ little for realistic composites; only if the *dominant* imperfection wavelength  $\frac{\bar{w}}{d} \sqrt{\frac{G^*}{E}}$  in the composite has an unrealistically small value less than 5 will the ratio  $\sigma_c^b/\sigma_c^k$  be substantially larger than unity.

Note that in the limit  $\frac{\bar{w}}{d} \sqrt{\frac{G^*}{E}} = 0$ , the imperfection vanishes and the bending theory gives a critical load  $\sigma_c/G^* = 1$  for all  $n$  and all  $\bar{\phi}_0/\gamma_Y^*$ .

### Prediction of kink band width

The normalized kink band width  $w/d$  is a function of the six non-dimensional parameters and groups

$$\epsilon_F, \gamma_Y^*, n, \tau_Y^*/E, \bar{w}/d, \bar{\phi}_0/\gamma_Y^*. \quad (36)$$

The effect of the wavelength  $\bar{w}/d$  of the initial misalignment upon kink width  $w/d$  is shown in Fig. 10 for  $n=3$  and  $\infty$  and typical values of  $\bar{\phi}_0/\gamma_Y^*$ ,  $\epsilon_F$ ,  $\gamma_Y^*$  and  $\tau_Y^*/E$ . The kink width  $w/d$  is little influenced by the wavelength  $\bar{w}/d$  or magnitude  $\bar{\phi}_0/\gamma_Y^*$  of the initial imperfection (and by the degree of material non-linearity  $n$ ). Note that the kink width arising from an initial misalignment is never far from the kink width for the perfectly aligned composite, given by the limit  $\bar{w}/d=0$  in Fig. 10. A definite minimum in kink width  $w/d$  occurs very near an imperfection width given by  $\bar{w}/d=w/d$ . This suggests a "lock-in" type of behavior, whereby the minimum kink width corresponds to the condition where it is nearly matched by the wavelength of the initial imperfection.

The effect of the non-dimensional groups  $\tau_Y^*/E$ ,  $\epsilon_F$ ,  $\gamma_Y^*$ , and  $n$  upon the kink band width  $w/d$  is explored in Figs. 11 and 12. Since the imperfection wavelength and magnitude play a minor role in setting the kink width, we consider only results for the perfectly aligned composite. The kink width is shown as a function of  $\tau_Y^*/E$  in Fig. 11, for a range of values of  $\epsilon_F$  and  $\gamma_Y^*$ , and  $n=3$  and  $\infty$ . Consider first the results given in Fig. 11(a) for the elastic-ideally plastic solid ( $n=\infty$ ). As shown in the Appendix, the curves in Fig. 11(a) satisfy

$$4(\tau_Y^*/E)^2 \left[ \left( \frac{4w}{\pi d} \right)^2 - 4(\tau_Y^*/E)^{-1} \right] = \left[ \epsilon_F + \left( \frac{4w}{\pi d} \right)^{-2} \right]^2 \quad (37)$$

For  $\epsilon_F = \gamma_Y^* = 0$ , this reduces to the Budiansky (1983) result given by Eq. (1). For unusually low values of  $\tau_Y^*/E$  (say, less than .0004), the kink width is seen to be sensitive to fiber failure strain  $\epsilon_F$ , but it is always very insensitive to the value of yield strain  $\gamma_Y^*$ . Further, if  $\tau_Y^*/E$  exceeds about .0004, changes in  $\tau_Y^*/E$  have only a minor effect upon kink width. This may also be seen from the analytic formula (1) for the rigid-ideally plastic solid ( $\gamma_Y^*=0$ ), where  $w/d$  varies with  $\tau_Y^*/E$  to the  $-1/3$  power. We note that  $w/d$  increases with both increasing  $\epsilon_F$  and increasing  $\gamma_Y^*$ .

Results for the non-linear solid ( $n=3$ ) are given for  $\gamma_Y^*=0.02$ , 0.01 and 0.005 in Figs. 11b, c and d, respectively. As  $n$  is decreased from  $\infty$  to 3, the kink width  $w/d$  becomes considerably less sensitive to the failure strain  $\epsilon_F$  and somewhat more sensitive to  $\gamma_Y^*$ ; otherwise, the trends are the same for  $n=3$  and for  $n=\infty$ . For finite  $n$ , the composite adopts an infinite initial stiffness in the limit  $\gamma_Y^*=0$ , and the constitutive description becomes unacceptable. We have found for  $n=3$  that as  $\gamma_Y^*$  is decreased from a value of 0.001 to zero,  $w/d$  drops steeply to zero; no curves are given to show this, as the effect is of no practical relevance.

The effect of strain hardening index  $n$  upon kink width is given in Fig. 12 for  $\epsilon_F = 0.01$  and  $\gamma_Y^* = 0.01$ . We observe that  $w/d$  increases only slightly with increasing  $n$ . In conclusion, the predicted kink width  $w/d$  is of the order 10-15 for a wide range of values for the 6 independent parameters (36) characterizing the imperfection and the material properties.

### CONCLUDING REMARKS

In this paper, a non-linear couple stress theory was used to incorporate the effect of fiber bending resistance into the analysis of compressive failure and kink-band formation of fiber composites. We have assumed an initial imperfection that was perfectly correlated in a direction inclined at an angle  $\beta$  to the transverse direction. It was found that while fiber bending resistance plays an essential role in the prediction of kink band width, it can be neglected in predicting failure strength. The imperfection wavelength has little effect on both compressive strength and kink width, and although the magnitude of the waviness strongly influences compressive strength, it has only a minor influence on kink width. Except for very low values of the composite shear yield stress or high values of the Ramberg-Osgood hardening parameter  $n$ , kink width is fairly insensitive to material properties. The predicted values of  $w/d$  in the neighborhood of 10-15 are roughly the same as the experimental data for polymer-matrix fiber composites collected and reviewed by Jelf and Fleck (1992).

### ACKNOWLEDGEMENTS

The authors are grateful for financial support from the National Science Foundation (contract MSS-9216135), the Office of Naval Research (contract 0014-91-J-1916), the Procurement Executive of the Ministry of Defense (contract 2029/267), the Department of Engineering, Cambridge University, and the Division of Applied Sciences, Harvard University.

### REFERENCES

- Argon, A.S. (1972). "Fracture of composites", *Treatise of Materials Science and Technology* Vol. 1, Academic Press, New York.
- Budiansky, B. (1983). "Micromechanics", *Computers and Structures*, **16**(1), pp. 3-12
- Budiansky, B. and Fleck, N.A. (1993). "Compressive failure of fiber composites", *J. Mech. Phys. Solids*, **41**, pp. 183-211.

- Hahn, H.T. (1987). "Compressive failure of unidirectional composites", 13th Annual Int. Symp. for Testing and Failure Analysis, Los Angeles, California.
- Jelf, P.M. and Fleck, N.A. (1992) "Compressive failure mechanisms in unidirectional composites", To appear in J. Composite Materials.
- Rosen, B.W. (1965). "Mechanics of composite strengthening", Fiber Composite Materials, Am. Soc. Metals Seminar, Chapter 3, pp. 37-75.
- Soutis, C. and Fleck, N.A. (1990). "Static compression failure of carbon fiber T800/924C composite plate with a single hole", J. Composite Materials, 24, pp. 536-558.

## APPENDIX

### ANALYTIC AND NUMERICAL SOLUTIONS

Here we describe the procedures used to calculate collapse response and the kink band width. We deal first with the differential equations (27) for the elastic-ideally plastic body, and then with Eq. (25) for  $1 < n < \infty$ ; the purely elastic case is governed by Eq. (27a). By symmetry, we need only consider the domain  $\xi \geq 0$  in all cases.

#### *Elastic-ideally plastic body ( $n = \infty$ )*

For the perfect ( $\bar{\omega} \equiv 0$ ) elastic-ideally plastic solid the governing equations (27) admit the following solution. Under increasing load  $\Lambda$ ,  $\omega$  stays equal to zero until the bifurcation load  $\Lambda = 1$  is reached, and then, in accordance with Eq. (27a),  $\omega$  increases everywhere, uniformly and elastically, up to the value  $\omega = 1$ , with  $\Lambda$  remaining equal to 1. If we presume that  $\omega(0)$  is infinitesimally larger than  $\omega$  elsewhere, we can anticipate that plastic yield will start at  $\xi = 0$  and spread into a finite vicinity of the origin within which  $\omega$  continues to increase. At the elastic-plastic boundary  $\xi_p$ , we have  $\gamma_e = \gamma_Y$ , which, by (20), (22), (23) requires

$$\omega(\xi_p) = 1 \quad (A1)$$

Solutions of Eqs. (27ab) satisfying this requirement are given by

$$\omega(\xi) = \begin{cases} \frac{1}{\Lambda} + \left(1 - \frac{1}{\Lambda}\right) \frac{\cos \sqrt{\Lambda} \xi}{\cos \sqrt{\Lambda} \xi_p} & 0 \leq \xi \leq \xi_p \\ \exp[-\sqrt{1-\Lambda}(\xi - \xi_p)] & \xi \geq \xi_p \end{cases} \quad (A2)$$

wherein the conditions  $\omega'(0) = 0$  and  $\omega'(\infty) = 0$  have been imposed. The additional bending continuity condition  $\omega'(\xi_p^+) = \omega'(\xi_p^-)$  implies

$$\cos(\sqrt{\Lambda} \xi_p) = -\sqrt{1-\Lambda} \quad (A3)$$



Hence

$$\omega(0) = \frac{1 + \sqrt{1 - \Lambda}}{\Lambda} \quad (\text{A4})$$

giving Eq. (32) of the text. Also, (A3) implies that  $\xi_p$  jumps discontinuously to the value  $\pi/2$  at  $\Lambda=1$  when  $\omega(0)$  just begins to increase beyond 1, and then continues to grow smoothly as  $\Lambda$  decreases.

Fiber fracture occurs where the magnitude  $|\omega'(\xi)|$  is a maximum, and hence where  $\omega''(\xi) = 0$ . It follows from (A2) that the fiber fracture location  $\xi_F$  is in the plastic region, and is related to the load  $\Lambda$  by

$$\xi_F = \frac{\pi}{2\sqrt{\Lambda}} \quad (\text{A5})$$

Then

$$|\omega'(\xi_F)| = \left| \frac{d\omega}{d\xi} \right|_{\max} = \sqrt{\frac{1 - \Lambda}{\Lambda}} \quad (\text{A6})$$

and using (A5) together with (A6) in (28) and (30) gives the analytic result (37) for the kink width.

For the imperfect composite ( $\bar{\omega} \neq 0$ ), the solutions of (27) satisfying  $\omega'(0) = \omega'(\infty) = 0$  are as follows. For  $\xi_p \leq \xi_I$

$$\omega(\xi) = \begin{cases} \frac{1}{\Lambda} + C_1 \cos(\sqrt{\Lambda}\xi) + \frac{\Lambda \bar{\omega}_0}{\left(\frac{\pi}{2\xi_I}\right)^2 - \Lambda} \cos\left(\frac{\pi\xi}{2\xi_I}\right) & 0 \leq \xi \leq \xi_p \\ C_2 e^{\sqrt{1-\Lambda}\xi} + C_3 e^{-\sqrt{1-\Lambda}\xi} + \frac{\Lambda \bar{\omega}_0}{1 - \Lambda + \left(\frac{\pi}{2\xi_I}\right)^2} \cos\left(\frac{\pi\xi}{2\xi_I}\right) & \xi_p \leq \xi \leq \xi_I \\ C_4 e^{-\sqrt{1-\Lambda}\xi} & \xi \geq \xi_I \end{cases} \quad (\text{A7a})$$

and for  $\xi_p \geq \xi_I$

$$\omega(\xi) = \begin{cases} \frac{1}{\Lambda} \cos(\sqrt{\Lambda}\xi) + \frac{\Lambda\bar{\omega}_0}{\left(\frac{\pi}{2\xi_I}\right)^2 - \Lambda} \cos\left(\frac{\pi\xi}{2\xi_I}\right) & 0 \leq \xi \leq \xi_P \\ \frac{1}{\Lambda} + C_2 \cos(\sqrt{\Lambda}\xi) + C_3 \sin(\sqrt{\Lambda}\xi) & \xi_I \leq \xi \leq \xi_P \\ C_4 e^{-\sqrt{1-\Lambda}\xi} & \xi \geq \xi_I \end{cases} \quad (\text{A7b})$$

The desired relation between the load and rotation variables  $\Lambda$  and  $\omega(0)$  is readily found by writing the equation

$$\omega(0) = \frac{1}{\Lambda} + C_1 + \frac{\Lambda\bar{\omega}_0}{\left(\frac{\pi}{2\xi_I}\right)^2 - \Lambda} \quad (\text{A8})$$

implied by (A7a), imposing the five consistency and continuity relations

$$\omega(\xi_P^+) = \omega(\xi_P^-) = 1, \quad \omega'(\xi_P^+) = \omega'(\xi_P^-), \quad \omega(\xi_I^+) = \omega(\xi_I^-), \quad \omega'(\xi_I^+) = \omega'(\xi_I^-), \quad (\text{A9})$$

and solving the system (A8-A9) of six nonlinear equations for the six unknowns  $\Lambda$ ,  $\xi_P$ ,  $C_1$ ,  $C_2$ ,  $C_3$ ,  $C_4$  in terms of prescribed values of  $\omega(0)$ . The solutions (obtained via a Newton-Raphson iterative scheme) provided the results for  $n=\infty$  in Figs. 5-9.

As in the case of the perfect composite, fiber fracture occurs at  $\xi = \xi_F$  when (28) is

satisfied, with  $\left|\frac{d\omega}{d\xi}\right|_{\max} = |\omega'(\xi_F)|$ , and

$$\omega''(\xi_F) = 0 \quad (\text{A10})$$

For prescribed values of  $\epsilon_F$ ,  $\tau_Y^*/E$ , and  $\gamma_Y^*$ , Eqs. (28), (A9) and (A10) now provide seven simultaneous equations for  $\xi_F$  and the values of  $\Lambda$ ,  $\xi_P$ , and  $C_1$ - $C_4$  at fracture. The solution (by the Newton-Raphson method) gives the width of kink band via (30).

*Ramberg-Osgood solid* ( $1 < n < \infty$ )

For the perfect composite ( $\bar{\omega} \equiv 0$ ), we can use (26), together with the assumed boundary conditions  $\omega(\infty) = \omega'(\infty) = 0$ , to get a first integral of the differential equation (25) in the form

$$\omega'^2 = g^2 + \frac{6}{7} \frac{n}{n+1} g^{n+1} - \Lambda \left( g + \frac{3}{7} g^n \right)^2 \quad (\text{A11})$$

At the origin,  $\omega'(0) = 0$  and (A19) implies

$$g(0) = \left[ \frac{7}{3} \frac{\sqrt{\left(\Lambda - \frac{n}{n+1}\right)^2 + \Lambda(1-\Lambda)} - \left(\Lambda - \frac{n}{n+1}\right)}{\Lambda} \right]^{\frac{1}{n-1}} \quad (\text{A12})$$

Equations (A12) and (26) provide the relation between  $\Lambda$  and  $\omega(0)$ .

Next we present a straightforward scheme for determining the kink band width for the perfect composite. Inserting into Eq. (25) the condition (A10) on the fracture location  $\xi_F$  gives

$$g(\xi_F) = \left[ \frac{7}{3} \left( \frac{1-\Lambda}{\Lambda} \right) \right]^{\frac{1}{n-1}} \quad (\text{A13})$$

and the corresponding value of  $|\omega'(\xi_F)|$  in terms of  $\Lambda$  follows from (A11). Substitution into the fiber failure criterion (28) then provides a nonlinear equation that can be solved numerically for the value of  $\Lambda$  at fracture. Finally, by use of (26) in the integration of (A11), the fiber fracture location  $\xi_F$  is given by

$$\xi_F = \int_{g(\xi_F)}^{g(0)} \frac{\left[1 + \frac{3}{7} n g^{n-1}\right] dg}{\sqrt{g^2 + \frac{6}{7} \frac{n}{n+1} g^{n+1} - \Lambda \left[g + \frac{3}{7} g^n\right]^2}} \quad (\text{A14})$$

where the limits of integration are given by (A12) and (A13). The kink band width  $w$  is related to  $\xi_F$  via (30).

Now consider the imperfect composite ( $\bar{\omega} > 0$ ), wherein the imperfection  $\bar{\omega}(\xi)$  defined by Eq. (24) extends over a region  $0 \leq \xi \leq \xi_1$ . Equation (A11) remains valid for  $\xi > \xi_1$ ; and integration from  $\xi_1$  to an arbitrary point  $\xi > \xi_1$  gives

$$\xi = \xi_1 + \int_{g(\xi_1)}^{g(\xi)} \frac{\left[1 + \frac{3}{7} n g^{n-1}\right] dg}{\sqrt{g^2 + \frac{6}{7} \frac{n}{n+1} g^{n+1} - \Lambda \left[g + \frac{3}{7} g^n\right]^2}} \quad (\text{A15})$$

Inside the imperfection band ( $\xi < \xi_1$ ), equation (25) may be reduced to a system of 3 first-order nonlinear equations for the dependent variables  $y_1 \equiv g$ ,  $y_2 \equiv g'$  and  $y_3 \equiv \Lambda$ . The resulting system is

$$\begin{cases} y_1' = y_2 \\ y_2' = \frac{1}{1 + \frac{3}{7}ny_1^{n-1}} \left[ y_1 - y_3\bar{\omega} - y_3 \left( y_1 + \frac{3}{7}y_1^n \right) - \frac{3}{7}n(n-1)y_1^{n-2}y_2^2 \right] \\ y_3' = 0 \end{cases} \quad (\text{A16})$$

To solve (A16), we prescribe the boundary condition  $y_1(0) \equiv g(0)$ , and the symmetry condition  $y_2(0)=0$ . The required third boundary condition is the following relation among  $y_1(\xi_1)$ ,  $y_2(\xi_1)$  and  $y_3(\xi_1)$ , that asserts Eq. (A11) at  $\xi = \xi_1$ :

$$y_2^2(\xi_1) \left[ 1 + \frac{3}{7}ny_1^{n-1}(\xi_1) \right]^2 - y_1^2(\xi_1) \left[ 1 + \frac{6}{7}\frac{n}{n+1}y_1^{n-1}(\xi_1) - y_3(\xi_1) \right] \left[ 1 + \frac{3}{7}y_1^{n-1}(\xi_1) \right]^2 = 0 \quad (\text{A17})$$

The numerical solution of the system of equations (A16) by a finite difference scheme and direct Gaussian elimination was found to be numerically stable, even when the load  $\Lambda$  exhibited a limit point. With use of the connection (26) between  $\omega$  and  $g$ , the solutions provide the connection between  $\Lambda$  and  $\omega(\xi)$ , and the desired response curves of  $\Lambda$  versus  $\omega(0)$ .

The fiber fracture location  $\xi_F$  to be used in Eq. (30) for the kink width was found by iteration. The boundary value  $y_1(0)$  was varied until the values of  $\Lambda$  and  $|\omega|_{\max}$  produced by the solution of Eqs. (A16) satisfied Eq. (28). At each iteration, the value of  $|\omega|_{\max}$ , and the current candidate value of  $\xi_F$ , may be found by use of Eqs. (A13), (A11) and (A14), whenever this current estimate of  $\xi_F$  exceeds  $\xi_1$ ; otherwise, local quadratic interpolation over the integration points used in the solution of (A16) may be used to discover  $|\omega|_{\max}$  and its location at the current estimate of  $\xi_F$  within the region  $0 \leq \xi \leq \xi_1$ .

#### *Elastic solid*

The response of the elastic solid, governed by Eq. (27a), is given by the last two members of Eqs. (A7a), with  $\xi_p=0$ . Applying the conditions of continuity of  $\omega$  and  $\omega'$  at  $\xi=\xi_1$  leads directly to the relation

$$\omega(0) = \frac{\bar{\omega}_0}{1 - \Lambda + \left( \frac{\pi}{2\xi_1} \right)^2} \left[ 1 + \frac{\pi}{2\xi_1} \frac{1}{\sqrt{1-\Lambda}} e^{-\sqrt{1-\Lambda}\xi_1} \right] \quad (\text{A18})$$

used to plot the elastic response curves in Fig. 7.

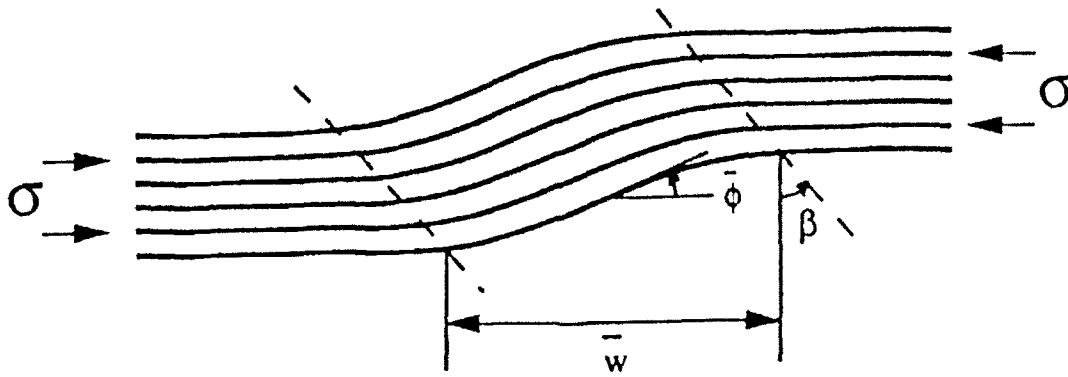


Fig. 1. The basic problem. A unidirectional composite with an initial fiber misalignment is subjected to a remote compressive stress  $\sigma$ . The fiber misalignment is correlated along the  $\beta$  direction.

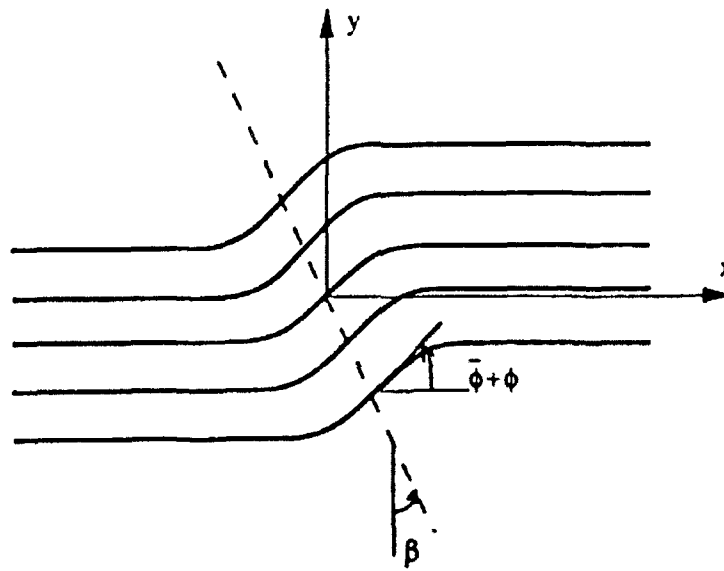


Fig. 2. Deformed geometry. Under load, the fibers rotate from an initial inclination  $\bar{\phi}(x)$  to a deformed inclination  $\bar{\phi}(x) + \phi(x)$ .

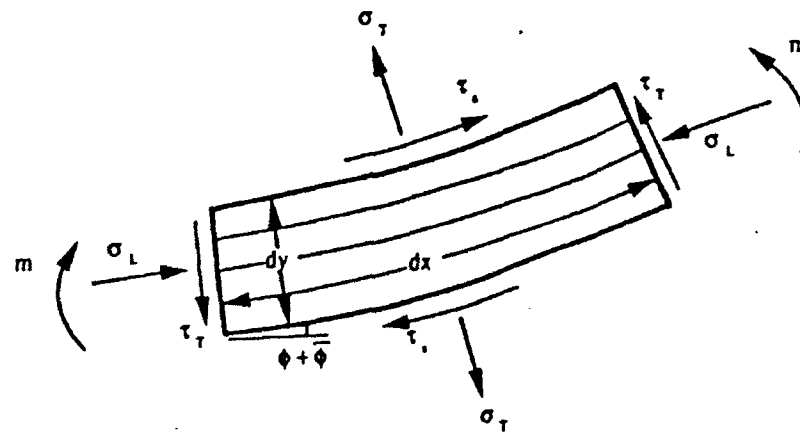


Fig. 3. Stresses on a representative element of the solid. The fibers and matrix have been smeared out to a continuum.

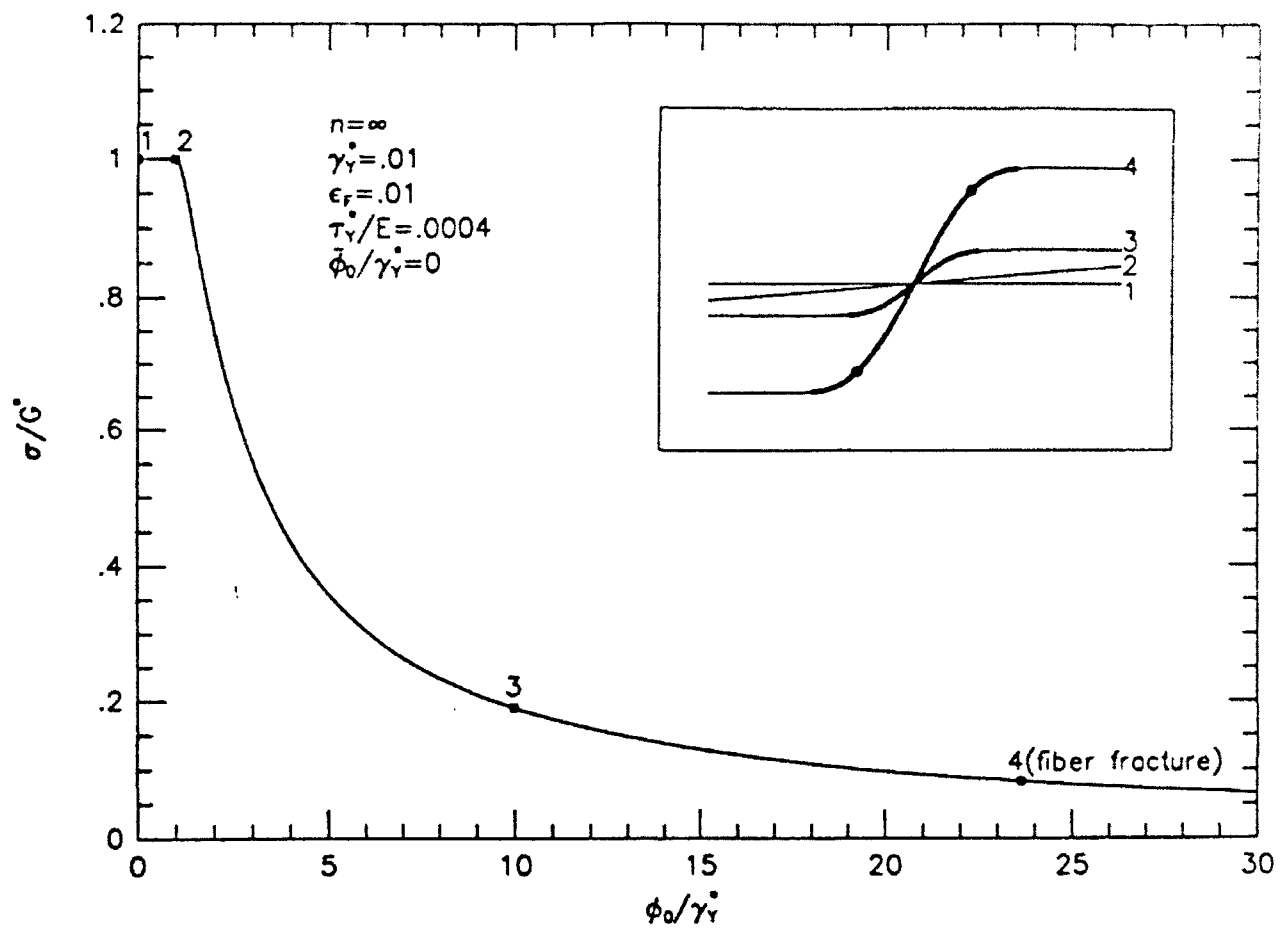


Fig. 4. Collapse response of an elastic-ideally plastic composite with zero initial misalignment. The insert gives the fiber shape at 4 stages of deformation, with the vertical deflection magnified by a factor of 100. The symbol • depicts the location of fiber fracture.

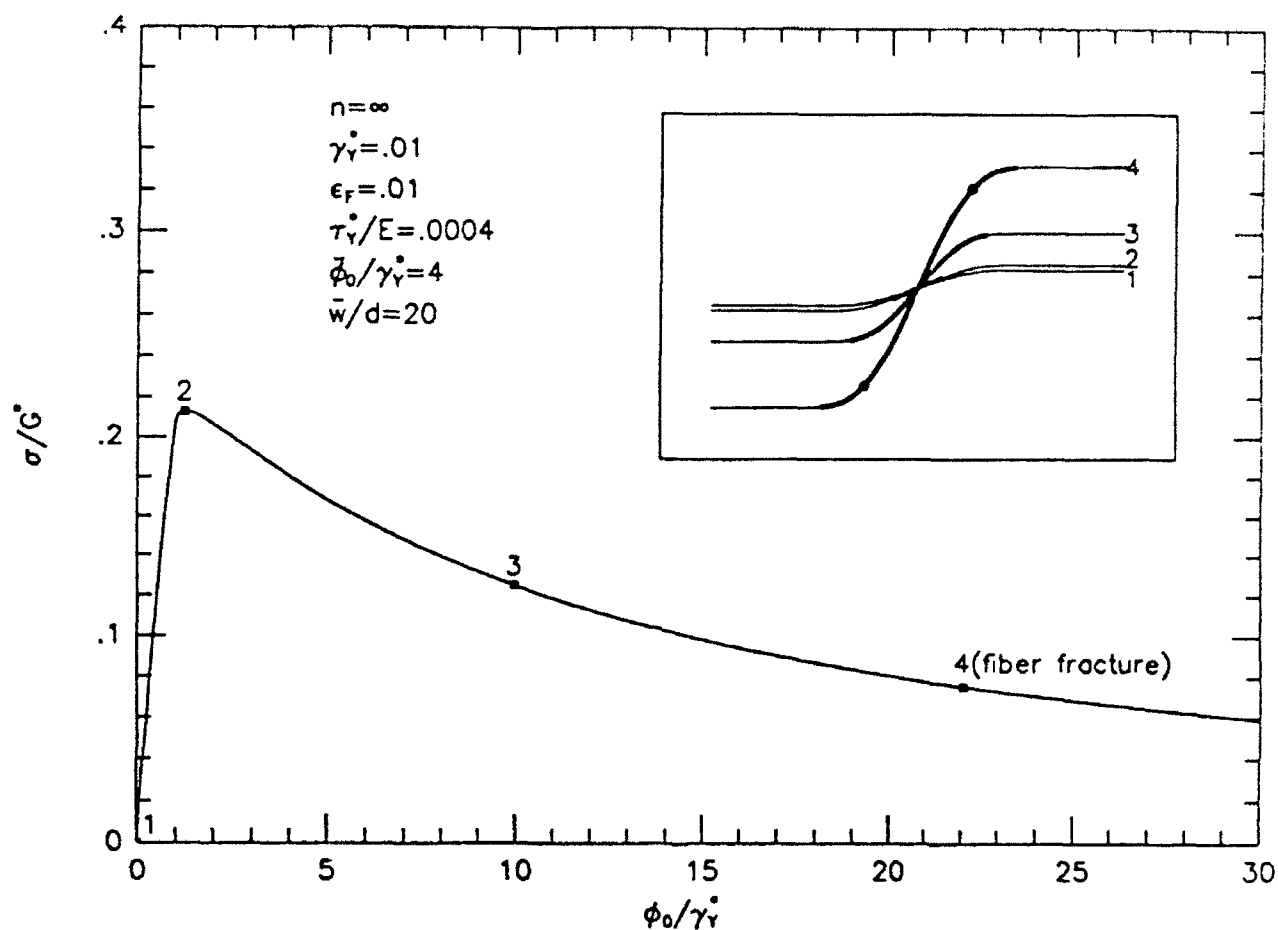


Fig. 5. Collapse response of an elastic-ideally plastic composite with an initial misalignment characterized by  $\bar{\phi}_0/\gamma_Y^* = 4$  and  $\bar{w}/d = 20$ . The insert gives the fiber shape at 4 stages of deformation, with the vertical deflection magnified by a factor of 100. The symbol • depicts the sites of fiber fracture.

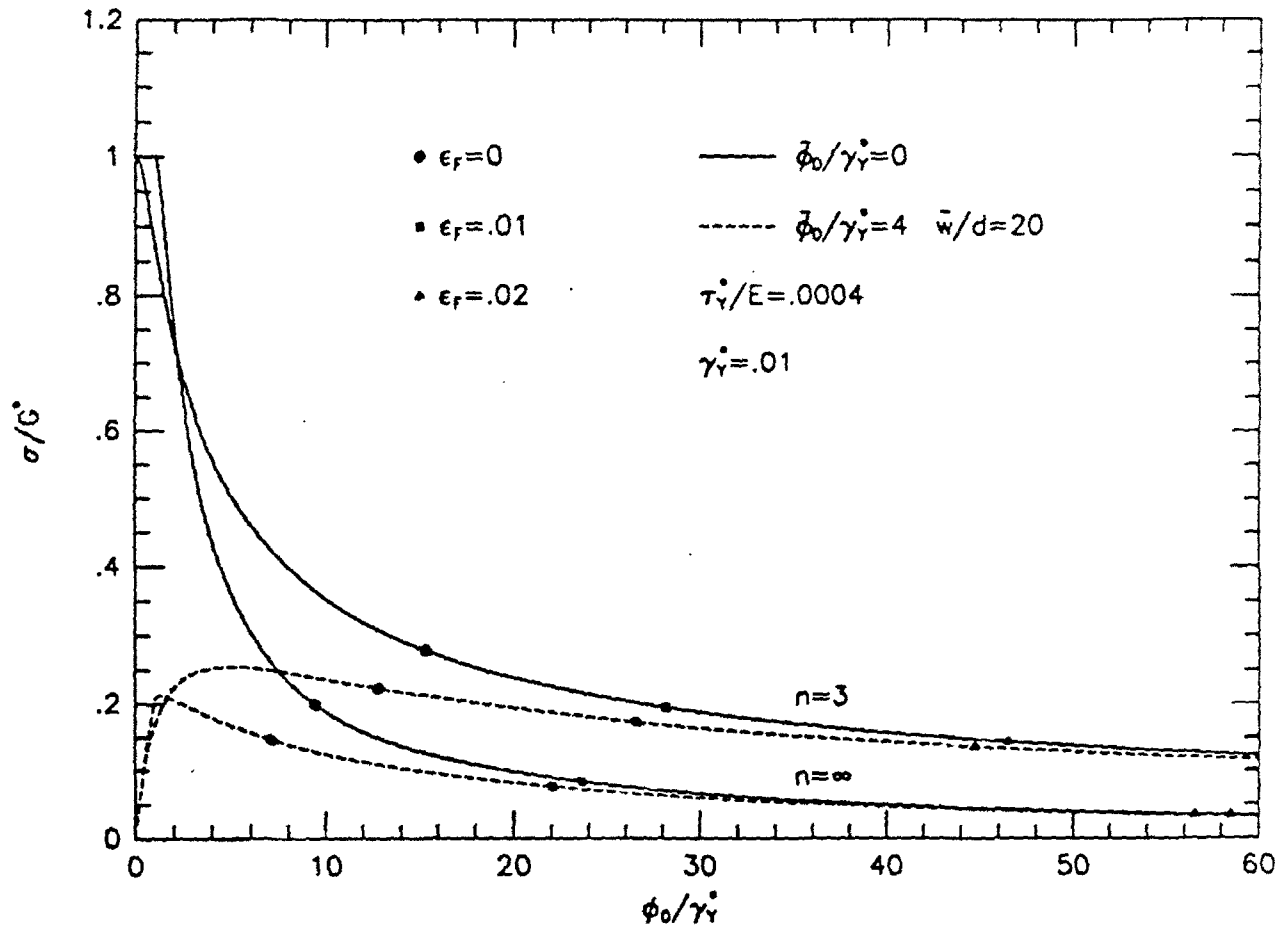


Fig. 6. Collapse response of perfectly aligned ( $\bar{\phi}_0/\gamma_Y^* = 0$ ) and misaligned composite ( $\bar{\phi}_0/\gamma_Y^* = 4$ ,  $\bar{w}/d = 20$ ), for  $n=3$  and  $\infty$ . The fiber rotation  $\phi_0/\gamma_Y^*$  at fiber fracture is sensitive to the value of the fiber fracture strain  $\epsilon_F$ , as shown.



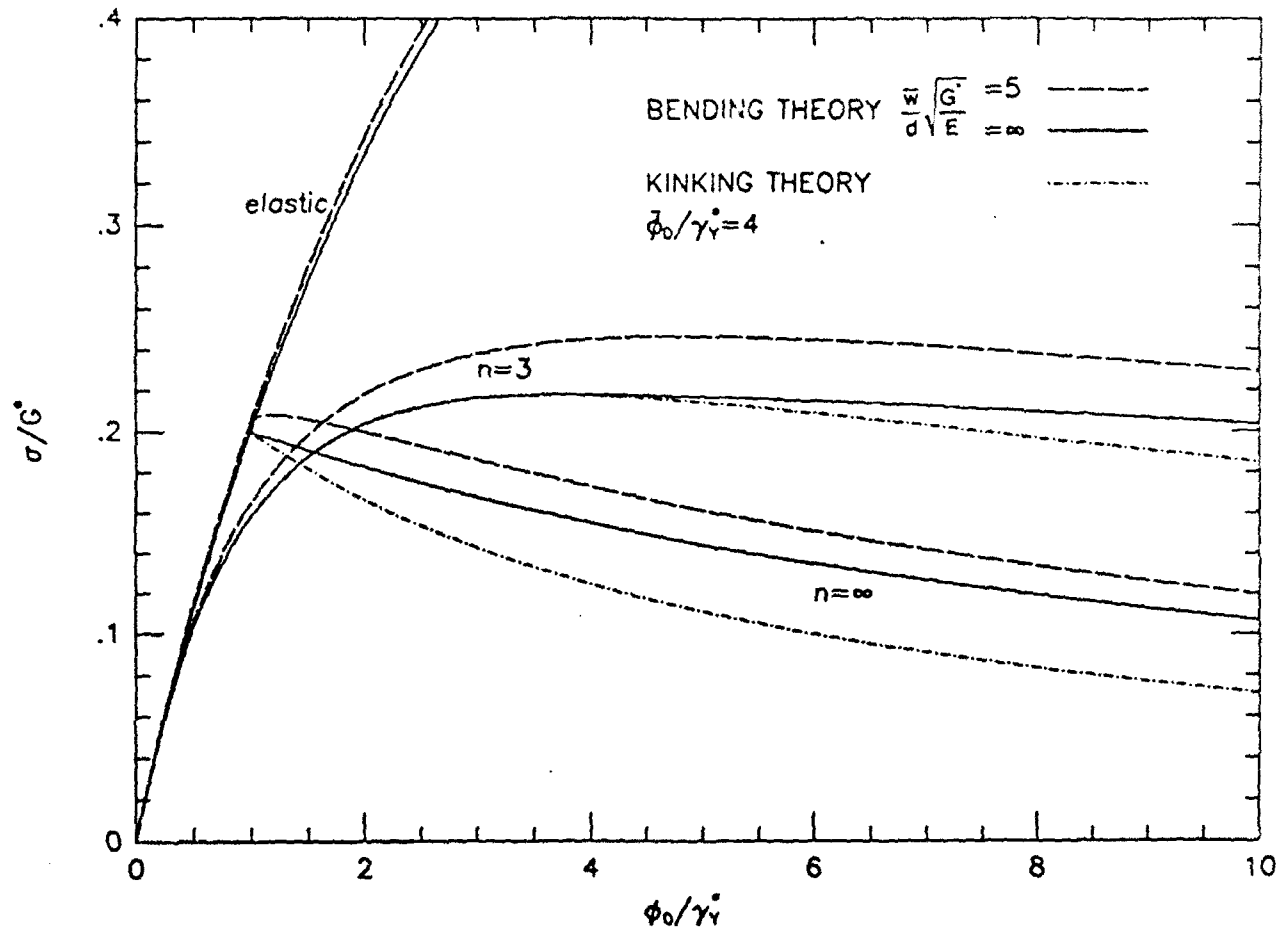


Fig. 7. Collapse response for a typical misalignment angle  $\bar{\phi}_0/\gamma_Y^* = 4$ . Predictions are given for two imperfection widths  $\frac{\bar{w}}{d} \sqrt{\frac{G^*}{E}} = 5, \infty$ , and for the full range of matrix non-linearity (elastic case,  $n=3$  and  $n=\infty$ ). The predictions of kinking theory are included.

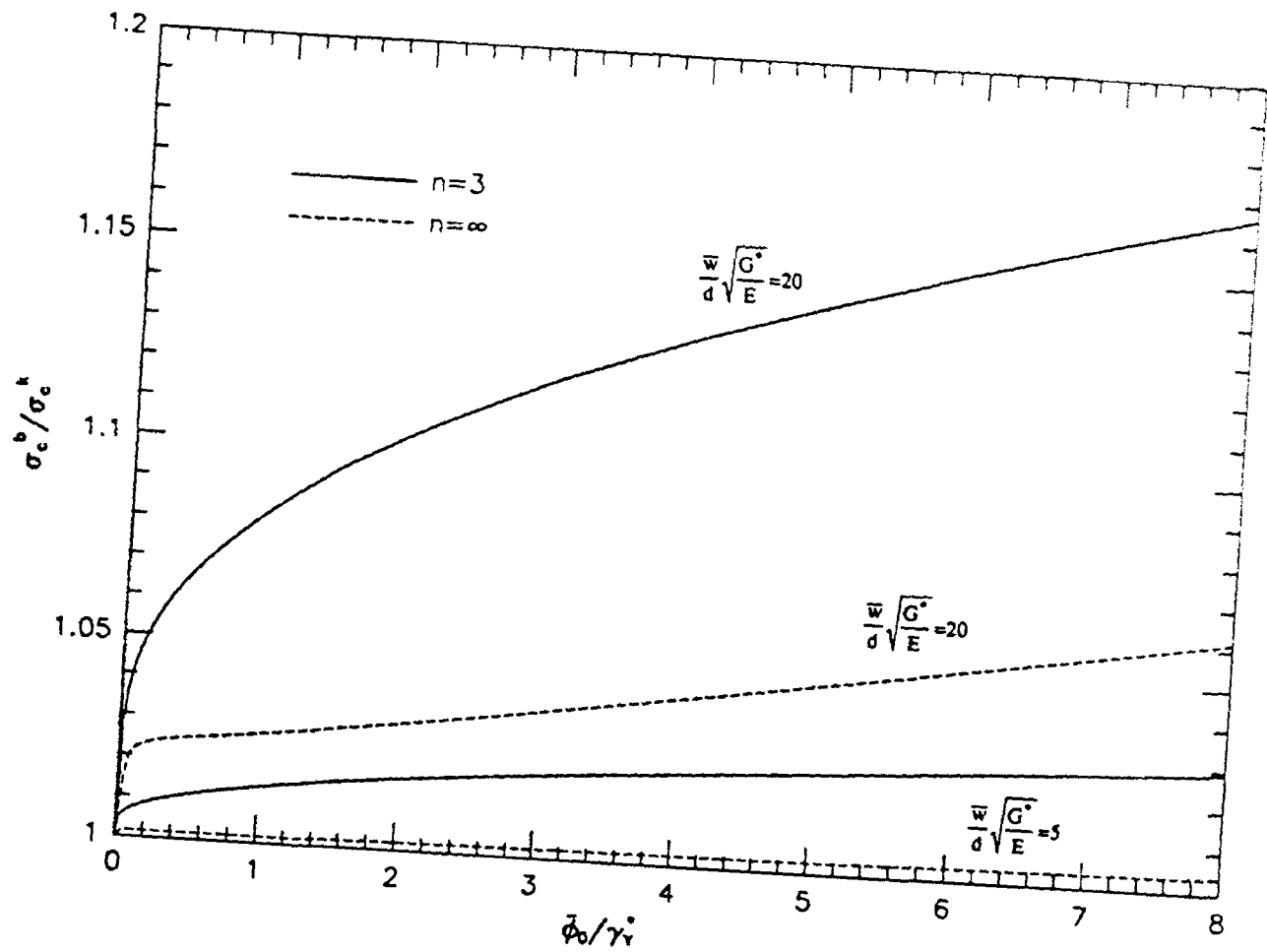


Fig. 8. Ratio of critical stress from bending theory  $\sigma_c^b$  to the critical stress from kinking theory  $\sigma_c^k$  as a function of fiber misalignment  $\bar{\phi}_0/\gamma_Y^*$ , for a wide range of matrix non-linearity  $n$  and misalignment wavelength  $\bar{w}/d\sqrt{G^*/E}$ .

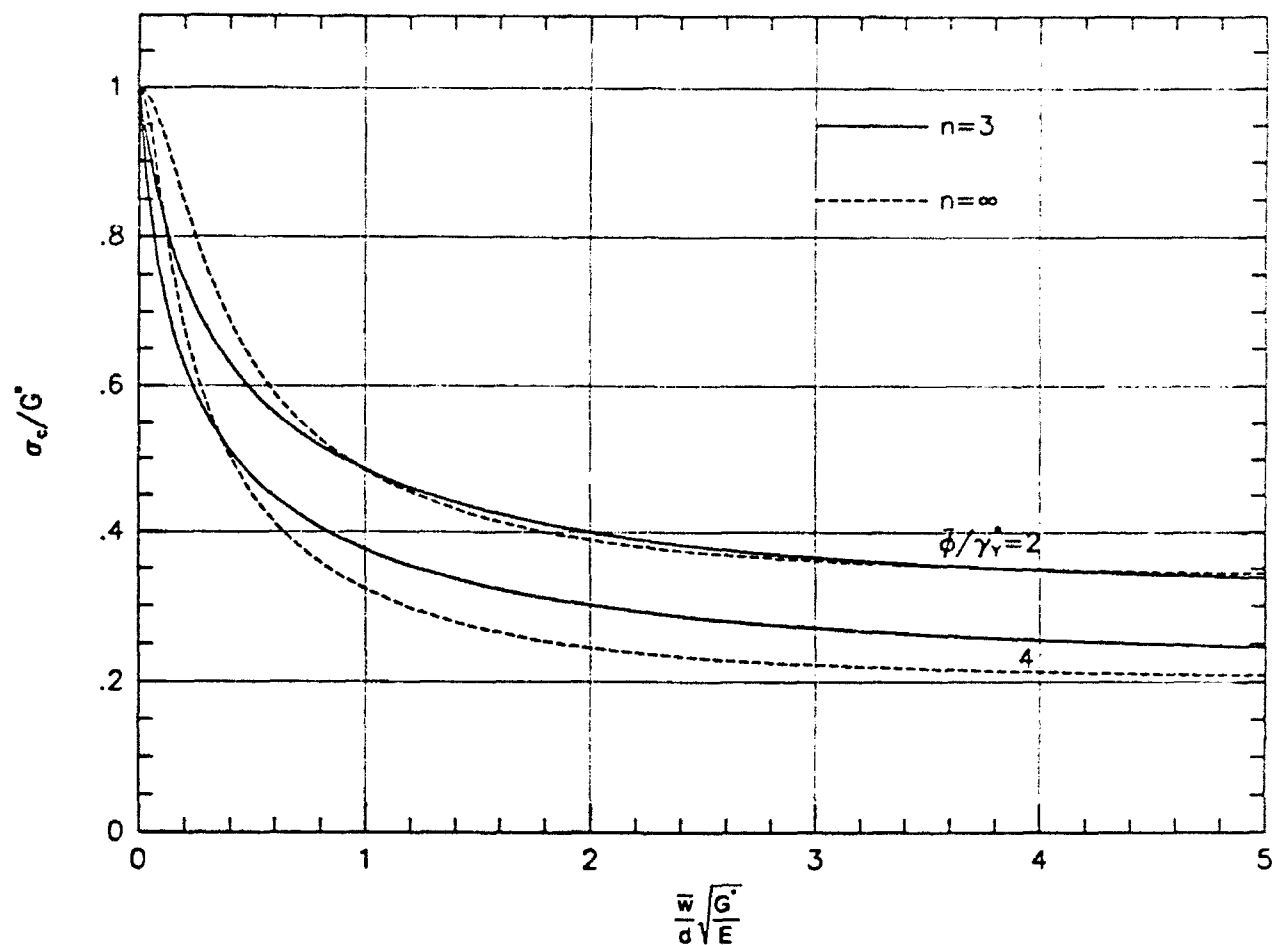


Fig. 9. The effect of wavelength of misalignment  $\frac{\bar{w}}{d} \sqrt{\frac{G^*}{E}}$  upon the critical stress  $\sigma_c/G^*$  for some typical values of matrix non-linearity  $n$  and misalignment angle  $\bar{\phi}_0/\gamma_Y^*$ ; bending theory.

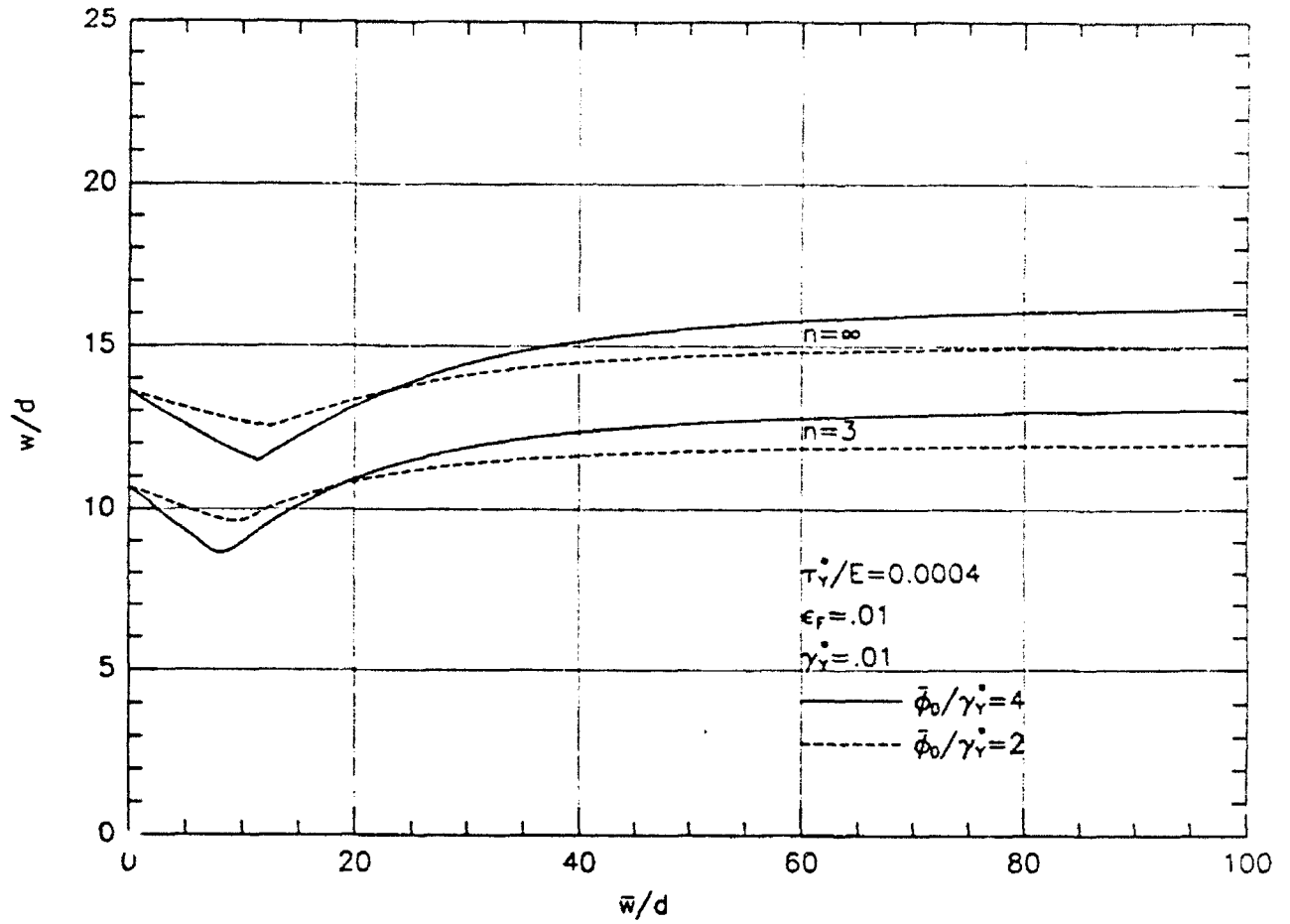


Fig. 10. Effect of misalignment wavelength  $\bar{w}/d$  upon width of kink band  $w/d$ , for  $n=3$  and  $\infty$ , and  $\bar{\phi}_0/\gamma_Y^*=2$  and 4.

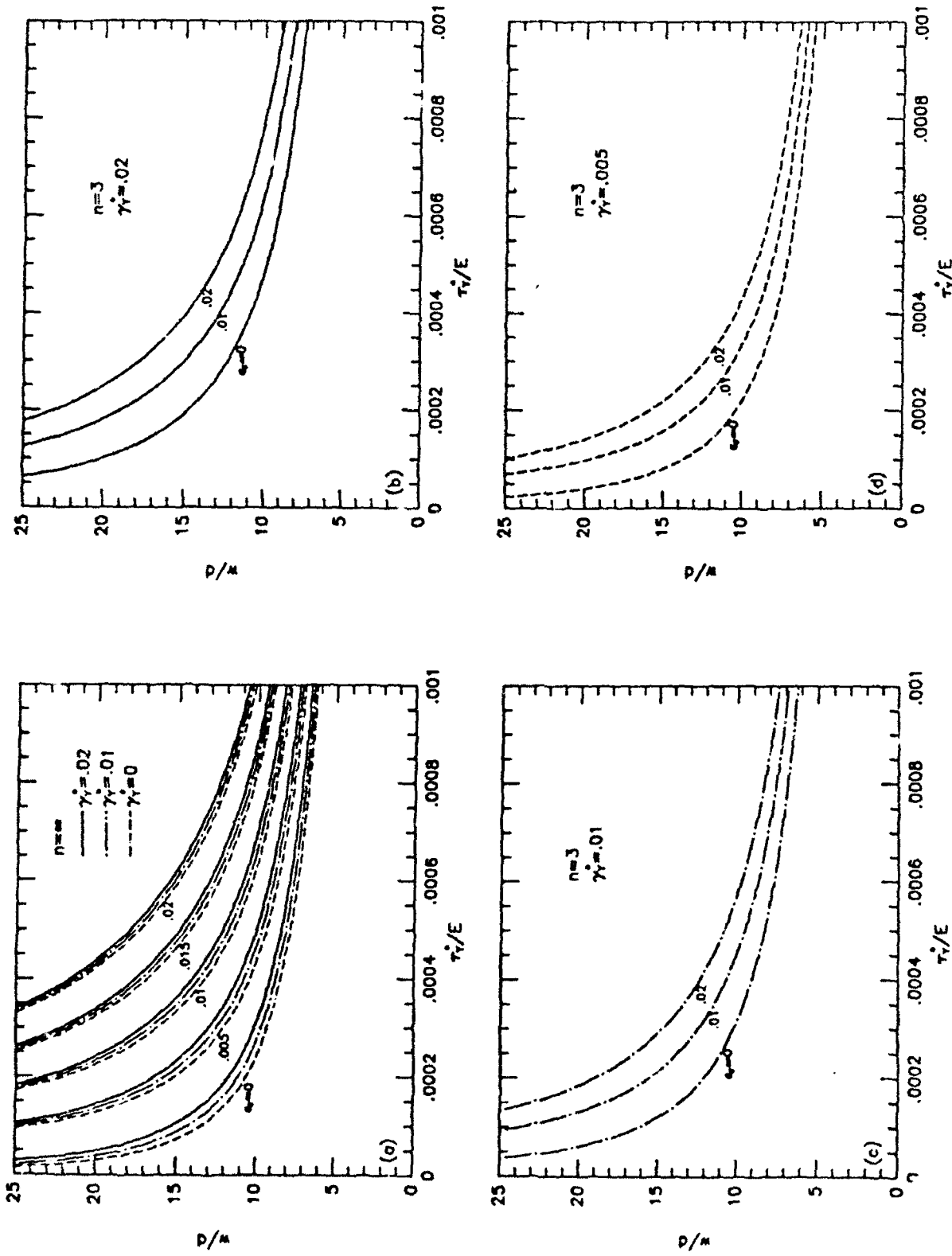


Fig. 11. Width of kink band for perfectly aligned composite ( $\bar{\Phi}_0/\gamma_v^* = 0$ ) as a function of  $\tau_v^*/E$ , and  $\epsilon_p$  in the range 0-.02. (a) Elastic-ideally plastic response, for  $\gamma_v^* = 0$ , .01 and .02. The remaining plots are for  $n=3$ : (b)  $\gamma_v^* = .02$ ; (c)  $\gamma_v^* = .01$ ; and (d)  $\gamma_v^* = .005$ .

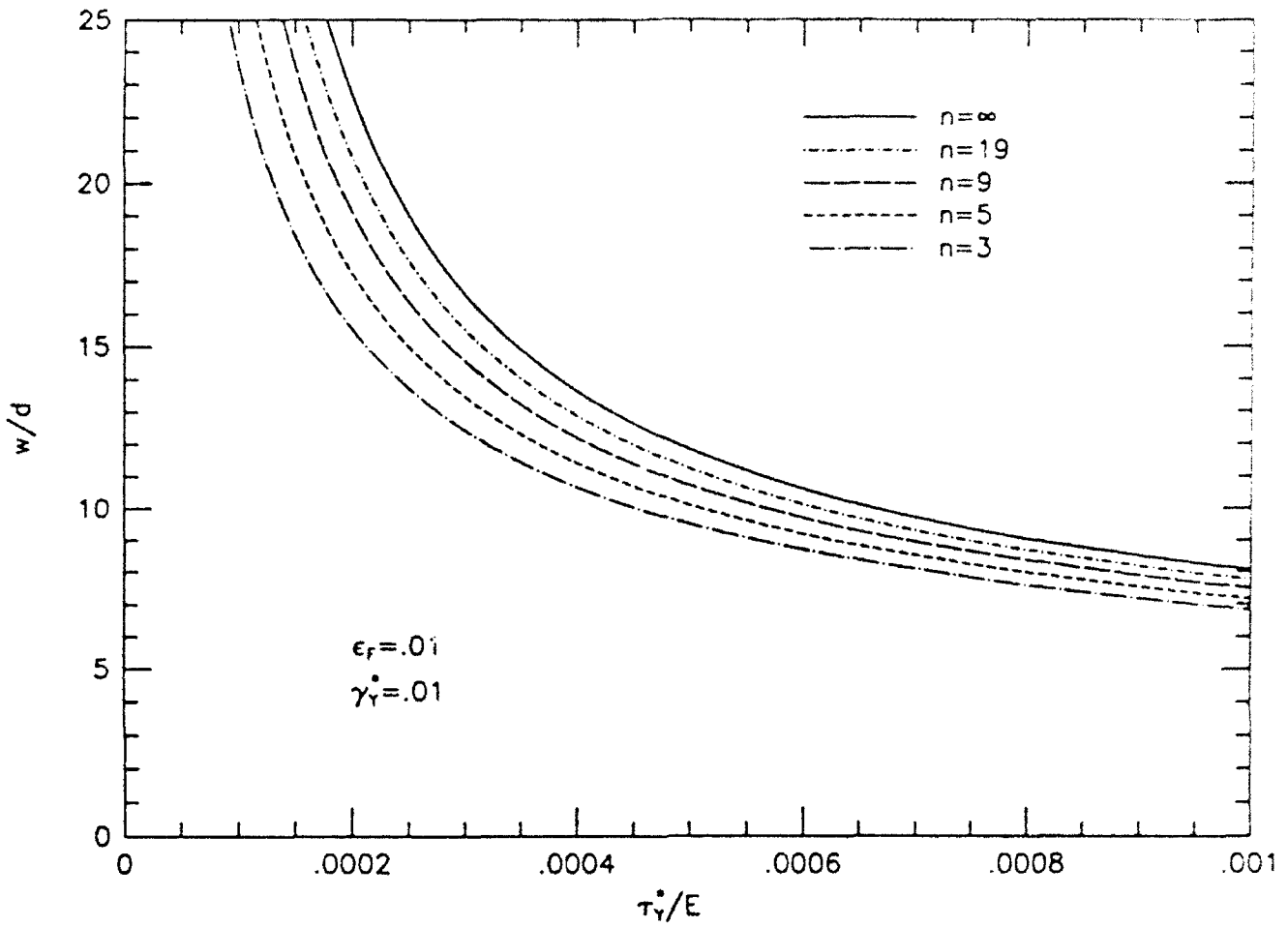
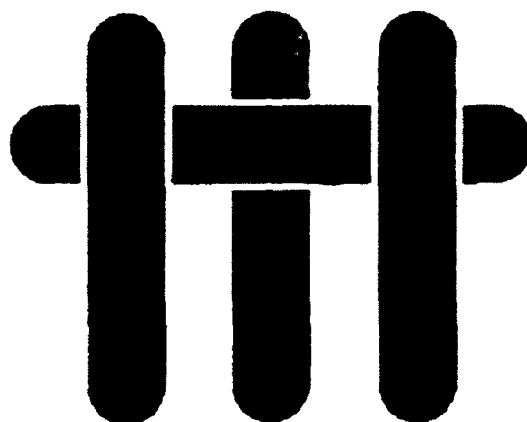


Fig. 12. Effect of  $\tau_Y^0/E$  upon width of kink band, for  $3 \leq n \leq \infty$  and  $\epsilon_f = 0.01$ ,  $\gamma_Y^0 = 0.01$ ; perfectly aligned composite ( $\bar{\phi}_0/\gamma_Y^0 = 0$ ).

# M A T E R I A L S



## Mechanical Properties of Partially Dense Alumina Produced from Powder Compacts

David C.C. Lam\*, F.F. Lange and A. G. Evans

Materials Department  
College of Engineering  
University of California  
Santa Barbara, California 93106

\* Current Address: Hitachi Research Laboratory, 1-1 Saiwaicho 3 chome, Hitachi-shi, Ibaraki-ken, 317 Japan

## Abstract

The elastic modulus ( $E$ ), critical strain energy released rate ( $G_c$ ), and flexural strength ( $\sigma$ ) have been determined for two partially dense alumina bodies produced from the same powder but with different initial densities. The mechanical properties were measured for specimens fabricated at four different relative densities. The measured elastic modulus, critical strain energy released rate and a calculated critical stress intensity factor ( $K_{Ic}$ ) were observed to be linearly related to  $(\rho - \rho_0)/(1 - \rho_0)$ , where  $\rho$  is the current relative density and  $\rho_0$  is the initial relative density of the powder compact. With the observed linear relations for  $E$ ,  $G_c$  (or  $K_{Ic}$ ) and the assumption that the crack length responsible for failure was present in the initial powder compact and shrunk in proportion to the relative density change, a Griffith equation was constructed to estimate the strength at any relative density. This relation was in good agreement with measurements.

## 1. Introduction

A variety of porous ceramics, viz., filters, membranes, electronic substrates, etc., fabricated by the partial densification of powders compacts, require mechanical reliability for their commercial performance. This article examines the effect of porosity on mechanical properties.

In their review of cellular materials, Gibson and Ashby<sup>1</sup> point out that porous materials can have higher specific mechanical properties relative to fully dense materials. Porous solids can also be formed with powders, which compartmentalize the void phase and transmit force through structural units having morphological characteristics which differ from those of cellular materials. Although powder compacts can be stable under applied pressures, neglecting relatively weak, interparticle attractive forces, their mechanical integrity under tension is initially zero, but increases as necks form between touching particles while the void content decreases and changes its morphology.

Although the elastic modulus<sup>2-14</sup> and strength<sup>15</sup> of materials containing isolated pores have been modeled and measured, only Young's Modulus has been extensively researched for porous materials formed with powders. One of the more interesting microstructural features was discovered by Green et al<sup>8</sup> who showed that prior to any densification, the formation of necks between touching particles by surface diffusion can substantially increase the elastic modulus. Further mass transport increased the



relative elastic modulus in a manner that appear to be linearly related to relative density, with the zero modulus intercept dependent on the initial density of the powder compact. The fracture resistance ( $G_c$  or  $K_{Ic}$ ) and strength of partially dense powder compacts have received much less attention. Because partially dense powder compacts could be used in a variety of structural applications, e.g., as matrices within continuous fiber composites, our objective was to obtain a greater understanding of how the mechanical properties of partially dense powder compacts are related to relative density.

## 2. Experiments

By controlling the interparticle potential,  $\alpha$ - $\text{Al}_2\text{O}_3$  powder <sup>a</sup> (mean particle diameter, 1  $\mu\text{m}$ , see ref. 16 for size distribution) compacts with an initial relative density,  $\rho_0$ , of either 0.50 or 0.62 were formed by pressure filtration with a method and reagents reported elsewhere <sup>16</sup>. Prior to filtration, the dispersed (pH 4) slurry, containing 20 volume %  $\text{Al}_2\text{O}_3$  was ultrasonicated for 20 minutes in an attempt to break up larger agglomerates. The lower density body was formed from a flocculated slurry (increasing the pH from 4 to 9), whereas the higher density body was formed from a dispersed slurry. Large cylindrical billets with a height of  $\sim 10$  cm. and a diameter of  $\sim 7.6$  cm. were formed. The bodies were dried and heat treated at 800  $^\circ\text{C}$  for 2 hours (shrinkage began at  $\approx 1100^\circ\text{C}$ ) to impart some mechanical integrity to diamond cut bars for Archimedes density measurement. The large bodies were further heat treated at 1100  $^\circ\text{C}$  for 2 hours to further increase the structural integrity of the material so that bars with the dimension 2.5 x 5 x 50 mm could be cut for property measurements. Different bars were then heated to temperatures between 1200  $^\circ\text{C}$  to 1500  $^\circ\text{C}$  for two hours for room temperature measurements of relative density, elastic modulus, crack growth resistance and strength.

The elastic modulus was measured with an ultrasonic technique used by Green and coworkers <sup>8</sup>. The sonic velocity of the partially dense bars was measured by gently clamping a set of dry contact transducers across two parallel surfaces. The ultrasonic velocity was measured by a computerized ultrasonic system <sup>b</sup>; 1 MHz transducers were used for lower density bars, while 2 MHz transducers were used for the higher density bars. With the velocity of sound  $v$  through the material, the Young's modulus can be calculated using the well known relation, <sup>17-22</sup>

---

<sup>a</sup> AKP 15, Sumitomo Corp., New York, NY.

<sup>b</sup> Model 7000; Ultrasonics, Inc State College PA.

$$E = \rho v^2 (1 - 2\mu)(1 - \mu^2), \quad (1)$$

where  $\mu$  is the Poisson's ratio which had been experimentally determined by Green ( $\mu = 0.17$ ) to be approximately independent of relative density<sup>8</sup>.

The critical stress intensity factor  $K_{IC}$  measure of the materials resistance to crack growth and is related to tensile strength ( $\sigma_c$ ) through the Griffith<sup>23</sup> fracture equation:

$$\sigma_c = Y \frac{K_{IC}}{\sqrt{2\pi c}}. \quad (2)$$

$K_{IC}$  is typically measured with a specimen configuration in which the  $K$  function is known, e.g., a compact tension specimen configuration that contains a preexisting crack of known dimension. Determination of the crack length in a porous body is subjective and renders conventional  $K_{IC}$  test configurations unreliable.

Alternately, a technique exists for measuring the critical strain energy release rate,  $G_c$ , which does not require knowledge of the initial crack length. In this measurement, the energy released during fracture is determined from the integrated area under the load-displacement curve and the cross sectional area of the fractured surface<sup>24, 25</sup>. In the present study, load-displacement curves are obtained from 3-point bend tests of chevron notched bars tested with a span length of 38 mm. Load was applied with a servo-hydraulic test frame<sup>c</sup> and deflection was measured directly by placing a spring loaded deflection arm on top of the center point of the bar. The chevron notch was sawn into the bar to improve crack propagation stability; in instances where no notch was used, the crack is known to become unstable and propagated catastrophically. In catastrophic failure, the work under the catastrophic load-displacement curve is larger than the real work and therefore overestimates the true energy released during fracture. Representative measurements of fracture energy must be determined from a stable load deflection curve shown in Fig 1. With knowledge of  $E$  and  $G_c$ ,  $K_{IC}$  was determined using

$$K_{IC} = \sqrt{E G_c}. \quad (3)$$

The strength of unnotched bars was measured using the same three point flexure test. Similar to other specimens, the bars for strength measurements were cut from the billets after the 1100 °C/2h treatment and further heat treated at high temperatures. No additional machining was performed after the initial 1100°C sintering step. Thus no new flaws that were introduced after the 1100 °C heat treatment.

<sup>c</sup> Model 810, Material Testing System

### 3. Results

All data are tabulated in Table 1. Plots for the relative elastic modulus  $\bar{E}$  and the relative critical strain energy release rate  $\bar{G}_c$  as a function of the current, relative density,  $\rho$ , appeared nearly linear as shown in Fig. 2. In these plots, both  $\bar{E}$  and  $\bar{G}_c$  extrapolate to 0 at the respective initial, relative densities,  $\rho_0$  for the two materials. Moreover when  $\bar{E}$  and  $\bar{G}_c$  are plotted against the density function <sup>a</sup>,  $(\rho - \rho_0)/(1 - \rho_0)$  all data appeared to produce the same linear function as shown in Figs. 2 and 3. In Fig. 2, the elastic modulus of the porous material is normalized by the elastic modulus of the fully dense material,  $E = 400$  GPa.<sup>26</sup> Likewise, in Fig. 3, the critical strain energy release rate for the porous material is normalized by the value for the fully dense material,  $G_c = 40$  J/m<sup>2</sup>.<sup>26</sup> Combining  $\bar{E}$  and  $\bar{G}_c$  with eq. (1), the mean  $\bar{K}_c$  is plotted in Fig. 4. Figure 5 reports the flexural strength vs the current, relative density,  $\rho$  for the two materials.

Representative micrographs of fractured surfaces that illustrate the microstructural evolution for material with an initial relative density of 0.50, after 2h heat treatments at 1200 °C, 1300 °C, and 1400 °C, are shown in Fig. 6. At 1200 °C, the grains appear to be nearly identical to the average and distributed <sup>16</sup> size of the initial particles, and the necks between the particles are large. At 1300 °C, the necks between the initial touching particles are fully formed. At 1400 °C, the substantial grain growth has occurred. Thus, it can be concluded that data for  $\bar{E}$ ,  $\bar{G}_c$  and  $\sigma_c$  were recorded for microstructures wherein necks between initial touching particle are fully formed, as well as being subject to grain coarsening.

### 4. Discussion

A linear relation was discovered between the relative elastic modulus and relative density for materials with different initial densities. The density function brings the data sets into coincidence (Fig 2) was determined through the more general relation,

$$\bar{E} = m\rho - k, \quad (4)$$

where the boundary conditions  $\bar{E} \rightarrow 1$  when  $\rho \rightarrow 1$  and  $\bar{E} \rightarrow 0$  when  $\rho \rightarrow \rho_0$  give

<sup>a</sup>  $(\rho - \rho_0)/(1 - \rho_0)$  is the current fractional porosity  $(\rho - \rho_0)$  divided by the initial, fractional porosity  $(1 - \rho_0)$

$$\bar{E} = \frac{\rho - \rho_0}{1 - \rho_0} \quad (5)$$

To understand the physics behind eq (4), it can be imagined that the first term,  $m\rho$ , represents a material formed with continuous, non-interacting, solid framework with a volume fraction,  $\rho$ . The rest of the material is void space. When all of the framework is oriented in the same direction as the stress,  $m = 1$ . Like-wise, when only a fraction of the framework,  $f$ , is oriented in the testing direction,  $m = f$ . The connective network in the partially dense powder compact supports stress only when  $\rho > \rho_0$ . Thus, after necks form between the particles, the connective network supports stress in proportion to the differential density. Unlike low density cellular and random fiber materials <sup>1</sup>, the particle network does not contribute to deformation through large bending moments.

A recent review <sup>9</sup> of modulus-density relations has proposed a relation,

$$\bar{E} = \left(1 - \frac{P}{P_c}\right)^n \quad (6)$$

where  $P$  is the current volume fraction of porosity ( $1 - \rho$ ),  $P_c$  is a critical volume fraction of porosity where  $\bar{E} = 0$ , and  $n$  is an exponent used to fit experimental data. Clearly,  $P_c = (1 - \rho_0)$  and when  $n = 1$ , eqs (5) and (6) are identical. Data for 6 rare-earth oxide systems <sup>10-12</sup> gave <sup>9</sup> ( $0.47 < \rho_0 < 0.63$ ) consistent with values generally achieved for powders (but not reported by the original authors). Values for  $n$  ranged around unity (0.74 and 1.3), suggests that the data could be approximated with a linear relation,  $n = 1$ . Figure 7 shows replots of data obtained for alumina bodies, <sup>8</sup> with three different initial densities illustrate that the data coincide and produce a linear relation when  $(\rho - \rho_0)/(1 - \rho_0)$  is used as the density coordinate.

In a similar manner, the relative strain energy release rate can be directly related to the density function

$$\bar{G}_c = \frac{\rho - \rho_0}{1 - \rho_0} \quad (7)$$

For this relation to apply, it is required that the crack front be continuous within the dense framework (as suggested in Fig. 6) and its area fraction be proportional to  $\rho$ . <sup>27</sup> Furthermore, since both  $\bar{E}$  and  $\bar{G}_c$  can be approximated by the same density function, eq (3) requires that the relative, critical stress intensity factor also have the same dependence on relative density, viz.,

$$\bar{K}_c = \frac{\rho - \rho_o}{1 - \rho_o} \quad (8)$$

The strength of the porous body is inversely related to the square root of the flaw size,  $c$ . Consequently, by assuming that the flaws (size  $c_i$ ) are incorporated into the powder compact during processing and shrink as the compact densifies, the current flaw size should be represented by

$$c = \alpha(1 - \epsilon) + \beta, \quad (9)$$

where  $\epsilon$  is the linear shrinkage strain given by

$$\epsilon = 1 - \left( \frac{\rho_o}{\rho} \right)^{1/3}. \quad (10)$$

The coefficients  $\alpha$  and  $\beta$  are determined by requiring that  $c \rightarrow c_i$  when  $\rho \rightarrow \rho_o$ , and  $c \rightarrow 0$  when  $\rho = 1$ . The final result is

$$\bar{c} = \frac{c}{c_i} = \frac{\left( \frac{\rho_o}{\rho} \right)^{1/3} - \rho_o^{1/3}}{1 - \rho_o^{1/3}}. \quad (11)$$

The effective flaw size  $c$ , at different densities, can be calculated from the measured strengths by using eq (3). The effective initial flaw size at  $\rho_o$  can then be obtained by fitting eq. (11) with the data. In this manner,  $c_i$  for both materials is  $\approx 350 \mu\text{m}$ .

By combining the preceding relations, the strength can be expressed as a function of the critical stress intensity factor of the dense body,  $K_{IC}$ , the size of the largest initial flaw within the powder compact,  $c_i$ , and density as

$$\sigma_c = Y \frac{K_{IC}}{\sqrt{2\pi c_i}} \frac{\rho - \rho_o}{1 - \rho_o} \left[ \frac{1 - \rho_o^{1/3}}{\left( \frac{\rho_o}{\rho} \right)^{1/3} - \rho_o^{1/3}} \right]^{1/2}. \quad (12)$$

Upon using  $c_i = 350 \mu\text{m}$  and  $K_{IC} = 4 \text{ MPam}^{1/2}$ ,<sup>29</sup> this strength relation, eq. (12), has been plotted on Fig. 5 to illustrate the reasonable agreement with experimental data.

## 5. Conclusion

It has been shown that the elastic modulus and critical strain energy release rate of a partially dense powder compact are linearly proportional to the density function,  $(\rho - \rho_0)/(1 - \rho_0)$ . This function arises because the solid and void phases are interpenetrating, where the solid phase is a framework that supports load without large bending moments, and allows crack extension in proportion to its area fraction (when  $\rho > \rho_0$ ). The variation in strength with relative density is consistent with the Griffith equation when the strength determining cracks within the powder shrink in proportion to the change in relative density.

### Acknowledgment

This research was supported by the Defense Advanced Research Projects through the University Research Initiative under the Office of Naval Research Contracts No. N00014-86-K-0753 and N00014-92-J-1808.

Table I Collective Data

Initial Relative Density,  $\rho_0 = 0.62$ 

Sintering	$\rho$	$\bar{E}$	$\bar{G}_c$	$\sigma_c$
1200°C/2h	0.71	$0.25 \pm 0.01$ (5)	$0.38 \pm 0.05$ (5)	$127 \pm 21$ MPa (9)
1300°C/2h	0.78	$0.42 \pm 0.01$ (5)	$0.50 \pm 0.03$ (3)	$168 \pm 43$ MPa (8)
1400°C/2h	0.85	$0.57 \pm 0.02$ (5)	$0.71 \pm 0.07$ (5)	$270 \pm 34$ MPa (8)
1500°C/2h	0.96	$0.91 \pm 0.01$ (5)	$0.78 \pm 0.08$ (6)	$474 \pm 67$ MPa (5)

Initial Relative Density,  $\rho_0 = 0.50$ 

Sintering	$\rho$	$\bar{E}$	$\bar{G}_c$	$\sigma_c$
1200°C/2h	0.58	$0.17 \pm 0.01$ (5)	$0.19 \pm 0.03$ (4)	$34 \pm 6$ MPa (3)
1300°C/2h	0.65	$0.30 \pm 0.01$ (5)	$0.31 \pm 0.06$ (5)	$81 \pm 17$ MPa (3)
1400°C/2h	0.73	$0.46 \pm 0.02$ (5)	$0.43 \pm 0.07$ (4)	$158 \pm 23$ MPa (5)
1500°C/2h	0.85	$0.69 \pm 0.02$ (5)	$0.62 \pm 0.07$ (3)	$318 \pm 39$ MPa (4)

Elastic modulus is normalized by  $E = 400$  GPa <sup>26</sup>Critical strain energy release rate is normalized by  $G_c = 40$  J/m<sup>2</sup> <sup>26</sup>

Number in parentheses indicates number of tests.

## References

1. L.J. Gibson and M.F. Ashby, Cellular Solids, Pergamon Press (1988).
2. R.L. Coble and W.D. Kingery, "Effect of Porosity on Physical Properties of Sintered Alumina," *J. Am. Ceram. Soc.* **39**, 377 (1956).
3. D.P.H. Hasselman and R.M. Fulrath, "Effect of Cylindrical Porosity on Young's Modulus of Polycrystalline Brittle Material," *J. Am. Ceram. Soc.* **47**, 545-5 (1965).
4. J.P. Watt, G.F. Davies and R.J. O'Connell, "The Elastic Properties of Composite Materials," *Rev. Geophys. Space Phys.* **14**, 541-63 (1976).
5. B. Budiansky and R.J. O'Connell, "Elastic Modulus of a Cracked Solid," *Int. J. Solids Structures.* **12**, 81-97 (1976).
6. F.P. Knudsen, "Effect of Porosity on Young's Modulus of Alumina," *J. Am. Ceram. Soc.* **45** 94-5 (1962).
7. J.C. Wang, "Young's Modulus of Porous Materials, Part I & II," *J. Mater. Sci.*, **19**, 801-814 (1984).
8. D. J. Green, C. Nader and R. Brezny, "The Elastic Behavior of Partially-Sintered Alumina," Sintering of Advanced Ceramics, Ceramics Transactions vol 7, ed. C.A. Handwerker, J.E. Blendell and W.A. Kaysser. 345-56.
9. K. K. Phani and S. K. Niyogi, "Elastic Modulus-Porosity Relation in Polycrystalline Rare-Earth Oxides, *J. Am. Ceram. Soc.* **70** [12] C362-66 (1987).
10. M. O. Marlowe and D. R. Wilder, "Elasticity and Internal Friction of Polycrystalline  $Y_2O_3$ ," *J. Am. ceram. Soc.* **48** [5] 227-33 (1965).
11. W. R. Manning, M. O Marlowe and D. R. Wilder, "Temperature and Porosity Dependence of Young's Modulus of Polycrystalline  $Dy_2O_3$  and  $Er_2O_3$  ," *J. Am. ceram. Soc.* **49** [4] 227-28 (1966); with O. Hunter, Jr. and B. R. Powell, Jr. "Elastic Properties of Polycrystalline  $Y_2O_3$ ,  $Dy_2O_3$ ,  $Ho_2O_3$ , and  $Er_2O_3$ : Room Temperature Measurements," *J. Am. ceram. Soc.* **52** [8] 436-42 (1969),
12. B. R. Powell, Jr. and W. R. Manning, "Elastic Properties of Polycrystalline  $Yb_2O_3$ ," *J. Am. Ceram. Soc.* **54** [10] 488-90 (1971).
13. O. Hunter, Jr. H. J. Korklan and R. R. Suchomel, "Elastic Properties of Polycrystalline Cubic  $Sm_2O_3$ ," *J. Am Ceram. Soc.* **57** [6] 267-68 (1974); with G. e. Graddy Jr., "Elastic Properties of Polycrystalline Cubic  $Lu_2O_3$ ," *J. Am Ceram. Soc.* **5** [1-2] 82 (1976).
14. S. L. Dole, O. Hunter, Jr. and F. W. Calderwood, "Elastic Properties of Polycrystalline Scandium and Thulium Sesquioxides," *J. Am Ceram. Soc.* **60** [3-4] 167-68 (1977).



15. R.M. Spriggs, "Expression For Effect Of Porosity on Elastic Modulus of Polycrystalline Refractory Materials, Particularly Aluminium Oxide," *J. Am. Ceram. Soc.* **44**, 628-29 (1961); "Effect of Open and Cloased Pores on Elastic Moduli of Polycrystalline Alumina," *J. Am. Ceram. Soc.* **45**, 454 (1962).
16. B.V. Velamakanni and F.F. Lange, "Effect of Interparticle Potentials and Sedimentation on Particle Packing Density of Bimodal Particle Distribution During Pressure Filtration," *J. Amer. Ceram. Soc.*, **74** [1] 166-72 (1991).
17. J. Krautkramer and H. Krautkramer, Ultrasonic Testing of Materials, 2nd ed. Springer, Berlin (1977).
18. M.C. Bhardwaj, "Principles and Methods of Ultrasonic Characterization of Materials," *Adv. Ceram. Mater.*, **1** [4] 311-24 (1986).
19. M.P. Jones, G.V. Blessing and C.R. Robbins, "Dry-Coupling Ultrasonic Elasticity Measurements of Sintered Ceramics and Their Green States," *Mater. Eval.*, **44** [6] 859-62 (1986).
20. J.A. Brunk, C.J. Valenza and M.C. Bhardwai, "Applications and Advantages of Dry Coupling Ultrasonic Transducers For Materials Characterization and Inspection," Acousto-Ultrasonics: Theory and Applications, J.C. Duke, Jr. ed. Plenum Press, N.Y. (1988).
22. D.S. Kupperman and H.B. Harplus, "Ultrasonic Wave Propagation Characteristics of Green Ceramics," *Ceram. Bull.*, **63** [12] 1505-9 (1984).
23. A.A. Griffith, "Phenomena of Rupture and Flow In Solids," *Phil. Trans. R. Soc. London*. A221, 163-90 (1920).
24. J. Nakayama, "Direct Measurements of Fracture Energies of Brittle Heterogeneous Material," *J. Amer. Ceram. Soc.*, **48** [11] 583-87 (1965).
25. F.J.P. Clarke, H.G. Tattersall, and G. Tappin, "Toughness of Ceramics and Their Work of Fracture," *Proc. Brit. Ceram. Soc.*, **6** 163-72 (1966).
26. A. Casagrande, D.C.C. Lam, B. Flynn and S. Kumar, unpublished work on the properties of fully dense alumina produced from Sumitomo AKP-15 and AKP-50 alumina powder, Materials Department, University of California, Santa Barabra (1990).
27. R.W. Rice and S.W. Freiman, "The Porosity Dependence of Fracture Energies," in Ceramics Microstructures '76, ed., R.M. Fulrath and J.A. Pask, 800-9 (1976).

### Figure Captions

Fig. 1      Typical load-displacement curve for fracture energy measurement.

- Fig. 2      Relative elastic modulus for both high and low initial density sets as a function of fractional densification. Fully dense elastic modulus corresponds to 400 GPa. <sup>26</sup>
- Fig. 3      Relative critical strain energy released rate for both high and low initial density sets as a function of fractional densification. Fully dense critical strain energy released rate equals 40 J/m<sup>2</sup>. <sup>26</sup>
- Fig. 4      Mean fracture toughness of porous alumina as a function of fractional densification calculated from elastic modulus and critical strain energy release rate data.
- Fig. 5      Strength of partially densified alumina plotted as a function of fractional densification.
- Fig. 6      SEM micrographs of the fractured surface of porous alumina ( $\rho_0 = 0.5$ ) at the initial stage of densification where necks are just formed (top, 1200 °C/2h); at the intermediate stage where the grain boundaries are fully formed before significant grain growth (middle, 1300 °C/2h); at the final stage where grain growth had taken place (1400 °C/2h).
- Fig. 7      Relative elastic modulus data for polycrystalline alumina <sup>8</sup> plotted as a function of fractional densification.

Fig. 1 Lam et al

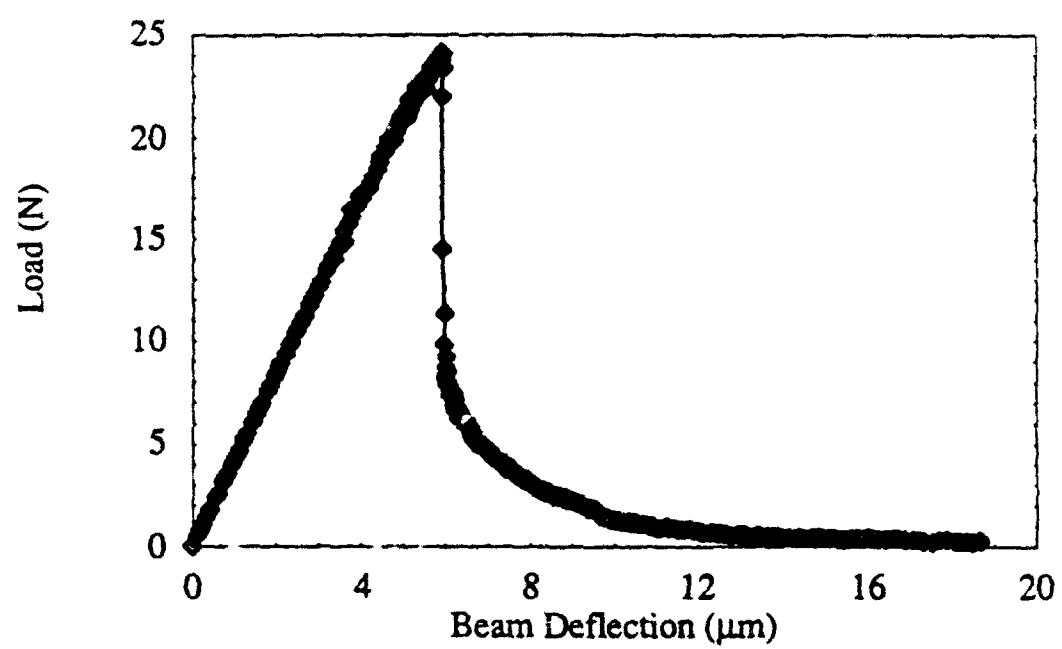


Fig. 2 Lam et al

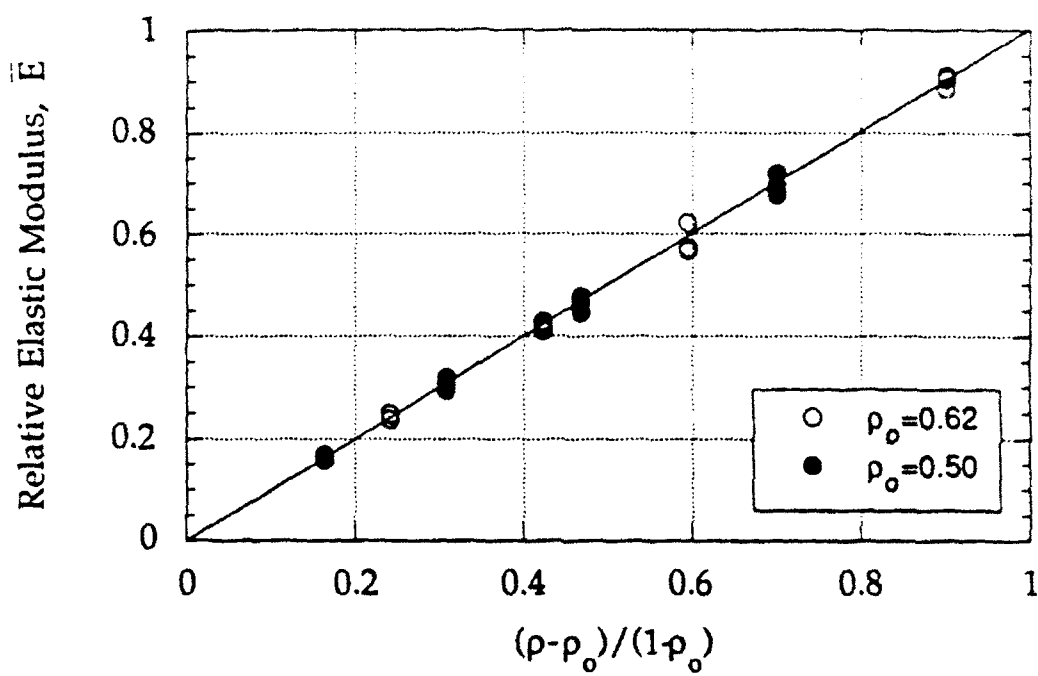


Fig. 3 Lam et al

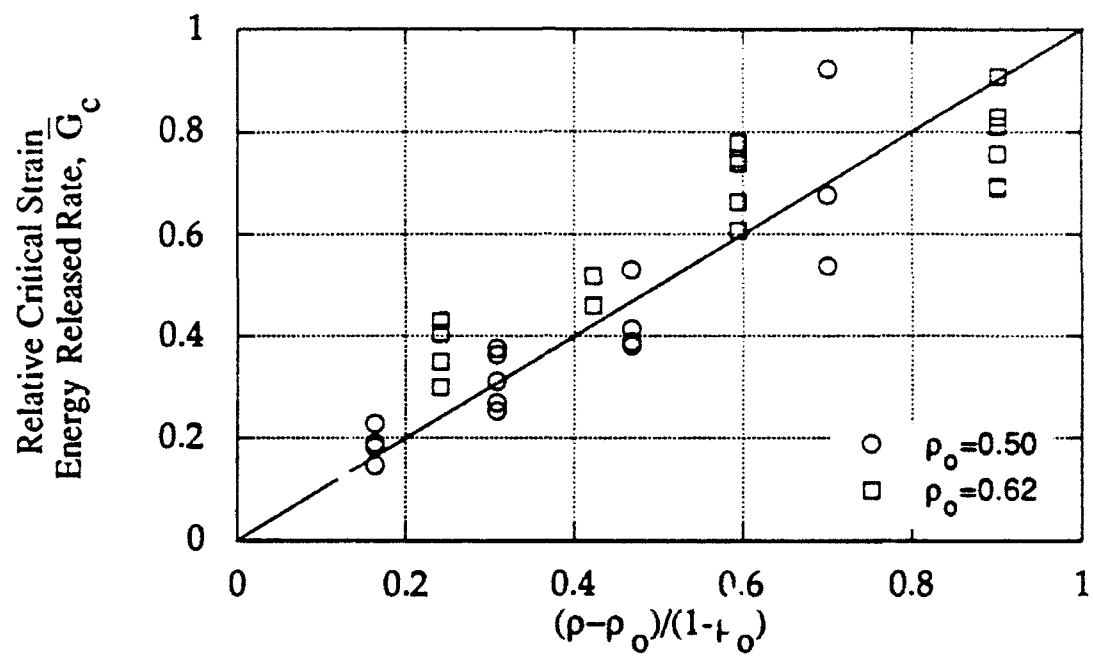


Fig. 4 Lam et al

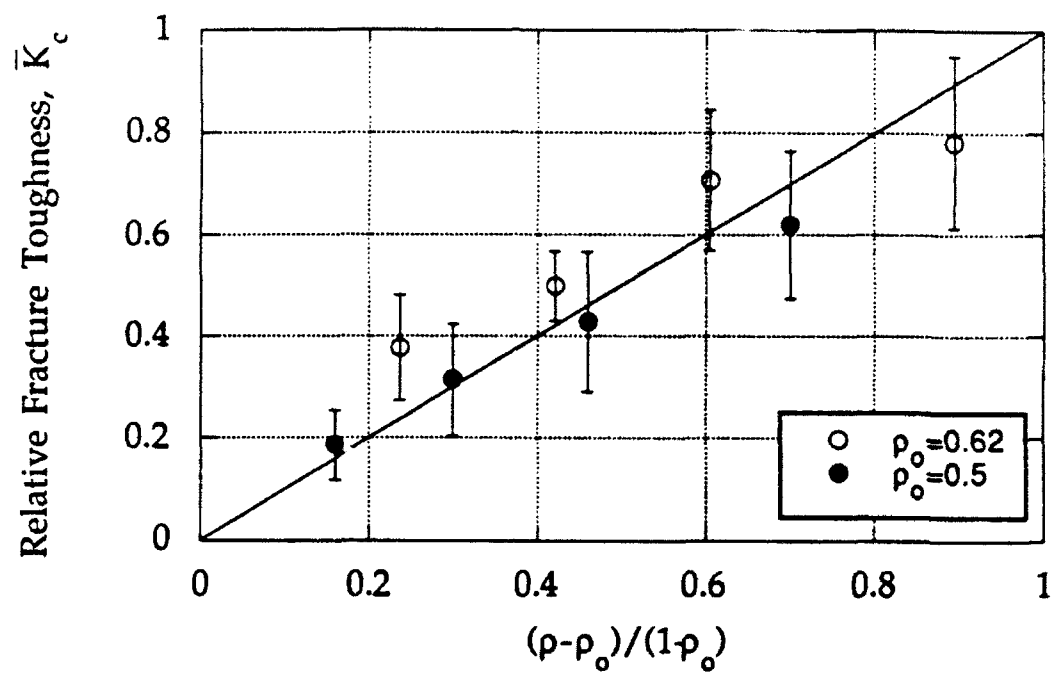


Fig. 5 Lam et al

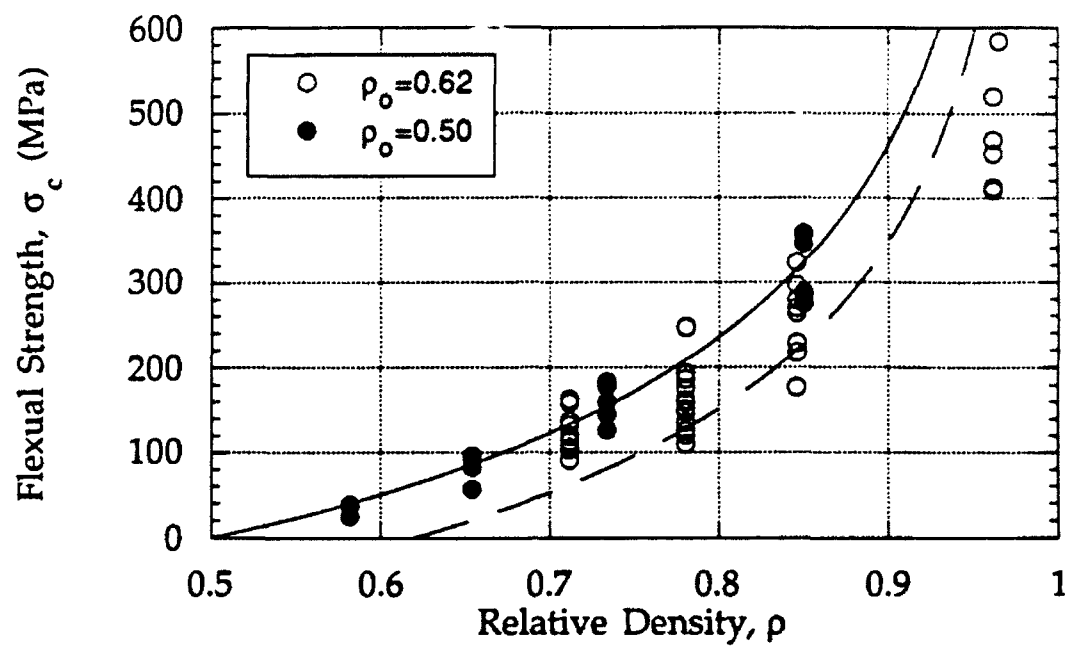


Fig 6 Lam et al

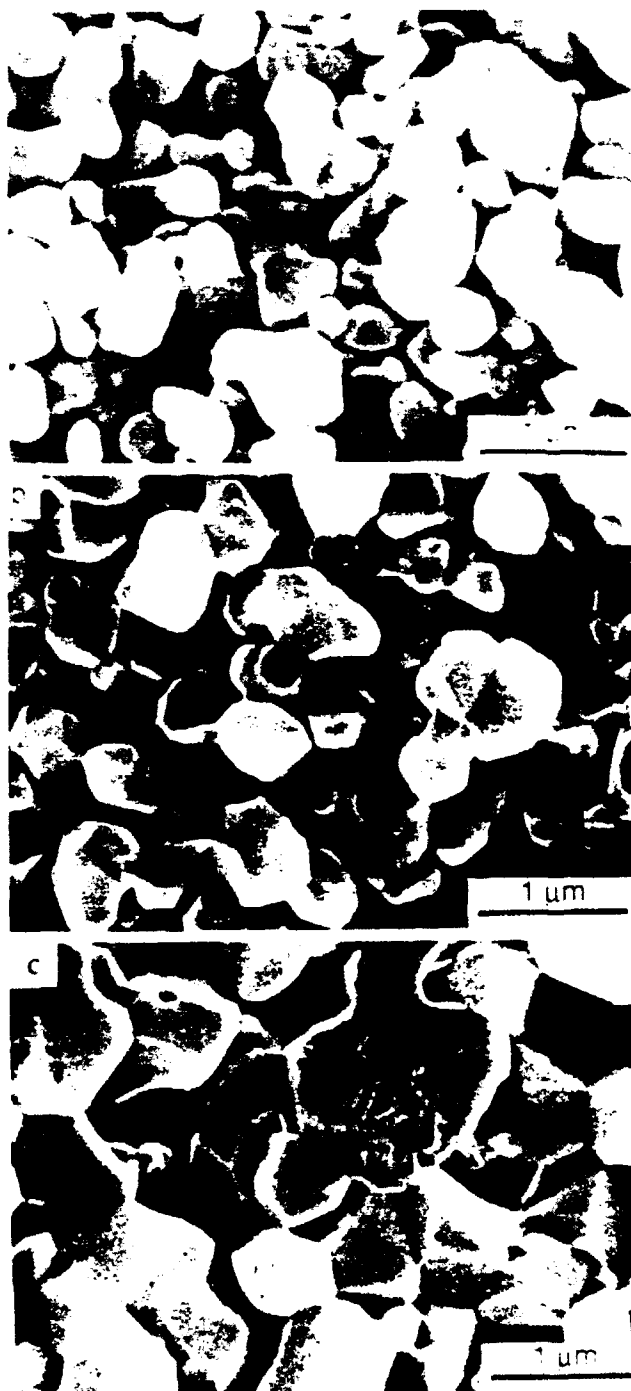
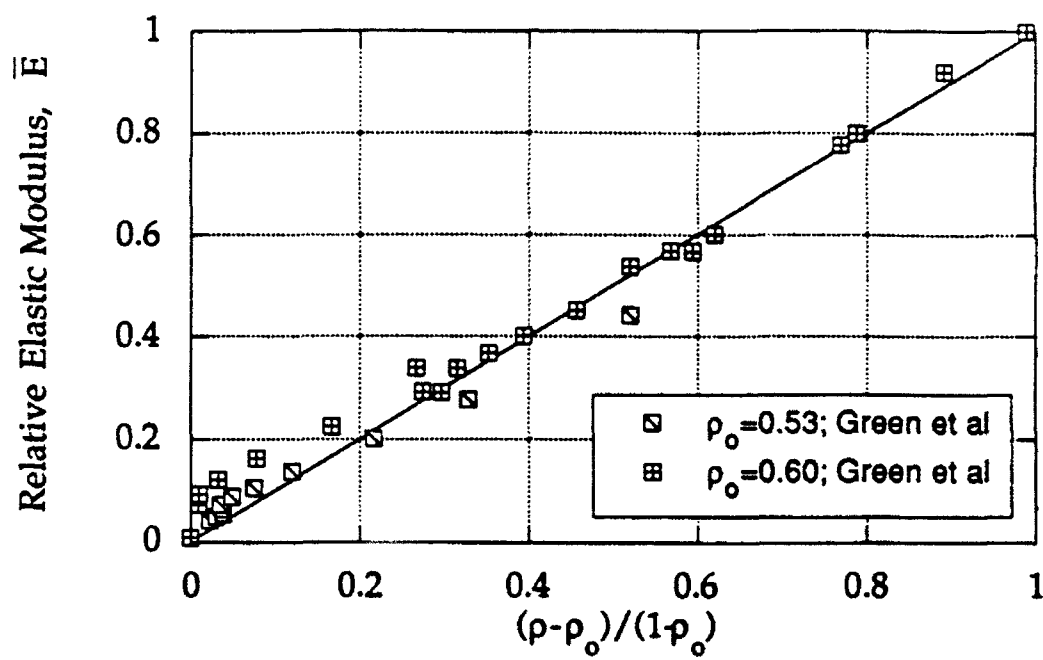




Fig. 7 Lam et al.



# Cracking due to Localized Hot Shock

Viggo Tvergaard

Technical University of Denmark, Lyngby, Denmark

Z. Cedric Xia and John W. Hutchinson\*

Harvard University, Cambridge, Massachusetts 02138

Results are presented for the cracking to be expected when a sudden temperature increase is applied over a localized region on a surface of a brittle solid. A localized temperature increase is applied to the surface of a body whose interior is initially at uniform temperature. A three-part analysis is conducted: (i) for the evolving temperature distribution, (ii) for the evolving thermal stresses induced by the nonuniform temperature field, and (iii) for stress intensity factors of cracks oriented either parallel to or perpendicular to the surface and initiated at times when the stresses are critical. Plane-strain and axisymmetric versions of the problems are considered. For the plane-strain problem, the complete trajectory of the crack is determined under the assumption that its tip advances maintaining a pure mode I field at all times. Conditions for excluding cracking due to localized hot shock are given.

## I. Introduction

THE problem addressed is the susceptibility to cracking of a brittle solid subject to localized heating at a spot on its surface. An example of current concern is spalling due to hot shock in the coating process of ceramic fibers where molten droplets of coating material impinge the fiber, as discussed by Backman.<sup>1</sup> Figure 1 shows the hot shock damage on sapphire fiber which has been coated by a titanium matrix material deposited as molten droplets. The matrix material was subsequently removed, revealing the spall damage. Another example is when the localized heating of a surface of a brittle material irradiated by a laser beam produces a hemispherically shaped spall chip. Generally speaking, localized heating of a surface induces compressive stresses parallel to the surface near the surface, and thus it is not intuitively apparent how cracking occurs in hot shock. By investigating the stresses induced in a semi-infinite half-space subject to a suddenly imposed localized temperature increase, one finds that tensile stresses do occur in regions below the surface and in some cases even at the surface outside the heated region. In this paper, both one-dimensional and axisymmetric temperature increase distributions are considered, as depicted in Fig. 2. These are suddenly imposed and subsequently held constant. The resulting temperature distributions are obtained as a function of time, as are the stresses induced by the nonuniform thermal expansion. The time and place where a particular component of stress reaches its maximum tensile value are identified, and cracking initiated at this

critical time is analyzed in some detail. This study does not deal with the coupled problem wherein a splat in contact with the substrate transfers its heat and consequently undergoes a change in temperature itself. The purpose of this paper is to gain insight into how cracking can arise in the simplest instances of localized hot shock. Subsequent work accounting for coupling and other effects, such as spalling due to bonding and subsequent cooling of the splat, will be necessary to refine the quantitative predictions arrived at here.

As a model to gain insight into the fiber spalling problem, Russell<sup>2</sup> has analyzed the effect of the sudden imposition of a uniform temperature increase  $\Delta T_0$  on the surface of a cylindrical body of radius  $R$ , i.e., the problem of an infinite solid cylinder suddenly thrust into a hot bath. Material at the surface of the cylinder experiences compressive stresses parallel to the surface, but the interior region near the axis of symmetry develops tensile stresses. The axial component of stress at the axis attains the largest tensile value, which is given by

$$\sigma_z(1 - \nu)/(\alpha E \Delta T_0) \cong 0.47 \quad (\nu = 0.3) \quad (1)$$

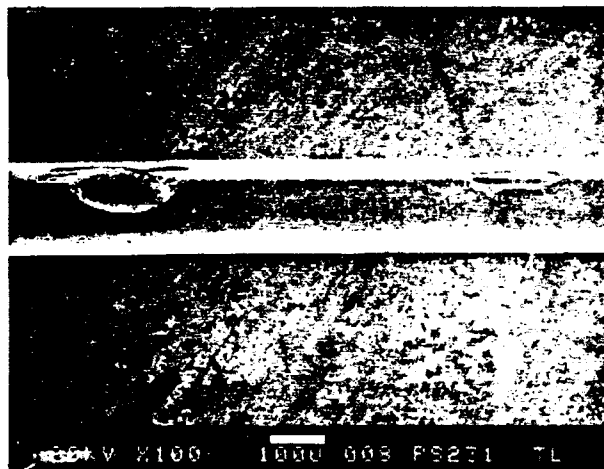


Fig. 1. Hot shock damage on a sapphire fiber (photograph supplied by E. S. Russell of GE Corp.).

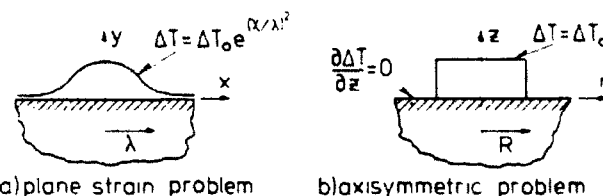


Fig. 2. Surface temperature distributions considered in this paper which are suddenly applied and subsequently held constant.

M. D. Thouless—contributing editor

Manuscript No. 195956. Received February 20, 1992; approved October 8, 1992.

The work of JWH and ZCX was supported in part by the DARPA University Research Initiative (Subagreement P.O. VB38639-0) with the University of California, Santa Barbara, ONR Prime Contract N00014-86-K0753) and the Division of Applied Sciences, Harvard University.

\*Member, American Ceramic Society

where  $E$  is Young's modulus,  $\nu$  is Poisson's ratio, and  $\alpha$  is the coefficient of thermal expansion. This value occurs after a time lapse from the imposition of  $\Delta T$  of

$$t = 0.075R^2/D \quad (2)$$

where  $D$  is the thermal diffusivity ( $D = k/\rho c$ ), where  $k$  is the thermal conductivity,  $\rho$  is the mass density, and  $c$  is the specific heat. Thus, if a critical stress  $\sigma_c$  for initiating a crack is invoked, the model predicts that no crack will be initiated if

$$\Delta T_c = 2.13(1 + \nu)\alpha E \sigma_c \quad (3)$$

Russell also considers the influence of barriers to perfect thermal conductivity at the fiber surface and their role in lowering the peak tensile stress.

## II. Hot Shock in Plane Strain

An infinite half-space lying below the  $x$ -axis has uniform  $E$ ,  $\nu$ ,  $\alpha$ , and  $D$ . At  $t = 0$  it has a uniform temperature, and at that instant a temperature increase

$$\Delta T = \Delta T_0 e^{-(x/\lambda)^2} \quad (\text{on } x = 0) \quad (4)$$

is suddenly imposed on the traction-free upper surface and is subsequently maintained for all time. As sketched in Fig. 2(a),  $\lambda$  is the approximate half-width of the localized hot spot. A three-part problem is solved: (i) the temperature distribution in the half-space for  $t > 0$ , (ii) the stress distribution in the half-space for  $t > 0$  which is induced by the nonuniform temperature field, and (iii) two cracking problems associated with cracks initiated at flaws located at the points where the maximum tensile stress components occur.

### (1) Temperature Distribution

The change of temperature in the interior of the half-space,  $\Delta T(x, y, t)$ , satisfies

$$\nabla^2(\Delta T) = D^{-1} \frac{\partial \Delta T}{\partial t} \quad (5)$$

subject to the initial conditions and Eq. (4) along with the condition that  $\Delta T \rightarrow 0$  as  $x^2 + y^2 \rightarrow \infty$ . This is a classical problem which can be solved with the aid of transform methods. The solution is

$$\Delta T(x, y, t) = \Delta T_0 \frac{(-y)}{\pi} \int_{-\infty}^{\infty} \frac{e^{-\eta^2 \lambda^2}}{[(x - \eta)^2 + y^2]} \exp\left[-\frac{(x - \eta)^2 + y^2}{4Dt}\right] d\eta \quad (6)$$

### (2) Stress Distribution

Under the assumption of plane strain conditions, the Airy stress function  $\Phi(x, y)$  at a given instant  $t$  satisfies

$$\nabla^4 \Phi = -[E\alpha(1 - \nu)]\nabla^2(\Delta T) \quad (7)$$

where the in-plane stress components are given by  $\sigma_{xx} = \Phi_{,yy}$ ,  $\sigma_{yy} = \Phi_{,xx}$ , and  $\sigma_{xy} = -\Phi_{,xy}$ . This equation is supplemented by traction-free conditions on  $y = 0$ , along with the requirement that the stresses vanish far from the hot spot. This problem, or others similar to it, have also appeared in the literature,<sup>11-14</sup> and neither the solution details nor the solution itself will be presented here. Closed-form expressions for the stress components  $\sigma_{ij}(x, y, t)$  are obtained which involve double integration over the half-space. These integrals are evaluated numerically to obtain the stress at any point at any time.

Plots of the two normal components directly beneath the center of the hot spot on  $x = 0$  are shown in Fig. 3 for various values of the nondimensional time variable,  $tD/\lambda^2$ . The maximum

tensile value of  $\sigma_{xx}(0, y, t)$  is given by the following and occurs at the position and time given by

$$\frac{(1 - \nu)\alpha E}{\alpha E \Delta T} = 0.0051 \quad \frac{y^*}{\lambda} = 0.508 \quad \frac{tD}{\lambda^2} = 0.023 \quad (8)$$

The maximum tensile value of  $\sigma_{xx}(0, y, t)$  and associated location and time are given by

$$\frac{(1 - \nu)\alpha E}{\alpha E \Delta T} = 0.0438 \quad \frac{y^*}{\lambda} = 1.23 \quad \frac{tD}{\lambda^2} = 0.098 \quad (9)$$

A feature of the plane-strain hot-shock problem which follows immediately from Eq. (7) is that the in-plane stresses approach zero as the temperature distribution approaches steady state (i.e., as  $\nabla^2(\Delta T) \rightarrow 0$  as  $t \rightarrow \infty$ ). This trend is reflected in the plots of Fig. 3.

### (3) Crack Trajectories and Stress Intensity Factors

At the time  $t^*$ , corresponding to either Eq. (8) or Eq. (9), a very short crack of length  $a \rightarrow 0$  is introduced at the point  $(0, y^*)$  where the maximum tensile stress occurs. For Eq. (8), the initiating crack is taken parallel to the  $y$ -axis, while for Eq. (9) it is taken parallel to the  $x$ -axis. Given the stress distribution at fixed time  $t^*$ , the crack trajectory is determined under the condition that the advancing tip is always in a state of pure mode I.

First, consider a crack initiated parallel to the  $y$ -axis at  $(0, y^*)$  with the stress distribution associated with  $t^*$ , as pictured in the insert of Fig. 4(a). Symmetry dictates that a crack extending along the  $y$ -axis will have mode I conditions at its crack tip. For

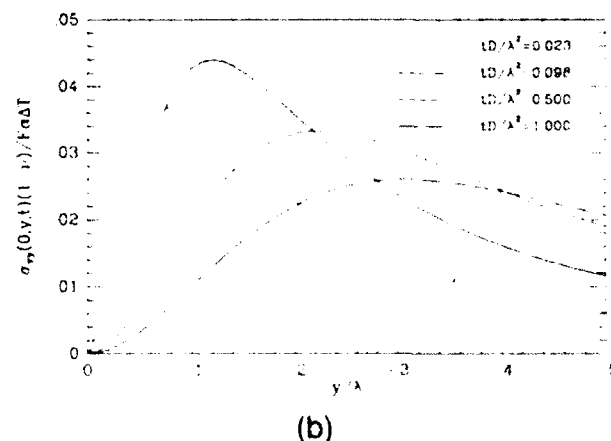
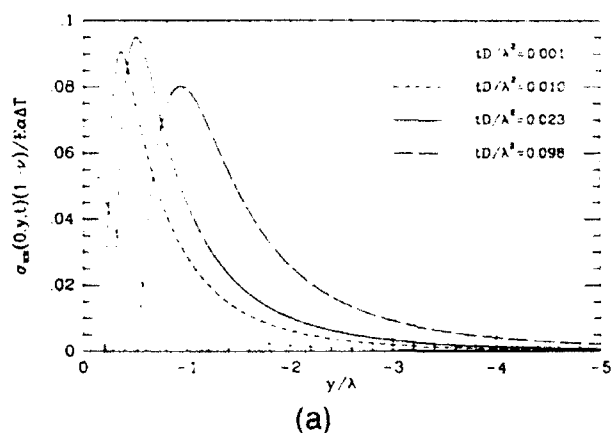


Fig. 3. Stress distributions directly beneath the hottest point on the surface for the plane strain problem.

a sufficiently small crack length compared to  $v^*$ , the mode I intensity factor at each tip is given by

$$K_I \approx \sigma_1^* \sqrt{\pi(a_1 + a_2)^2} \quad (10)$$

Plots of  $K_I$  at the top and bottom crack tips are given in Fig. 4. The solution method for determining  $K_I$  is discussed in the Appendix. The stress intensity factor of the upper tip increases as the crack length initially increases but then goes to zero as the tip approaches the free surface, advancing into the region where  $\sigma_1$  is compressive. As the lower tip dives deeper into the half-space, the stress intensity factor also decreases after first increasing. Given the toughness of the material,  $K_{Ic}$ , one can determine arrest lengths,  $a_1^*$  and  $a_2^*$ , from the information in Fig. 4. If  $\sigma_1$  is the critical stress associated with some initial flaw size, then, by Eq. (8), cracks parallel to the  $x$ -axis will not be initiated if

$$\Delta T_0 < 10.5(1 - \nu)\sigma_1/(\alpha E) \quad (11)$$

Now, consider cracks initiated parallel to the  $x$ -axis at  $(0, y^*)$  at time  $t^*$  given by Eq. (9). A very short crack extending from  $(-a, y^*)$  to  $(a, y^*)$  will be in mode I at each tip with

$$K_I \approx \sigma_1^* \sqrt{\pi a} \quad (12)$$

If it were to extend as a straight crack, it would develop a mode II stress intensity factor in addition to mode I. Curved trajectories for the crack extending symmetrically about its midpoint have been computed under the criterion that pure mode I conditions exist at all times at its tips. The calculations are therefore for a crack of increasing length (with symmetry enforced with respect to  $x = 0$ ) advancing with a curved trajectory determined incrementally such that  $K_{II} = 0$  is always in effect. The calculation, which is discussed further in the Appendix, is started with a very short, straight crack. The stresses in the

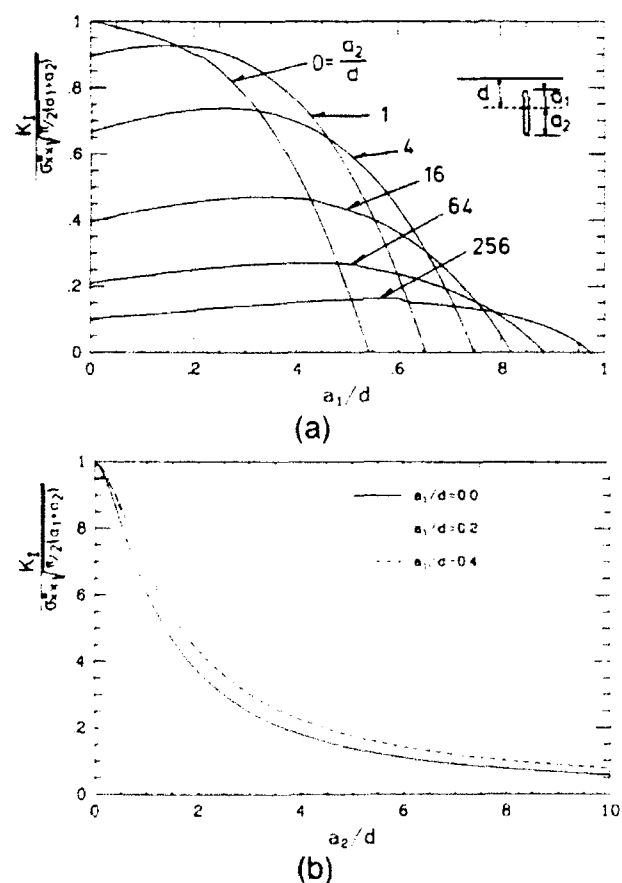


Fig. 4. Stress intensity factor in plane-strain problem for (a) upper tip and (b) lower tip. In each figure  $\sigma_1^*$  is given by Eq. (8) and  $d = -v^* = 0.505\lambda$ .

uncracked half-space as determined in Section II(2) is  $\sigma_1(x, y, t^*)$ , and this distribution is used in carrying out the calculations for the subsequent development of the cracks. Calculations of crack trajectories based on the criterion of pure mode I growth have been carried out in other contexts by Wasistrach and Ingraffea, Swenson and Kaushik, Fleck, and Freund and Kim.

Three crack trajectories are shown in Fig. 5(a). The curve labeled A is initiated at  $(0, y^*)$ , and those labeled B and C are initiated above and below  $(0, y^*)$ , respectively, as can be seen from where each trajectory crosses the  $y$ -axis. There clearly is a tendency for the cracks to seek out a depth roughly equal to  $v^* = -1.23\lambda$  and then propagate parallel to the interface. The mode I stress intensity factor is shown with different normalizations in Figs. 5(b) and 5(c), where it is plotted against the horizontal coordinate of the right tip and *not* against the half-length of the curved trajectory. From Fig. 5(b) it is noted that the result (Eq. (12)) for the short crack remains a good approximation for cracks with half-widths up to  $\lambda$  or larger. From Fig. 5(c), it is seen that the peak value of  $K_I$  occurs at a half-width of about  $1.4\lambda$  with

$$K_I \approx \sigma_1^* \sqrt{\pi \lambda} = 0.078\alpha E \Delta T_0 \sqrt{\lambda} (1 - \nu) \quad (13)$$

For crack half-widths greater than  $1.4\lambda$ ,  $K_I$  falls slowly and has decreased only to about one-half of the peak value for a half-width of  $5\lambda$ . Thus, the plane-strain model suggests that fairly extensive subsurface cracking, more or less parallel to the free surface, is possible if the temperature is high enough to initiate growth. With  $\sigma_1$  as the critical stress for initiation, Eq. (9) implies that these cracks will not be initiated if

$$\Delta T_0 < 22.8(1 - \nu)\sigma_1/(\alpha E) \quad (14)$$

Alternatively, since the peak value of  $K_I$  is given by Eq. (13), no crack parallel to the free surface, irrespective of size, can propagate if  $(K_I)_{\text{peak}} < K_{Ic}$  or, equivalently,

$$\Delta T_0 < 12.9(1 - \nu)K_{Ic}/(\alpha E \sqrt{\lambda}) \quad (15)$$

### III. Axisymmetric Hot Shock

The axisymmetric problem shown in Fig. 2(b) has somewhat different boundary conditions than the plane-strain problem just considered. The half-space has uniform temperature prior to the sudden imposition of an axisymmetric temperature increase,  $\Delta T(r, 0, t) = \Delta T_0$ , for  $t \geq 0$  on the free surface for  $r < R$ . For  $r > R$ , the free surface is taken to be perfectly insulated with  $\partial(\Delta T)/\partial z = 0$  on  $z = 0$ . The three-part problem solved for the two-dimensional model is solved here. In the axisymmetric problem, however, a finite element method is used to solve each of the three parts. Discussion of some of the details of the computational procedures is given in the Appendix.

#### (1) Temperature Distribution

Contours of constant temperature at three times within the range of interest are shown in Fig. 6. These contours display the progression of the heated region as it expands downward into the half-space. The three times are  $t = t_0$ ,  $t = 2t_0$ , and  $t = 4t_0$ , where  $t_0 = 0.016R^2/D$ .

#### (2) Stress Distribution

Contours of constant values of the two stress components,  $\sigma_{rr}$  and  $\sigma_{zz}$ , are shown in Figs. 7 and 8, respectively, at the same three times. The maximum tensile value of  $\sigma_{rr}$ , the location on the axis of symmetry where it occurs, and the time it is attained are

$$\frac{(1 - \nu)\sigma_{rr}^*}{\alpha E \Delta T_0} = 0.085 \quad \frac{z^*}{R} = -0.46 \quad \frac{t^* D}{R^2} = 0.016 \quad (16)$$

These calculations were carried out using the value of Poisson's ratio,  $\nu = 0.23$ , and the quantities shown do have some dependence on  $\nu$ . Nevertheless, the above combination including the

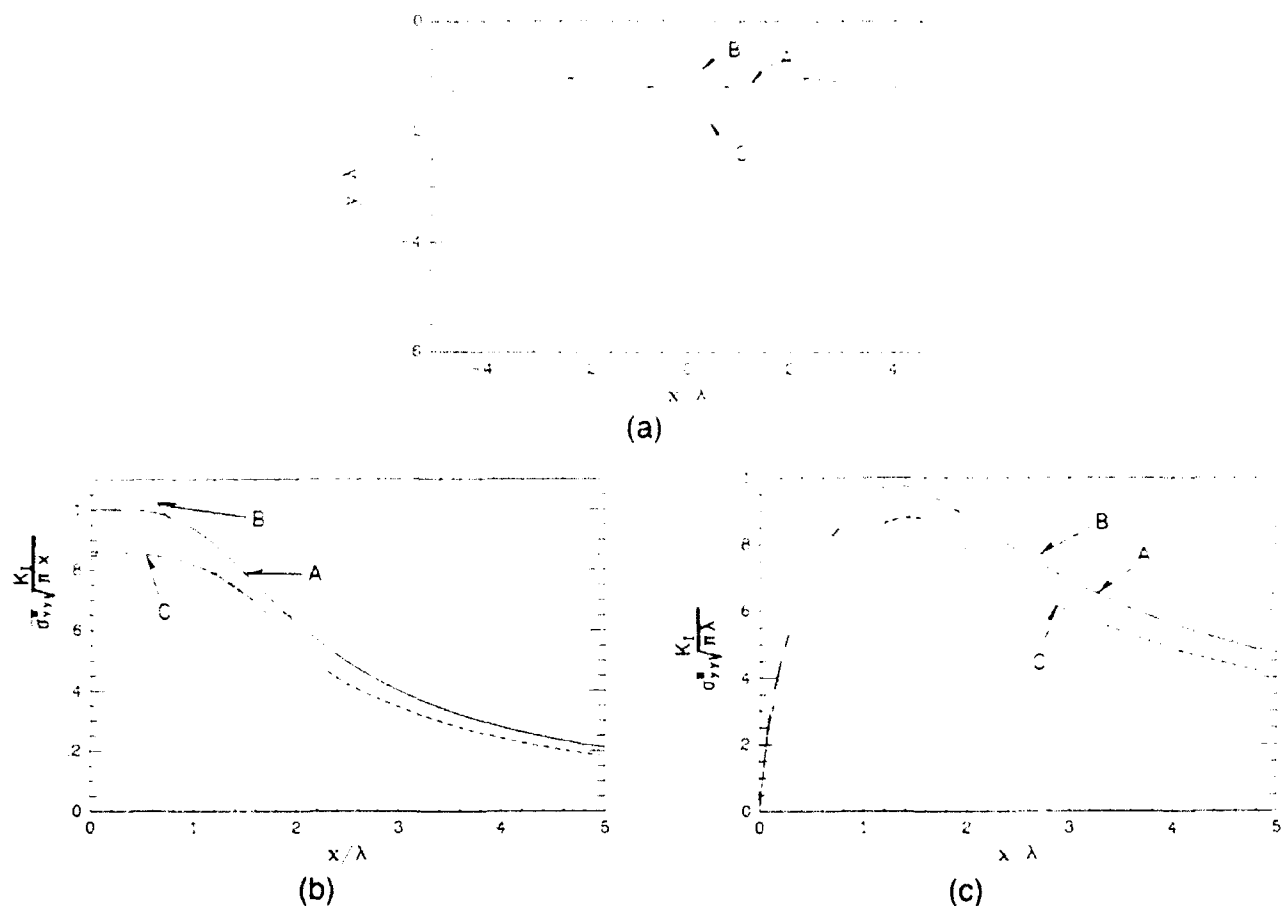


Fig. 5. (a) Mode I crack trajectories in the plane-strain problem. (b) and (c) Normalized stress intensity factor for crack in (a).

factor  $(1 - \nu)$  does capture the approximate  $\nu$ -dependence. This was established by repeating a few selected calculations with other values of  $\nu$ . The circumferential component of stress also attains tensile values at the surface of the half-space outside the circular heated region, as can be seen in Fig. 7. The maximum tensile value of the circumferential stress at the surface, its position, and time of occurrence are approximately

$$\frac{(1 - \nu)\sigma_{\theta}^*}{\alpha E \Delta T_0} \approx 0.035 \quad \frac{r^*}{R} \approx 1.63 \quad \frac{t^* D}{R^2} \approx 0.064 \quad (17)$$

The maximum tensile value of  $\sigma_{\theta}$  occurs along the axis of symmetry, and its value, position, and time of occurrence are

$$\frac{(1 - \nu)\sigma_{\theta}^*}{\alpha E \Delta T_0} \approx 0.070 \quad \frac{z^*}{R} \approx -0.95 \quad \frac{t^* D}{R^2} \approx 0.064 \quad (18)$$

The similarities between the tensile stresses in the axisymmetric and plane-strain problems are striking as can be seen by comparing Eq. (16) with (8) and Eq. (18) with (9). Of course, Eq. (17) has no analogue in plane strain. The maximum tensile stresses which occur in localized hot shock are about one order of magnitude smaller than the maximum compressive stress induced at the surface, which is  $\alpha E \Delta T_0 (1 - \nu)$ . In the axisymmetric problem, the peak tensile value of  $\sigma_{\theta}$  is slightly larger than the peak value of  $\sigma_r$  and is attained earlier. Both the radial cracks aligned perpendicular to the surface and the spalling

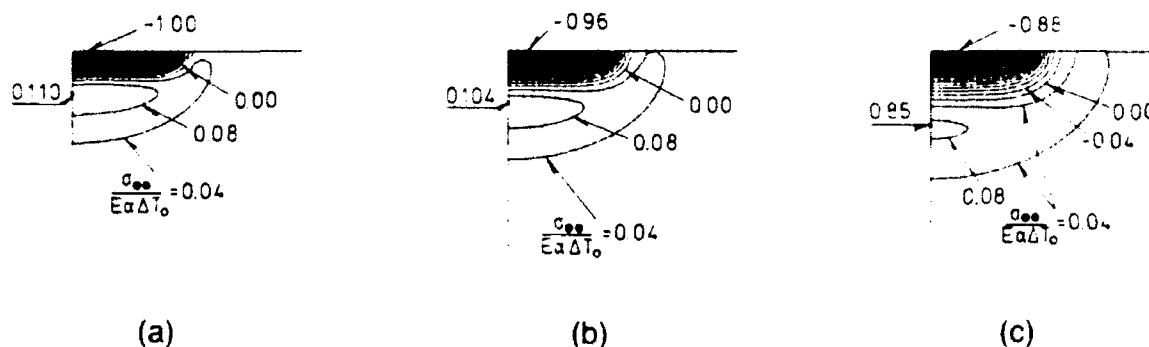


Fig. 6. Temperature distributions for the axisymmetric problem at (a)  $t = t^* = 0.016R^2/D$ , (b)  $t = 2t^*$ , and (c)  $t = 4t^*$ .

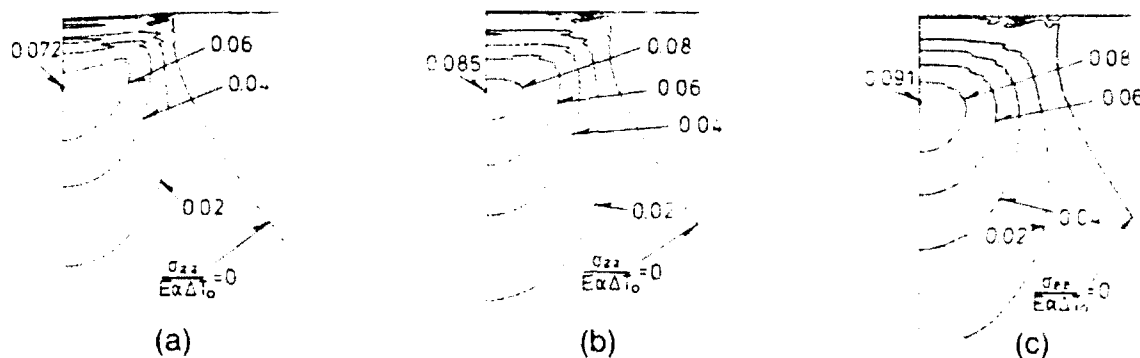


Fig. 7. Distributions of  $\sigma_{xx}$  in the axisymmetric problem at (a)  $t = t_0$ , (b)  $t = 2t_0$ , and (c)  $t = 4t_0$

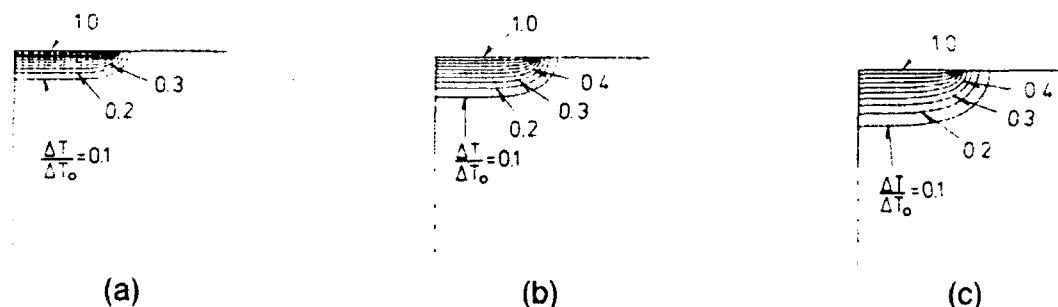


Fig. 8. Distributions of  $\sigma_{yy}$  in the axisymmetric problem at (a)  $t = t_0$ , (b)  $t = 2t_0$ , and (c)  $t = 4t_0$

cracks aligned parallel to the surface can be produced by localized axisymmetric hot shock, although the radial cracks may be more prevalent than the spalling cracks for the reasons just mentioned. Both are most likely to be nucleated below the hot spot by subsurface flaws. The distribution of the circumferential stress is such that we can conjecture that a radial crack nucleated below the hot spot would arrest in the form of a crescent, which, if it reached the surface, would intersect the surface as a relatively short segment of radial crack lying just outside the perimeter of the hot spot.

A spalling crack nucleated parallel to the surface in the vicinity of the peak tensile value of  $\sigma_{xx}$  will spread outward as a penny-shaped crack, curving in response to the nonuniform stress distribution. No attempt has been made to compute the surface trajectories of pure mode I advance for the axisymmetric problem. Instead, calculations have been performed to determine the energy release rate and the mode I and mode II intensity factors for flat penny-shaped cracks spreading from small cracks centered at the axis of symmetry at a selection of depths and times. As in the plane-strain problem, it is found that cracks spreading from the point of maximum tensile stress will tend to spread more or less in a plane parallel to the surface.

### (3) Stress Intensity Factors for Penny-Shaped Cracks Parallel to the Surface

Let  $\sigma_x^*$  be the maximum tensile stress given by Eq. (18) at time  $t^*$ . A sufficiently small penny-shaped crack of radius  $a$ , aligned parallel to the surface and located on the axis at  $z = z^*$ , will be in mode I with

$$K_I \equiv \frac{2}{\pi} \sigma_x^* \sqrt{\pi a} = 0.079 \alpha E \Delta T_0 \sqrt{a/(1-\nu)} \quad (19)$$

The energy release rate is given by

$$G = \frac{(1-\nu^2)K_I^2}{E} = 0.0063 \left( \frac{1+\nu}{1-\nu} \right) (\alpha \Delta T_0)^2 E a \quad (20)$$

This result, which represents the maximum possible energy release rate for very short cracks, is shown in Fig. 9.

As the radius of the flat penny-shaped crack extends away from the axis, a mode II component of stress intensity will develop. Calculations have been carried out for a number of cases for flat penny-shaped cracks centered at various points along the axis of symmetry and subject to the stress field existing in the half-space at various times. Curves for the energy release rate,

$$G = \frac{(1-\nu^2)}{E} (K_I^2 + K_{II}^2) \quad (21)$$

normalized by  $[(1+\nu)/(1-\nu)]ER(\alpha\Delta T_0)^2$ , as a function of  $a/R$  are shown in Fig. 9. The curves are labeled by the depth,  $d$ , below the surface where the crack lies and the nondimensional time characterizing the stress distribution. The results in Fig. 9 were calculated with  $\nu = 0.23$ , but several calculations

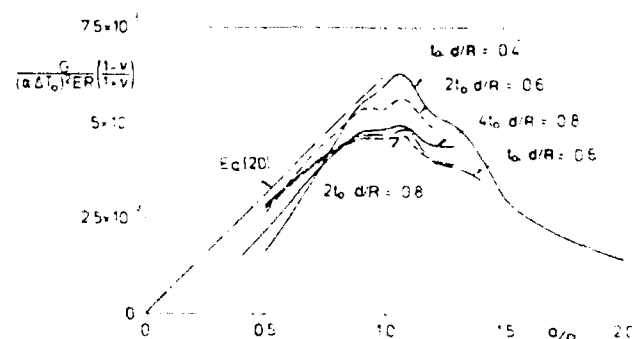


Fig. 9. Normalized energy release rate for penny-shaped cracks oriented parallel to the surface at a depth  $d$  below the surface and advancing into the stress distribution of the uncracked body associated with the times indicated

repeated with  $\nu = 0.4$  suggest that the normalization captures the Poisson's ratio dependence to a very good approximation. It can be noted from the results in Fig. 9 that the short crack limit (Eq. (20)) provides an excellent approximation for cracks with radii as large as the radius  $R$  of the heated spot. The companion curves giving the relative amount of mode II to mode I are plotted in Fig. 9, where the measure of mode mixity is taken as

$$\psi = \tan^{-1}(K_{II}/K_I) \quad (22)$$

Over the range of  $a/R$  for which calculations have been made, the mode II component of the stress intensity is relatively small compared to the mode I component. The general trend noted with respect to the trajectories in the plane-strain problem can be expected for this axisymmetric problem. Namely, when the crack is initiated at a depth which places it above the maximum of  $\sigma_{xx}$  on the axis, it will head downward but then begin to head upward again after it has reached a radius on the order of  $R$ . The present calculations do not allow one to conclude that the cracks will more or less parallel the surface at radii well in excess of  $R$ , as is the case in the plane-strain problem, but over the range of  $a/R$  considered there is no suggestion of any strong tendency for the crack to curve upward.

The maximum value of  $G$  over all the cases considered is

$$G = 0.0063 \left( \frac{1+\nu}{1-\nu} \right) (\alpha \Delta T_0)^2 ER \quad (23)$$

occurring for the case  $t = t_0$  with a crack depth of  $d = 0.4R$  at a crack radius of  $a = R$ . From Fig. 10 it is seen that the crack is nearly mode I at this point, and thus the associated value of  $K_I$  is

$$K_I = 0.079 \alpha E \Delta T_0 \sqrt{R}/(1-\nu) \quad (24)$$

This result is remarkably close to the plane-strain result (Eq. (13)) when the effective half-width of the hot spot in plane strain is identified with the radius of the axisymmetric hot spot. Thus, it follows that the condition (Eq. (15)) for excluding cracking applies to axisymmetric cracking parallel to the surface as well if  $\lambda$  is exchanged with  $R$ .

To complete the results for the penny-shaped cracks, we have displayed the variations of the normalized energy release rate and  $\psi$  as a function of depth below the surface in Figs. 11 and 12, in each instance for  $a/R = 1$ . These variations are in accord with the previous discussion. In particular, it is noted that the largest energy release rates at finite crack radius (i.e.,  $a = R$ ) occur for cracks nucleated at times well before  $t^*$  associated with the peak tensile value of  $\sigma_{xx}^*$  in Eq. (18) and at a depth which is only about one-half of the critical depth for the smallest cracks.

#### IV. Discussion

When a temperature increase is suddenly imposed on the surface of a body at uniform temperature, the stress just below the hot spot is compressive with magnitude  $\alpha E \Delta T_0/(1-\nu)$ . Tensile stresses develop below the surface as the temperature increase diffuses into the solid. The magnitude of the largest tensile stresses documented in this work are not more than about one-tenth of the magnitude of the above maximum compressive

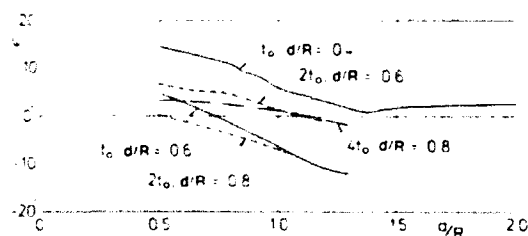


Fig. 10. Measure of mode mixity for cracks whose energy release rates are shown in Fig. 9.



Fig. 11. Normalized energy release rate for penny-shaped cracks at various depths  $d$ , all with  $a = R$ , and advancing into the stress distribution of the uncracked body associated with the times indicated.

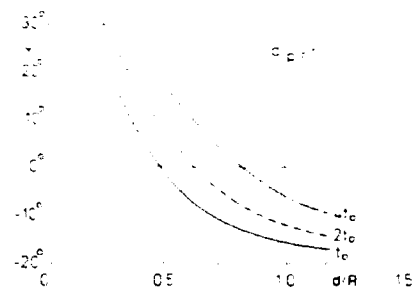


Fig. 12. Measure of mode mixity for cracks whose energy release rates are shown in Fig. 11.

stress. These tensile stresses develop on planes which are parallel to the surface and also on planes which are perpendicular to the surface. They occur at depths which are between one-half and one times the half-width or radius of the hot spot. In the case of the axisymmetric hot spot, circumferential tensile stresses develop at the surface outside the perimeter of the hot spot, but these stresses are only about one-half as large as the maximum subsurface tensile stresses.

The crack analyses indicate that subsurface cracks initiated parallel to the surface will tend to spread more or less parallel to the surface, and not necessarily curve up to the surface to generate a spall chip. Cracks initiated under the hot spot on planes perpendicular to the surface will remain in their plane and extend both upward and downward, and they also will not necessarily break through to the surface. In other words, the analyses suggest that hot shock may in some instances create subsurface damage which cannot be observed on the surface. There are several mechanisms not discussed here by which the cracks can travel to the surface and create a spall. If the radius of a crack running parallel to the surface becomes large enough relative to its depth below the surface, the compressive stress parallel to the surface can cause the platelike region above the crack to buckle away from the substrate. This, in turn, will induce mixed-mode conditions at the crack tip which will drive the tip to the surface as discussed in Ref. 9. Another possibility, noted in some model experiments (private communication by Eric Matthys, University of California, Santa Barbara), has not been discussed, where a splat solidifies and bonds to the substrate and then cools and contracts at a faster rate than the substrate, due to its higher coefficient of thermal expansion. This gives rise to a stress distribution somewhat akin to cold shock, which may be analyzed along the lines discussed in Section V. E of the article by Hutchinson and Suo.<sup>10</sup>

Matthys impinged molten drops of Ni at 1600°C on a quartz substrate. Using acoustic measurements, he observed two distinct cracking events: the first about 2 s after the droplet hit, which appeared to be entirely subsurface, and the second about 30 s later, involving spalling of the previously established

crack. The splat radius was typically 0.5 cm. Using the value for fused quartz of  $D = 9.5 \times 10^{-7} \text{ m}^2/\text{s}$  in Eq. (18) to predict the time at which the maximum tensile occurs, one finds  $t^* = 1.7 \text{ s}$ . This value compares favorably with the first cracking event reported by Matthys. The second event is believed to be associated with the cooling phase of the bonded solidified splat mentioned above. The tensile stress levels induced by the splat from Eq. (18), on the other hand, appear to be too low to initiate cracking. Equivalently, the quartz substrate material appears to readily meet the condition (Eq. (14)) on temperature for the 1600°C splat. Thus, it remains to understand how the cracks are initiated in this particular experiment.

Coupling in the heat transfer problem between the splat and the substrate has not been considered here nor has the role of a thermal coating considered in Ref. 2. If the time at which cracking is predicted to occur, typically  $t/D \approx 0.02$  to 0.1, is short compared to the time it takes the splat to undergo significant cooling, then the present results may be reasonably accurate without further modification. This might be the case, for example, for a splat medium undergoing solidification. The coupled problem should be considered if the splat temperature drops significantly prior to the predicted time of cracking or if for any reason the temperature at the surface of the solid varies rapidly with time after the first sudden increase.

## APPENDIX

### (1) Plane-Strain Cracking Problems

The problem of the subsurface crack oriented perpendicular to the free surface is solved using standard integral equation techniques. The geometry and the stress distribution of the uncracked half-space possess symmetry with respect to the crack line, so only opening displacements need be considered. The crack is represented by a dislocation distribution which is chosen to cancel the traction on the crack faces. The solution for a dislocation below the traction-free surface of the half-space is available in the literature, and the numerical procedure of Erdogan and Gupta<sup>10</sup> for solving the integral equation can be effectively used.

The problem of generating the trajectory of a very short crack initiated parallel to and below the surface when the crack is required to advance as a pure mode I crack has been treated in other contexts.<sup>11,12</sup> Given a smoothly curved subsurface crack, the solution can be produced using the same procedures as described in the previous paragraph, except that both tangential and opening displacements of the crack face must be considered. Because of the symmetry of the stress distribution with respect to the plane  $x = 0$ , only trajectories which were symmetric with respect to that plane were considered. Assuming that the crack at its current length has  $K_{II} = 0$ , then the crack length is increased with a change in curvature of the next increment chosen such that the advanced tip also is in a state of pure mode I. The procedure used here for incrementing the crack was identical to that used in Refs. 7 and 8.

### (2) Axisymmetric Problems

As mentioned in the body of the paper, finite element methods were used to solve each of the three subproblems. Eight-noded isoparametric elements were used, and the same mesh is employed for the heat conduction problem as for the stresses induced in the uncracked half-space.

Equation (5) governs the evolving temperature change,  $\Delta T(r, z, t)$ . The following variational statement of Eq. (5) is used as the basis of the numerical solution to the transient problem:

$$D^{-1} \int_V \frac{\partial \Delta T}{\partial t} \delta T \, dV = - \int_V \nabla \Delta T \cdot \nabla \delta T \, dV + \int_S (\hat{n} \cdot \nabla \Delta T) \delta T \, dS \quad (25)$$

where  $\delta T$  is the variation of  $T$ . A finite body was used in the numerical solution. It was taken to be a circular cylinder with

outer radius  $R = 10R_0$  and height  $H = 10R_0$ . Apart from the region  $r \leq R_0$  on the top surface, where  $\Delta T$  is prescribed to be  $\Delta T_0$  for  $t \geq 0$ , the surface is everywhere taken to be perfectly insulated, assuming that negligible heat is lost from the unheated portion of the surface. The choices for  $R$  and  $H$  ensure that the zone of appreciable temperature increase is confined to a relatively small volume of the body and that the thermal stresses induced remain negligible in most of the volume analyzed. The stress-strain relations for the elastic material, subject to a field of temperature increase  $\Delta T$  relative to the initial uniform temperature are

$$\sigma = E \epsilon, \quad \epsilon = \alpha \Delta T \mathbf{1}_0 \quad (26)$$

At a given time  $t$ , the temperature field  $\Delta T$  is known from the numerical solution of Eq. (25), and the corresponding stress fields and strain fields are found by a numerical solution based on using Eq. (26) in the principle of virtual work. At the bottom surface,  $z = -10R_0$ , far from the heated region, symmetry conditions have been prescribed with  $u = 0$  and zero shear tractions. All the other surfaces are taken to be traction free.

As mentioned in the body of the paper, the crack is imagined to develop in the uncracked half-space at a given time  $t$  with its associated temperature and stress distribution. In other words, the crack is assumed to grow after the temperature and stress distributions in the uncracked body have been established. The growth process is likely to be dynamic, and any subsequent influence of the crack on the temperature distribution has not been considered.

In each crack analysis, the energy release rate  $G$  is determined by the stiffness derivative finite-element technique,<sup>13</sup> which involves derivatives with respect to crack advance for element stiffness and load terms resulting from thermal expansion. The computations are still based on the principle of virtual work with Eq. (26) substituted for the thermoelastic behavior, but the mesh is highly refined near the crack tip, with several rings of small elements around the tip. The  $J$ -integral is used to evaluate the energy release rate, using the actual strain energy density expansion accounting for thermal expansion.<sup>14</sup> For these axisymmetric crack problems, the  $J$ -integral values obtained on contours of very small radius around the tip agree with the values obtained by the stiffness derivative technique within 2%–4%. The ratio of the stress intensity factors,  $K_{II}/K_I$ , is needed to evaluate  $\psi$  in Eq. (22). Approximate values of the stress intensity factors were obtained by substituting stress values at two integration points symmetrically placed about the crack plane into the well-known analytical expressions for the singular near-tip fields. Corresponding values of the energy release rate evaluated using the  $K$ 's obtained in this manner in Eq. (21) differ by from 5% to 15% from the accurate values obtained from the methods mentioned above. Thus, the magnitudes of the values of  $K_I$  and  $K_{II}$  obtained from the singular fields are not very accurate, but it is assumed that the ratio of their values in Eq. (22) should give a reasonable representation of mode mixity.

Finally, it is noted again that the assumption of traction-free surfaces used in the present studies excludes the type of spalling mentioned in the Conclusions, where a hot splat solidifies, bonds to the substrate, and then drives a crack through surface tractions upon cooling.

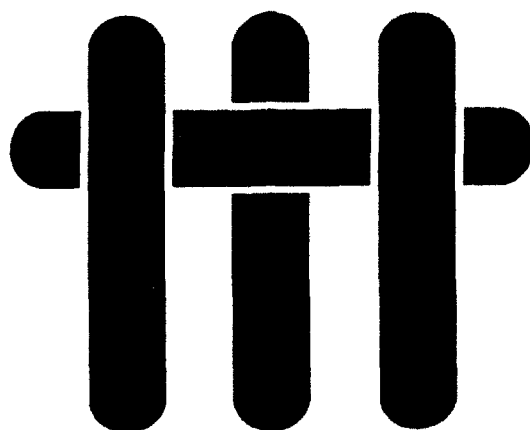
## References

1. Backman, "Metal-Matrix Composites and BPS: A Modeling Perspective," *J. Aer.*, July, 17–20 (1990).
2. E. S. Russell, "Model for Fiber Thermal Shock during Plasma Spray Deposition," Rep. No. R90ALB1039, Technical Information Series, GE Aircraft Engines, Lynn, MA, Oct. 1990.
3. W. Jaunzemis and E. Sternberg, "Transient Thermal Stresses in a Semi-Infinite Slab," *J. Appl. Mech.*, 27, 93–103 (1960).
4. A. Jahanbakhsh, "Transient Stresses Induced by Heating a Plane Boundary," *Int. J. Solids Struct.*, 9, 1–14 (1973).



10. P. A. Wawrzyniec and A. R. Ingerotto, "Interactive Finite Element Analysis of Fracture Processes: An Integrated Approach," *Eng. Appl. Mech.*, **8**, 137-50 (1987).
11. D. A. Swenson and N. Kaushik, "Finite Element Analysis of Edge Cracks in Plates," *Eng. Fract. Mech.*, **37**, 643-55 (1990).
12. N. A. Fleck, "Brittle Fracture Initiation and Arrest in Microcracks," *Proc. R. Soc. London, A*, **432**, 85-70 (1991).
13. T. B. Fredrick and K. S. Kim, "Spall Cracking around a Strained Ceramic Inclusion in a Brittle Material and Implications for Viable Integrated Circuits," in the proceedings of the 1991 MRS Spring Meeting, Anaheim, CA in Symposium H, Mechanical Behavior of Materials and Structures in Microelectronics (1991). Materials Research Society, Pittsburgh, PA (1991).
14. J. W. Hutchinson and Z. Suo, "Mixed Mode Cracking in Elastic Materials: pp. 64-135, in *Advances in Fracture Mechanics*, Vol. 29, Edited by J. W. Hutchinson and T. Y. Wu, Academic Press, New York (1990).
15. T. E. Eversman and C. D. Gifford, "On the Generalized Solution of Strain Energy Formulation," *Q. Appl. Mech.*, **30**, 171-72 (1974).
16. T. M. Heug, "A Strain Energy Formulation for the Calculation of the Distribution of Stress Tip Stress Intensity Factors," *Eng. Fract. Mech.*, **10**, 477-90 (1976).
17. C. E. Smith, B. Mottram, and J. Newman, "Finite Element Analysis of Three-Dimensional Crack Fronts in Elastic Structures," *Eng. Fract. Mech.*, **30**, 131-40 (1988).

# M A T E R I A L S



## THE PHYSICS AND MECHANICS OF BRITTLE MATRIX COMPOSITES

by

A.G. Evans, F.W. Zok  
Materials Department  
College of Engineering  
University of California  
Santa Barbara, California 93106-5050

## TABLE OF CONTENTS

1.	INTRODUCTION.....	8
1.1	Rationale .....	8
1.2	Objective .....	9
1.3	Approach .....	12
2.	INTERFACES.....	13
2.1	Thermomechanical Representation .....	13
2.2	Measurement Methods.....	14
2.3	Sliding Models .....	15
2.4	Experimental Results .....	16
2.5	Environmental Influences .....	17
3.	RESIDUAL STRESSES .....	18
4.	FIBER PROPERTIES.....	21
4.1	Load Sharing .....	21
4.2	The Ultimate Tensile Strength.....	23
4.3	Fiber Pull-Out .....	25
4.4	Influence of Flaws .....	26
4.5	<i>In Situ</i> Strength Measurements .....	27
4.6	Experimental Results .....	28
5.	MATRIX CRACKING IN UNIDIRECTIONAL MATERIALS.....	29
5.1	Basic Mechanics .....	30
5.2	The Matrix Cracking Stress.....	34
5.3	Crack Evolution.....	36
5.4	Constitutive Law .....	39
	5.4.1 Stresses Below Saturation.....	40
	(i) Small Debond Energy .....	40
	(ii) Large Debond Energy.....	41
	5.4.2 Stresses Above Saturation.....	42
5.5	Simulations.....	43
5.6	Experiments .....	44
6.	MATRIX CRACKING IN 2-D MATERIALS .....	45
6.1	Tensile Properties .....	45
6.2	Shear Properties.....	47
	(i) In-Plane Shear .....	48
	(ii) Interlaminar Shear.....	49
6.3	Transverse Tensile Properties.....	49
7.	STRESS REDISTRIBUTION .....	51

7.1	Background .....	51
7.2	Mechanism Transitions .....	52
7.3	Mechanics Methodology .....	53
	(i) Class I Materials .....	53
	(ii) Class II Materials .....	54
	(iii) Class III Materials .....	54
7.4	Measurements .....	55
8.	FATIGUE .....	57
8.1	Basic Phenomena .....	57
8.2	Cyclic Crack Growth .....	58
8.3	Thermomechanical Fatigue .....	62
8.4	Experimental Results .....	63
9.	CREEP .....	65
9.1	Basic Behavior .....	65
9.2	Effect of Fiber Failures .....	69
9.3	Interface Debonding .....	70
9.4	Matrix Cracking .....	70
9.5	Strain Recovery .....	71
9.6	Experimental Results .....	72
10.	CHALLENGES AND OPPORTUNITIES .....	73

## NOMENCLATURE

$a_i$	parameters found in the paper by Hutchinson and Jensen (1990)—Table II
$a_o$	length of unbridged matrix crack
$a_m$	fracture mirror radius
$a_N$	notch size
$a_t$	transition flaw size
$b$	plate dimension
$b_i$	parameters found in the paper by Hutchinson and Jensen (1990)—Table II
$c_i$	parameters found in the paper by Hutchinson and Jensen (1990)—Table II
$d$	matrix crack spacing
$d_s$	saturation crack spacing
$f$	fiber volume fraction
$f_l$	fiber volume fraction in loading direction
$h$	fiber pull-out length
$l$	sliding length
$m$	shape parameter for fiber strength distribution
$n$	creep exponent
$q$	residual stress in matrix in axial orientation
$s_{ij}$	deviatoric stress
$t$	time
$t_p$	ply thickness
$t_b$	beam thickness
$u$	crack opening displacement (COD)
$u_a$	COD due to applied stress
$u_b$	COD due to bridging
$w$	beam width
$C_v$	specific heat at constant strain
$E$	Young's modulus
$\bar{E}$	unloading modulus
$E_*$	Young's modulus of material with matrix cracks
$E_f$	Young's modulus of fiber
$E_m$	Young's modulus of matrix
$E_L$	ply modulus in longitudinal orientation
$E_T$	ply modulus in transverse orientation
$E_t$	tangent modulus
$E_s$	secant modulus
$G$	shear modulus
$\dot{G}$	energy release rate (ERR)

$G_{tip}$	tip ERR
$G_{up}^o$	tip ERR at lower bound
$K$	stress intensity factor (SIF)
$K_b$	SIF caused by bridging
$K_f$	critical SIF for fibers
$K_m$	critical SIF for matrix
$K_R$	crack growth resistance
$K_{tip}$	SIF at crack tip
$I_o$	moment of inertia
$L$	crack spacing in 90° plies
$L_g$	gauge length
$L_o$	reference length
$R$	fiber radius
$\mathcal{R}$	radius of curvature
$S$	tensile strength of fiber
$S_b$	dry bundle strength
$S_c$	characteristic fiber strength
$S_g$	UTS subject to global load sharing
$S_o$	scale factor for fiber strength
$S_p$	pull-out strength
$S_u$	ultimate tensile strength (UTS)
$S_*$	UTS in presence of a flaw
$T$	temperature
$\alpha$	linear thermal coefficient of expansion (TCE)
$\alpha_f$	TCE of fiber
$\alpha_m$	TCE of matrix
$\gamma$	shear strain
$\gamma_c$	shear ductility
$\delta_c$	characteristic length
$\delta\epsilon$	hysteresis loop width
$\epsilon$	strain
$\epsilon_*$	strain caused by relief of residual stress upon matrix cracking
$\epsilon_e$	elastic strain
$\epsilon_o$	permanent strain
$\epsilon_\tau$	transient creep strain
$\lambda$	pull-out parameter
$\mu$	friction coefficient

$\nu$	Poisson's ratio
$\phi$	orientation of interlaminar cracks
$\rho$	density
$\sigma$	stress
$\sigma_b$	bridging stress
$\bar{\sigma}_b$	peak, reference stress
$\sigma_e$	effective stress
$\sigma_f$	stress in fiber
$\sigma_i$	debond stress
$\sigma_m$	stress in matrix
$\sigma_{mc}$	matrix cracking stress
$\sigma^0$	stress on $0^\circ$ plies
$\sigma_0$	creep reference stress
$\sigma_{rr}$	radial stress
$\sigma^R$	residual stress
$\sigma_s$	saturation stress
$\sigma_s^*$	peak stress for traction law
$\sigma_t$	lower bound stress for tunnel cracking
$c$	misfit stress
$\tau$	interface sliding stress
$\tau_0$	constant component of interface sliding stress
$\tau_s$	shear strength
$\Delta^R$	displacement caused by matrix removal
$\Delta T$	change in temperature
$\Delta \epsilon_p$	unloading strain differential
$\Delta \epsilon_0$	reloading strain differential
$\Gamma$	fracture energy
$\Gamma_i$	interface debond energy
$\Gamma_f$	fiber fracture energy
$\Gamma_m$	matrix fracture energy
$\Gamma_R$	fracture resistance
$\Gamma_S$	steady-state fracture resistance
$\Gamma_T$	transverse fracture energy
$\Omega$	misfit strain
$\Omega_0$	misfit strain at ambient temperature

## SYNOPSIS

This review compiles knowledge about the mechanical and structural performance of ceramic-matrix composites. The overall philosophy recognizes the need for models that allow efficient interpolation between experimental results, as the constituents and the fiber architecture are varied. This approach is necessary because empirical methods are prohibitively expensive. Moreover, the field is not yet mature, though evolving rapidly. Consequently, an attempt is made to provide a framework into which models could be inserted, and then validated by means of an efficient experimental matrix. The most comprehensive available models and the status of experimental assessments are reviewed. The phenomena given emphasis include: the stress/strain behavior in tension and shear, the ultimate tensile strength and notch sensitivity, fatigue, stress corrosion and creep.



## 1. INTRODUCTION

### 1.1 Rationale

The strong interest in continuous fiber-reinforced ceramic matrix composites (CMC) has arisen primarily because of their ability to retain good tensile strength in the presence of holes and notches (Prewo, 1982; Mall *et al.*, 1993; Cady *et al.*, 1993). This characteristic is important because CMC components generally need to be attached to other components. At these attachments (whether mechanical or bonded), stress concentrations arise, which dominate the design and reliability. Inelastic deformation at these sites is crucial. It alleviates the elastic stress concentration by locally redistributing stress (Evans, Domergue and Vagaggini, 1993). Such inelasticity is present in CMCs (Nardonne and Prewo, 1988; Kim and Pagano, 1991; Cao *et al.*, 1990; Pryce and Smith, 1992). In association with the inelastic deformation, various degradation processes occur which affect the useful life of the material. Several fatigue effects are involved (Prewo, 1987; Zawada *et al.*, 1991): cyclic, static and thermal. The most severe degradation appears to occur subject to out-of-phase thermomechanical fatigue (TMF). In addition, creep and creep rupture occurs at high temperatures (Weber and Evans, 1993).

All of the CMC properties that govern structural utility and life depend upon the constituent properties (fibers, matrix, interfaces), as well as the fiber architecture. Since the constituents are variables, optimization of the property profiles needed for design and lifing become prohibitively expensive if traditional empirical procedures are used. The philosophy of this article is based on the recognition that mechanism-based models are needed, which allow efficient interpolation between a well-conceived experimental matrix. The emphasis is on the creation of a framework which allows models to be inserted, as they are developed, which can also be validated by carefully chosen experiments.

## 1.2 Objectives

The initial intent of this review is to address the *mechanisms* of stress redistribution upon monotonic and cyclic loading, as well as the *mechanics* needed to characterize the notch sensitivity (Evans, Domergue and Vagaggini, 1993; Bao and Suo, 1992). This assessment is conducted primarily for CMCs with 2-D reinforcements. The basic *phenomena* occurring in CMCs that give rise to inelastic strains are matrix cracks and fiber failures subject to interfaces that debond and slide (Fig. 1.1) (Aveston *et al.*, 1967; Evans and Marshall, 1990; Curtin, 1991). These phenomena identify the essential constituent properties, which have the typical values indicated on Table I.

Three underlying *mechanisms* are responsible for the non-linearity (Evans and Zok, 1992; Vagaggini and Evans, 1993). (i) *Frictional dissipation* occurs at the fiber/matrix interfaces, whereupon the sliding resistance of debonded interfaces,  $\tau$ , becomes a key parameter. *Control of  $\tau$  is critical*. This behavior is dominated by the fiber coating, as well as the fiber morphology (Evans, Zok and Davis, 1991; Davis *et al.*, 1993). By varying  $\tau$ , the prevalent damage mechanism and the resultant non-linearity can be dramatically modified. (ii) The matrix cracks increase the *elastic compliance* (He *et al.*, 1993). (iii) The matrix cracks also cause changes in the residual stress distribution, resulting in a *permanent strain* (He *et al.*, 1993).

The relative ability of these mechanisms to operate depends on the loading, as well as the fiber orientation. It is necessary to address and understand the mechanisms that operate for loadings which vary from tension along one fiber direction to shear at various orientations. For *tensile loading*, several damage mechanisms have been found, involving matrix cracks combined with sliding interfaces (Fig. 1.2). These can be visualized by mechanism maps (Evans, 1991), which then become an integral part of the testing and design activity. *One* damage mechanism involves mode I cracks with simultaneous fiber failure, referred to as *class I behavior* (Fig. 1.2). Stress redistribution is

provided by the tractions exerted on the crack by the failed fibers, as they *pull out* (Bao and Suo, 1992; Cox and Marshall, 1992; Cox, 1991; Cox and Lo, 1992). A *second* damage mechanism involves multiple matrix cracks, with minimal fiber failure, referred to as *class II behavior* (Fig. 1.2). In this case, the plastic deformation caused by matrix cracks allows stress redistribution (Evans *et al.*, 1992; Cady *et al.*, 1993). A schematic of a mechanism map based on these two damage mechanisms (Fig. 1.3) illustrates another important issue: the use of *non-dimensional parameters* to interpolate over a range of constituent properties.<sup>‡</sup> On the mechanism map, the ordinate is a non-dimensional measure of sliding stress and the abscissa is a non-dimensional *in situ* fiber strength. A *third* damage mechanism also exists (Fig. 1.2), referred to as *class III*. It involves matrix shear damage prior to composite failure as a means for redistributing stress. A proposed mechanism map is presented in Fig. 1.4 (Brøndsted *et al.*, 1993).

A summary of tensile stress-strain curves obtained for a variety of 2-D CMCs (Fig. 1.5) highlights the most fundamental characteristic relevant to the application of CMCs. Among these four materials, the SiC/CAS system is found to be *notch insensitive* in tension (Cady *et al.*, 1993), even for quite large notches (~ 5 mm long). The other three materials exhibit varying degrees of *notch sensitivity* (Heredia *et al.*, 1993). Moreover, the notch insensitivity in SiC/CAS arises *despite relatively small plastic strains*. These results delineate two issues that need resolution. (i) How much plastic strain is needed to impart notch insensitivity. (ii) Is the ratio of the 'yield' strength to ultimate tensile strength (UTS) an important factor in notch sensitivity? This review will address both questions.

The *shear behavior* of CMCs also involves matrix cracking and fiber failure (Brøndsted *et al.*, 1993). However, the ranking of the shear stress/strain curves between materials (Fig. 1.6) differs appreciably from that found for tension (Fig. 1.5). Preliminary

---

<sup>‡</sup> For ease of reference, all of the most important non-dimensional parameters are listed on a separate table (Table II).

efforts at understanding this difference and for providing a methodology to interpolate between shear and tension will be described.

Analyses of damage and failure in CMCs have established that certain *constituent properties* are basic to composite performance (Table I). These need to be *measured*, independently, and then used as characterizing parameters, analogous to the yield strength and fracture toughness in monolithic materials. The six major *independent* parameters are the interfacial sliding stress,  $\tau$ , and debond energy,  $\Gamma_i$ , the *in situ* fiber properties,  $S_c$  and  $m$ , the fiber/matrix misfit strain,  $\Omega$ , and the matrix fracture energy  $\Gamma_m$ , as well as the elastic properties,  $E$ ,  $\nu$  (Evans *et al.*, 1993). *Dependent* parameters that can often be used to infer the constituent properties include: the fiber pull-out length (Curtin, 1991; Cao *et al.*, 1990), the fracture mirror radius on the fibers (Jamet *et al.*, 1984) and the saturation crack spacing in the matrix (Zok and Spearing, 1992). Approaches for measuring the constituent properties in a *consistent, straightforward* manner will be emphasized and their relevance to composite behavior explored through models of damage and failure. Moreover, the expressions that relate composite behavior to constituent properties are often unwieldy, because a large number of parameters are involved. Consequently, throughout this article, the formulae used to represent CMC behaviors are the *simplest* capable of describing the major phenomena.†

In most CMCs with desirable tensile properties, linear elastic fracture mechanics (LEFM) criteria are violated (Marshall and Cox, 1988; Marshall *et al.*, 1985). Instead, various large-scale non-linearities arise, associated with matrix damage and fiber pull-out. In consequence, an alternate mechanics is needed to specify the relevant *material and loading parameters* and to establish *design rules*. Some progress toward this objective will be described and related to test data. This has been achieved using large-scale

---

† The behaviors represented by these formulae are often applicable only to composites: the equivalent phenomenon being absent in monolithic ceramics. Consequently, the expressions should be restricted to CMCs with fiber volume fractions in the range of practical interest ( $f$  between 0.3–0.5). Extrapolation to small  $f$  would lead to erroneous interpretations, because mechanism changes usually occur.

bridging mechanics (LSBM), combined with continuum damage mechanics (CDM) (Cox and Lo, 1992; Bao and Suo, 1992; Hayhurst *et al.*, 1991; Cox and Marshall, 1991).

The preceding considerations dictate the ability of the material to survive thermal and mechanical loads imposed for short durations. In many cases, long-term survivability at elevated temperatures dictates the applicability of the material. Life models based on *degradation* mechanisms are needed to address this issue. For this purpose, generalized fatigue and creep models are required, especially in regions that contain matrix cracks. It is inevitable that such cracks exist in regions subject to strain concentrations and, indeed, are required to redistribute stress. In this situation, degradation of the interface and the fibers may occur as the matrix cracks open and close upon thermomechanical cycling, with access of the atmosphere being possible, through the matrix cracks. The rate of such degradation dictates the useful life.

### 1.3 Approach

To address the preceding issues, this article is organized in the following manner. Some of the basic thermomechanical characteristics of CMCs are first established, with emphasis on interfaces and interface properties, as well as residual stresses. Then, the fundamental response of *unidirectional* (1-D) materials, subject to *tensile loading*, is addressed, in accordance with several sub-topics: (i) Mechanisms of non-linear deformation and failure; (ii) Constitutive laws that relate macroscopic performance to constituent properties; (iii) The use of stress/strain measurements to determine constituent properties in a consistent, straightforward manner; (iv) The simulation of stress/strain curves. The discussion of 1-D materials is followed by the application of the same concepts to 2-D materials, subject to combinations of tensile and shear loading. At this stage, it is possible to address the *mechanisms of stress redistribution* around flaws, holes, attachments and notches. In turn, these mechanisms suggest a *mechanics*

*methodology* for relating strength to the size and shape of the flaws, attachment loading, etc.

Data regarding the effects of cyclic loading and creep on CMC life are limited. The concepts to be developed thus draw upon knowledge and experience gained with other composite systems, such as metal matrix (MMCs) and polymer matrix (PMCs) materials. The overall philosophy is depicted in Fig. 1.7.

## 2. INTERFACES

### 2.1 Thermomechanical Representation

The thermomechanical properties of coatings at fiber/matrix interfaces are critically important. A consistent characterization approach is necessary. The most commonly adopted hypothesis is that there are two parameters (Fig. 2.1). One is associated with *fracture* and the other with *slip* (Hutchinson and Jensen, 1990; Mackin *et al.*, 1992; Kerans, *et al.*, 1992). Fracture, or debonding, is considered to involve a debond energy,  $\Gamma_i$  (Evans *et al.*, 1990; He and Hutchinson, 1989). Slip is expected to occur with a shear resistance,  $\tau$ . A schematic representation (Fig. 2.2) illustrates the issues. *Debonding* must be a mode II (shear) fracture phenomenon. In brittle systems, mode II fracture typically occurs by the coalescence of microcracks within a material layer (Fleck *et al.*, 1991). In some cases, in CMCs, this layer coincides with the coating itself, such that debonding involves a diffuse zone of microcrack damage (Fig. 2.2). In other cases, the layer is very thin and the debond has the appearance of a *single crack*. For both situations, it is believed that debond propagation can be represented by a debond energy,  $\Gamma_i$ , with an associated stress jump above and below the debond front (Hutchinson and Jensen, 1990). Albeit that, in several instances,  $\Gamma_i$  is essentially zero (Marshall and Oliver, 1987). When a discrete debond crack exists, *frictional sliding* of the

crack faces provides the shear resistance. Such sliding occurs in accordance with a friction law (Mackin *et al.*, 1992; Jero *et al.*, 1992; Marshall, 1992),

$$\tau = \tau_0 - \mu \sigma_{rr} \quad (2.1)$$

where  $\mu$  is the Coulomb friction coefficient,  $\sigma_{rr}$  is the compression normal to the interface and  $\tau_0$  is a term associated with fiber roughness. When the debond process occurs by diffuse microcracking in the coating, it is again assumed (without justification) that the interface has a constant shear resistance,  $\tau_0$ .

For debonding and sliding to occur, rather than brittle cracking through the fiber, the debond energy  $\Gamma_i$  must not exceed an upper bound, relative to the fiber fracture energy,  $\Gamma_f$  (He and Hutchinson, 1989). Calculations have suggested that the following inequality must be satisfied (Fig. 2.3)

$$\Gamma_i \lesssim (1/4)\Gamma_f \quad (2.2)$$

Noting that most ceramic fibers have a fracture energy,  $\Gamma_f \approx 20 \text{ Jm}^{-2}$ , Eqn. (2.2) indicates that the upper bound on the debond energy,  $\Gamma_i \approx 5 \text{ Jm}^{-2}$ . This magnitude is broadly consistent with experience obtained on fiber coatings that impart requisite properties to CMCs (Davis *et al.*, 1993; Evans *et al.*, 1992; Rice, 1987; Rice *et al.*, 1984; Bender *et al.*, 1986; Cranmer, 1989; Brennan and Prewo, 1982).

## 2.2 Measurement Methods

Measurements of the sliding stress  $\tau$  and the debond energy,  $\Gamma_i$ , have been obtained by a variety of approaches (Table I). The most direct involve displacement measurements. These are conducted in two ways: (i) fiber push-through/push-in, by using a small-diameter indenter (Marshall and Oliver, 1987; Jero *et al.*, 1992; Mackin

*et al.*, 1992); (ii) tensile loading in the presence of matrix cracks (Marshall and Evans, 1985; Kotil *et al.*, 1990; Evans *et al.*, 1993). Indirect methods for obtaining  $\tau$  also exist. These include measurement of the saturation matrix crack spacing (Zok and Spearing, 1993) and the fiber pull-out length (Curtin, 1991). The *direct* measurement methods require accurate determination of displacements, coupled with an analysis that allows rigorous deconvolution of load/displacement curves. The basic analyses used for this purpose are contained in papers by Hutchinson and Jensen (1990), Liang and Hutchinson (1993), Marshall (1992) and Jero *et al* (1992). The fundamental features are illustrated by the behavior found upon tensile loading, subsequent to matrix cracking (Fig. 2.4). The hysteresis that occurs during an unload/reload cycle relates to the sliding stress,  $\tau$ . *Accurate values for  $\tau$  can be obtained from hysteresis measurements* (Kotil *et al.*, 1991; Evans *et al.*, 1993; Vagaggini *et al.*, 1993). Furthermore, these results are *relevant to the small sliding displacements* ‡ that occur during matrix crack evolution in actual composites. The plastic strains contain *combined* information about  $\tau$ ,  $\Omega$  and  $\Gamma_i$ . Consequently, if  $\tau$  is already known,  $\Gamma_i$  can be evaluated from the plastic strains measured as a function of load, especially if  $\Omega$  has been obtained from independent determinations (Evans *et al.*, 1993). The basic formulae that connect  $\tau$ ,  $\Gamma_i$  and  $\Omega$  to the stress/strain behavior are presented in a subsequent section.

## 2.3 Sliding Models

The manipulations of interfaces needed to control  $\tau$  can be appreciated by using a model to simulate the sliding behavior. A simplified sliding model has been developed (Fig. 2.3) which embodies the role of the pressure at contact points, due to the combined effects of a mismatch strain and roughness (Mackin *et al.*, 1992; Marshall, 1992; Jero *et al.*, 1992). Coulomb friction is regarded as the *fundamental* friction law operating at

---

‡ Information about  $\tau$  at larger sliding displacements is usually obtained from fiber push-through measurements.



contacts. Otherwise, the system is considered to be elastic. The variables in the analysis are (i) the amplitude and wavelength of the roughness; (ii) the mismatch strain,  $\Omega$ ; (iii) the Coulomb friction coefficient,  $\mu$ ; (iv) the elastic properties of the constituents. With these parameters as input, the sliding can be simulated for various loading situations. One set of simulations conducted for comparison with fiber push-out tests (Fig. 2.5) illustrates the relative importance of each of the variables. For this set, the fiber roughness was characterized using a fractal method. The roughness within the section was selected at random, from the measured amplitude distribution, causing some differences in the push-out spectrum for each simulation. By using this simulation, *substantial* systematic changes in the sliding resistance have been predicted when the friction coefficient, the mismatch strain and the roughness amplitude are changed.<sup>‡</sup> Generally, the mismatch strain and the roughness can be measured independently (Mackin *et al.*, 1992). Consequently, the comparison between simulation and experiment actually provides an estimate of the *friction coefficient*,  $\mu$ . If this is found to be within an acceptable range, the inferred  $\mu$  is, thereafter, used to predict how  $\tau$  can be expected to vary as either the misfit or the roughnesses are changed, if  $\mu$  is fixed. This approach indicates that  $\mu \approx 0.1$  for either C or BN coatings (Lamon *et al.*, 1993), whereas  $\mu \approx 0.5$  for oxide coatings (Mackin *et al.*, 1993). Such values are compatible with macroscopic friction measurements made on bulk materials and thus appear to be reasonable. However, much additional testing is needed to validate the sliding model.

## 2.4 Experimental Results

All of the experience with CMCs is on C, BN, or Mo fiber coatings (Evans *et al.*, 1991; Davis *et al.*, 1993; Rice, 1984; Brennan, 1986; Bender *et al.*, 1986). Such coatings usually have a relatively low debond energy,  $\Gamma_i$ , and can provide a range of sliding

---

<sup>‡</sup> There are only minor effects of Poisson's ratio.

stresses,  $\tau$  (Table I), as illustrated by comparison of three different carbon coatings on sapphire fibers in TiAl (Fig. 2.6a). A considerable range in  $\tau$  has even been achieved with C coatings. Values between 2 and 200 MPa have been found. Furthermore, this range obtains even at comparable values of the misfit strain. The different values may relate to fiber roughness. Roughness effects are best illustrated by the sliding behavior of sapphire fibers in a glass matrix. During fiber manufacture, sinusoidal asperities are grown onto the surface of the sapphire fibers. The sinusoidal fiber surface roughness is manifest as a wavelength modulation in the sliding stress during push-out (Fig. 2.6b) (Mackin *et al.*, 1992). However, there must also be influences of the coating thickness and microstructure. A model that includes an explicit influence of the coating has yet to be developed.

In most CMC systems, the debond energy  $\Gamma_i$  has been found to be negligibly small ( $\Gamma_i < 0.1 \text{ Jm}^{-2}$ ). Such systems include all of the glass ceramic matrix systems reinforced with Nicalon fibers, which have a C interphase formed by reaction during composite processing. Low values also seem to obtain for SiC matrix composites with BN fiber coatings. The clear exception is SiC/SiC composites made by chemical vapor infiltration (CVI), which use a C *interphase*, introduced by chemical vapor deposition (Naslain, 1993). For such composites, the non-linear behavior indicates a debond energy,  $\Gamma_i \approx 5 \text{ Jm}^{-2}$  (Table I). The interphase in this case debonds by a diffuse damage mechanism (Burrat, 1993). Moreover, it has been found that the coating behavior can be changed into one with  $\Gamma_i \approx 0$ , either by heat treatment of the composite (after CVI) or by chemical treatment of the fiber (Naslain, 1993). A basic understanding of these changes in  $\Gamma_i$  does not exist.

## 2.5 Environmental Influences

There are temperature and environmental effects on  $\tau$  and  $\Gamma_i$ . There are also effects on  $\tau$  of fiber displacement and cyclic sliding (Fig. 2.6c). These effects can critically

influence composite performance. The basic effect of temperature on  $\tau$  (Luh and Evans, 1987) concerns changes in the misfit strain and friction coefficient, evident from the simulations shown in Fig. 2.5. Environmental influences can be pronounced, especially in oxidizing atmospheres. The major effects arise either at high temperatures, or during fatigue.† When either C or Mo coatings are used,  $\tau$  initially decreases upon either exposure or fatigue (Fig. 2.6d), because a gap is created between the fiber and matrix, caused by elimination of the coating, through volatile oxide formation (Cao *et al.*, 1990; Holmes and Schuler, 1990; Holmes and Cho, 1992; Davis *et al.*, 1993). This process occurs when the *local* temperature reaches  $\sim 800^\circ\text{C}$ . The subsequent behavior depends on the fibers. When SiC fibers are used, further exposure causes  $\text{SiO}_2$  formation (Bischoff *et al.*, 1989). This layer gradually fills the gap, leading to large values of  $\tau$ . Eventually, a 'strong' interface bond forms (with large  $\Gamma_i$ ) that produces brittle behavior, without fiber pull-out. Conversely, oxide fibers in oxide matrices are inherently resistant to this embrittlement phenomenon (Mackin *et al.*, 1993; Davis *et al.*, 1993) and are environmentally desirable, provided that the matrix does not sinter to the fibers.

### 3. RESIDUAL STRESSES

The development of damage in CMCs is sensitive to the residual stress caused by the misfit strain,  $\Omega$ . Measurement of these stresses thus becomes an important aspect of the analysis and prediction of damage. These stresses arise at inter- and intra-laminate levels. Within a laminate, the axial stress in the matrix is (Budiansky *et al.*, 1986),

$$q = (E_m/E)\sigma^f \quad (3.1)$$

---

† A consequence of internal heating associated with cyclic frictional sliding at the interfaces.

where  $\sigma^T$  is the misfit stress, which is related to the misfit strain by (Table II)

$$\sigma^T = (c_2/c_1)E_m \Omega. \quad (3.2)$$

The average residual stress in a 0/90 laminate, with uniform laminate thickness,  $\sigma^R$ , depends on constituent properties in approximate accordance with (Zok and Evans, 1993),

$$\sigma^R \approx \frac{\Omega(1-f)E_L[1-E_m/E_L]}{(1+\nu_{LT})(1+E_L/E_T)} \quad (3.3)$$

Note that the residual stress  $\sigma^R \rightarrow 0$  on the elastic properties becomes homogeneous ( $E_f = E_m = E_L$ ). While connections between the residual stresses and constituent properties are rigorous, experimental determination is still necessary, because  $\Omega$  is not readily predictable. In general,  $\Omega$  includes terms associated with the thermal expansion difference,  $\alpha_f - \alpha_m$ , as well as volume changes that occur either upon crystallization or during phase transformations. For CVI systems, 'intrinsic' stresses may also be present.

Several experimental procedures can be used to measure the residual stresses. The three preferred methods involve diffraction (X-ray or neutron), beam deflection and permanent strain determination. X-ray diffraction measurements have the limitation that the penetration depth is small, such that only near-surface information is obtained. Moreover, in composites, residual stresses are *redistributed* near surfaces (Liang and Hutchinson, 1993). Consequently, a full stress analysis is needed to relate the measured strains to either  $q$  or  $\sigma^R$ .

Beam deflection and permanent strain measurements have the advantage that they provide information *averaged* over the composite. The results thus relate directly to the

misfit strain,  $\Omega$ . An experimental approach having high reliability involves curvature measurements on beams made from 0/90 composites (Beyerle *et al.*, 1992). For such material, polishing to produce one 0° layer and one 90° layer results in elastic bending (Fig. 3.1).† The radius of curvature  $\mathcal{R}$  is related to the residual stress by (Beyerle *et al.*, 1992a);\*

$$\sigma^R = E_L I_o / \mathcal{R} t_b^2 w \quad (3.4)$$

where  $I_o$  is the second moment of inertia,  $t_b$  is the beam thickness and  $w$  the beam width.

When only 1-D material is available, the preferred approach is to measure the displacement,  $\Delta_R$ , that occurs when a section of matrix, length  $L_d$ , is removed by dissolution (when possible). The residual stress in the matrix is then (Beyerle *et al.*, 1992b),

$$q = E_f f \Delta^R / (1 - f) L_d \quad (3.5)$$

Typical results are plotted on Fig. 3.2.

Finally, the permanent strains that arise following tensile plastic deformation also relate to  $\Omega$ . Measurement of these strains allows  $\Omega$  to be assessed (Vagaggini *et al.*, 1993). The relevant formulae are presented in a later section.

Once the ambient misfit strain,  $\Omega_o$ , has been inferred for the above measurements, the temperature dependence can be assessed from the thermal expansion mismatch, using,

---

† Unless the material has a plain weave.

\* There is a typographical error in Beyerle *et al.*: the width  $w$  was omitted in their equation.

$$\Omega = \Omega_o - (\alpha_m - \alpha_f) \Delta T_R \quad (3.6)$$

where  $\Delta T_R$  is the temperature change from ambient.

## 4. FIBER PROPERTIES

### 4.1 Load Sharing

The strength properties of fibers are *statistical* in nature. Consequently, it is necessary to apply principles of weakest link statistics, which define the properties of fibers *within a composite*. The initial decision to be made concerns the potential for interactions between failed fibers and matrix cracks. It has generally been assumed that matrix cracks and fiber failure are non-interacting and that global load sharing (GLS) conditions obtain<sup>‡</sup> (Curtin, 1991; Phoenix and Raj, 1992, Hild *et al.*, 1993). In this case, the stress along a material plane that intersects a failed fiber is equally distributed among all of the intact fibers. Experience has indicated that these assumptions are essentially valid for a variety of CMCs.

Subject to the validity of GLS, several key results have been derived. Two characterizing parameters emerge (Hentenberg and Phoenix, 1991): a characteristic length

$$\delta_c^{m+1} = L_o [S_o R / \tau]^m \quad (4.1)$$

and a characteristic strength

$$S_c^{m+1} = S_o^m [L_o \tau / R] \quad (4.2)$$

---

<sup>‡</sup> However, a criterion for GLS breakdown has yet to be devised.

where  $m$  is the shape parameter,  $S_0$  the scale parameter,  $L_0$  the reference length, and  $R$  the fiber radius. Various GLS results based on these parameters are described below.

When fibers do not interact, analysis begins by considering a fiber of length  $2L$  divided into  $2N$  elements, each of length  $\delta z$ . The probability that fiber element will fail, when the stress is less than  $\sigma$ , is the area under the probability density curve (Matthews *et al.*, 1976; Freudenthal, 1967)

$$\delta\phi(\sigma) = \frac{\delta z}{L_0} \int_0^\sigma g(S) dS \quad (4.3)$$

where  $g(S)dS/L_0$  represents the number of flaws per unit length of fiber having a 'strength' between  $S$  and  $S + dS$ . The local stress,  $\sigma$ , is a function of both the distance along the fiber,  $z$ , and the reference stress,  $\bar{\sigma}_b$ . The survival probability  $P_s$  for all elements in the fiber of length  $2L$  is the product of the survival probabilities of each element,

$$P_s(\bar{\sigma}_b, L) = \prod_{n=-N}^N [1 - \delta\phi(\bar{\sigma}_b, z)] \quad (4.4)$$

where  $z = n\delta z$  and  $L = N\delta z$ . Furthermore, the probability  $\Phi_s$  that the element at  $z$  will fail when the peak, reference stress is between  $\bar{\sigma}_b$  and  $\bar{\sigma}_b + \delta\bar{\sigma}_b$ , but not when the stress is less than  $\bar{\sigma}_b$ , is the change in  $\delta\phi$  when the stress is increased by  $\delta\bar{\sigma}_b$  divided by the survival probability up to  $\bar{\sigma}_b$ , given by (Matthews *et al.*, 1976; Freudenthal, 1967; Oh and Finnie, 1970)

$$\Phi_s(\bar{\sigma}_b, z) = [1 - \delta\phi(\bar{\sigma}_b, z)]^{-1} \left[ \frac{\partial \delta\phi(\bar{\sigma}_b, z)}{\partial \bar{\sigma}_b} \right] d\bar{\sigma}_b. \quad (4.5)$$

Denoting the probability density function for fiber failure by  $\Phi(\bar{\sigma}_b, z)$ , the probability that fracture occurs at a location  $z$ , when the peak stress is  $\bar{\sigma}_b$ , is governed by the probability that all elements *survive up to a peak stress*  $\bar{\sigma}_b$ , but that failure occurs, at  $z$ , when the stress reaches  $\bar{\sigma}_b$  (Thouless and Evans, 1988; Oh and Finnie, 1970). It is given by the product of Eqn. (4.4) with Eqn. (4.5)

$$\Phi_s(\bar{\sigma}_b, z) \delta \bar{\sigma}_b \delta z = \frac{\prod_{i=1}^N [1 - \delta \phi(\bar{\sigma}_b, z)]}{[1 - \delta \phi(\bar{\sigma}_b, z)]} \left[ \frac{\partial \delta \phi(\bar{\sigma}_b, z)}{\partial \bar{\sigma}_b} \right] d\bar{\sigma}_b. \quad (4.6)$$

While the above results are quite general, it is convenient to use a power law to represent  $g(S)$ ,

$$\int_0^\sigma g(S) dS = (\sigma/S_0)^m. \quad (4.7)$$

Alternative representations of  $g(S)$  are not warranted at the present level of development. Using this assumption, Eqn. (4.6) becomes (Thouless and Evans, 1988)

$$\Phi(\bar{\sigma}_b, z) = \exp \left\{ -2 \int_0^L \left[ \frac{\sigma(\bar{\sigma}_b, z)}{S_0} \right]^m \frac{dz}{L_0} \right\} \left( \frac{2}{L_0} \right) \frac{\partial}{\partial \bar{\sigma}_b} \left[ \frac{\sigma(\bar{\sigma}_b, z)}{S_0} \right]^m. \quad (4.8)$$

This basic result has been used to obtain solutions for several problems (Thouless and Evans, 1988; Sutcu, 1988; Curtin, 1991), described below.

## 4.2 The Ultimate Tensile Strength

When multiple matrix cracking precedes failure of the fibers in the  $0^\circ$  bundles, the load along each matrix crack plane is borne entirely by the fibers. *Nevertheless, the matrix has a crucial role*, because stress transfer between the fibers and the matrix still occurs



through the sliding resistance,  $\tau$ . Consequently, some stress can be sustained by the failed fibers. This stress transfer process occurs over a distance related to the characteristic length,  $\delta_c$ . As a result, the stresses on the intact fibers along any plane through the material are less than those experienced within a 'dry' fiber bundle (in the absence of matrix). The transfer process also allows the stress in a failed fiber to be unaffected at distance  $\geq \delta_c$  from the fiber fracture site (Fig. 4.1). Consequently, composite failure requires that fiber bundle failure occurs *within*  $\delta_c$  (Curtin, 1991). This phenomenon leads to an ultimate tensile strength (UTS) *independent of gauge length*,  $L_g$ , provided that  $L_g > \delta_c$ .† The magnitude of the UTS can be computed by first evaluating the average stress on *all* fibers, failed plus intact, along an arbitrary plane through the material. Then, by differentiating with respect to the stress on the *intact* fibers, in order to obtain the maximum, the UTS becomes,

$$S_g = f_t S_c F(m) \quad (4.9a)$$

with

$$F(m) = \left[ 2/(m+1) \right]^{1/(m+1)} \left[ (m+1)/(m+2) \right]$$

It is of interest to compare this result to that found for a 'dry' bundle. Then, the 'fiber bundle' strength  $S_b$ , depends on the gauge length in accordance with (Corten, 1967),

$$S_b = f S_o (L_o/L_g)^{1/m} e^{-1/m} \quad (4.9b)$$

---

† At small gauge lengths ( $L_g < \delta_c$ ), the UTS becomes gauge length dependent and exceeds  $S_u$  (Hild *et al.*, 1993).

In all cases,  $S_g > S_b$ .

As the load increases, the fibers fail systematically, resulting in a characteristic fiber fragment length. At composite failure, there can be multiple cracks within some fibers. The existence of many fiber fragments is still compatible with a high ultimate tensile strength.<sup>‡</sup> However, a diminished creep strength may ensue, as elaborated below (Section 9).

The above results are applicable to *tensile loading*. When a bending moment is applied, the behavior is modified. In this case, the stress is redistributed by both matrix cracking and fiber failure. Predictions of the UTS in pure flexure (Fig. 4.2) indicate the salient phenomena (Hild *et al.*, 1993).

#### 4.3 Fiber Pull-Out

In CMCs with good composite properties, fiber pull-out is evident on the tensile fracture surfaces (Thouless *et al.*, 1989). Various measurements conducted on these surfaces provide valuable information. Regions with highly correlated fiber failures, with minimal pull-out, are indicative of *manufacturing flaws*. Such flaws often occur in regions where fiber coating problems existed. In zones where fiber failures are *uncorrelated*, the distribution of fiber pull-out lengths, provides essential information. The pull-out lengths are related explicitly to the *stochastics* of fiber failure (Thouless and Evans, 1988; Curtin, 1991). The basic realization is that, on average, fibers do not fail on the plane of the matrix crack, even though the stress in the fibers has its *maximum value* at this site. This unusual phenomenon relies exclusively on statistics, wherein the locations of fiber failure may be identified as a distribution function that depends on the shape parameter,  $m$ . Furthermore, the mean pull-out length  $\bar{h}$  has a connection with the

---

<sup>‡</sup> A good analogy being the strength of a wire rope.

characteristic length,  $\delta_c$ . Consequently, a functional dependence exists, dictated by the non-dimensional parameters,  $\tau \bar{h}/RS_c$  and  $m$ ,

$$\bar{h}\tau/RS_c = \lambda(m) \quad (4.10)$$

There are two bounding solutions for the function  $\lambda$  (Fig. 4.3). Composite failure subject to *multiple matrix cracking* gives the *upper bound*. Failure in the presence of a *single crack* gives the *lower bound*.

Because of pull-out, a frictional *pull-out resistance* exists, which allows the material to sustain load, beyond the UTS. The associated 'pull-out' strength  $S_p$  is an important property of the composite (Fig. 4.4). The strength,  $S_p$ , is given by (Phillips, 1974),

$$\begin{aligned} S_p &= 2\tau f \bar{h}/R \\ &\equiv 2f S_c \lambda(m) \end{aligned} \quad (4.11)$$

#### 4.4 Influence of Flaws

The preceding results are applicable provided that there are no unbridged segments along the matrix crack. *Unbridged regions* concentrate the stress in the adjacent fibers and weaken the composite (Cui and Budiansky, 1993; Bao and Suo, 1992). Simple linear scaling considerations indicate that the diminished UTS depends on a non-dimensional *flaw index* (Table II),

$$\mathcal{A} = a_0 S_g^2 / E_L \Gamma \quad (4.12)$$

where  $\Gamma$  is the area under the stress/displacement curve for the bridging fibers,  $E$  is Young's modulus and  $2a_0$  is the length of the unbridged segment. The flaw index  $\mathcal{A}$  can be specified, based on  $\Gamma$ , using Large-Scale Bridging Mechanics (LSBM). The

dependence of the UTS, designated  $S^*$ , on the flaw index  $\mathcal{A}$  can be determined from LSBM by numerical analysis (Fig. 4.4) (Suo *et al.*, 1993). The results reveal that the ratio,  $S_p/S_g$ , is an important factor. Notably, relatively large values of the 'pull-out' strength alleviate the strength degradation caused by unbridged cracks.

#### 4.5 *In Situ* Strength Measurements

In general, composite consolidation degrades fiber properties and it becomes necessary to devise procedures that allow determination of  $S_c$  and  $m$  to be evaluated relevant to the fibers *within the composite*. This is a challenging problem. In some cases, it is possible to dissolve the matrix without further degrading the fibers and then measure the bundle strength (Prewo, 1986). This is not feasible with most CMCs of interest. The following two alternatives exist.

Some fibers exhibit fracture mirrors when they fail within a composite (e.g., Nicalon). A semi-empirical calibration has been developed that relates the mirror radius,  $a_m$ , to the *in situ* fiber tensile strength,  $S$ , given by (Fig. 4.5),

$$S \approx 3.5K_f/\sqrt{a_m} \quad (4.13)$$

where  $K_f$  is the fracture toughness of the fiber (Eckel and Bradt, 1989; Cao *et al.*, 1990; Jamet *et al.*, 1984). By measuring  $S$  on many fibers, and then plotting the cumulative distribution  $G(S)$ , both the shape parameter,  $m$ , and the characteristic *in situ* fiber strength,  $S_c$ , can be ascertained. Results of this type have been obtained for Nicalon fibers in a variety of different matrices (Fig. 4.6). This compilation indicates the sensitivity of the *in situ* strength to the composite processing approach. This fiber strength variation is also reflected in the range in UTS found among CMCs reinforced with these fibers (Fig. 1.4).

A problem in implementing the fracture mirror approach arises when a significant fraction of the fibers does not exhibit well-defined mirrors. Those fibers that do not have mirrors usually have a smooth fracture surface. It has thus been assumed that these are the weakest fibers in the distribution (Beyerle *et al.*, 1992; Eckel and Bradt, 1989). The order statistics used to determine  $G(S)$  are adjusted accordingly. This assumption has not been validated.

The only alternative approaches for evaluating  $S_c$ , known to the authors, are based on pull-out and fragment length measurements (Curtin, 1991). Both quantities depend on  $S_c$  and  $m$ , as well as  $\tau$ . Consequently, if  $\tau$  is known,  $S_c$  can be determined. For example,  $m$  can be evaluated by fitting the distribution of fiber pull-out lengths to the calculated function. Then,  $S_c$  can be obtained for the mean value,  $\bar{h}$ , using Eqn. (4.4). This approach has not been extensively used and checked.

#### 4.6 Experimental Results

Several studies have compared the multiple matrix cracking GLS prediction,  $S_g$  (Eqn. 4.9) with the UTS measured for either 1-D or 2-D CMCs. In most cases, the UTS is in the range  $(0.7-1) S_g$ , as indicated on Fig. 4.7. The two obvious discrepancies are the SiC/SiC<sub>CVI</sub> material and one of the SiC/C materials. In these cases, the GLS predictions overestimate the measured values. Moreover,  $\tau$  is relatively large for both materials, as reflected in the magnitude of the stress concentration index (Fig. 4.7). Two factors have to be considered as these results are interpreted. (i) In some materials, the fraction of fibers that exhibit mirrors is not large enough to provide confidence in the inferred values of  $S_c$  and  $m$ . This issue is a particular concern for the SiC/SiC<sub>CVI</sub> material. (ii) In other materials, manufacturing flaws are present that provide unbridged crack segments, which cause the UTS to be smaller than  $S_g$  (Section 4.4).

With the above provisos, it is surprising that the UTS measured for several 2-D CMCs is close to the GLS prediction. In these materials, cracks exist in the 90° plies at

low stresses and these cracks should concentrate the stress on the neighboring fibers in the  $0^\circ$  plies. The UTS would thus be expected to follow the strength degradation diagram (Fig. 4.4). That this weakening does not occur remains to be explained. It probably reflects the influence on the strength degradation of elastic anisotropy, as well as pull-out (Fig. 4.4).

## 5. MATRIX CRACKING IN UNIDIRECTIONAL MATERIALS

The development of damage in the form of matrix cracks within 1-D CMCs subject to tensile loading has been traced by direct optical observations on specimens with carefully polished surfaces and by acoustic emission detection (Kim and Pagano, 1991; Beyerle *et al.*, 1992; Pryce and Smith, 1992; Kim, 1992, Cho *et al.*, 1992; Kim and Katz, 1988), as well as by ultrasonic velocity measurements (Baste *et al.*, 1992). Interrupted tests, in conjunction with sectioning and SEM observations, have also been used. Analyses of the matrix damage found in 1-D CMCs provides the basis upon which the behavior of 2-D and 3-D CMCs may be addressed. The *matrix cracks* are found to interact with predominantly intact fibers, subject to interfaces that debond and slide. This process commences at a lower bound stress,  $\bar{\sigma}_{mc}$ . The crack density increases with increase in stress above  $\bar{\sigma}_{mc}$  and may eventually attain a saturation spacing,  $\bar{d}_s$ , at stress  $\bar{\sigma}_s$ . The details of crack evolution are governed by the distribution of matrix flaws. The matrix cracks reduce the unloading elastic modulus,  $\bar{E}$ , and also induce a permanent strain,  $\epsilon_0$  (Fig. 2.2). Relationships between  $\bar{E}$ ,  $\epsilon_p$  and constituent properties provide the key connections between processing and macroscopic performance, via the properties of the constituents.

The deformations caused by matrix cracking, in conjunction with interface debonding and sliding, exhibit three regimes that depend on the magnitude of the

debond stress,  $\bar{\sigma}_i$ . In turn,  $\bar{\sigma}_i$  depends on the debond energy through the relationship (Hutchinson and Jensen, 1990),

$$\bar{\sigma}_i = (1/c_i) \sqrt{E_m \Gamma_i / R} - \sigma^T \quad (5.1a)$$

which has a useful non-dimensional form

$$\Sigma_i = \bar{\sigma}_i / \sigma \quad (5.1b)$$

A mechanism map that identifies the three regimes is shown in Fig. 5.1 (Vagaggini *et al.*, 1993). When  $\Sigma_i > 1$ , debonding does not occur, whereupon matrix crack growth is an entirely elastic phenomenon. This condition is referred to as the no debond (ND) regime. When  $\Sigma_i < 1/2$ , small debond energy (SDE) behavior arises. The characteristic of this regime is that the reverse slip length at the interface, upon complete unloading, exceeds the debond length. In the SDE regime,  $\Gamma_i$  is typically small and does not affect certain properties, such as the hysteresis loop width. The term SDE is thus used, loosely, to represent the behavior expected when  $\Gamma_i = 0$ . An intermediate, large debond energy (LDE) regime also exists, when  $1/2 \leq \Sigma_i \leq 1$ . In this situation, reverse slip is impeded by the debond.

## 5.1 Basic Mechanics

The approach used to simulate mode I cracking under monotonic loading is to define tractions  $\sigma_b$  acting on the crack faces, induced by the fibers (Fig. 1.1) and to determine their effect on the crack tip by using the J-integral (Marshall *et al.*, 1985; Budiansky *et al.*, 1986),

$$G_{up} = G - \int_0^u \sigma_b du \quad (5.2)$$

where  $G$  is the energy release rate and  $u$  is the crack opening displacement. Cracking is considered to proceed when  $G_{tip}$  attains the pertinent fracture energy. Since the fibers are not failing, the crack growth criterion involves matrix cracking only. A lower bound is given by (Budiansky *et al.*, 1986; McCartney, 1987)

$$G_{up} = \Gamma_m(1-f) \quad (5.3)$$

with  $\Gamma_m$  being the matrix toughness. Upon crack extension,  $G$  becomes the crack growth resistance,  $\Gamma_R$ , whereupon

$$\Gamma_R = \Gamma_m(1-f) + \int_0^u \sigma_b du. \quad (5.4)$$

A traction law  $\sigma_b(u)$  is now needed to predict  $\Gamma_R$ . A law based on frictional sliding along debonded interfaces has been used most extensively and appears to provide a reasonable description of many of the observed mechanical responses (Eqn. 2.1). The traction law also includes effects of the interface debond energy,  $\Gamma_i$  (Hutchinson and Jensen, 1990). For many CMCs,  $\Gamma_i$  is small, as reflected in the magnitude of the debond stress,  $\Sigma_i$ .

For SDE, with a constant sliding stress,  $\tau_o$ , the sliding distance  $\ell$ , in the absence of fiber failure, is related to the crack surface tractions,  $\sigma_b$ , by (Aveston *et al.*, 1971; Marshall *et al.*, 1985)

$$\ell = [RE_m(1-f)/2\tau_o E_f f](\sigma_b + \sigma^T) \quad (5.5a)$$

For LDE, the corresponding solution is (Hutchinson and Jensen, 1990)



$$\ell = [RE_m(1-f)/2\tau_0 E, f](\sigma_b - \bar{\sigma}_i) \quad (5.5b)$$

The sliding length is, in turn, related to the crack opening displacement. The corresponding traction laws are thus (Marshall *et al.*, 1985; Budiansky *et al.*, 1986): for SDE,

$$\sigma_b + \sigma^T = [2\xi\tau_0 E f u/R]^{1/2} \quad (5.6a)$$

for LDE,

$$\sigma_b - \bar{\sigma}_i = [2\xi\tau_0 E f u/R] \quad (5.6b)$$

where  $\xi$  is defined in Table II. When fiber failure occurs, statistical considerations are needed to determine  $\sigma_b(u)$ .

The matrix fracture behavior can also be described by using stress intensity factors,  $K$ . This approach is more convenient than the J-integral in some cases: particularly for short cracks and for fatigue (Marshall *et al.*, 1985; McMeeking and Evans, 1990). To apply this approach, it is first necessary to specify the contribution to the crack opening induced by the applied stress, as well as that provided by the bridging fibers. For a plane strain crack of length  $2a$  in an infinite plate, these are given by (Tada *et al.*, 1985). The contribution due to the applied stress is

$$u_{\infty} = (4/E)\sigma\sqrt{a^2 - x^2} \quad (5.7a)$$

and that caused by bridging is

$$u_b = -(4/E) \int_0^a \sigma_b(\hat{x}) H d\hat{x} \quad (5.7b)$$

with  $H$  being a weight function. The net crack opening displacement is

$$u = u_- + u_b \quad (5.8)$$

The contribution to  $K$  from the bridging fibers is obtained using (Tada *et al.*, 1985),

$$K_b = -2 \sqrt{\frac{2}{\pi}} \int_0^a \frac{\sigma_b(x) dx}{\sqrt{a^2 - x^2}} \quad (5.9)$$

With  $\sigma_b$  given by Eqn. (5.5). The shielding associated with  $K_b$  leads to a tip stress intensity factor

$$K_{up} = K + K_b \quad (5.10)$$

where  $K$  depends on the loading and specimen geometry.

A criterion for matrix crack extension, based on  $K_{tip}$ , is needed. For this purpose, to be consistent with the energy criterion (Eqn. 5.3), the critical stress intensity factor is taken to be

$$K_{up} = \sqrt{E \Gamma_m (1-f)} \quad (5.11)$$

Then, as demonstrated below, the two approaches ( $K$  and  $\mathcal{G}$ ) lead to the same steady-state matrix cracking stress.

## 5.2 The Matrix Cracking Stress

The preceding basic results can be used to obtain solutions for matrix cracking (Aveston, Cooper and Kelly (ACK), 1971; Marshall *et al.*, 1985; Budiansky *et al.*, 1986; McCartney, 1987; Zok and Spearing, 1992; Singh, 1989). Present understanding involves the following factors. Because the fibers are intact, a steady-state condition exists wherein the tractions on the fibers in the crack wake balance the applied stress. This special case may be addressed by integrating Eqn. (5.2) up to a limit  $u = u_0$ . This limit is obtained from Eqn. (5.6) by equating  $\sigma_b$  to  $\sigma$ . For SDE, this procedure gives (Budiansky *et al.*, 1986)

$$\mathcal{G}_{up}^0 = \frac{(\sigma + \sigma^T)^3 E_m^2 (1-f)^2 R}{6 \tau_0 f^2 E_f E_L^2} \quad (5.12)$$

A lower bound to the matrix cracking stress,  $\sigma_{mc}$ , is then obtained by invoking Eqn. (5.3), such that (Budiansky *et al.*, 1986)\*

$$\begin{aligned} \bar{\sigma}_{mc} &= E_L \left[ \frac{6 \tau_0 \Gamma_m f^2 E_f}{(1-f) E_m^2 R E_L} \right]^{1/3} - \sigma^T \\ &\equiv \sigma_{mc}^* - \sigma^T \end{aligned} \quad (5.13)$$

Analogous results can be obtained using stress intensity factors (Marshall *et al.*, 1985; McMeeking and Evans, 1990). For the example of a small center crack in a tensile

---

\* In some cases, *small* matrix cracks can form at stresses below  $\bar{\sigma}_{mc}$  (Kim and Pagano, 1991). These occur either within matrix-rich regions or around processing flaws. However, the non-linear composite properties are usually dominated by fully-developed matrix cracks that form at stresses above  $\bar{\sigma}_{mc}$ .

specimen,† (Eqns. 5.9 and 5.11) give a steady-state result at large crack lengths (McMeeking and Evans, 1990),

$$K_{up} = \frac{\sigma \sqrt{R}}{\sqrt{6} \mathcal{T}} \quad (5.14)$$

and  $\mathcal{T}$  is a sliding index defined in Table II. When combined with the fracture criterion (Eqn. 5.11), the matrix cracking stress,  $\bar{\sigma}_{mc}$  is predicted to be the same as that given by Eqn. (5.13).

The K approach may also be used to define a transition crack length  $a_t$  above which steady-state applies. This transition length is given by (Marshall *et al.*, 1985; McCartney, 1987),

$$a_t/R = E_m \left[ \Gamma_m (1 + \xi)^2 (1 - f)^4 / \tau_0^2 f^4 E_f^2 R \right]^{1/6}. \quad (5.15)$$

Namely, when the initial flaw size  $a_i > a_t$ , cracking occurs at  $\sigma = \bar{\sigma}_{mc}$ . Conversely, when the initial flaws are small,  $a_i < a_t$ , it has been shown that (McMeeking and Evans, 1990)

$$K_{up} \approx K \left[ 1 - \frac{3.05}{\mathcal{E}} \sqrt{\mathcal{E} + 3.3} + \frac{5.5}{\mathcal{E}} \right]. \quad (5.16)$$

where  $\mathcal{E}$  is a loading index defined as, (Table II),

$$\mathcal{E} = 2R(1 - f)^2 E_m^2 \sigma / E_f E \tau_0 a f^2 (1 - \nu^2).$$

---

†  $K = \sigma \sqrt{\pi a}$

This result for  $K_{tip}$ , when combined with Eqn. (5.11), gives a revised matrix cracking stress, which *exceeds*  $\bar{\sigma}_{mc}$ .

Analogous results can be derived for the LDE regime. In this case, Eqn. (5.6b) may be used with Eqn. (5.2) to derive an energy release rate, which can be combined with the fracture criterion (Eqn. 5.3) to predict  $\sigma_{mc}$ . The result is contained within the implicit formula (Evans and Domergue, 1993),

$$\left( \frac{\sigma_{mc}}{\bar{\sigma}_i} - 1 \right)^3 + 3 \sqrt{\frac{E_m \Gamma_i}{R \bar{\sigma}_i}} \left( \frac{\sigma_{mc}}{\bar{\sigma}_i} - 1 \right)^2 = \left( \frac{\sigma_{mc}^*}{\bar{\sigma}_i} \right)^3 \quad (5.17)$$

### 5.3 Crack Evolution

The evolution of additional cracks at stresses above  $\sigma_{mc}$  is less well understood, because two factors are involved: *screening* and *statistics* (Beyerle *et al.*, 1992; Zok and Spearing, 1992; Cho *et al.*, 1992). When the sliding zones between neighboring cracks overlap, *screening* occurs and  $G_{tip}$  differs from  $G_{up}^0$ . The relationship is dictated by the location of the neighboring cracks. When a crack forms midway between two existing cracks with a separation  $2d$ , subject to SDE,  $G_{tip}$  is related to  $G_{up}^0$  by (Zok and Spearing, 1992)

$$G_{up}/G_{up}^0 = 4(d/2\ell)^3 \quad (\text{for } 0 \leq d/\ell \leq 1) \quad (5.18a)$$

and

$$G_{up}/G_{up}^0 = 1 - 4(1 - d/2\ell)^3 \quad (\text{for } 1 \leq d/\ell \leq 2) \quad (5.18b)$$

When  $d$  is sufficiently small, Eqn. (5.19a) applies and  $G_{tip}$  is independent of the stress. Once this occurs,  $G_{tip}$  cannot increase and is unable to again satisfy the matrix crack growth criterion (Eqn. 5.3). This occurs with spacing,  $\bar{d}_s$ , at an associated stress  $\bar{\sigma}_s$  (Fig. 2.4). This spacing is given by,

$$\bar{d}_s/R = \chi \left[ \Gamma_m (1-f)^2 E_f E_m / f \tau_o^2 E_L R \right]^{1/2} \quad (5.19)$$

Note that this result is *independent* of the residual stress, because the terms containing  $(\sigma_b + \sigma^T)$  in Eqns. (5.5) and (5.12) cancel when inserted into Eqn. (5.19a). The coefficient  $\chi$  depends on the spatial aspects of crack evolution: periodic, random, etc.. Simulations for spatial randomness indicate that,  $\chi \approx 1.6$  (Zok and Spearing, 1992). Moreover, these same simulations indicate that the saturation stress should scale with  $\bar{\sigma}_{mc}$ , such that

$$\bar{\sigma}_s / \sigma_{mc} = 1.26 \quad (5.20)$$

This stress ratio depends *only* on the spatial characteristics of the cracks.

In addition to these screening effects, the actual *evolution of matrix cracks* at stresses above  $\sigma_{mc}$  is governed by *statistics* that relate to the size and spatial distribution of matrix flaws. If this distribution is known, the evolution can be predicted. Such statistical effects arise when the matrix flaws are smaller than the transition size,  $a_t$ , at which steady-state commences (Eqn. 5.15). In this case, a flaw size distribution must be combined with the short crack solution for  $K_{tip}$  (Eqn. 5.16) in order to predict crack evolution. At the simplest level, this has been done by assuming an exponential distribution for the matrix flaw size (Spearing and Zok, 1993),

$$p = \exp(L/L_o) (a_t/a)^{-\omega} \quad (5.21)$$

where  $p$  is the fraction of flaws in length  $L$  having size larger than  $a$ ,  $\omega$  is a shape parameter related to the Weibull modulus for the matrix,  $m_m$  ( $\omega = m_m/2$ ) and  $L_0$  is a scale parameter

$$L_0 = \lambda_s \ell_0$$

with  $\ell_0$  being the slip distance at  $\sigma = \sigma_{mc}$  and  $\lambda_s$  a numerical coefficient. The condition  $\lambda_s \leq 1$  corresponds to a high density of matrix flaws already large enough to be at steady-state. Conversely,  $\lambda_s > 1$  refers to a situation wherein most matrix flaws are smaller than the transition size,  $a_t$ .

Simulations can be performed in which the key variables are the shape parameter  $\omega$  and the scale parameter  $\lambda_s$ . The simulated crack densities (Fig. 5.2a) indicate a sudden burst of cracking at  $\sigma = \sigma_{mc}$ , when  $\lambda_s < 1$ , followed by a gradual increase with continued elevation of the stress. The saturation stress is similar to that given by Eqn. (5.20). In contrast, when  $\lambda_s \gg 1$ , the cracks evolve more gradually with stress, reaching saturation at substantially higher levels of stress. Nevertheless, the saturation spacing remains insensitive to  $\lambda_s$ . These simulated behaviors are qualitatively similar to those measured by experiment (Fig. 5.2b). Moreover, the values found for  $\omega$  are in a reasonable range ( $m_m = 2\omega \approx 4-8$ ). However, since  $\omega$  and  $a_0$  are not known, a priori, in practice this approach becomes a fitting procedure rather than a predictive model. Despite this limitation, it has been found that a simple formula can be used to approximate crack evolution in most CMCs (Evans *et al.*, 1993), given by (Fig. 5.2b),

$$\bar{d} \approx \bar{d}_s \frac{[\bar{\sigma}_s/\bar{\sigma}_{mc} - 1]}{[\bar{\sigma}/\bar{\sigma}_{mc} - 1]} \quad (5.22)$$

Analogous results can be derived for LDE, with the debond length given by Eqn. (5.5b) and the reference energy release rate by Eqn. (5.17). In this case, the saturation crack spacing is smaller than that given by Eqn. (5.20)

#### 5.4 Constitutive Law

Analyses of the plastic strains caused by matrix cracks, combined with calculations of the compliance change, provide a constitutive law for the material. The important parameters are the permanent strain,  $\epsilon_0$  and the unloading modulus,  $\bar{E}$ . These quantities, in turn, depend on several constituent properties; the sliding stress,  $\tau$ , the debond energy,  $\Gamma_d$ , and the misfit strain,  $\Omega$ . The most important results are summarized below.

Matrix cracks *increase* the elastic compliance. Numerical calculations indicate that the *unloading elastic modulus*,  $E^*$ , is given by (He *et al.*, 1993),

$$E_L/E^* - 1 = (R/\bar{d}) \mathcal{B}[f, E_f/E_m] \quad (5.23)$$

where  $\mathcal{B}$  is the function plotted on Fig. 5.3. The matrix cracks also cause a permanent strain associated with relief of the residual stress. This strain,  $\epsilon^*$ , is related to the modulus and the misfit stress by (Fig. 5.4) (He *et al.*, 1993),

$$\epsilon^* \equiv \sigma^T [1/E^* - 1/E_L] \quad (5.24)$$

The preceding effects occur *without* interface sliding. The incidence of *sliding* leads to *plastic strains* that superpose onto  $\epsilon^*$ . The magnitude of these strains depends on  $\Sigma_i$  (Fig. 5.1) and on the stress relative to the saturation stress,  $\sigma_s$ .



### 5.4.1 Stresses Below Saturation

#### (i) Small Debond Energy

For SDE, when  $\sigma < \sigma_s$ , the unloading modulus  $\bar{E}$  depends on  $\tau_o$ , but is *independent* of  $\Gamma_i$  and  $\Omega$ . However, the permanent strain  $\epsilon_o$  depends on  $\Gamma_i$  and  $\Omega$ , as well as  $\tau_o$ . These differing dependencies of  $\bar{E}$  and  $\epsilon_o$  on constituent properties have the following two implications. (i) To *simulate* the stress/strain curve, both  $\epsilon_o$  and  $\bar{E}$  are required. Consequently,  $\tau_o$ ,  $\Gamma_i$  and  $\Omega$  *must be known*. (ii) The use of unloading and reloading to *evaluate the constituent properties* has the convenience that the hysteresis is dependent *only on  $\tau_o$* . Consequently, precise determination of  $\tau_o$  is possible. Moreover, with  $\tau_o$  known from the hysteresis, both  $\Gamma_i$  and  $\Omega$  can be evaluated from the permanent strain. The principal SDE results are as follows.

The permanent strain is (Evans *et al.*, 1993; Pryce and Smith, 1992; Vagaggini *et al.*, 1993)

$$(\epsilon_o - \epsilon^*) \mathcal{H}^{-1} = 4(1 - \Sigma_i) \Sigma_T + 1 - 2 \Sigma_i^2 \quad (5.25)$$

where  $\mathcal{H}$  is a hysteresis index (Table II)

$$\mathcal{H} = b_2 (1 - a_i f)^2 R \bar{\sigma}^2 / 4 \bar{d} \tau_o E_m f^2 \quad (5.26)$$

and

$$\Sigma_T = \sigma^T / \bar{\sigma}. \quad (5.27)$$

The maximum width of the hysteresis loop, at half maximum,  $\delta \epsilon_{1/2}$ , is (Figs. 2.2, 5.4)

$$\delta \epsilon_{\mathcal{H}} = \mathcal{H}/2. \quad (5.28)$$

The unloading strain is (Fig. 5.4),

$$\Delta \epsilon_p = \mathcal{H} \quad (5.29)$$

and the unloading modulus is

$$(\bar{E})^{-1} = (E^*)^{-1} + \mathcal{H}/\bar{\sigma} \quad (5.30)$$

### (ii) Large Debond Energy

For LDE (Fig. 5.1), when  $\sigma < \sigma_s$ , the unloading modulus depends on both  $\tau$  and  $\Gamma_i$  (Fig. 5.4). There are also linear segments to the unloading and reloading curves. These segments can be used to establish constructions that allow the constituent properties to be conveniently established. The principal results are as follows. The permanent strain is (Vagaggini *et al.*, 1993),

$$(\epsilon_o - \epsilon^*) \mathcal{H}^{-1} = 2(1 - \Sigma_i)(1 - \Sigma_i + 2\Sigma_\tau) \quad (5.31)$$

and the unloading modulus is

$$(\bar{E})^{-1} = (E^*)^{-1} + 4\Sigma_i(1 - \Sigma_i)\mathcal{H}/\bar{\sigma} \quad (5.32)$$

In this case, the hysteresis loop width depends on the magnitude of  $\Sigma_i$ . For intermediate values,  $1/2 \leq \Sigma_i \leq 3/4$

$$\delta \epsilon_{\mathcal{H}} = \mathcal{H} \left[ 1/2 - (1 - 2\Sigma_i)^2 \right] \quad (5.33)$$

whereas, for  $3/4 \leq \Sigma_i \leq 1$

$$\delta \varepsilon_{\gamma} = 4 \mathcal{H} [1 - \Sigma_i]^2 \quad (5.34)$$

#### 5.4.2 Stresses Above Saturation

At stress,  $\sigma > \sigma_s$ , the crack density remains essentially constant. It has thus been assumed that there is no additional stress transfer between the fibers and the matrix. In this case, the tangent modulus is given by (Aveston *et al.*, 1971):

$$E_t \equiv d\sigma/d\varepsilon = fE_f \quad (5.35)$$

In practice, the tangent modulus is usually found to be smaller than predicted by Eqn. (5.35). Two factors are involved: changes in the sliding stress and fiber failure. At high fiber stresses, the Poisson condition of the fiber reduces the radial stress,  $\sigma_r$ . Consequently, whenever the sliding stress can be represented by Eqn. (2.1),  $\tau$  decreases as the stress increases. The associated tangent modulus at fixed crack spacing is (Hutchinson and Jensen, 1990)

$$d\bar{\sigma}/d\bar{\varepsilon} = b_1 E_m \bar{d}/a_3 b_2 R [1 + \vartheta + \exp(-\vartheta)] \quad (5.36)$$

where  $\vartheta = 2\mu b_1 d/R$ , with  $\mu$  being the friction coefficient.

As the UTS is approached, significant fiber failures occur, which further reduce the tangent modulus. The basic stress/strain relationship is (Hild *et al.*, 1993),

$$\bar{\sigma} = fE_f \bar{\varepsilon} \left\{ 1 + \sum_{n=1} \frac{(-1)^n}{2n!} \left[ \frac{2+n(m+1)}{1+n(m+1)} \right] (E_f \bar{\varepsilon}/S_c)^{n(m+1)} \right\} \quad (5.37)$$

## 5.5 Simulations

The preceding constitutive laws may be used to simulate stress/strain curves for comparison with experiments. In order to conduct the simulations, the constituent properties,  $\tau$ ,  $\Gamma_i$  and  $\Omega$  are first assembled into the non-dimensional parameters  $\mathcal{H}$ ,  $\Sigma_i$ , and  $\Sigma_T$ . For this purpose, it is necessary to have independent knowledge of  $\bar{d}(\bar{\sigma})$ . When this does not exist, an estimation procedure is needed, based on Eqn. (5.22), through evaluation of  $\bar{d}_s$ ,  $\bar{\sigma}_{mc}$  and  $\bar{\sigma}_s$ . The first step is to use Eqn. (5.20a) to evaluate the saturation crack spacing  $\bar{d}_s$  from the constituent properties. One limitation of this procedure concerns the accuracy with which  $\chi$  and  $\Gamma_m$  are known. An alternative option exists when crack spacing data are available for another CMC with the *same matrix*. Then, Eqn. (5.20a) can be used to *scale*  $\bar{d}_s$  in accordance with,

$$\bar{d}_s^3 \sim E_f R^2 / \tau_o^2 E_L$$

It is also possible to estimate  $\bar{\sigma}_{mc}$  from the constituent properties, by using Eqn. (5.18). Then Eqn. (5.20) is used to estimate,  $\sigma_s$ .

When  $d(\bar{\sigma})$  has been established in this manner, stress/strain curves can be simulated for 1-D materials. Upon recognizing the need for internal consistency. Notably, both  $\bar{d}_s$  and  $\sigma_{mc}$  depend on  $\tau_o$  and  $\Gamma_i$ . Moreover,  $\sigma_s$  scales with  $\sigma_{mc}$ . In addition,  $\sigma_{mc}$  depends on the misfit stress  $\sigma_i^T$ , whereas  $\bar{d}_s$  and the ratio  $\sigma_s/\sigma_{mc}$  are  $\sigma_i^T$  independent. Based on this approach, simulations have been used to conduct sensitivity studies of the effects of constituent properties on the inelastic strain. Examples (Fig. 5.5) indicate the spectrum of possibilities for CMCs.

## 5.6 Experiments

Relatively complete matrix cracking and inelastic strain measurements have been made on two unidirectional CMCs (Evans *et al.*, 1993; Domergue *et al.*, 1993; Vagaggini *et al.*, 1993; Lamon *et al.*, 1993): SiC/CAS, as well as SiC/SiC (produced by CVI). The stress/strain curves for these two materials (Fig. 5.6) indicate a contrast in inelastic strain capability, which demand interpretation. Some typical hysteresis measurements for these materials (Fig. 5.6) reveal major differences, which must reflect differences in constituent properties. There are also considerable differences in the evolution of matrix cracks (Fig. 5.2). An analysis of the hysteresis loops (Fig. 5.7) and the permanent strain (Fig. 5.8), as well as other characteristics, indicate the substantial differences in interface properties summarized on Table III. These differences arise despite the fact that the fibers are the same and that the fiber coatings are C in both cases.<sup>‡</sup>

The constituent properties from Table III can, in turn, be used to simulate the stress/strain curves (Fig. 5.9). The agreement with measurements affirms the simulation capability, whenever the constituent properties have been obtained from *con., letely independent tests* (Table I). This has been done for the SiC/CAS material, but not yet for SiC/SiC. While the comparison between simulation and experiment is encouraging, an unresolved problem concerns the predictability of the saturation stress,  $\sigma_s$ . In most cases, *ab initio* determination cannot be expected, because the flaw parameters for the matrix are processing sensitive. Reliance must therefore be placed on experimental measurements, which are rationalized, *post facto*. Further research is needed to establish whether formalisms can be generated from the theoretical results which provide useful bounds on  $\sigma_s$ . A related issue concerns the necessity for matrix crack density information. Again, additional insight is needed to establish meaningful

---

<sup>‡</sup> Analysis of the coating structure by TEM provides a rationale for specifying the differing interface responses in accordance with the basic model (Fig. 2.2).

bounds. Meanwhile, experimental methods that provide crack density information in an efficient, straightforward manner require development. One possibility involves measurements of the acoustic velocity,  $v$ , which can be conducted continuously, during testing (Baste *et al.*, 1992). These measurements relate to changes in the elastic modulus  $E^*$  as matrix cracks develop ( $E^* = \rho_0 v^2$ ). This modulus can be related to the crack spacing, through a model (Eqn. 5.23).

## 6. MATRIX CRACKING IN 2-D MATERIALS

General loadings of 2-D CMCs involve mixtures of tension and shear. For design purposes, it is necessary to have models and experiments that combine these loadings. Matrix cracking and fiber failure are the basic phenomena that dictate all of the nonlinearities. However, there are important differences between tension and shear. The behavior subject to tensile loading has been widely investigated (Harris *et al.*, 1992; Cooper and Chyung, 1987; Holmes and Schuler, 1990; Cranmer, 1989; Coyle *et al.*, 1986; Prewo and Brennan, 1982; Prewo, 1986). The behavior in shear is only appreciated at an elementary level (Brøndsted *et al.*, 1993). Furthermore, the intermediate behaviors have had even less study (Harris *et al.*, 1990; Sbaizero and Evans, 1986). Nevertheless, the basic concept is clear. It is required that matrix cracking, as well as fiber failure, phenomena be incorporated into the models in a consistent manner, such that *interpolation* procedures can be devised and implemented.

### 6.1 Tensile Properties

General comparison between the tensile stress/strain [ $\sigma(\epsilon)$ ], curves for 1-D and 2-D materials (Fig. 6.1) provides important perspective. It is found that  $\sigma(\epsilon)$  for 2-D materials is quite closely matched by simply scaling down the 1-D curves by 1/2. The

behavior of 2-D materials must, therefore, be *dominated* by the 0° plies,<sup>‡</sup> because these plies provide a fiber volume fraction in the loading direction about half that present in 1-D material (Evans *et al.*, 1993).

The only significant 2-D effects occur at the *initial deviation from linearity*. At this stage, matrix cracks that form either in matrix-rich regions or in 90° plies evolve at somewhat lower stresses than cracks in 1-D materials. However, the associated non-linearities are usually slight and do not normally contribute in an important manner to the overall non-linear response of the material. For example, matrix cracking in the 90° plies often proceeds by a tunneling mechanism (Fig. 6.2). Tunnel cracking occurs subject to a lower bound stress (Xia *et al.*, 1993; Hutchinson and Suo, 1992),

$$\sigma_i = \sigma_i^o - \sigma^R (E_L + E_T) / 2E_T \quad (6.1)$$

with

$$\sigma_i^o = [E\Gamma_R/gt_f]^K$$

where  $g$  is a coefficient that ranges between 1/3 and 3/2. The unloading modulus associated with such tunnel cracks is (Xia *et al.*, 1993; Laws and Dvorak, 1990),

$$\bar{E}/E = H^*(E_f/E_m, f, t_p/\bar{L}) \quad (6.2)$$

with  $\bar{L}$  being the mean crack spacing in the 90° plies and  $H^*$  is a function that varies from 1 to 0.6, as  $t_p/\bar{L}$  increases from 0 to above 1. The corresponding permanent strain is

---

<sup>‡</sup> Furthermore, since some of the 2-D materials are woven, the 1/2 scaling infers that the curvatures introduced by weaving have minimal effect on the stress/strain behaviors.

$$\epsilon_p = (1 - E_T v_L^2 / E_L) (\sigma^R / E_L) \quad (6.3)$$

The overall stress/strain response is summarized in Fig. 6.3. In practice, the stresses may be larger because the actual evolution of cracks, at stresses above  $\sigma_c$ , depends on the availability of flaws in the 90° plies.

Extension of tunnel cracks into the matrix of the 0° plies (Fig. 6.2) results in behavior similar to that found in 1-D material. Moreover, if the stress  $\sigma^0$  acting on the 0° plies is known, the 1-D solutions may be used directly to predict the plastic strain. Otherwise, this stress must be estimated. For a typical 0/90 system,  $\sigma^0$  must range between  $\bar{\sigma}$  and  $2\bar{\sigma}$ , depending upon the extent of matrix cracking in the 90° plies and upon  $E_T/E_L$ . A sound rationale for choosing  $\sigma^0$  within this range does not yet exist. Preliminary analysis has been conducted using,  $\sigma^0 = 2\bar{\sigma}$ , as implied by the comparison between 1-D and 2-D stress/strain curves (Fig. 6.1). Additional modelling on this topic is in progress.

Using this simplified approach, simulations of stress/strain curves have been conducted (Domergue *et al.*, 1993; Aubard, 1992). These curves have been compared with experimental measurements for several 2-D CMCs. The results are summarized in Fig. 6.4. It is apparent that the simulations lead to somewhat larger flow strengths than the experiments, especially at small inelastic strains. To address this discrepancy, further modelling effort is in progress, which attempts to couple the behavior of the tunnel cracks with the matrix cracks in the 0° plies.

## 6.2 Shear Properties

The matrix cracking that occurs in 2-D CMCs, subject to shear loading depends on the loading orientation and the properties of the matrix. Two dominant loading orientations are of interest: in-plane shear along one fiber orientation and out-of-plane



(or interlaminar) shear. The key difference between these loading orientations concerns the potential for interaction between the matrix cracks and the fibers (Fig. 6.5). For the out-of-plane case, matrix cracks evolve without significant interaction with the fibers. Conversely, for in-plane loading, the matrix crack *must interact* with the fibers. These interactions impede matrix crack development. Consequently, the in-plane shear strength always exceeds the interlaminar shear strength.

### *i) In-Plane Shear*

Experiments that probe the in-plane shear properties have been performed by using Iosipescu test specimens (Brøndsted *et al.*, 1993). A summary of experimental results (Fig. 1.6) indicates that the matrix has a major influence on the shear flow strength  $\tau_s$  and the shear ductility,  $\gamma_c$ . Moreover, it has been found that the shear flow strengths can be ranked using a parameter,  $\mathcal{W}$ , derived from the matrix cracking stress in the absence of interface sliding, given by (Fig. 6.6),

$$\mathcal{W} = \sqrt{\Gamma_m/RG} \quad (6.4)$$

Within  $\mathcal{W}$ , the property of principal importance is the shear modulus,  $G$ , which reflects the increase in compliance caused by the matrix cracks. However, it remains to develop a model that gives a complete relationship between the composite strength and the constituent properties.

The shear ductility also appears to be influenced by the shear modulus, but in the opposite sense—high modulus matrices result in low ductility. This behavior has been rationalized in terms of the effect of matrix modulus on the bending deformation experienced by fibers between matrix cracks (Brøndsted *et al.* 1993). As yet, there have been no calculations that address this phenomenon.

## ii) Interlaminar Shear

The matrix cracks that form upon interlaminar shear loading and provide the plastic strains are material dependent. The simplest case, depicted in Fig. 6.5b, involves multiple tunnel cracks that extend across the layer and orient normal to the maximum tensile stress *within* the layer (Sbaizero and Evans, 1985). In other cases, the matrix cracks are confined primarily to the matrix-only layers between plies (Beyerle *et al.*, 1992). A general understanding of these different behaviors does not yet exist.

When the interlaminar cracks form by tunneling (Fig. 6.5), the solutions are straightforward and have a direct analogy within the transverse cracking results described above (Bao, 1993). The behaviors can be expressed in terms of the tensile stress  $\sigma$  acting normal to the prospective crack plane. Then, the *lower bound* value of this stress at which tunnel cracks form,  $\sigma_{cs}$ , is given by

$$\sigma_{cs} \sqrt{t_1/E_T \Gamma_R} = \mathcal{F}(E_L/E_T, \phi, \nu_L/\nu_T) \quad (6.5)$$

where  $t_1$  is the thickness of the layer subject to interlaminar cracking and  $\phi$  is the crack orientation. The function  $\mathcal{F}^{-2}$  is plotted on Fig. 6.7 for orthotropic materials (with  $\nu_T/\nu_L = 3$ ). Evidently, these interlaminar shear cracks form more readily than the transverse cracks that develop upon tensile loading. This accounts for the inferior performance of CMCs in the presence of interlaminar shear loads.

## 6.3 Transverse Tensile Properties

CMCs with 2-D fiber architecture are susceptible to interlaminar cracking in various component configurations (Fig. 6.8). In such cases, as the crack extends through the component, conditions range from mode I to mode II. Tests and analyses are needed that relate to these issues. Most experience has been gained from PMCs (Chai, 1984).

The major issue is the manner whereby the interlaminar (transverse) cracks interact with the fibers. In principle, it is possible to conduct tests in which the cracks do not interact. In practice, such interactions always occur in CMCs, as the crack front meanders and crosses over inclined fibers (Spearing and Evans, 1992; Kaute *et al.*, 1993). These interactions dominate the measured fracture loads in conventional cantilever (DCB) specimens, as well as in flexure specimens (Bordia *et al.*, 1991; Bao *et al.*, 1992). Some typical results for the transverse fracture energy (Fig. 6.9), indicate the large values (compared with  $\Gamma_m \approx 20 \text{ Jm}^{-2}$ ) induced by these interactions.

Analysis indicates that large-scale bridging (LSB) is involved and the bridging behavior can be explicitly ascertained from the measured curves (Bao *et al.*, 1992). For the particular case of a DCB specimen (Fig. 6.8a), the J-integral is explicitly defined in terms of the bending moment,  $M$  and the traction law (Bao and Suo, 1992). For example, the steady-state resistance,  $\Gamma_s$ , for a linear softening traction law, is

$$\begin{aligned}\Gamma_s &\equiv 12\hat{M}^2/Et_b^3 \\ &= \sigma_s u_s/2 + \Gamma_m\end{aligned}\tag{6.5}$$

and the zone length at steady-state is

$$L_s = (Eu_s/3\sigma_s)^{1/2}t_b^{3/2}\tag{6.6}$$

where  $2t_b$  is the DCB beam thickness, with the quantities  $\Gamma_s$  and  $L_s$  defined on Fig. 6.9. Experimental measurements made with DCB specimens can be used to evaluate the parameters,  $\sigma_s$  and  $u_s$ , by simply fitting the data to Eqns. (6.5) and (6.6). This information can then be used to *predict*  $\Gamma_s$  for other configurations.

An example is given for SiC/CAS composites (Fig. 6.9). Experimental results for this material (Spearing and Evans 1992) give  $u_s \approx 100 \mu\text{m}$  and  $\sigma_s \approx 10 \text{ MPa}$ . One

application of these results is the prediction of the tunnel cracking found in 0/90 laminates (Eqn. 6.1). The analysis of tunnel cracking (Xia *et al.*, 1993) has established that for typical laminate thicknesses, the crack opening displacements are small ( $< 1 \mu\text{m}$ ). For such small displacements, there is a *negligible influence of the fibers*. Consequently,  $\Gamma_R = \Gamma_m (1 - f)$ . Other applications to C-specimens and T-junction are in progress.

An obvious limitations of the procedure is the uncertainty about the manner whereby the matrix crack interacts with the fibers in other geometries and hence, the universality of  $\sigma_s$  and  $u_s$ . This is a topic for further research.

## 7. STRESS REDISTRIBUTION

### 7.1 Background

CMCs usually have substantially lower notch sensitivity than monolithic brittle materials and, in several cases, exhibit notch insensitive behavior (Cady *et al.*, 1993; Mall *et al.*, 1993). This desirable characteristic of CMCs arises because the material may *redistribute stresses* around strain concentration sites. Notch effects appear to depend on the class of behavior. Moreover, a different *mechanics* is required for each class, because the stress redistribution mechanisms class operate over different physical scales. Class I behavior involves stress redistribution by fiber bridging/pull-out, which occurs along the crack plane (Bao and Suo, 1992; Zok *et al.*, 1991). Large-Scale Bridging Mechanics (LSBM) is preferred for such materials. Class II behavior allows stress redistribution by large-scale matrix cracking (Cady *et al.*, 1993) and Continuum Damage Mechanics (CDM) is regarded as most appropriate. Class III behavior involves material responses similar to those found in metals, and a comparable mechanics might be used (Heredia *et al.*, 1993): either LEFM for small-scale yielding or non-linear fracture mechanics for large-scale yielding. Since a unified mechanics has not yet been identified, it is necessary to use *mechanism maps* that distinguish the various classes (Figs. 1.3, 1.4).

## 7.2 Mechanism Transitions

The transition between class I and class II behaviors involves considerations of both matrix crack growth and fiber failure. One hypothesis for the transition may be analyzed using LSBM. Such analysis allows the condition for fiber failure at the end of an unbridged crack segment to be solved simultaneously with the energy release rate of the matrix front. The latter is equated to the matrix fracture energy (Cui and Budiansky, 1993). By using this solution to specify that fiber failure occurs *before the matrix crack extends into steady-state*, class I behavior is presumed to ensue. Conversely, class II behavior is assigned when the steady-state matrix cracking condition is achieved prior to fiber failure. The resulting mechanism map involves two indices (Table II),

$$\begin{aligned} S &= (RS/a_o\tau)(E_m^2/E_L E_f)[(1-f)/f]^2 \\ &\equiv 3/\mathcal{A}_b \end{aligned} \quad (7.1)$$

and

$$\mathcal{U} = \sigma_{mc}/S \quad (7.2)$$

With  $S$  and  $\mathcal{U}$  as coordinates, a mechanism map may be constructed that distinguishes class I and class II behavior (Fig. 1.3). While this map has qualitative features consistent with experience, the experiments required for validation have not been completed. In practice, the mechanism transition in CMCs probably involves additional considerations.

The incidence of class III behavior is found at relatively small magnitudes of the ratio of shear strength,  $\tau_s$ , to tensile strength  $S$ . When  $\tau_s/S$  is small, a shear band develops at the notch front and extends normal to the notch plane. Furthermore, since

$\tau_s$  is related to  $G$ , the parameter  $G/S$  is selected as the ordinate of a mechanism map. Experimental results suggest that class III behavior arises when  $G/S \gtrsim 50$  (Fig. 1.4).

### 7.3 Mechanics Methodology

#### (i) Class I Materials

The class I mechanism, when dominant, has features compatible with LSBM (Bowling and Groves, 1979; Zok *et al.*, 1991; Zok and Hom, 1990). These mechanics may be used to characterize effects of notches, holes and manufacturing flaws on tensile properties, whenever a single matrix crack is prevalent. For cases wherein the flaw or notch is small compared with specimen dimensions, the tensile strength may be plotted as functions of *both* flaw indices:  $\mathcal{A}_b$  and  $\mathcal{A}_p$  (Fig. 4.3). For the former, the results are sensitive to the ratio of the pull-out strength  $S_p$  to the UTS (Suo *et al.*, 1993). These results should be used whenever the unnotched tensile properties are compatible with global load sharing. Conversely,  $\mathcal{A}_p$  should be used as the notch index when the unnotched properties appear to be pull-out dominated.

When the notch and hole have dimensions that are significant fraction of the plate width ( $a_0/b > 0$ ), *net section* effects must be included (Suo *et al.*, 1993). Some results (Fig. 7.1) illustrate the behavior for different values of the notch sensitivity index,  $\mathcal{A}$ . Experimental validation has not been undertaken. Nevertheless, partial results for one material (SiC/C<sub>B</sub>) are compatible with LSBM (Heredia *et al.*, 1993), as shown for data obtained with center notches and center holes (Fig. 7.1). The promising feature is that LSBM explains the difference between notches and holes (upon requiring that  $\mathcal{A} = 0.8$ ). Moreover, if this material is pull-out controlled, the constituent properties give a notch sensitivity index, consistent with LSBM ( $\mathcal{A}_p = 0.76$ ).

### (ii) Class II Materials

The non-linear stress/strain behavior governed by matrix cracking (expressed through  $\bar{\epsilon}$ , Eqn. (5.32), and  $\epsilon_o$ , Eqn. (5.31), provides a basis for a Damage Mechanics (CDM) approach that may be used to predict the effects of notches and holes (Hayhurst *et al.*, 1990). Such developments are in progress.<sup>†</sup> In practice, several class II CMCs have been shown to exhibit notch insensitive behavior, at notch sizes up to 5 mm (Cady *et al.*, 1993; Mall *et al.*, 1993). The notch insensitivity is manifest in the effect of the relative notch size,  $a_o/b$ , on the ratio of the UTS measured in the presence of notches (designated  $S^*$ ), to the strength in the absence of notches (designated  $S$ ). Results for SiC/CAS are illustrated on Fig. 7.2. In this material, the non-linearity provided by the matrix cracks allows sufficient stress redistribution that the stress concentration is *eliminated*. This occurs despite the low ductility ( $< 1\%$ ). Moreover, since a basic stress/strain simulation capability based on constituent properties, is imminent (Figs. 5.3, 6.3, 6.4), it can be expected that a CDM procedure will be available in the near future, capable of predicting this behavior.

### (iii) Class III Materials

Class III behavior has been found in several C matrix composites (Heredia *et al.*, 1993). In these materials, the shear bands can be imaged using an X-ray dye penetrant method. Based on such images, the extent of the shear deformation zone  $\ell_s$  is found to be predictable from measured shear strengths,  $\tau_s$  (Fig. 1.6), in approximate accordance with (Fig. 7.3)

$$\ell_s/a_o \approx \sigma/\tau_s \quad (7.3)$$

---

<sup>†</sup> An important factor that dictates whether continuum or discrete methods are used concerns the ratio of the matrix crack spacing to the radius of curvature of the notch.

Calculations have indicated that this shear zone diminishes the stress ahead of the notch (Fig. 7.4), analogous to the effect of a plastic zone in metals. For C/C materials, it has been found that the shear band lengths are small enough that LEFM is able to characterize the experimental data over a range of notch lengths, such that,  $K_{IC} = 16 \text{ MPa}\sqrt{\text{m}}$  (Fig. 7.5). However, conditions must exist where LEFM is violated. For example, when  $l_s/a_0 \gtrsim 4$ , the stress concentration is essentially eliminated (Fig. 7.4) and the material must then become notch insensitive. Further work is needed to identify parameters that bound the applicability of LEFM, as well as establish the requirements for notch insensitivity.

#### 7.4 Measurements

Notch sensitivity data (Fig. 7.1, 7.2 and 7.5) provide an explicit measure of stress redistribution. However, further understanding requires techniques that probe the stress and strain around notches, as CMCs are loaded to failure. Many of the methods have been developed and used for the same purpose on PMCs (Stinchcombe and Bakis, 1990; Bakis *et al.*, 1989). These techniques can measure both strain and stress distributions.

Strain distributions are measured with high spatial resolution by using Moiré interferometry. In this method, the fringe spacings relate to the in-plane displacements which, in turn, govern the strains. There has been only limited use of this technique for CMCs (Shaw *et al.*, 1993). Preliminary measurements suggest that the inelastic deformations that arise from matrix cracking result in strains similar to *elastic* strains. Based on such similarity, it may be speculated that the reduced stress concentrations may relate explicitly to the lower stresses that arise upon inelastic deformation at fixed strain (Fig. 7.6). Further exploration of this simple concept is in progress.

Since strain measurements appear to have minimal sensitivity to the stress redistribution mechanisms operative in CMCs, a technique then measures the *stress*



distribution is preferred. One such method involves measurement of thermoelastic emission. This method relies on the *temperature rise*  $\Delta T$  that occurs when an element of the composite is subject to a *hydrostatic stress*  $\Delta \sigma_{kk}$  under adiabatic conditions. The fundamental adiabatic relationship for a homogeneous solid is (Harwood and Cummings, 1991),

$$\Delta \sigma_{kk} = (C_v \rho_0 / \alpha T_0) \Delta T \quad (7.4)$$

where  $C_v$  is the specific heat at constant strain and  $\rho_0$  is the density. One experimental implementation of this concept is a technique referred to as Stress Pattern Analysis by Thermoelastic Emission (SPATE) (Harwood and Cummings, 1991). It involves the use of high sensitivity infrared detectors, which measure the temperature in a lock-in mode, as a cyclic stress is applied to the material. This feature essentially eliminates background problems and has good signal-to-noise characteristics. SPATE measurements are conventionally performed at small stress amplitudes, which elicit 'elastic' behavior in the material. Experimental results (Mackin *et al.*, 1993) for a class II material (SiC/CAS) have confirmed that the stress concentration can be eliminated by matrix cracks (Fig. 7.7). In addition, results for a class III material (C/C) have provided a direct measure of the stress redistribution caused by shear bands (Fig. 7.8).

Another method for strain measurement uses fluorescence spectroscopy (Molis and Clarke, 1990). This method has particular applicability to oxides, especially  $Al_2O_3$  (either as fiber or matrix). The technique has the special advantage that strains can be measured in individual fibers, such that stress changes caused by matrix cracks can be measured. Such measurements permit the material to be probed at the spatial resolution needed to understand mechanisms, in detail.

## 8. FATIGUE

### 8.1 Basic Phenomena

While experimental information exists regarding the cyclic, static and thermomechanical fatigue of CMC, as yet, there has not been a concerted attempt at relating the fatigue measurements to constituent properties (Prewo, 1986; Rousseau, 1990; Holmes and Cho, 1992; Holmes, 1991, Zawada *et al.*, 1991). Nevertheless, methodologies for predictions of crack growth and fatigue life can be derived from the mechanisms associated with failure under monotonic loading. Furthermore, the development of such methodologies may be hastened by the observations, measurements and modelling performed for metal (MMC) and polymer (PMC) matrix composites.

Matrix cracking in CMCs has been observed under cyclic and static loading conditions. In both cases, the fibers remain intact and bridge the cracks. Consequently, the basic matrix cracking models can be used in conjunction with suitable crack growth criteria to predict damage evolution and fracture. Application of these models to cyclic fatigue requires two modifications. (i) A transformation is needed to convert the influence of fiber bridging from monotonic,  $K_b$  (Eqn. 5.10) to cyclic,  $\Delta K_b$ . (ii) The matrix crack growth criterion is changed. For cyclic loading, the Paris law relates crack growth in the matrix to the stress intensity range at the crack front,  $\Delta K_{tip}$ , by

$$da/dN = \beta (\Delta K_{tip}/E)^{n_f} \quad (8.1)$$

where  $N$  is the number of cycles,  $n_f$  is a power law exponent and  $\beta$  is a material dependent coefficient. When the dominant mechanism involves stress corrosion, crack growth can be described in terms of  $G_{tip}$  through the commonly-used power law

$$\frac{da}{dt} = \dot{a}_0 \left( \frac{G_{up}}{G_m} \right)^\eta \quad (8.2)$$

where  $\dot{a}_0$  is a reference velocity,  $\eta$  is the power law exponent and  $G_m$  is the toughness, taken to be  $\Gamma_m (1 - f)$ .

In fatigue, the same three classes of behavior found for the monotonic loading of CMCs have been identified (Fig. 1.2). Emphasis has been given to class I behavior, with either notches or unbridged segments being a major consideration. The models are thus most relevant to high cycle fatigue (HCF) in the presence of features (flaws, notches, holes, etc.), which represent crack-like regions, having initial, unbridged segments. However, multiple matrix cracking (class II) behavior also occurs and has importance with regard to non-linearity and stress redistribution, as well as to low cycle fatigue (LCF). In some cases, class III behavior has been noted.

## 8.2 Cyclic Crack Growth

A key factor in matrix crack growth is the nature of the interface. When the interface is strong, there can be no contribution to the fatigue resistance from frictional dissipation and the composite behaves in approximate accordance with the rule-of-mixtures expected from fatigue properties of the matrix and reinforcement (Shang *et al.*, 1987). Conversely, when the interfaces are 'weak,' fibers can remain intact in the crack wake and cyclic frictional dissipation resists fatigue crack growth (McMeeking and Evans, 1990). The latter has been extensively demonstrated on Ti matrix composites reinforced with SiC fibers (Walls *et al.*, 1991; Sensmeier and Wright, 1989). The essential features of the 'weak' interface behavior are as follows: intact, sliding fibers acting in the crack wake shield the crack tip, such that the stress intensity range at the crack tip,  $\Delta K_{tip}$ , is less than that expected for the applied loads,  $\Delta K$ . Using this approach, a simple transformation converts the monotonic crack growth parameters into cyclic parameters

that can be used to interpret and simulate fatigue crack growth. The key transformation is based on the relationship between interface sliding during loading and unloading, which relates the monotonic result to the cyclic equivalent through (McMeeking and Evans, 1990)

$$\left(\frac{1}{2}\right)\Delta\sigma_b(x/a, \Delta\sigma) = \sigma_b(x/a, \Delta\sigma/2) \quad (8.3)$$

where  $\Delta\sigma$  is the range in the applied stress. Notably, the amplitude of the *change* in fiber traction  $\Delta\sigma_b$  caused by a change in applied stress,  $\Delta\sigma$ , is twice the fiber traction  $\sigma_b$  which would arise in the monotonic loading of a previously unopened crack, caused by an applied stress equal to half the stress change. This result is *fundamental to all subsequent developments* (McMeeking and Evans, 1990).

The stress intensity factor for bridging fibers subject to cyclic conditions is

$$\Delta K_b(\Delta\sigma) = -2\sqrt{\frac{a}{\pi}} \int_0^a \frac{\Delta\sigma_b(x, \Delta\sigma)}{\sqrt{a^2 - x^2}} dx \quad (8.4)$$

which, with the use of Eqn. (8.3), becomes

$$\Delta K_b(\Delta\sigma) = 2K_b^{\max}(\Delta\sigma/2) \quad (8.5)$$

where the superscript 'max' refers to the maximum values of the parameters achieved in the loading cycle and thus,  $K_b^{\max}$  is the bridging contribution that would arise when the crack is loaded by an applied stress equal to  $\Delta\sigma/2$ . Furthermore, since  $\Delta K$  is linear, Eqn. (8.3) is also valid for the tip stress intensity factor:

$$\Delta K_{up} = 2K_{up}(\Delta\sigma/2). \quad (8.6)$$

When the fibers remain intact, a cyclic *steady-state* ( $\Delta K$  independent of crack length) is obtained when the cracks are long, given by the condition  $\Delta \mathcal{E} \leq 4$  (McMeeking and Evans, 1990), where  $\Delta \mathcal{E}$  is defined in Table II. The result is:<sup>‡</sup>

$$\Delta K_{up} = \Delta \sigma \sqrt{R} (\sqrt{12} \Delta \mathcal{T})^{-1}. \quad (8.7)$$

where  $\Delta \mathcal{T}$  is defined in Table II.

The corresponding crack growth rate is determined from Eqns. (8.1) and (8.7) (McMeeking and Evans, 1990) as

$$\frac{da}{dN} = \beta \left[ \frac{\Delta \sigma \sqrt{R}}{\sqrt{6} \Delta \mathcal{T} E_m} \right]^n. \quad (8.8)$$

When short cracks are of relevance ( $\Delta \mathcal{E} > 4$ ),

$$\Delta K_{up} = \Delta \sigma \sqrt{\pi a} \left[ 1 - \frac{4.31}{\Delta \mathcal{E}} \sqrt{\Delta \mathcal{E} + 6.6} + \frac{11}{\Delta \mathcal{E}} \right]. \quad (8.9)$$

Consequently, at fixed  $\Delta \sigma$ ,  $\Delta K_{tip}$  increases as the crack extends, and the crack growth accelerates. However, the bridged matrix fatigue crack always grows at a *slower rate* than an unbridged crack of the same length. Consequently, the composite always has *superior* crack growth resistance relative to the monolith.

To incorporate the effects of fiber breaking into the fatigue crack growth model, a deterministic criterion has been used (Bao and McMeeking, 1993): the statistical characteristics of fiber failure have yet to be incorporated. To conduct the calculation,

---

<sup>‡</sup> For cyclic loading, the residual stress  $q$  does not affect  $\Delta K_{tip}$ .

once the fibers begin to fail, the unbridged crack length has been continuously adjusted to maintain a stress at the unbridged crack tip equal to the fiber strength. These conditions lead to the determination of the crack length,  $a_f$ , when the first fibers fail, as a function of the fiber strength and the maximum applied load (Fig. 8.1). Note that when either the fiber strength is high or the applied stress is low, no corresponding value of  $a_f$  can be identified and the fibers do not fail.

After the first fiber failure, fibers continue to break as the crack grows. Continuing fiber failure creates an unbridged segment larger than the original notch size. However, only the current unbridged length  $2a_u$  and the current total crack length  $2a$  are relevant (Fig. 8.2) (Bao and McMeeking, 1993).

If the fibers are relatively weak and break close to the crack tip ( $a_0/a \rightarrow 1$ ), the bridging zone is always a small fraction of the crack length. In this case, there is minimal shielding. If the fibers are moderately strong, the fibers remain intact at first. But when the first fibers fail, subsequent failure occurs quite rapidly as the crack grows. The unbridged crack length then increases more rapidly than the total crack length and the  $\Delta K_{tip}$  also increases as the crack grows. When the fibers are even stronger, first fiber failure is delayed. But once such failure occurs, many fibers fail simultaneously and the unbridged length increases rapidly. This causes a sudden increase in the crack growth rate. Finally, when the fiber strength exceeds a critical value, they never break and the fatigue crack growth rate always diminishes as the crack grows. The sensitivity of these behaviors to fiber strength is quite marked (Fig. 8.2), with the different types of behavior occurring over a narrow range of fiber strength. Some typical crack growth curves predicted using this approach are plotted on Fig. 8.3. Finite geometry effects associated with LSB also exist (Bao and McMeeking, 1993).

The results of Fig. 8.1 can be used to develop a criterion for a 'threshold' stress range,  $\Delta\sigma_t$ , below which fiber failure does not occur for *any* crack length. Within such a regime, the crack growth rate approaches the steady-state value given by Eqn. (8.8),

with all fibers in the crack wake remaining intact. The variation in the 'threshold' stress range with fiber strength is plotted on Fig. 8.4.

A notable feature of the predictions pertains to the role of the stress ratio  $\mathcal{R}_s$  in composite behavior. Prior to fiber failure, the crack growth rate is independent of  $\mathcal{R}_s$  (except for its effect on the fatigue properties of the matrix itself). However,  $\mathcal{R}_s$  has a strong influence on the transition to fiber failure, as manifest in its effect on the maximum stress. It thus plays a dominant role in the fatigue lifetime.

In many cases, CMCs are subject to multiple matrix cracking upon cyclic and static loading, which leads to reductions in the unloading modulus  $\bar{E}$ , as well as changes in the hysteresis. The basic mechanics is essentially the same as that described for monotonic loading, except that the matrix crack growth criterion must be changed.

### 8.3 Thermomechanical Fatigue

The basic matrix crack growth model can be extended to include thermomechanical fatigue (TMF). This can be achieved by means of another transformation wherein all of the stress range terms in Eqns. (8.3) to (8.9) are replaced, as follows (McMeeking, 1993),

$$\begin{aligned}\Delta\sigma \Rightarrow \Delta t &= \Delta\sigma + fE_f(\alpha_f - \alpha_m)\Delta T \\ \Delta\sigma_b \Rightarrow \Delta t_b &= \Delta\sigma_b + fE_f(\alpha_f - \alpha_m)\Delta T\end{aligned}\tag{8.10}$$

where  $\Delta T$  represents the temperature cycle and  $\Delta\sigma$  the stress cycle. With these transformations, it is possible to represent the crack growth using two non-dimensional parameters,  $\Delta\mathcal{E}_0$  and  $\Delta\mathcal{E}_T$  (Table II) that specify the stress cycling and the temperature cycling, respectively. It is immediately apparent that matrix crack growth and fiber failure are expected to be quite different for out-of-phase and in-phase TMF. The salient predictions are presented for both cases.

For materials in which  $\alpha_m > \alpha_f$ , in-phase TMF causes  $\Delta T$  to be *less* than that expected for stress cycling alone and vice versa. These effects are apparent from trends in the stress intensity range,  $\Delta K_{tip}$  (Fig. 8.5), calculated for cases wherein fiber failure does not occur. A key result is that, whereas  $\Delta K_{tip}$  always reduces upon initial crack extension either for stress cycling alone or for in-phase TMF, it can *increase* for out-of-phase TMF. Furthermore, for extreme ratio of  $\Delta \epsilon_T$  to  $\Delta \epsilon_0$ ,  $\Delta K_{tip}$  can *exceed* that for the monolithic matrix without fibers. This result implies that the crack growth rate also *exceeds* that for the monolith (at the equivalent  $\Delta K$ ). Then, the composite has crack growth resistance *inferior* to the monolithic matrix. The implications for the choice of fiber and the allowable temperature range  $\Delta T$  are immediate.

When fiber failure effects are introduced, in-phase and out-of-phase cycling result in behaviors *that oppose* those associated with matrix crack growth. Namely, the crack size,  $a_f$ , at which fiber failure commences is *smaller* for in-phase loading than for out-of-phase loading (Fig. 8.6). Consequently, in order to ensure a threshold, the material is required to operate under conditions of fiber integrity. Then, in-phase TMF represents the more severe problem.

#### 8.4 Experimental Results

Experimental results in Ti MMCs are in broad agreement with the predictions of the above models (Fig. 8.7). One of the important phenomena found in these materials is that the sliding stress  $\tau$  decreases upon cycling, because of 'wear' mechanisms operating within the fiber coating. However, the reduction in  $\tau$  occurs after a relatively small number of cycles ( $< 1,000$ ) and thereafter, remains at an essentially constant value. It is also evident for these materials that the fiber strength is *not degraded by cyclic sliding of the interface*, even after  $> 10^5$  cycles. Conversely, substantial fiber degradation effects may occur in CMCs.



Tensile fatigue testing of CMCs has indicated that there are both cyclic and environmental influences. These behaviors include: changes in the modulus  $\bar{E}$ , changes in the hysteresis loop width and internal heating. In all cases, the interpretation of existing data is complicated by the role of the environment, manifest as stress corrosion, oxidation, etc.

Reductions in modulus  $\bar{E}$  usually accompany cyclic loading at fixed stress amplitude (Fig. 8.8) (Zawada *et al.*, 1991; Spearing *et al.*, 1993). In some cases, there is also a small subsequent increase. The modulus changes are caused by multiple matrix cracks. The modulus can be analyzed (Section 5), such that changes in constituent properties during fatigue may be obtained. Measurements made for SiC/CAS at low frequencies ( $< 10$  Hz) have been correlated with the crack density (Fig. 8.9). Comparisons with simulations indicate that cyclic sliding results in substantial reductions in  $\tau$ , from  $\sim 15$  MPa for the pristine composite (Mackin and Zok, 1993) to  $\sim 4$  MPa. Such behavior is consistent with that found for Ti MMCs. At higher frequencies ( $\geq 50$  Hz), frictional heating also occurs, accompanied by a *larger reduction* in  $\tau$  (Holmes, 1991).<sup>\*</sup> The hypothesis is that the frictional heating causes the C fiber coating to be eliminated. Such behavior would be consistent with that found upon isothermal heat treatment (Sbaizero *et al.*, 1990).

Related behavior has been found at *constant stress* (Spearing *et al.*, 1993). This effect has been attributed to *stress corrosion* of the matrix by moisture. Substantial crack growth has been found at stresses below that required to produce cracks in short duration, monotonic tensile tests. Furthermore, the crack densities following extended periods under load ( $\sim 10^6$  s) are *higher* than those obtained in the short duration tests. The development of cracks with time and stress has been successfully simulated

---

<sup>\*</sup> A reduction in  $\tau$  during fatigue is well substantiated for Ti MMCs. This has been attributed to an interface wear mechanism.

(Fig. 8.10) by using the above fiber bridging models, coupled with a stress corrosion law for the matrix (Eqn. 8.2).

The occurrence of fatigue failure at peak stresses substantially lower than the UTS (Fig. 8.11), has important implications. There are two contributions to this behavior. One relates to the reduction in  $\tau$  caused by cycling. The other concerns fiber weakening. Reductions in  $\tau$  diminish the UTS in accordance with the scaling (Eqn. 4.9),  $S_g \sim \tau^{1/m}$ . For example, in the SiC/CAS material, a change in  $\tau$  from 15 to 3 MPa (Fig. 8.8) would reduce  $S_g$  by  $\sim 30\%$ . The fatigue threshold would thus occur at 0.7 UTS, despite the fiber strength being retained. Fatigue failure occurring at even smaller stresses would indicate that the fiber strength systematically diminishes with cycling. Such effects would also be evident from reductions in the retained strength (Zawada *et al.*, 1991). There are three primary mechanisms of fiber weakening: abrasion, oxidation and stress corrosion. These mechanisms may be distinguished in the following manner. The strength degradation caused by stress corrosion occurs abruptly, following *time* accumulated at *peak load*. It should not be accelerated by thermal cycling. Abrasion occurs systematically with cyclic sliding at the interfaces (Fig. 8.12) and should be enhanced by out-of-phase TMF, which accentuates the sliding displacement. Oxidation is strictly time and temperature dependent. The strong effect of out-of-phase TMF on the fatigue life at high temperature (Mall *et al.*, 1993) suggests that fiber degradation by abrasion is an important mechanism, perhaps accentuated by oxide formation at higher temperatures. Much additional study is required on this topic.

## 9. CREEP

### 9.1 Basic Behavior

The creep behavior and relationships with constituent properties are critically influenced by fiber failure, matrix cracks and interface debonding. Some of the basic

stress/time characteristics are sketched in Fig. 9.1 and 9.2. When the fibers and matrix are intact and the interfaces are bonded, the creep deformations of the composite and the constituent properties are related in a straightforward manner (McLean, 1990; McMeeking, 1993). When one constituent is elastic (fiber or matrix) and the other creeps, the *longitudinal* creep strain is *transient* and stops when all of the strain is transferred onto the elastic material (Figs. 9.1 and 9.2) (McMeeking, 1993). The creep law needed to describe this behavior is

$$\dot{\epsilon}_{ij} = \frac{1}{2G} \dot{s}_{ij} + \frac{1}{9K} \delta_{ij} \dot{\sigma}_{kk} + \frac{3}{2} B \sigma_e^{n-1} s_{ij} + \alpha \delta_{ij} \dot{T} \quad (9.1)$$

where  $\dot{\epsilon}$  is the strain rate,  $\dot{\sigma}$  is the stress rate,  $\delta_{ij}$  is the Kronecker delta,  $n$  is the creep index,  $\underline{s}$  is the deviatoric stress and the effective stress  $\sigma_e$  is defined by

$$\sigma_e = \sqrt{\frac{3}{2} s_{ij} s_{ij}}, \quad (9.2)$$

and  $B$  is the rheology parameter for steady-state creep,

$$B = \dot{\epsilon}_0 / \sigma_0^n$$

with  $\sigma_0$  being the reference stress and  $\dot{\epsilon}_0$  the reference strain rate. If the fibers are elastic and the matrix creeps, the stress in the matrix,  $\sigma_m$ , evolves at constant applied stress as ( $n \neq 1$ ) (McLean, 1985, McMeeking, 1993),

$$\sigma_m(t) = \left\{ \frac{(n-1)f E_f E_m B t}{E_L} + \frac{1}{[\sigma_m(0)^{n-1}]} \right\}^{1-n} \quad (9.3)$$

where  $\sigma_m(0)$  is the matrix stress at time,  $t = 0$ . When the matrix stress,  $\sigma_m \rightarrow 0$ , the stress on the fibers increases to,  $\sigma_f = \sigma/(1 - f)$ , such that the transient strain  $\epsilon_t$  is

$$\epsilon_t = \sigma/E_f(1 - f) \quad (9.4)$$

Similar results apply when the fibers creep, but the matrix is elastic.

When both the fiber and the matrix creep, steady-state develops in the composite following an initial transient (Fig. 9.2). The evolution of the matrix stress occurs according to ((McLean, 1972),

$$\left[ \frac{E}{fE_mE_f} \right] \dot{\sigma}_m = B_m \sigma_m^{n_m} - B_f \left[ \frac{\sigma - (1 - f)\sigma_m}{f} \right]^{n_f} \quad (9.5)$$

where  $n_m$  and  $n_f$  are the creep indices for the matrix and fibers, respectively. When a steady-state is reached ( $\dot{\sigma}_m = 0$ )  $\sigma_m$  and  $\sigma_f$  are related by,

$$\left[ \sigma_m^{n_m} (B_m/B_f) \right]^{1/n_f} + \frac{(1 - f)}{f} \sigma_m = \frac{\sigma}{f} \quad (9.6)$$

and

$$\sigma_m(1 - f) + \sigma_f f = \sigma \quad (9.7)$$

These formulae can be solved for specific  $n_m$  and  $n_f$  to obtain  $\sigma_m$  and  $\sigma_f$ . With the stresses known the composite creep rate can be readily obtained.

*Transverse* creep with well-bonded fibers is usually *matrix dominated*. Solutions which have been generated for bonded rigid fibers thus have utility. All such solutions

indicate that the creep attains steady-state, with a creep-rate *lower* than that for the matrix alone (Fig. 9.1). Moreover, strengthening solutions derived for transverse deformation with a power law hardening matrix (Fig. 9.3) also apply to a power law creeping matrix, in steady-state.† The reduction in creep rate depends on the power law exponent for the matrix and the spatial arrangement of the fibers. For a composite with a square arrangement of fibers, and a matrix subject to diffusional creep ( $n_m = 1$ ), since there is no creep in the fiber direction ( $z$ ) (McMeeking, 1993),

$$\dot{\epsilon}_{yy} = -\dot{\epsilon}_{xx} = (\sigma_{yy} - \sigma_{xx})k_1(f) \quad (9.8)$$

with

$$k_1(f) = (3/4)[(1-f)/(1+2f)] \quad (9.9)$$

In essence,  $k_1$  gives the *reduction* in creep-rate upon incorporating the bonded fibers. For non-linear matrices, the equivalent results have the form

$$\dot{\epsilon}_{xx} = -\dot{\epsilon}_{yy} = B_m (\sigma_{xx} - \sigma_{yy})^{n_m-1} (\sigma_{xx} - \sigma_{yy}) k_n(f) \quad (9.10)$$

where  $k_n$  is a function of the fiber volume fraction and spatial arrangement. For example, when  $n_m = 5$  and a square array is used,

$$k_n = 0.42[(1-f)/(1+f^2)]^5 \quad (9.11)$$

---

† With the strains becoming the strain-rates.

## 9.2 Effect of Fiber Failures

When stresses are applied along the fiber axis in a system with a creeping matrix, the time-dependent stress elevation on the fibers may cause some fiber failures. Following fiber failure, *sliding* would initiate at the interface, accompanied by further creep in the matrix. The time constant for this process is much longer than that for the initial transient, described above, and can be analyzed as a separate creep problem. While the process is complicated, several factors are important. If the stress on the fibers reaches their strength,  $S$ , the composite will fail. Moreover, the relevant  $S$  is probably that with a *small*  $\tau$ , associated with creep sliding of the interface. In this limit, composite failure is possible at all stresses above the 'dry bundle' strength,  $S_b$  (Eqn. 4.9b). Conversely, the composite *cannot* rupture at stress below  $S_b$ , unless the fibers are degraded by creep. The dry bundle strength thus represents a 'threshold.' At stresses below  $S_b$ , creep must be transient.

At higher stresses, the fibers will fracture and may fragment. Then, steady-state creep is possible (Fig. 9.1), proceeding in accordance with a creep law devised for a material with aligned rigid reinforcements of *finite aspect ratio*. This behavior is represented by the Mileiko (1970) model. The solution for a non-sliding interface is (Kelly and Street, 1972; McMeeking, 1993),

$$\dot{\epsilon} = B_m \sigma^{n_m} (R/L_f)^{n_m+1} \mathcal{L}(n_m, f) \quad (9.12)$$

where  $L_f$  is the fragment length and

$$\mathcal{L}(n_m, f) = 2^{n_m+1} \sqrt{3} \left[ \frac{\sqrt{3}(2n_m+1)}{2n_m f} \right]^{n_m} \frac{(1-f)^{(n_m+1)/2}}{(n_m-1)}$$

However, the fragment length *decreases* as the stress increases. This occurs in accordance with the scaling,

$$L_f/R \sim (S_c/\sigma)^m \quad (9.13)$$

Consequently, steady-state creep-rate should occur with a large power law exponent,  $n_m + m + mn_m$ . Such behavior has been reported in composites with discontinuous fibers (Nieh, 1984). The overall behavior is sketched on Fig. 9.4. In practice, because of the large stress exponent at stress above  $S_b$ , adequate creep performance can only be ensured at stresses below  $S_b$ .

### 9.3 Interface Debonding

While there are no solutions for transverse creep with debonding interfaces, the analogy noted above between power law deformation and steady-state creep provides insight. Calculations of transverse deformation with and without interface bonding (Fig. 9.5) indicate a major strength degradation when debonding occurs (Gunawadena *et al.*, 1993; Jansson and Leckie, 1992). Furthermore, the composite behavior approaches that for a body containing cylindrical holes. Creep results for porous bodies may thus provide rough estimates of the transverse creep strength when the interfaces debond.

### 9.4 Matrix Cracking

In some CMCs, the fibers creep more readily than the matrix. Such materials include SiC/SiC and SiC/C. In this case, fiber creep and matrix cracking appear to proceed in a synergetic manner that accelerates the creep and causes premature creep rupture. The basic phenomenon is as follows. Creep in the fiber increases the stress on the matrix, as described above. The stress on the matrix then exceeds  $\sigma_{mc}$  (Eqn. 5.18), causing cracks to form in the matrix. These cracks permit the matrix to exhibit plastic

strain, as elaborated in Section 5. As a result, the stress on the fibers increases, again, and they continue to creep. This process proceeds until creep rupture occurs in the fibers (Fig. 9.6). A model of this phenomenon has yet to be developed.

### 9.5 Strain Recovery

Since creep in composites redistributes stresses between matrix and fiber, strain recovery *must occur when the loads are removed* (Holmes, 1992) This behavior is well established for a system with one elastic constituent and one viscoplastic constituent, in accordance with standard Kelvin concepts. Notably, the elastic stretch in one constituent is gradually relaxed when the load is removed. The specifics depend, of course, on the nature of the viscoplasticity. A simple example illustrates the salient phenomena. A composite with elastic fibers and a creeping matrix, loaded along the fiber direction, has been crept until the stress in the matrix is essentially zero (Fig. 9.7). The load is then removed. The instantaneous elastic shrinkage  $\Delta\epsilon$  must satisfy

$$\Delta\epsilon = \frac{\sigma_m}{E_m} = \frac{\Delta\sigma_f}{E_f}. \quad (9.15)$$

The stresses after elastic unloading are thus

$$\sigma_m = -\frac{f\sigma E_m}{(1-f)E_L} \quad (9.16)$$

$$\sigma_f = \sigma E_m/E_L$$

Thereafter, holding at temperature causes  $\sigma_m$  to relax according to Eqn. (9.3), with  $\sigma_m(0)$  given by Eqn. (9.16).



## 9.6 Experimental Results

Experimental data for a range of different composites are used to illustrate some of the features described above and to anticipate trends. The longitudinal behaviors found when the fibers are elastic are addressed first. Results obtained on TiAl reinforced with sapphire fibers (Fig. 9.8) establish the existence of transient creep in the longitudinal orientation when the fibers are elastic and intact, but the matrix is subject to creep (Weber *et al.*, 1993). At higher loads, when some fibers fail, creep can continue and rupture may occur, as demonstrated by data obtained on a Ti matrix composite reinforced with SiC fibers (Fig. 9.9). Removal of the load after creep results in reverse deformation, as demonstrated for a SiC/Si<sub>3</sub>N<sub>4</sub> composite (Fig. 7.7). Upon using a creep index applicable to monolithic Si<sub>3</sub>N<sub>4</sub> ( $n = 2$ ), the stress in the matrix relaxes in the manner

$$\sigma_m = \left[ \frac{f E_f E_m B t}{E_L} - \frac{(1-f) E_L}{f \sigma E_m} \right]^{-1} \quad (9.17)$$

The inverse situation may also be important in some CMCs, wherein the fibers creep but the matrix is *elastic* (Weber *et al.*, 1993b; Abbe *et al.*, 1989). Typical examples include SiC/SiC and SiC/C composites, which have SiC fibers with fine grain size (such as Nicalon). In these materials, matrix cracks either pre-exist from processing or are created upon loading. When these cracks exist, fiber creep (accompanied by interface sliding) results in continuous composite deformation and eventual creep rupture (Fig. 9.6). Moreover, polycrystalline ceramic fibers usually develop grain boundary cavities during creep and have a low creep ductility (Weber *et al.*, 1993b).

When both the matrix and fibers creep, continued deformation of the composite proceeds in the longitudinal orientation (Weber and Evans, 1993). Results obtained on

CAS/SiC (Fig. 9.10) verify that creep continues. However, interpretation is complicated by microstructural changes occurring in the fibers, which lead to creep hardening. The deformation is thus entirely primary in nature. These results identify microstructural stability as an important fiber selection criterion.

## 10. CHALLENGES AND OPPORTUNITIES

It is suggested that reasonable progress has been made in understanding inelastic mechanisms that operate in CMCs, although the continued development of models and experimental validation is necessary. Consequently, it is now possible to appreciate how stress redistribution occurs and to characterize the notch sensitivity of these materials. The analysis of degradation mechanism is much less mature. In particular, the mechanisms that operate upon cyclic loading (thermal and mechanical) have not been clearly identified.

There are several challenges and opportunities that arise from this status. With regard to the short duration performance of CMCs, it is necessary to develop simple constitutive laws that can be used with finite element codes in order to calculate stresses around attachments, holes, etc. The mechanism-based models of the inelastic strain are preferred for this purpose. However, further research is needed to achieve this objective. Most importantly, there is insufficient basic understanding about the inelastic strains that occur upon shear loading and their dependence on constituent properties. Basic inelastic strain models with matrix cracks inclined to the fibers are needed to address this deficiency.

Degradation mechanisms that operate upon cyclic loading in the presence of matrix cracks require concerted study. Interface changes and fiber degradation are both possible. Moreover, there may be detrimental synergistic interaction with the environment. The models developed for MMCs indicate that the retention of fiber

strength upon cyclic loading is particularly important, because this strength governs the fatigue threshold. Mechanism and models that relate to fiber strength degradation are critically important. Interface properties are less important, provided that the debond energy remains small enough to prevent fiber failure at the matrix cracks.

TABLE I

## Constituent Properties of CMCs and Methods of Measurement

CONSTITUENT PROPERTY	MEASUREMENT METHODS	TYPICAL RANGE
Sliding Stress, $\tau$ (MPa)	<ul style="list-style-type: none"> <li>• Push-Out Force</li> <li>• Pull-Out Length, <math>\bar{h}</math></li> <li>• Saturation Crack Spacing, <math>\bar{l}_s</math></li> <li>• Hysteresis Loop, <math>\delta\epsilon</math></li> <li>• Unloading Modulus, <math>\bar{E}_L</math></li> </ul>	1-200
Characteristic Strength, $S_c$ (GPa)	<ul style="list-style-type: none"> <li>• Fracture Mirrors</li> <li>• Pull-Out Length, <math>\bar{h}</math></li> </ul>	1.2-3.0
Misfit Strain, $\Omega$	<ul style="list-style-type: none"> <li>• Bilayer Distortion</li> <li>• Permanent Strain, <math>\epsilon_p</math></li> <li>• Residual Crack Opening</li> </ul>	$0-2 \cdot 10^{-3}$
Matrix Fracture Energy, $\Gamma_m$ (Jm <sup>-2</sup> )	<ul style="list-style-type: none"> <li>• Monolithic Material</li> <li>• Saturation Crack Spacing, <math>\bar{l}_s</math></li> <li>• Matrix Cracking Stress, <math>\bar{\sigma}_{mc}</math></li> </ul>	5-50
Debond Energy, $\Gamma_i$ (Jm <sup>-2</sup> )	<ul style="list-style-type: none"> <li>• Permanent Strain, <math>\epsilon_p</math></li> <li>• Residual Crack Opening, <math>u_p</math></li> </ul>	0-5

**TABLE II**  
**Inventory of Non-Dimensional Functions**

Relative Stiffness.....	$\xi \rightarrow fE_f/(1-f)E_m$
Sliding Index.....	$\tau \rightarrow \xi[\tau_0 E/\sigma E_f]^{1/2}$
Cyclic Sliding Index.....	$\Delta\tau \rightarrow \xi[\tau_0 E/\Delta\sigma E_f]^{1/2}$
Loading Index.....	$\mathcal{E} \rightarrow [2R\sigma/f\xi^2 a\tau_0]$
Cyclic Loading Indices .....	$\Delta\mathcal{E} \rightarrow [2R(\Delta\sigma)/f\xi^2 a\tau_0]$
.....	$\Delta\mathcal{E}_0 \rightarrow [2R(\Delta\sigma)/f\xi^2 a_0\tau_0]$
Bridging Index.....	$\mathcal{E}_b \rightarrow [2R\sigma_b/f\xi^2 a\tau_0]$
Cyclic Bridging Indices.....	$\Delta\mathcal{E}_b \rightarrow [2R(\Delta\sigma_b)/f\xi^2 a\tau_0]$
.....	$\Delta\mathcal{E}_T \rightarrow [2RE_f(\alpha_f - \alpha_m)\Delta T/\xi^2 f\tau_0 a]$
Misfit Index .....	$\Sigma_T \rightarrow \frac{\bar{\sigma}_T}{\bar{\sigma}_p} = (c_2/c_1)E_m\Omega/\bar{\sigma}_p$
Debond Index.....	$\Sigma_d \rightarrow \frac{\bar{\sigma}_d}{\bar{\sigma}_p} = (1/c_1)\sqrt{E_m\Gamma_i/R\bar{\sigma}_p^2} - \Sigma_T$
Hysteresis Index.....	$\mathcal{H} \rightarrow b_2(1-a_1f)^2 R\bar{\sigma}_p^2/4\bar{\ell}\tau E_m f^2$
Crack Spacing Index .....	$\mathcal{L} \rightarrow \Gamma_m(1-f)^2 E_f E_m/f\tau^2 E_L R$
Matrix Cracking Index .....	$M \rightarrow 6\tau\Gamma_m f^2 E_f/(1-f)E_m^2 R E_L$
Residual Stress Index.....	$\mathcal{Q} \rightarrow E_f f\Omega/E_L(1-\nu)$
Flaw Index .....	$\mathcal{A} \rightarrow a_0 S^2/E_L \Gamma$
Flaw Index for Bridging .....	$\mathcal{A}_b \rightarrow [f/(1-f)]^2 (E_f E_L/E_m^2)(a_0\tau/RS_u)$
Flaw Index for Pull-Out .....	$\mathcal{A}_p \rightarrow (a_0/\bar{h})(S_p/E_L)$

TABLE IIb

Summary of H J Constants For Type II Boundary Conditions

$$a_1 = E_f/E$$

$$a_2 = \frac{(1-f)E_f[1+E_f/E]}{[E_f + (1-2\nu)E]}$$

$$b_2 = \frac{(1+\nu)E_m \{2(1-\nu)^2 E_f + (1-2\nu)[1-\nu + f(1+\nu)](E_m - E_f)\}}{(1-\nu)E_f[(1+\nu)E_o + (1-\nu)E_m]}$$

$$b_3 = \frac{f(1+\nu) \{ (1-f)(1+\nu)(1-2\nu)(E_f - E_m) + 2(1-\nu)^2 E_m \}}{(1-\nu)(1-f)[(1+\nu)E_o + (1-\nu)E_m]}$$

$$c_1 = \frac{(1-fa_1)(b_2 + b_3)^{1/2}}{2f}$$

$$c_2 = \frac{a_2(b_2 + b_3)^{1/2}}{2}$$

$$c_1/c_2 = \frac{1-a_1f}{a_2f}$$

with

$$E = fE_f + (1-f)E_m$$

$$E_o = (1-f)E_f + fE_m$$

TABLE III

Important Constituent Properties For Two Typical CMCs:  
Comparison Between SiC/SiC and SiC/CAS

PROPERTY	MATERIAL	
	SiC/CAS	SiC/SiC
Matrix Modulus, $E_m$ (GPa)	100	400
Fiber Modulus, $E_f$ (GPa)	200	200
Sliding Stress, $\tau$ (MPa)	15-20	100-150
Debond Energy, $\Gamma_i$ (Jm <sup>-2</sup> )	~ 0.1	~ 2
Residual Stress, $q$ (MPa)	80-100	50-100
Fiber Strength, $S_c$ (GPa)	2.0-2.2	1.3-1.6
Shape Parameter, $m$	3.3-3.8	4.2-4.7
Matrix Fracture Energy, $\Gamma_m$ (Jm <sup>-2</sup> )	20-25	5-10

## REFERENCES

- Abbe, F., Vicens, J. and Chermant, J.L. (1989) *J. Mater. Sci. Lett.*, **8**, 1026–28.
- Aubard, X. (Nov. 1992) Thèse de Doctorat de L'Université de Paris.
- Aveston, J., Cooper, G.A. and Kelly, A., in *The Properties of Fiber Composites*, NPL Conf. Proc., pp. 15–26.
- Bakis, H.R., Yih, H.R., Stinchcomb, W.W. and Reifsnider, K.L. (1989) *ASTM STP 1012*, 66–83.
- Bao, G. and McMeeking, R. (1993) *Acta Metall. Mater.*, in press.
- Bao, G. and Suo, Z. (1992) *Appl. Mech. Rev.*, **45** [8] 355–66.
- Bao, G., Fan, B. and Evans, A.G. (1992) *Mech. of Mtls.*, **13**, 59–66.
- Baste, S., El Guerjouma, R. and Andoin, B. (1992) *Mech. of Mtls.*, **14**, 15–32.
- Bender, B., Shadwell, Bulik, C., Incorvati, L. and Lewis, D., III (February 1986) *Am. Ceram. Soc. Bull.*, **65**[2] 363–69.
- Beyerle, D., Spearing, S.M. and Evans, A.G. (1992a) *J. Am. Ceram. Soc.*, **75**[12] 3321–30.
- Beyerle, D., Spearing, S.M., Zok, F. and Evans, A.G. (1992b) *J. Am. Ceram. Soc.*, **75**[10] 2719–25.
- Bischoff, E., Rühle, M., Sbaizero, O. and Evans, A.G. (1989) *J. Am. Ceram. Soc.*, **72** [5] 741–45.
- Bordia, R., Dalgleish, B.J., Charalambides, P.G. and Evans, A.G. (1991) *J. Am. Ceram. Soc.*, **74** [11] 2776–80.
- Bowling, J. and Groves, G.W. (1979) *J. Mater. Sci.*, **14**, 43.
- Brennan, J.J. (1986) *Tailoring of Multiphase Ceramics*, (ed. Tressler, R.E. et al.) **20**, 549.
- Brennan, J.J. and Prewo, K.M. (1982) *J. Mater. Sci.*, **17**, 2371–83.
- Brøndsted, P.A., Heredia, F.E. and Evans, A.G. (1993) *J. Am. Ceram. Soc.*, to be published.
- Budiansky, B., Hutchinson, J.W. and Evans, A.G. (1986) *J. Mech. Phys. Solids*, **34**, 167–89.
- Cady, C., Mackin, T.J. and Evans, A.G. (1993) *J. Am. Ceram. Soc.*, to be published.



- Cao, H.C., Bischoff, E., Sbaizero, O., Rühle, M. and Evans, A.G. (1990) *73* [6] 1691–99.
- Chai, H. (1984) *Composites* **15**[4] 277–90.
- Chawla, K.K. (1987) *Composite Materials Science and Engineering*, Springer-Verlag, NY.
- Cho, C., Holmes, J.W. and Barber, J.R. (1992) *J. Am. Ceram. Soc.*, **75**[2] 316–24.
- Cooper, R.F. and Chyung, K. (1987) *J. Mater. Sci.*, **22**, 126.
- Corten, H.T. (1967) *Modern Composite Materials* (eds. Brontman, L.J. and Krock, R.H.) Addison, p. 27.
- Cox, B.N. (1991) *Acta Metall. Mater.*, **39** [6] 1189–1201.
- Cox, B.N. and Lo, C.S. (1992) *Acta Metall. Mater.*, **40**, 69.
- Cox, B.N. and Marshall, D.B. (1991) *Fatigue and Fracture of Eng. Mtls.*, **14**, 847.
- Coyle, T.W., Guyot, M.H. and Jamet, J.F. (1986) *Cer. Eng. & Sci. Proc.*, **7**[7–8] 947–57.
- Cranmer, D.C. (1989) *Am. Ceram. Soc. Bull.*, **68**[2] 415.
- Cui, L. and Budiansky, B., to be published.
- Curtin, W.A. (1991a) *J. Mater. Sci.*, **26**.
- Curtin, W.A. (1991b) *J. Am. Ceram. Soc.*, **74**, 2837.
- Daniels, H.E. (1945) *Proc. Roy. Soc.*, **A183**, 405.
- Davis, J.B., Löfvander, J.P.A., Evans, A.G., Bischoff, E. and Emiliani, M.L. (1993) *J. Am. Ceram. Soc.*, in press.
- Domergue, J.M., Evans, A.G. and Roach, D., *J. Am. Ceram. Soc.*, to be published.
- Eckel, A.J. and Bradt, R.C. (1989) *J. Am. Ceram. Soc.*, **72**, 435.
- Evans, A.G. (1990) *J. Am. Ceram. Soc.*, **73** [2] 187–206.
- Evans, A.G. (1991), *Mat. Sci. Eng.*, **A143**, 63.
- Evans, A.G. and Dalglish, B.J. (Sept.–Oct. 1986) *Ceramic Eng. & Sci. Proceedings*, **7** [9–10].
- Evans, A.G. and Domergue, J.M. (1993) *J. Am. Ceram. Soc.*, in press.
- Evans, A.G., Domergue, J.M. and Vagaggini, E. (1993) *J. Am. Ceram. Soc.*, to be published.
- Evans, A.G. and Marshall, D.G. (1989) *Acta Metall.*, **37**, 2567–83.

- Evans, A.G. and McMeeking (1986) *Acta Metall.*, **34** [12] 2435–41.
- Evans, A.G. and Zok, F.W., (1992) *Topics In Fracture and Fatigue* (ed. A.S. Argon) pp. 271–308.
- Evans, A.G., Zok, F.W. and Davis, J. (1991) *Composites Science and Technology*, **42**, 3–24.
- Fleck, N.A., Hutchinson, J.W. and Suo, Z. (1991) *Intl. Jnl. Solids Structures*, 1683.
- Freudenthal, A., *Fracture* (1967) (ed. Liebowitz, H.) Academic Press.
- Gunawadena, S., Jansson, S. and Leckie, F.E. (1993) *Acta Metall. Mater.*, in press.
- Harris, B., Habib, R.A. and Cooke, R.G. (1992) *Proc. Roy. Soc., Series A*, **437**, 109–31.
- Harwood, N. and Cummings, W.M. (1991) *Thermoelastic Stress Analysis*, Adam Hilger IOP Publishing.
- He, M. and Hutchinson, J.W. (1989) *Intl. Jnl. Solids Structures*, **25**[9] 1-53–67.
- Hayhurst, D., Leckie, F.A. and Evans, A.G. (1991) *Proc. Roy. Soc., London*, **A434**, 369.
- He, M.Y., Wu, B.X., Evans, A.G. and Hutchinson, J.W. (1993) *Mech. of Mtls.*, in press.
- Heredia, F., Spearing, S.M. and Evans, A.G. (1992) *J. Am. Ceram. Soc.*, **75**[11] 3017–25.
- Heredia, F.E., Spearing, S.M., He, M.Y., Mackin, T.J., Brøndsted, P.A., Evans, A.G. and Mosher, P. (1993) *J. Am. Ceram. Soc.*, to be published.
- Heredia, F.E., Spearing, S.M., Mosher, P., Evans, A.G. and Curtin, W.A. (1992) *J. Am. Ceram. Soc.*, **75**, 3017–25.
- Hild, F., Domergue, J.M., Leckie, F.A. and Evans, A.G. (1993) *Intl. Jnl. Solids Structures*, to be published.
- Holmes, J.W. (1991) *J. Am. Ceram. Soc.*, **74**[7] 639–45.
- Holmes, J.W. (1991) *J. Mater. Sci.*, **26** 1808–14.
- Holmes, J.W. and Cho, C. (1992) *J. Am. Ceram. Soc.*, **75** [4] 929–38.
- Holmes, J.W. and Shuler, S.F. (1990) *J. Mater. Sci. Lett.*, **9** 1290–91.
- Hutchinson, J.W. and Jensen, H. (1990) *Mech. of Mtls.*, **9**, 139.
- Hutchinson, J.W. and Suo, Z. (1991) *Appl. Mech. Rev.*, **28**.
- Jamet, J.F., Lewis, D. and Luh, E.Y. (1984) *Ceram. Eng. Sci. Proc.*, **5**, 625.

- Jannson, S. and Leckie, F.A. (1992) *Journal of the Mechanics and Physics of Solids*, **40**, 593–612.
- Jero, P.D., Kerans, R.J. and Parthasarathy, T.A. (1991) *J. Am. Ceram. Soc.*, **74**, 2793.
- Kaute, D.A.W., Shercliff, H.R. and Ashby, (1993) M.F., *Acta Metall. Mater.*, to be published.
- Kelly, A. and Street, K.N. (1972) *Proceedings of the Royal Society, London*, **A328**, 283–293.
- Kerans, R.J. and Parthasarathy, T.A. (1991) *J. Am. Ceram. Soc.*, **74**, 1585.
- Khobaib, M. and Zawada, L.P. (1991) *Ceram. Eng. Sci. Proc.*, **12** [7–8] 1537–55.
- Kim, B.Y. and Pagano, N. (1991) *J. Am. Ceram. Soc.*, **74**, 1082–90.
- Kim, R.Y. (1992) *Ceram. Eng. Sci. Proc.*, **13** [7–8] 281–300.
- Kim, R.Y. and Katz, A.P. (1988) *Ceram. Eng. Sci. Proc.*, **9** 853–60.
- Kotil, T.J., Holmes, J.W. and Cominou, M. (1990) *J. Am. Ceram. Soc.*, **73**, 1879.
- Lamon, J., Raballiat, P. and Evans, A.G., *J. Am. Ceram. Soc.*, in press.
- Laws, N. and Dvorak, G., (1980) *Jnl. Composite Mtls.*, **22**, 900.
- Luh, E.Y. and Evans, A.G. (1987) *J. Am. Ceram. Soc.*, **70** [7].
- Mackin, T.J., Evans, A.G., He, M.Y. and Purcell, T.E. (1993) to be published.
- Mackin, T., Warren, P. and Evans, A.G. (1992) *Acta Metall. Mater.*, **40** [6] 1251–57.
- Mackin, T., Yang, J., Levi, C. and Evans, A.G. (1993) *Acta Metall. Mater.*, in press.
- Mackin, T. and Zok, F.W. (1993) *J. Am. Ceram. Soc.*, **75**, 3169–71.
- Mall, S., Bullock, D.E. and Pernot, J.J., to be published.
- Marshall, D.B. (1992) *Acta Metall. Mater.*, **40**, 427–41.
- Marshall, D.B., Cox, B.N. and Evans, A.G. (1985) *Acta Metall.*, **33**, 2013–21.
- Marshall, D.B. and Cox, B.N. (1985) *Mech. of Mtls.*, **7**, 127.
- Marshall, D.B. and Evans, A.G. (1985) *J. Am. Ceram. Soc.*, **68**, 225–31.
- Marshall, D.B., and Evans, A.G. (1988) *Materials Forum*, **11**, 304–12
- Matthews, J.R., Shack, W.J. and McClintock, F.A. (1976) *J. Am. Ceram. Soc.*, **59**, 304.

- McCartney, L.N. (1987) *Proc. Roy. Soc.*, **A409**, 329-50.
- McLean, D. (1972) *Journal of Materials Science*, **7**, 98-104.
- McLean, M. (1985) *Composites Science and Technology*, **23**, 37-52.
- McMeeking, R.M. (1993) *International Journal of Solids and Structures*, in press.
- McMeeking, R.M. and Evans, A.G. (1990) *Mech. of Mtls.*, **9**, 217-27.
- Mileiko, S.T. (1970) *Journal of Materials Science*, **5**, 254-261.
- Molis, S.E. and Clarke, D.R. (1990) *J. Am. Ceram. Soc.*, **73**, 3189.
- Nardonne, V.C. and Prewo, K.M. (1988) *J. Mater. Sci.*, **23**, 168.
- Nieh, T.G. (1984) *Metallurgical Transactions A*, **15A**, 139-146.
- Oh, H.L. and Finnie, I. (1970) *Intl. J. Frac.*, **6**, 287.
- Phillips, D.C. (1974) *J. Mater. Sci.*, **9**[11] 1874-54.
- Phoenix, L. and Raj, R. (1992) *Acta Metall. Mater.*, **40**, 2813-28.
- Prewo, K.M. (1982) *J. Mater. Sci.*, **17**, 3549.
- Prewo, K.M. (1986) *J. Mater. Sci.*, **21**, 3590-600.
- Prewo, K.M. (1987) *J. Mater. Sci.*, **22**, 2595-701.
- Prewo, K. and Brennan, J.J. (1982) *J. Mater. Sci.*, **17**[4] 1201-06.
- Prewo, K.M. and Brennan, J.J. (1980) *J. Mater. Sci.*, **17**[2] 463-68.
- Prewo, K.M. and Brennan, J.J. (1982) *J. Mater. Sci.*, **17**, 1201-06.
- Pryce, A.W. and Smith, P. (1992) *J. Mater. Sci.*, **27**, 2695-2704.
- Rice, R.W., U.S. Patent 4,642,271, BN Coating of Ceramic Fibers for Ceramic Fiber Composites, February 10, 1987; assigned to the United States of America as represented by the Secretary of the Navy.
- Rice, R.W., Spann, J.R., Lewis, D. and Coblenz, W. (1984) *Ceram. Eng. Sci. Proc.*, **5**[7-8] 614-24.
- Rousseou, C.Q. (1990) *Thermal and Mechanical Behavior of metal Matrix and Ceramic Matrix Composites*, ASTM STP 1080, eds. Kennedy, J.M., Moeller, H.H. and Johnson, W.S., American society for Testing and Materials, Philadelphia, PA.
- Sbaizero, C. and Evans, A.G. (1986) *J. Am. Ceram. Soc.*, **69** [6] 481.

- Sensmeier, M. and Wright, K. (1989) *Proceedings TMS Fall Meeting*, ed. Law, P.K. and Gungor, M.N. 441.
- Shang, J.K., Tzou, J.L. and Ritchie, R.V. (1987) *Met. Trans.*, **A18**, 1613.
- Singh, R. (1989) *J. Am. Ceram. Soc.*, **72**, 1764.
- Spearing, S.M. and Evans, A.G. (1992) *Acta Metall.*, **40** [9] 2191-99.
- Spearing, S.M. and Zok, F.W. (1993) *Jnl. Eng. Mtls. Tech.*, in press.
- Spearing, S.M., Zok, F.W. and Evans, A.G. (1993) *J. Am. Ceram. Soc.*, to be published.
- Stinchcomb, W. and Bakis, C.E. (1992) *Fatigue of Composite Materials*, ed. Reifsnider, K.L., Elsevier Science Publishers B.V. (1990) pp. 105-80.
- Suo, Z., Ho, S. and Gong, X., *J. Matl. Engr. Tech.*, in press.
- Sutcu, M. (1989) *Acta Metall.*, **37**[2] 651-61.
- Tada, H.I., Paris, P.C. and Irwin, G.R. (1985) *The Stress Analysis of Cracks Handbook*, Del Research Corp., St. Louis.
- Thouless, M.D. and Evans, A.G. (1988) *Acta Metall.*, **36**, 517.
- Thouless, M.D., Sbaizero, O., Sigl, L.S. and Evans, A.G. (1989) *J. Am. Ceram. Soc.*, **72** [4] 525-32.
- Vagaggini, E. and Evans, A.G. (1993) *J. Am. Ceram. Soc.*, in press.
- Walls, D. and Zok, F.W., (1991) in *Advanced Metal Matrix Composites for Elevated Temperatures*, eds. Gungor, M.N., Lavernia, E.J. and Fishman, S.G., ASM, Metals Park, p. 101.
- Walls, D., Bao, G. and Zok, F.W., (1993) *Acta Metall. Mater.*, in press.
- Walls, D., Bao, G. and Zok, F. (1991) *Scripta Metall. Mater.*, **25**, 911.
- Weber, C. and Evans, A.G. (1993) to be published.
- Weber, C. and Zok, F.W. (1993) to be published.
- Weber, C., Yang, J.Y., Löfvander, J.P.A., Levi, C.G. and Evans, A.G. (1993) *Acta Metall. Mater.*, in press.
- Xia, C., Carr, R.R. and Hutchinson, J.W. (1992) *Harvard Univ. Report Mech-202*, to be published.
- Zawada, L.P., Butkus, L.M. and Hartman, G.A. (1991) *J. Am. Ceram. Soc.*, **74**, 2851-58.

Zok, F.W. and Evans, A.G. (1993) to be published.

Zok, F.W. and Hom, C.L. (1990) *Acta Metall. Mater.*, **38**, 1895.

Zok, F.W. and Spearing, S.M. (1992) *Acta Metall. Mater.*, **40**, 2033.

Zok, F.W., Sbaizero, O., Hom, C. and Evans, A.G. (1991) *J. Am. Ceram. Soc.*, **74** [1] 187-93.

## FIGURE CAPTIONS

- Fig. 1.1 The fundamental mechanisms that operate as a crack extends through the matrix.
- Fig. 1.2 Three prevalent damage mechanisms occurring around notches in CMCs. Each mechanism allows stress redistribution by a combination of matrix cracking and fiber pull-out.
- Fig. 1.3 A proposed mechanism map that distinguishes class I and class II behavior.
- Fig. 1.4 A proposed mechanism map that distinguishes class III behavior.
- Fig. 1.5 Tensile stress/strain curves measured for a variety of 2-D CMCs.
- Fig. 1.6 Shear stress/strain curves measured for 2-D CMCs.
- Fig. 1.7 The philosophy adopted for using models in the design and application of CMCs.
- Fig. 2.1 A schematic indicating the sliding and debonding behavior envisaged in CMCs.
- Fig. 2.2 The fiber sliding model.
- Fig. 2.3 A debond diagram for CMCs.
- Fig. 2.4 A typical load/unload cycle showing the parameters that can be measured which relate to the interface properties.
- Fig. 2.5 Simulation of the effects of the key variables on the push-out behavior a) roughness, b) residual stress, c) friction coefficient.
- Fig. 2.6 Some typical fiber push-out measurements conducted on CMCs and intermetallic matrix composites a)  $\text{Al}_2\text{O}_3/\text{TiAl}$  within  $\text{C}/\text{Al}_2\text{O}_3$  double coatings, b)  $\text{SiC}/\text{glass}$  and  $\text{Al}_2\text{O}_3/\text{glass}$  showing effect of fiber roughness, c)  $\text{SiC}/\text{Ti}$  with  $\text{C}$  coating showing influence of fatigue, d)  $\text{Al}_2\text{O}_3/\text{Al}_2\text{O}_3$  with fugitive  $\text{Mo}$  coating.

- Fig. 3.1 A schematic of the beam bending effect used to evaluate the residual stress.
- Fig. 3.2 Displacements caused by matrix dissolution as a function of length removed.
- Fig. 4.1 A schematic illustrating the load transfer process from failed fibers.
- Fig. 4.2 Relationship between ultimate strengths measured in flexure and tension.
- Fig. 4.3 Bounds on the relationship between the non-dimensional fiber pull-out length and the Weibull modulus.
- Fig. 4.4 The effect of unbridged regions, length  $2a_0$ , on the ultimate tensile strength.
- Fig. 4.5 A schematic indicating a fracture mirror and the dimension used to predict the *in situ* strength.
- Fig. 4.6 *In situ* strength distributions measured for Nicalon fibers on three CMCs, using the fracture mirror approach.
- Fig. 4.7 Comparison of the measured UTS with  $S_g$  predicted from GLS (Eqn. 4.9a) plotted against a stress concentration index. Note that  $\bar{h}$  is inversely proportional to  $\tau$ .
- Fig. 5.1 A mechanism map representing the various modes of interface response.
- Fig. 5.2 a) Simulation of crack evolution for various matrix flaw distributions characterized by  $\lambda_s$  when the shape parameter  $\omega = 2$ .  
b) Evolution of matrix crack density with stress for unidirectional SiC/CAS.
- Fig. 5.3 Effects of modulus mismatch and fiber volume fraction on the elastic compliance.
- Fig. 5.4 Basic parameters involved in the stress/strain behavior of CMCs.  
a) debonding and sliding subject to SDE b) in the absence of debonding.
- Fig. 5.5 Simulated stress/strain curves for 1-D CMCs indicating the relative importance of constituent properties.
- Fig. 5.6 Stress-strain curves and typical hysteresis measurements obtained on SiC/CAS and SiC/SiC unidirectional composites.



- Fig. 5.7 Analysis of hysteresis loop results for unidirectional SiC/CAS and SiC/SiC.
- Fig. 5.8 Analysis of permanent strains for unidirectional SiC/CAS and SiC/SiC.
- Fig. 5.9 Simulated stress/strain curve for unidirectional SiC/SiC and comparison with experiment.
- Fig. 6.1 A comparison of stress/strain curves measured for 1-D and 2-D CMCs. The dotted lines labelled 1/2 (1-D) represent the behavior expected in 2-D materials when the 90° plies carry zero load.
- Fig. 6.2 The matrix crack growth mechanisms that operate in 2-D CMCs.
- Fig. 6.3 Simulated stress/strain response for a 2-D CMCs subject to tunnel cracking.
- Fig. 6.4 A simulated stress/strain curve for a 2-D SiC/SiC in which the plastic strains are dominated by the 0° plies. The experimental results for a SiC/SiC composite are shown for comparison.
- Fig. 6.5 Schematic indicating the two modes of shear damage: a) in-plane b) interlaminar.
- Fig. 6.6 Normalized in-plane shear stress/strain curves with the non-dimensional parameter  $\mathcal{W}$  indicated.
- Fig. 6.7 The interlaminar strength as a function of interlaminar crack orientation,  $\phi$ .
- Fig. 6.8 Schematic of the various modes of transverse cracking in CMCs.
- Fig. 6.9 The transverse fracture resistance of a SiC/CAS material. Also shown are the traction law assumed for inclined bridging fibers upon transverse cracking and the predicted resistance curves.
- Fig. 7.1 Effects of relative notch size on the UTS. Also shown are experimental data for a SiC/C material.
- Fig. 7.2 Experimental results for SiC/CAS indicating notch insensitivity.
- Fig. 7.3 Relationship between shear band length and stress for a C/C composite. The calculated curve is also shown.

- Fig. 7.4 Effect of shear bands on the stress ahead of a notch.
- Fig. 7.5 LEFM representation of notch data for C/C.
- Fig. 7.6 A schematic indicating an approximate method for obtaining the stress by using the strain obtained from elastic calculations.
- Fig. 7.7 A SPATE image obtained from a SiC/CAS composite compared with that for a monolithic material.
- Fig. 7.8 A SPATE image obtained from a C/C composite.
- Fig. 8.1 The length of crack  $a_f$  at first fiber failure as a function of fiber strength for a range of stress amplitudes,  $\Delta\mathcal{E}$ .
- Fig. 8.2 Fiber breaking rate as manifest in the current unbridged crack length  $2a_u$  as a function of total crack length  $2a$ .
- Fig. 8.3 Predicted fatigue crack growth curves.
- Fig. 8.4 The threshold stress diagram. Also shown are experimental results.
- Fig. 8.5 Effects of TMF on the tip stress intensity factor a) in phase, b) out-of-phase.
- Fig. 8.6 Effects of TMF on the crack size at which fiber failure occurs a) in phase, b) out-of-phase.
- Fig. 8.7 Comparison between experimental crack growth results and predictions for unidirectional SiC/Ti composites.
- Fig. 8.8 Modulus reduction found upon fatigue in a glass matrix composite (Zawada *et al.*).
- Fig. 8.9 Influence of cyclic loading on modulus reduction as a function of crack density for a unidirectional CAS/SiC composite indicating that  $\tau$  has been decreased by fatigue.
- Fig. 8.10 Experimental measurements and simulations of matrix crack evolution in a SiC/CAS composite caused by stress corrosion at constant stress.
- Fig. 8.11 Fatigue and TMF data for a glass matrix composite (Mall *et al.*).

- Fig. 8.12 Mechanism of fiber degradation by fatigue, coupled with oxidation.
- Fig. 9.1 Schematic indicating creep anisotropy in unidirectional CMCs.
- Fig. 9.2 Schematic indicating effects of intact and creeping fibers, as well as fiber failure on the longitudinal creep.
- Fig. 9.3 Transverse strength of a unidirectional composite with a power law hardening matrix.
- Fig. 9.4 A sketch indicating the longitudinal creep threshold and the behavior above the threshold.
- Fig. 9.5 Comparison of transverse behavior with and without interface debonding.
- Fig. 9.6 Creep rupture data for a SiC/C composite which is susceptible to fiber creep and matrix cracking.
- Fig. 9.7 Creep recovery effects in a SiC/Si<sub>3</sub>N<sub>4</sub> with 'elastic' fibers and a creeping matrix (Holmes *et al.*, 1993).
- Fig. 9.8 Transient longitudinal creep in a TiAl matrix composite reinforced with sapphire fibers (Weber *et al.*, 1993).
- Fig. 9.9 Transient creep and rupture data obtained for a SiC/Ti composite subject to incremental loading (Weber and Zok, 1993).
- Fig. 9.10 Longitudinal creep of a SiC/CAS composite (Weber and Evans, 1993).

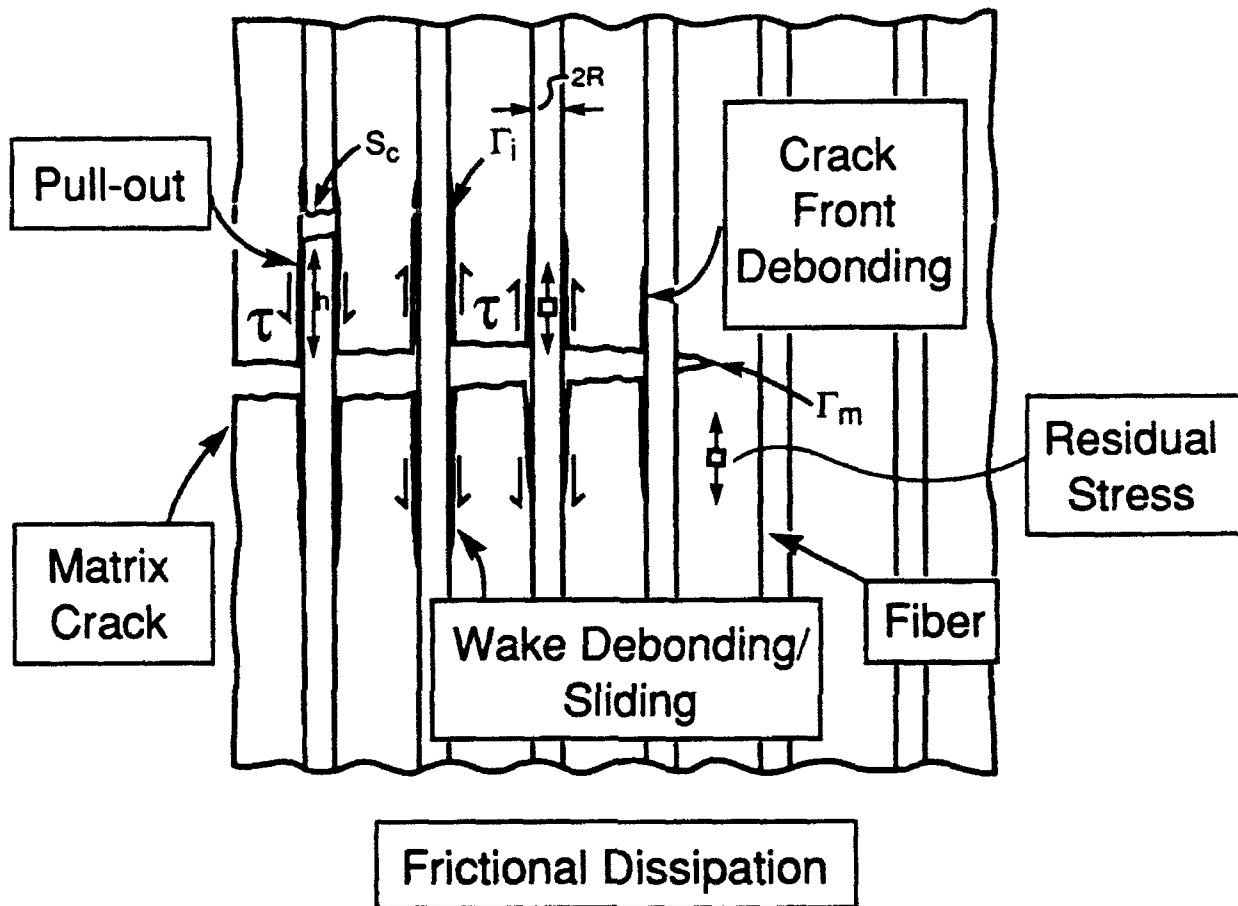
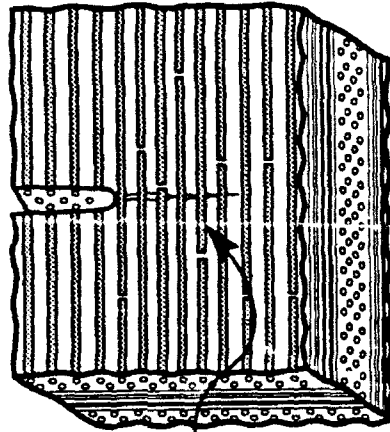


Fig. 1-1

### Class I

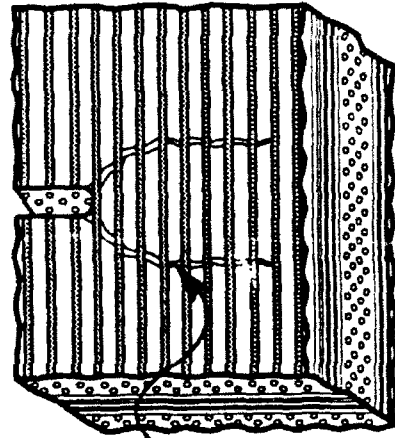
Matrix Cracking + Fiber Failure



Pull-Out Traction  
Redistribute Stress

### Class II

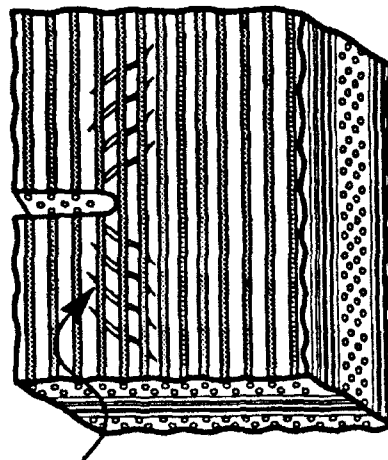
Matrix Cracking: No Fiber Failure



Matrix Cracks  
Redistribute Stress

### Class III

Shear Damage By Matrix Cracking



Shear Damage Zone  
Redistributes Stress

Figure 1.2

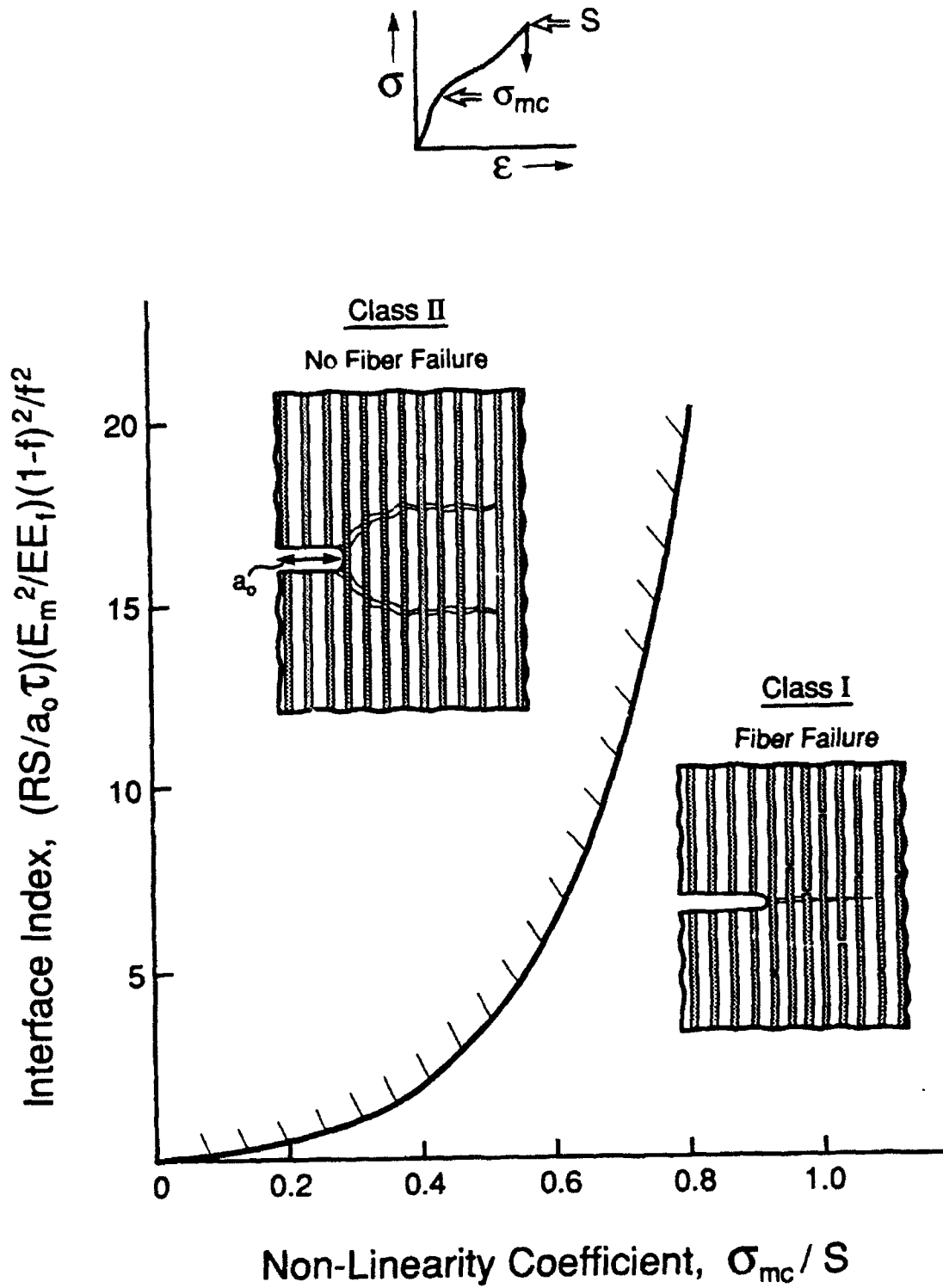


Figure 1.3

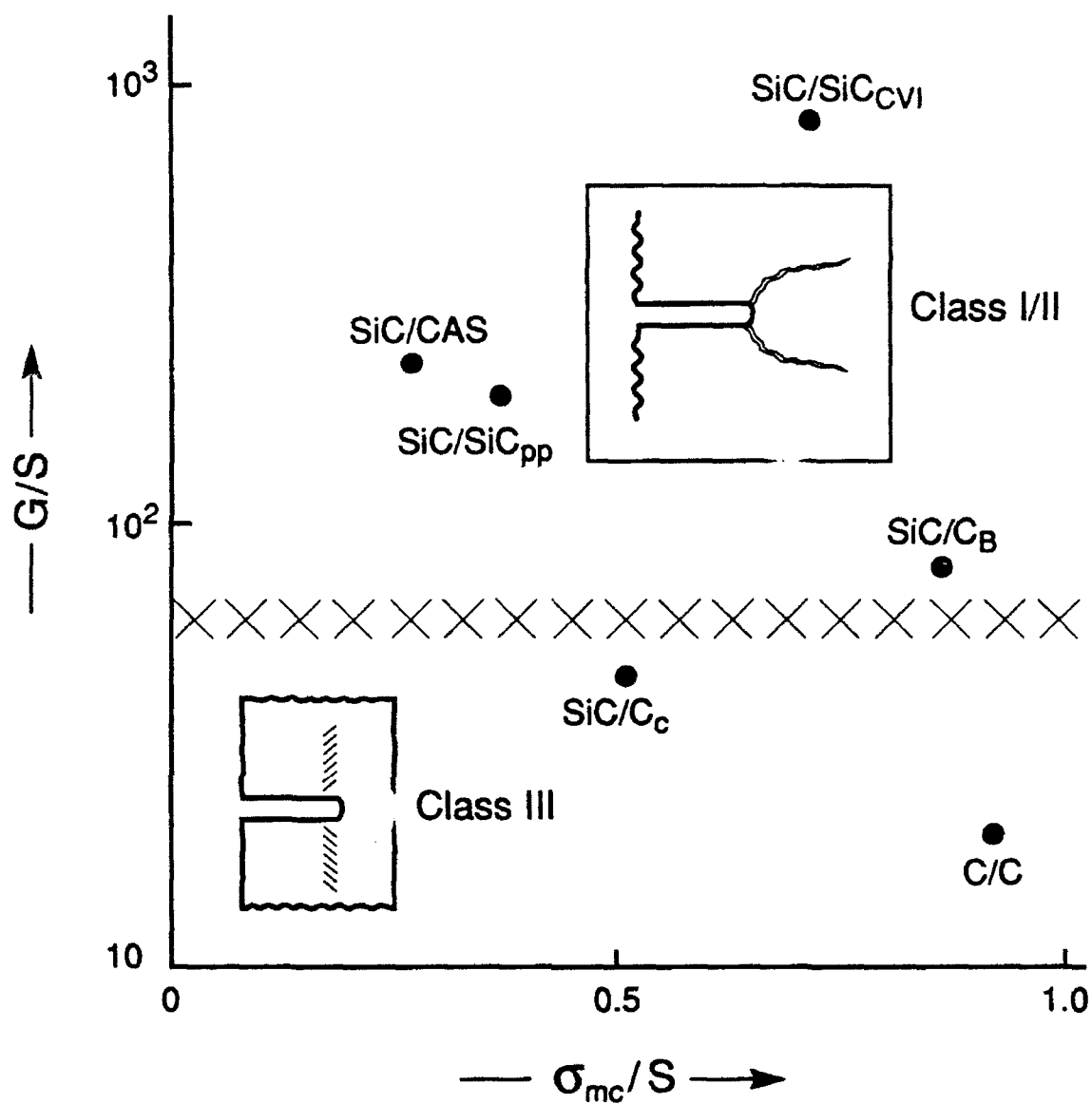


Figure 1.4

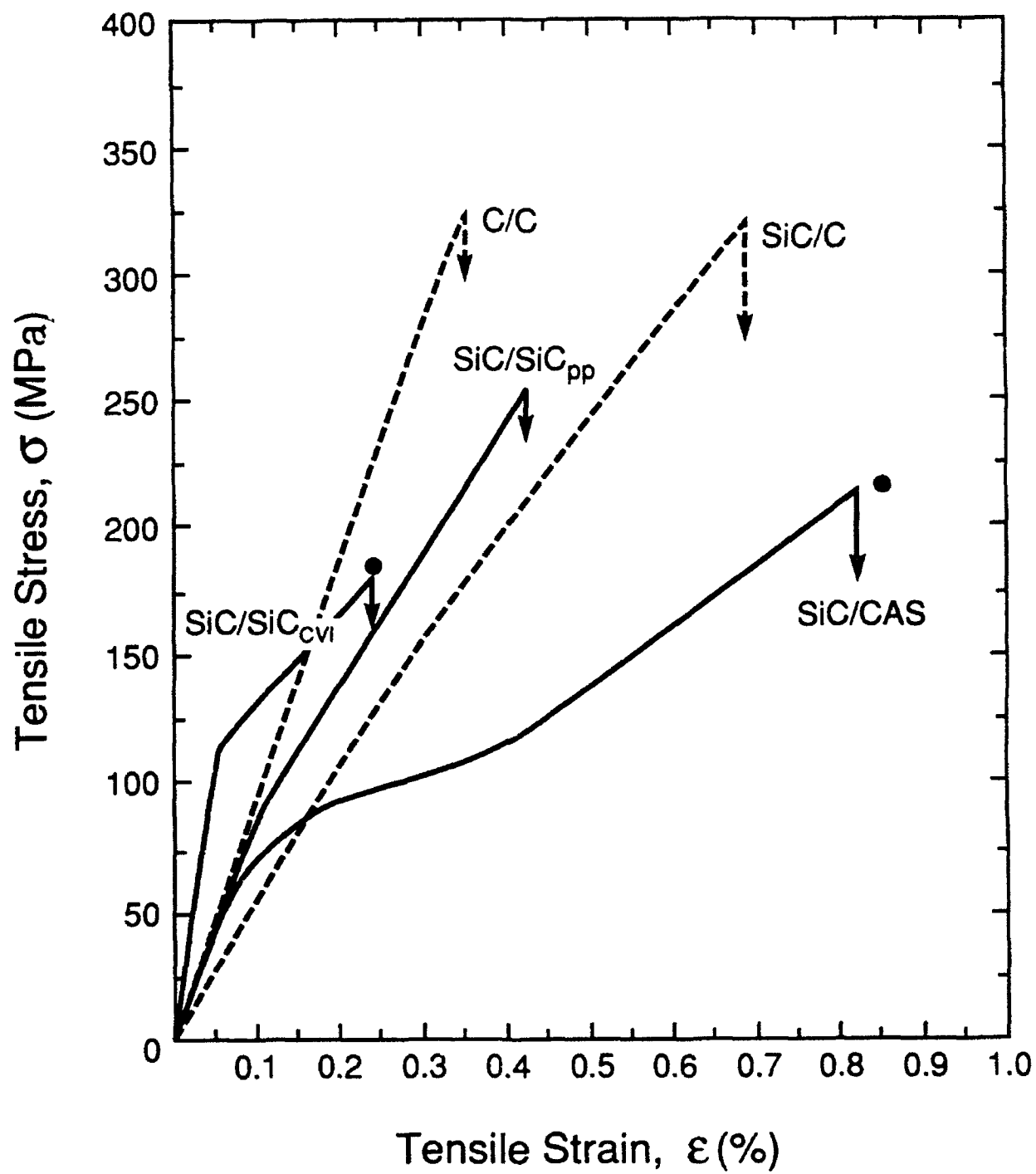


Figure 1.5



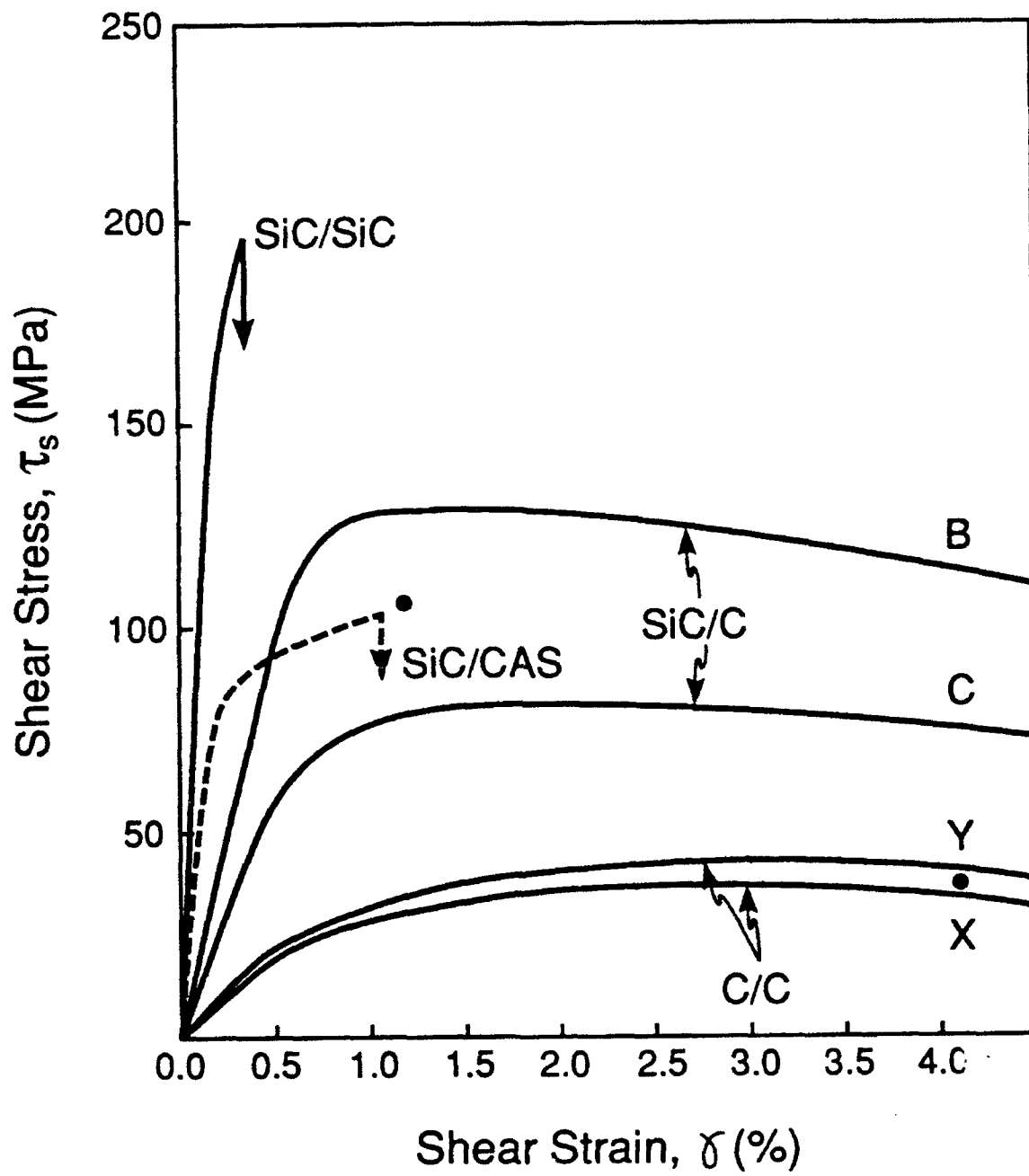


Figure 1.6

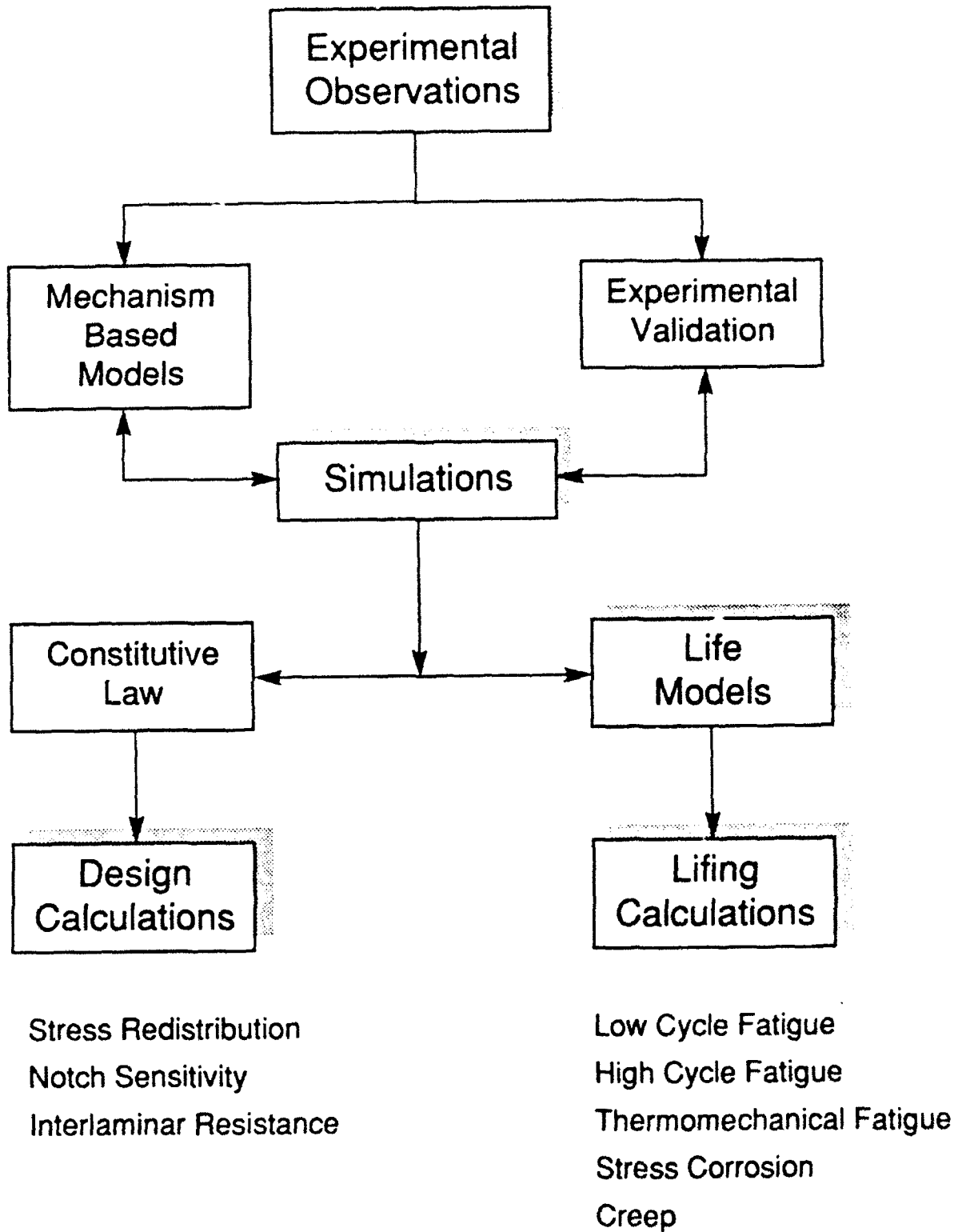


Figure 1.7

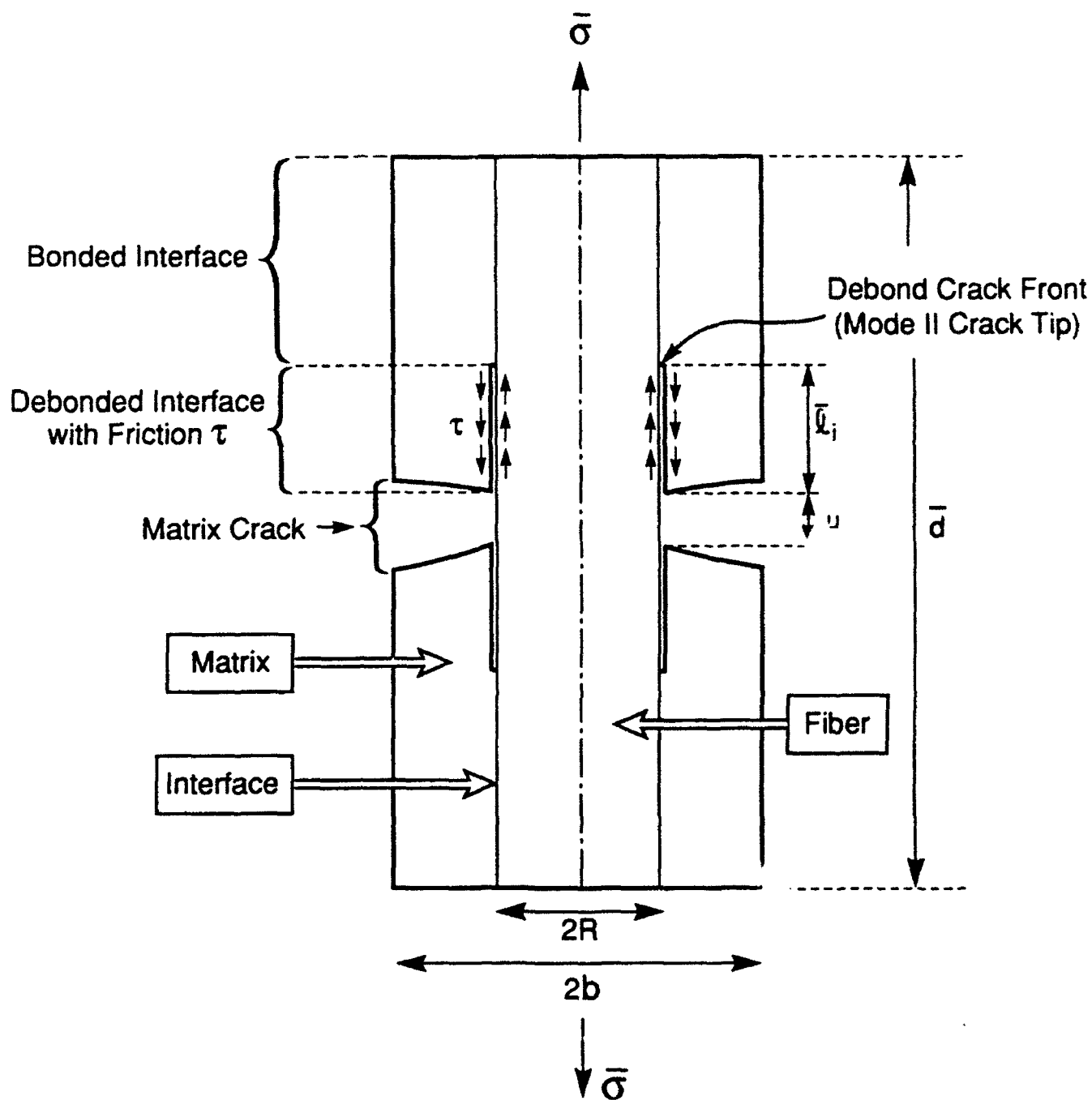


Fig. 2.1

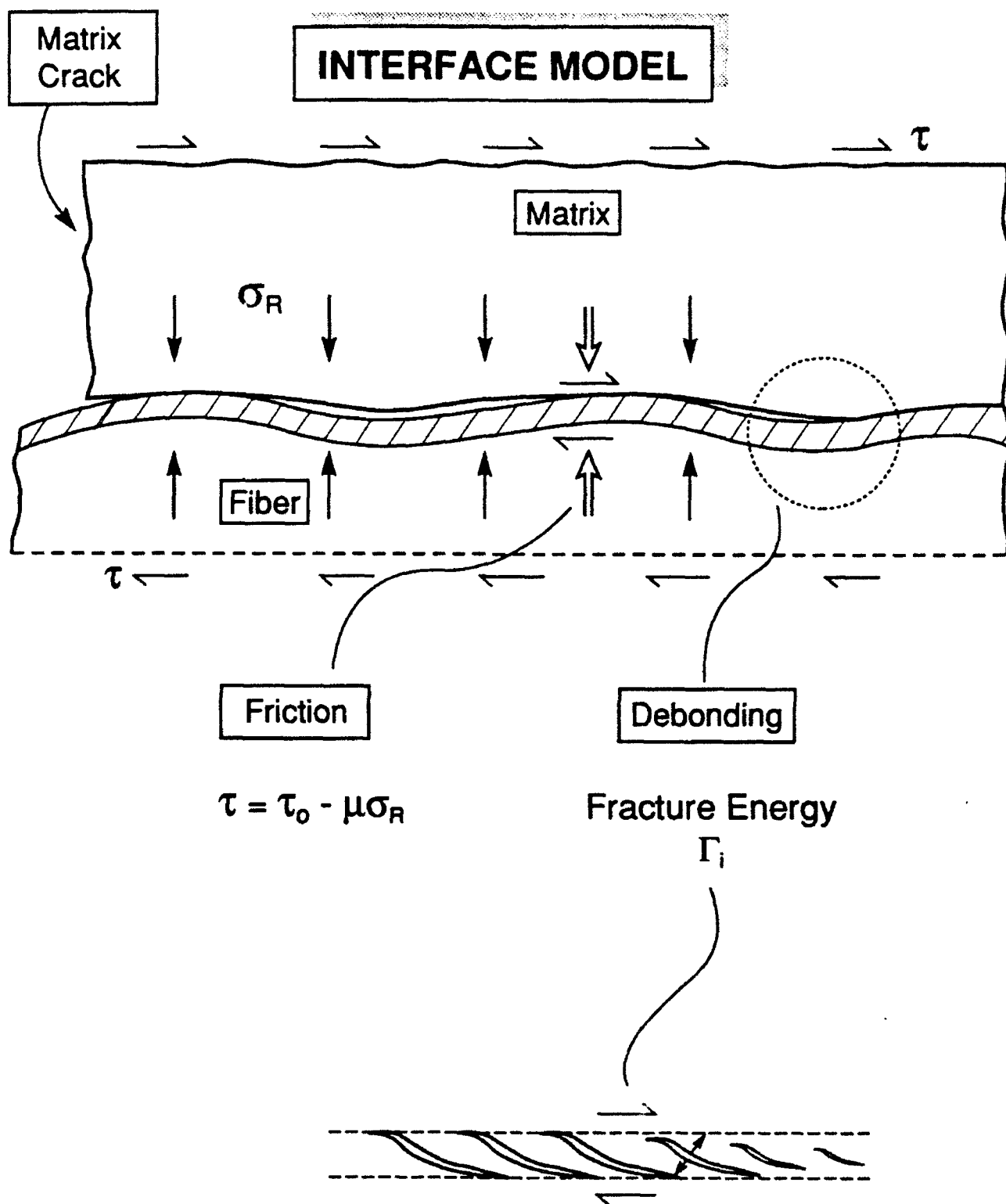


Fig. 2-2

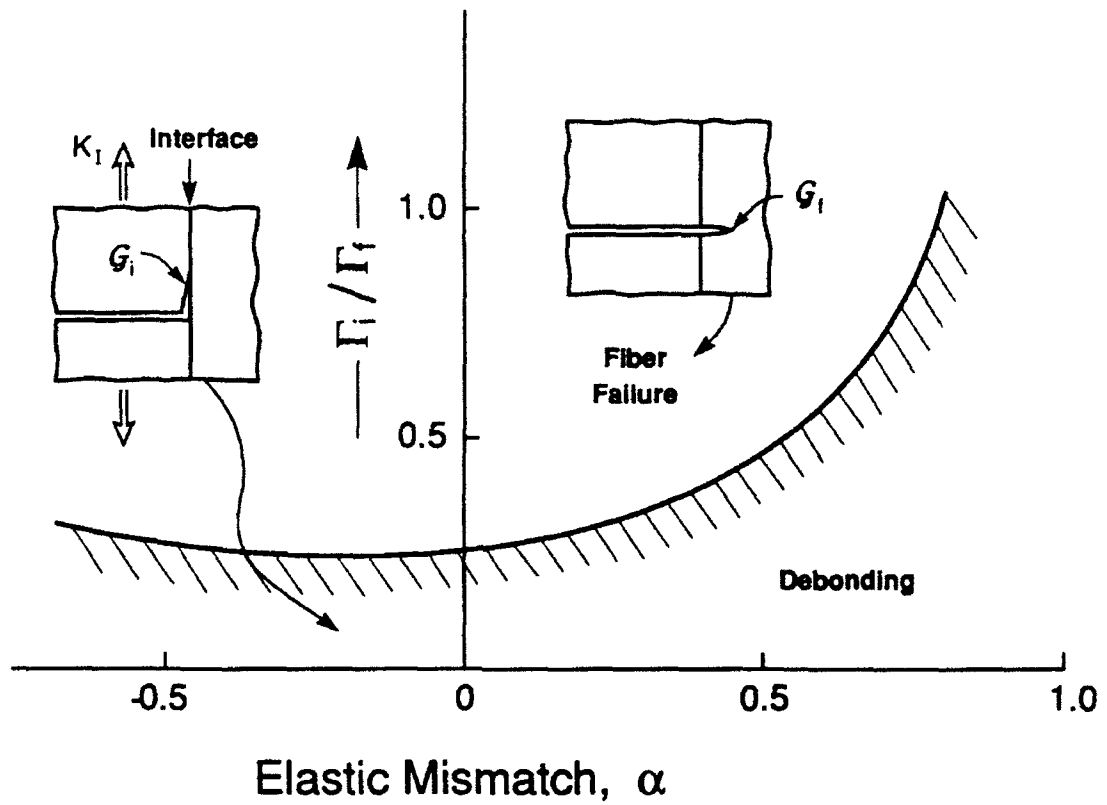


Figure 2.3

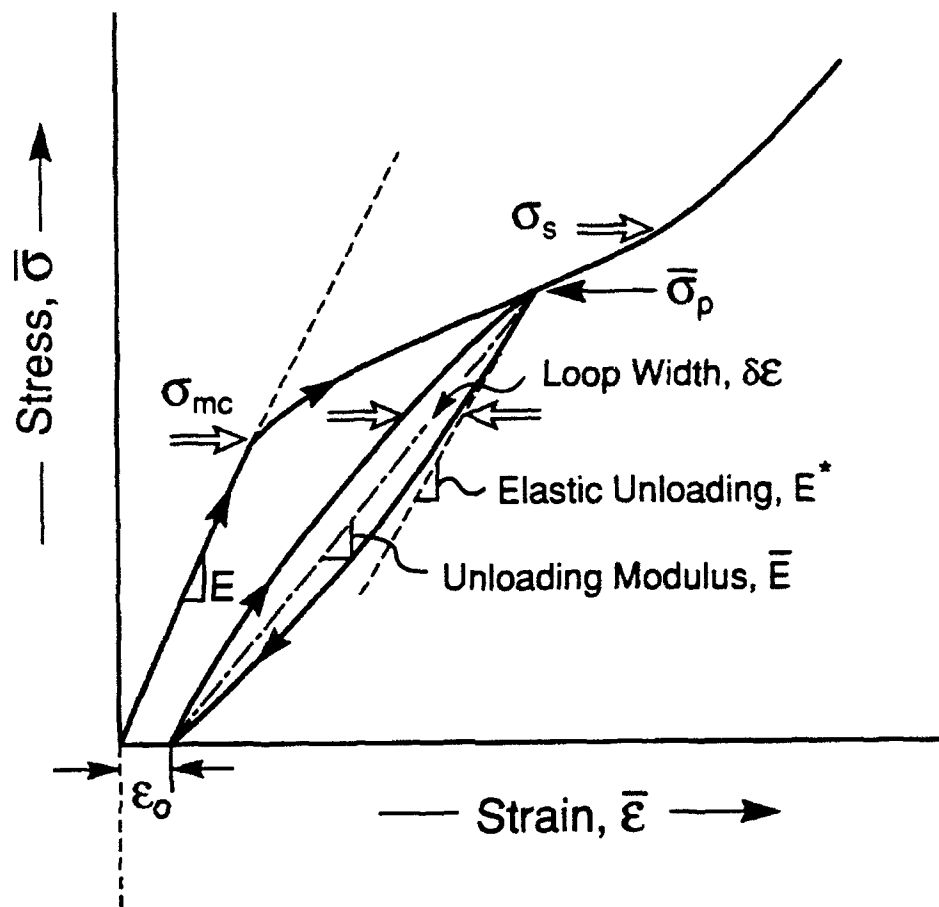


Figure 2.4

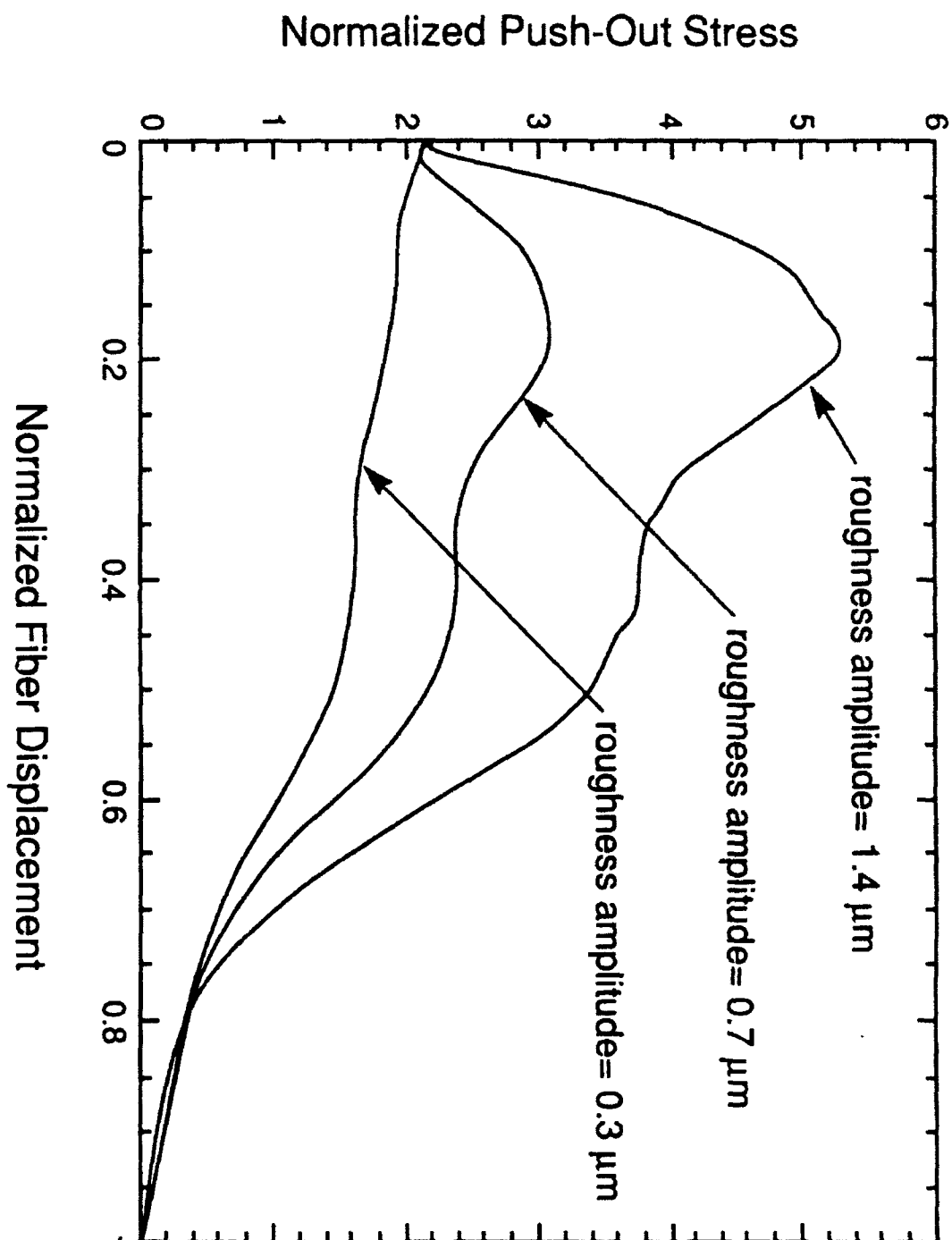


Fig 2. 5a

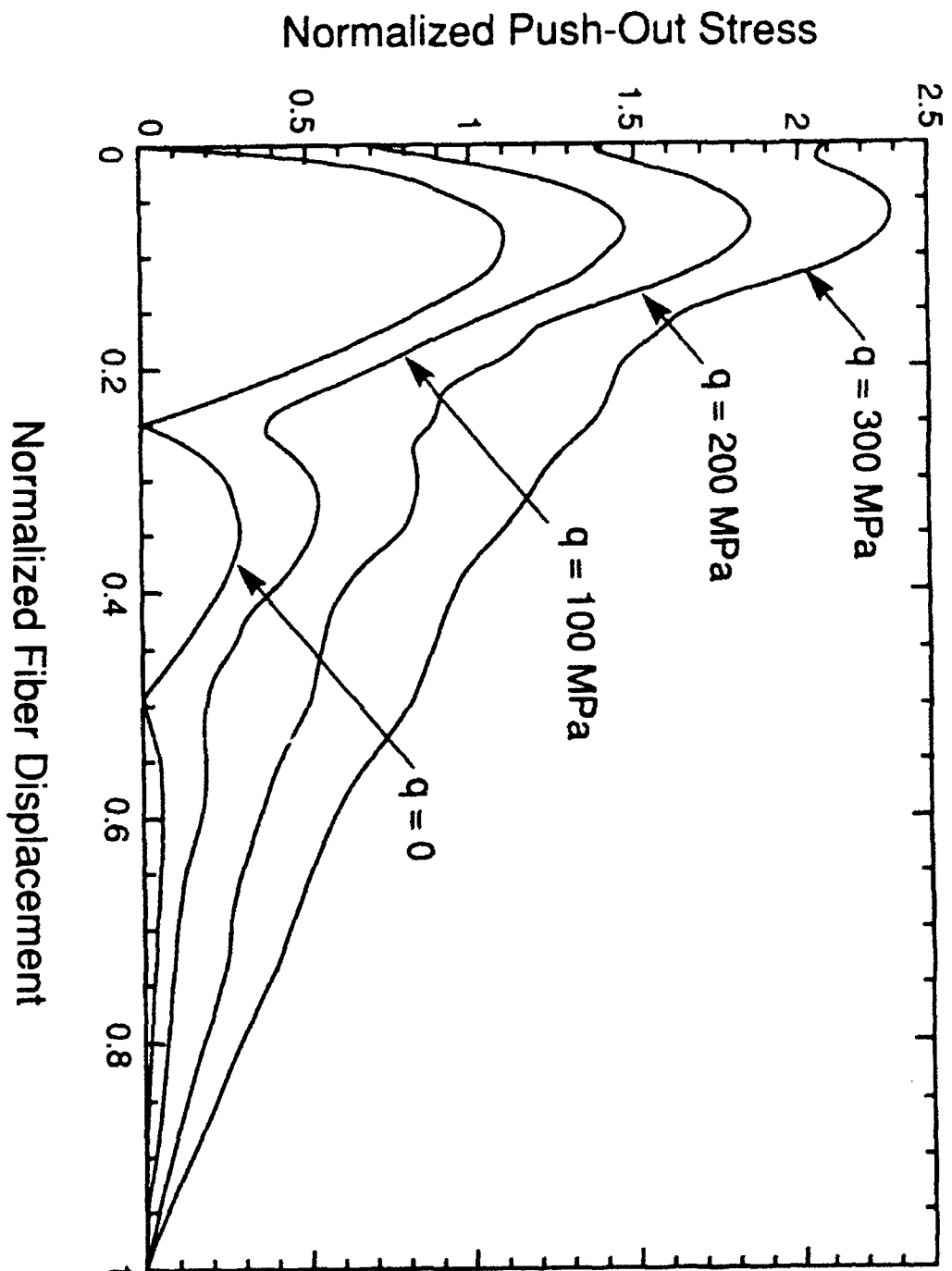


Fig 2.5b



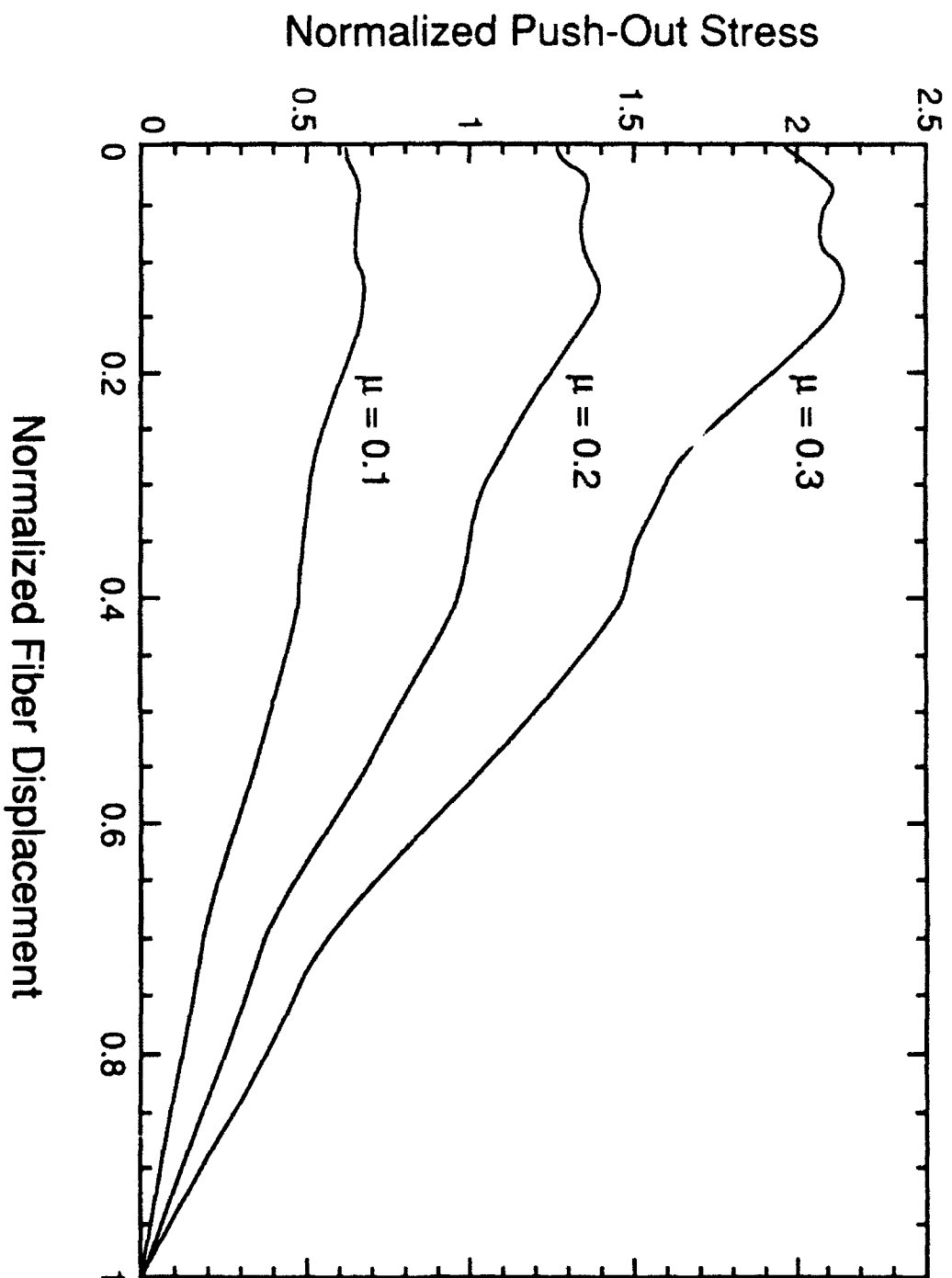


Fig 2.5c

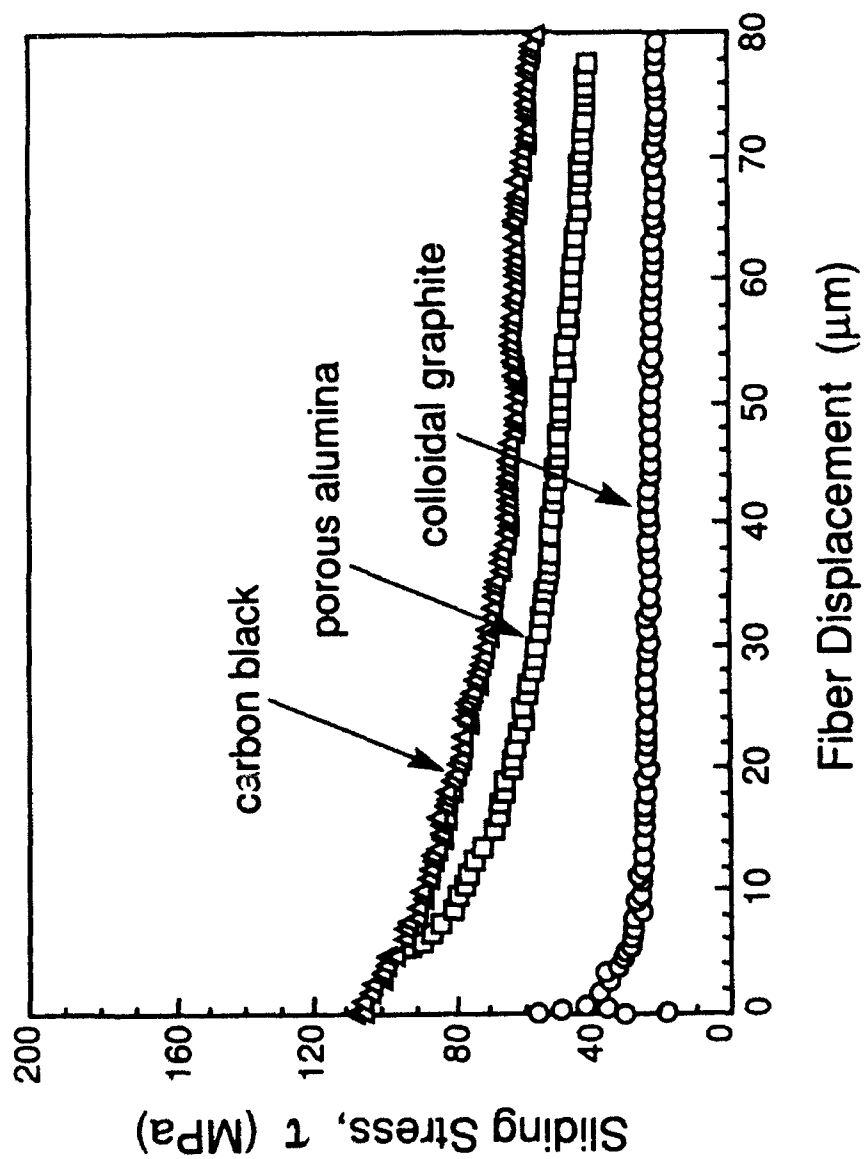


Fig 2.6a

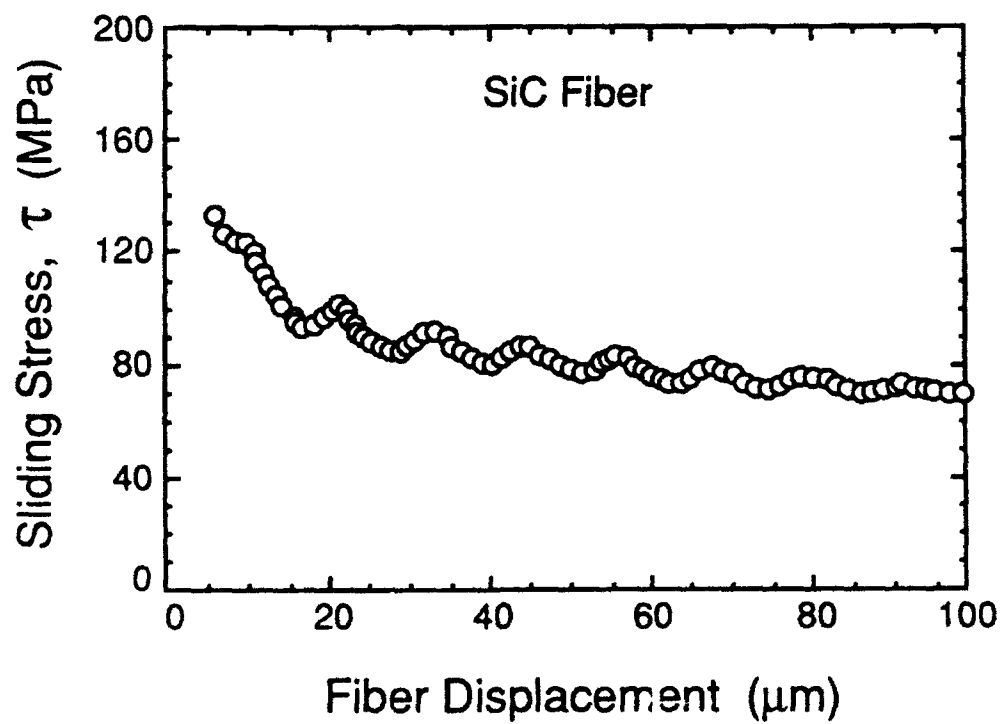
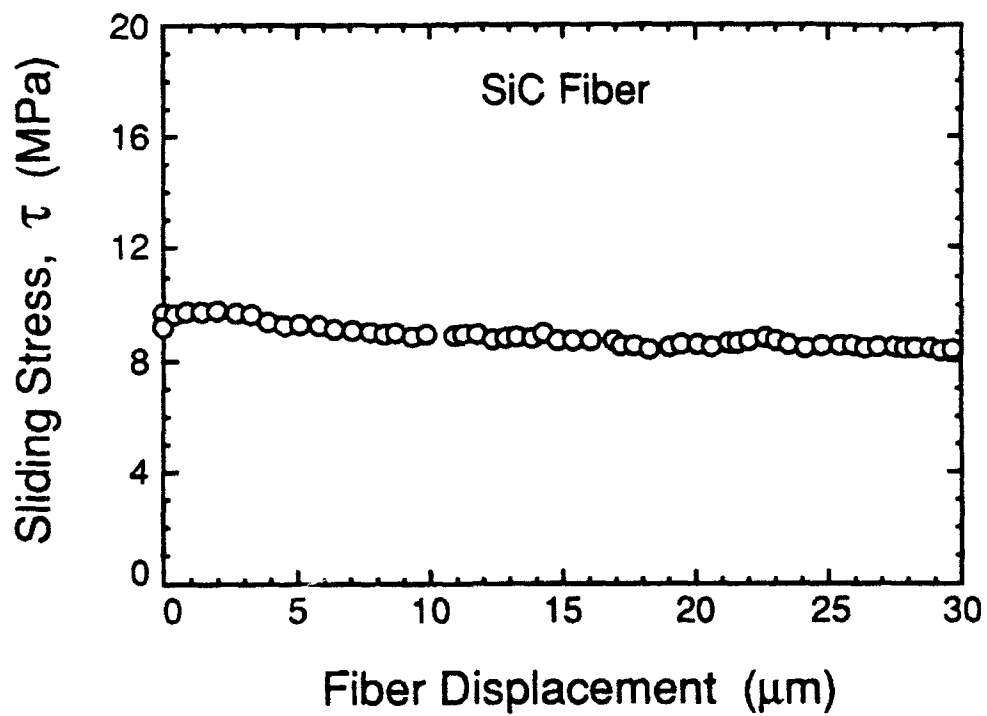


Fig 2.6b

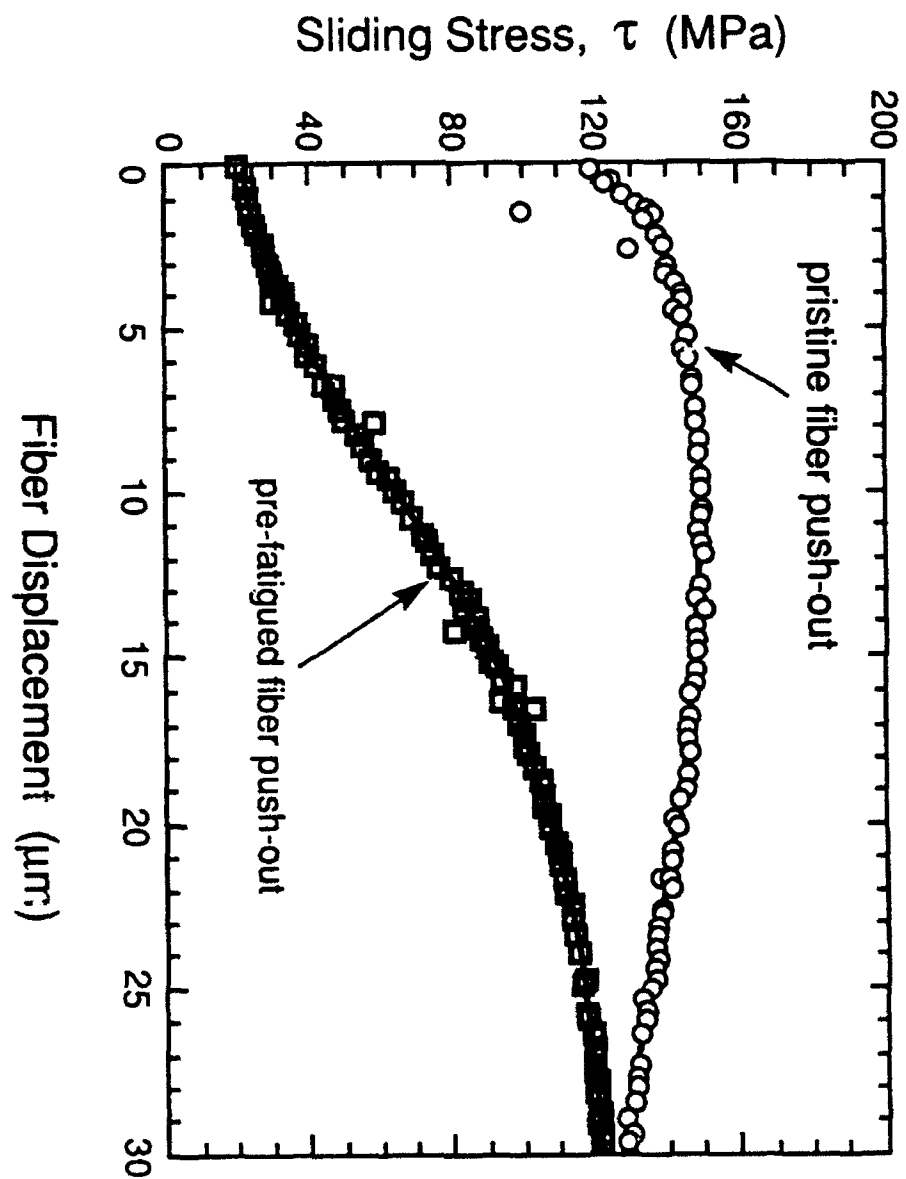


Fig 2.6c

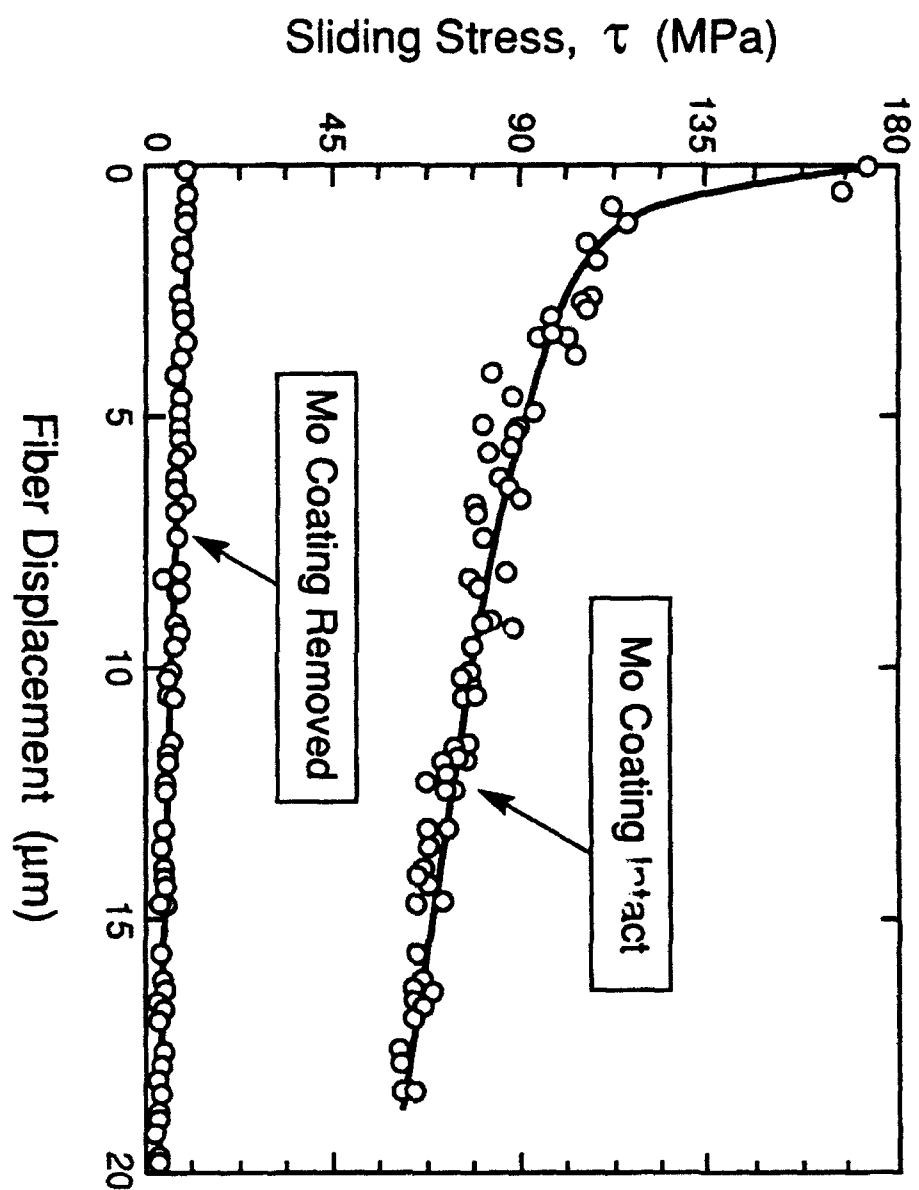


Fig 2.6 d

## BEAM BENDING

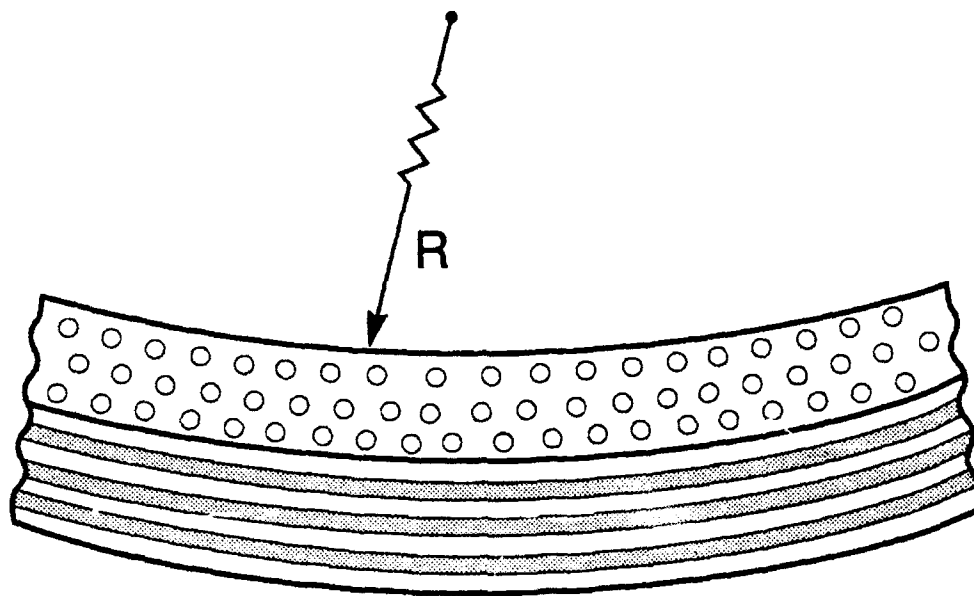


Figure 3.1

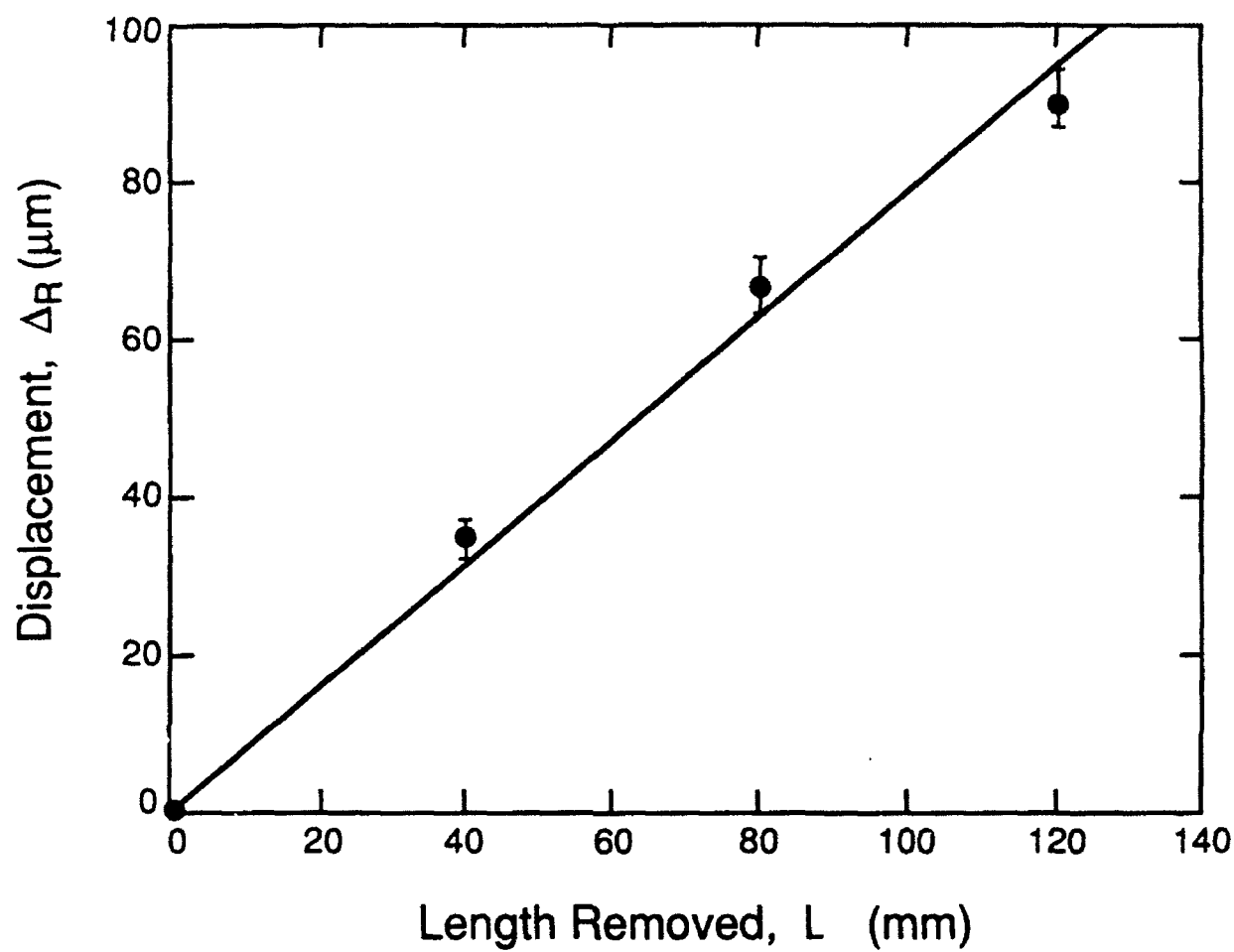


Figure 3.2

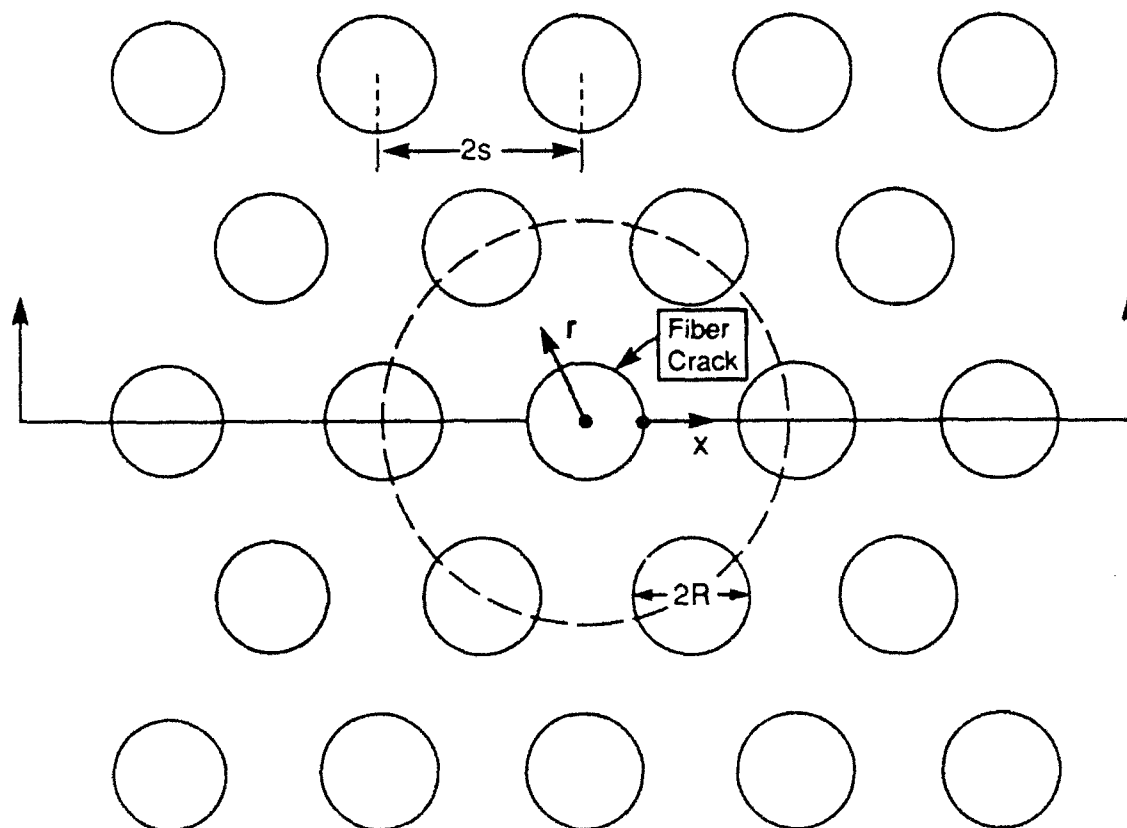
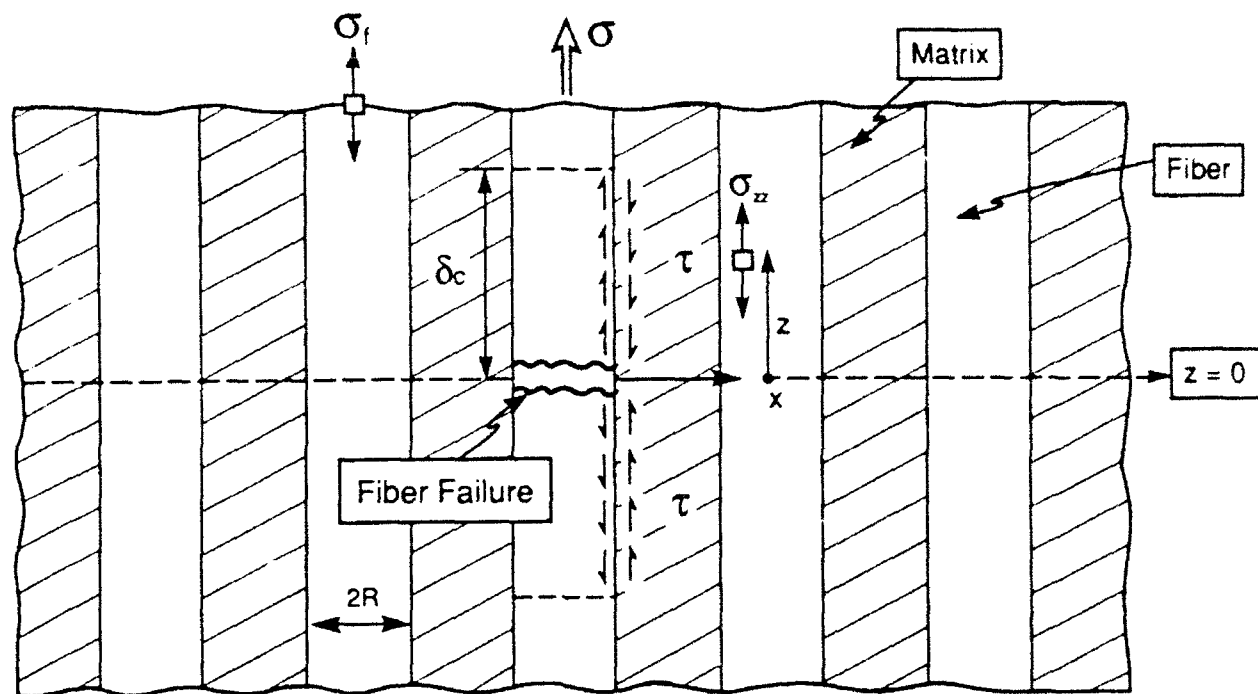
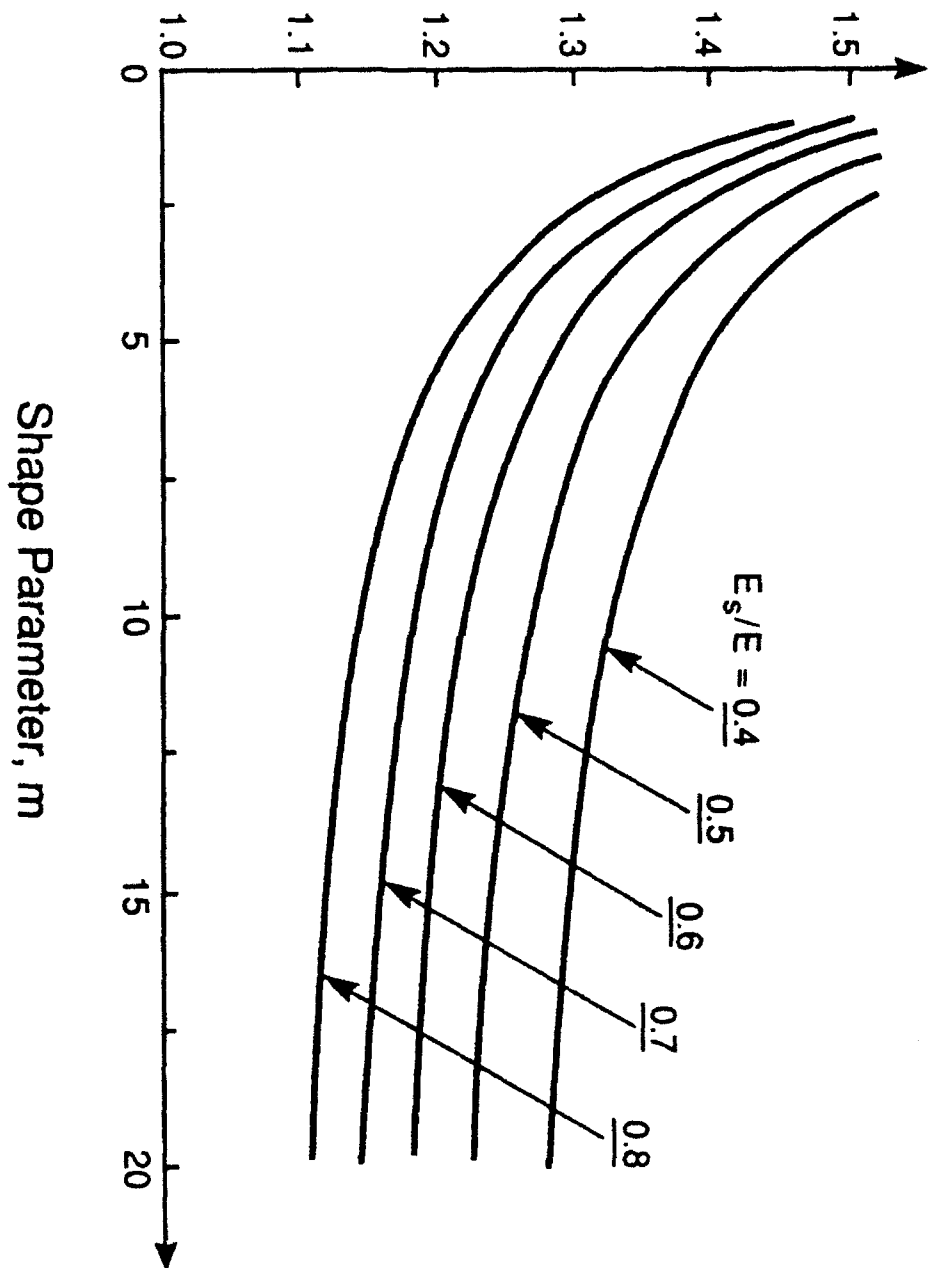


Figure 4.1



Normalized Ultimate Flexural Strength,  
 $S_F / S_U$



Shape Parameter,  $m$

Fig 4.2

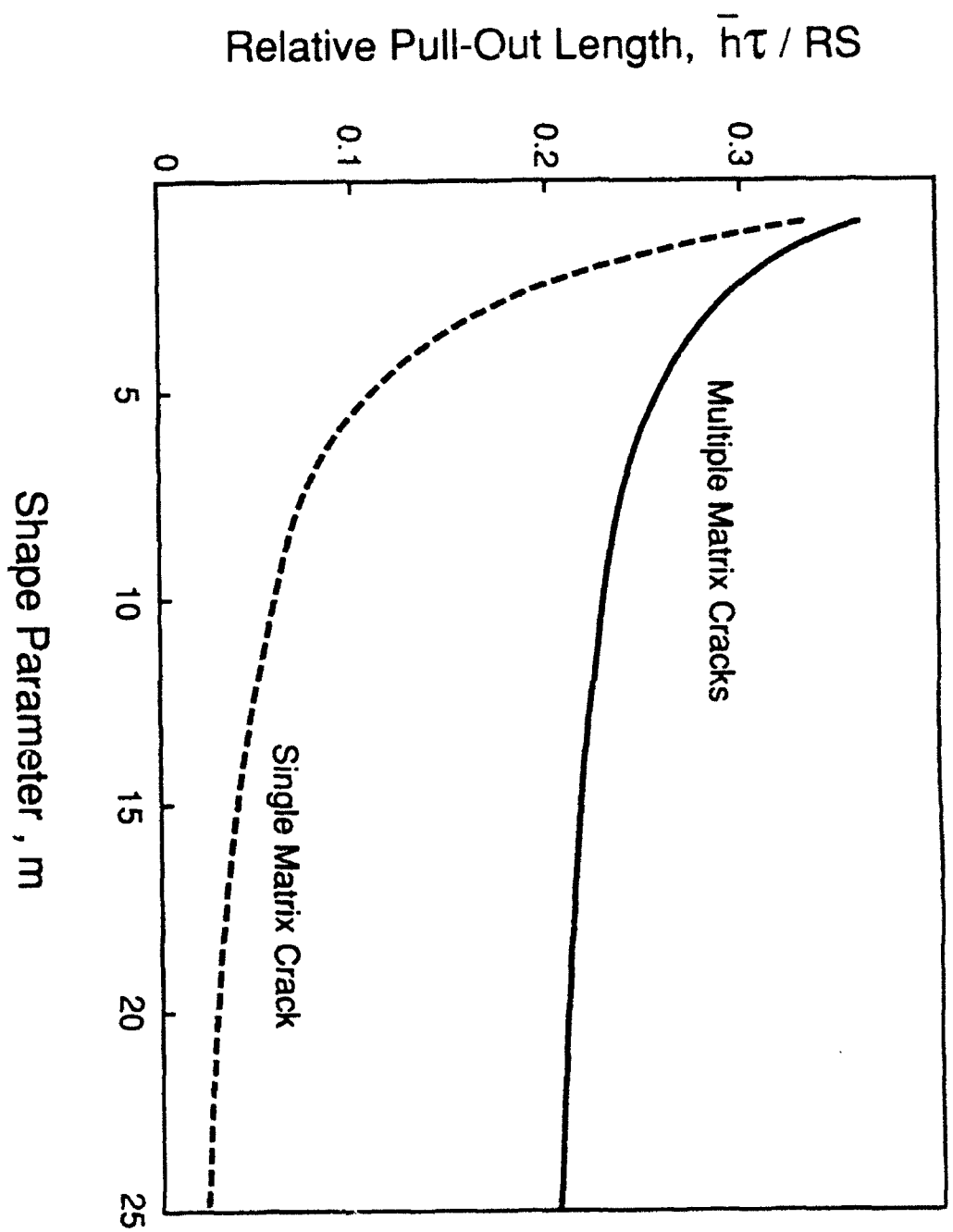
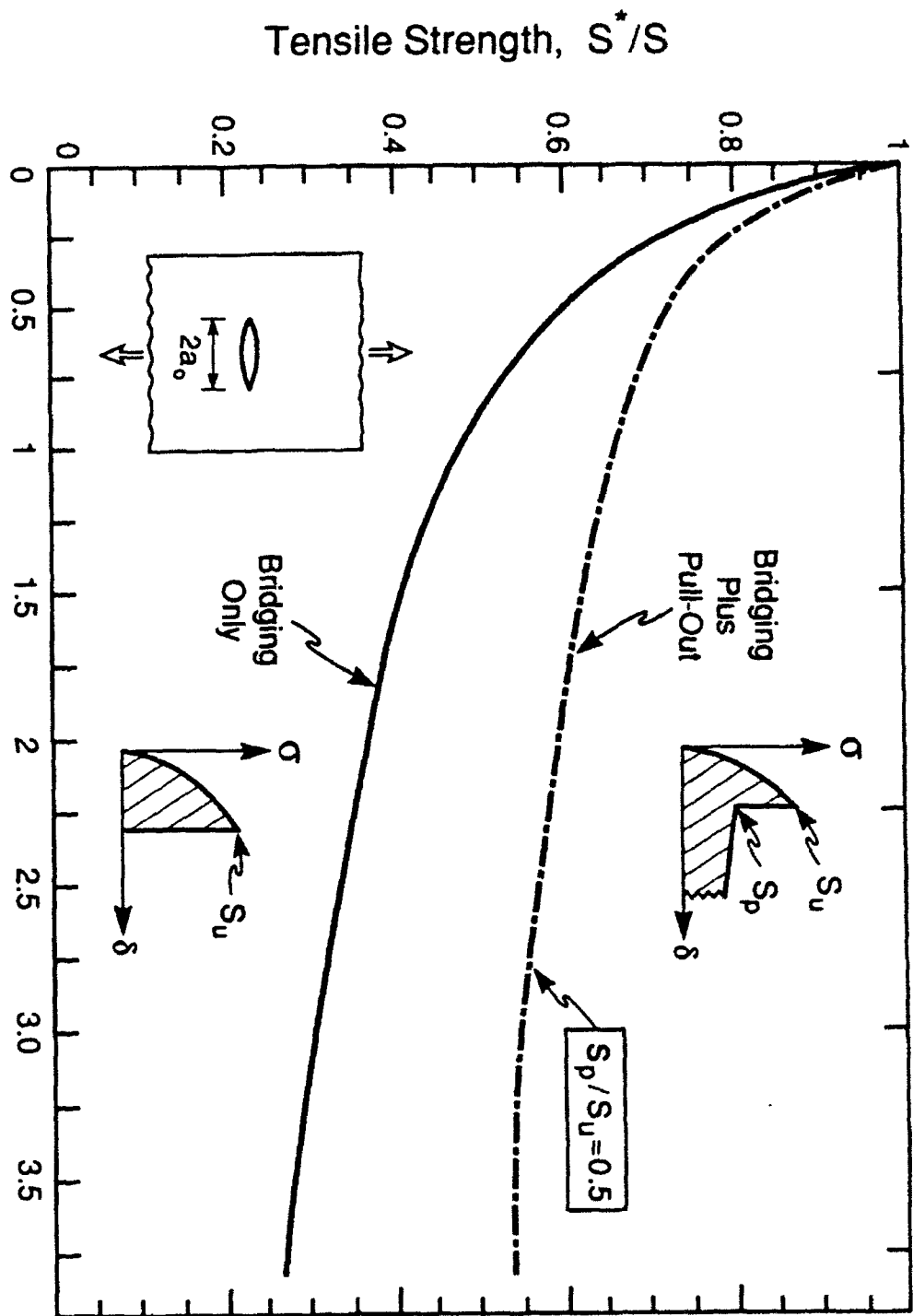


Figure 4.3



$$\text{Flaw Index, } A_b = \frac{f^2}{(1-f)^2} \left( \frac{E_f E}{E_m^2} \right) \left( \frac{a_0 \tau}{RS} \right)$$

Figure 4. 4

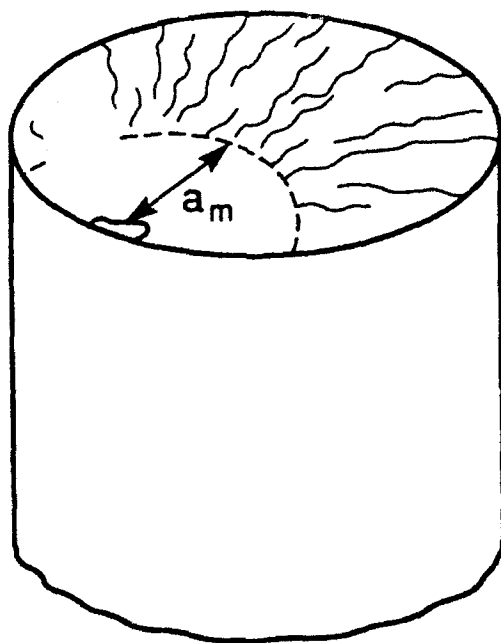


Figure 4.5

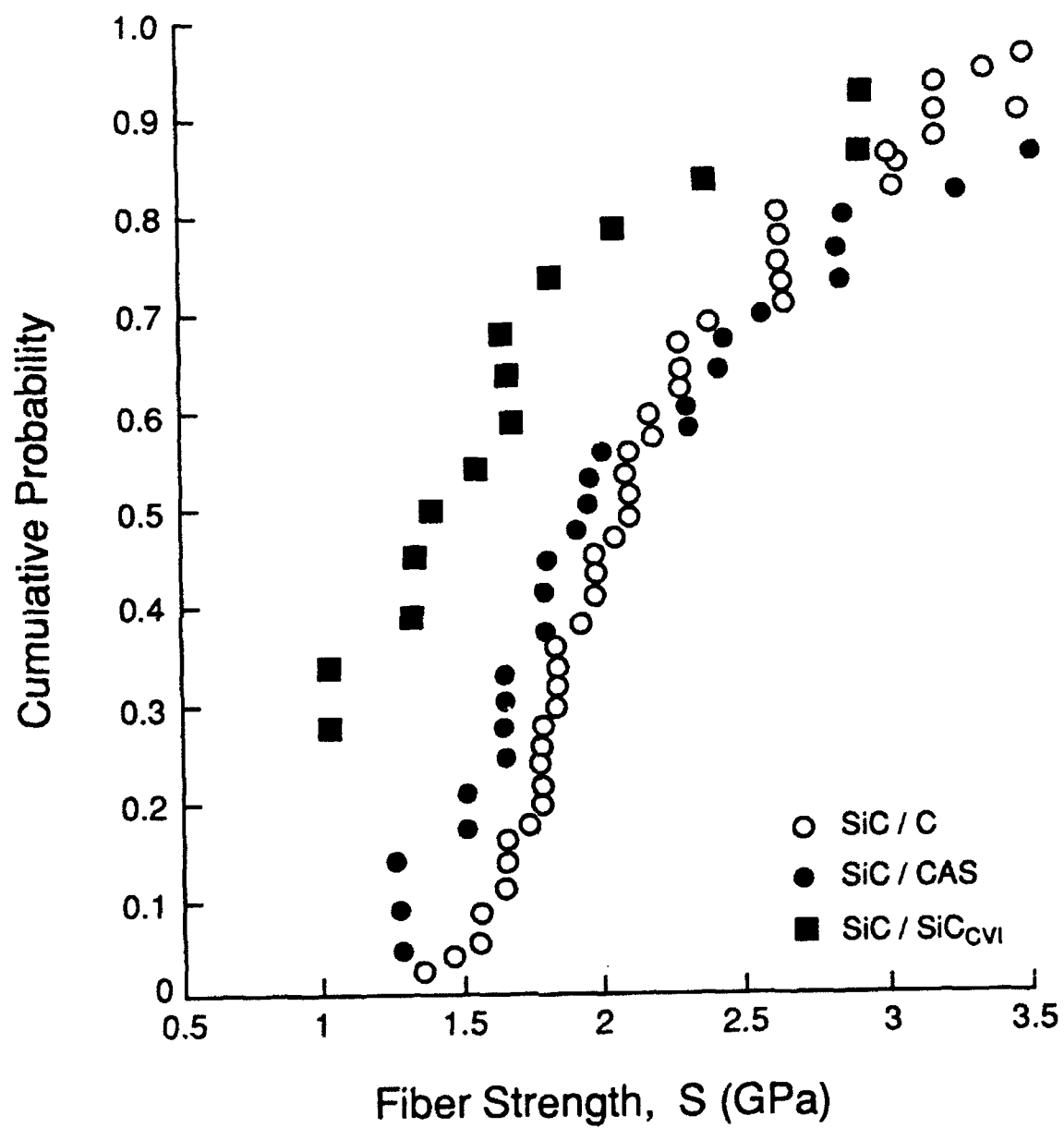


Fig 4.6

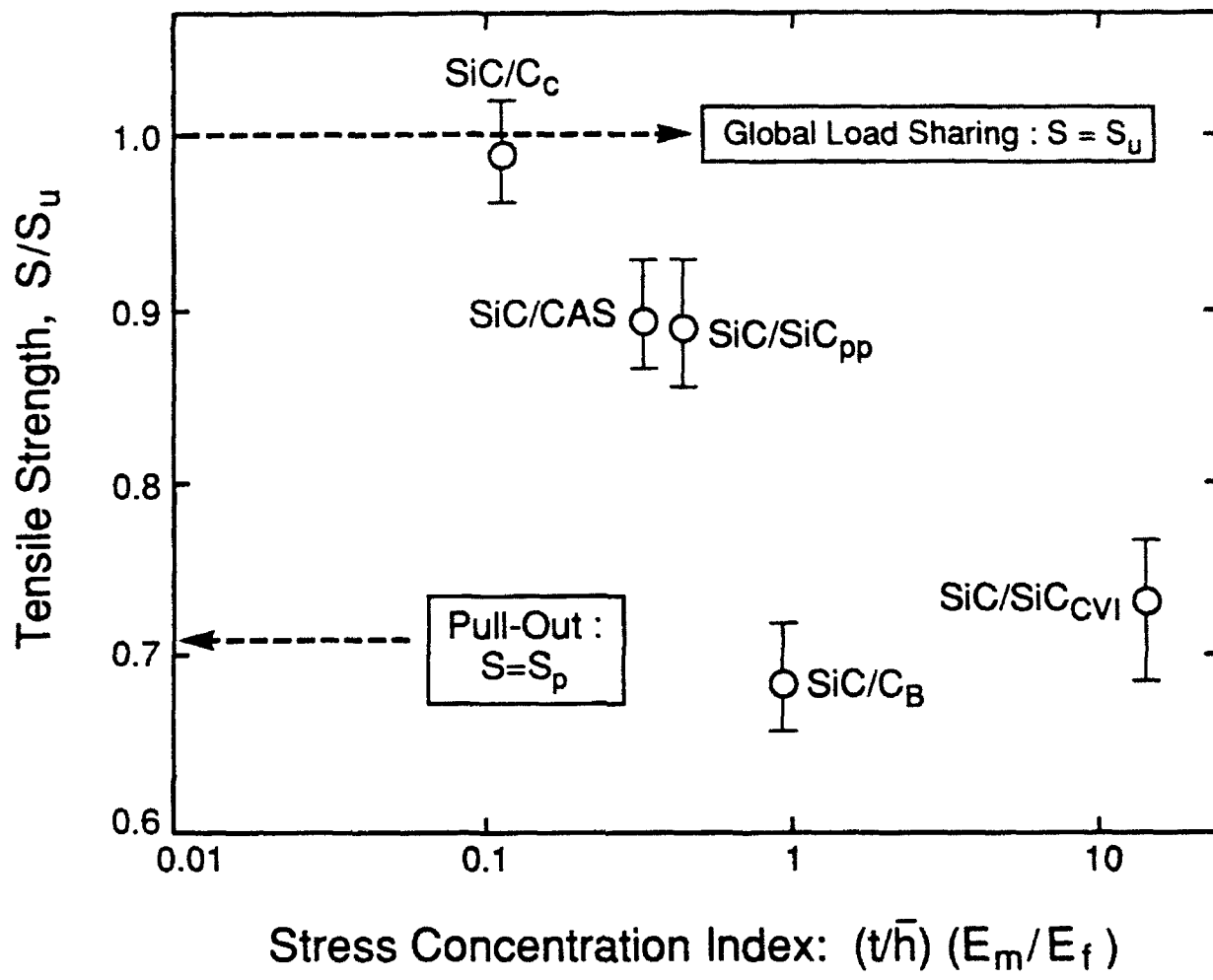


Figure 4. 7

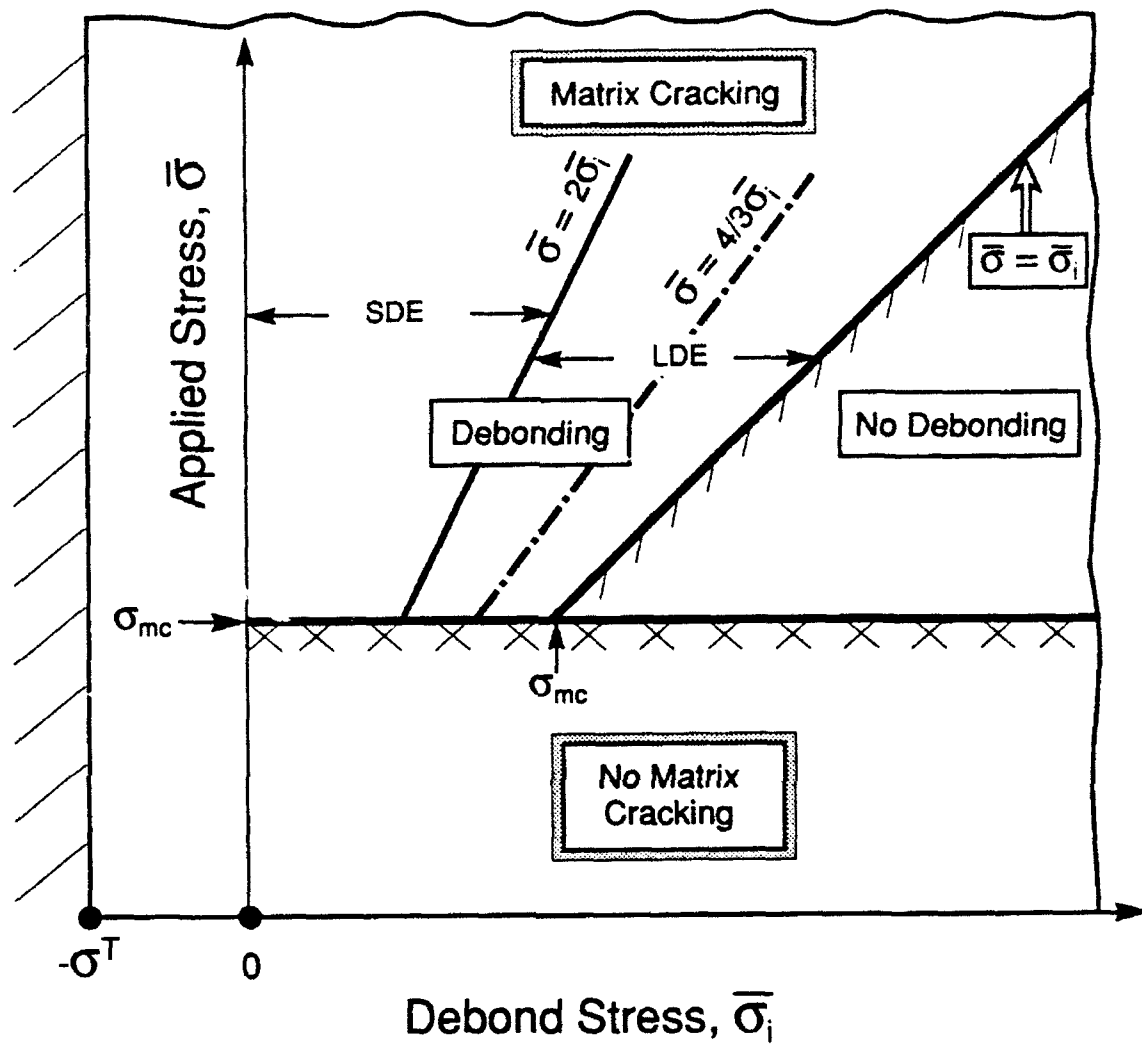


Figure 5.1

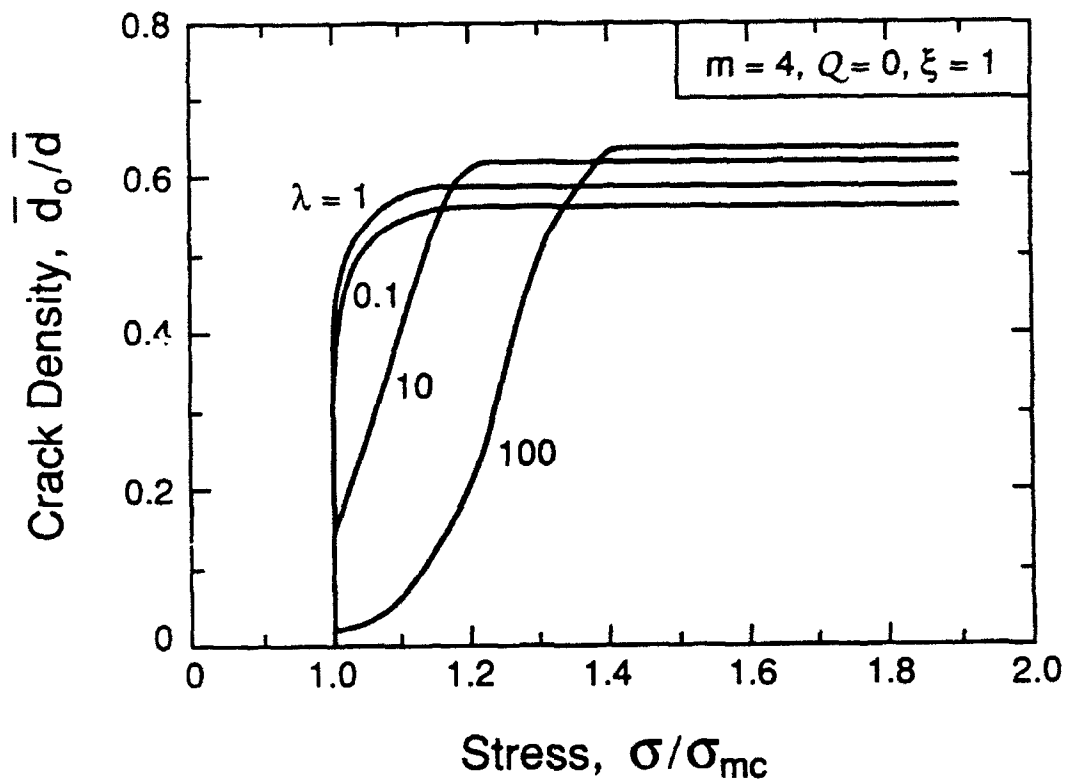


Fig 5.2a



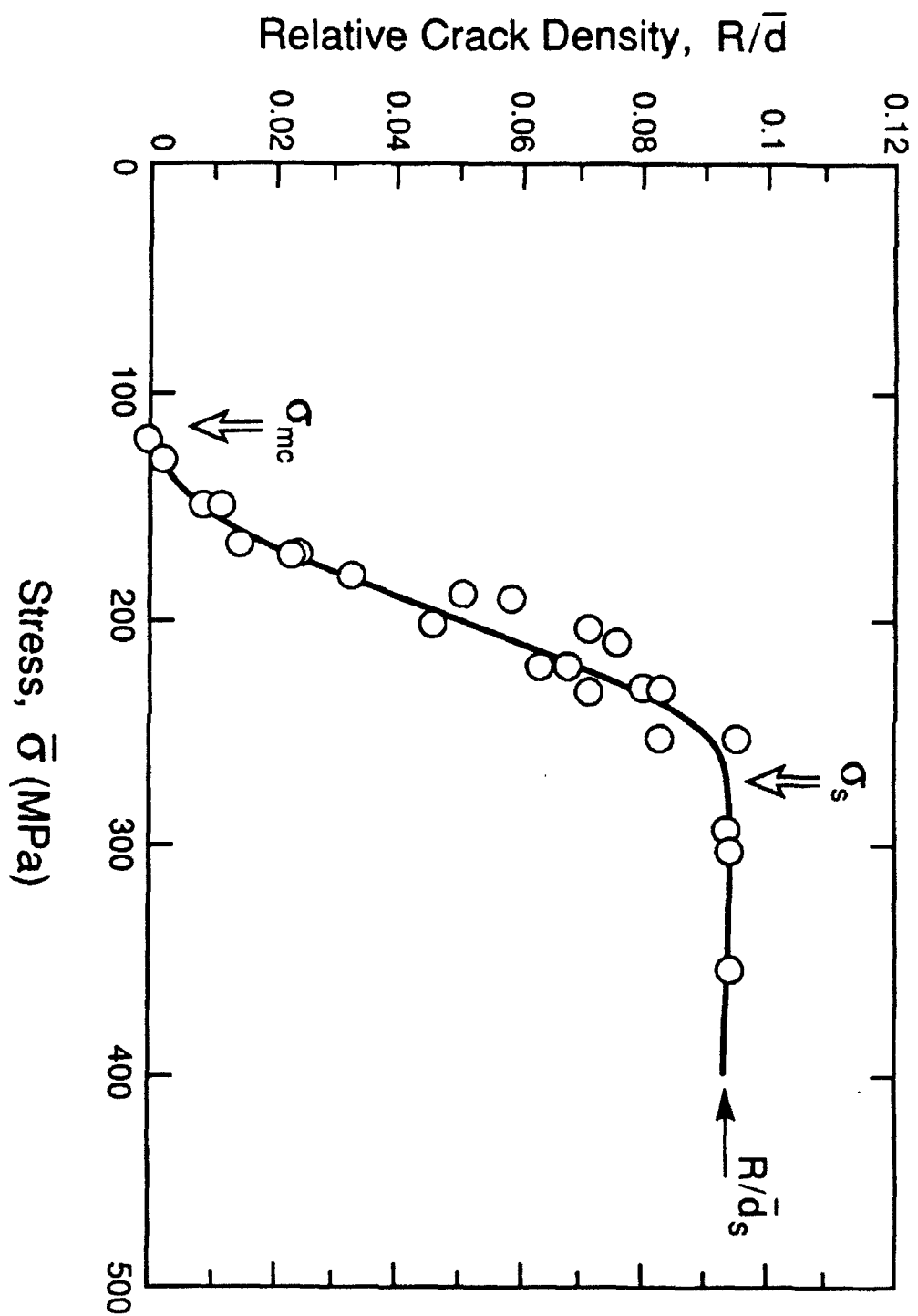


Fig 5 2 b

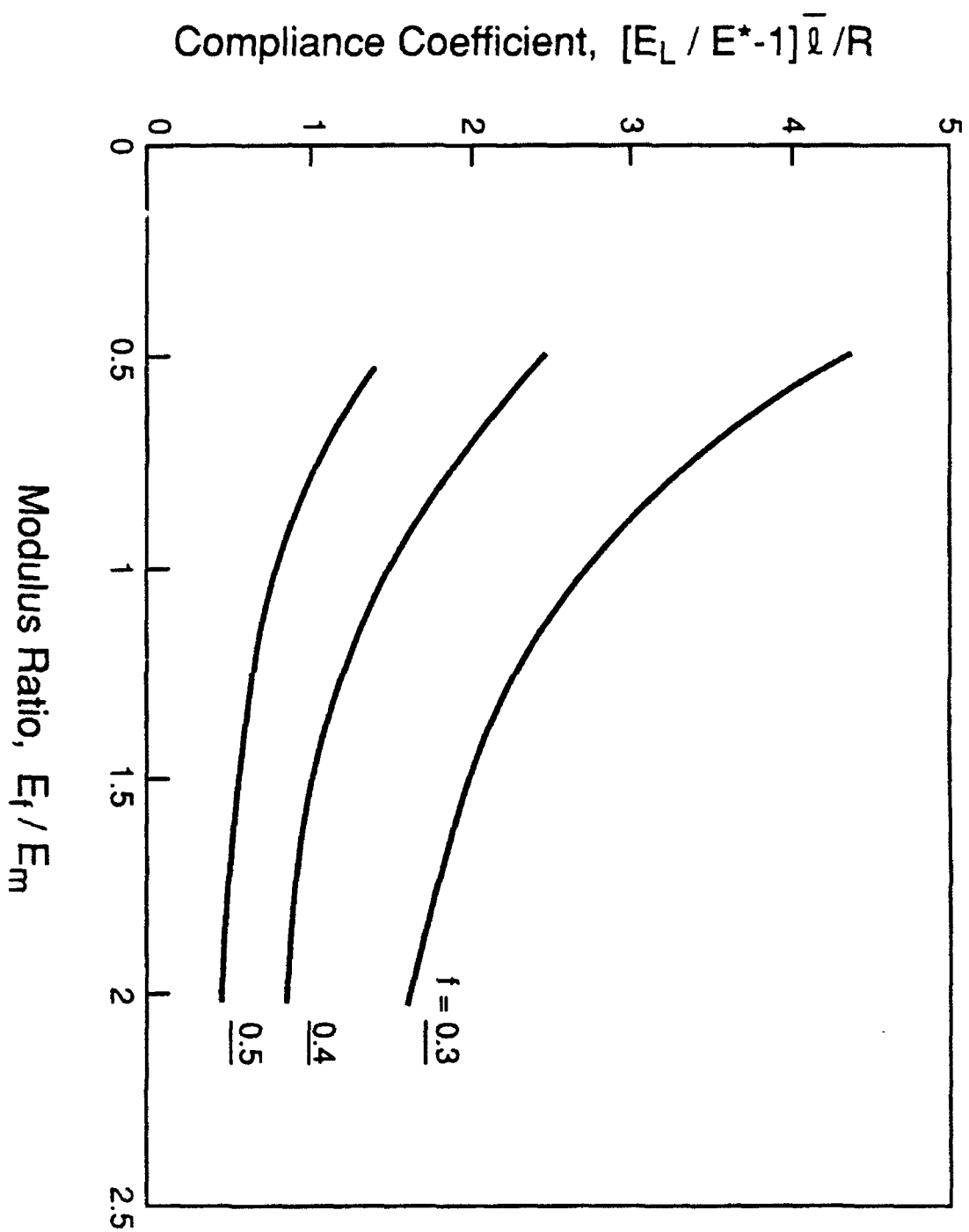
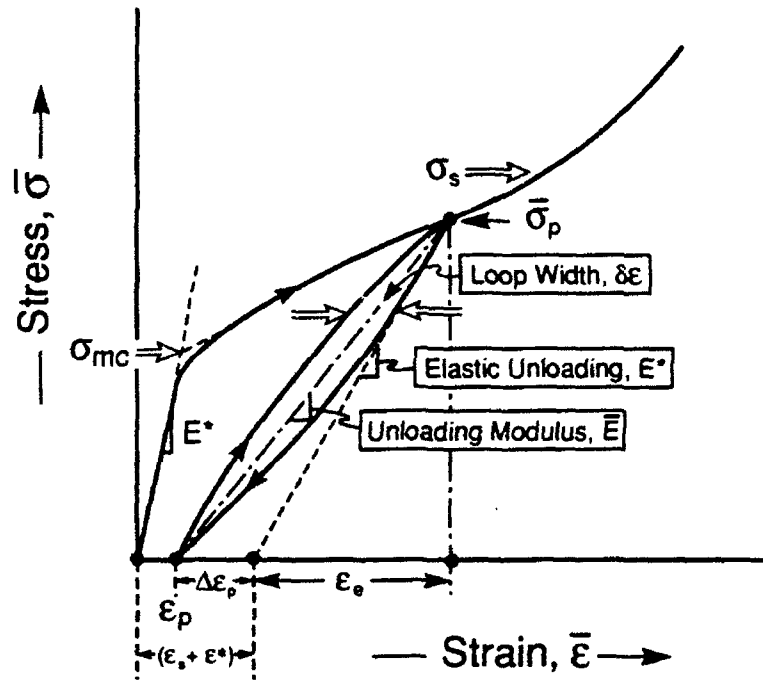
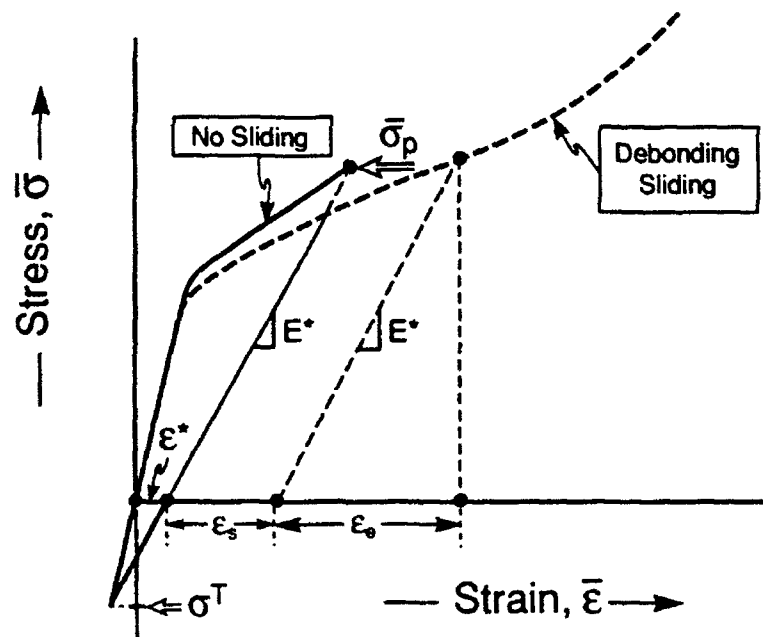


Figure 5.3



a) Debonding and Sliding Interface



b) Behavior When Debonding Inhibited

Figure 5.4

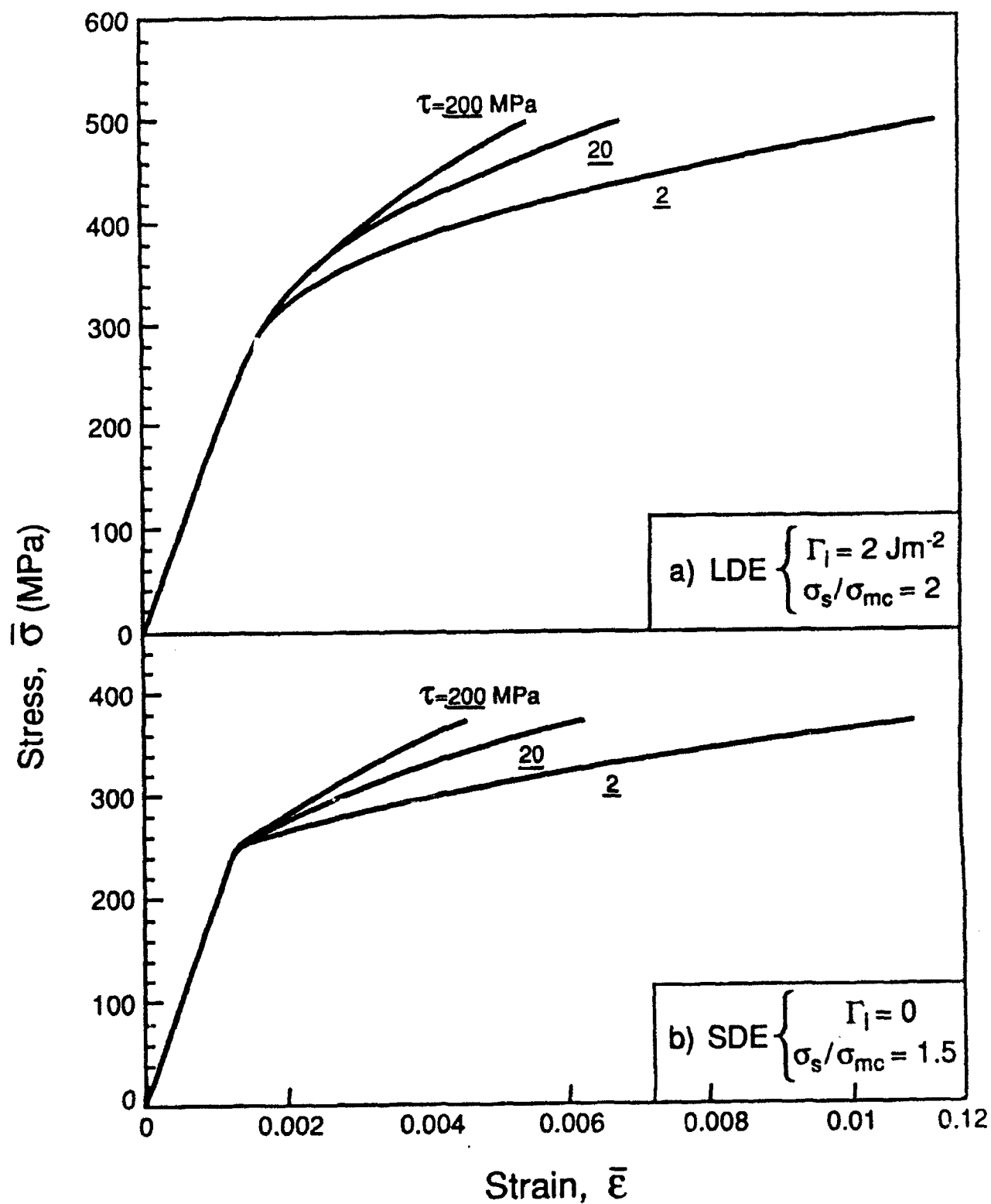


Figure 5.5

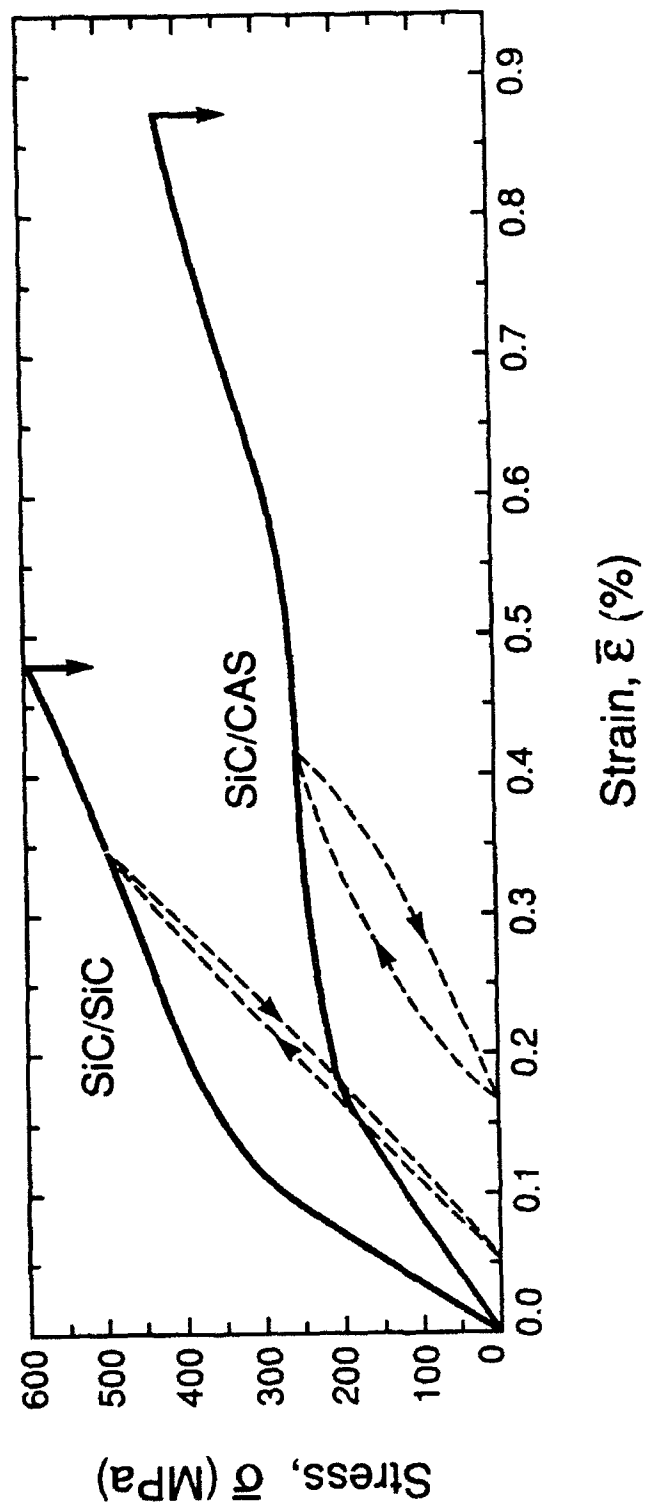


Fig 5.6

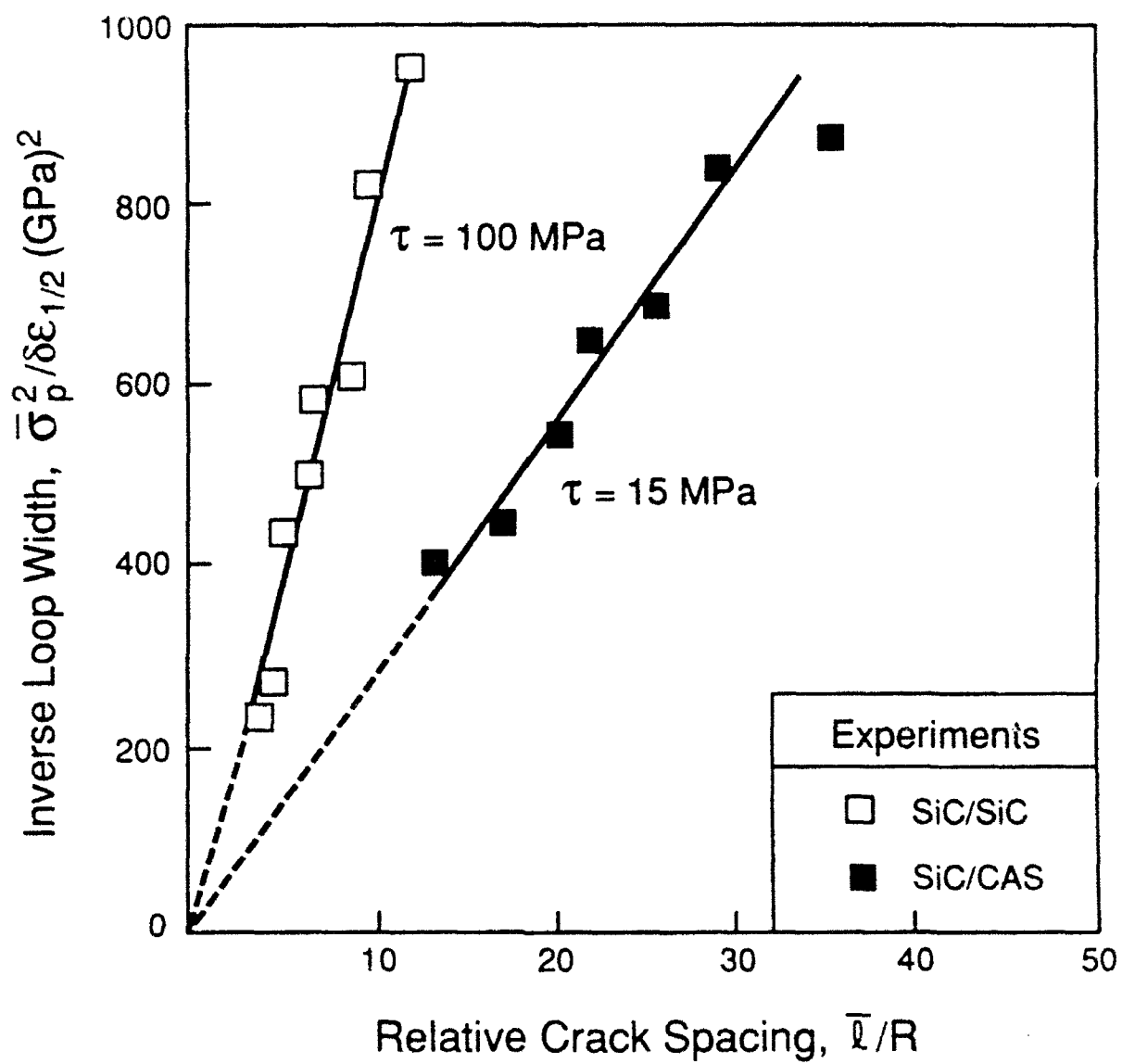


Fig 57

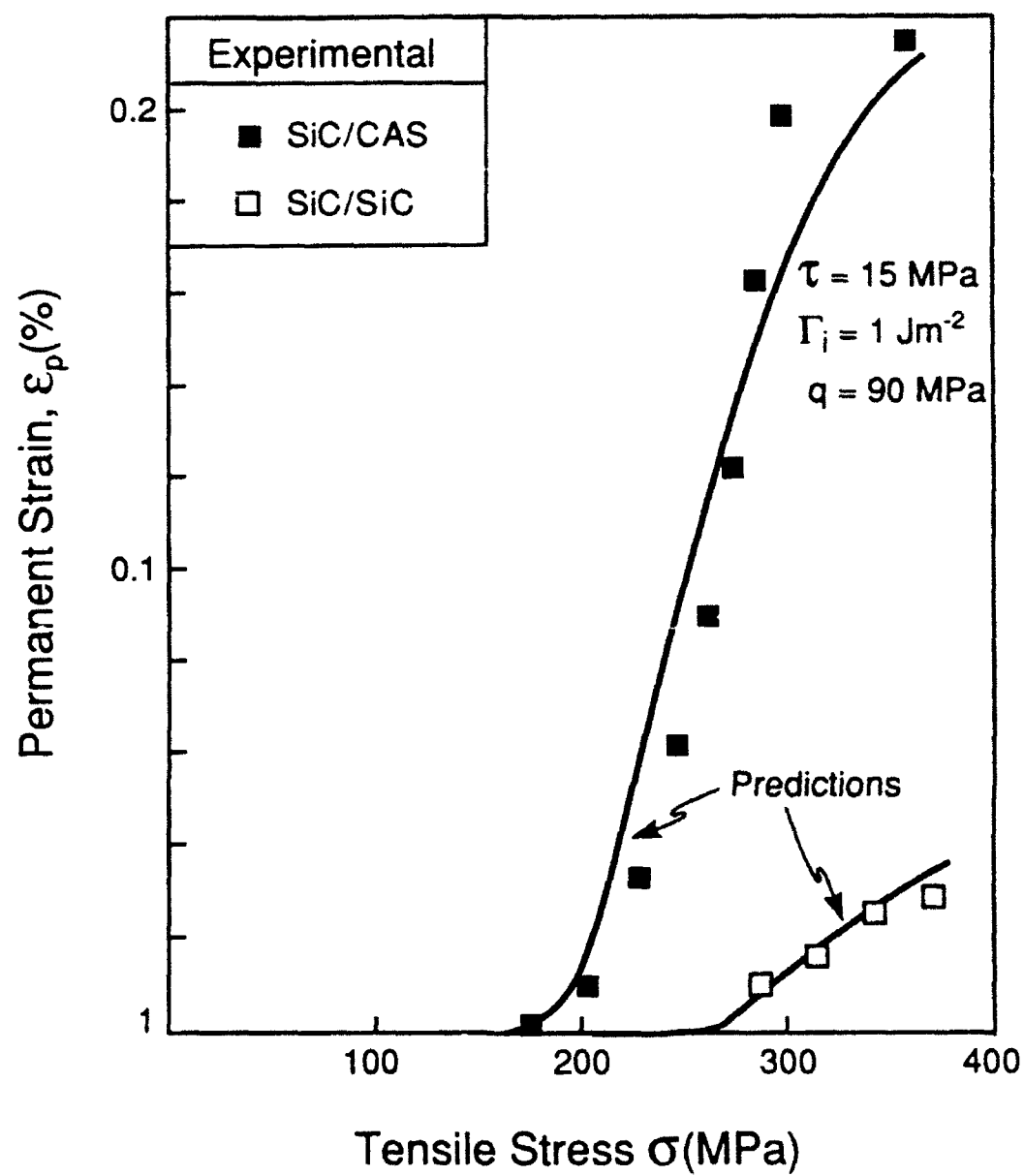


Fig. 5 8

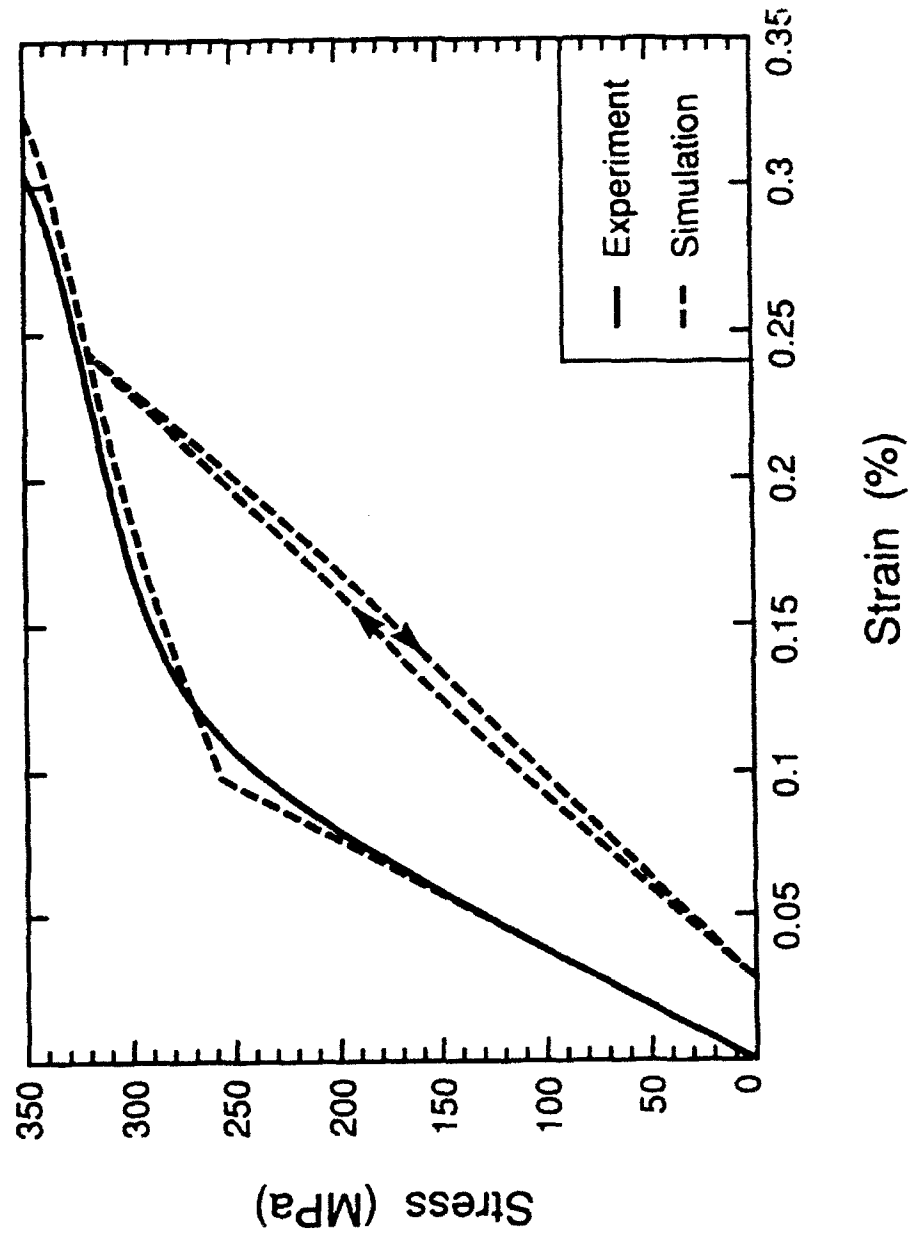


Fig 5.9



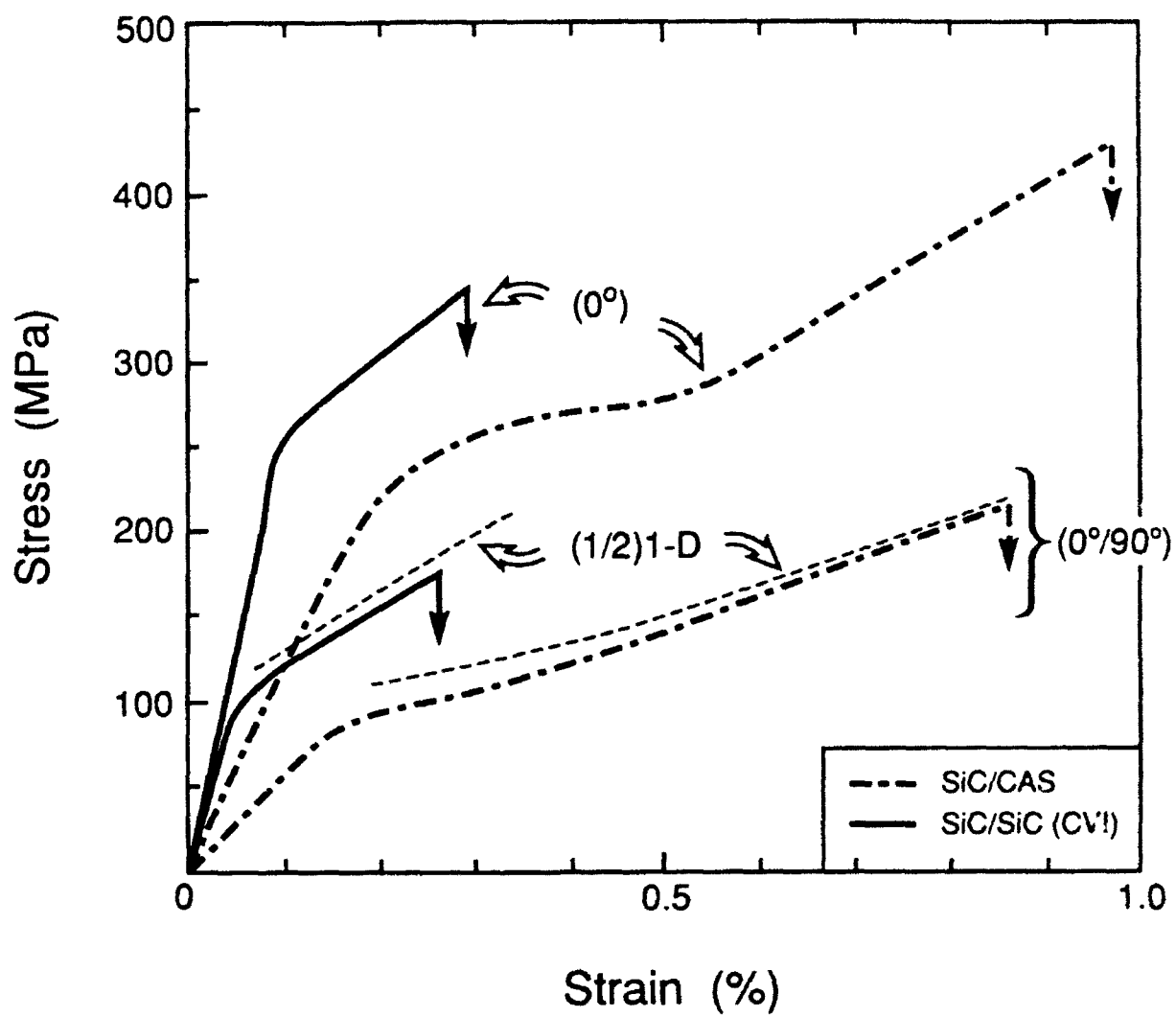


Figure 6.1

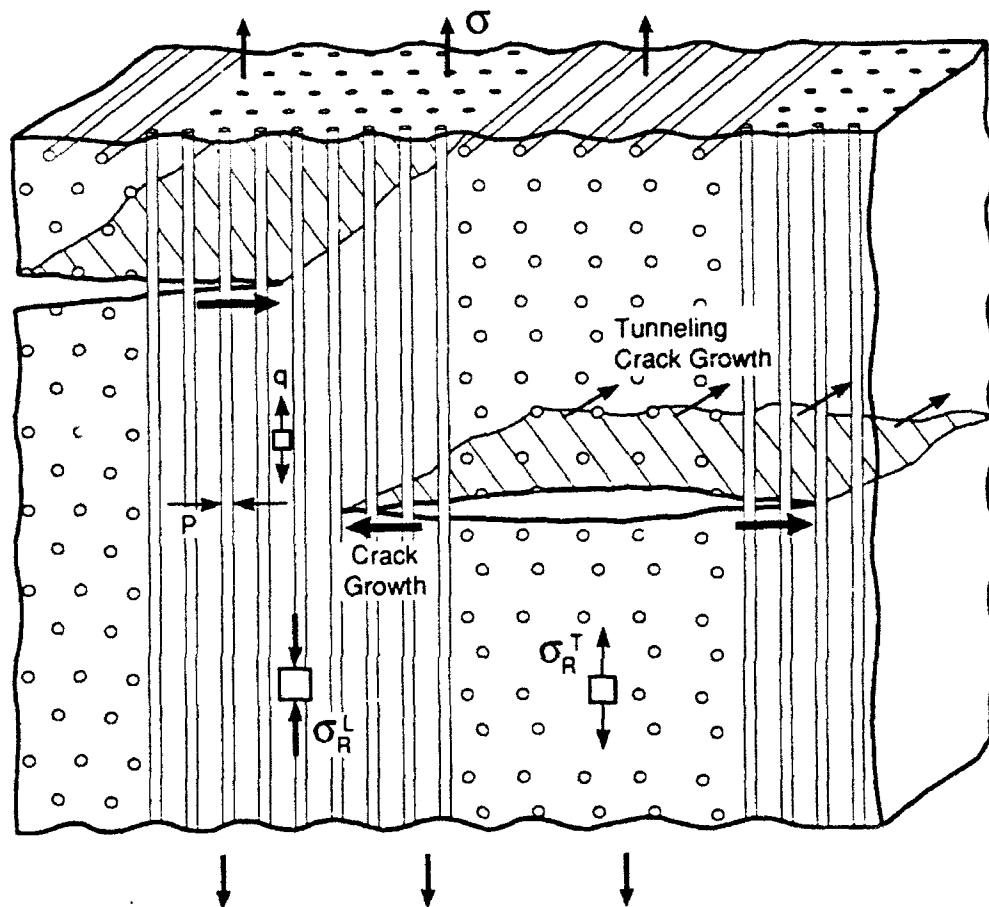


Figure 62

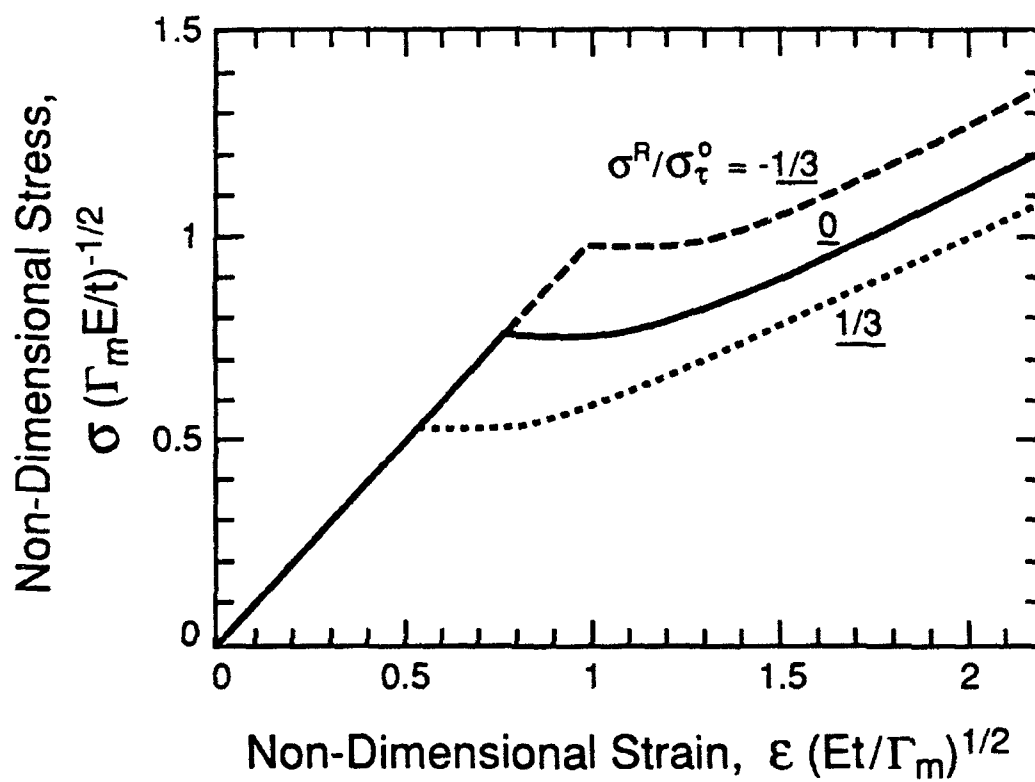


Figure 6.3

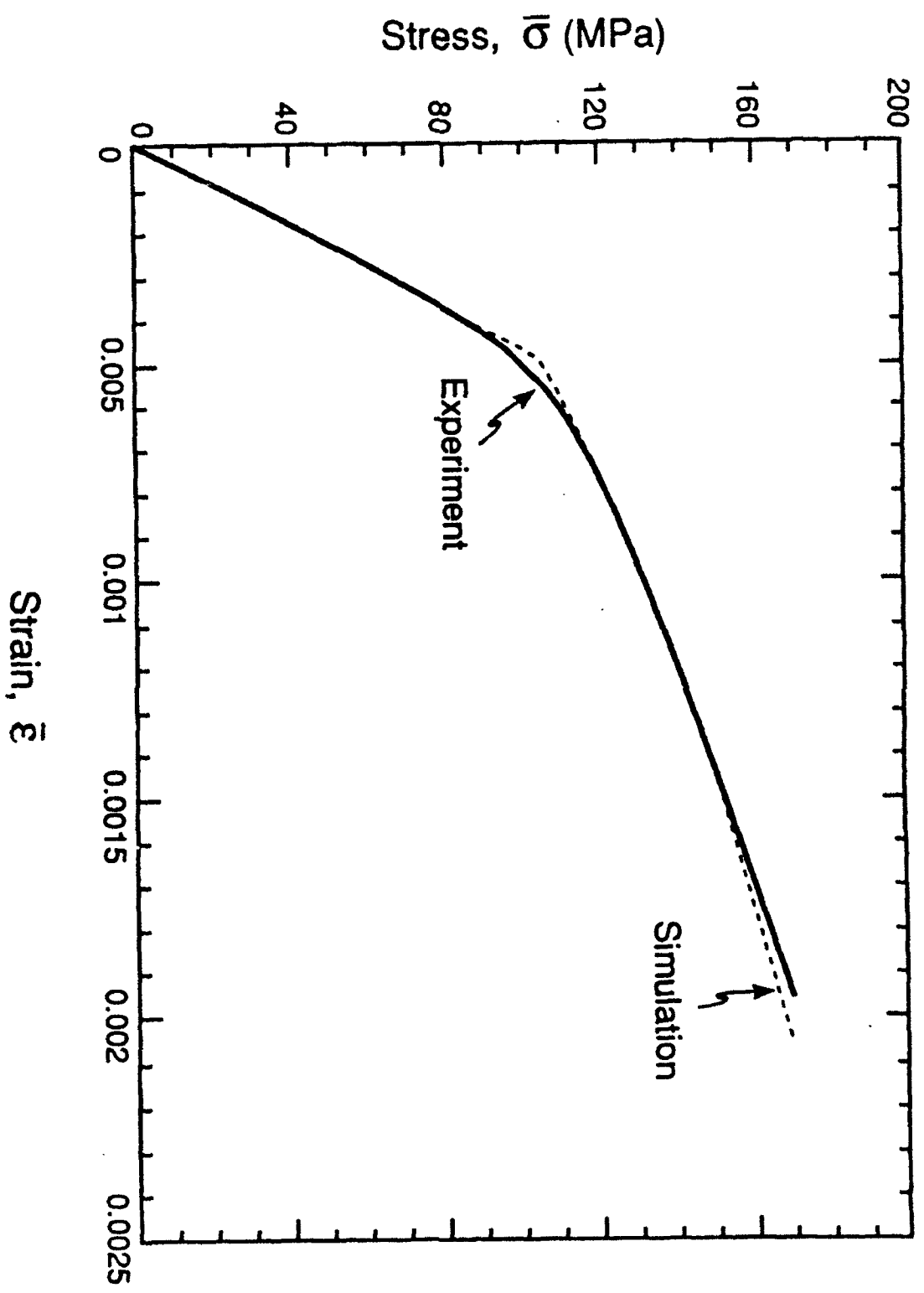
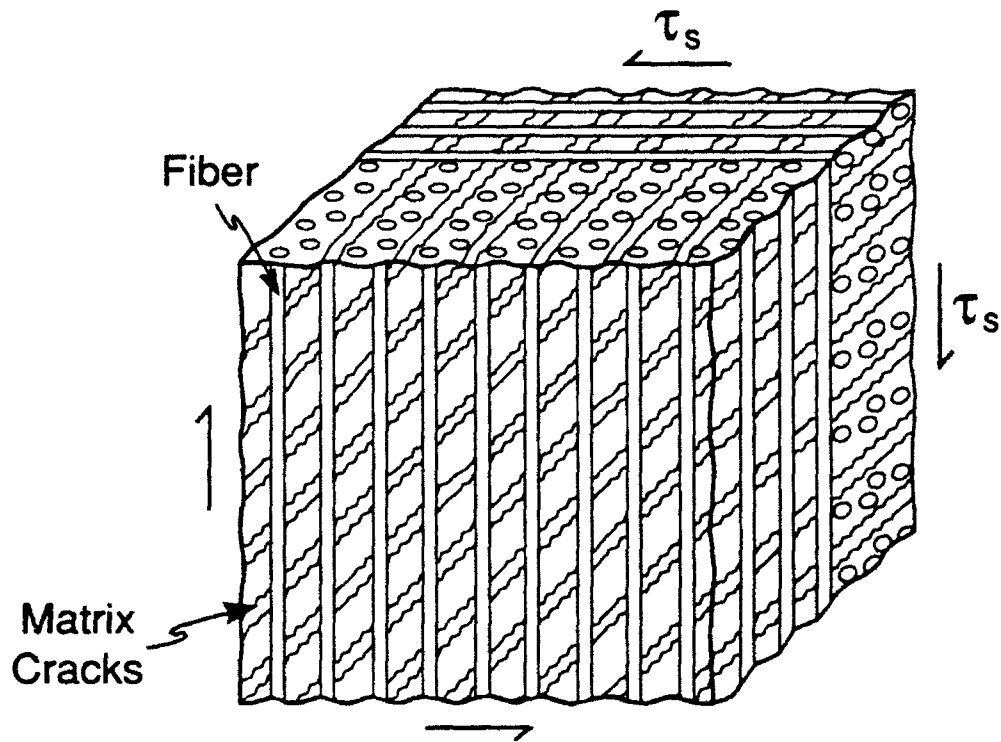
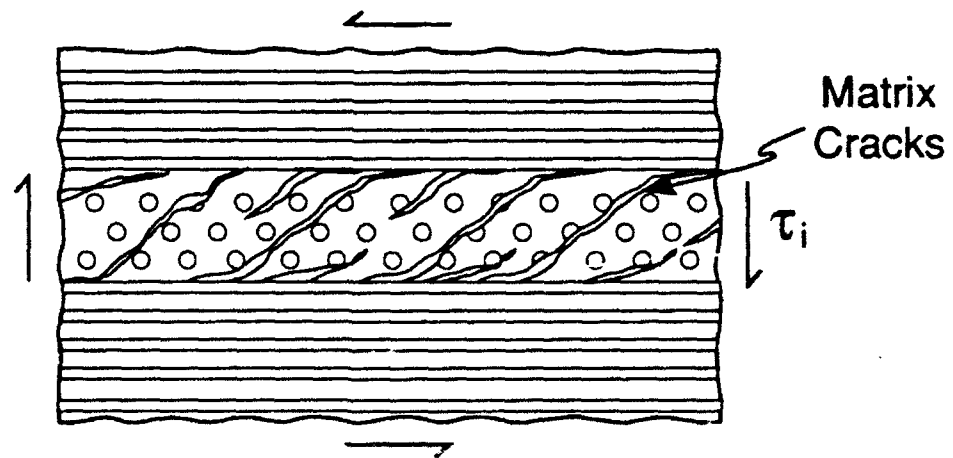


Figure 6.4



a) In-Plane Shear



b) Interlaminar Shear

Figure 6.5

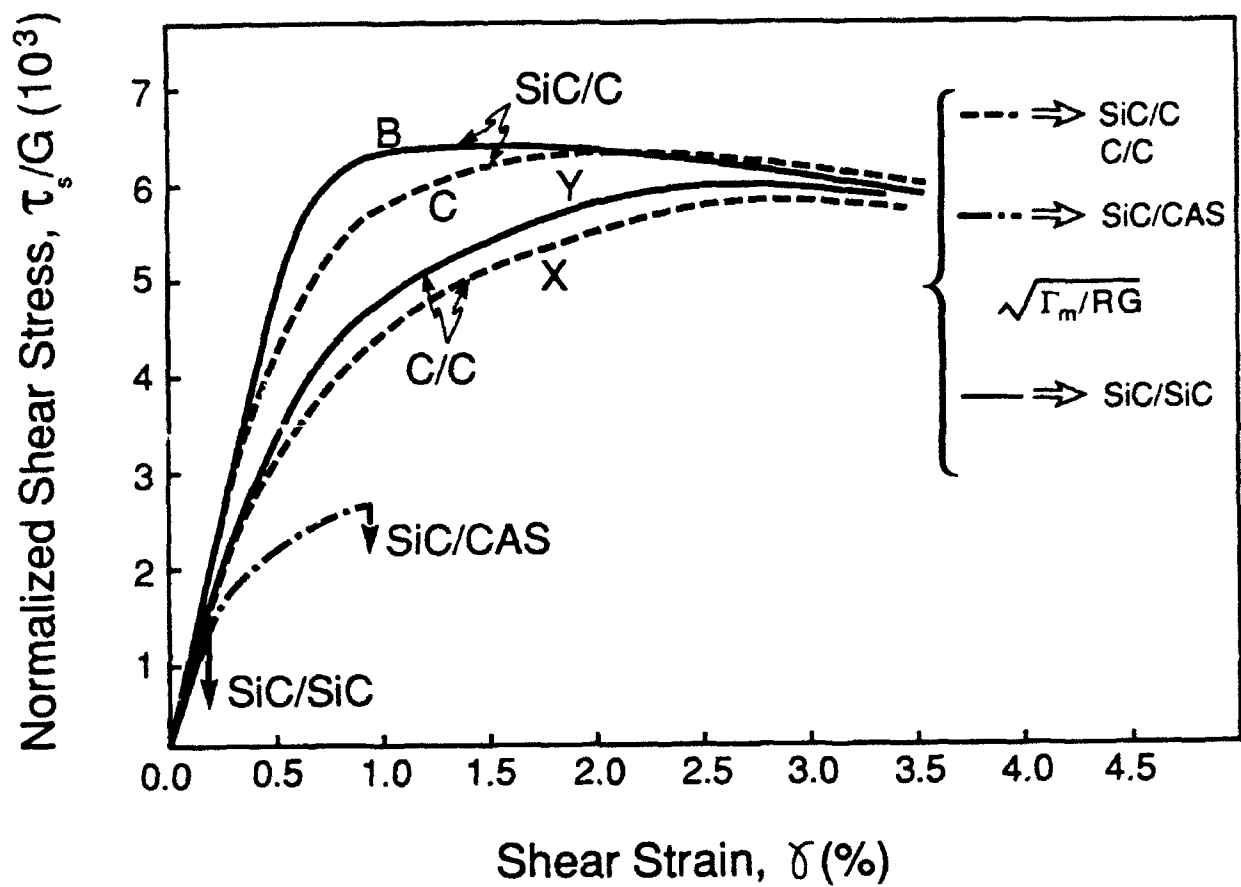


Figure 6.6

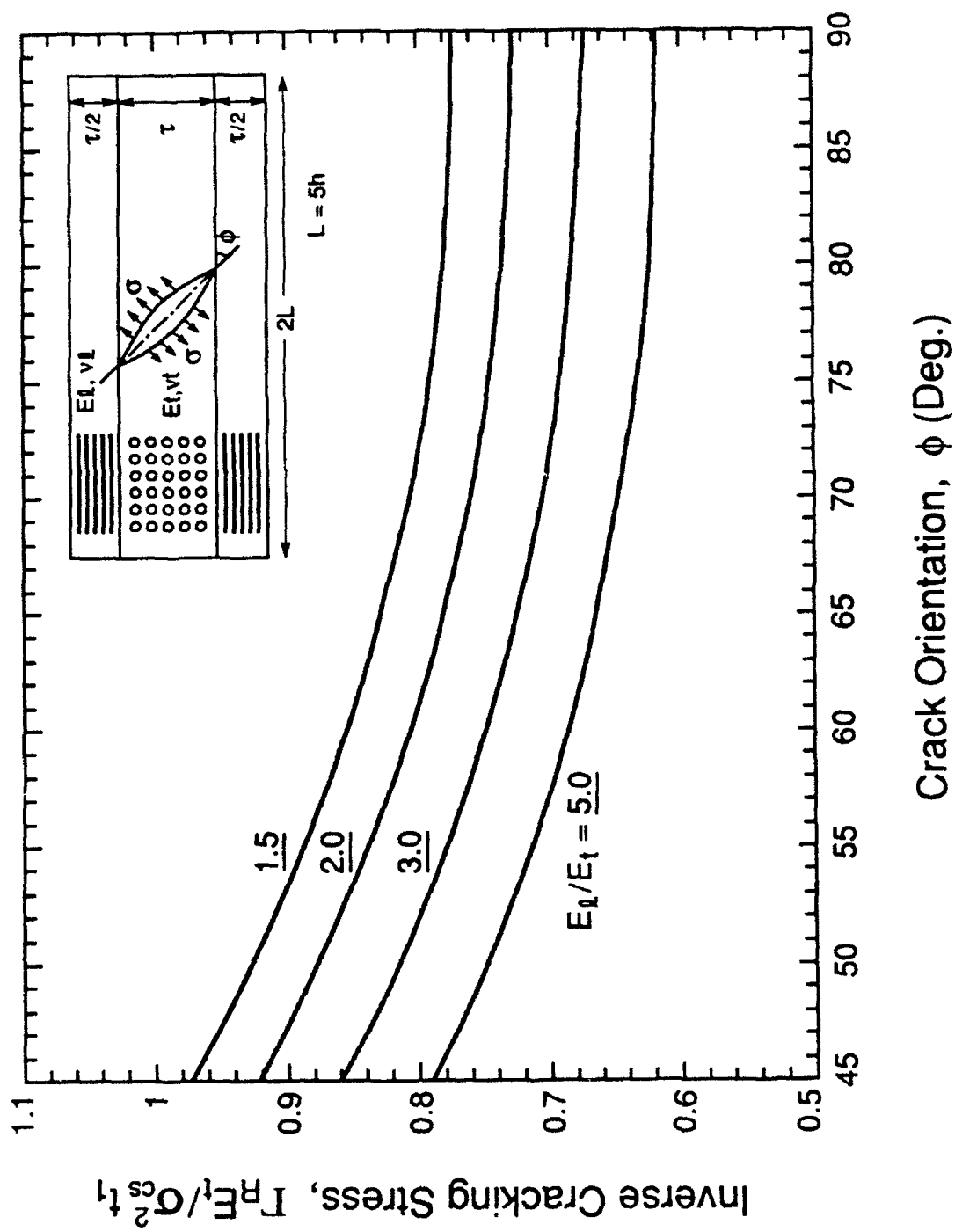
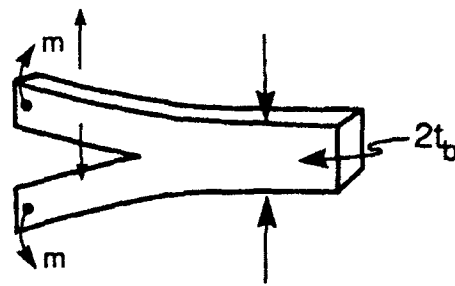
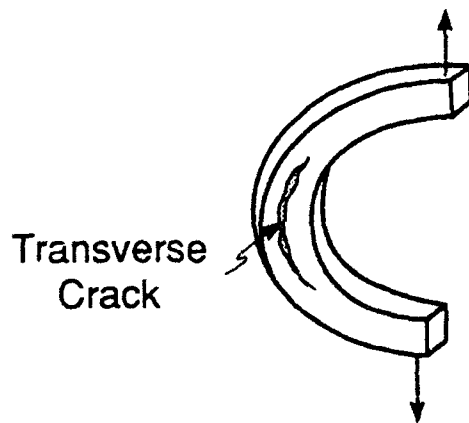


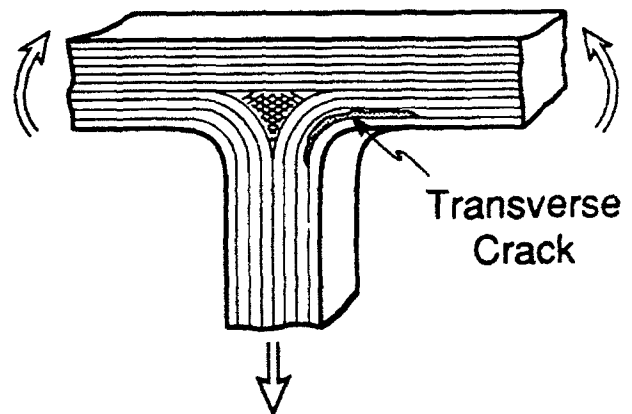
Figure 6.7



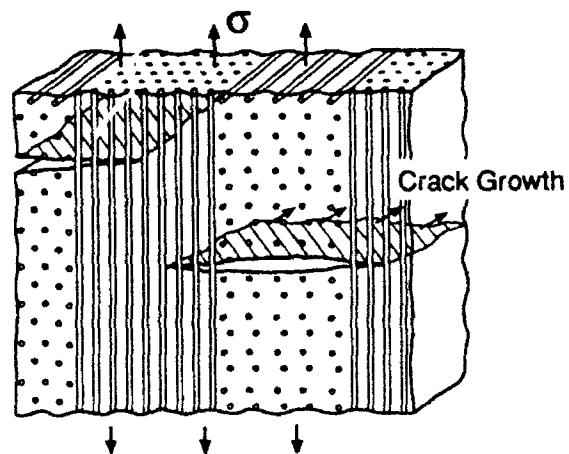
a) Cantilever Beam



b) C-Specimen



c) T - Junction



d) Tunnel Cracks

Figure 6.8



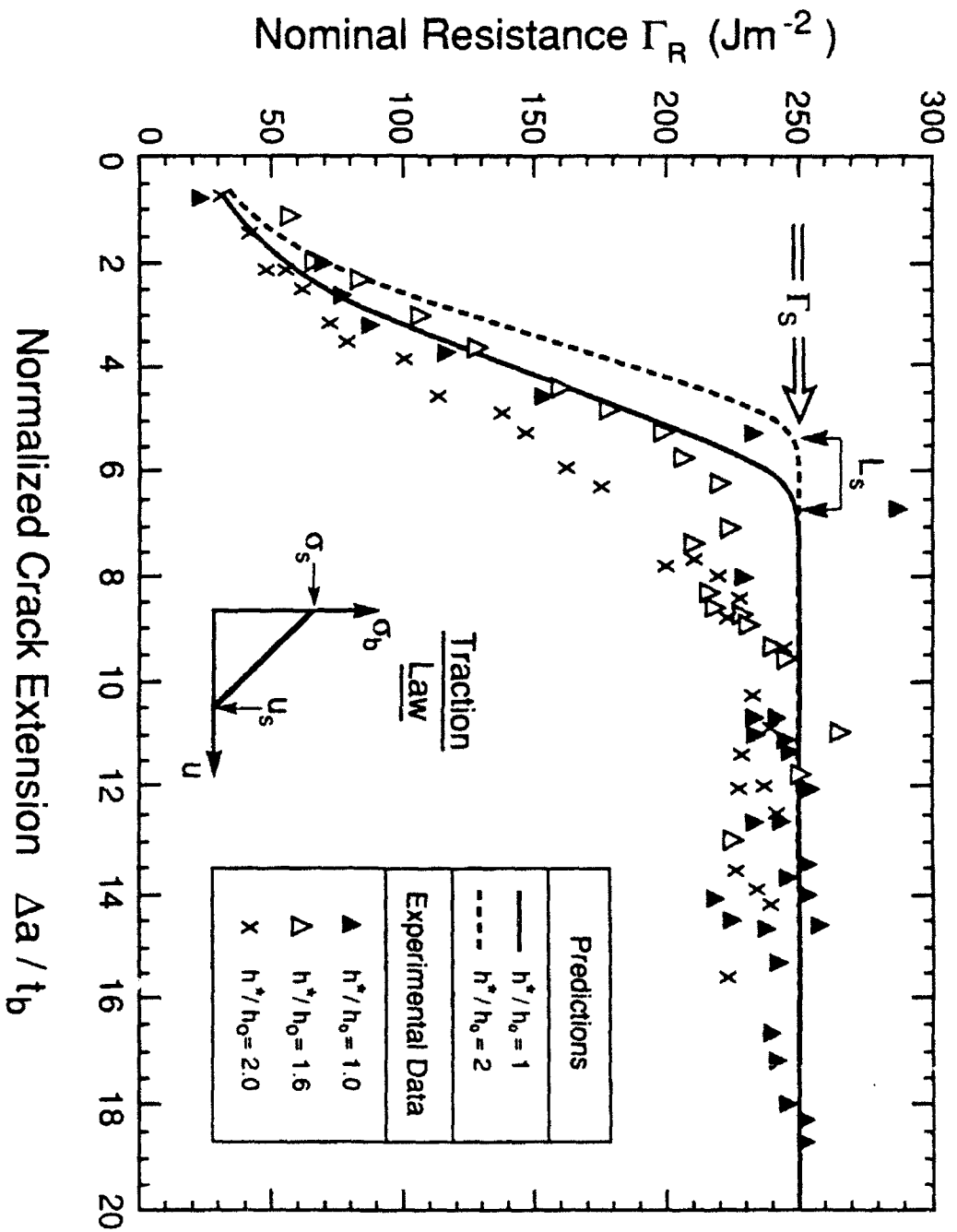


Figure 6.9

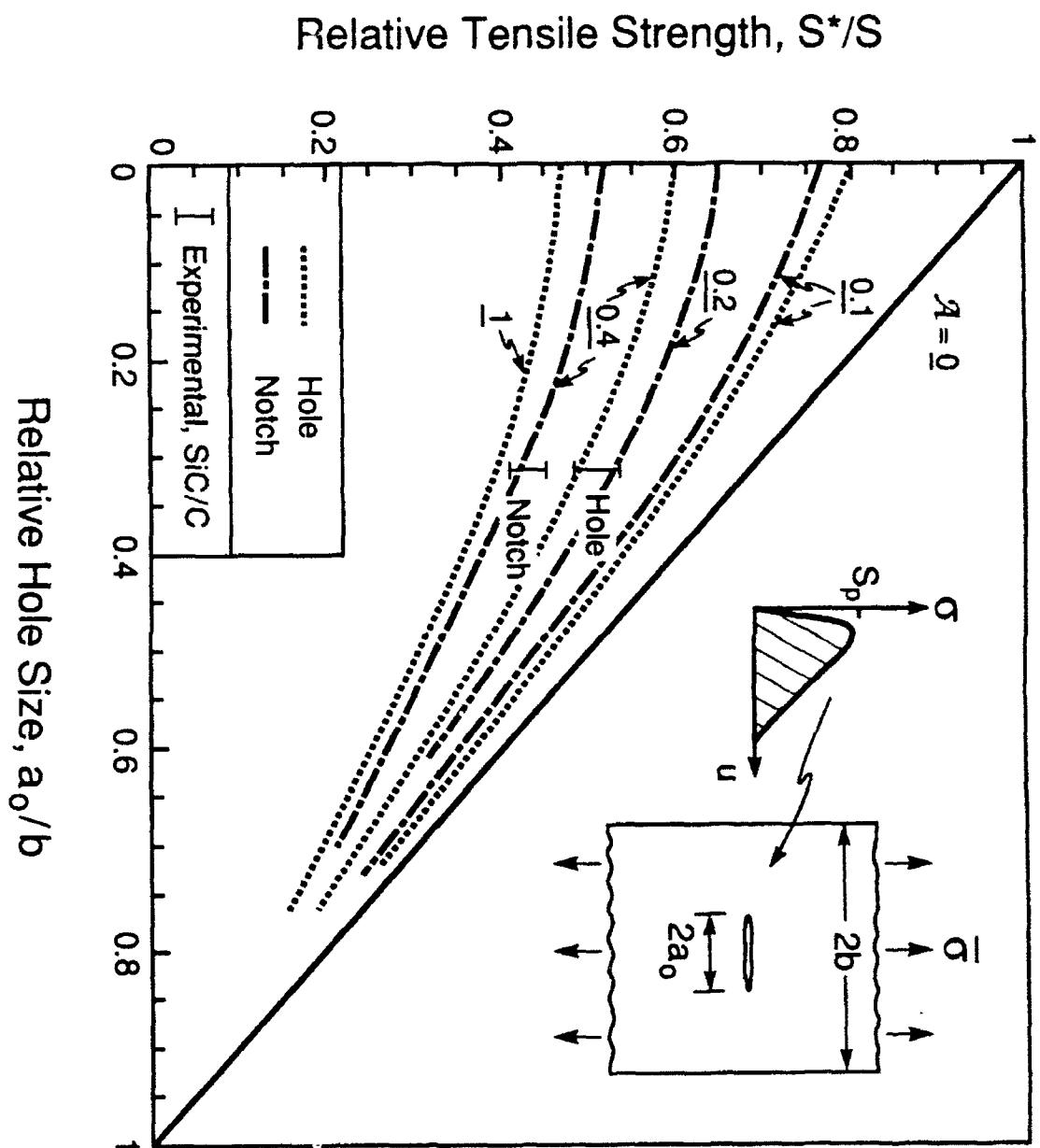


Figure 7.1

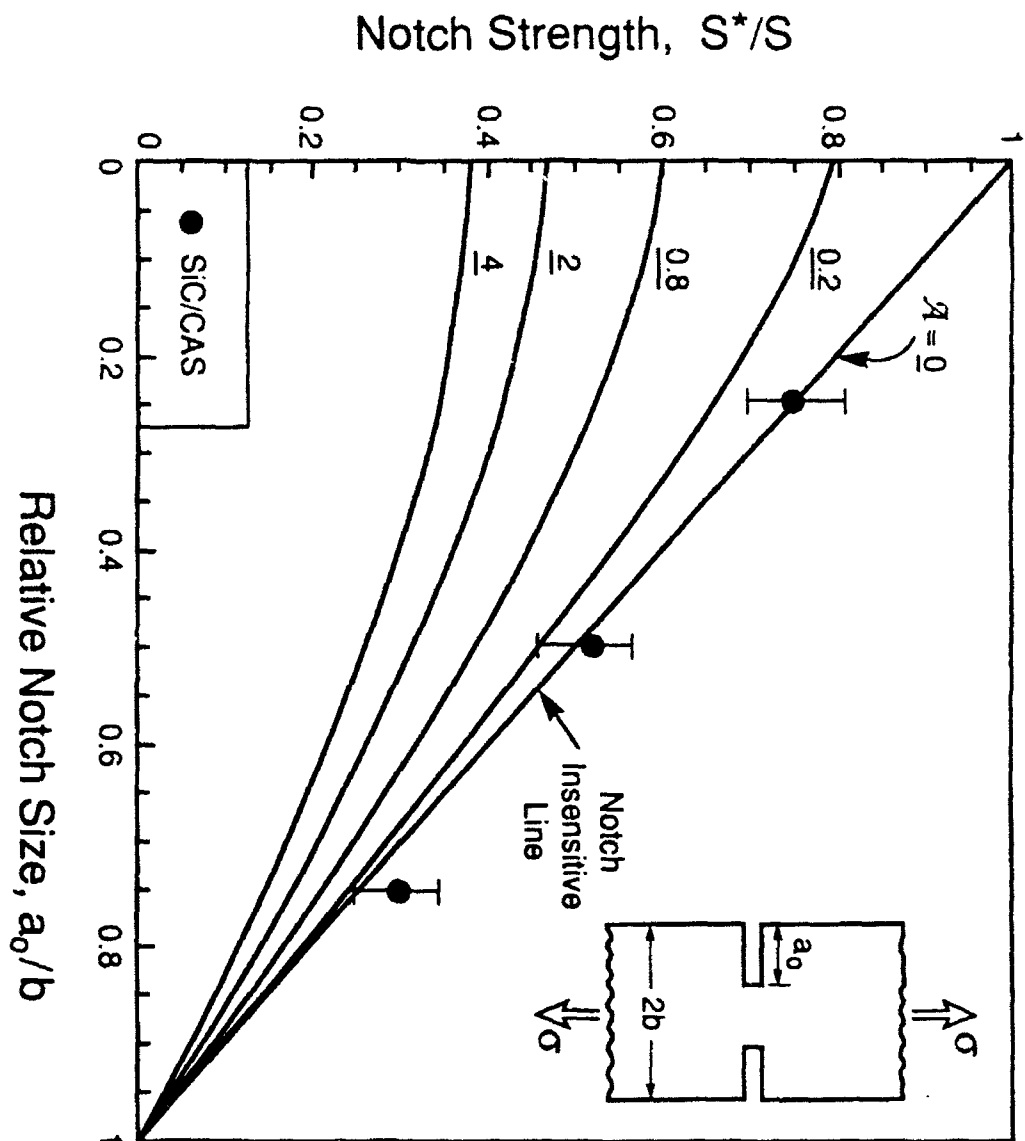


Figure 7.2

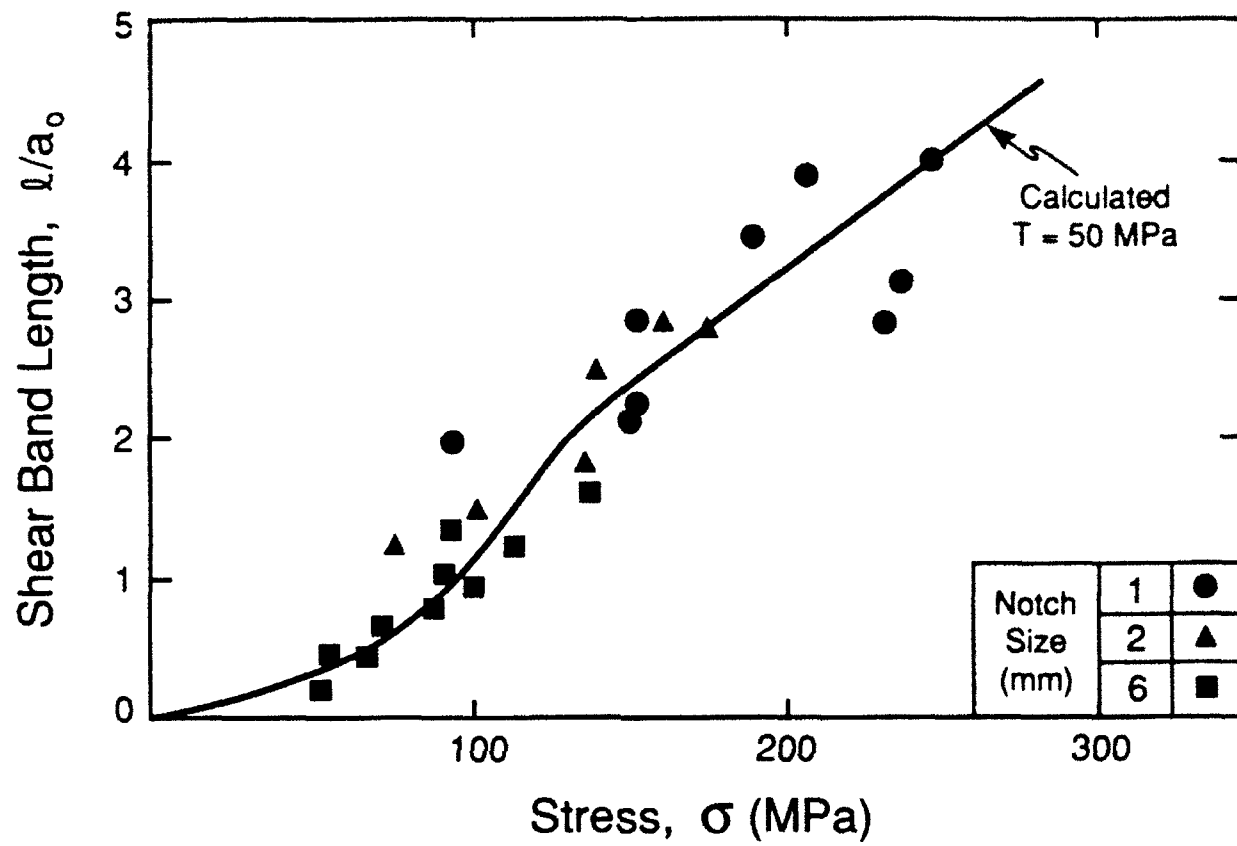


Figure 7.3

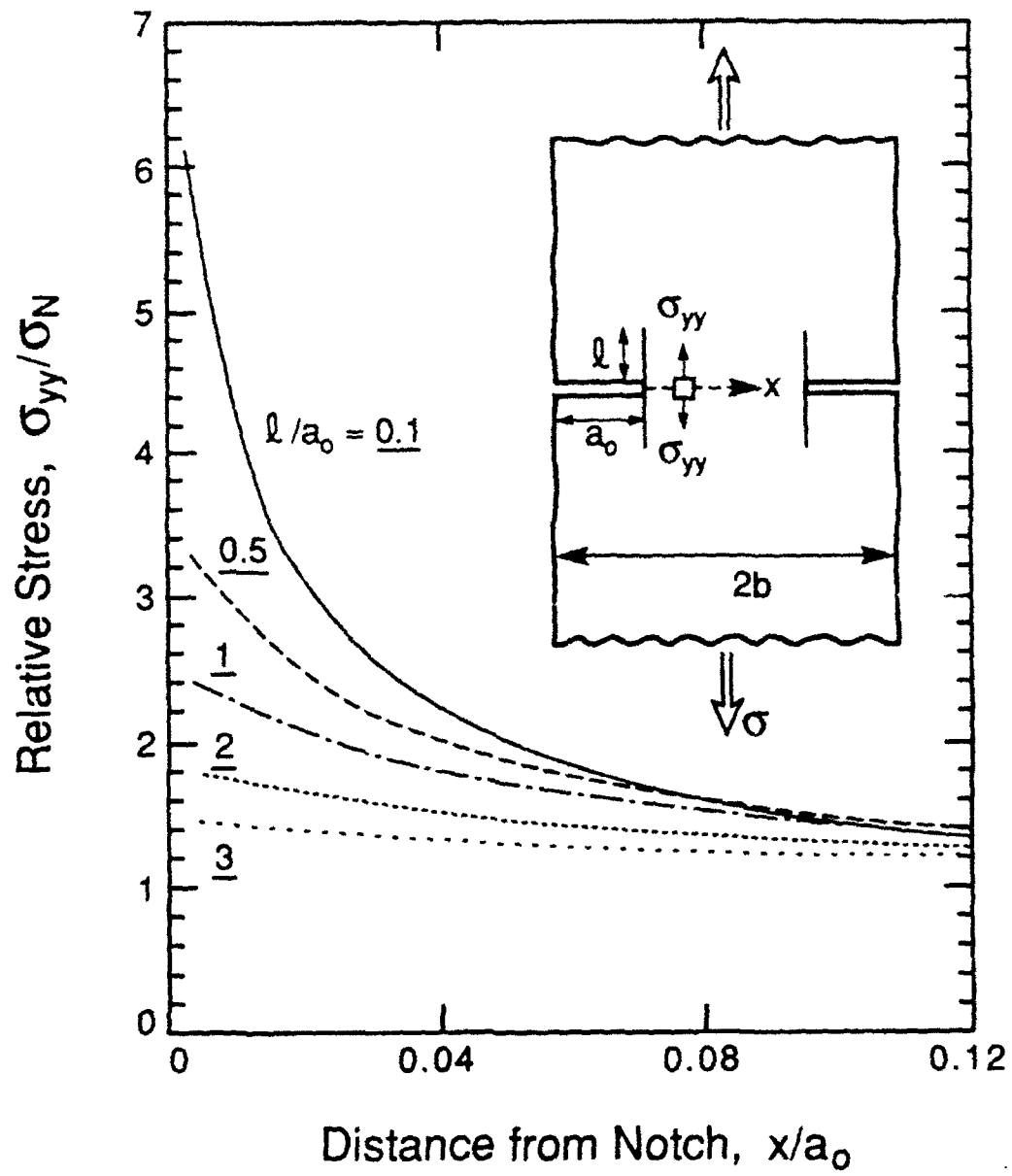


Figure 7.4

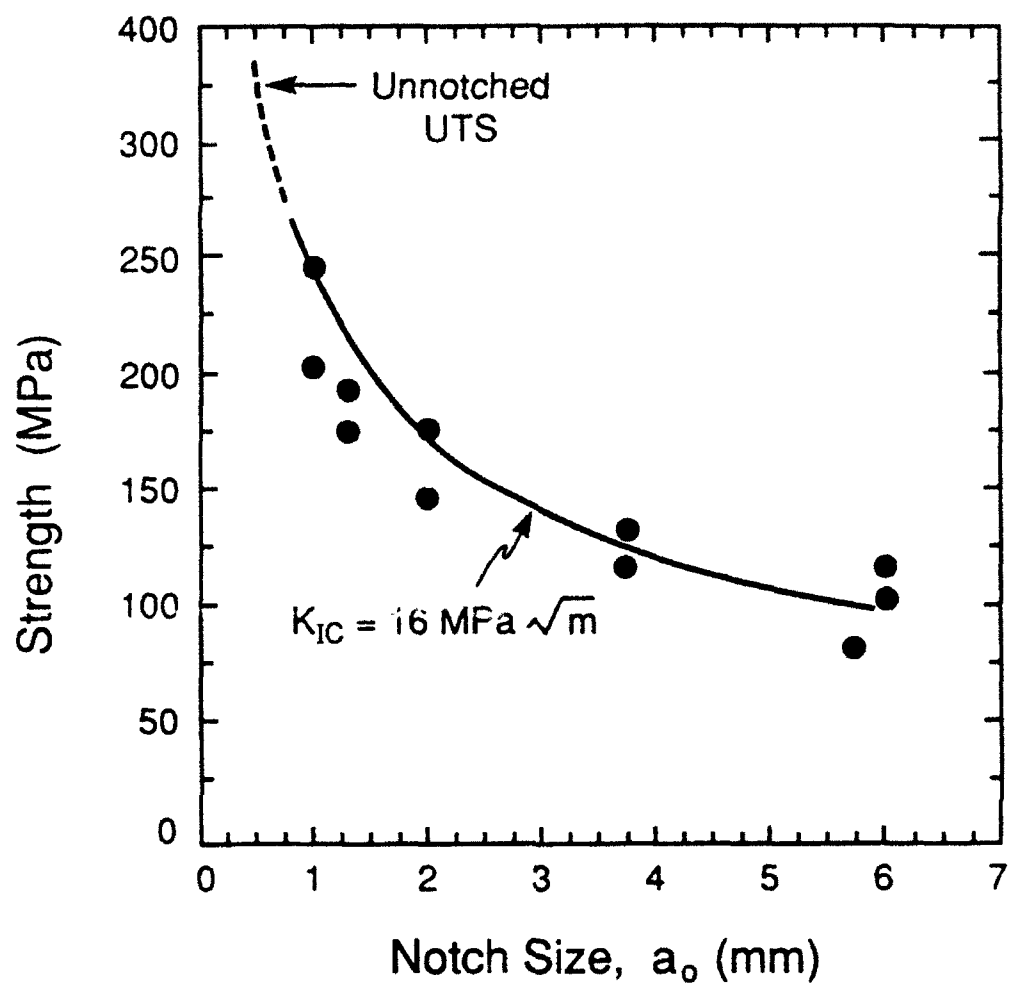


Figure 7.5

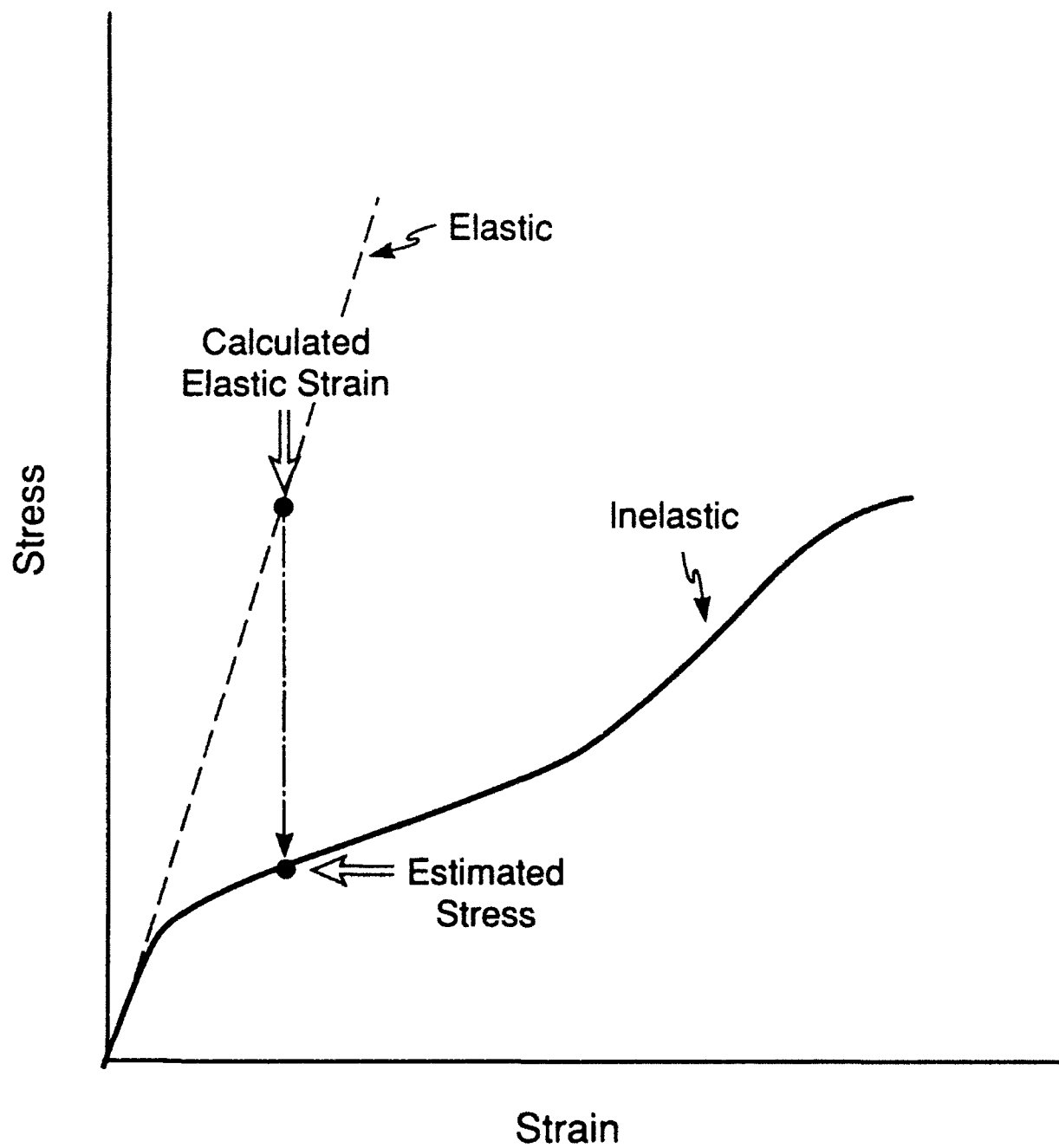
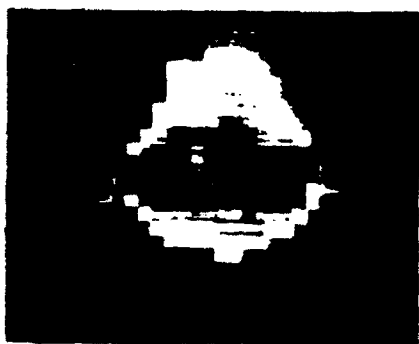
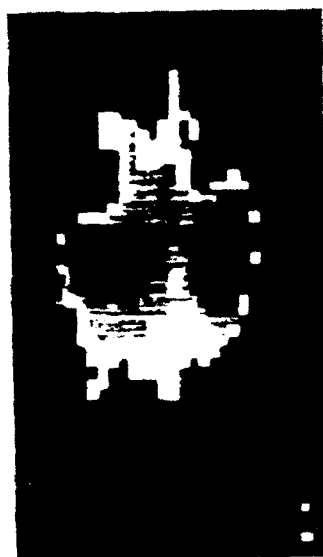


Fig 7.6



a



b

Fig 7.7





Fig 7.8

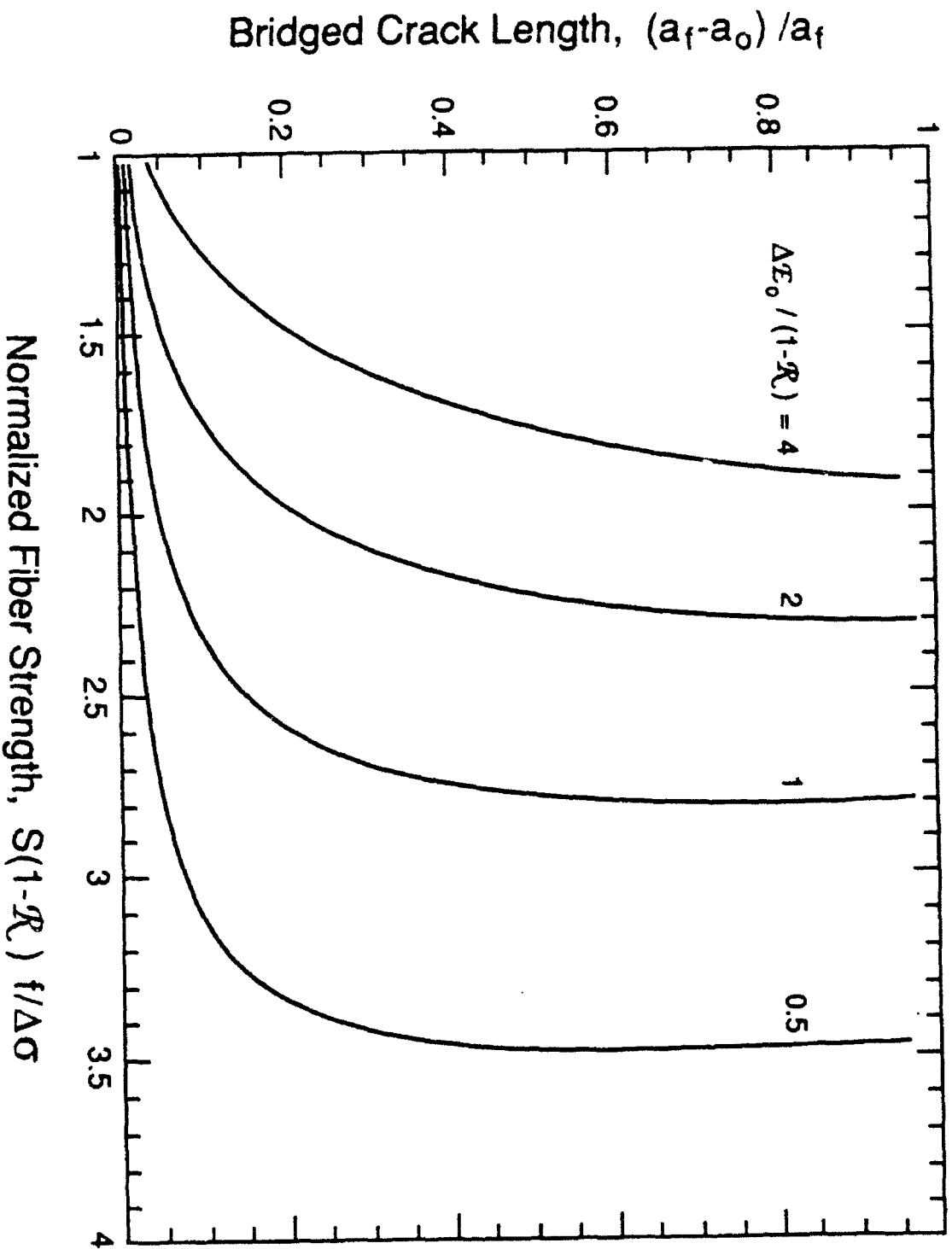


Fig 8.1

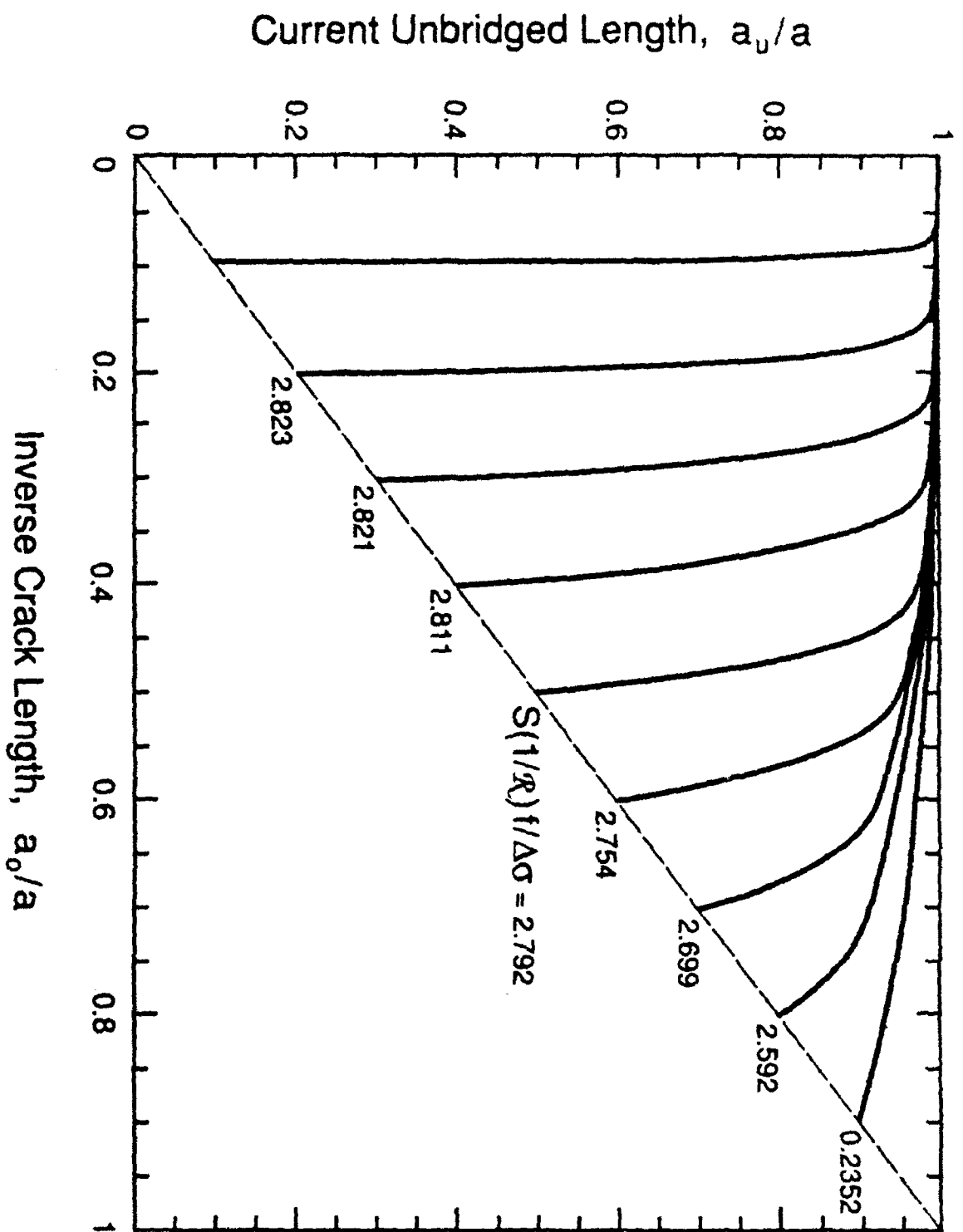


Fig 8.2

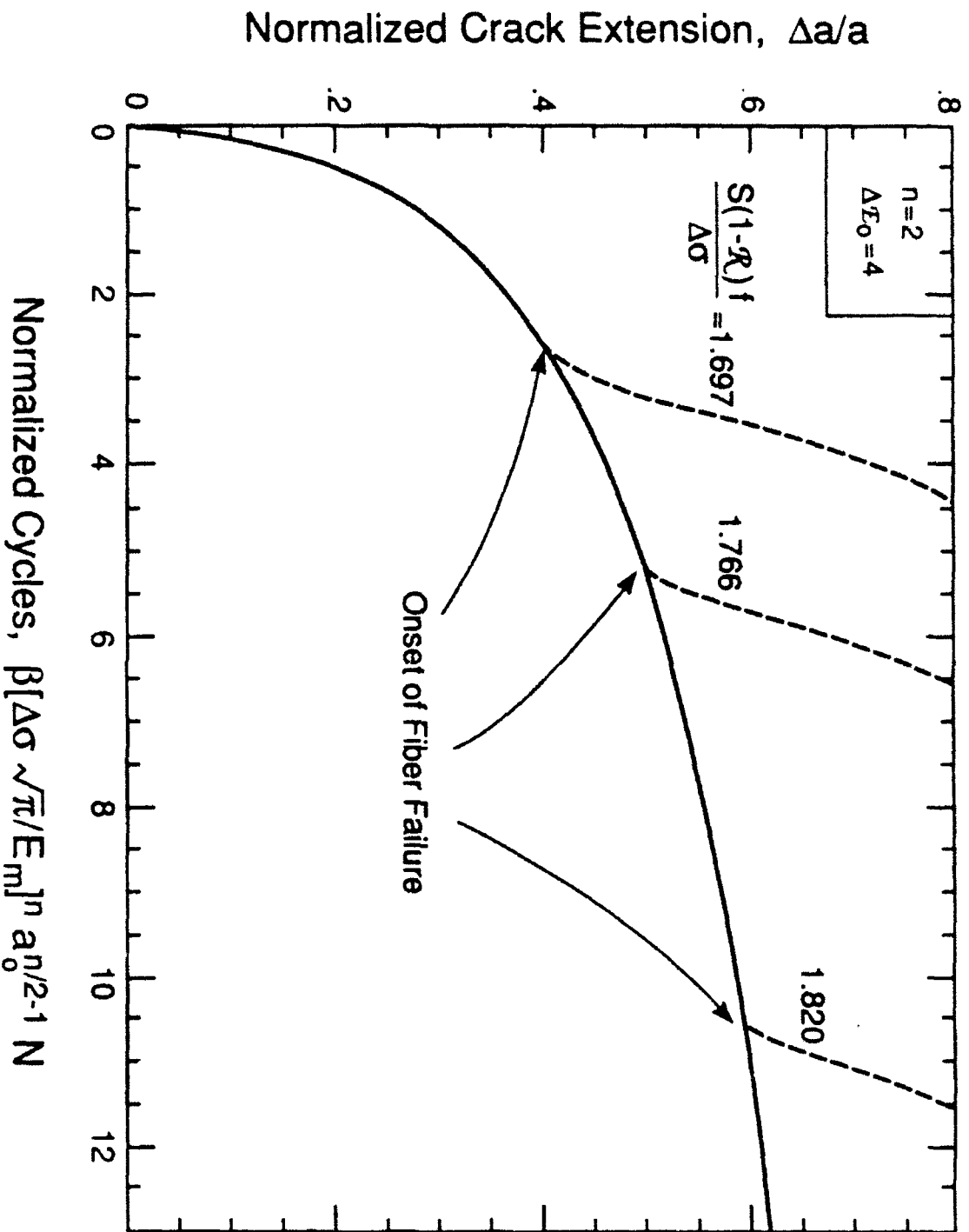


Fig 8.3

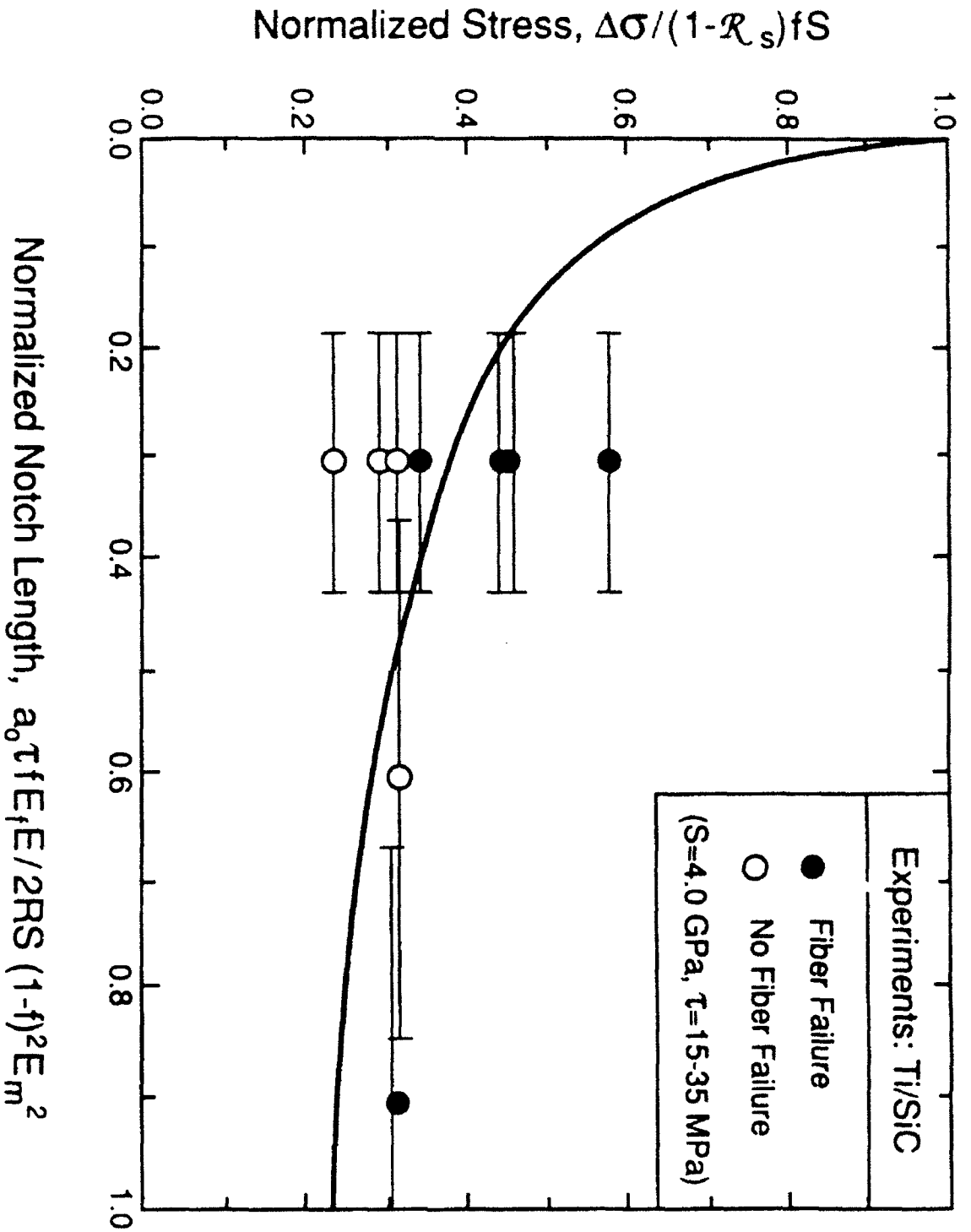


Figure 8.4

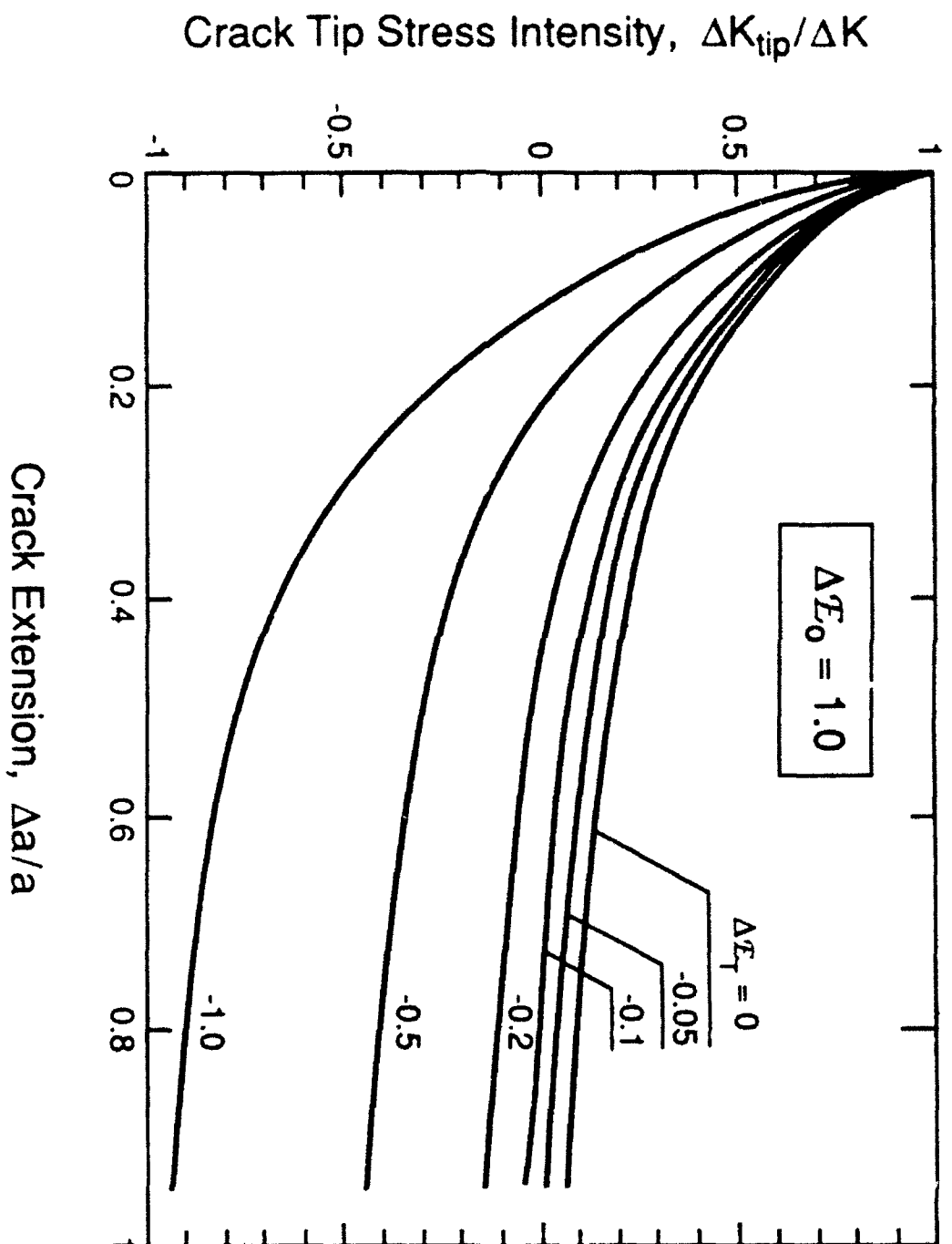


Fig 8.5a

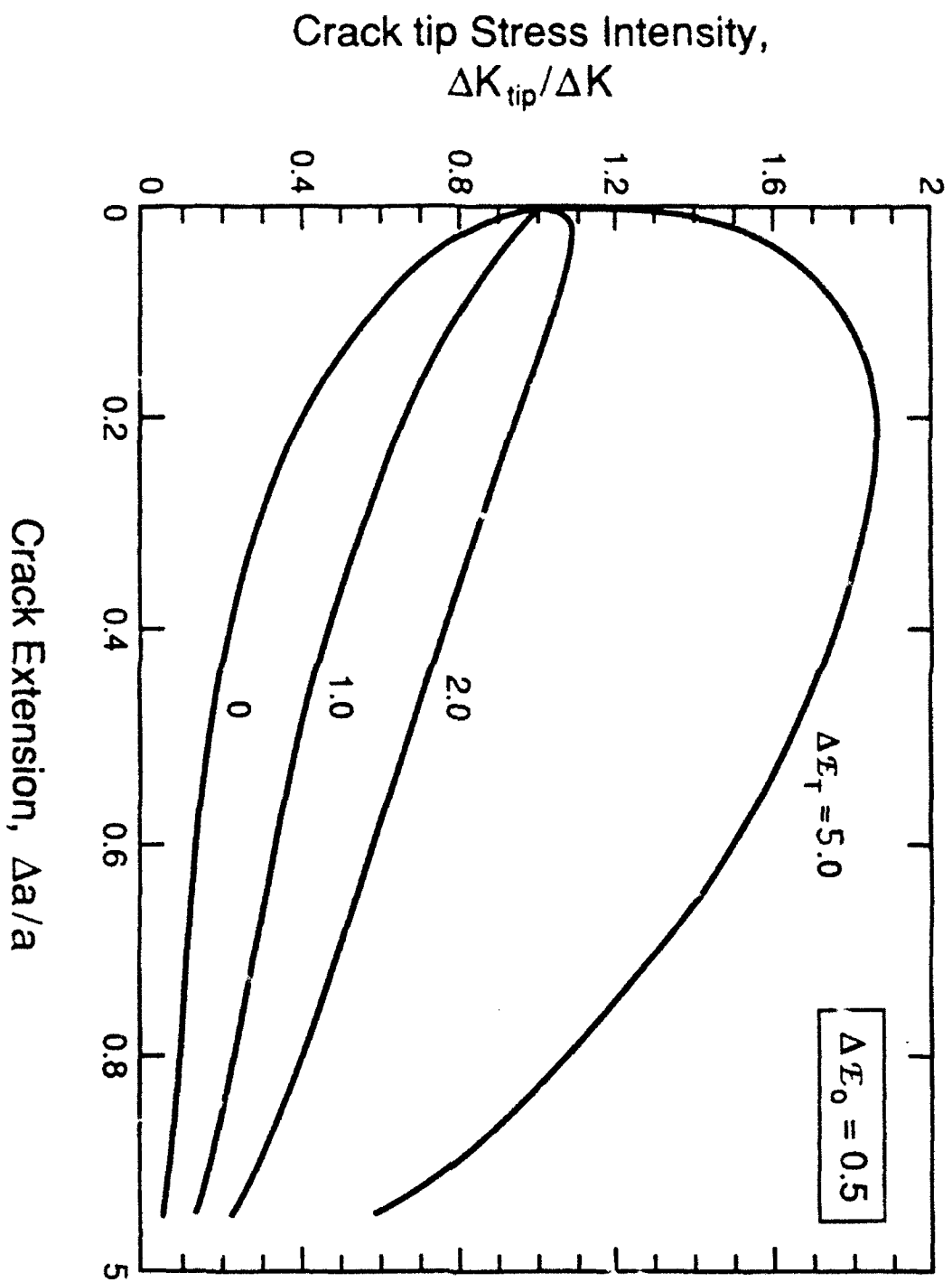
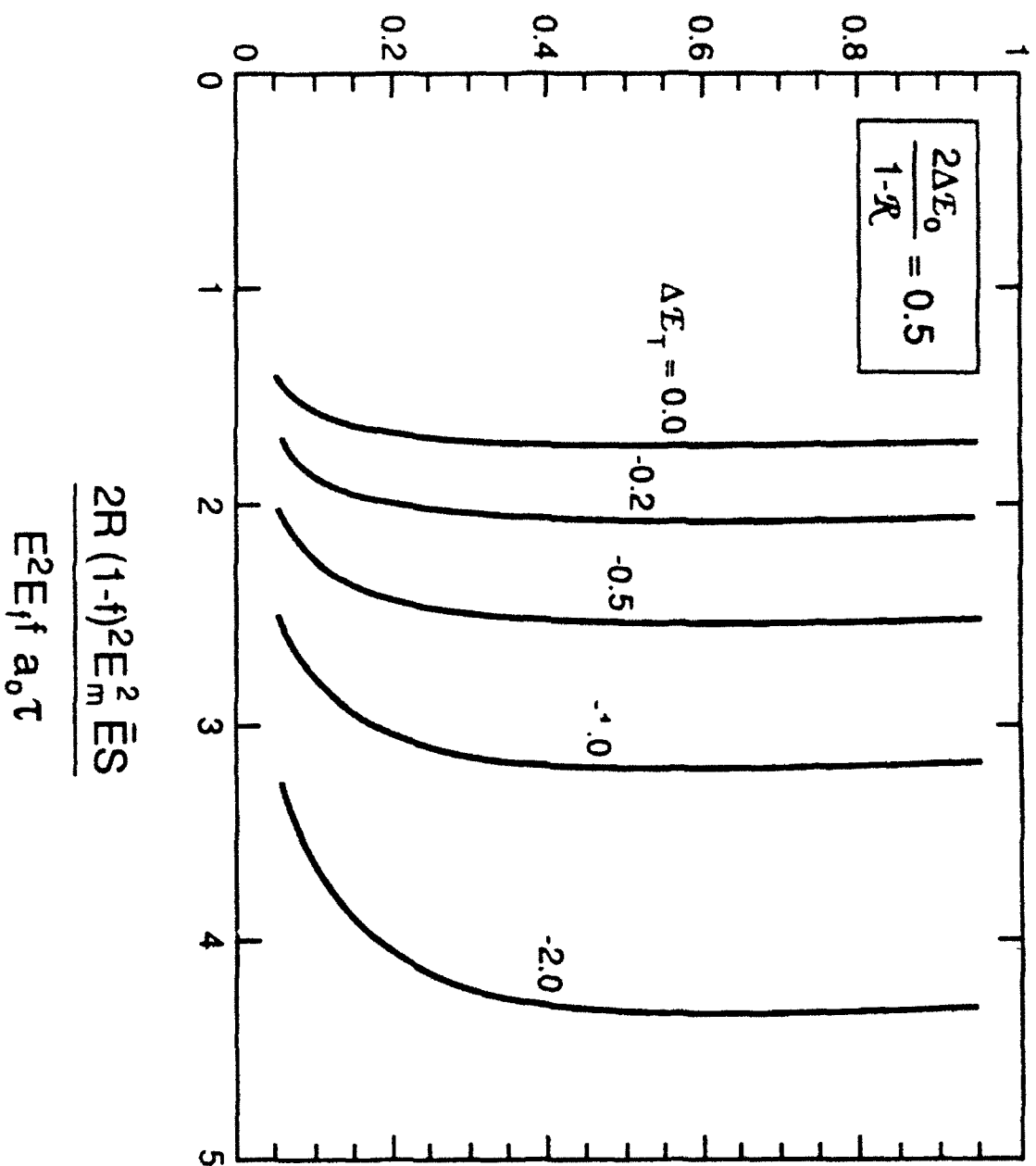


Fig 8 5 b

Relative Crack Size at Failure,  
 $[(a_f - a_o)/a_f]$



$$\frac{2R(1-f)^2 E_n^2 \bar{E} S}{E^2 E_f a_o \tau}$$

Fig 8.6a



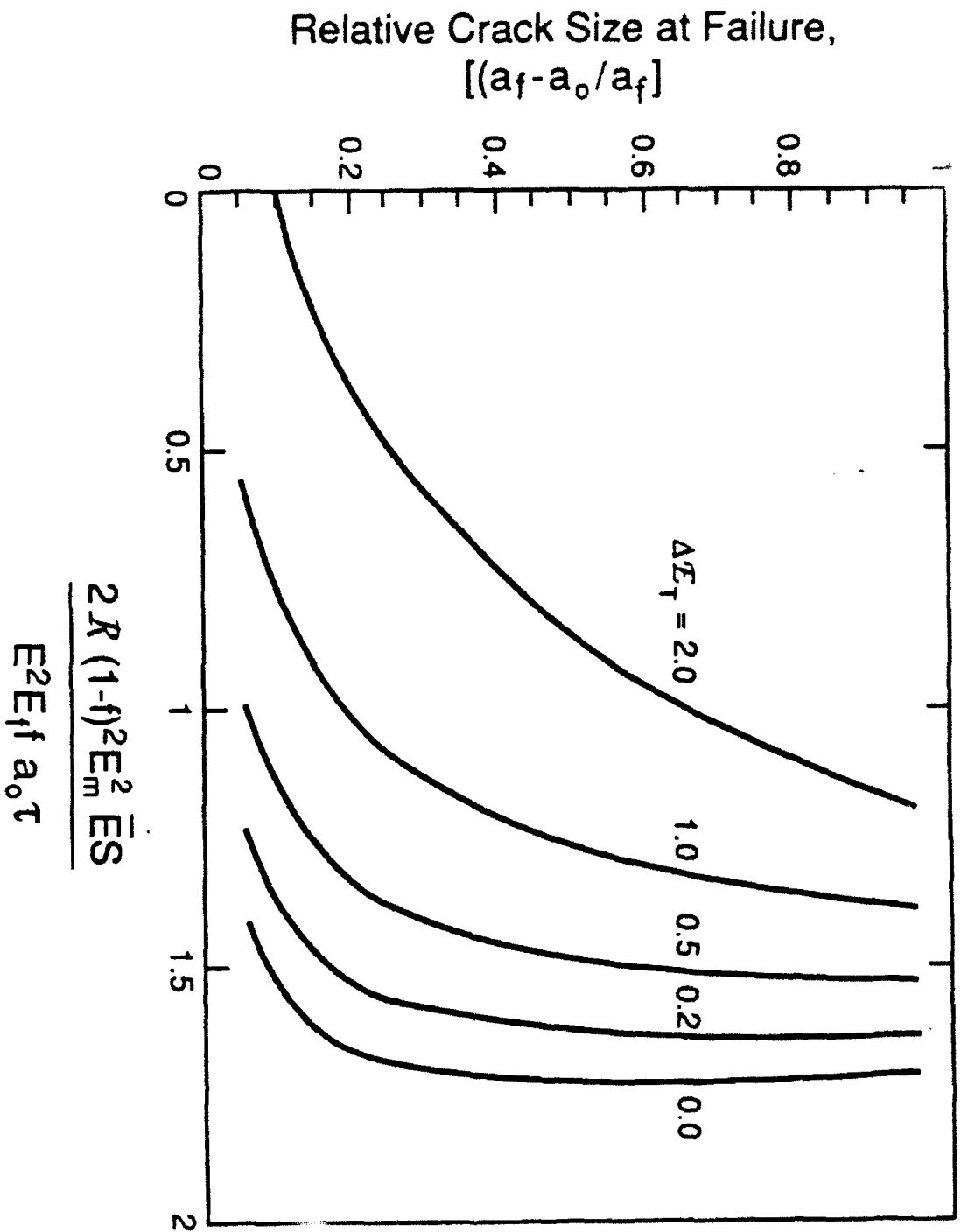


Fig 8 6 b

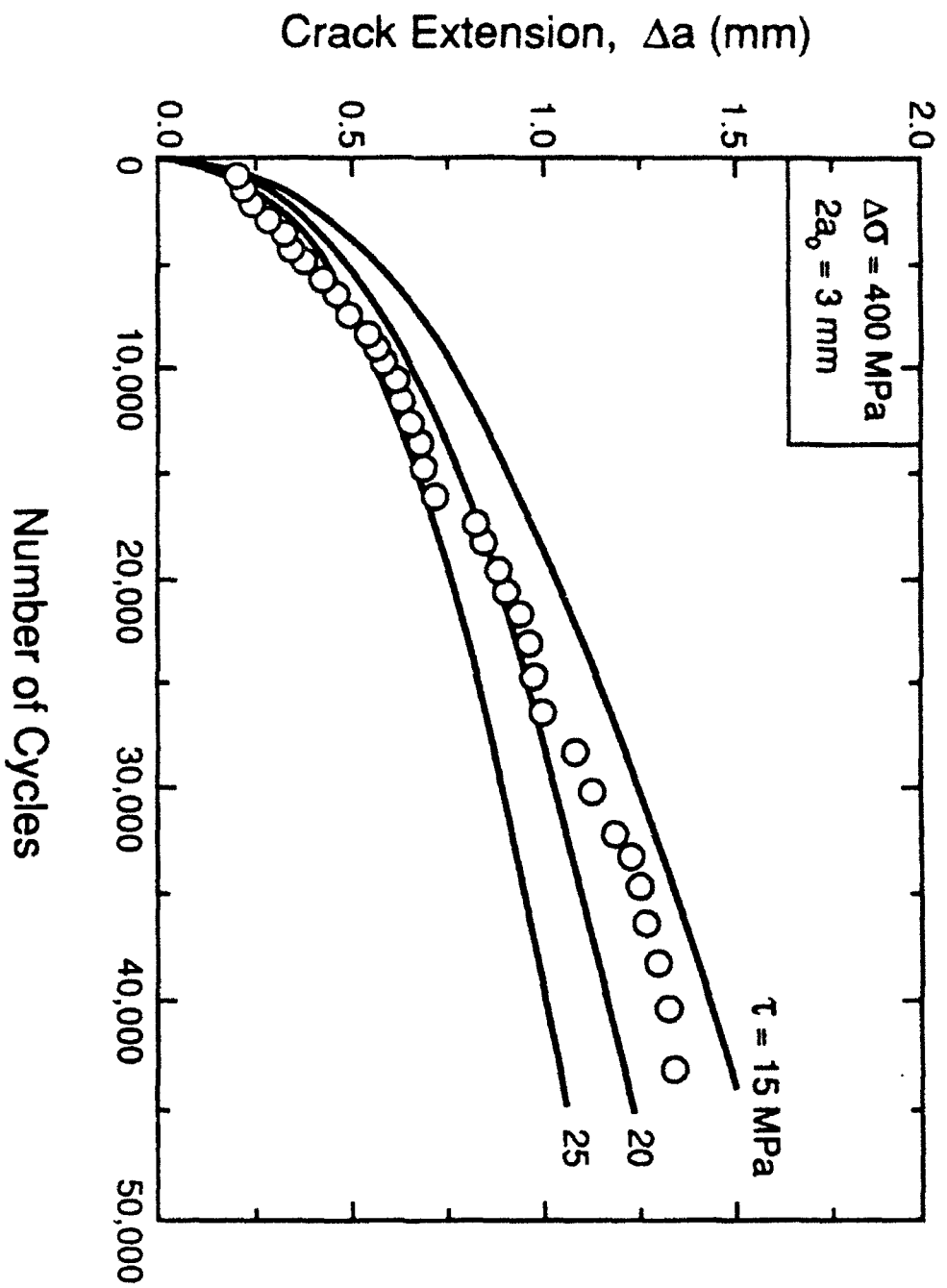


Figure 8.7 (a)

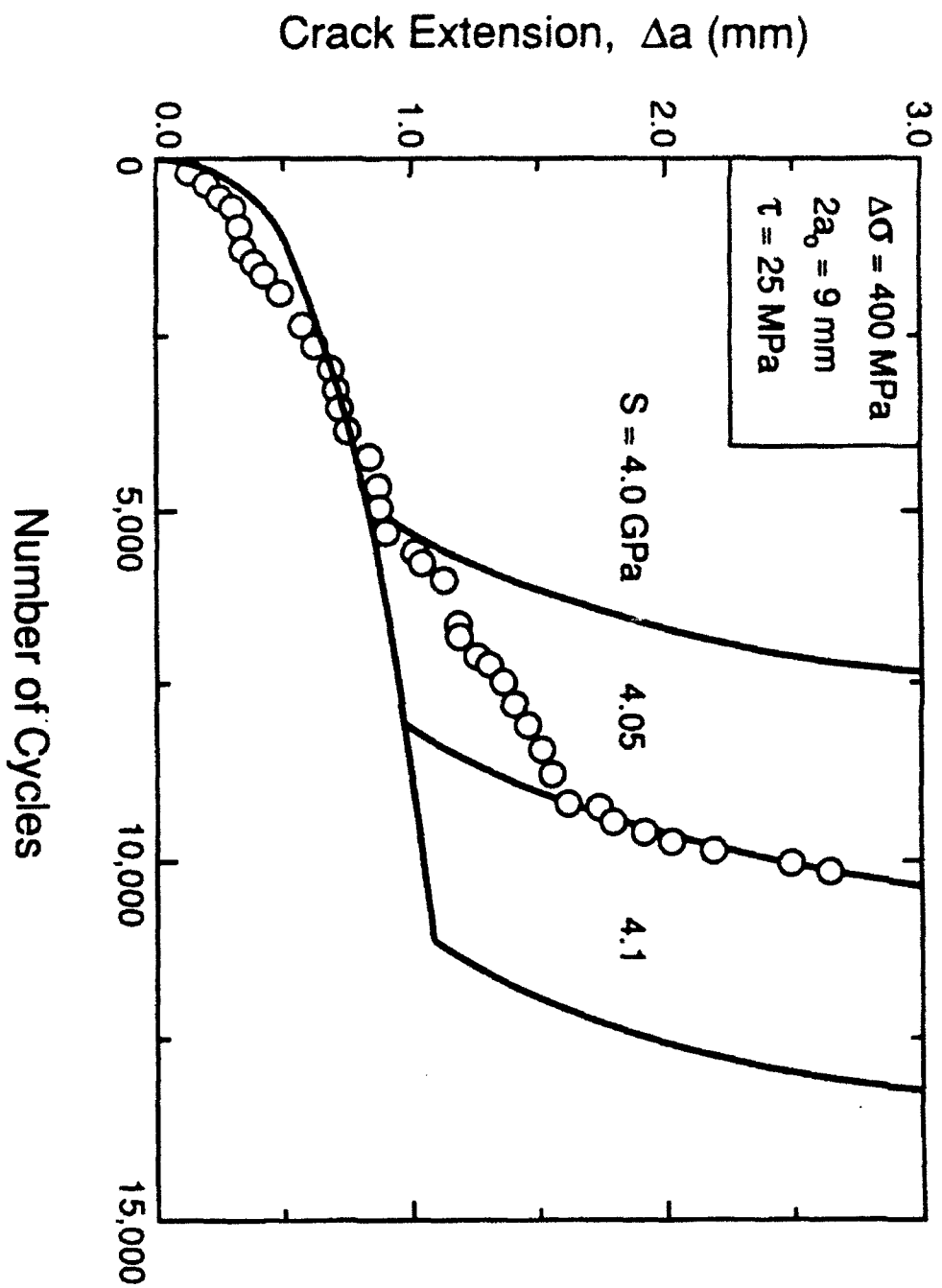


Figure 8.7 (b)

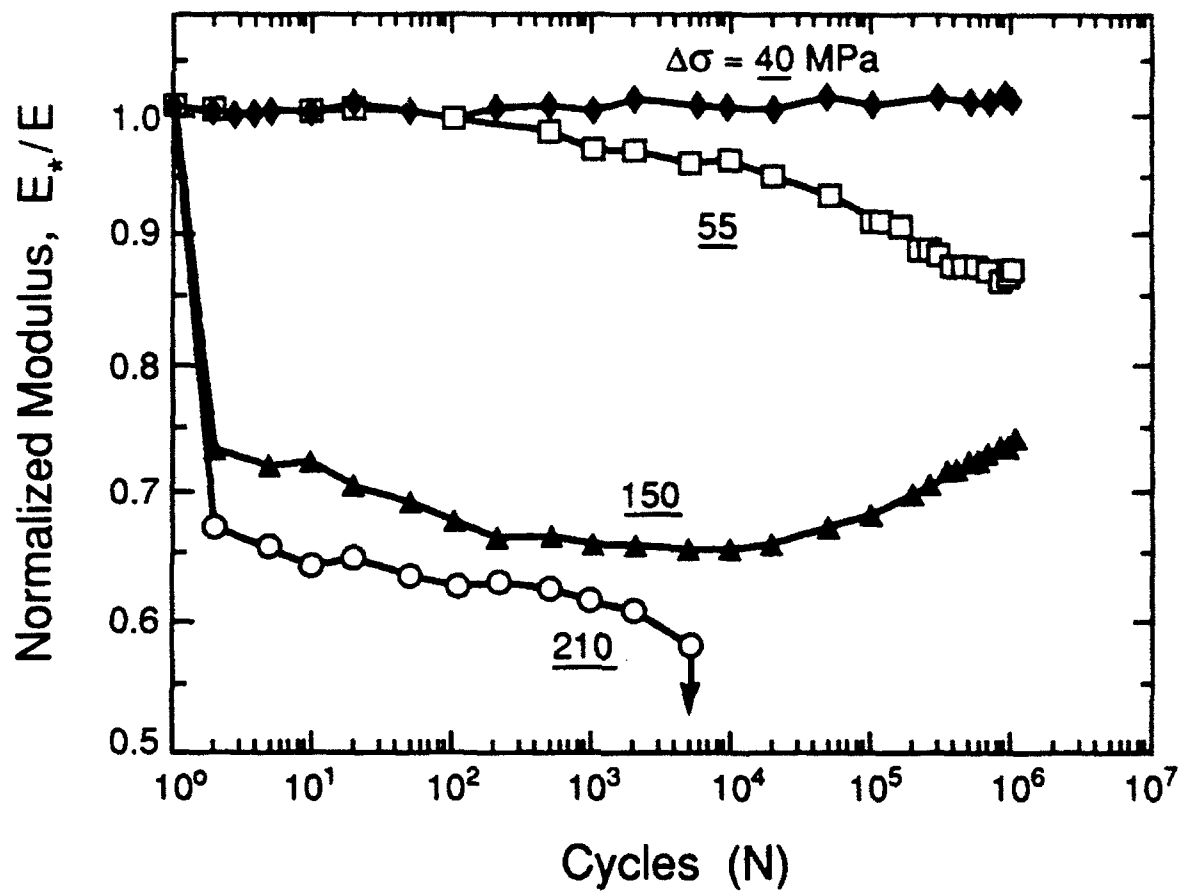


Fig 8.8

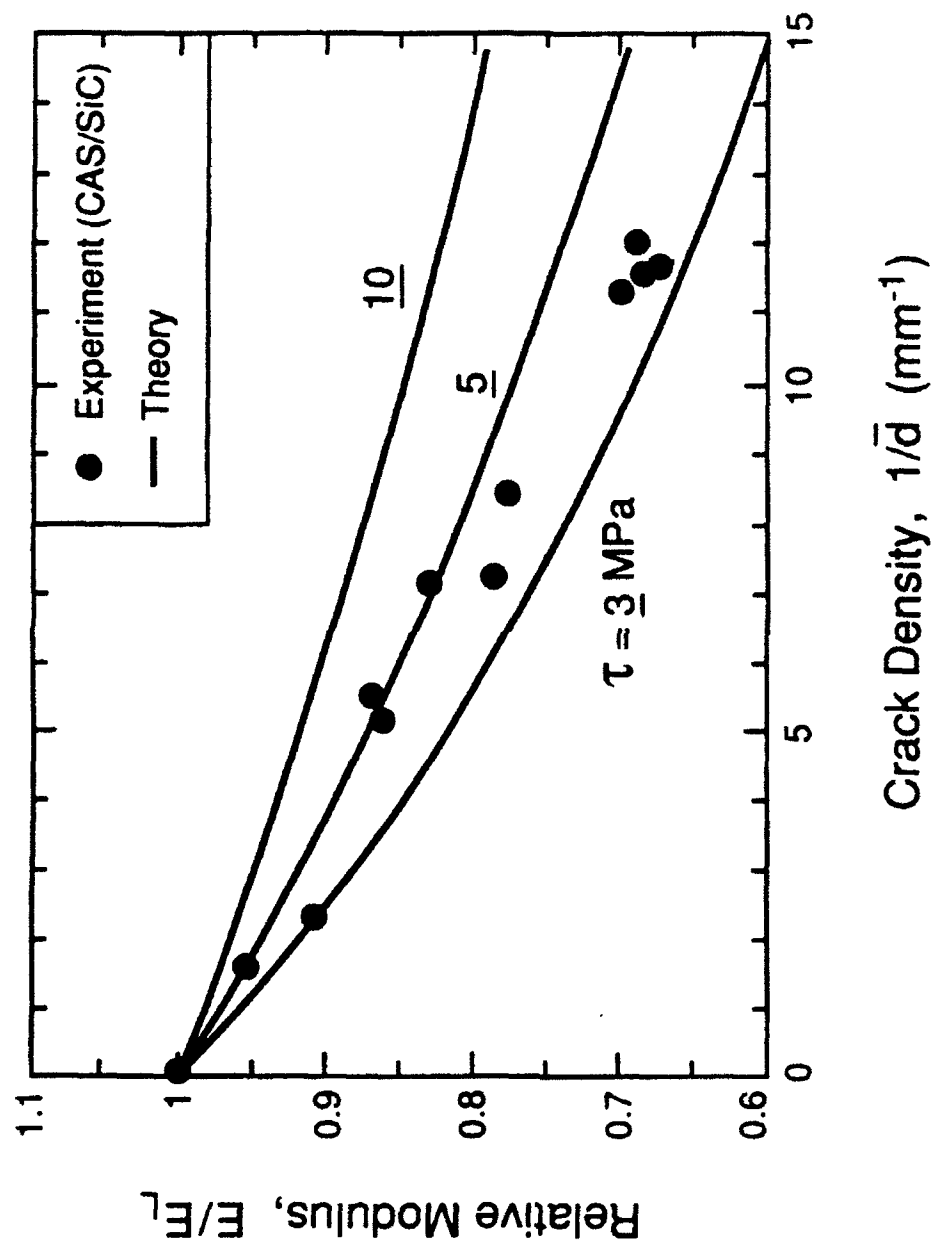


Figure 8.9

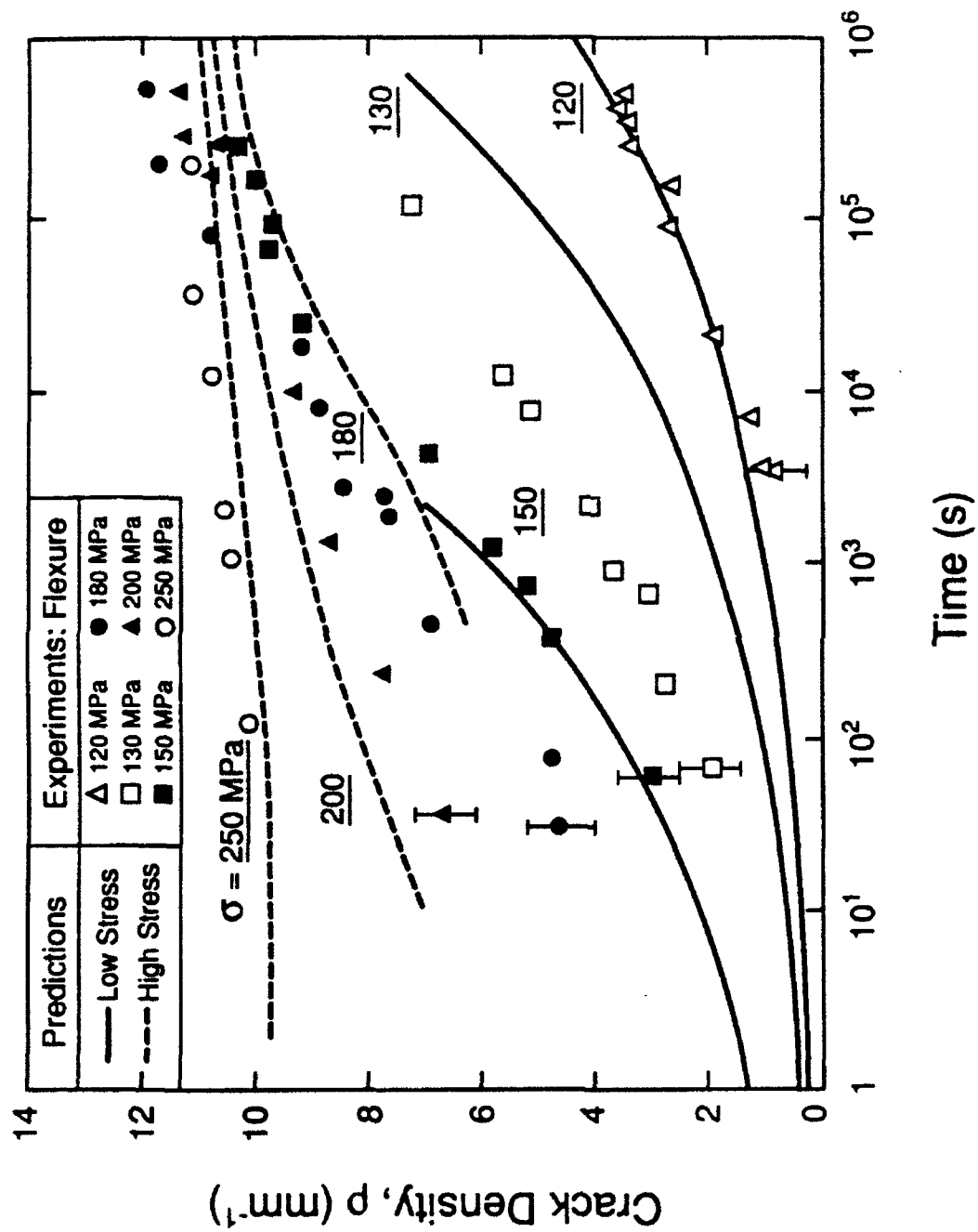


Figure 9.10

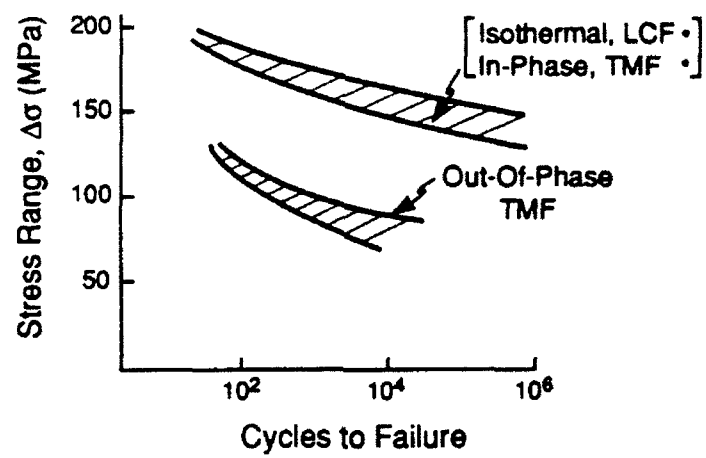


Fig. 8.11 Fatigue Behavior of CMCs

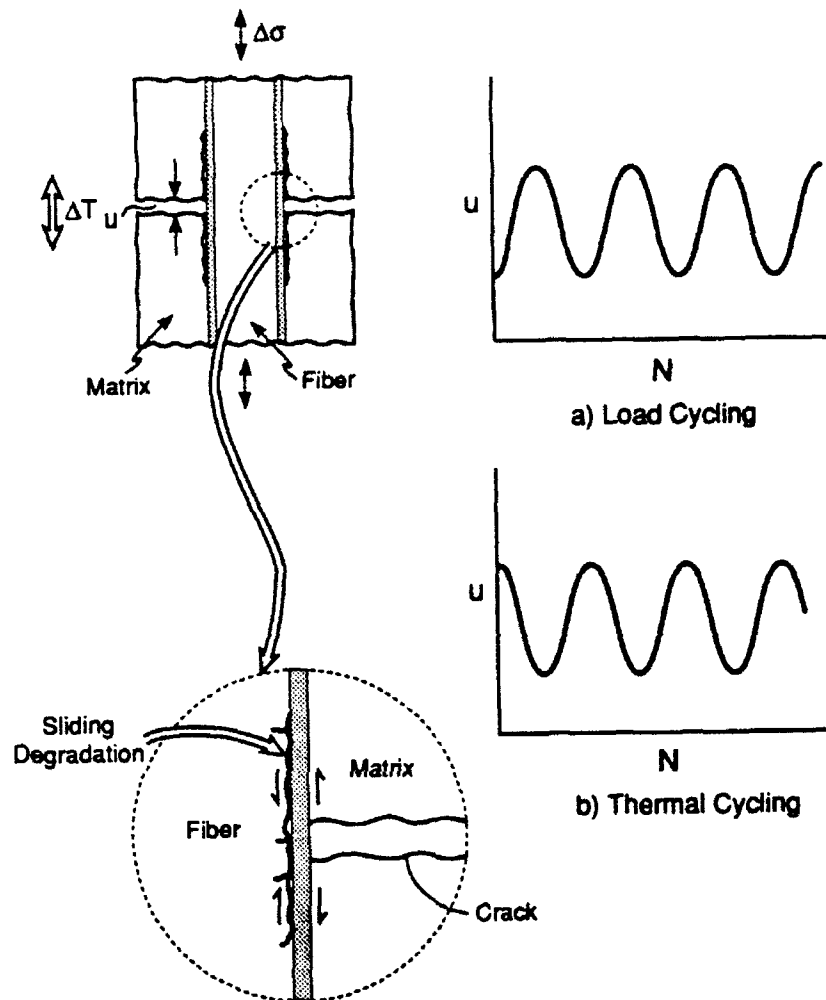


Fig. 8.12 Mechanisms of Fiber Degradation Upon Thermomechanical Cycling



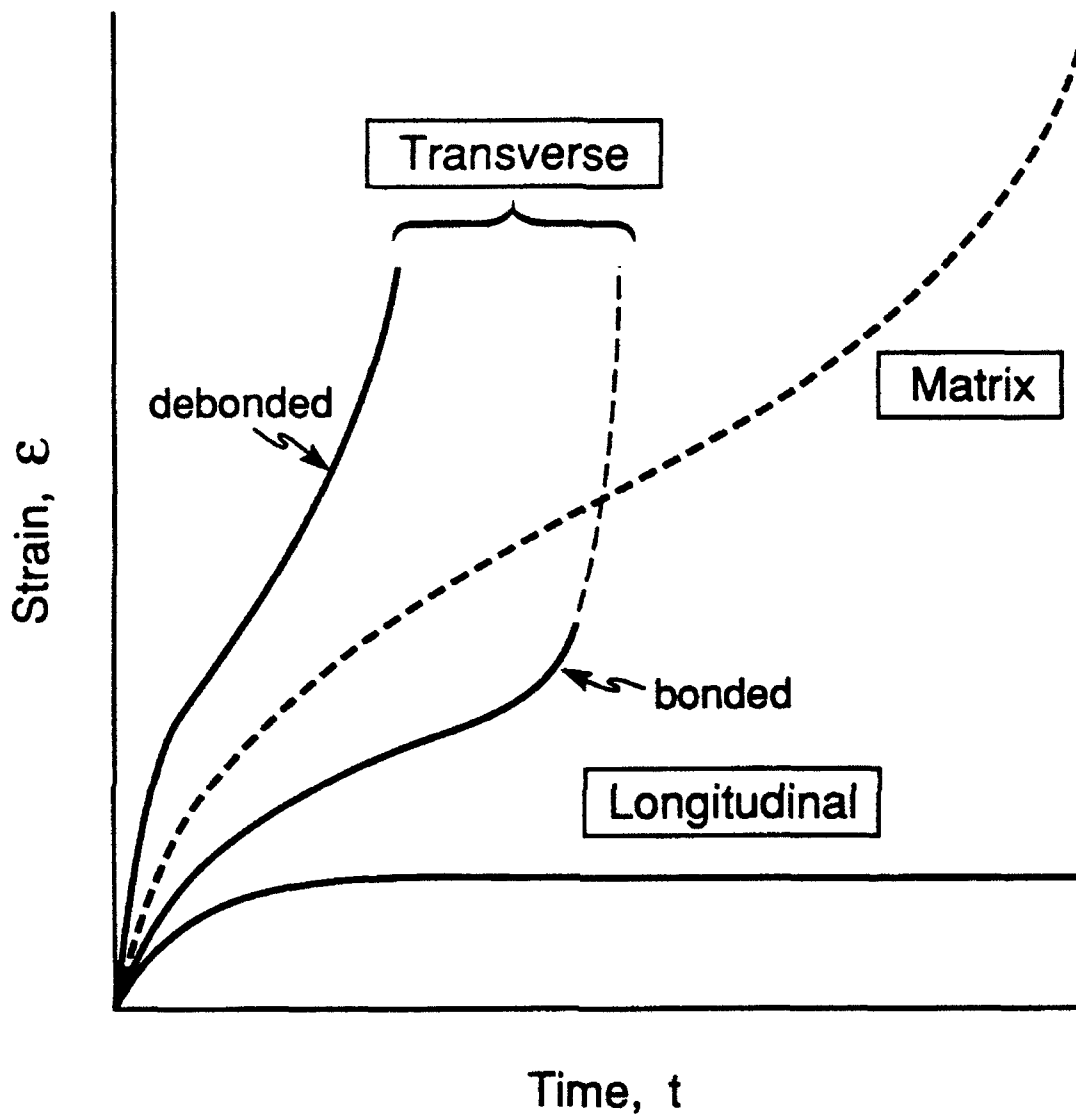


Fig 9.1

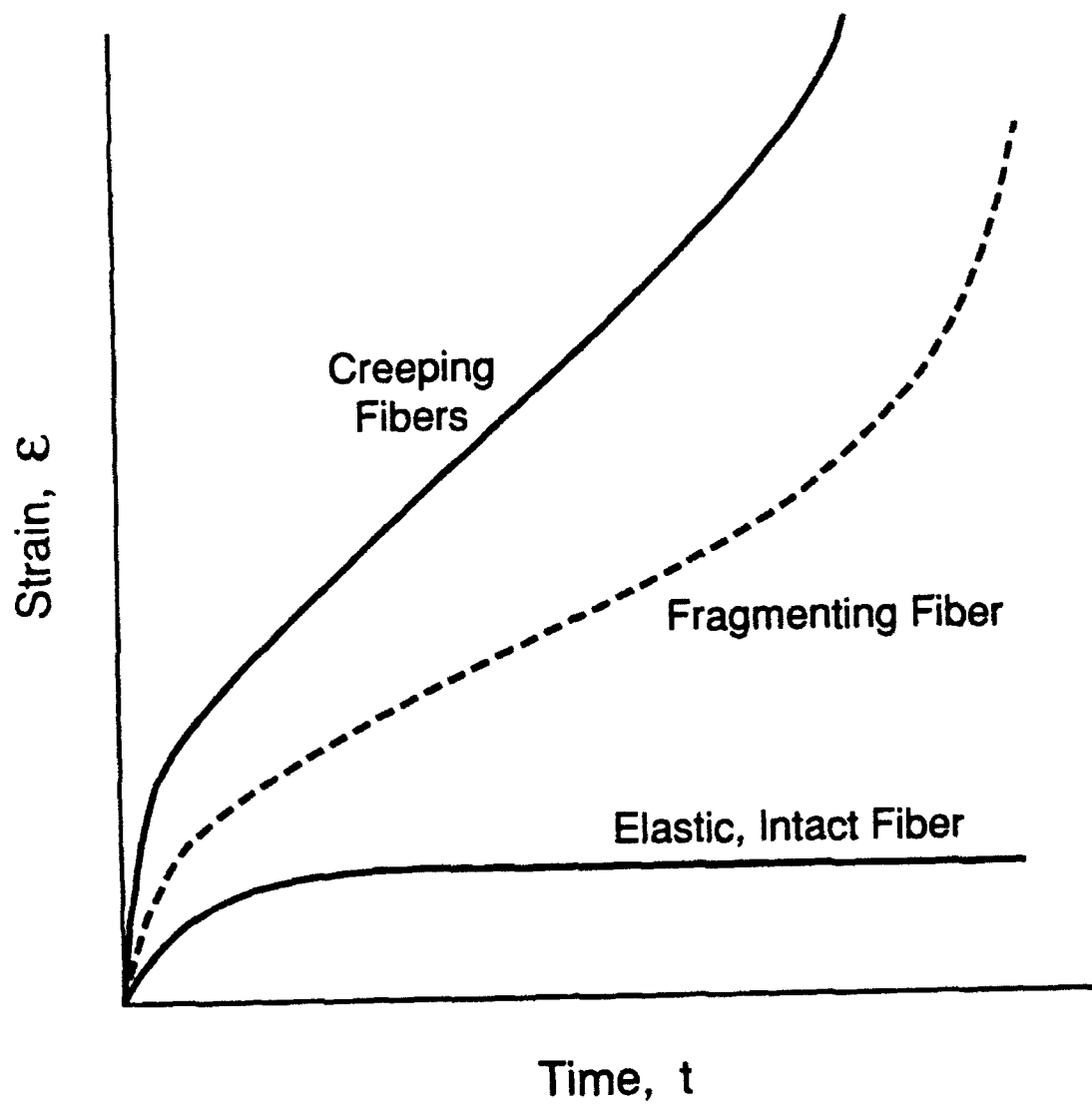


Fig 9 2

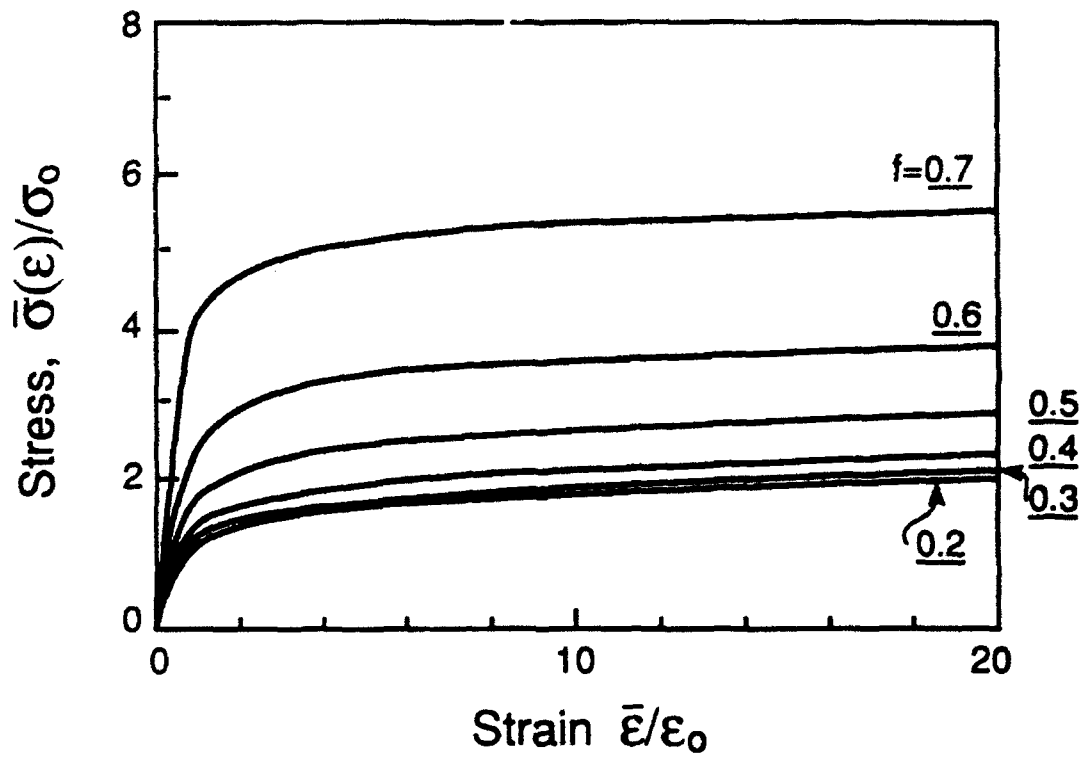


Figure 9.3 Calculated transverse stress/strain curves (normalized by the matrix yield stress and strain).

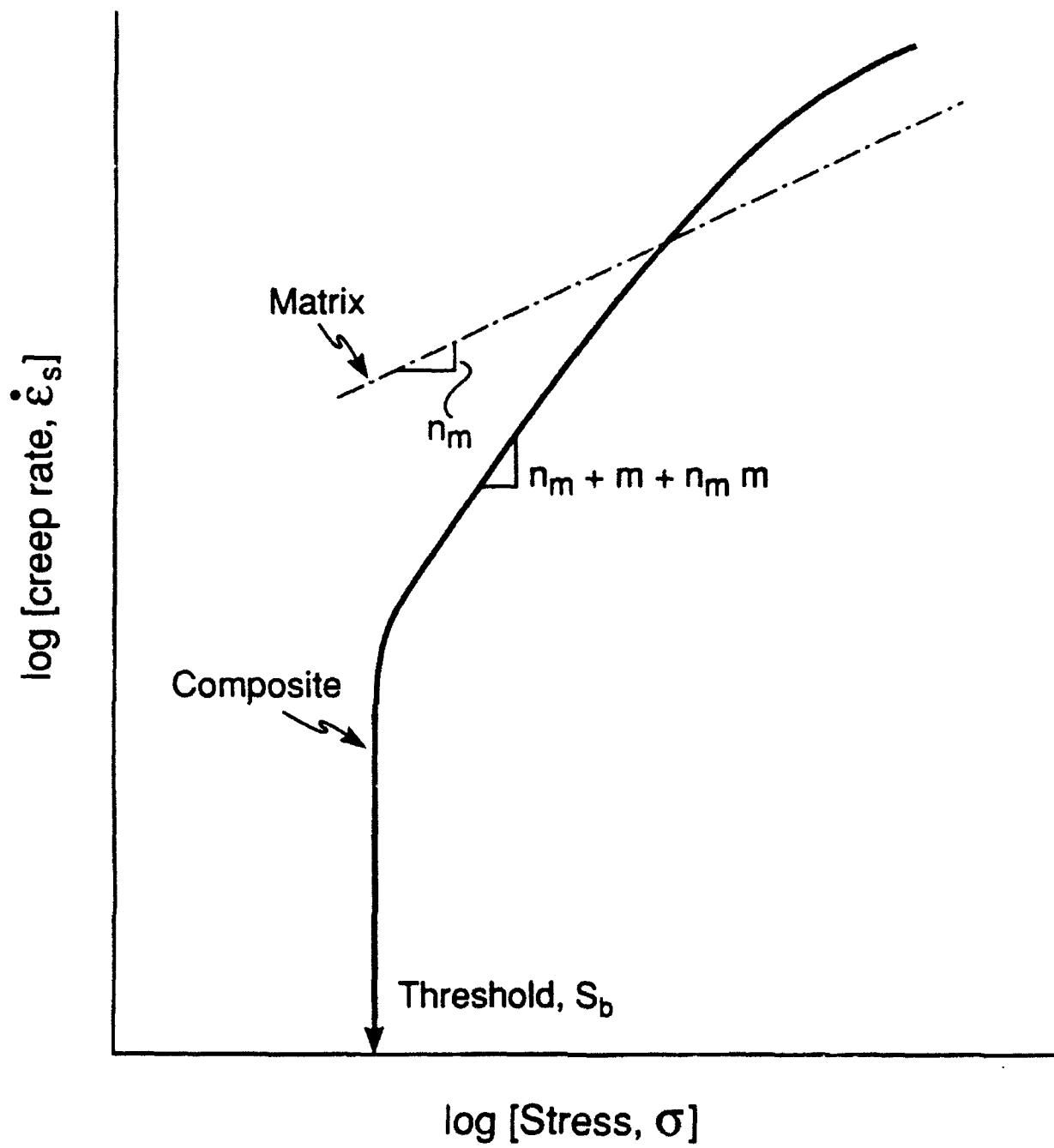


Fig 9 4

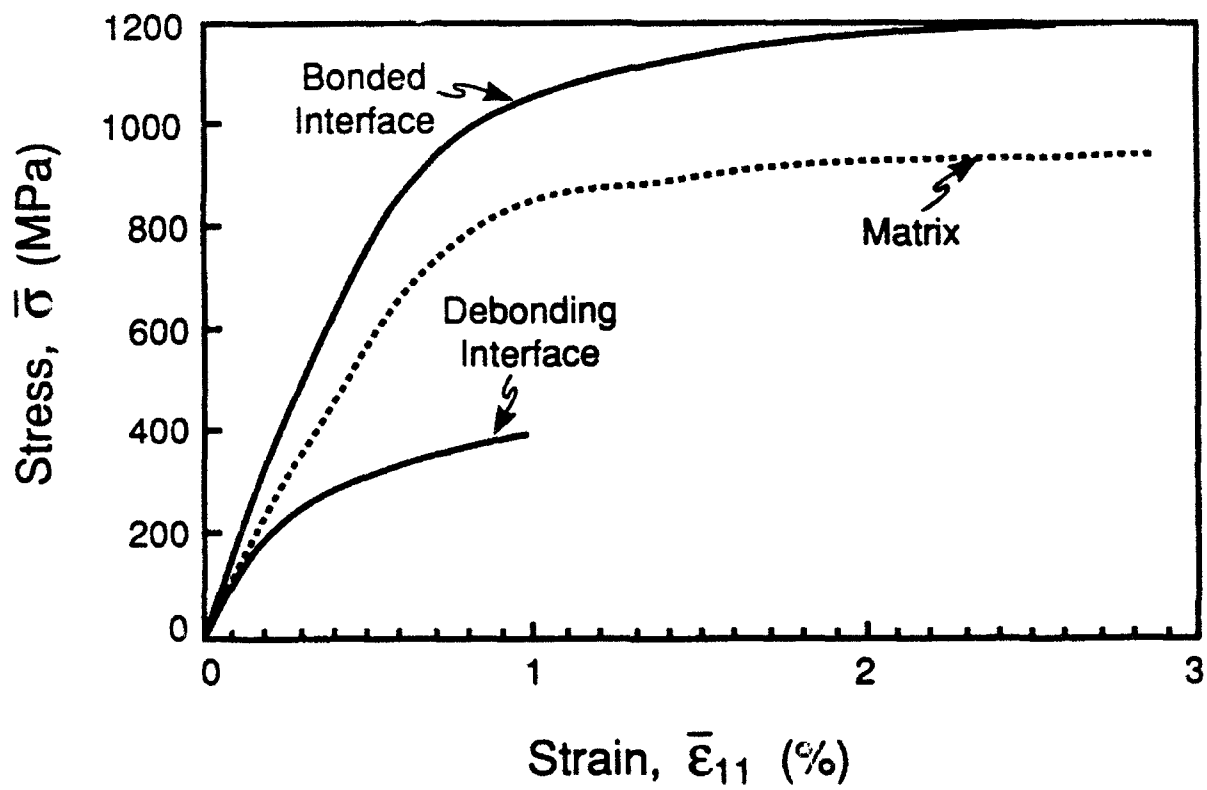


Figure 9.5

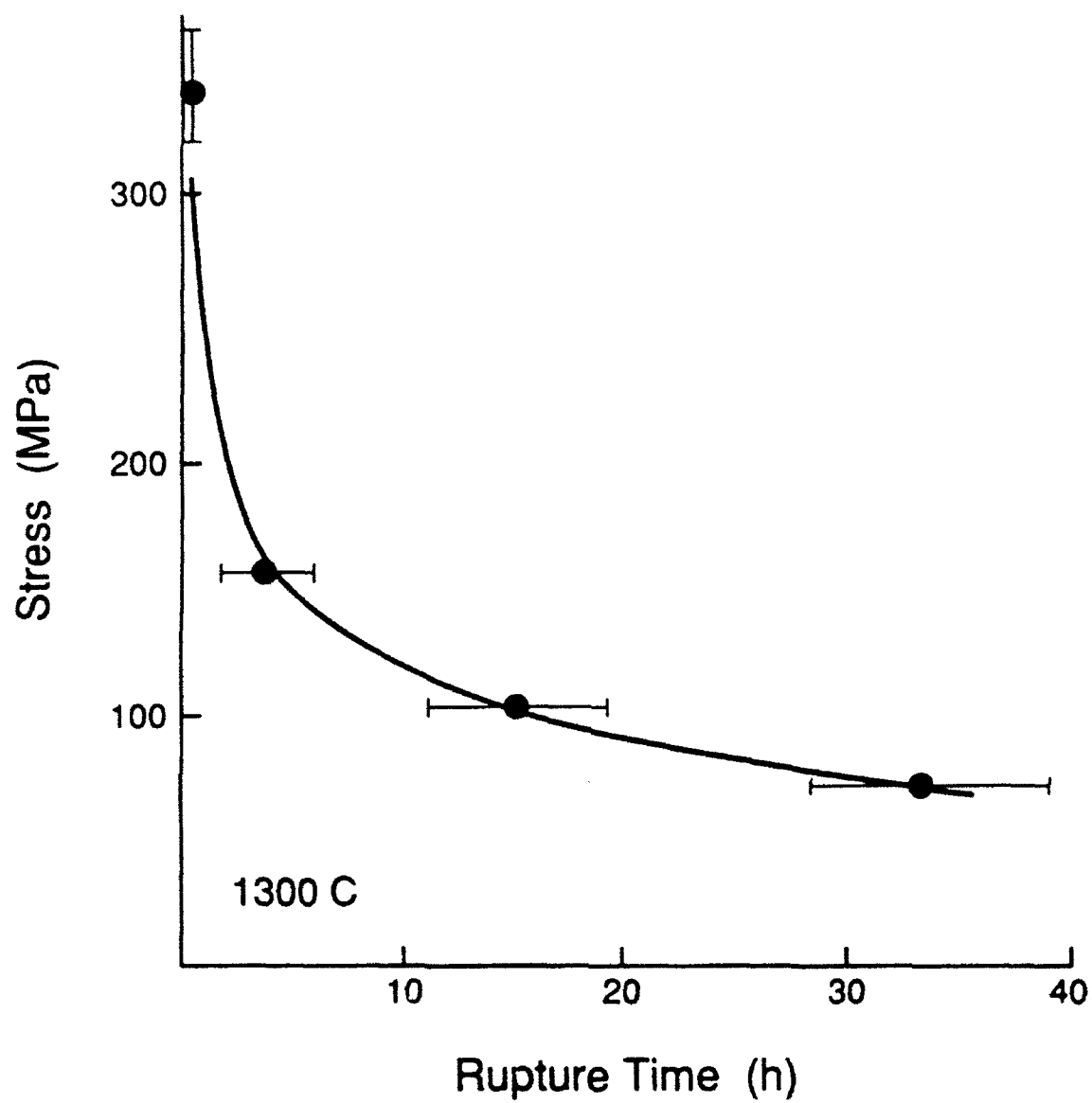


Fig 9.6

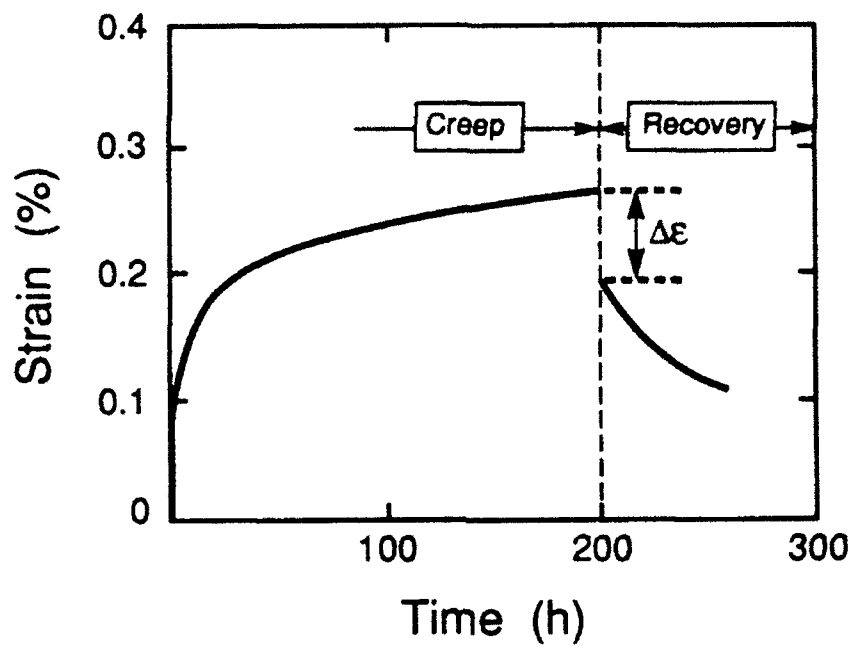


Fig 9.7

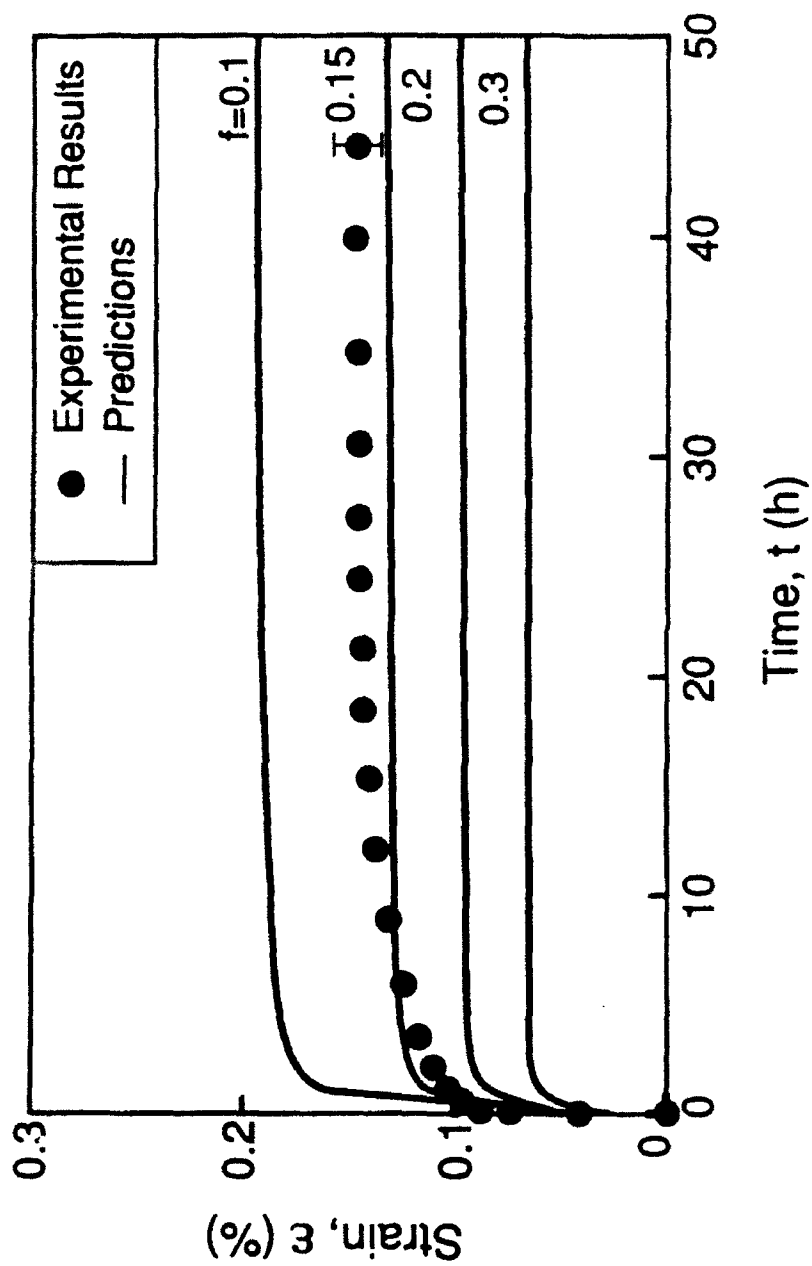


Figure 9.8



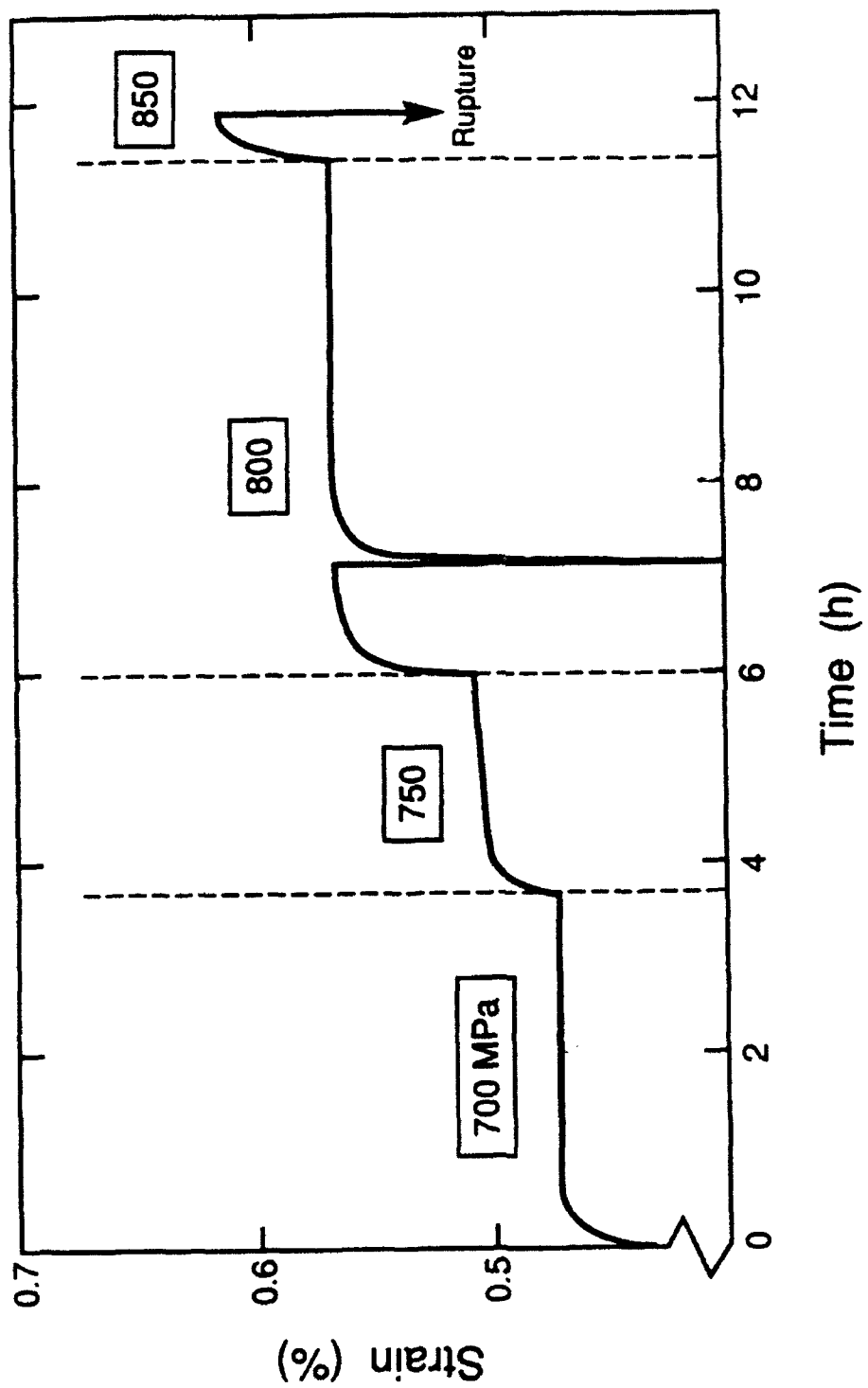


Fig 9.9

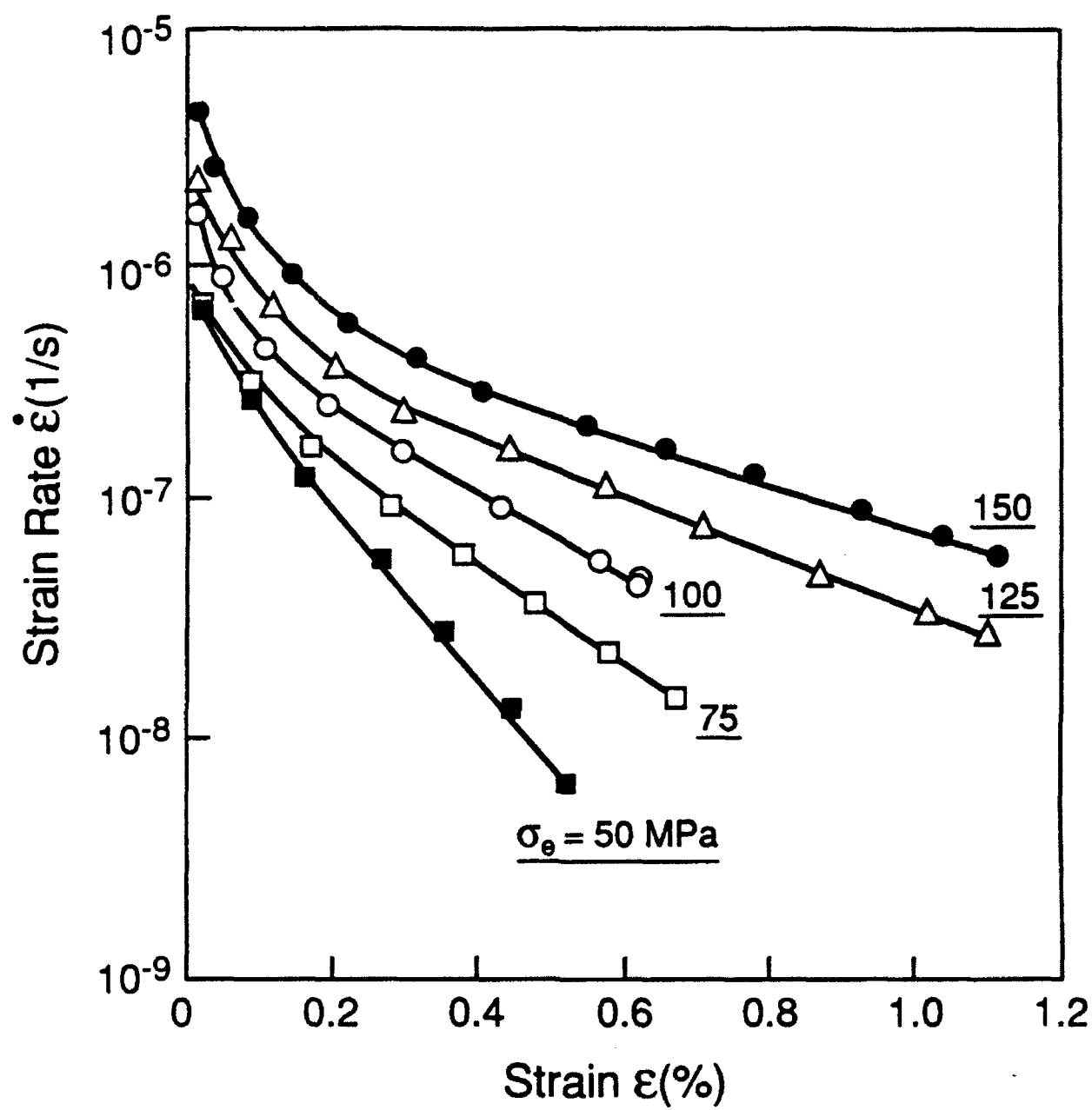
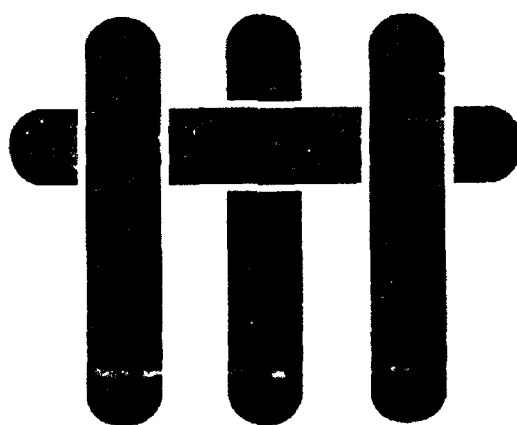


Figure 9.10

M A T E R I A L S



# In-Situ Growth of SiC in MoSi<sub>2</sub> by Melt Processing

D.J. Tilly, J.P.A. Löfvander and C.G. Levi

High Performance Composites Center  
Engineering Materials Department  
University of California  
Santa Barbara, CA

published in

*Intermetallic Matrix Composites II*

MRS Symposium Proceedings Vol. 273  
D.B. Miracle, J. Graves and D.L. Anton, eds.  
Materials Research Society, Pittsburgh, PA, 1992

# IN-SITU GROWTH OF SiC IN MoSi<sub>2</sub> BY MELT PROCESSING

DANIEL J. TILLY, J.P.A. LÖFVANDER and C.G. LEVI  
Engineering Materials Department, University of California,  
Santa Barbara CA 93106

## ABSTRACT

The growth of SiC during solidification of Mo-Si-C melts was investigated to explore the potential for developing *in-situ* refractory reinforcements for MoSi<sub>2</sub> matrices. Volume fractions of up to 20% were readily incorporated by arc melting. Primary  $\beta$ -SiC grows as equiaxed particles, plates and hopper crystals, whereas secondary SiC grows with ribbon, thin flake or whisker morphologies. The dominant facets of both primary and secondary SiC are of the {111} and {002} type, which are also characteristic of the equilibrium crystal shape. There is a clear orientation relationship between the phases wherein the close packed planes and directions of the C11<sub>b</sub> and B3 structures are parallel.

## INTRODUCTION

Molybdenum disilicide (MoSi<sub>2</sub>) is attractive for high temperature structural applications owing to its high melting point ( $T_M = 2300$  K) and good oxidation resistance associated with the formation of a protective silica scale [1,2]. The ordered tetragonal C11<sub>b</sub> structure offers the potential of high strength and stiffness at elevated temperatures, but its intrinsic brittleness hinders the application of monolithic MoSi<sub>2</sub> as a structural material. Compositing schemes based on ceramic fibers or ductile refractory metal reinforcements are under investigation to improve both the toughness and creep strength of MoSi<sub>2</sub> [3-6]. Thermal expansion mismatch between MoSi<sub>2</sub> and the reinforcements may cause matrix cracking during processing or thermal cycling [7]. Introduction of SiC into MoSi<sub>2</sub> has been successfully used to lower the thermal expansion coefficient of the matrix and suppress cracking in Mo-wire reinforced composites [6]. SiC whiskers and particulates have also been shown to improve the creep resistance of MoSi<sub>2</sub> [2,8]. Thus, SiC additions to MoSi<sub>2</sub> are of significant interest, but often lead to less than optimal microstructures if implemented by powder blending approaches. This paper reports on a study aimed at growing SiC-reinforcements *in-situ* by solidification processing of Mo-Si-C melts of suitable compositions.

## EXPERIMENTAL TECHNIQUES

The alloys investigated in this study were produced with high purity elemental components; 99.97% Mo, 99.995% Si and 99.9% C (all in weight percent). Alloys were prepared by arc-melting under an atmosphere of purified argon containing less than 0.1 ppb oxygen. The buttons, weighing approximately 15 g each, were flipped and remelted several times to ensure macroscopic chemical homogeneity. The materials were characterized by optical, scanning (SEM) and transmission (TEM) electron microscopy. Specimens were prepared for optical and SEM microscopy by standard grinding and polishing techniques; a solution consisting of 2 % hydrofluoric acid, 25 % nitric acid (by volume) and lactic acid making up the balance was used for deep-etching to reveal the SiC phase morphologies. SEM

examination was performed in a JEOL SM840A microscope equipped with a Tracor Northern TN5500 Energy Dispersive X-ray Spectroscopy (EDS) system. Samples suitable for TEM were produced by cutting with a low-speed diamond wafering blade, polishing to  $\sim 80\ \mu\text{m}$  and subsequently dimple ground to a final thickness of  $< 10\ \text{nm}$ . The disks were thoroughly washed in acetone and methanol before ion milling. Subsequent TEM analysis was performed in a JEOL 2000FX microscope operated at 200 kV equipped with a Link Analytical eXL EDS system.

## RESULTS AND DISCUSSION

A tentative liquidus projection for the Mo-Si-C system is given in Figure 1. This diagram modifies the original version of Nowotny et al. [9] by incorporating recent revisions of the binary systems and experimental work in the vicinity of the  $\text{MoSi}_2$ -SiC eutectic, as discussed in greater detail elsewhere [10]. This liquidus projection has three main regions representing the solidification of primary graphite, SiC and  $\text{MoSi}_2$ . The graphite and SiC liquidi are separated by the monovariant line  $\text{L}+\text{SiC}+\text{C}$  emerging from the peritectic in the Si-C binary. A two-fold saturation line  $\text{L} \rightarrow \text{MoSi}_2+\text{SiC}$  originates at the quasi-binary eutectic Mo-66Si-2C (in at.%). Thus, SiC is not only thermochemically stable in  $\text{MoSi}_2$  at elevated temperatures, but may also be grown from the melt as a primary and/or secondary phase by suitable control of the alloy chemistry. According to Figure 1, the maximum volume fraction of primary SiC which can be produced through melt processing is  $\sim 35\%$ .

Alloys with the compositions noted in Figure 1 were prepared to explore the microstructural development and morphologies of the SiC phases produced. (Both alloys were slightly richer in Si than the quasi-binary compositions to ensure that their solidification paths were on the same side of the liquidus surface.)

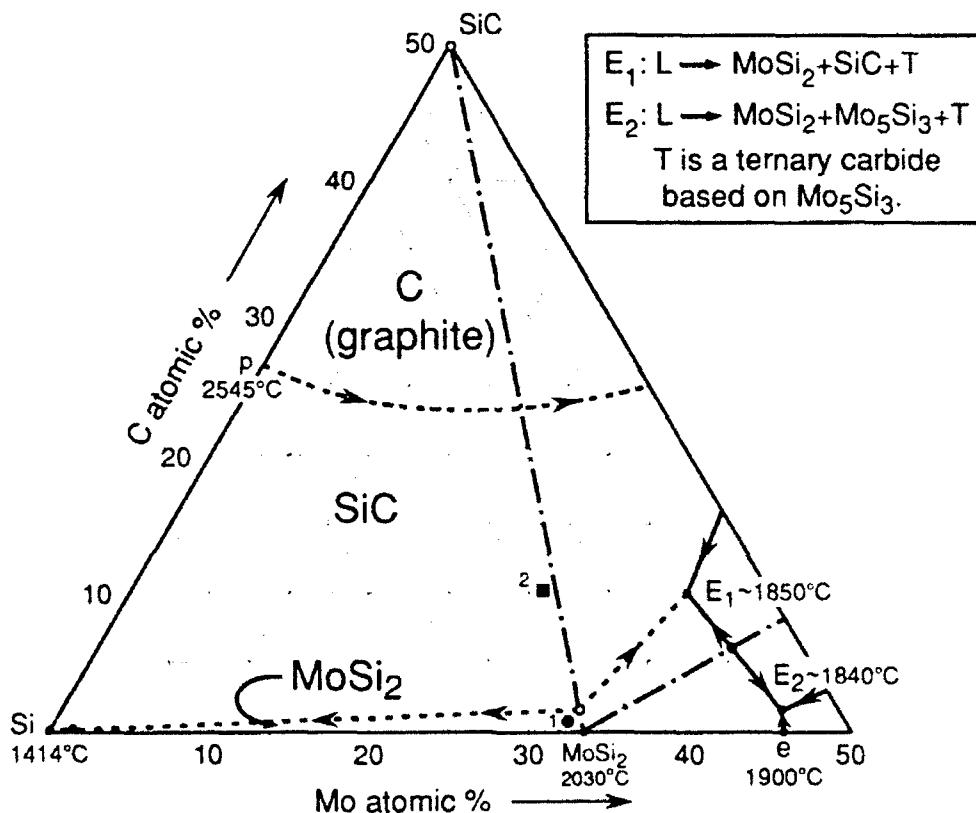


Figure 1. Tentative partial liquidus projection for the Si-rich corner of the Mo-Si-C system, from reference [10].

The hypoeutectic alloy (1) is Mo-67Si-1C and should produce primary MoSi<sub>2</sub>, whereas the hypereutectic alloy (2) is Mo-63.5Si-10C and should form primary SiC. Since both phases are essentially stoichiometric compounds, the liquid composition should trace a straight path on the liquidus surface directly away from the composition of the primary phase as temperature decreases and solidification progresses. Once the liquid composition reaches the line of two-fold saturation, both phases should grow concurrently provided there is no significant kinetic hindrance for nucleation of SiC on MoSi<sub>2</sub> and vice-versa. If neither phase can accommodate the excess Si in solid solution, the liquid composition will become progressively enriched in Si as solidification proceeds along the monovariant line toward the Si-rich corner. Eventually, a small amount of elemental Si should form from the last pockets of liquid.

The hypoeutectic alloy (1) exhibited only secondary SiC phases, mostly in the form of (sub-micron) thin ribbons or flakes with very high aspect ratios, as illustrated in the SEM micrograph of a deep etched specimen in Figure 2(a). (Whiskers were also observed but are not shown in this figure). The array of parallel ribbons suggests that the two MoSi<sub>2</sub> and SiC phases can grow coupled along the line of two-fold saturation; the structure appears as an irregular eutectic in metallographic sections. TEM analysis of secondary phases consistently revealed the sphalerite (B3) structure of  $\beta$ -SiC (cubic, space group F43m). The cross section of the ribbon in Figure 2(b) is oriented along an  $\langle 011 \rangle_{\beta\text{-SiC}}$  zone axis (which is also the axis of the ribbon), whereupon the dominant facets are found to be of the {111} type and the edges of the {002} and {111} type.

An orientation relationship was observed wherein the close packed planes and directions of both phases are parallel, i.e.

$$(11\bar{1})_{\text{SiC}} \parallel (110)_{\text{MoSi}_2} \text{ and } [011]_{\text{SiC}} \parallel [001]_{\text{MoSi}_2}$$

This is consistent with the suggested coupled growth of the eutectic-like structure along the line of two-fold saturation.

The hypereutectic alloy (2) produced a substantial amount (~20%) of primary SiC, growing primarily in equiaxed and platelike morphologies as revealed in the SEM views of deep etched specimens, Figure 3(a). Hopper crystal variations of these morphologies were also observed, as illustrated in Figures 3(b-d).

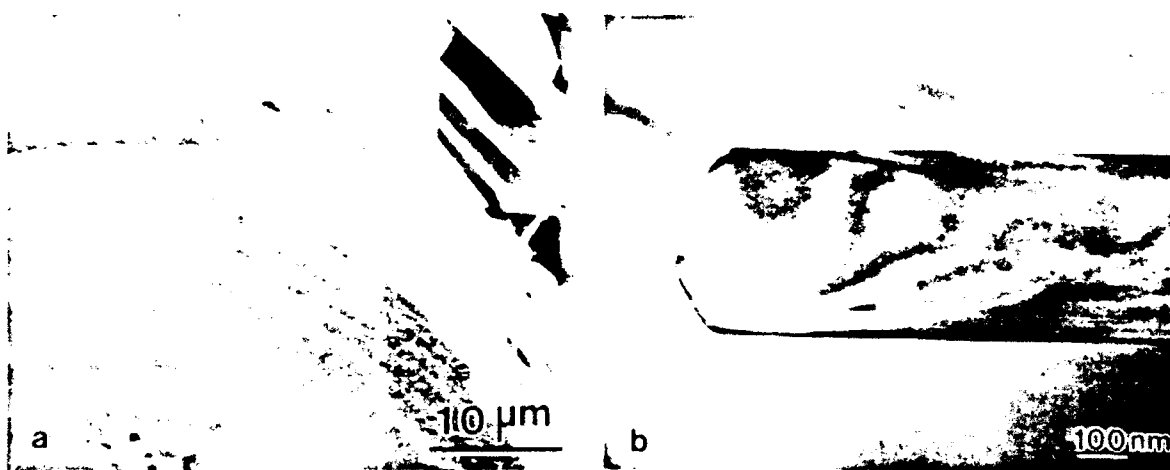


Figure 2. Secondary SiC in hypoeutectic alloy 1: (a) SEM view of secondary SiC ribbons and flakes with MoSi<sub>2</sub> matrix partially etched away. (b) TEM view of SiC ribbon along its axis, corresponding to the  $[011]_{\beta\text{-SiC}}$  zone.

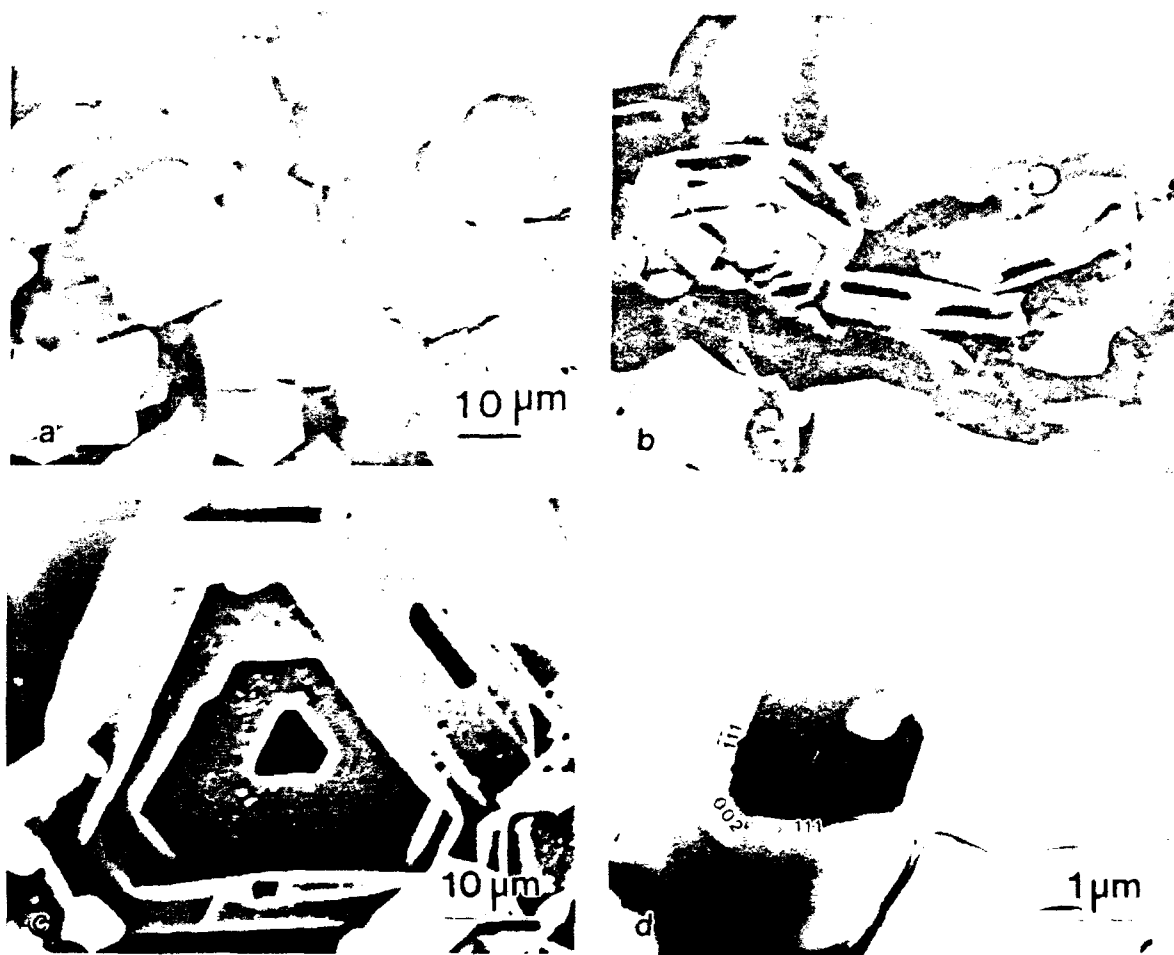


Figure 3. Primary SiC morphologies in hypereutectic alloy 2: (a) Equiaxed particles and platelets revealed by deep etching MoSi<sub>2</sub> matrix, (b) cluster of hopper crystals in the same specimen, and (c) closer view of a hopper crystal showing preferential growth at the edges of a {111} facet. (d) TEM micrograph of a hopper crystal normal to a [110] zone showing MoSi<sub>2</sub> matrix solidified within a triangular cavity similar to that in (c). Note the shrinkage porosity and the bounding {111} and {002} facets.

Hopper crystals are believed to evolve from edge instabilities during growth owing to the evolution of different supersaturations between the center and the edges of a crystal facet [11]. In the present case, these variations arise from the local buildup of Mo and concomitant depletion of Si and C in front of the SiC/melt interface. The SEM micrograph in Figure 3(c) clearly shows the preferential nucleation and growth of ledges in the periphery of a {111} crystal facet, consistent with the classical hopper growth mechanism. Note the progressive expansion of the triangular cavity in the primary SiC as growth evolves out of the plane of the micrograph. The cavity is later filled with solid MoSi<sub>2</sub> when the solidification path reaches the two-fold saturation line in Figure 1. The TEM micrograph in Figure 3(d) reveals MoSi<sub>2</sub> present in the center of a large SiC hopper crystal in a separate specimen.

TEM analysis of the primary particles confirm that they also have the  $\beta$ -SiC structure. Figure 4(a) shows a primary SiC platelet along a  $\langle 011 \rangle$  zone axis, similar to that in Figure 2(b). The corresponding projection in Figure 4(b) shows the facets to be of the  $\{11\bar{1}\}$  and  $\{002\}$  type, which are thus inferred to be the planes of slowest growth. (Note the same facets on the ledges of the hopper crystal, Figure 3d.) In contrast, growth along the  $[011]$  axis seems to be relatively easy, as suggested by the

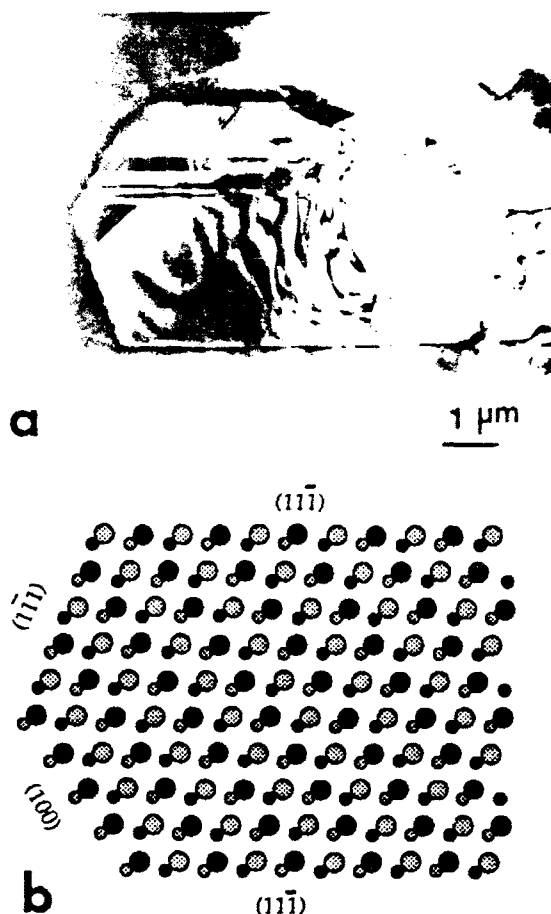


Figure 4. TEM of primary  $\beta$ -SiC platelet (a) showing  $\langle 011 \rangle_{\beta\text{-SiC}}$  zone axis with  $\{111\}$  and  $\{002\}$  facets and twins parallel to the  $\{111\}$  planes. (b) Structure projection corresponding to the zone axis in (a); the larger circles are Si atoms and the smaller C atoms; the two shades represent the  $1/2$  and  $1/4$  levels along  $[011]$ .



Figure 5. SEM view of deep-etched sample showing possible re-entrant twins at the edge of a primary SiC plate.

evolution of long ribbons in this direction. Analysis of Figure 4(b) reveals that growth along the slower  $\langle 11\bar{1} \rangle$  and  $\langle 002 \rangle$  directions involves the stacking of alternating layers consisting of all C or all Si atoms, whereas growth along the faster  $\langle 011 \rangle$  direction involves layers containing C and Si in the proper stoichiometry. Similar relationships between stacking pattern and ease of propagation have been observed in the growth of TiB and TiB<sub>2</sub> from Ti alloy melts [12-14]. While these observations provide some insight on the role of crystallography on the growth behavior, the understanding of the relevant mechanisms is far from complete.

The dominant facets observed in these SiC crystals are consistent with their equilibrium shape predicted from interfacial energy considerations [15]. It is not clear, however, why plate crystals also evolve in addition to the equiaxed particles expected for the cubic  $\beta$ -SiC phase [15]. One possible explanation is suggested by Figure 5, which shows features reminiscent of re-entrant twins with the relevant twin planes parallel to the long  $\{111\}$  facets of the plate. Re-entrant twins are known to enable the platelike growth of Si [16] and could play a similar role in  $\beta$ -SiC. Twins are indeed present in many particles, as confirmed by high resolution TEM of the striations in Figure 4(a) reported elsewhere [10]. Understanding the evolution of these twins and their role in the growth process may open an avenue for morphological control in MoSi<sub>2</sub>/SiC microstructures.

The orientation relationship noted between the MoSi<sub>2</sub> matrix and the secondary SiC is also consistently observed with the primary SiC phases. This suggests that MoSi<sub>2</sub> can readily nucleate and grow epitaxially on the primary SiC. The implications of the orientation relationship and the details of the interfacial structure have been elaborated in a separate publication [10].



## CONCLUDING REMARKS

It has been shown that SiC additions can be developed *in-situ* during solidification processing of Mo-Si-C melts with appropriate chemistries.  $\beta$ -SiC can grow as primary or secondary phases and evolves in a variety of morphologies including equiaxed particles, plates, ribbons, flakes and whiskers. Hopper crystal forms of the plates and equiaxed particles were also observed, presumably arising from instabilities associated with the segregation of Mo during growth. Both primary and secondary particles show dominant facets of the  $\{111\}_{\beta\text{-SiC}}$  and  $\{002\}_{\beta\text{-SiC}}$  type, and exhibit a clear and consistent orientation relationship with the matrix. Preliminary evidence suggests that a re-entrant twin growth mechanism may be responsible for the development of platelike shapes in primary SiC.

## ACKNOWLEDGMENTS

This work was sponsored by DARPA under a University Research Initiative grant N00014-86-K-0753 supervised by Dr. W. Coblenz and monitored by Dr. S.G. Fishman of the Office of Naval Research.

## REFERENCES

- [1] P.J. Meschter and D.S. Schwartz: *Journal of Metals*, **41**(11), pp. 11, (1989).
- [2] F.D. Gac and J.J. Petrovic: *Journal of the American Ceramic Society*, **68**, pp. 200, (1985).
- [3] J.P.A. Löfvander, J.Y. Yang, C.G. Levi and R. Mehrabian: *Advanced Metal Matrix Composites for Elevated Temperatures*, eds. M.N. Gungor, E.J. Lavernia and S.G. Fishman, ASM International, Materials Park, OH, pp. 1-10, (1991).
- [4] T.C. Lu, A.G. Evans, R.J. Hecht and R. Mehrabian: *Acta Metall. & Mater.*, **39**(8) pp. 1853-1862, (1991).
- [5] J. Besson, M. De Graef, J.P.A. Löfvander and S.M. Spearing: accepted for publication in *Journal of Materials Science*, (1992).
- [6] M. Maloney and R.J. Hecht: to be published in the *Proceedings of the First High Temperature Structural Silicides Workshop*, eds. A.K. Vasudevan and J.J. Petrovic, (1992).
- [7] T.C. Lu, J. Yang, Z. Suo, A.G. Evans, R. Hecht and R. Mehrabian: *Acta Metall. & Mater.* **39**(8), pp. 1883-1890, (1991).
- [8] R.M. Aikin, Jr. and L. Christodoulou: to be published in the *Proceedings of the First High Temperature Structural Silicides Workshop*, eds. A.K. Vasudevan and J.J. Petrovic, (1992).
- [9] H. Nowotny, E. Parthé, R. Kieffer and F. Benesousky: *Monatsh. Chem.*, **85**, pp. 255-272, (1954).
- [10] D.J. Tilly, J.P.A. Löfvander and C.G. Levi: submitted to *Materials Science and Engineering*.
- [11] I. Minkoff and B. Lux: *J. Crystal Growth*, **22**, pp. 163, (1974).
- [12] M.E. Hyman, C. McCullough, J.J. Valencia, C.G. Levi and R. Mehrabian: *Metallurgical Transactions A*, **20A**, pp. 1847-1859, (1989).
- [13] M.E. Hyman, C. McCullough, C.G. Levi, R. Mehrabian: *Metallurgical Transactions A*, **22A**(7), pp. 1647-1662, (1991).
- [14] M. De Graef, J.P.A. Löfvander and C.G. Levi: *Acta Metall. & Mater.*, **39**(10), pp. 2381-2391, (1991).
- [15] G. A. Wolff: *Intermetallic Compounds*, ed. J. H. Westbrook, John Wiley & Sons New York, NY, pp. 91-92, (1967).
- [16] G.F. Bolling and W.A. Tiller: *Metallurgy of Elemental and Compound Semiconductors*, Interscience, NY, (1961).